To the Graduate Council:

I am submitting herewith a thesis written by Young Dae Lee entitled "Characteristics and Annealing Behavior of Polyethylenes Designed for Use as Underground Cable Insulation". I have examined the final copy for form and content and recommend that it be accepted in partial fulfillment of the requirements for the degree of Doctor of Philosophy, with a major in Polymer Engineering.

Paul J. Phillips, Major Professor

We have read this thesis
and recommend its acceptance:

Accepted for the Council:

Vice Provost
and Dean of The Graduate School

# CHARACTERISTICS AND ANNEALING BEHAVIOR OF POLYETHYLENE DESIGNED FOR USE AS UNDERGROUND CABLE INSULATION

A Dissertation

Presented for the

Doctor of Philosophy

Degree

The University of Tennessee, Knoxville

Young Dae Lee

August 1989

Copyright © Young Dae Lee, 1989
All rights reserved

# ACKNOWLEDGEMENTS

The author would like to express his sincere appreciation to Professor Paul J. Phillips, his advisor, for his contributions, guidance, suggestions and constructive criticism throughout this research and for his help. The author wishes to thank his former advisor, Professor J. E. Spruiell for his guidance at the beginning of this work.

The author thanks Department of Energy, Oak Ridge National Laboratory, The Electric Power Research Institute and The Center of Material Processing at the University of Tennessee, Knoxville for the financial support.

The author would like to express his appreciation to Dr. J. S. Lin at Oak Ridge National Laboratories for his help and useful discussions for small angle x-ray scattering work.

The author is indebted to Mr. Russell P. Wong for his assistance in the preparation of Fourier Transform Infrared spectra and Mr. Larry Effler for his help in the preparation of small angle light scattering patterns.

The author appreciates the discussions with current and former fellow graduate students, Dr. Ali Vatansever, Dr. Deepak R. Parikh, Mr. William Scott Lambert, Ms. Trishna Ray-Chaudhuri, Mr. Rajen M. Patel and Mr. Scott Dibrell of Department of Materials Science and Engineering and Dr. Paul A. Flowers in the Department of Chemistry.

The technical help provided by the departmental electronic and machine shops is appreciated.

The author wishes to thank his committee members, Professors, P. J. Phillips, J. E. Spruiell, E. S. Clark, R. Benson, and M. O. Pace.

The author expresses his sincere appreciation to his wife Young-Oak Lee for her encouragement and endurance throughout this work.

# ABSTRACT

A series of polyethylenes developed for use as high voltage electric cable insulation have been characterized. All crosslinked polyethylene materials show similar melting behavior, whereas linear-low-density polyethylene shows complicated melting behavior due to the variation of copolymer content. The IR investigation shows that tree retardant polyethylenes contain additional chemical additives. The basic functions of the additives are thought to be antioxidation and voltage stabilization, on the basis of higher oxidative induction time (OIT) and higher breakdown strength. The density, heat of fusion and crystallinity of TR-XLPE was found to be higher than the other crosslinked polyethylenes, presumably due to the presence of the additive.

SAXS results of various polyethylenes were interpreted based on model simulations. Among the various models, the variable stack model was found to fit marginally better than others for XLPE, LDPE and LLDPE. The absence of a definite Bragg peak in the SAXS pattern of LLDPE was considered to be due to the wide distribution of local crystallinity, resulting from fractionation during crystallization according to branch levels.

DSC experiments showed that isothermal annealing of polyethylene results in the generation of a new peak or a shoulder next to the annealing temperature. The origin of the double melting peak in XLPE annealed at 107$^{o}$C was investigated using in-situ

methods. The crystallinity determined from DSC, WAXD and density measurement was found to increase with annealing time. Morphological changes with annealing time based on the SAXS studies indicated a large increase of crystallinity distribution among the stacks, a small decrease of thickness distribution within each stack and an increase of mean long periodicity.

In the DSC study, clear evidence of room temperature annealing was found for all XLPEs and LLDPE. It was found that room temperature annealing causes a shoulder around 45$^{o}$C as well as a shift of melting peak, resulting in an increase of crystallinity.

Large spherulites clustered in dense patterns were observed in the electrically ruptured regions of all polyethylenes. IR spectra of the ruptured region shows clear evidence of severe oxidation and chain scission during breakdown. Molecular chain scission appears to occur at the crosslink and branch points within the amorphous region, due to oxidation and temperature rise. The resulting short chain sections are believed to have crystallized to form large spherulites.

# TABLE OF CONTENTS

SECTION PAGE

1. INTRODUCTION....1

2. LITERATURE REVIEW....5

2.1. Electrical Properties of Polymeric Insulation....5
2.1.1. Introduction....5
2.1.2. Dielectric Breakdown....6
2.1.3. Electrical Breakdown Mechanisms in Solids....8
2.1.3.1. Electronic Breakdown....10
2.1.3.2. Thermal Breakdown....13
2.1.3.3. Electro-mechanical Breakdown....15
2.1.4. Electrical Breakdown of Polymers....17
2.1.4.1. Environmental Factors....18
2.1.4.1.1. Specimen Geometry....18
2.1.4.1.2. Temperature....19
2.1.4.1.3. Time....19
2.1.4.1.4. Electrode, Voltage Application, And Other Effects....20
2.1.4.2. Material Factors....21
2.1.4.2.1. Chemical Structure....22
2.1.4.2.2. Solid Structure....23
2.1.5. Electrical Treeing....30
2.1.5.1. Experimental Observations of Electrical Trees....32
2.1.5.2. Mechanisms of Electrical Treeing....35
2.1.5.3. Inhibition of Electrical Treeing....39
2.1.6. Water Treeing....42
2.1.6.1. Experimental Observations of Water Trees....43
2.1.6.2. Factors Affecting Water Treeing....46
2.1.6.3. Mechanisms of Water Treeing....56
2.1.6.4. Inhibition of Water Treeing....60
2.2. Small Angle X-ray Scattering....61
2.2.1. Introduction....61
2.2.2. Basic Scattering Theory....63
2.2.3. Diffuse Scattering....65
2.2.3.1. Guinier Theory....67
2.2.3.2. Porod Data Treatment....68
2.2.3.3. Distance Distribution Function....72
2.2.4. SAXS by Solid Semicrystalline Polymers....75
2.2.5. General Interpretation of SAXS from Polyethylenes....82

2.2.5.1. Near Zero Angle Intensity of SAXS of Solid Polymers....87
2.2.5.2. The Integrated Intensity, Q....90
2.3. Polyethylenes Used in Cable Insulation....94
2.3.1. Introduction....94
2.3.2. Low-Density Polyethylene....94
2.3.3. Crosslinked Polyethylene....96
2.3.3.1. Crosslinking....96
2.3.3.2. Effects of Crosslinking....99
2.3.3.3. Morphology of XLPE....102
2.3.3.4. Degradation of XLPE....104
2.3.4. Linear Low Density Polyethylene....109

3. EXPERIMENTAL....111

3.1. Materials....111
3.2. Sample Preparation....113
3.2.1. Molding....113
3.2.2. Annealing Procedures....114
3.3. Characterization....115
3.3.1. Infrared Spectroscopy....115
3.3.2. Thermal Analysis....118
3.3.3. Oxidative Induction Time....122
3.3.4. Small Angle X-ray Scattering....124
3.3.5. In-situ SAXS....129
3.3.6. Electrical Breakdown Studies....131

4. EXPERIMENTAL RESULTS....132

4.1. Characterization....132
4.1.1. Crosslinking of XLPE....132
4.1.2. Infrared Analysis....133
4.1.3. DSC Study....142
4.1.4. Density Measurement....153
4.1.5. Wide Angle X-ray Study....155
4.1.6. Oxidative Induction Time Measurement....157
4.2. Annealing and Thermal Effects....160
4.2.1. DSC Study....161
4.2.2. Density Measurement....179
4.2.3. Wide Angle X-ray Diffraction....182
4.3. Experimental Results of SAXS....184
4.3.1. General Observations....184
4.3.2. Unaged Polyethylenes....185
4.3.3. Annealed Polyethylenes....197
4.3.4. SAXS Data at High Temperature....223
4.4. Theoretical Study of SAXS....252
4.4.1. Introduction....252
4.4.2. Simple Lamellar Stack Model....254
4.4.3. Variable Stack Model....264
4.5. Electric Breakdown....272

4.5.1. Electrical Breakdown Strength .....272
4.5.2. Morphology of The Breakdown Area .....278
4.5.3. Infrared Spectroscopy .....287

5. DISCUSSIONS.....293

5.1. Interpretation of SAXS data.....294
5.1.1. SAXS Model Study.....294
5.1.2. Physical Meanings of Models.....306
5.1.3. Interpretation of Experimental SAXS Data.....315
5.2. Characterization of Various Polyethylenes.....318
5.2.1. IR Study.....318
5.2.2. DSC Study.....322
5.2.3. Density Measurement.....337
5.2.4. Wide Angle X-ray Study.....338
5.2.5. Small Angle X-ray Study.....339
5.2.6. Dielectric Property and OIT Measurements.....345
5.2.7. Effect of Crosslinking.....350
5.3. Annealing of Polyethylene.....357
5.3.1. DSC Study.....357
5.3.2. Density measurement and Wide Angle X-ray Study.....359
5.3.3. Small Angle X-ray Study.....361
5.3.4. Morphological Influence.....371
5.3.5. Effects of Annealing Environment.....376
5.4. Phase Separation of XLPE.....391
5.4.1. Physical Evidence of Phase Separation.....391
5.4.2. In-situ SAXS Analysis.....395
5.4.3. Distance Distribution Curves.....398
5.4.4. Proposed Mechanisms of Melt Separation and Annealing.....415
5.5. Electrical Breakdown.....418
5.5.1. IR Analysis.....418
5.5.2. Morphological Effects.....420
5.5.3. Breakdown Mechanisms.....422

6. CONCLUSIONS.....425

6.1. SAXS Model Study .....425
6.2. Characterization of Various Polyethylenes.....426
6.3. Annealing of Polyethylene.....427
6.4. Phase Separation of XLPE.....428
6.5. Electrical Breakdown.....429

7. SUGGESTIONS FOR FURTHER WORK.....431

7.1. SAXS Model.....431
7.2. Direct Observation.....431
7.3. The Effects of Annealing Time and Temperature .....432
7.4. The Room Temperature Annealing Effect.....432

7.5. Visco-Elasticity of XLPE Melt.....432
7.6. Thermo-Oxidative Degradation.....433
7.7. Mechanisms for Water treeing .....433

REFERENCES.....435

APPENDICES.....448

I. LISTING OF FORTRAN PROGRAM FOR SIMPLE SAXS MODEL WITH GAUSSIAN THICKNESS DISTRIBUTION.....449
II. LISTING OF FORTRAN PROGRAM FOR SIMPLE SAXS MODEL WITH ASYMMETRIC THICKNESS DISTRIBUTION.....457
III. LISTING OF FORTRAN PROGRAM FOR VARIABLE SAXS MODEL WITH GAUSSIAN THICKNESS DISTRIBUTION AND GAUSSIAN CRYSTALLINITY DISTRIBUTION.....466
IV. LISTING OF FORTRAN PROGRAM FOR VARIABLE SAXS MODEL WITH ASYMMETRIC THICKNESS DISTRIBUTION AND GAUSSIAN CRYSTALLINITY DISTRIBUTION.....475
V. LISTING OF PASCAL PROGRAM FOR IN-SITU SAXS DATA TREATMENT.....485

VITA.....507

# LIST OF TABLES


| TABLE | | PAGE |
|---|---|---|
| 3.1.1 | Comparison of polyethylene used in this work | 112 |
| 5.1.1. | Results from variable stack model simulations | 300 |
| 5.3.1 | Variation of crystalline and amorphous thickness of TR-XLPE, EC-XLPE, PL-XLPE and TR-LLDPE annealed at 107°C in air | 372 |
| 5.3.2 | Variation of crystalline and amorphous thickness of TR-XLPE, EC-XLPE, PL-XLPE and TR-LLDPE annealed at 107°C in silicone oil | 379 |
| 5.4.1 | Variation of material parameters of TR-XLPE at various in-situ temperatures | 394 |
| 5.4.2 | Dimensions of major entities of TR-XLPE for various in-situ conditions | 416 |

# LIST OF FIGURES


| FIGURE | | PAGE |
|---|---|---|
| 2.1.1 | Schematic of dielectrical strength test | 9 |
| 2.1.2 | Effect of crystallinity on the electrical strength of HDPE. (Ref. Miyauchi and Wayagi, 1972) | 24 |
| 2.1.3 | Influence of electrical stress on bow tie tree formation. (Ref. Mizukami, 1978) | 49 |
| 2.2.1 | One-dimensional correlation function of an ideal lamellar structure: (a) crystallinity 0.2, (b) 0.4. (Ref. Vonk, 1985b) | 85 |
| 3.3.1 | Schematic representation of a typical DSC system | 119 |
| 3.3.2 | Typical DSC melting curve of XLPE | 121 |
| 3.3.3 | Typical oxidative exotherm of XLPE | 125 |
| 3.3.4 | Schematics of the ORNL ten meter SAXS spectrometer | 126 |
| 3.3.5 | Schematic of in-situ SAXS experiment | 130 |
| 4.1.1 | IR spectra of TR-XLPE, EC-XLPE, PL-XLPE and TR-LLDPE | 135 |
| 4.1.2 | FTIR spectra of TR-XLPE, EC-XLPE, PL-XLPE and TR-LLDPE | 136 |
| 4.1.3 | Difference IR spectra of TR-XLPE (EC-XLPE or PL-XLPE subtracted) | 138 |
| 4.1.4 | FTIR spectra of TR-XLPE, TR-LDPE, sol and gel fractions of TR-XLPE | 140 |
| 4.1.5 | FTIR spectra of TR-XLPE, EC-XLPE, PL-XLPE and TR-LLDPE in the region of 1050 - 800 $cm^{-1}$ | 141 |
| 4.1.6 | FTIR spectra of TR-XLPE, TR-LDPE, sol and gel fractions of TR-XLPE in the region of 1050 - 800 $cm^{-1}$ | 143 |
| 4.1.7 | DSC thermograms of TR-XLPE, EC-XLPE, PL-XLPE and TR-LLDPE | 144 |

4.1.8 DSC thermograms of TR-XLPE held at room temperature and quenched in the DSC.....145

4.1.9 Difference DSC curve of TR-XLPE held at room temperature having subtracted from it the curve of TR-XLPE quenched in the DSC.....146

4.1.10 DSC curves of TR-LLDPE solidified under different conditions.....148

4.1.11 DSC curves of gel, extractables, cured and uncured TR-XLPE.....150

4.1.12 Variation of melting points with curing for TR-XLPE, EC-XLPE and PL-XLPE.....151

4.1.13 Variation of heat of fusion with curing for TR-XLPE, EC-XLPE and PL-XLPE.....152

4.1.14 Densities of uncured, cured and gel fraction of EC-XLPE, TR-XLPE and PL-XLPE.....154

4.1.15 Wide angle x-ray diffraction curve of TR-XLPE.....156

4.1.16 WAXD crystallinities of uncured, cured and gel fraction of TR-XLPE and PL-XLPE.....158

4.1.17 Oxidative exotherms of TR-XLPE, EC-XLPE, PL-XLPE and TR-LLDPE.....159

4.2.1 Variation of DSC curves of TR-XLPE annealed at different temperatures for 3 hours.....162

4.2.2 Variation of DSC curves of TR-LLDPE annealed at different temperatures for 3 hours.....163

4.2.3 DSC curves of TR-XLPE annealed at 107$^{o}$C for various periods of time.....165

4.2.4 DSC curves of TR-LLDPE annealed at 117$^{o}$C for various periods of time.....166

4.2.5 Plots of second melting peak temperatures of TR-XLPE, EC-XLPE, PL-XLPE and TR-LLDPE as a function of annealing time at 107$^{o}$C.....167

4.2.6 Plots of second melting peak temperatures of TR-XLPE, EC-XLPE, PL-XLPE and TR-LLDPE as a function of annealing time at 100$^{o}$C.....169

4.2.7 Variation of heat of fusion of TR-XLPE, EC-XLPE, PL-XLPE and TR-LLDPE with annealing time.....170

4.2.8 Variation of heat of fusion of first melting peaks of TR-XLPE, EC-XLPE, PL-XLPE and TR-LLDPE with annealing time.....171

4.2.9 Variation of heat of fusion of second melting peaks of TR-XLPE, EC-XLPE, PL-XLPE and TR-LLDPE with annealing time.....173

4.2.10 Variation of second melting peak temperatures of TR-XLPE, EC-XLPE, PL-XLPE and TR-LLDPE as a function of annealing time at 107°C in silicone oil.....175

4.2.11 Variation of heat of fusion of TR-XLPE, EC-XLPE, PL-XLPE and TR-LLDPE with annealing time at 107°C in silicone oil.....176

4.2.12 DSC curves of PL-XLPE and EC-XLPE annealed at 107°C in transformer oil for 8 hours.....177

4.2.13 DSC curves of TR-XLPE and TR-LLDPE annealed at 107°C in transformer oil for 8 hours.....178

4.2.14 DSC curves of PL-XLPE and EC-XLPE annealed at 78°C in transformer oil for 8 hours.....180

4.2.15 Variation of densities of TR-XLPE, EC-XLPE and PL-XLPE with annealing time at 107°C.....181

4.2.16 Variation of WAXD crystallinities of TR-XLPE, EC-XLPE and PL-XLPE with annealing time at 107°C.....183

4.3.1 SAXS contour plot of unannealed TR-XLPE.....186

4.3.2 SAXS intensity curves of HDPE, TR-XLPE, TR-LDPE and TR-LLDPE.....187

4.3.3 Lorentz-corrected SAXS intensity curves of HDPE, TR-XLPE, TR-LDPE and TR-LLDPE.....188

4.3.4 SAXS intensity curves of TR-XLPE, TR-LDPE and gel fraction of TR-XLPE.....190

4.3.5 Lorentz-corrected SAXS intensity curves of TR-XLPE, TR-LDPE and gel fraction of TR-XLPE.....191

4.3.6 SAXS intensity curves of EC-XLPE and EC-LDPE.....192

4.3.7 Lorentz-corrected SAXS intensity curves of EC-XLPE and EC-LDPE.....193

4.3.8 SAXS intensity curves of TR-XLPE, EC-XLPE and PL-XLPE.....194

4.3.9 Lorentz-corrected SAXS intensity curves of TR-XLPE, EC-XLPE and PL-XLPE.....195

4.3.10 SAXS intensity curves of TR-LDPE and EC-LDPE.....196

4.3.11 Variation of SAXS intensity curves of TR-XLPE annealed at 107°C in air with annealing time.....198

4.3.12 Variation of SAXS intensity curves of EC-XLPE annealed at 107°C in air with annealing time.....199

4.3.13 Variation of SAXS intensity curves of PL-XLPE annealed at 107°C in air with annealing time.....200

4.3.14 Variation of SAXS intensity curves of TR-LLDPE annealed at 107°C in air with annealing time.....201

4.3.15 Variation of Lorentz-corrected SAXS intensity curves of TR-XLPE annealed at 107°C in air with annealing time.....202

4.3.16 Variation of Lorentz-corrected SAXS intensity curves of EC-XLPE annealed at 107°C in air with annealing time.....203

4.3.17 Variation of Lorentz-corrected SAXS intensity curves of PL-XLPE annealed at 107°C in air with annealing time.....204

4.3.18 Variation of Lorentz-corrected SAXS intensity curves of TR-LLDPE annealed at 107°C in air with annealing time.....205

4.3.19 Variation of SAXS intensity curves of TR-LDPE annealed at 107°C in air with annealing time.....206

4.3.20 Variation of SAXS intensity curves of EC-LDPE annealed at 107°C in air with annealing time.....207

4.3.21 Variation of SAXS intensity curves of PL-LDPE annealed at 107°C in air with annealing time.....208

4.3.22 Variation of SAXS intensity curves of HDPE annealed at 107°C in air with annealing time.....209

4.3.23 Variation of Lorentz-corrected SAXS intensity curves of TR-LDPE annealed at 107°C in air with annealing time.....210

4.3.24 Variation of Lorentz-corrected SAXS intensity curves of EC-LDPE annealed at 107°C in air with annealing time.....211

4.3.25 Variation of Lorentz-corrected SAXS intensity curves of PL-LDPE annealed at 107°C in air with annealing time.....212

4.3.26 Variation of Lorentz-corrected SAXS intensity curves of HDPE annealed at 107°C in air with annealing time.....213

4.3.27 Variation of SAXS intensity curves of TR-XLPE annealed at 107°C in silicone oil with annealing time.....215

4.3.28 Variation of SAXS intensity curves of EC-XLPE annealed at 107°C in silicone oil with annealing time.....216

4.3.29 Variation of SAXS intensity curves of PL-XLPE annealed at 107°C in silicone oil with annealing time.....217

4.3.30 Variation of SAXS intensity curves of TR-LLDPE annealed at 107°C in silicone oil with annealing time.....218

4.3.31 Variation of Lorentz-corrected SAXS intensity curves of TR-XLPE annealed at 107°C in silicone oil with annealing time.....219

4.3.32 Variation of Lorentz-corrected SAXS intensity curves of EC-XLPE annealed at 107°C in silicone oil with annealing time.....220

4.3.33 Variation of Lorentz-corrected SAXS intensity curves of PL-XLPE annealed at 107°C in silicone oil with annealing time.....221

4.3.34 Variation of Lorentz-corrected SAXS intensity curves of TR-LLDPE annealed at 107°C in silicone oil with annealing time.....222

4.3.35 Variation of SAXS intensity curves of TR-XLPE annealed at 107°C in air with annealing time. (immersed in transformer oil after annealing).....224

4.3.36 Variation of SAXS intensity curves of EC-XLPE annealed at 107°C in air with annealing time. (immersed in transformer oil after annealing).....225

4.3.37 Variation of SAXS intensity curves of PL-XLPE annealed at 107°C in air with annealing time. (immersed in transformer oil after annealing).....226

4.3.38 Variation of SAXS intensity curves of TR-LLDPE annealed at 107°C in air with annealing time. (immersed in transformer oil after annealing).....227

4.3.39 Variation of SAXS intensity curves of TR-XLPE held at various in-situ temperatures.....229

4.3.40 SAXS intensity curves of various XLPE held at various in-situ temperatures.....230

4.3.41 Lorentz-corrected SAXS intensity curves of various XLPE held at various in-situ temperatures.....232

4.3.42 SAXS intensity curves of TR-XLPE held at in-situ temperature of 107.5°C for various periods of time....233

4.3.43 Lorentz-corrected SAXS intensity curves of TR-XLPE held at in-situ temperature of 107.5°C for various periods of time.....234

4.3.44 SAXS intensity curves of EC-XLPE held at in-situ temperature of 107°C for various periods of time.....236

4.3.45 Lorentz-corrected SAXS intensity curves of EC-XLPE held at in-situ temperature of 107°C for various periods of time.....237

4.3.46 SAXS intensity curves of PL-XLPE held at in-situ temperature of 106°C for various periods of time.....238

4.3.47 Lorentz-corrected SAXS intensity curves of PL-XLPE held at in-situ temperature of 106°C for various periods of time.....239

4.3.48 SAXS intensity curves of PL-XLPE held at in-situ temperature of 25°C, 90°C and 106°C for about 30 minutes.....240

4.3.49 Lorentz-corrected SAXS intensity curves of PL-XLPE held at in-situ temperature of 25°C, 90°C and 106°C for about 30 minutes.....241

4.3.50 In-situ SAXS intensity curves of pre-annealed TR-XLPE measured at room temperature and 108°C. (annealed at 106°C prior to the experiment).....243

4.3.51 In-situ SAXS intensity curves of pre-annealed EC-XLPE measured at room temperature and 108°C. (annealed at 106°C prior to the experiment).....244

4.3.52 In-situ SAXS intensity curves of pre-annealed PL-XLPE measured at room temperature and 108°C. (annealed at 106°C prior to the experiment).....245

4.3.53 Lorentz-corrected SAXS intensity curves of pre-annealed TR-XLPE measured at room temperature and 108°C. (annealed at 106°C prior to the experiment).....246

4.3.54 Lorentz-corrected SAXS intensity curves of pre-annealed EC-XLPE measured at room temperature and 108°C. (annealed at 106°C prior to the experiment).....247

4.3.55 Lorentz-corrected SAXS intensity curves of pre-annealed PL-XLPE measured at room temperature and 108°C. (annealed at 106°C prior to the experiment).....248

4.3.56 In-situ SAXS intensity curves of pre-annealed TR-LLDPE measured at room temperature and 108°C. (annealed at 106°C prior to the experiment).....249

4.3.57 In-situ SAXS intensities of TR-XLPE for various conditions on a log-log scale.....250

4.3.58 In-situ SAXS intensities of PL-XLPE for various conditions on a log-log scale.....251

4.4.1 Gaussian distribution functions with the average of 0.5 and various standard deviations.....256

4.4.2 Calculated SAXS intensity curves based on the simple stack model with Gaussian thickness distributions.....258

4.4.3 Calculated one-dimensional SAXS intensity curves based on the simple stack model with Gaussian thickness distributions.....259

4.4.4 Modified Exponential distribution functions with the average of 0.5 and various standard deviations.....260

4.4.5 Calculated SAXS intensity curves based on the simple stack model with modified exponential thickness distributions.....262

4.4.6 Calculated one-dimensional SAXS intensity curves based on the simple stack model with modified exponential thickness distributions.....263

4.4.7 Calculated SAXS intensity curves based on the variable stack model with Gaussian thickness distributions and Gaussian crystallinity distributions among stacks. ($\sigma_x$ = 0.05) .....266

4.4.8 Calculated SAXS intensity curves based on the variable stack model with Gaussian thickness distributions and Gaussian crystallinity distributions among stacks. ($\sigma_x$ = 0.1) .....267

4.4.9 Calculated SAXS intensity curves based on the variable stack model with Gaussian thickness distributions and Gaussian crystallinity distributions among stacks. ($\sigma_x$ = 0.125) .....268

4.4.10 Calculated SAXS intensity curves based on the variable stack model with Gaussian thickness distributions and Gaussian crystallinity distributions among stacks. ($\sigma_x$ = 0.15) .....269

4.4.11 Calculated SAXS intensity curves based on the variable stack model with Gaussian thickness distributions and Gaussian crystallinity distributions among stacks. ($\sigma_x$ = 0.175) .....270

4.4.12 Calculated SAXS intensity curves based on the variable stack model with Gaussian thickness distributions and Gaussian crystallinity distributions among stacks. ($\sigma_x$ = 0.2) .....271

4.4.13 Calculated one-dimensional SAXS intensity curves based on the variable stack model with Gaussian thickness distributions and Gaussian crystallinity distributions among stacks. ($\sigma_x$ = 0.1) .....273

4.4.14 Calculated one-dimensional SAXS intensity curves based on the variable stack model with Gaussian thickness distributions and Gaussian crystallinity distributions among stacks. ($\sigma_x$ = 0.15) .....274

4.4.15 Calculated SAXS intensity curves based on the variable stack model with modified exponential thickness distributions and Gaussian crystallinity distributions among stacks. ($\sigma_x$ = 0.05) .....275

4.4.16 Calculated SAXS intensity curves based on the variable stack model with modified exponential thickness distributions and Gaussian crystallinity distributions among stacks. ($\sigma_x$ = 0.15) .....276

4.4.17 Calculated SAXS intensity curves based on the variable stack model with modified exponential thickness distributions and Gaussian crystallinity distributions among stacks. ($\sigma_x$ = 0.2) .....277

4.5.1 Weibull distribution plot of breakdown strength of TR-XLPE, EC-XLPE, TR-LLDPE and biaxially stretched TR-LLDPE.....279

4.5.2 Overview of the electrically ruptured area of TR-XLPE.....281

4.5.3 Microphotograph of the electrically ruptured area of TR-XLPE.....282

4.5.4 Microphotograph of spherulites in the electrically ruptured area of TR-XLPE under cross polars.....283

4.5.5 Microphotograph of star-like breakdown streaks in the electrically ruptured area of TR-XLPE under cross polars.....284

4.5.6 Microphotograph of the etched surface of electrically ruptured area of TR-XLPE.....285

4.5.7 SALS patterns of the electrically ruptured area of TR-XLPE(a) and extractable portion quenched to room temperature(b).....286

4.5.8 FTIR spectra of the electrically ruptured area, cured and uncured TR-XLPE in the region of 2000-1500 $cm^{-1}$...288

4.5.9 FTIR spectra of sol and gel fractions of TR-XLPE in the region of 2000-1500 $cm^{-1}$.....289

4.5.10 FTIR spectra of the electrically ruptured area, cured and uncured TR-XLPE in the region of 1050-800 $cm^{-1}$....291

4.5.11 FTIR spectra of sol and gel fractions of TR-XLPE in the region of 1050-800 $cm^{-1}$.....292

5.1.1 Calculated difference SAXS intensity curves based on the variable stack model with Gaussian thickness distributions with $\sigma_x$ of 0.10. (Intensities of $\sigma_c$ of 0.05 subtracted).....297

5.1.2 Calculated difference SAXS intensity curves based on the variable stack model with Gaussian thickness distributions with $\sigma_x$ of 0.15. (Intensities of $\sigma_c$ of 0.05 subtracted).....298

5.1.3 Schematics of typical SAXS intensity curves and definitions of characteristic parameters.....302

5.1.4 Calculated one-dimensional correlation function based on the variable stack model ($\sigma_x$= 0.15) .....304

5.1.5 Calculated one-dimensional correlation function based on the variable stack model ($\sigma_x$= 0.175) .....305

5.1.6 Calculated SAXS intensity curves based on the variable stack model with Gaussian thickness distributions and Gaussian crystallinity distributions among stacks. ($\sigma_c$ =0.1) .....307

5.1.7 Calculated SAXS intensity curves based on the variable stack model with Gaussian thickness distributions and Gaussian crystallinity distributions among stacks. ($\sigma_c$ =0.175) .....308

5.1.8 SAXS intensity curves of slow-cooled (1.5°C/ min) and quenched TR-LLDPE.....310

5.1.9 SAXS intensity curves of slow-cooled (1.5°C/ min) and quenched TR-XLPE.....311

5.1.10 SAXS intensity curves of slow-cooled (1.5°C/ min) and quenched TR-LDPE.....313

5.1.11 Schematics of the variable stack model.....314

5.2.1 DSC thermograms of TR-XLPE held at room temperature for two years and quenched in the DSC.....324

5.2.2 Difference DSC curve of TR-XLPE held at room temperature having subtracted from it the curve of TR-XLPE quenched in the DSC.....325

5.2.3 DSC thermograms of TR-XLPE gel held at room temperature for two years and quenched in the DSC.....327

5.2.4 Difference DSC curve of TR-XLPE gel held at room temperature having subtracted from it the curve of TR-XLPE gel quenched in the DSC.....328

5.2.5 DSC thermograms of TR-XLPE sol held at room temperature for two years and quenched in the DSC.....329

5.2.6 Difference DSC curve of TR-XLPE sol held at room temperature having subtracted from it the curve of TR-XLPE sol quenched in the DSC.....331

5.2.7 DSC thermograms of TR-LLDPE held at room temperature for two years and quenched in the DSC.....335

5.2.8 Difference DSC curve of TR-LLDPE held at room temperature having subtracted from it the curve of TR-LLDPE quenched in the DSC.....336

5.2.9 SAXS intensity curves of TR-XLPE held at room temperature for two years and quenched in the DSC.....341

5.2.10 SAXS intensity curves of TR-LLDPE held at room temperature for two years and quenched in the DSC.....346

5.2.11 Variation of BD strength of TR-XLPE and EC-XLPE with aging time. (Source: Chan, 1985).....347

5.2.12 Variation of maximum tree length of TR-XLPE and EC-XLPE with aging time. (Source: Chan, 1985).....348

5.3.1 Variation of long period of TR-XLPE, EC-XLPE, PL-XLPE and TR-LLDPE with annealing time at 107°C in air.....363

5.3.2 Variation of long period of uncured TR-LDPE, EC-LDPE, PL-LDPE and HDPE with annealing time at 107°C in air..364

5.3.3 Difference SAXS intensity curves of TR-XLPE annealed at 107°C for various period of time in air (Fresh TR-XLPE subtracted).....365

5.3.4 Difference SAXS intensity curves of TR-LLDPE annealed at 107°C for various period of time in air (Fresh TR-LLDPE subtracted).....366

5.3.5 Variation of long period of TR-XLPE, EC-XLPE, PL-XLPE and TR-LLDPE with annealing time at 107°C in silicone oil.....377

5.3.6 SAXS intensity curves of TR-XLPE annealed at 107°C for 3 hours in the Univolt oil and in air.....381

5.3.7 SAXS intensity curves of TR-LLDPE annealed at 117°C for 3 hours in the Univolt oil and fresh TR-LLDPE.....382

5.3.8 SAXS intensity curves of E-1 and E-2 cables immersed in the Univolt oil at 60°C for 3 hours prior to the measurement and without treatment.....383

5.3.9 Lorentz-corrected SAXS intensity curves of E-1 and E-2 cables immersed in the Univolt oil at 60°C for 3 hours prior to the measurement and without treatment.....384

5.3.10 Difference SAXS curves of E-1 and E-2 cables immersed in the transformer oil subtracted from them the curves of the untreated cables.....386

5.3.11 Difference SAXS curves of immersed and untreated cables (E-1 was subtracted from E-2).....387

5.3.12 Difference SAXS curve caused by oil diffusion into additional E-2 structure on a log-log scale.....389

5.4.1 DSC melting curves of TR-XLPE after holding at various temperatures for 30 minutes.....392

5.4.2 Typical fitted SAXS intensity curves of TR-XLPE held at the various in-situ temperatures for 30 minutes for the evaluation of the distance distribution function.....400

5.4.3 Theoretical distance distribution curves of spheres, rod-like particles and disk-shape particles.....401

5.4.4 Theoretical F(r) function curves of spheres, rod-like particles and disk-shape particles.....402

5.4.5 The distance distribution curves of various polyethylenes at various in-situ conditions.....404

5.4.6 The F(r) function curves of various polyethylenes at various in-situ conditions.....405

5.4.7 Variation of the distance distribution curves of TR-XLPE held at 107.5°C with in-situ time.....407

5.4.8 Variation of the F(r) curves of TR-XLPE held at 107.5°C with in-situ time.....408

5.4.9 Variation of the distance distribution curves of EC-XLPE held at 107°C with in-situ time.....409

5.4.10 Variation of the F(r) curves of EC-XLPE held at 107°C with in-situ time.....410

5.4.11 Variation of the distance distribution curves of PL-XLPE held at 106°C with in-situ time.....411

5.4.12 Variation of the F(r) curves of PL-XLPE held at 106°C with in-situ time.....412

5.4.13 Variation of the distance distribution curves of PL-XLPE with various in-situ temperature and time.....413

5.4.14 Variation of the F(r) curves of PL-XLPE with various in-situ temperature and time.....414

VOLUME I

# 1. INTRODUCTION

Electric equipment generally consists of three basic components, namely, structural parts, electric conductors, and electric insulating materials. Among these elements, insulating materials play a major role in the satisfactory operation of electric machines. Hence, electric insulation has been the subject of exhaustive studies by scientists as well as engineers, and countless articles have been published dealing with the engineering and scientific problems of insulation designs and applications. However, insulation performance is still one of the major considerations that challenge the reliability of electric equipment for a long life, especially at elevated temperatures, and for higher voltage applications. The design and development of suitable insulation materials must not only be based on a thorough knowledge of the electrical and physical functions to be performed by the insulation, but also on a proper understanding of the electrical, mechanical, chemical, and physical properties of the insulation material under the conditions of use.

A prime example of the electrical system in which the insulation performance is the most important factor for the satisfactory operation is underground transmission cables. The need for insulated underground transmission cables in urban areas is growing due to the their safety. The insulation function of those electrical cables has been predominantly performed by semi-

crystalline polymers. In recent years, the use of low-density polyethylene, crosslinked using dicumyl peroxide, and linear-low-density polyethylene for the insulation of for transmission cables has prevailed. They are preferred over the traditional oil impregnated paper insulation because of their better dielectric properties, good processability, lower cost and low specific gravity. Crosslinked polyethylene and linear-low-density polyethylene are also considered to be a better selection than conventional low-density polyethylene because of their higher resistance to thermal overload. However, these materials are not immune from a long term aging process known as "treeing".

In order to improve the insulation function of polyethylene and to reduce the problems associated with the failure of insulation, many investigators have studied the mechanism of insulation aging. So far, however, it is agreed among most investigators that a definite understanding of aging mechanisms is beyond our reach unless the insulation materials themselves are fully understood. Without a sound understanding of the effects of such operation factors on the various properties of insulation material, simple phenomenological projection to the failure mechanism tends to cause errors.

Several mechanisms have been proposed for the damaging process by electrical stress. Factors that affect the damaging process have long been studied and traditionally, much effort has been paid for environmental factor such as geometry of the specimen, nature of the

electrical stress, temperature and so on. The major reason for this trend is due to the fact that the damaging process is normally a very localizing phenomenon.

Over the past decade, more researchers recognized the importance of the effects of the material factors on the electrical properties and the damaging process (eg.,Phillips, 1978, 1984). Molecular structure (Ieda, 1978; Filippini, 1986), morphology (Phillips, 1978; Ceres and Kolesov, 1980; Schultz, 1984), crystallinity (Fukuda, 1980) and the presence of chemical additives (Bamji, 1986a) have been found to influence the dielectric properties of polymeric insulation. More recently, due to the perfection of new characterization techniques, the chemical nature of the polymer has been recognized as the major contributory factors along with the physical and morphological structures. Recent findings (Laurent, 1983; Bamji, 1984, 1986a, 1986b) of electroluminescence phenomena occurring during the initiation phase of trees in polyethylene at room temperature support the electro-chemical nature of the damaging process by the electrical stress.

In this study, chemical, physical and morphological properties of various polyethylenes are characterized for the elucidation of their relationships with the electrical properties. The materials used in this research are three different grades of crosslinked polyethylene and one grade of linear-low-density polyethylene introduced by Union Carbide Corp. in the early 1980's. The difference in chemical composition was monitored using FTIR. The

physical property changes were also evaluated using DSC and a density gradient column. The morphological nature was examined using WAXD and SAXS. The electrical properties were studied by measuring breakdown strength.

The effects of thermal stress were also investigated for all these materials using in-situ SAXS and in-situ DSC techniques along with the same techniques used for the characterization. For the interpretation of the SAXS results, numerical simulation was made based on the model proposed by Blundell (1978). The distance distribution function proposed by Glatter (1977, 1979, 1982) for dilute solution, was also utilized for the interpretation of in-situ SAXS results.

Finally, electrical breakdown mechanism has also been reevaluated based on the findings of the electrically ruptured areas made by several different techniques. A possible explanation for these findings was made based on the thermal and chemical damaging process.

# 2. LITERATURE REVIEW

## 2.1. Electrical Properties of Polymeric Insulation

### 2.1.1. Introduction

Electrical insulation is made from materials that have very high resistivity. It is used to separate conductors of different potential (Clark, 1962; Sillars, 1973). The primary function of electrical insulation is to insulate, i.e. to prevent the flow of electric current between oppositely charged conductors. To serve this function it is necessary that insulation should supply a means for physically separating the conductors. This means that insulation must also serve a mechanical function. To properly provide this function, insulation must possess satisfactory mechanical properties. A final major property of most insulation is that of thermal stability and heat transfer, since most electric machines generate heat in their normal operation. Heat is also generated by dielectric losses in the insulation. This heat must be adequately dissipated to prevent excessive heat accumulation leading to the destruction of the machine. The insulation itself must endure elevated temperatures.

There are many solids used for insulation such as ceramics, glasses, papers, porcelains, and plastics. Among these solid insulations, polymers have been found to be the most desirable insulation in certain applications due to their unique combination of characteristics. The favored characteristics of polymeric

insulation include ease of fabrication, low cost, low density, excellent electrical and mechanical properties. Plastics not only act as effective insulators but also provide structural support for field carrying conductors. However, the low thermal stability of polymeric materials at elevated temperatures, with few exceptions, places limits on the application of polymeric insulation systems in which a large amount of heat is generated.

In this section, the major dielectric properties of polymeric insulation will be reviewed such as dielectric breakdown strength, and their mechanism. In a later part, two of the major problems associated with the polymeric insulation - electrical treeing and water treeing - will be reviewed.

### 2.1.2. Dielectric Breakdown

Under the condition of strong fields, insulating materials may be permanently altered, a situation that ultimately leads to failure. Electrical strength is a measure of a materials resistance to this permanent damage, and it can be defined and measured. Electrical strength is the electrical stress (voltage gradient) required to produce failure of an insulation by a dielectric breakdown.

Obviously, dielectric strength, being a measure of the electrical strength of a material is a very important characteristic of an insulating material, in the same way that the tensile strength relates to the mechanical properties. However, difficulties associated with the definition and the measurement of this property

arise because of the importance of a large number of variables which influence the results. The difficulties are also caused by a number of different modes in which breakdown can occur. Since breakdown is a destructive and weak link phenomenon, these difficulties and various factors are brought into play.

No insulation can be completely free from small current leakage, even though insulation by its definition should be free from any current leakage. The small current leakage may cause electron injection, generate heat, or produce mechanical stress, leading to failure of the insulation. Theories for electrical breakdown and details of how it is affected by these variables will be discussed in the following section.

The measurement of breakdown strength can normally be carried out using three basic procedures (Shah, 1984). The first procedure is known as the short-term method. In this method, the voltage is increased from zero at a uniform rate until the failure occurs. The failure is made evident by actual rupture or decomposition of the specimen. The second method is known as the slow-rate-of-rise method. The test is carried out by applying an initial voltage approximately equal to 50% of the breakdown strength as determined in a short-term test. Next, the voltage is increased at a uniform rate to breakdown. Thirdly, the step-by-step test method requires applying initial voltage as in the second method and then increasing the voltage in equal increments and holding for specified time periods until the material fails. In most cases the dielectric

strength values obtained by the step growth method correspond better with actual use conditions (Shah, 1984). However, service failure generally occurs at a voltage below the rated dielectric strength due to the time factor involved. Normally, the voltage to be applied in commercial use of insulation is designed not to exceed about 1/3 of the dielectric strength value obtained by the step-by-step method (Clark, 1962). Figure 2.1.1 illustrates schematically the basic set-up for a dielectric strength test (Shah, 1984).

### 2.1.3. Electrical Breakdown Mechanisms in Solids

There have been several mechanisms proposed for electrical breakdown of solids. A classification of these several breakdown theories is always to a certain extent personally biased and differs among authors (Graneua, 1979; Sillars, 1973; O'Tooles, 1984; Saums, 1973; Fischer, 1982; Ieda, 1983; Schultz 1974). For this review, breakdown mechanisms are defined as dependent largely on the inherent properties of the material itself. From this point of view, the fundamental breakdown processes are roughly classified into electronic, thermal and mechanical breakdown processes. In addition, partial discharge in voids or contaminants and various treeing phenomena are sometimes considered as partial or prebreakdown. However, their occurrence is invariably associated with the presence of defects in the insulation and they are normally long-term phenomena. Thus, they are considered here as an electric aging effect rather than a breakdown phenomenon and are dealt with in a separate section.

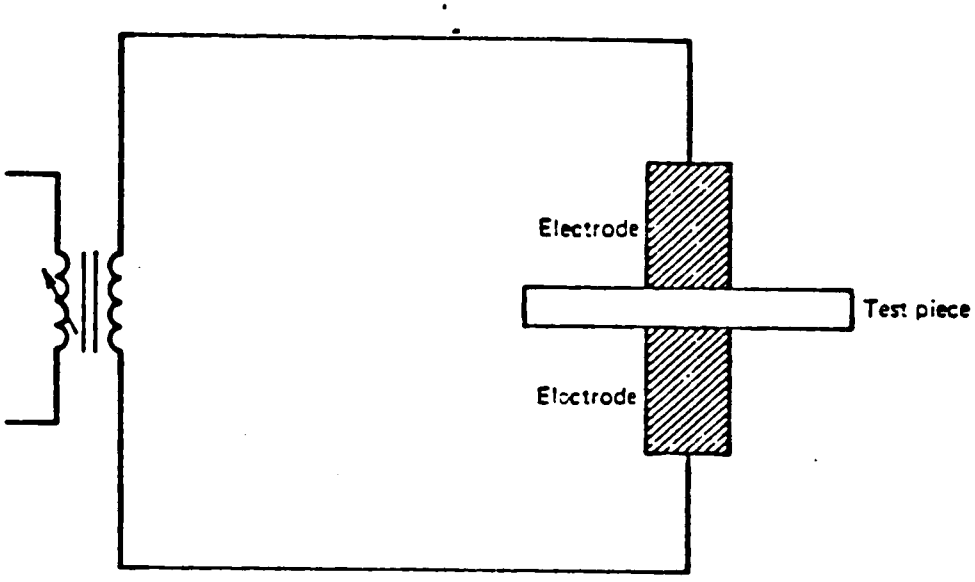



Figure 2.1.1 Schematic of dielectrical strength test.

2.1.3.1. Electronic Breakdown

Electronic breakdown, which is a purely laboratory phenomenon, involves the concept of the highest electrical stress that a particular material will withstand in the absence of any recognizable secondary effects such as heating by dielectric loss or bombardment by charged particles from extraneous discharge (Ieda, 1983; Schultz, 1974). This purely electrical or 'intrinsic' breakdown depends directly on the number of mobile electrons in the insulation and on their energy distribution. The energy, in turn, depends directly on the applied electrical field stress. This purely electronic breakdown entails an instability in the free electron distribution and an onset of collision ionization. The breakdown strength depends only on the physical state of the dielectric and is not influenced by surrounding conditions including sample geometry.

Two approaches have been used in attempting understanding of electronic breakdown; namely, that of calculating the field strength for which an instability in electron distribution causes the onset of collision ionization (collective theories) and that which investigates how the carriers produced by collision ionization multiply to cause the almost instantaneous build-up of a thermal breakdown current (avalanche theory). It is generally agreed that any electronic breakdown must be somehow a property of the field-induced flow of charge carriers. The question in this regard

concerns what characteristic of the carrier motion produces some critical effect leading to breakdown. The critical condition is most probably one in which the rate of production of charge carriers (electrons) is larger than their rate of recombination. The instability may occur either directly through the breakdown of the binding forces or by the generation of heat.

All collective electronic breakdown mechanisms consist of essentially two basic processes. The first process is the transfer of energy from the electric field to the system via mobile electrons (carriers). The second process can be considered as the interaction of the electrons with the lattice of the insulating material. The criterion for breakdown is therefore that the rate of energy gain by the electrons exceed the rate of loss to the lattice. There are two main conditions for collective breakdown mechanisms— low- and high-energy criteria — depending on the assumptions and boundary conditions applied (Nelson, 1983). The low-energy criterion is determined by the average behavior of all electrons, whereas the high-energy criterion is based on the fluctuation occurring in the energy of the electrons. These two approaches, however, assume that the concentration of mobile electrons is so small that inter-electron interaction and energy exchange can be neglected. The breakdown strength calculated using these two criteria shows a slight increase with increasing temperature because the rate of energy loss to the lattice increases as a result of enhanced electron-phonon interaction.

There are other theories of collective electronic breakdown mechanism which include the electron-electron interaction. One such theory was proposed by Frohlich for amorphous dielectrics in 1947 (Frohlich, 1947). In his theory, below a transition temperature, inter-electron interaction was neglected whereas above that temperature the interaction was considered to dominate. The breakdown strength above the transition temperature was derived as

$$F_{am} = A \exp (\triangle V/2kT) \qquad 2.1.1.$$

where $\triangle V$ is the average energy of shallow trap levels below the bottom of the 'conductive band'. Even though the absolute value of $F_{am}$ is not meaningful for polymers, this equation has the advantage of predicting a decrease in breakdown strength above a certain temperature.

As reviewed by Nelson (1983), there are lots of experimental observations which are not accounted for by the basic single electron theory or collective theories of intrinsic breakdown. Moreover, Phillips (1983) argued that for polymeric materials intrinsic electronic breakdown mechanisms except that of the Frohlich theory can be eliminated in all probability. The merit of these collective theories, however, lies in the fact that they should predict a true intrinsic breakdown strength value which is independent of electrode, voltage application and specimen geometry.

The avalanche mechanism which is known to be mainly responsible for breakdown in gases, has been adapted to solid

dielectrics (Sillars, 1973). The avalanche mechanism deals with the ability of fast electrons to ionize atomic or molecular species in their path. In other words, electrons injected from the cathode are accelerated by the electron field until some portion of them acquire energies high enough to cause ionization. This ionization liberates new electrons and photons, which in turn act to cause further ionization in a channel extending between the electrodes. When the ionization avalanche reaches the cathode, there exists between the electrodes a channel containing positive ions and electrons. This path then acts effectively as an electron conduit between electrodes.

Avalanche theories investigate the conditions and requirements for the chance of a high-energy electron causing collision ionization to develop into an avalanche of critical, thermally destructive size. According to these theories, breakdown strength increases with rising temperature.

2.1.3.2. Thermal Breakdown

Thermal breakdown is a type of insulation failure that can be adequately described in terms of the macroscopic thermal and electrical properties of a given dielectric configuration. In this theory the electrical breakdown is discussed by the condition causing loss of the thermal balance between Joule heating, due to the conduction current, and its dissipation (Varlow, 1980). For dc fields, insulation loss current leads to Joule heating of the dielectric, while for a.c. fields, the dielectric losses due to

relaxation phenomena also contribute to the thermal balance between energy gain and heat dissipation. The thermal balance is described by the differential equation

$$C\ d\ (dT/dt) = \sigma\ E^2 + \text{div}\ (k\ \text{grad}\ T) \qquad 2.1.2$$

where C and d are the specific heat and the density of dielectric and T is the temperature of the lattice, k the thermal conductivity, $\sigma$ the electrical conductivity, or the equivalent when heating is by dielectric loss, E the electric field, and grad T the space gradient of the temperature. For a solution of the above equation it is assumed that the insulating properties are lost and breakdown considered to start at a certain point above the critical temperature, $T_c$. The solution of this equation gives the time needed to reach $T_c$ for a given applied field and given boundary conditions.

This theory has been used frequently in explaining qualitatively electrical breakdown phenomena of practical devices in the high temperature region. However, the quantitative experimental realization of thermal breakdown depends on the period of application of the applied voltage and there are two extremes to consider. In the first case, when the stress is applied for a sufficient length of time to permit near steady-state conditions to prevail, i.e. dT/dt -> 0, the field necessary to raise the temperature to Tc is calculated. This gives the lowest field for thermal breakdown and the 'minimum thermal breakdown voltage' is

obtained. This form of breakdown is essentially a phenomenon associated with continuously stressed dielectrics.

The other limiting case occurs when the field is applied rapidly, and it can be assumed that no heat is conducted away from the specimen, i.e. no heat conduction term. The electric strength corresponding to this form of breakdown is called the impulse thermal breakdown strength. This breakdown strength varies with time of application of the field, being larger for an applied voltage pulse of short duration, but does not depend greatly on the size and shape of the sample.

However, under normal conditions and even under the better controlled condition of laboratory experiments, it is known to be difficult to realize the above equation due to uncertainty in dielectric conductivity and field stress (Nelson, 1983). The dielectric conductivity sums over all the dissipation processes occurring within the dielectric and will be a function of various parameters, such as temperature, electrical field strength, frequency, and even locality. The electrical field strength may also vary locally because of electrode geometries, but also as a result of unrecognized factors such as thermal properties of contact electrodes and surrounding media.

2.1.3.3. Electro-mechanical Breakdown

Electro-mechanical breakdown mainly deals with instability in the balance between mechanical and electrical forces. On this basis Stark and Garton (1955) proposed that an electrically stressed

material may fail by mechanical collapse. In materials such as thermoplastic polymers, the initial thickness of specimen ($L_o$) is known to decrease as the voltage is raised. The force due to the attraction of the oppositely charged electrodes will be balanced by the mechanical rigidity of the polymer in question. With an applied voltage V and relative permittivity, $\Phi_r$, of dielectric and the permittivity of free space, $\Phi_o$, the balance of electrostatic and mechanical forces is given for large strain by

$$1/2\ \Phi_r\ \Phi_o\ (V/L)^2 = Y\ \ln\ (L_o/L) \qquad 2.2.3.$$

where Y is the Young's modulus of the polymer at the given temperature, L the equilibrium thickness, and $L_o$ the initial thickness of specimen. It should be pointed out that a stable state is possible only if $L/L_o$ is greater than 0.6. In other words, $L^2$ $\ln(L_o/L)$ has a maximum at $L/L_o$=0.6, i.e. $\ln(L_o/L)$=0.5. the critical stress, $F_c$, is $(Y/\Phi_r\Phi_o)^{1/2}$ and the highest apparent intrinsic strength that can be observed as

$$F= V/L = \exp\ (-1/2)\ F_c= (Y/\Phi_r\Phi_o)^{1/2}\ x\ 0.6 \qquad 2.1.4.$$

With this equation satisfactory agreement between calculated and observed breakdown strength has been obtained for certain polymers, particularly nonpolar, thermoplastic ones, such as polybutylene and polyethylene. Stark and Gorton (1955) also observed an increased breakdown strength at elevated temperature upon improving the mechanical rigidity of polyethylene.

In summary, there exists sufficient evidence in favor of the possibility of electro-mechanical breakdown in certain polymers in certain electrode arrangements. However the basic equation for this theory was derived assuming the validity of Hooke's law and no lateral constraint. Accordingly, as far as nonlinearity of the stress strain relationship is concerned, this equation must be modified. The concept of this breakdown is usually applied at elevated temperature well above the transition range from electronic to electro-mechanical breakdown.

### 2.1.4. Electrical Breakdown of Polymers

Dielectric breakdown is influenced by many factors that are not directly related to the material to be tested; examples include sample geometry, impurities present, environment, and voltage application methods. Moreover, it is commonly agreed that it is difficult to interpret the breakdown phenomena in solid dielectrics, including polymeric materials, by a single breakdown mechanism. Thus, there are two alternative ways to construct the breakdown model. In the first approach the various effects and processes are regarded as secondary effects of a basic single breakdown mechanism. In the other approach it is assumed that all the considerable processes are included in the breakdown model as a multi-step breakdown process. It has been argued that the second alternative is somewhat better than the first for the purpose of understanding the relationship between theory and experiment quantitatively (Ieda, 1980, 1983; Jonscher, 1984).

In this section the effects of various factors on breakdown will be reviewed. All the factors which are directly related to the material as well as pertaining to the environment will be considered. These factors influence not only the dielectric breakdown but also other electrical properties including dielectric constant, loss factor, electric aging phenomena, etc.

### 2.1.4.1. Environmental Factors

#### 2.1.4.1.1. Specimen Geometry

Although intrinsic breakdown strength should not be affected by sample geometry, experimental evidence has made it clear that the breakdown strength decreases with increasing specimen thickness (Koo, 1984). The thicker specimen requires a higher voltage to achieve the same voltage gradient. It was believed that since thicker specimens have more defects such as internal voids, moisture and nonuniformity, and since greater current leakage due to these defects causes early failure of the specimen, increasing thickness implies an increased probability for weak points of breakdown strength in the material (Shah, 1984). For a similar reason Milton and Wentz (1966) reported that there is a logarithmic dependence of electric strength on electrode area. However, it was concluded that the area effect is more or less purely statistical, whereas the thickness effect is physical in origin (Nelson, 1984).

2.1.4.1.2. Temperature

Since the physical properties of polymers change with temperature, the temperature dependence of their breakdown strength is plausible. In his review papers Ieda (1980,1983) divided the temperature dependence modes of the breakdown strength of several polymers into two regions. He matched the boundary temperature between these two regions to the glass transition temperature. According to Ieda, in region I, below Tg, breakdown strength of non-polar polymers is almost independent of temperature. In the higher temperature region, however, breakdown strength decreases with increasing temperature. The transition temperature between Region I and II does not exist for polar polymers. In this case, it was noted that as temperature rises, breakdown strength decreases slowly from an extremely low temperature to a critical temperature from which strength falls steeply. This critical temperature for polar polymers was matched to the crystalline melting temperature.

2.1.4.1.3. Time

In general, electrical breakdown occurs some time after voltage application. This time scale was reported to range from nanoseconds under high-field impulse conditions to many years under normal operating conditions, depending on the breakdown mechanism (Jonscher, 1984). This time delay is also known as time lag. For short time lag, the electrical breakdown is believed to be primarily associated with electronic processes. In research on short time lag (c.a. 30 nsec) for polymethylmethacrylate, Auckland et al. (1977)

suggested that during this time lag the progressive ionization of the eventual breakdown channel takes place, followed by the collapse of the voltage across the specimen.

However it has been controversial to distinguish the border line between short and long time delay, since the destruction of material in any case is considered as a progressive process. Some researchers considered all time effects as a kind of aging phenomenon no matter what the length of time lag (Jonscher,1984). However, in this review long time effects will be dealt with separately in the section on aging phenomena.

2.1.4.1.4. Electrode, Voltage Application, And Other Effects

Dielectric breakdown strength is also affected by the electrode geometry, the electrode area, and electrode base material composition (Shah, 1984; Varlow, 1980). Generally, it is known that the breakdown voltage decreases with increasing electrode area (the same effect as sample geometry). Due to the effects of electrode geometry and composition, direct comparison of experimental results for different electrodes sometimes leads to confusion and disagreement.

Along with the electrode effects, the mode of voltage application is another major factor in breakdown strength. There are mainly three different modes of voltage application; alternating, direct, and impulse voltage. For the long-term alternating voltage, the frequency is considered as an accelerating factor in the breakdown (Bahder, 1973; Mckean, 1976). However, the

strength obtained by this method was argued to be easily affected by electrical and electrochemical deterioration of the material (Varlow, 1980). Short-term alternating voltage breakdown is normally accomplished by raising the voltage either stepwise or at a constant rate to achieve breakdown in a few minutes or less. However short-term alternating voltage along with direct voltage breakdown is thought to be subject to the influence of injected space charge (Varlow, 1980). Impulse breakdown is considered to approach most closely the 'intrinsic' strength, being relatively less influenced by space charge injection if the impulse duration is sufficiently short (Bradwell, 1971). Other factors affecting breakdown strength which do not pertain to the material itself include humidity, pressure, etc.

2.1.4.2. Material Factors

The structural characteristics, either chemical or morphological, of polymers have a pronounced influence on their mechanical, physical, and chemical properties. It is not surprising that these characteristics also affect the electrical properties of the polymers, including dielectric strength. Such dependences on structure have been investigated by comparison of densities (Prigent, 1975), molecular weight (Fischer, 1976), crystallinities (Ieda, 1980; Fukuda, 1980; Gryzybowski, 1980; Miyauchi, 1972) and so on.

The intimate relationship between the critical temperature of breakdown strength and glass transition temperature also suggests

the possible influence of polymer structure on electrical properties. There are a relatively small number of papers dealing with the effects of morphology and structure of polymeric insulation on the dielectric breakdown strength compared with the effects of other parameters not pertaining to the materials.

2.1.4.2.1. Chemical Structure

The effects of molecular weight on the breakdown strength at room temperature for polyethylene were studied by Fisher and Nissen (1976). They reported that breakdown strength increases with increasing molecular weight. However, their report was questioned by Ieda (1983) because the critical temperature for the breakdown strength is located near room temperature. Ieda stated that the influence of molecular weight at low temperatures ( $< 40^{o}C$) is insignificant, whereas in a higher temperature range, an increase in molecular weight increases breakdown strength.

It is of interest to note that a relationship exists between the electrical strength and cohesive energy density (CED). Sabuni and Nelson (1976) reported that polar polymers, having a high CED yield the highest electric strength. Actually, CED is a parameter which characterizes the energy required to separate a close molecular structure into infinitely separated molecules. In other words, the CED gives a measure of the strength of secondary bonding between molecules. As described earlier, polar polymers usually show a continuously decreasing breakdown strength with increasing temperature. This phenomenon is thought to be due mainly to the

breakup of the dipole-dipole interactions (Sabuni, 1976). The introduction of a polar group in a polymer structure was also reported to result in an increase of breakdown strength at low temperature.

For the effects of other chemical structures, the breakdown strength is known to increase with crosslinking especially at higher temperatures (Ieda, 1980). Generally, crosslinking leads to an increase of softening point beyond which the breakdown strength of the material normally decreases.

2.1.4.2.2. Solid Structure

Among the various morphological factors influencing the electrical breakdown strength, crystallinity is one of the most thoroughly studied factors. Miyauchi and Yahagi (1972) have investigated the dependence of electrical strength of polyethylene with dc voltage on the degree of crystallinity. The crystallinity was changed by varying the annealing process on the same high density polyethylene film. Their results are shown in Figure 2.1.2. Below 80°C electrical strength increases with a decrease of crystallinity, but above 80°C the effect of crystallinity is reversed. The results above 80°C were considered to be related to the electro-mechanical breakdown, whereas for the results below 80°C, a modified Frohlich's amorphous breakdown theory was employed.

For crosslinked polyethylene, the degree of crystallinity was also found to be closely related to impulse voltage breakdown strength by Fukuda et al. (1980). However, crosslinked polyethylene

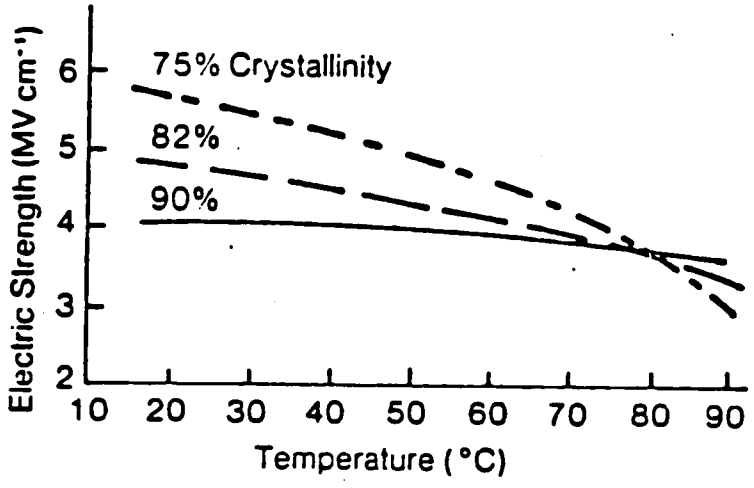



Figure 2.1.2 Effect of crystallinity on the electrical strength of HDPE. (Ref. Miyauchi and Wayagi, 1972).

showed an increase of breakdown strength as crystallinity was raised. They also observed a decrease of breakdown strength with an increase of temperature. This observation was attributed to a decrease in crystallinity with increasing temperature after noting that the thickness of the amorphous zone increased with temperature without any severe change in crystal thickness. Thus, the amorphous zone was postulated to play an important role in the occurrence of impulse breakdown. Moreover, the impulse breakdown was thought to originate from the amorphous region.

An interesting example as to how morphology affects breakdown was reported by Kolesov (1980). His results for the breakdown strength of both high-density polyethylene and polypropylene were plotted as a function of the diameter of spherulites. These tests were conducted with an impulse voltage on specimens whose spherulite sizes were modified by heat treatment in the range of 5 to 145 μm. The results of a 6 mm diameter sphere-plane electrode system showed that strength is reduced with increase of the spherulite radius until the latter becomes about equal to the specimen thickness. Kolesov concluded from this result that breakdown channels occur mainly in the interspherulite space of the insulation. This view had been reported earlier by Wagner (1975), who showed microphotographs of the breakdown of the inter-spherulite region for polypropylene.

Kolesov (1980), in addition, observed the breakdown of spherulites and inter-spherulite portions of polypropylene independently by accessing relevant areas using microscopic

examination in polarized light. However, the electrical strength of defect-free spherulites was reported to be independent of spherulite size. Thus, the size effect shown in his results was accounted for by the inter-spherulite regions having low density and irregular structure. This situation is expected, since impurities are known to segregate in the boundary regions between spherulites. Furthermore, Kolesov (1980) reported that as the spherulite size increases, the density of polymer within the inter-spherulite space decreases, yielding the observed reduction in electrical strength and other properties. Kolesov's results present the possibility that by a change in morphology, a modification in electrical properties may be engineered.

Kolesov's results of spherulite size effect have recently been criticized from the viewpoint that variation in solidification conditions usually causes simultaneous variations in spherulite size, lamellar thickness, degree of crystallinity, and other microstructures (Phillips, 1983; Ceres, 1984). In a review paper, Phillips (1983) maintained that considerable caution needs to be exerted in assuming that spherulite size is the controlling variable in electrical breakdown, since large spherulites are formed at a low supercooling condition under which exclusion of impurities and low-molecular weight materials can occur from the crystals into interspherulitic regions. Thus, the observed correlations between spherulite size and electric strength might actually be a correlation between boundary structures and electrical strength.

In a very recent study, Ceres and Schultz (1984) investigated the effect of spherulite size on electrical properties, while other parameters, such as lamellar thickness and degree of crystallinity, were held constant. They utilized a self-seeding technique coupled with isothermal crystallization. With this technique they were also able to prepare samples with different crystallinity but with similar spherulite size. They measured electrical lifetime of each sample with a needle electrode system.

Their results are similar to those of Kolesov, showing the electrical lifetime to decrease with increasing spherulite size and, more weakly, with decreasing crystallinity at a given spherulite size. It is of interest to note that they tried to explain the size effect in terms of modification of interspherulitic regions which were observed as paths of electrical breakdown. They expected that the more rapid the spherulite growth rate, the less selective is the spherulite with regard to poorly crystallizable molecules, and the less different the interspherulitic material is from the material that the spherulite is composed of. However, their results reveal that the sample which should have the greatest foreign material concentration at interspherulitic regions (i.e., slower crystallized sample) shows the highest electrical life. They also reviewed other possible mechanisms for the underlying source of spherulite boundary weakness; such as the mechanical fragility and less dense material with higher voiding. However, they actually observed effects opposite to those expected for these sources and concluded that

these possible mechanisms are either unimportant or are only weakly dependent on crystallization.

Commercial insulation such as cable insulation may have a non-uniform distribution of spherulite size. This comes about since crystallization from the melt depends critically on the cooling conditions, so that for a thick slab of insulation the surface region will suffer a higher rate of change of temperature and thus tend to have smaller spherulite size. Changes in morphology and density due to the annealing of polymer cables may have some impact on subsequent electrical strength.

The impulse breakdown strength was investigated as a function of the draw ratio as well as orientation functions for crosslinked polyethylene by Yahagi (1980). His results show that breakdown strength increases with increasing draw ratio for samples drawn at room temperature. As the c-axis orientation factor increased, impulse strength also increased. He suggested from these results that breakdown easily occurs along the direction of the main chain. He also reported the relation between impulse breakdown strength and rate of drawing. Even though measured values of the breakdown strength are scattered, the average value was found to have a minimum at a certain draw rate which increases with drawing temperature.

Ambrosio et al. (1987) investigated the effects of processing parameters on the morphology and dielectric breakdown of the XLPE. Molding pressure and cooling rate were noted to be important for the

processing. They reported that higher molding pressures and slower cooling rates increase the degree of crystallinity. The impulse breakdown strength was also noted to have increased with an increase in the degree of crystallinity.

The influence of heat treatment on the electrical strength of polyethylene was presented by Cooper et al. (1976, 1977). Film specimens of polyethylene were subjected to heat treatment over a range of temperature between 20°C and 100°C, followed by quenching to room temperature. They observed both transient (Cooper, 1976) and permanent (Cooper, 1977) influences for electrical properties. In the first hour following quenching from 100°C, the electrical strength of polyethylene film samples falls to a very low value before recovering to approximately the value obtained on a similar specimen without heat treatment. Breakdown was carried out by impulse voltage following prestressing in the fields-opposing sense. This demonstrates the influence of the transient morphological change following heat treatment on the ability of the polymer to accumulate the trapped space charge to which the prestressing phenomenon has been attributed. They also reported that there is no transient or permanent effect on the electrical strength of the specimens determined using impulse voltage alone, where there is insufficient time for the development of the prestressing space. Permanent changes in the prestressed samples vary in magnitude depending on the temperature of the heat treatment, producing a maximum effect between 60°C and 70°C.

The amorphous area was reported to be crucial to the breakdown strength of polymeric insulators (Kaminaga, 1986). With an increase of amorphous thickness, polyethylene was noted to have a lower impulse breakdown strength. The amorphous area under tension also revealed higher values of breakdown strength. They found a proportional relationship between impulse breakdown strength and amorphous birefringence.

The general conclusions from these morphological investigations are that the breakdown strength is closely related to the morphological features as in the case of chemical structure. Morphology can be modified normally by thermal and mechanical treatments. Thus, it is expected that the thermal and mechanical histories of the materials are important variables. A detailed understanding of the effect of morphology on electrical behavior of polymer is yet to be established.

### 2.1.5. Electrical Treeing

Treeing is a type of electrical prebreakdown damage which progresses through a dielectric section under electrical stress so that its path resembles the shape of a tree (Eichhorn, 1976). Although polymeric insulations have outstanding dielectric properties, almost all polymeric materials exhibit treeing phenomena. Treeing can be classified mainly into two types-- electrical and water trees-- according to the growth environment and its characteristics. Electrical trees are known to be dark, branch-like structures, and grow in a dry dielectric; whereas, water trees

are diffuse structures with a bush- or fan-like appearance, and grow in the presence of moisture. Electrical stress and stress concentration are required for both trees.

According to their shape, the trees can also be classified into two types-- vented and non-vented trees. Vented trees are initiated from the interface between the insulation and another material. Thus, the interface acts as the source from which water or air is drawn into the tree. Such vented trees are capable of growing continuously for a long enough time to bridge the electrode and cause failure. A more likely case with water trees is that they will grow long enough to reduce the effective insulation thickness to a value below that required to support the electrical stress.

On the other hand, trees which start at internal voids or contaminants are called non-vented trees or bow-tie trees. Since they do not have a free supply of air or water, their growth appears to be limited. Even though there is little likelihood of bow-tie trees growing large enough to bridge the conductors in commercial service conditions, there is a statistical chance that bow-tie trees can add to the length of vented trees (Shaw, 1984).

Trees are generally accepted as defects which contribute to long term electrical failure in solid dielectrics. Therefore, in order to predict the service life of insulation, it is necessary to study the effect of various variables on the initiation and the growth rate of trees as well as the morphology, initiation and growth mechanism of trees. With the present state of knowledge,

electrical and water trees appear so different with respect to their mechanisms and their structures that they are usually studied separately.

In a review paper by Eichhorn (1974) it was stated that one of the earliest works on the subject of damage by corona or partial discharge is that of Rayner in 1912. Since then, interesting publications have appeared on the subject of electrical treeing or internal tracking, and several mechanisms for treeing have been proposed. In spite of the enormous efforts by numerous investigators, however, many controversies persist, and most investigators agree that considerable future research will be required to resolve them.

Since all breakdown of insulation involves a time period and electrical treeing is thought to be a type of prebreakdown phenomenon, much of the detailed behavior of electrical trees can be understood in terms of breakdown processes. However, most workers still consider treeing as long term-aging at relatively low stress and electrical breakdown as a short-term destructive process. Due to the ambiguous border line between these two phenomena, several investigators have dealt with these two subjects at the same time (eg., Jonscher,1984; Bahder, 1982).

2.1.5.1. Experimental Observations of Electrical Trees

Except under the special circumstances which pertain to intrinsic breakdown, the initiation and growth of tiny tree-like defects is involved in breakdown of polymers. Such trees have been

observed and studied by various workers using needles or sharp-pointed holes (eg., Olyphant, 1963; Bolton, 1965; Bulinski, 1981; Mcmahon, 1964). In an early work, Bolton et al. (1965) made a statistical study in polymethylmethacrylate using a needle-shaped hole having an end radius of about 25 μm, coated with a conducting film. They applied impulses of some 150 kV amplitude and 30 μs duration to this system. They noted that each time a visible discharge was seen the tree system had been extended.

Using a similar electrode geometry, Eichhorn (1974) investigated the morphology of electrical trees by means of electron microscopy. He observed different external appearances of trees in wet polyethylene (moisture content of 0.12 % or more) from those of dry polyethylene. However, scanning electron microscopy (SEM) of both trees did not show any significant differences in the shape of the hollow channels. At that time he named the trees in wet samples as wet trees. Later, in other reports he mentioned that both are electrical trees with a morphology of hollow channels (Eichhorn, 1976). There is a great variation in the external appearance of electrical trees. The differences are due mainly to variations of the growth environment such as magnitude of voltage applied (Bahder, 1975) and presence of moisture (Eichhorn, 1974).

Although early studies suggested that tree growth was largely random (Bolton, 1965; Billing, 1974), other investigators did not agree with such observations. Wagner (1975) prepared a special pointed electrode arrangement producing an extremely inhomogeneous

electric field to observe the actual progression of tree channels inside polyethylene and polypropylene. He reported that the discharge channels pass along the spherulitic boundaries. This observation has been confirmed by many other researchers (Kolesov, 1980; Kitagawa, 1980, 1981). Since the interspherulitic regions appear to be mechanically weak areas, this observation indicates that breakdown or growth of trees is a weak link phenomenon. He also mentioned that the configuration of adjoining superstructures precluded a uniform coaxial enlargement of the discharge channel. For the mechanism of the treeing phenomenon it was also noted that very high temperature had to be associated with the formation of the trees since small spherulites, which were thought to be formed by melting and recrystallization, could be observed around trees.

There have been a number of factors reported which affect the treeing phenomenon, such as is the case for electrical breakdown. These factors can be divided into two categories, environmental and material. For the environmental factors, geometry and composition of the electrode have been studied extensively (Billing, 1974; Kitagawa, 1980; Kitchin, 1958; 1962). Other environmental factors include temperature, pressure, and mode of voltage application. For the factors pertaining to the specimen itself, chemical structure, presence of voids or contaminants, mechanical prestress (Billig, 1974), presence of additives, and thermal history have been considered. For the most part the results of these studies parallel those reviewed previously for electrical breakdown phenomena.

Therefore, in this section more emphasis will be placed on the specific mechanism of channel-like treeing phenomena and tree inhibition.

2.1.5.2. Mechanisms of Electrical Treeing

The mechanisms of electrical treeing have been studied extensively along with those of electrical breakdown. Most investigators agree that partial discharges are generally responsible for the initiation of electrical treeing (Eichhorn, 1976; Shaw, 1984; Tanaka, 1978; Eichhorn, 1983; Bernstein, 1984). However, there have been differences of opinion about the mechanisms by which partial discharge affects the insulation. These mechanisms include electron injection, the presence of hot electrons, and thermal decomposition.

In recent review articles Eichhorn (1976, 1983) considered electron injection as the most likely explanation for the initiation of electrical trees. Due to the stress concentration at a certain geometry, electron injection into the dielectric solid is thought to occur. After emission into the solid some electrons may be trapped and others may return to the electrode on the next half cycle of alternating current. During this return, the electrons are thought to fall into a very high field and accumulating energy. After absorption of sufficient energy for ionization, decomposition of material is followed by formation of a cavity within which partial discharge can occur and propagate the breakdown as a channel, which ultimately becomes a tree.

Recent findings (Laurent, 1983; Bamji, 1984) of electro-luminescence phenomena occurring during the initiation phase of electrical trees in polyethylene at room temperature strongly supports the view of Eichhorn. This emission of light, emanating from the bulk of the polymer, is attributed to the re-combination of carriers injected at the metal-dielectric interface and trapped in deep trapping centers of the polymer. Thus, the emission of light observed in the period proceeding the first measurable partial discharge appears to be characteristic of the initiation process of electrical treeing. The mode of degradation of the material introduces a process of bond breaking brought about by the injected carriers, thus, forming free radicals and low molecular weight products. The light has been detected not only in the degassed samples but also in normal samples, as well as in those impregnated with other gases (Bamji, 1984).

Bamji and his colleague (1986a, 1986b) also reported that photoemission due to the electroluminescence occurs not only in the visible light range, but also in the UV range. At low voltage, they observed light in the visible range, but at relatively high voltage the polymer emitted UV light. They speculated that UV light at high voltage is crucial in causing rapid degradation leading to electrical trees.

Cartier and Pfluger (1987), on the other hand, detected hot electrons in linear hydrocarbon n-$C_{36}H_{74}$ under high voltage using a thermally and optically stimulated exoelectron emission detector.

These hot-electrons were thought to initiate chemical damage in solid organic dielectrics. They estimated the degradation threshold at electron kinetic energies of 3 to 4 eV for the sample. Their results indicate that hot electrons break bonds, which leads to crosslinking and/or polymerization even under high vacuum with no oxygen present. It was also noted that bonds are broken as soon as the kinetic energy of injected electrons is of the order of C-H and C-C bond energies.

Another mechanism which has been proposed by Mason (1959) to explain the initiation of electrical trees and dielectric breakdown in general, is that partial discharge causes Joule or localized heating and thermal decomposition.

In addition to the effect of the partial discharge on the initiation of electrical treeing, there is a mechanical consideration. Ieda and Nawata (1973) presented a model of crazing phenomena due to a periodic Maxwell stress. A repeated Maxwell stress induced around a needle electrode was thought to cause a compressive stress in the insulation, which produced cracks or crazes parallel to the direction of the field. Chemical chain scission by injected charge and oxidation have also been attributed to the initiation of the electrical treeing (Shimizu, 1987). They proposed chain scission to be caused by the injected charge and that oxygen molecules moved by a diffusion process to further promote channel growth.

Although there is controversy concerning the detailed mechanisms of tree initiation, most investigators agree on the growth mechanism (Eichhorn, 1976, 1983; Bahder, 1982). After the initiation of electrical trees, growth begins due to discharge (Lu, 1986). The initiation of trees means that a cavity has been formed at the point of concentrated stress which is large enough to undergo partial discharge.

Due to the low value of the dielectric constant within the gas-filled cavity and to the sharp geometry of the cavity, electrical stress concentration occurs around this cavity (Wagner, 1975; Timpe, 1979; Yahagi, 1977). Furthermore, the dielectric strength of the gas within such space is lower than that of the matrix of the surrounding dielectric solid. Therefore, partial discharge causing ionization may appear in this space without causing an immediate breakdown of the polymeric insulation (Bahder, 1982). The trees will continue to grow because of the periodic effect of discharge and propagation through the weakest part of the structure as already mentioned.

The analytical identification and quantification of the products resulting from discharge degradation have previously been investigated. The discharge products which have been identified in most of these studies may be divided into two main categories, namely: gases such as $CO_2$, CO, and $H_2O$ (Wolter, 1982) and liquid droplets in association with solids (McMahon, 1968).

Gamez-Garcia et al. (1984, 1987) recently investigated the mechanism of formation of solid and liquid by-products. They reported that the degradation of XLPE, resulting from its exposure to partial discharges, leads to the formation of solid, liquid and gaseous products, direct results of the discharge synthesis reactions. They noted the reaction had taken placed within the intervening electrode gap space. In their initial report they speculated that the presence of acetophenone, $CO_2$, and $H_2O$ in a discharge degradation test of XLPE may give rise to various synthesis products (Gamez-Garcia, 1984). In a later study (Gamez-Garcia, 1987) they confirmed their first report and found that CO, $CO_2$, $H_2O$, and acetophenone are the main reagents implicated in this synthesis process. They found oxalic acid and other non-aromatic compounds resulted from the discharge synthesis process involving only CO and $H_2O$. They attributed the presence of acetophenone to the formation of benzoic acid, benzamide, toluene, and other aromatic compound during the process. In the absence of $CO_2$, CO, $H_2O$, and acetophenone in a discharge test was found to lead only to pitting and erosion with no by-product formation on the surface.

2.1.5.3. Inhibition of Electrical Treeing

There have been many attempts to reduce or eliminate electrical treeing in insulation since the treeing problem was discovered in cable insulation. These approaches can be divided largely into two groups. One is modification of the cable construction method, and the other is the modification of the

material or material structure, often with the aid of additives. The modification of cable construction includes the replacement of impregnated conductive tapes by extruded layers of semiconductive polymer (Fjisawa, 1968). This modification eliminates the loose ends of conductive tapes which often protrude onto the insulation layer and act as needle points to initiate treeing easily. Subsequent improvements of cable construction have been made by extruding multi-layer shielding and by maintaining an absolutely clean and smooth interface between insulation and conductor. Bahder et al. (1976) reported that a cable manufactured with very smooth interfaces as well as free of contaminants or voids was not subject to electrical treeing under normal operating conditions.

An achievement in the second category is the introduction of crosslinked polyethylene as an insulation material. This offered higher temperature service and improved chemical resistance over the uncross-linked counterparts (Eichhorn, 1981). At first the improvement of electrical properties and resistance to treeing phenomena were attributed to crosslinking. However, several workers proved that some improvement resulted from the presence of acetophenone, one of three chemical residues from the peroxide crosslinking reaction (Braun, 1980). Thus, this improvement is thought to be due to the modification of polymer structure with additives.

The modification of the structure of the insulation material with additives began by filling the cavities with another material

of higher permittivity and breakdown strength such as oil (Hayami, 1973), sulfur hexafluoride (Morita, 1974), and water (Tanaka, 1975). With these modifications, partial discharges could be prevented, and propagation of trees was retarded. In a recent paper Bamji reported the effectiveness of the use of a UV stabilizer (Bamji, 1986a) to retard the electrical treeing. Their results were based on findings from electroluminescence especially in the UV range. They reported that a sample with UV stabilizer emitted no UV light at 364 or 300 nm, contrary to what was found in their regular samples without UV stabilizer. The sample treated with UV stabilizer was observed to have a longer tree inception time (17 h) than the ones without stabilizer (0.5 h).

There have been other additives used for the purpose of reducing electrical treeing by capturing energetic electrons chemically, retarding propagation of trees electrically, and interfering physically with tree propagation. Detailed mechanisms with various additives were reviewed by Eichhorn (1983).

Other researchers have attempted to improve the structure by other methods. One of these is thermal treatment. As reviewed earlier, variation of supercooling causes a change in superstructure which also brings about a reduction of treeing as well as improvement of electrical properties (Kolesov, 1980; Ceres, 1984). Namiki et al.(1980) reported that heat treatment of crosslinked polyethylene cause morphological changes in microvoids. Their scanning electron microscopy results revealed that the initial

microvoids were transformed into spherical particles with heat treatment. However, their experiments showed no improvement in treeing resistance.

### 2.1.6. Water Treeing

Water treeing is known as a degradation phenomenon that occurs in polymers in the presence of water and an electric field. The water tree has a diffuse structure with a bush- or fan-like appearance (Shaw, 1984; Eichhorn, 1974). This phenomenon was first observed in underground cables around 1968 (Tabata, 1972). Since then, the phenomenon has been studied extensively. However, progress has been slow in establishing definitively how and why such trees initiate, propagate, and ultimately contribute to the failure (Shaw, 1984; Bernstein, 1984).

At an early stage a water tree may be distinguished from an electrical tree by its external appearance and its disappearance upon drying. The disappearance is thought to be the result of some sort of collapsing of the trees. Due to its collapsing feature the water tree had not been studied extensively until Matsubara and Yamanouchi (1975) developed a staining technique in 1974. Moreover, Lawson et al. (1973, 1980) reported that failed cables from service conditions contain various kinds of water trees. They suggested that there is a correlation between water trees and cable failure. In a recent paper, Kothe and co-workers (1986) reported reduced impulse breakdown strength in cables with water treeing. They also noted that the electrical trees generated by impulse, initiate at the

periphery of a water tree and grow within the water tree to complete the breakdown.

Fukuda (1975), on the other hand, maintained that some kinds of water trees do not affect the physical strength, including electrical strength. This group studied bow-tie water trees with lengths up to 1.0 mm. On the whole, most researchers agree that water trees reduce ac breakdown strength, a common measure of cable deterioration (Cooper, 1976, 1977; Bulinski, 1981; Bahder, 1975; Bernstein, 1978; Chan, 1978; Gryzybowski, 1978; Kirkland, 1982; Srinivas, 1978).

More definite evidence was obtained in the form of direct observation that a water tree may initiate an electrical tree (Lanctoe, 1979). Chen and his co-workers (1986) proposed the initiation mechanism of electrical trees from water trees. The first transition step of water treeing to breakdown is thought to be through the formation of the electrical tree out of the water tree region. They (Chen, 1986) observed a large density of microcavities near the initiation point of water trees. The microcavities then form a larger channel by coalescing each other. The actual formation of electrical tree even at low voltage was observed to be caused by the partial discharge.

2.1.6.1. Experimental Observations of Water Trees

In an early extensive examination of water trees from underground cables Iwata and his co-workers (1973) observed a wide range in the external appearance of water trees from nearly

invisible to those penetrating 5 mm thick crosslinked polyethylene cables and bridging the inner and outer electrodes. They reported that after bridging the electrodes the cable could still hold some voltage. They thought that this was due to a non-carbonized inside wall of the cables.

Along with the variety of external appearances, it was known that unless dyed, water trees disappeared upon drying and reappeared on wetting (Matsubara, 1975; Isshiki, 1974). The disappearance was thought to imply collapse of water trees while their reappearance implied a permanent alteration of the insulation material. Fukuda et al. (1973) reported that infrared spectra of a crosslinked polyethylene cable with water trees showed the existence of water. The presence of water in water trees has been also directly demonstrated by water analysis recently (Nunes, 1982.

In some reports the morphology of water trees was suggested to resemble that of electrical trees with channel-like defects all connecting back to the point from which growth started (Iwata, 1973; Isshiki, 1974). The fine branches have been assumed to have a diameter of the order of 1 μm (Meyer, 1979). It was also suggested (Dakin, 1975) that the voids constituting the water trees are interconnected by channels which develop under the influence of electrical stress and collapse due to surface tension once the field is removed.

However, others demonstrated that the trees are simply comprised of small voids (Tanaka, 1975). In a recent study, Bamji et

al. (1983) presented scanning electron microscopic pictures of a section of a water tree which was prepared by freeze fracture. The section shows microvoids without any evidence of connecting channels. Other experiments that relate to this point were made by Cross and Koo (1984). They studied gas permeation through water trees of low-density polyethylene. The results show that water trees simply contain water in dispersed form and that interconnecting channels are absent. Similar results were also reported by the Gorton and Shaw (1986) using permeation apparatus filled with a 3% aqueous solution of sodium chloride.

In spite of extensive efforts, most researchers agree that the detailed structure is not yet complete understood (Shaw, 1984). However, it has been recognized that the treed areas have a higher numerical density of voids compared to untreed areas (Braun, 1980; Tanaka, 1975; Tabata, 1972; Fukuda, 1975; Bamji, 1983; Barlow, 1983; Dissado, 1982; Franke, 1978; Gryzybowski, 1982; Naybour, 1983; Orton, 1982). Scanning transmission electron micrographs prepared by Naybour (1983) show that the higher density of voids up to 10 /$mm^3$ in the size range of 1 μm or less was formed around larger vented trees. However, they did not observe any voids or channels for smaller vented trees nor for the non-vented trees. Their results also revealed that the number of voids increased with tree growth.

Another interesting but controversial observation is the relation between voids and the superstructure of polymers. Dissado et al. (1982) reported that voids were found on spherulitic surfaces

and the growth of trees was influenced by spherulitic boundaries. On the other hand, Orton et al. (1982) concluded that void locations in water trees can not correlated with the nodular texture revealed by etched transmission electron microscopic technique, and these nodules have little relation with the spherulites found in polyethylene. So far, the difficulties associated with scanning or transmission electron microscopic technique for the study of water tree morphology have been claimed to be related to the probability that preparation of samples tends to collapse the structure of water trees (Shaw, 1984). Moreover, unwanted artifacts can be associated with direct observation using electron microscopy.

2.1.6.2. Factors Affecting Water Treeing

Most investigators who have studied water treeing have measured the number of trees in unit area or the length of trees. As is the case of polymerization or crystallization, the number of trees appearing in a given duration of time may give an indication of tree initiation rate, whereas the change in length of trees provides a measure of propagation rate. The process of treeing has been divided into the separate considerations of initiation and propagation by many authors (Shaw, 1984; Nitta, 1974; Sletbak, 1979). However, as Bernstein (1984) claimed in his review paper, very few attempts have been made to actually study these effects separately. The reason for this is due to difficulties associated with the definition of initiation and correlation with the growth of trees.

In a theoretical study Sletbak (1979) referred to initiation as the formation of the first tree branch, and considered that further growth represented propagation. On the other hand, Nitta (1974) considered initiation as the process of water gathering around the region of high electric field stress. In a very recent study, Bernstein (1984) defined the initiation phase as electron injection from discontinuities leading to cation radicals followed by free radical formation. This pre-partial discharge series of events was considered as being common to both water and electrical treeings. He also noted that the commonly observed induction period was part of the initiation.

Growth of water trees have been investigated as a measure of aging of insulation by determining the length of the longest tree, median length, or the entire distribution of tree lengths (Sletbak, 1983; Soma, 1980). On the other hand, some authors investigated growth rate by studying the variation of tree length with time. Some of them reported a linear relationship (Nitta, 1974; Filippini, 1983; Yamada, 1979; Yamanouchi, 1978), whereas others proposed a logarithmic correlation (Braun, 1980; Tabata, 1972). In a recent series of papers Dissado et al.(1982, 1983) tried to make a master curve of tree growth rate for various tree data available with a six-parameter model. Most authors proposing such equations have attempted to define the dependence of various factors on treeing quantitatively.

As is the case of electrical breakdown, there have been many factors studied influencing the initiation and growth of water trees. The factors pertaining to the environment are electrical variables, nature of water, time, and temperature. Among these, electrical variables have been studied most extensively. The effects of frequency, polarity, and electrical stress have all been discussed.

Increasing the electrical stress is reported to increase the tree initiation rate (Matsubara, 1975; Fukuda, 1975; Dissado, 1980; Mizukami, 1978; Yoshimura, 1982; Sletbak, 1977) and growth rate (Bahder, 1973; Matsubara, 1975; Srinivas, 1978; Bamji, 1983; Franke, 1978; Filippini, 1983; Yoshimura, 1982; Ashcraft, 1979; Hossam Eldin, 1983; Noto, 1980). However, some researchers disagree with the positive dependence of electrical stress on the growth rate. As shown in Figure 2.1.3, Mizukami et al.(1978) reported that after 300 hours of aging at 2 to 12 MV/m, the bow-tie tree population increased with an increase in stress, whereas the tree length became shorter. However, most other authors found no evidence of negative dependence of voltage on the growth rate of water trees. No disagreement concerning the effect of electrical stress on the tree initiation rate was found.

The role of frequency, however, has not been fully established. While most investigators have found that higher frequency increases the growth rate monotonically (Fukuda, 1975; Srinivas, 1978; Hossam Eldin, 1983; Noto, 1980), some authors have

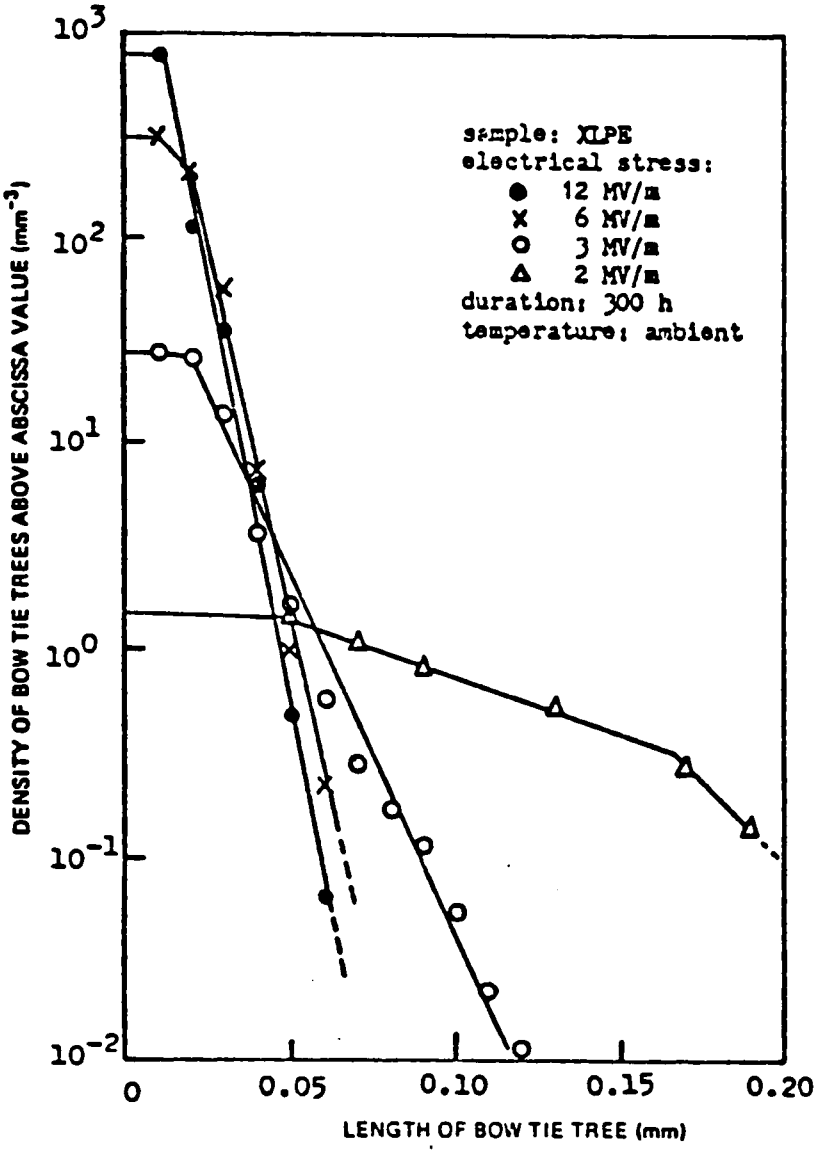



Figure 2.1.3 Influence of electrical stress on bow tie tree formation. (Ref. Mizukami, 1978).

reported that there is a maximum in this effect (Favrie, 1980; Michel, 1979). However, Sletback (1977) reported no significant effect of frequency on tree growth. Filippini and Meyer (1983) reported that growth rate went through a maximum at about 5 kHz for the cable sample geometry. Similar results were reported by Favrie and Auclair (1980) for the water needle test geometry. On the other hand, Sletbak and Botne (1977) found that the average length of bow-tie trees changed very little over the period up to 3000 hours at the frequency from 50 to 5 kHz.

The influence of frequency on tree initiation rate has been reported with even more mixed results. For example, Densley and his co-workers (1980) measured the numerical density of vented trees at 60, 400, 1000 Hz at voltages up to 8 KV. Their results indicated that more trees were generated at 400 Hz than at 1000 Hz. However, at 60 Hz no trees were observed up to 745 hours.

In studying the effects of polarity, several authors have investigated the nature of water trees grown at high dc stresses (Franke, 1978a, 1978b; Hossam Eldin, 1983; Noto, 1980). However in most cases, water trees were grown with alternating currents. Dc water trees have been reported to have a different external appearance from ac trees and to grow at much higher stresses.

Since the water tree is normally observed in the presence of water, it is natural to expect that the nature of the water might influence water treeing. Many authors have studied the effect of dissolved ionic substances on treeing. Most of them have found that

ionic substances increased the tree growth rate (Filippini, 1982, 1983; Hossam Eldin, 1983; Noto, 1980; Michel, 1979; Ashcraft, 1978; Nunes, 1984), but some of them saw an insignificant or negative effect (Favrie, 1980; Katz, 1975). There are also many reports on the effects of non-ionic additives (Favrie, 1980; Katz, 1974), oxygen (Nunes, 1984) and other chemicals on water treeing.

Temperature is one of the major factors affecting most chemical and physical processes. However, studies of the effect of temperature on treeing behavior do not show unequivocal tendencies. There are some works showing positive effects of temperature on initiation (Matsubara, 1975; Sletbak, 1983; Katz, 1974; Morita, 1978; Yoshimitsu, 1978) and on growth (Favrie, 1980; Franke, 1978). On the other hand, there are also some reports of negative dependence with temperature on initiation as well as growth rate. For example, Morita et al.(1978) reported a positive dependence on water tree initiation for crosslinked polyethylene, while observing a negative temperature dependence for low-density polyethylene. Sletbak and his co-workers (1983) found a mixed dependence of temperature in temperature cycling studies for crosslinked polyethylene. Favrie and Auclair (1980) observed an increase in tree growth rate of low-density and crosslinked polyethylenes with an increase of temperature at 15 kV, but a decrease in tree growth rate at 10 kV. A similar temperature dependence was also reported by Ren and co-workers (1986). They reported the increasing rate of growth of water trees with temperature reaches a maximum for XLPE with

different types of antioxidants. They also noted the external shapes of water trees at high temperatures are different from those at low temperatures. Bulinski (1988), however, reported that the length of trees grown at room temperature were longer than those grown at 60°C, but the times to breakdown at 60°C were significantly less than those at room temperature.

Such contradictions may imply relatively small dependence on temperature of water treeing compared with other variables, or they may reflect differences between the materials themselves or the test procedures. Actually, detailed variances in different materials with same name (eg., crosslinked or low-density polyethylene) are far beyond simple consideration. There may be different antioxidant levels, void contents, nature and content of contaminants, and so on. Moreover, polyethylenes and other polymers are very sensitive to thermal and mechanical treatments. Thermal energy may change the nature of voids and contaminants, molecular weight, superstructure, and other physical properties. Thus, without an understanding of the effect of thermal treatment on structure and properties, it is very difficult to clarify the effect of temperature on water treeing, and the nature of water trees themselves.

There is also a report of the effect of pressure on the water treeing. Tu and Kao (1984) molded low density polyethylene samples with needle shaped recesses for water point electrode. They placed these samples in a pressure chamber and studied the effect of pressure on the electric properties and water treeing. Their results

show that the ac breakdown voltage increases rapidly with increasing pressure below 10 bar and that this pressure dependence is gradually diminished for higher pressure. They also noted that pressure enhances the initiation of water trees, but suppresses their propagation, indicating that external pressure enhances the water to penetrate into preexisting microvoids. However, they could not explain the effect of pressure on water tree propagation with existing mechanisms.

The material variables seem to include chemical and structural variables. The difference in material composition (eg., polarity) is one of the major material factors which influences electrical properties as reviewed earlier. However, Isshiki et al. (1974) concluded that polarity and crystallinity were not important factors, but that modulus affected the treeing phenomena of various polymers such as low- and high-density polyethylenes, crosslinked polyethylene, polypropylene, polystyrene, polyvinylcloride, polycarbonate, ethylene-co-vinyl acetate, and nylon.

There are several reports concerning the effects of morphological variables such as crystallinity and orientation on water treeing. Namiki et al.(1980) studied the effects of annealing on the initiation rate of bow-tie trees in polyethylene cables. Their results showed an increase in tree initiation upon annealing. They also observed that annealing caused the partial filling of voids which, in turn, created sharp-crack like defects. They explained that the increase of tree initiation on annealing was due

to the formation of crack-like defects. Similar results were reported by Chan (1978). He found no improvement in the breakdown voltage of crosslinked polyethylene cables with annealing at 70°C. He also reported a higher susceptibility of subsequent water treeing for annealed samples. He pointed out that annealing of crosslinked polyethylene may accelerate the loss of acetophenone, which might result in a decreasing resistance to water treeing.

In a study of the relationship between water treeing, morphology, and microstructure of polymers, de Bellet et al. (1987) maintained that by controlling crystalline or spherulite morphology or mechanical properties, formation of channels or voids during treeing can be inhibited or modified.

The influence of the molecular weight of polyethylene on the propagation of water trees was investigated by Filippini et al. (1986). Their results show that samples with higher molecular weight show a much reduced water tree growth rate similar to what is observed for stress cracking. They interpreted the results with the aid of mechanical damage mechanism of water tree.

Phillips and Vatansever (1984) investigated the effects of annealing at maximum use temperature for crosslinked polyethylene cables (105°C-110°C) on initiation and growth of water trees. They observed that the ultimate number of water trees present and the average length of the largest trees are both increased significantly by annealing at 107°C. It was noted interestingly that the DSC curves for annealed samples at 107°C clearly showed two separate

melting regions while those for quenched ones showed only one broad peak. After confirming the new peak to belong to the sol fraction of crosslinked polyethylene, they concluded that the sol had separated from the crosslinked material during annealing at 107°C. In their report they also maintained that the thermal history is crucial to the electrical properties and is responsible for the discrepancies present among other studies on electrical properties.

Another material variable which influences water treeing is the presence of chemical additives. It is known that if crosslinked polyethylene is cured with dicumyl peroxide, it has a high resistance to water treeing relative to an uncured polyethylene. As is the case of electrical treeing, this resistance was thought to result from the presence of acetophenone. Braun (1980) reported that if the acetophenone is removed using vacuum, the susceptibility of crosslinked polyethylene to water treeing is almost as great as for an uncured polyethylene. Even though the detailed morphologies and mechanisms of water trees are thought to be different from those of electrical trees, the coincidence of other additives which work to suppress both electrical and water trees is reported to be very high (Morita, 1974; Eichhorn, 1979; Mcmahon, 1981).

The presence of contaminants has also been discussed as an influencing factor for water treeing. It is well recognized that contaminants of many sorts (Isshiki, 1974; Katz, 1974) can accelerate the initiation of bow-tie trees. However, a recent paper by Nagasaki et al. (1983) has demonstrated that certain polymeric

contaminants or certain inorganic fillers can retard both tree initiation and propagation in crosslinked polyethylene.

2.1.6.3. Mechanisms of Water Treeing

There are not many different mechanisms proposed to explain water treeing. Most of them lead to propagation by cracking or a splitting type of mechanical failure. Two major differences in the observation of water trees from those of electrical trees are the collapse of water trees on drying and a low voltage requirement for formation of water trees. These two observations lead to the three different proposed mechanisms for water tree initiation and growth, an electrostatic effect on moisture, a thermal mechanism, and a chemical mechanism.

The electrostatic effect was first introduced by Iwata et al. (1973) as a possible mechanism for the water filled treeing phenomenon. They suggested that the water could be pushed into a dielectric by Maxwell force. At almost the same time, Tanaka et al. (1973) explained that water could be drawn into the cable insulation by dielectrophoresis which is an electrokinetic phenomenon for the movement of uncharged but polarizable particles or molecules in a divergent field. However, these proposed mechanisms were used to explain the saturation of electrical insulation exposed in wet surroundings rather than treeing. A few years later Mizukami et al. (1978) proposed that water vapor in insulation, condensed under electrical stress, could push aside polymer chains to form voids. Other groups have examined the mechanism of electrostriction, which

describes the variation in the volume of dielectrics under the influence of an electric field, to explain the water treeing phenomenon (Tanaka, 1976). In a recent report Koo and his co-workers (1984) proposed that electrostatic pressure is responsible for creating microcavities, although the creation rate may be diffusion controlled. Other authors have discussed the effect of electrically originated mechanical stresses and strain in the formation of water trees.

Direct thermal effects for the formation of water trees is unlikely due to a low required power factor and electric stress. However Tanaka et al. (1975, 1976) proposed that water filled cavities will be enlarged when water within them expands due to dielectric heating. Such expansion was proposed to generate a mechanical force that strains the insulation material and breaks molecular chains, thus increasing the size of the voids or forming new ones. Isshiki et al. (1974) combined several pre-existing proposals to postulate that an alternating field causes vibration of water 'electrodes' which generate fatigue and rupture of the polymer aided by joule or dielectric heating of the water. They also introduced the concept that oxidation occurs, proposing that electric discharges could be responsible.

Morita et al. (1978) proposed that oxidation of the polymer might accelerate the penetration of water, but maintained that the initiation step was a mechanical fracture of the polymer chains in regions of high electrical stress. In a review paper, Shaw and Shaw

(1984) emphasized the roles of oxygen in the treeing process. They mentioned that oxidation is a secondary process in water treeing, helping only to increase water and ion transport rates to the tips of trees by lowering the surface energy between water and polymer. They also proposed that oxidation may be a highly influential factor in the rate of conversion from water to electrical trees.

Similar views have been also proposed more recently (Ren, 1986; Henkel, 1985, 1987; Garton, 1986). Ren and co-workers (1985) claimed that water trees are initiated by the scission of chemical bonds under the action of electrical stress in the presence of water. In the same paper, they reported that XLPE with antioxidants shows a much lower rate of water tree propagation and initiation. Henkel and Müller (1985, 1987) also emphasized the consequence of oxidation. They hypothesized that the decomposition of hydroperoxides occurred during thermal oxidation was a major factor in the water treeing process, forming radicals. The radicals formed then initiated the degradation process.

Garton and co-workers, on the other hand, detected the difference between infrared spectra of treed and non-treed regions of same field aged cable. They reported the treed regions show additional peaks at 1725 $cm^{-1}$ , 625 $cm^{-1}$, 1130 $cm^{-1}$, and 1610 $cm^{-1}$. These additional peaks were noted to be associated with oxidation products such as carbonyl (1725 $cm^{-1}$), sulphate ions ($SO_4^{2-}$, 625 and 1130 $cm^{-1}$) and carboxylate anion ($-COO^-$, 1610 $cm^{-1}$ ). Even though they did not claim that oxidation alone is not responsible for the

whole treeing process, they assured that the some oxidation, particularly on the walls of cavities, is occurring. They also noted that the treed regions are prone to extensive oxidation, this being indicated by oxidative induction time (OIT) measurements. It was also noted that oxidation may play a major role in the final breakdown of insulation after the formation of water trees.

Taking the chemical point of view, Bernstein (1984) argued that the initiation of water trees is similar to that of electrical trees, occurring by electron injection. He considered the initiation phase of water treeing as electron injection from the discontinuities leading to, first, cation radical and then free radical formation. He also proposed that antioxidants and voltage stabilizers limit damage by those electrons or the subsequent products. This hypothesis explains the observation that stabilizers for electric trees are often effective against water trees. However, this suggests that the growth rate of trees, once initiated, should not be influenced by retardants.

A similar view was also reported by Given and his colleagues (1987). They maintained that the penetration of the polymer by the ions is the first stage of water tree formation. The initial penetration of ions into the polymer distorts its structure by forcing polymer chains apart in the amorphous regions. In addition, they maintain that each ion will introduce water into polymer due to its associated hydration sheaths, leading a void formation. They observed that ions present in solution will alter the growth rate of

the water trees, with the growth rate being dependent on the properties of the ions present.

In a recent paper Filippini and his co-workers (1986) concluded that there is no basic difference in the very nature of the mechanisms which govern the initiation and propagation phases of growth of water treeing. They reported that no emission of light, either before the onset of growth of the water trees or during their propagation, contrary to that reported in electrical treeing. Electroluminescence phenomena occurring during the initiation phase of electrical treeing has been attributed to the re-combination of carriers injected at the metal-dielectric interface and trapped in polymer. The absence of light emission was interpreted by the absence of a local preliminary degradation of the polymer due to an action of the electrical field.

2.1.6.4. Inhibition of Water Treeing

Since water trees are initiated by stress concentration and the presence of water, many of the methods reviewed in electrical treeing inhibition are also applied. Again the methods of reducing treeing can be categorized as material improvement, improvement of cable construction, elimination of voids and contaminants, and application of additives such as voltage stabilizers and antioxidants.

In a recent paper (Kim, 1986), Kim and Lim selected eleven chemical compounds for tree retardation based on their thermal stability during the fabrication process of cables. Samples were

prepared by mixing homogeneously 10 wt% of the additives to the matrix material. They found that the additives ( such as m-cresol and α- or β-naphthol), which have higher electron affinities, were more effective in the suppression of water treeing. They considered the reason for this behavior to be that more electrons are trapped at the inner surface of the water channel due to the presence of additives with higher electron affinities.

In order to relieve the thermal oxidation process of the water tree initiation phase, Henkel and his colleague (1987) tried various additives. They reported barbituric acid as the best effective additive. They believed that the inhibition was enhanced by the presence of easily dissociated H atoms in the molecules. This allows the additive to function as radical scavengers, thereby stopping the oxidative degradation of the polymers.

In addition to these chemical modifications, there are other improvements that prevent water from penetrating the cable by using a water-tight sheath (Favrie, 1980). Introduction of wetting agents (Soma, 1980) and an emission shield (Bahder, 1982) are also ways to inhibit the water treeing phenomenon.

## 2.2. Small Angle X-ray Scattering

### 2.2.1. Introduction

Small angle x-ray scattering (SAXS) is a useful and important technique for studying semicrystalline polymers. This technique has been extensively utilized for the elucidation of overall

superstructures in the range of 50 to 1500 Å, even though this indirect method of analysis sometimes contradicts the findings of direct methods such as SEM and TEM (Geil, 1963). However, the latter techniques have been also criticized for showing very localized features ranging up to few microns and being subject to artifacts generated during preparation of samples, such as microtoming. There is an additional deficiency in SAXS technique alone, since SAXS data alone may result in an ambiguity because of the nature of scattering, e.g. the principle of Babinet's reciprocity and the complexity of theory.

X-ray scattering stems from the fluctuation of electron density among the entities within a given material. It has been realized that most semi-crystalline polymers give rise to rather a broad diffraction maxima in the small angle range (ca. $1^{o}$) with diffuse scattering extending to zero degree. This type of scattering usually produces discrete scattering and is thought to be due to interference within the dense system. There is another type of scattering, diffuse scattering which may result from the presence of other entities such as microvoids or particles which tend to be dispersed dilutely throughout the material. The prime assumption of a dilute system is that the entities do not interfere with other entities within the system. The broad peaks caused by discrete scattering in a dense polymer system have been interpreted in terms of the simplest model of regularly alternating crystalline and amorphous regions, while the diffuse near-zero-angle intensities in

a polymer melt or in some polymer solids have not been interpretable using a generalized method. So far, theories and subsequent interpretations in SAXS applications have not been very conclusive. Even though the scattering theory from one case can be extended another case, most studies have been carried out for separate case.

In this review, basic scattering theory will be considered first; it forms the basis of any detailed theory. Diffuse scattering theory for the dilute system will also be discussed before reviewing scattering for dense systems. General approaches for the experimental interpretation of scattering in semi-crystalline polymers will also be discussed.

## 2.2.2. Basic Scattering Theory

Scattered waves in the small angle range are regarded as coherent, meaning that the amplitudes are additive, and the intensity is given by the absolute square of the resulting amplitude. The amplitudes are of equal magnitude (= $F_e$), and differ only in their phase $\varphi$, which, in turn, depends on the position of the electron ($\bar{r}_i$) in space and the scattered vector defined by

$$\bar{k} = \bar{S} - \bar{S}_o \qquad 2.2.1$$

$\bar{S}$ and $\bar{S}_o$ are unit vectors along the incident and scattered waves respectively. The magnitude of $\bar{k}$ is

$$k = |\bar{k}| = 4\pi/\lambda \sin \theta \qquad 2.2.2$$

where $\lambda$ is the wavelength of the x-rays, and $\theta$ is half of the scattering angle. Then, the scattered amplitude and the intensity from a collection of electrons, respectively, are given by

$$F(\bar{k}) = F_e \int_V dV \cdot d(\bar{r}) \cdot \exp(-i\bar{k}\,\bar{r}) \qquad 2.2.3$$

$$I(\bar{k}) = FF^* \qquad 2.2.4$$

$$I(\bar{k}) = I_e \int_V \int_V dV_1 \cdot dV_2 \cdot d(\bar{r}_1) \cdot d(\bar{r}_2) \cdot \exp(-i\bar{k}\,(\bar{r}_1 - \bar{r}_2)) \qquad 2.2.5$$

where $d(\bar{r})$ is the electron density at position $\bar{r}$.

The amplitude $F(\bar{k})$ of diffraction in a certain direction is the Fourier transform of the electron density distribution within the object. The intensity is also a Fourier integral, involving only the relative distance $(\bar{r}_1 - \bar{r}_2)$ for every pair of points. The double integration can be carried out using two different steps: first, summarize all pairs having equal relative separation, and then integrate over all relative separations. The first step can be carried out by adopting the operation of convolution square or auto-correlation defined by

$$\bar{d}^2(\bar{r}) = \int_V dV_1 \cdot d(\bar{r}_1) \cdot d(\bar{r}_2) \qquad 2.2.6$$

$$\text{with: } \bar{r} = (\bar{r}_1 - \bar{r}_2) = \text{constant} \qquad 2.2.7$$

The second step consists of an integration over reciprocal space, since every electron pair of relative separation r can be represented by a point in reciprocal space.

$$I(\bar{k}) = I_e \int_V dV \cdot \bar{d}^2(r) \exp(-i\bar{k}\,\bar{r}) \qquad 2.2.8$$

We can further develop the above equation by considering two different cases, since there are two kinds of inhomogenieties responsible for small-angle x-ray scattering from polymers. These are (a) alternation of crystalline and amorphous regions, which in general will possess different electron densities, and (b) the presence of small particles in a matrix such as microvoids or particles in a solid polymer matrix or crystallites in a polymer melt. In one of the cases (case (a)) SAXS is treated in terms of an one-dimensional lattice. The lattice is composed of lamellar crystals separated by intervening amorphous layers. In the other cases the system can be assumed to be randomly oriented and spherically isotropic without any long range order. The equation can be simplified for the statistically isotropic systems. In the next two sections these two cases will be reviewed individually.

### 2.2.3. Diffuse Scattering

Diffuse scattering extending to zero angle is found in a simple theoretical treatment for scattering at very small angles for

simple geometries, as summarized in Guinier's textbook (Guinier, 1955). Such theoretical treatments are normally based on the assumption that there is no interference inside the system, termed the dilute system. In a dilute system of identical particles of constant electron density d, embedded in a medium of constant density $d_o$, the difference $\Delta d = (d-d_o)$ will be relevant for diffraction. The simplest case is that of particles showing spherical symmetry, such as a sphere of radius $R_o$ and volume V. The resultant intensity was derived by Rayleigh(1911):

$$I_1(k) = (\Delta d)^2 V^2 \left[ 3 \frac{\sin kR_o - kR_o \cos kR_o}{(kR_o)^3} \right]^2 \qquad 2.2.9$$

For particles of different shape but with a center of symmetry, a similar simplification can be applied to equation 2.2.9. The phase factor exp(-ikr) can then be replaced by cos kr, giving the amplitude as:

$$F_1(k) = (\Delta d) \int dV \cdot \cos kr \qquad 2.2.10$$

$$I_1(k) = F_1^2(k) \qquad 2.2.11$$

where the integration should be carried out beyond the volume of the particle. The intensity is then found by taking the average of $F^2$ over all orientations. Many theoretical intensity functions have been calculated for simple geometries such as ellipsoids

(Guinier,1939; Porod, 1948), disks (Porod, 1948) and cylinders (Porod, 1948).

2.2.3.1. Guinier Theory

Another approach to data treatment in a dilute system uses the Guinier approximation. For the central part of the intensity function near zero-angle, a universal approximation can be made. This was first given by Guinier (1939) as

$$I_1(k) = I_1(0) \cdot \exp(-k^2 R_g^2 / 3) \qquad 2.2.12$$

with the "radius of gyration" $R_g$ as the only parameter. It is defined as the mean square distance from the center of gravity. Thus, by measuring the slope of $\ln(I(k))$ against $k^2$, the size of the particle can be evaluated in term of the radius of gyration. The governing equation for a general spherical geometry was derived as

$$\frac{I(k)}{I_1(0)} = \mathrm{Exp}\left(-\frac{1}{3} R_g^2 k^2\right) \qquad 2.2.13$$

This relationship is widely recognized to be nearly exact for a very dilute suspension of spherical particles. For other geometries similar derivations have been made. Two of the modifications that are appropriate for polymers are the geometry of narrow cylinders of diameter 2R and length 2H, and that of thin discs of diameter 2R and 2H. For long rods, the approximation can be derived as

$$\frac{I(k)}{I_1(0)} = \frac{1}{2Hk} \text{Exp}(-\frac{1}{4} R^2 k^2) \qquad 2.2.14$$

where the dimension H is extremely large with respect to dimension R. On the other hand, for discs the approximation can be made as

$$\frac{I(k)}{I_1(0)} = \frac{2}{k^2R^2} \text{Exp}(-\frac{1}{3} H^2 k^2) \qquad 2.2.15$$

which differs in that $\ln(k^2 I(k))$ of discs is linearly dependent on $k^2$, while for the rod geometry $\ln(k I(k))$ is linearly dependent on $k^2$. However, it is widely recognized that the above theoretical treatments becomes increasingly inaccurate as the suspension becomes more closely packed (Alexander, 1969).

2.2.3.2. Porod Data Treatment

Another theory that involves scattering from particles was developed by Porod (1951). This theory deals with the final slope of the intensity curve, which is related to the finer structure of the particles, due to the nature of reciprocity in dimension in scattering theory. As the scattering vector approaches large values, a simplification can be made to form an intensity function that is inversely proportional to the fourth power of the scattering vector:

$$I_1(k) = (\Delta\rho)^2 \frac{2\pi}{k^4} S \qquad 2.2.16$$

where S is the total interface. In fact it is known that this fourth power law is valid not only for single particles, but also for densely packed systems, provided that there exists a well defined fine structure.

The general case for particle scattering is best treated by the use of a correlation function $\tau(r)$ defined as the average of the product of two electron density fluctuations at a distance r.

$$\tau(r) = \langle \mu(r_1)\ \mu(r_2) \rangle \qquad 2.2.17$$

where the electron density fluctuation $\mu$ is defined as $\bar{d}$-d. The correlation function also has the property that $\tau(0) = \overline{\mu^2}$, and $\tau$ becomes 0 for large r. Then, the general intensity function for the isotropic case can be rewritten as

$$I(k) = V \int 4\ \pi r^2\ dr\ \ \tau(r)\ \exp(-ikr) \qquad 2.2.18$$

where the phase factor exp(-ikr) in isotropic system is not a function of distance r and can be replaced with the average value $\langle \exp(-ikr) \rangle$. The averaged value can also be replaced by the fundamental formula of Debye (1915):

$$\langle \exp(-ikr) \rangle = \frac{\sin kr}{kr} \qquad 2.2.19$$

By combining the appropriate equations, the intensity function can be written in the form of a Fourier transform:

$$I(k) = V \int 4\pi r^2 \, dr \cdot \tau(r) \frac{\sin kr}{kr} \qquad 2.2.20$$

On the other hand, the correlation function can also be obtained by the inverse Fourier transform given by:

$$V \, \tau(r) = \frac{1}{2\pi^2} \int_0^\infty k^2 \, dk \cdot I(k) \frac{\sin kr}{kr} \qquad 2.2.21$$

where the Debye factor sin(kr)/kr can be replaced with the simple mathematical notation of Si(kr). Due to the Si function the above functions have a special meaning for h = 0 and r = 0 and the Debye factor attains a value of 1. The above equations then become simple.

$$I(0) = V \int_0^\infty 4\pi r^2 \, dr \cdot \tau(r) \qquad 2.2.22$$

$$V \, \tau(r) = \frac{1}{2\pi^2} \int_0^\infty k^2 \, dk \cdot I(k) \qquad 2.2.23$$

$$V \, \tau(r) = V \, \overline{\mu^2} \qquad 2.2.24$$

Furthermore, from the integral part of the above equation 2.2.23, it can be inferred that, no matter what the actual structure is, the integral part must remain invariant and is directly related to the mean square fluctuation of the electron density. Thus, it is called "invariant," Q being given as

$$Q = \int_0^{\infty} k^2 \, dk \cdot I(k) \qquad 2.2.25$$

Even though the intensity function is defined as a function of h in reciprocal space, the correlation function is defined as a function of the real distance r in real space. Therefore, the interpretation of the correlation function becomes straightforward. Since these above simple forms of function are defined only for single particles without large scale interactions, a more generalized function has to be derived for interpretation of actual experimental data. Normally, the primary modification for a real system with some sort of interaction involves a certain distribution function, the surrounding function and statistical fluctuation for different phases. However, the correlation function can remain in simple form by means of the structural invariant Q, as given:

$$\tau(r) = \frac{1}{Q} \int_0^{\infty} k^2 \, dk \cdot I(k) \frac{\sin kr}{kr} \qquad 2.2.26$$

The corresponding equation for intensity is also given using a normalized correlation function $\tau_o$ that is solely dependent on the shape of the particles.

$$I(k) = V \overline{\mu^2} \int_0^{\infty} 4\pi r^2 \, dr \cdot \tau_o(r) \frac{\sin kr}{kr} \qquad 2.2.27$$

2.2.3.3. Distance Distribution Function

The intensity function has been defined as a function of both the correlation function, $\tau(r)$, and the square of distance $r^2$. This leads to the development of a new function called the distance distribution function P(r) (Porod, 1948; Guinier & Fournet 1955). The distance distribution function P(r) is defined as $\tau(r)$ multiplied by $r^2$ :

$$P(r) = \tau(r)\, r^2 \qquad 2.2.28$$

By using this function the generalized intensity function can be written in the simpler form:

$$I(k) = 4\pi \int_0^\infty P(r) \cdot \frac{\sin kr}{kr}\, dr \qquad 2.2.29$$

The relation between the scattering intensity function and the distance distribution function will be a direct Fourier transform. The scattering intensity at zero angle becomes a constant; $4\pi$ times the integral of P(r).

$$I(0) = 4\pi \int_0^\infty P(r)\, dr \qquad 2.2.30$$

In the reverse manner, the distance distribution function can be obtained by a conventional Fourier transformation:

$$P(r) = \frac{1}{2\pi^2} \int_0^\infty I(k)\cdot(kr)\cdot\sin(kr)\, dk \qquad 2.2.31$$

Due to the nature of the Fourier transformation, problems will arise from the termination effect and the influence of any remaining background scattering. These two effects may cause a strong artificial oscillation in the P(r) function that is somewhat useless. So far several techniques have been proposed for the calculation of the distance distribution function, mostly from the data obtained from the slit geometry (Glatter, 1977, 1979; Glatter & Kratky, 1982).

A quantitative classification of shape and internal structure of a particle has then been obtained directly from P(r) (Glatter, 1979). In addition, several major structural parameters can be derived from the function. For a simple system with homogeneous particles having a constant electron density of $p_c$, the distance distribution can be evaluated. The distance distribution function of a sphere has been derived (Porod, 1948) as:

$$P(r) = 12\ x^2\ (2 - 3x + x^3) \qquad 2.2.32$$

where x is r/D and D is the diameter of the sphere. This function has its maximum near r=D/2 (x = 0.525). It is known also that for any deviation from spherical shape , the ratio M (=r(max) /D) decreases in the following sequence: globular particles, flat disk particles, and rod-like particles (Glatter & Kratky, 1982).

For the rod-like particle where the cross-section A (with maximum dimension d) should be small in comparison to the length L

of the whole particle, P(r) will increase linearly with decreasing r-values, starting from r=L.

$$P(r) = \frac{1}{2\pi} p_c \cdot A^2 (L-r) \qquad 2.2.33$$

The slope of the linear part of the equation in the tail region is proportional to the area of the cross-section.

An analytical expression of the P(r) function of infinite flat particles, i.e. particles elongated in two dimensions, is given (Porod, 1948) as

$$P(r) = \frac{16}{\pi} x (\arccos x - x \sqrt{(1-x^2)}) \qquad 2.2.34$$

where x is r/D. The complex mathematical form of this function can be more easily understood by looking at the actual change of the function with distance r. For the region where r is less than the thickness of the disk d, the P(r) function will increase with the second power of r. If r > d, the increase will change more or less linearly. The situation is much clearer if the new function f(r), that is the function P(r) divided by r, is considered.

$$f(r) = \tau(r) \cdot r = P(r) / r \qquad 2.2.35$$

This function more easily shows changes dependent on the shape of disk. The curve begins with a linear increase until r approaches the thickness of the disk. After that point the f(r) function will

decrease linearly. The limiting value A of the function, obtained from an extrapolation of the linear part, will contain information about the area of the basal plane of the disk.

$$A = f(r)_{r-0} = p_c^2 \cdot V \cdot d/2 \qquad 2.2.36$$

The returning point of the F(r) function in any derivation will be the maximum dimension of the particles. The distance distribution function is also related to the radius of gyration. The square of the radius of gyration can be obtained as half of the normalized second moment of this function, viz.

$$R_g^2 = \frac{\int_0^\infty P(r) \cdot r^2 \, dr}{2 \int_0^\infty P(r) \, dr} \qquad 2.2.37$$

## 2.2.4. SAXS by Solid Semicrystalline Polymers

In most cases, SAXS by dense materials, such as solid semicrystalline polymers shows a rather broad diffraction maxima in the small-angle region. It is generally agreed that this maximum arises from periodic fluctuations of order (crystalline and amorphous regions) on the scale of a few tens or hundreds of angstroms within the system. The maximum is considered to result from constructive interference over the plane normal to the diffraction rays, according to simple Bragg's law. Bragg's law is given as

$$\sin \Theta = \frac{n\lambda}{2d} \qquad 2.2.38$$

where n is an integer, and $\Theta$ is the angle between the incident beam and the platelet, and d is a spacing or long period.

For the broad peaks, the angular position of the diffraction maxima can thus be interpreted using Bragg's law to yield the average structural period of the system.

Difficulties with the above mentioned approach using Bragg's law have been recognized as falling into two classes. First, the sizes calculated by this method do not agree with those obtained from other experiments such as SEM and TEM. One such example was reported by Geil (1964). Secondly, the treatment by this simple method may ignore additional information that can be obtained from experiment, particularly the distribution of intensity within the scattering pattern. The breadth of the peak is related to the distribution of the dimensions that causes the broad peak. However, this simple method of data treatment inhibits acquisition of the important information. These two major difficulties are further complicated by the presence of two or more maxima, which are normally referred to as first- and second-order scattering maxima, which arise from same microstructure. These two effects stimulated several investigators to consider refinements to the simple two-phase model. Tsvankin (1964) included a transition zone between crystalline and amorphous regions as a modification to a two-phase

model. There have been other modifications to explain these abnormalities (reviewed by Buchanan (1971) and Crist (1973)).

One of the most important alterations to this simple application of Bragg's Law was proposed by Hosemann (1962). He considered two independent distributions of crystalline and amorphous layers in an one-dimensional paracrystalline lattice model. The lattice is assembled by selecting amorphous and crystalline layers alternatively. The crystalline thickness, amorphous thickness and total periodic thickness of the jth lamella will be $Y_j$, $Z_j$, and $X_j$, respectively. The independent distribution of crystalline and amorphous thickness are H(Y) and h(Z), respectively. The number average crystalline thickness will then be

$$\bar{Y} = \int H(Y) \cdot Y dY \qquad 2.2.39$$

In a similar way, the number average amorphous thickness can be obtained as:

$$\bar{Z} = \int h(Z) \cdot Z dZ \qquad 2.2.40$$

The overall number average long period $\bar{X}$ and overall crystallinity $\varphi$ are given in terms of Y and Z.

$$\bar{X} = \bar{Y} + \bar{Z} \qquad 2.2.41$$

$$\varphi = \bar{Y} \; / \; \bar{X} \qquad 2.2.42$$

The width of the distribution functions can be characterized by the standard deviations:

$$\sigma_y^2 = \int H(Y) \; (Y - \bar{Y})^2 dY \qquad 2.2.43$$

$$\sigma_z^2 = \int h(Z) \; (Z - \bar{Z})^2 dZ \qquad 2.2.44$$

$$\sigma_x^2 = (\sigma_y^2 + \sigma_z^2) \qquad 2.2.45$$

The intensity function for such a lattice has been derived by Hosemann (1962) for arbitrary functions H(Yj) and h(Zj) for the case of constant electron density over the thickness of the scattering particles. His result may be written for a lattice of length L = N·X as

$$I(k) = I_\infty * |s(k)|2 \; / \; \bar{X} \qquad 2.2.46$$

where $I_\infty$ is an intensity function for an infinitely extended one-dimensional lattice and $|s(k)|2$ is defined as a shape factor that is a function solely of the overall size (length) of the lattice. The infinite intensity function $I_\infty$ is given as

$$I_\infty = \frac{\hat{}d^2}{2\pi^2 k^2} \; Re\left[\frac{(1 - F_y)(1 - F_z)}{1 - F_y F_z}\right] \qquad 2.2.47$$

where $\hat{}p$ is the difference of the densities of crystalline and amorphous region, and $F_y$ and $F_z$ are Fourier transforms of the distribution functions H(Y) and h(Z), respectively, e.g.

$$F_y = \int H(Y) \exp(-2 \pi i k Y) \, dY \qquad 2.2.48$$

Reduction of the equation leads to two different terms, one of which depends on the lattice length or the number of lamellae within a stack, i.e.

$$I(k) = I_B(k) + I_C(k) \qquad 2.2.49$$

$$I_B(k) = \frac{\hat{} d^2}{4\pi^2 k^2 X} \frac{|1-F_y|^2 \cdot (1-|F_z|^2) + |1-F_z|^2 \cdot (1-|F_y|^2)}{|1 - F_y F_z|^2} \qquad 2.2.50$$

$$I_C(k) = \frac{\hat{} d^2}{2\pi^2 k^2 X N} \; Re\left[\frac{F_z(1-F_y)^2 \cdot (1-(F_y F_z)^N)}{(1 - Fy\, Fz)^2}\right] \qquad 2.2.51$$

where $I_B(k)$ is denoted as the Babinet component and $I_C(k)$ as the crystalline component. As N becomes large enough to be effectively infinite, the term $I_C$ becomes negligible, so that the observed intensity is given entirely by $I_B$. This term has the effect of

broadening the diffraction peak and introduces a central diffuse scattering around the beam stop (Hosemann, 1962).

This generalized paracrystalline model has been considered to be more representative of the structure of the macro-lattices of semicrystalline polymers than other paracrystalline models such as the restricted paracrystalline model (Hosemann, 1962; Crist, 1973).

Several investigators have applied various distribution functions to obtain a better theoretical representation of semi-crystalline polymers. Reinhold et al. (1964) utilized a delta function of $Y_j$ for $H(Y_j)$ and an asymmetric distribution function for $h(Z_j)$. On the other hand, Tsvankin (1964) considered the SAXS of a disordered infinite one-dimensional lattice in which the amorphous thickness obeys an exponential distribution function, and the crystalline thickness is symmetric and rectangular. He also included in this model a transition region of thickness over which the density linearly increased from $p_a$ to $p_c$. Such a transition region results in a trapezoidal density profile along the lattice. The effect of a symmetric distribution of the size of the constituents of the lattice on theoretical SAXS intensity was also studied by Hosemann (1962), Blundell (1970), and Crist (1973).

In an elegant paper, Blundell investigated three types of models based on the generalized paracrystalline model for the explanation of experimental SAXS intensity of low-density polyethylene, which normally has a density of 50% (Blundell 1978). The first type consists of 'effectively' infinite stacks in which

the amorphous and crystalline thicknesses follow various combinations of Gaussian and exponential distributions. For the second type he considered a model consisting of stacks with a finite size of N lamellae. The third type consists of the volume of stacks involving localized dispersity of crystallinity, within which the amorphous and crystalline thickness vary with a Gaussian symmetric distribution. For the third type he utilized a normalized Gaussian distribution $P(\varphi)$ for the variation of local crystallinity. The overall intensity per unit volume was thought to be the volume-average of the intensities of the component single stack intensities.

$$I(k) = \int I(h,\varphi)\cdot P(\varphi)\, d\varphi \qquad 2.2.52$$

where the overall crystallinity $\bar{\varphi}$ of the system and dispersion $\sigma_c$ are given by:

$$\bar{\varphi} = \int \varphi\cdot P(\varphi)\, d\varphi \qquad 2.2.53$$

$$\sigma_c^2 = \int (\varphi - \bar{\varphi})^2\cdot P(\varphi)\, d\varphi \qquad 2.2.54$$

During data treatment, Blundell assumed that the average amorphous thickness is constant for all lamellar stacks and independent of the local crystallinity of the stack, so that the local long period will

therefore be larger in those stacks where the crystallinity is higher. For simplicity he obtained values with the intrinsic intensity of each component stack, $I(h,\varphi)$ taken to be pure Gaussian case with:

$$\sigma_y / \bar{Y} = \sigma_z / \bar{Z} \qquad 2.2.55$$

Upon comparison with experimental data, Blundell suggested that the third type is most representative of low-density polyethylene. This variable stack model was interpreted in terms of phase separation during crystallization. The first model was concluded to be the poorest and an inappropriate model for LDPE. However, he failed to ascribe a physical meaning to the various parameters within the model. In fact, the boundary of the volume of stacks in the third type is not clearly defined. For the second model it was necessary to assume the number of lamellar stacks to be unrealistically small in order to fit data properly. Blundell was also unable to obtain experimental data near the beam stop region because of the limits of experimentation. Thus, he could not compare theoretical values in this region with experimentally observed values.

### 2.2.5. General Interpretation of SAXS from Polyethylenes

Most studies of SAXS from crystalline polymers are based on the theories that were reviewed in the previous section. In some cases, experimental data has been compared with theoretical

predictions. On other occasions, some important material parameters were calculated from the scattering data on the basis of the theories. Most SAXS data from melt-crystallized polyethylene show both zero-angle diffuse scattering near the beam stop and one or more broad Bragg peaks. It is generally agreed that the broad diffraction maxima are a consequence of a regular alternation with an average periodicity of 50 to 300 Å. This arises from the presence of crystalline and amorphous regions. Even though there have been frequent discrepancies between the structural size inferred from SAXS and those from other quantitative measurements such as in electron microscopy (Geil, 1963), the application of Bragg theory to the first-order peak is accepted as giving a good measure of the average periodic repeat distance of layered structures (Alexander, 1969). However, SAXS data in general have been considered to give a wide range of information about the structure investigated.

In a series of papers by Schultz and his colleagues (1970, 1971, 1976, 1978, 1979) the SAXS data from melt-crystallized polyethylene were studied. In interpreting their data, they generally examined the following five topics.

1) Shape and slope of the zero-angle scattering curve.
2) Location of the Bragg Maxima.
3) Ratio of two intensity maxima, if present.
4) The breadths of the Bragg Peaks.
5) Integrated Intensity ($Q_o$).

For the calculation of the parameters in 2), 3), and 4), they utilized the normal two phase model consisting of crystalline and amorphous regions rather than the ambiguous modified two phase model developed by other researchers. However, in their earlier work Kavesh and Schultz (1970) reviewed the difficulties associated with the simple two phase model normally used for data measured by slit geometry, this being all that were available at that time.

One of the modifications for the simple one-dimensional lamellar model was made by Vonk and his co-workers (1973, 1985a, 1985b) in order to reduce the discrepancies in the structural parameters inferred from two different methods including SAXS. They generalized the treatment such that the variation in density between the amorphous and the crystalline area was generated by an arbitrary function. They assumed that the density changed gradually from the amorphous to the crystalline phase. They obtained the thickness of the diffuse transition layer, E, from the SAXS pattern by fitting SAXS data in an I vs. $1/k^2$ plot (Vonk, 1973). However, this treatment has been criticized in that the result is very sensitive to the position of the background in the SAXS pattern (Roe, 1982).

In a recent paper Vonk and Pijpers (Vonk, 1985a) calculated other structural parameters from the one-dimensional correlation function $\tau$, which was obtained directly from the smeared intensity function after subtraction of the background. A schematic presentation of such correlation functions for crystallinities of 0.2 and 0.4 is given in Figure 2.2.1. The first minimum with a

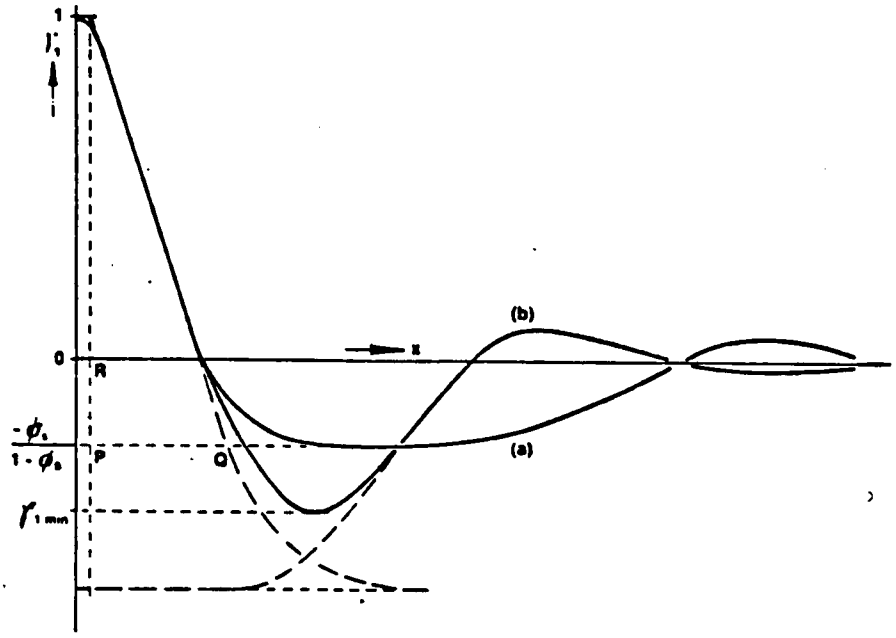



Figure 2.2.1 One-dimensional correlation function of an ideal lamellar structure: (a) crystallinity 0.2, (b) 0.4. (Ref. Vonk, 1985b).

horizontal region, they associated with the crystallinity $\varphi$ through $\tau = -\varphi/(1-\varphi)$ if $\varphi < 0.5$, or $\tau = -(1-\varphi)/\varphi$ if $\varphi > 0.5$. If, however, this horizontal region is followed by a neighboring maximum, they concluded that the baseline at $-\varphi/(1-\varphi)$ or at $-(1-\varphi)/\varphi$ is below the value $\tau_{min}$ of $\tau$ at the first minimum. In that case $\varphi$ has a interval such that $\varphi_{min} < \varphi < 1-\varphi_{min}$ where $\tau_{min} = -\varphi_{min}/(1-\varphi_{min})$. They also obtained the specific surface, S/V, of the boundary layer from the same fitted one-dimensional correlation function, using the following equation.

$$\left.\frac{d\tau}{dx}\right|_{x>E} = -\frac{S}{2V}\Big/\left(\varphi(1-\varphi) - \frac{E}{6}\frac{S}{V}\right) \qquad 2.2.56$$

For the ideal lamellar structure, where the lamellar stacks are large enough not to affect the small angle scattering, they derived the equation for the evaluation of the number average long periodicity $\langle L\rangle_n$ by

$$S / V = 2 / \langle L\rangle_n \qquad 2.2.57$$

However, they utilized Bragg theory to determine the weight average long periodicity $\langle L\rangle_w$. The ratio $\langle L\rangle_w / \langle L\rangle_n$, which must be greater that 1, was identified with the polydispersity of the identity periods. They also obtained a number--averaged crystal thickness, $\langle T_c\rangle_n$ , from the one dimensional correlation function (Vonk, 1985a). There are other parameters that have been derived from the SAXS pattern by many investigators. However, the most informative but

controversial parts are zero-angle intensity and the invariant Q. In the next two sections we will review the treatment of SAXS data near the beam stop and invariant, using examples from a series of works by Schultz et al. (1970, 1971, 1976, 1978, 1979).

2.2.5.1. Near Zero Angle Intensity of SAXS of Solid Polymers

The interpretation of the diffuse scattering extending to zero degree has not been agreed upon among its investigators. Part of the reason is that the zero angle intensity is hard to measure and even measured intensity at room temperature is not all that outstanding. Furthermore, the Lorentz correction, which is necessary for the interpretation of non-spherically symmetric systems such as solid polymer particles, makes this zero scattering intensity negligible. Another reason appears to arise from the fact that there may be interparticle interference in a solid polymer. This makes the theoretical interpretation, as well as theoretical and quantitative analysis of SAXS data very complicated.

In the works by Schultz and his co-workers (1976, 1978) diffuse zero-angle scattering intensity was considered in the interpretation of structural data from melt crystallization. Later, they also utilized this interpretation for their zero-angle scattering intensity data at room temperature measured for melt crystallized polyethylene (McCready, 1979).

In the course of a dynamic study of high density polyethylene from the melt, Schultz and his co-workers (1978) carried out in situ experiments utilizing the ORNL 10-meter SAXS camera. Specimens were

rapidly cooled in the x-ray beam in a tandem birdcage furnace from 180°C to a temperature between 115°C and 126°C, and scattering patterns were recorded for 30 seconds in 50 seconds intervals. They prepared the Lorentz corrected scattering curves. The patterns were observed to be a superposition of diffuse scattering extending to zero angle and a Bragg maximum. At high crystallization temperatures, or at short crystallization times at each crystallization temperature (ranging from 118°C to 124°C), they found that the scattering curves decreasing monotonically from zero angle. As crystallization proceded, the zero hump was seen to develop on the zero angle peak and grow ultimately into a Bragg maximum. This phenomenon was noted to occur at the expense of the zero-angle peak.

They suggested that 'zero angle scattering be emanated from amorphous gaps in the lamellar stacking within a spherulite.' As for reasoning for this interpretation, they provided the following three hypotheses, which they proved in the same paper (1978).

1) The zero angle scattering should yield a straight line Guinier plot.
2) the Guinier plot, interpreted in terms of scattering by isolated platelets, should give a platelet thickness value similar to that found for crystalline platelets at the same temperature.
3) The Guinier slope (i.e. the platelet thickness) should be invariant with time for each isothermal crystallization.

In addition to proving the above hypotheses, they calculated the dimensions of platelets from the Guinier slope (which was found to be constant at the given temperature) using the following equation.

$$l_g = \frac{\sqrt{3}}{\pi} \sqrt{d\{ \ln[ k^2 I(k)]\}/ dk^2} \qquad 2.2.58$$

where $l_g$ is the dimension (thickness) of the platelets and k is a scattering vector. This relationship is known to be nearly exact for a very dilute suspension of the platelet system (Guinier, 1955). The platelet thickness $l_g$ was found to range from 167 to 267 Å.

In a later work (Shultz, 1979), it was noted that one of the prime observations was 'diminishing a diffused scattering extending to zero angle as crystallization time is increased.' This was found for SAXS patterns of samples crystallized at high temperatures but measured at 'room temperature' without Lorentz correction, which was considered in a former work (Schultz, 1976). If corrected, the zero angle intensity will not show any slope, as observed in the former work, but will show a tiny hump at the angle near the beam stop due to the factor of $k^2$. However, they claimed that the diminishing of the zero-angle peak signifies that new crystallites have grown within the gap.' Another consideration to be made is that 'diminishing in a linear manner' does not necessary mean 'reducing slope of the Guinier plot in a logarithmic scale'. There is a big difference in dimension between linear and logarithmic scales. In other words, $\{\ln I_1 - \ln I_2\}$ is not $\{I_1 - I_2\}$, but $\{\ln[I_1/I_2]\}$. The

plot, in fact, appears to show an increase of the slope in a logarithmic scale with crystallization time.

Similar change in SAXS pattern upon crystallization of polyethylenes was noted by Song and his co-workers with synchrotron radiation (Song, 1988). They agreed that the change of in-situ SAXS patterns with crystallization reflects a transition from the single particle scattering pattern to an interference pattern. However, they could not get the corrected intensity, $I(k)\cdot k^2$, to yield a straight line in the Guinier Plot as did Schultz (1978). They suggest that the scattering pattern change reflected structural change from a disordered lamellar structure, with a broad distribution of lamellar spacing and a large amount of amorphous gap, to well-defined lamellar stacks.

2.2.5.2. The Integrated Intensity, Q

The integrated intensity, Q (in photons per second) is obtained from the circularly averaged numerical SAXS intensities, I(k), using

$$Q = 4\pi \int_0^\infty k^2 I(k)\, dk \qquad 2.2.59$$

where k is a scattering vector as introduced in equation 2.2.1. For a system of two phases separated by sharp interfaces such as crystalline and amorphous phases in a simple two phase model, there exists a general relationship among $Q_o$, the absolute density

difference ( $d_c$ - $d_a$) between two phases, and the volume fractions, $\varphi c$ and (1 - $\varphi c$), of the phases (Guinier, 1955):

$$Q = [ N_a (Z/M)]^2 (d_c - d_a)^2 \varphi c(1 - \varphi c) \qquad 2.2.60$$

where $N_a$ is Avogadro's number and Z and M are the number of electrons per molecule and the molecular weight of the material, respectively. For relative comparison, M and Z do not have to be specified.

The integrated scattering intensity has been used as a measure of the scattering power of the material to be inspected. A plot of the integrated intensities and temperature or time reflects the kinetic behavior of the material at the specific conditions (Song, 1988; Kawaguchi, 1984).

During in-situ investigations, Schultz and co-workers (Schultz, 1978) noted two major effects concerning SAXS intensity: the integrated intensity diminishes and the ratio of first and second-order Bragg maxima decreases, during cooling. Due to the nature of in-situ experimentations, the areas under these curves represent relative and comparable values of the integrated intensities with time. An integrated intensity plot with actual angles on the x-axis, instead of the usual scattering vector, reveals that the area under the intensity plot measured at 121$^{o}$C is much larger than that measured at room temperature (c.a. 4 times).

On the other hand, normal crystalline peaks in WAXS usually decrease in area with temperature, indicating a reduction in the

volume fraction of the crystalline phase. The opposite behavior in the SAXS curve should not be surprising due to the nature of the integrated SAXS intensities (reciprocity) as shown in equations 2.2.60. Schultz also explained this phenomenon to be related to a decrease in the degree of crystallinity by noting 'an increase in $\varphi c$ above 0.5 results in decreasing $Q_o$, as observed'. However, all the values of crystallinity in this case were not necessary smaller than 50%. Earlier work by Kavesh and Schultz (1971) shows that the bulk density measured at 120°C is 0.91 $g/cm^3$ and that of room temperature is shown to be 0.97 $g/cm^3$ (Kavesh, 1971). On the other hand, a more recent paper by the same group (McCready, 1979) shows that calculated theoretical mean densities of amorphous and crystalline phase of the same material at room temperature are 0.829 and 1.0005 $g/cm^3$, respectively. With the aid of this recent data, the overall density change from room temperature to 121°C is calculated to correspond to a change in crystallinity from 81% to 46%. The variation of these values shows that, during experiment, the actual crystallinity passes through the value of 50%, which is thought to be critical (Schultz, 1978). For a more detailed analysis of the invariant $Q_o$, the density difference between two phases at different temperatures must be assessed.

A possible solution to the above mentioned contradictions may be the presence of a third phase, such as microvoids, and/or the presence of a non-discrete boundary between the amorphous and the crystalline regions. Beginning in the 1950's, there have been many

papers concerning the contribution from microvoids in polymeric materials. For scattering generated by a natural and artificial fiber, it is well known that the presence of microvoids, even less than 1% of the total volume, will cause a large amount of diffuse scattering at the equatorial region (Statton, 1962, 1965; Hermans, 1959) due to the large degree of density difference between voids and other phases. During crystallization, formation of microvoids is very likely because of a contraction from the amorphous or partially melted regions. Densities of the amorphous phases or melt phases are smaller than those of the crystalline region. In other words, the specific volume of loosely packed regions is larger than those of crystalline regions. If the fraction of microvoids has any effect on total scattering intensity, it will contribute to the diffused scattering extending to zero angle and initial stage of Bragg maxima.

The other factor to be considered is the temperature factor, as reported by Raman et al. (1977) and by Zubov et al. (1967). Beyond the crystallization temperature of 120°C, chain mobility increases due to a greater freedom on the internal rotation around a single bond. This thermal vibration, which causes irreversible structural modification, may cause additional scattering which was not accounted for in the comparison of whole data. For the same reason, the invariant methods suggest the possibility that there must be some other phase which will account for the difference

between the simulated numerical data and the experimentally obtained data.

## 2.3. Polyethylenes Used in Cable Insulation

### 2.3.1. Introduction

The polymer pre-breakdown phenomenon known as treeing has been a cause of the concern within the cable industry, as discussed in the preceding section. Despite many studies devoted to this problem the phenomenon of treeing is still poorly understood. A major reason for this is considered to be the poor understanding of the structure and properties of the materials used in this application. It is widely realized that sound understanding of these materials is crucial to the elucidation of this degradation phenomenon and the prevention of the problem.

In this section, the general understanding of the polyethylenes used in the cable insulation will be reviewed with a special emphasis on crosslinked polyethylene. However, the simple chemistry of low-density polyethylene and linear-low-density polyethylene will be also discussed.

### 2.3.2. Low-Density Polyethylene

Polyethylene is a partially crystalline thermoplastic, polymerized from ethylene gas at a controlled temperature and pressure with a catalyst in a continuous process. Upon exposure to the catalyst and heat, a carbon-to-carbon chain reaction occurs producing large polymer molecules. Basically, there are two common

methods of making polyethylene: high-pressure and low-pressure method. The base material for most crosslinkable polyethylenes is prepared using the high-pressure method. In the high-pressure method, polymerization occurs randomly and continuously. The product is highly branched and has a limited density. Also, the material has good clarity, toughness, and flexibility. The resins prepared using this method are commonly known as conventional low-density polyethylene, with a range of density of 0.91 to 0.925 g/cm3 (Glover, 1986).

During the polymerization, the molecular weight, its distribution, crystallinity and long chain branching of the resin are determined by the reaction pressure, temperature, and type and concentration of the initiator. In order to keep the molecular weight essentially constant with varing pressure or temperature, a certain amount of chain transfer agents are added.

The homopolymerization of ethylene by the free radical mechanism can be characterized by three different steps, so called, initiation, propagation and termination steps. Initiation of polymer radicals is normally performed either by thermal energy or by sources of free radicals such as organic peroxides. Chain growth takes place by the successive addition of ethylene units to the growing chains. The growth of these polymer chains is finally terminated by addition or disproportionation of radicals.

During the polymerization process branching reactions occur by either intra- or inter-molecular chain transfer. The intra-molecular

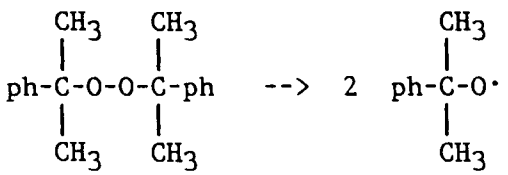
type of chain transfer causes short chain branching, while the inter-molecular type leads to long chain branching. Branching is known to influence the physical properties and rheological properties.

## 2.3.3. Crosslinked Polyethylene

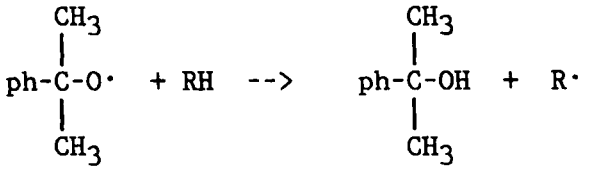
### 2.3.3.1. Crosslinking

Crosslinkable polyethylene resins are supplied as a compound of low-density polyethylene and cross-linking agents. Thus, polyethylene can be crosslinked, converting it from a thermoplastic to a thermoset. This is done by the addition of crosslinking agents, normally peroxides. Moderate doses of irradiation via an electron beam can also lead to a crosslinked polyethylene.

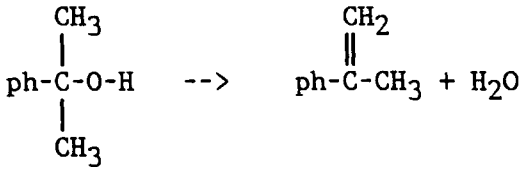
Peroxide crosslinking proceeds through first order decomposition of peroxide. This decomposed agent, then, abstracts protons from polyethylene, forming macroradicals. Combination of these macroradicals results in tetrafunctional crosslinking. The chemical scheme of dicumylperoxide (DCP) crosslinking, which is most widely known as the peroxide crosslinking procedure, is given as follows (DeBoer and Pennings, 1976):



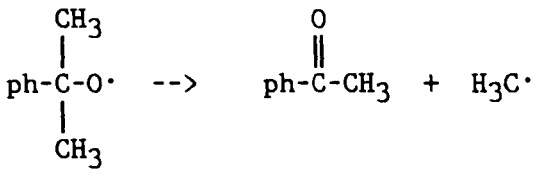
2.3.1



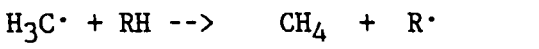
2.3.2



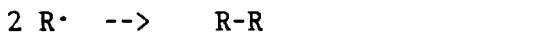
2.3.3



2.3.4

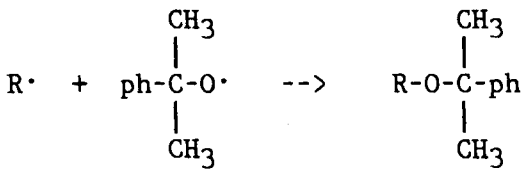


2.3.5

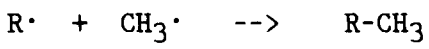


2.3.6

During peroxide crosslinking, chemical modification of the polymer chains can occur by combination of polymer radicals with peroxy or methyl radicals:

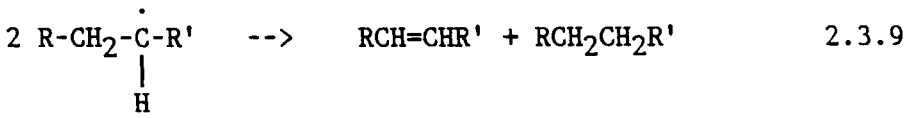


2.3.7

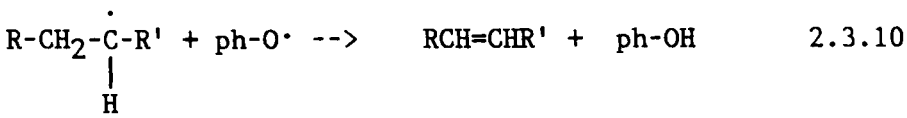


2.3.8

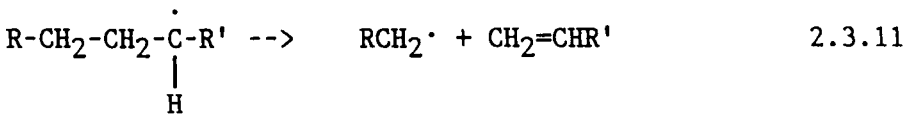
There are other possible reactions involving the macroradicals such as disproportionation, unsaturation, and β-scission as given:



$$2\ R\text{-}CH_2\text{-}\dot{C}H\text{-}R' \longrightarrow RCH{=}CHR' + RCH_2CH_2R' \qquad 2.3.9$$



$$R\text{-}CH_2\text{-}\dot{C}H\text{-}R' + ph\text{-}O\cdot \longrightarrow RCH{=}CHR' + ph\text{-}OH \qquad 2.3.10$$



$$R\text{-}CH_2\text{-}CH_2\text{-}\dot{C}H\text{-}R' \longrightarrow RCH_2\cdot + CH_2{=}CHR' \qquad 2.3.11$$

On the other hand, dicumyl peroxide (DCP) crosslinking generates some other by-products such as hydrogen, methane, ethane, acetone, phenol, methanol, water, α-methylstyrene, cumylalcohol and acetophenone (Wagner and Wartusch, 1977; Kato, 1987). Especially, cumylalcohol and acetophenone are considered the main components from the decomposition of DCP as shown in equations 2.3.2 and 2.3.4.

Additives other than crosslinking agent used in the manufacturing of crosslinkable polyethylene include antioxidants, UV protector, fillers, color addition, slip agent, anti-block agents, and photodegradable agents (Glover, 1986).

Crosslinkable polyethylenes are used mainly for wire and cable coatings because of their good dielectric, thermal, and mechanical properties. The resins range in melt index from less than 1 g/10 min

to 2 g/10 min. Resins with low melt index are used for cable insulation and jacketing to give toughness and abrasion resistance.

2.3.3.2. Effects of Crosslinking

The effect of crosslinking on the properties of LDPE has been reported in a extensive way. However, most studies proved that the actual effects have to be understood through consideration of the different types of PE used and the methods of the crosslinking process. Peroxide crosslinking of LDPE, for instance, has been considered to reduce the melting point (Kao and Phillips, 1986; Narkis, 1987) and crystallinity (Vatansever, 1987; Narkis, 1987; Salyer, 1983), to improve some mechanical properties (Andreopoulos and Kampouris, 1986; Narkis, 1987), and to enhance solvent resistance (Manley and Qayyum, 1971). Crosslinking was also reported to cause chain scission of low-density polyethylene from the difference of molecular weight distribution of LDPE and sol fraction after crosslinking (Kato, 1987).

Kao and Phillips (1986) reported that the melting point of crosslinked polyethylene and the gel fraction of crosslinked polyethylene decreased as the amount of DCP used during crosslinking increases. They also noted that the percent of extractable (sol fraction) is dependent on the level of dicumylperoxide present. From the experimental results they speculated a possible phase separation of sol and gel in the melt and put an emphasis on the importance of the amount of sol fraction in their crystallization and melting behavior.

The crystallization kinetics of whole or gel fraction of crosslinked polyethylene was further reported to be different from those of noncrosslinked system (Phillips and Kao, 1986). Phillips and Kao's analyses of crystallization kinetics of crosslinked polyethylene and their gel fractions show that the estimated values of $\sigma\sigma_e$ are comparable with those obtained for linear polyethylene at Regime III transition. On the contrary, the corresponding values of noncrosslinked polyethylene and sol fractions alone were noted to have reasonable values of $\sigma\sigma_e$ when Regime II was assumed. They also reported that literal interpretation of the Avrami exponents indicates a sheaf-like morphology for low levels of crosslinking which changes to fibrillar as crosslinking density increases. They claimed that the crosslinking agent (DCP) also serves as a nucleating agent for polyethylene.

The effect of crosslinking by two different methods such as irradiation and peroxide has been recently reported by Narkis and his colleague (1987). Their results showed that the crosslinking density can be enhanced by the increase amount of irradiation or by increasing the level of DCP present, but the maximum attainable gel content by peroxide crosslinking was higher than that by irradiation. Melting point depression by thermal crosslinking was observed for all three different types of polyethylene-UHMWPE, HMWPE, and NMWPE. However, the melting points of the polyethylenes cured by irradiation were noted to show a complicated feature. First run of the thermal analysis showed an increase of melting point as

the amount of dose increased, but the second run showed the reverse trend. The results were attributed to the fact that crosslinking in the solid state, such as irradiation, enhanced crystal perfection due to the scission of strained tie-molecules in the amorphous region. On the other hand, the peroxide crosslinking was viewed as a more homogeneous process, resulting in uniform crosslinking throughout the material. Once polyethylene crosslinked by either method crystallizes from the melt, the effect of the level of crosslinking on the melting point was noted to be same.

Narkis and his colleague (1987) also reported that the effect of crosslinking on the mechanical properties depends on the types of polyethylene and curing methods. UHMWPE and HMWPE showed drastic decrease in tensile strength at break, whereas NMWPE showed a slight increase. The yield strengths of all types of thermally crosslinked polyethylene was reported to decrease with the amount of crosslinking. However, the radiation cured polyethylenes showed increased values of yield strength. These complex features were interpreted from the view point of the material structure, stating that the yield strength is directly related to the degree of crystallinity whereas tensile strength at break depends on the polymer drawability, where strain hardening is in effect.

Similar results of the effect of crosslinking on the mechanical behavior were described by Andreopulos and Kampouris (1986). They prepared samples by crosslinking low-density polyethylene with DCP. Their results showed that the tensile

strength and elongation at room temperature increased with increase of the gel content whereas the Young's modulus decreased.

2.3.3.3. Morphology of XLPE

Morphology of polyethylene has been studied generally for high and low-density polyethylene. The general understanding of LDPE morphology is that most of LDPE is spherulitic. Spherulites are considered to be formed from the melt in the absence of significant stress by either homogeneous or heterogeneous nucleation. The crystals, formed initially either by foreign nuclei or its own nuclei, spawn new crystals alongside them, leading to the development of a sheaf and ultimately to the spherulite. The characteristic internal shape is that of a thin long ribbon-like structure known as a lamella.

In a series of paper, Phillips and Gohil (1986a, 1986b) reported the morphology of low-density polyethylene and crosslinked polyethylene. They carefully prepared samples for electron microscopy with an etching-replicating technique. They described that the branched polyethylene and the sol fraction of the crosslinked polyethylene showed well-developed banded spherulites over the whole range of crystallization temperatures ($T_c$= 88$^{o}$C - 104$^{o}$C). They also noted that there are regions where the regular banding is disrupted and relatively linear growth has occurred. These irregularities were noticed to increase with the increase of crystallization temperature. The overall size of spherulites varies from 10 to 15 μm. The band periodicity in the spherulites was

associated with the crystallization temperature, ranging from 0.6 to 1.5 μm.

Crosslinked polyethylene, on the other hand, was reported to have a sheaf- or bundle-like morphology over the entire range of crystallization temperatures from 88°C to 104°C. Even though the crosslinking was done by the introduction of a small amount of DCP, the effect of the crosslinking on the crystallization kinetics and over-all morphology was noted to be remarkable. It was also stated that the size of the sheaves is in the range of 2 to 6 μm and the ultimate size of this growth feature is five times smaller than the spherulites produced in the uncured LDPE counterpart. Crystallization at a higher temperature ( > 102°C) resulted in formation of banded sheaves, whose periodicity is considerably smaller than the branched counter-part polyethylene (0.8 to 1 μm). The presence of 'S' shaped lamellae were also observed that were thought to be characteristic of the twisting nature of the lamellae. The absence of lamellar banding in the sheaves of the gel fraction of crosslinked polyethylene was thought to be attributed to pre-existent tie-molecules, which are an inherent feature of network junctions in a crosslinked system.

In the comparison of morphologies in branched and crosslinked polyethylene, Phillips and Gohil considered that the absence of banded spherulites in crosslinked polyethylene is due to the lack of long range mobility and the presence of pre-existing tie-molecules amongst the growing lamellar crystals. The introduction of a small

amount of crosslinking was also considered to result in an increase of nucleation density.

However, their DSC results indicate that the introduction of crosslinks does little to alter the basic nature of the thermal behavior, except that the returning melting point of crosslinked polyethylene is about 5°C lower than that of the uncured material. Their DSC results were interpreted as indicating that the nature of the lamellae as well as the distribution of the surrounding amorphous region was not changed drastically.

The observation of similar morphologies, such as sheaf-like morphology or lamellar bundles, for various crosslinked low-density polyethylenes was also remarked on a paper by de Ballet (1987). In a recent publication the sheaf-like morphology was also confirmed for extruded XLPE cable insulation (Vatansever, 1987; Phillips, 1988). It was noted, however, that the sheaves do not usually fill the entire volume of the material and the intervening space is filled by worm-like lamellae. In addition, the crystal thickness of the commercially available extruded materials was estimated to be in the range from 70 Å to 85 Å according to the location of the sample within the cable.

2.3.3.4. Degradation of XLPE

The major degradation problem in crosslinked polyethylenes used for cable insulation is thermal degradation and oxidation. Joule heating by the dissipation of electric energy under the normal operation conditions cause overheating of the material in service.

To achieve satisfactory operation of electrical equipment, the insulating materials have to show thermal stability and retain their properties at elevated temperatures. Furthermore, cable insulation material may be exposed occasionally to even higher temperatures, up to above 150°C for, relatively short periods of time during the joining procedure of cables (Kato, 1987).

Recent reports regarding the importance of oxidation to the formation and growth of trees have generated major concern regarding the role of oxidation in the general performance of polyethylene insulation. (Shimizu, 1985, 1987; Garton 1986; Henkel and Müller (1985). An initial FTIR study by Bamji and his colleague (1984) showed that the water-treed region of field aged cables revealed evidence of some oxidation and that it was more prone to oxidation than the non-treed region, as observed by shorter oxidation induction times. A later report by the same group (Garton, 1986) showed more definite evidence that supported their earlier assertion. They observed strong absorption peaks at 1725, 625, 1130, and 1610 $cm^{-1}$ in the treed region in their FTIR study. They considered that the carbonyl (1725 $cm^{-1}$), sulphate (615 and 1130 $cm^{-1}$) and carboxylate ions (1610 $cm^{-1}$) caused these peaks, indicating oxidation during water treeing. Shimizu et al. (1985) concluded that chemical scission of the polymer chain caused by carriers injected from the conductor is the first stage of tree initiation and that the presence of oxygen accelerates the channel growth due to the formation of radicals by the oxygen.

Röhl and Andreß (1985) investigated the thermo-oxidation degradation process of low-density polyethylene by means of UV spectroscopy. They found the absorption maxima of the spectra at the wavelength of 217 nm, corresponding to the absorption of carbonyl groups, on a slab that had been exposed to atmospheric air at a temperature of 90°C for 600 hours. They noted that only the surface had such damage, indicating that penetrating oxygen plays an important role. The oxidation processes for crosslinked polyethylene have been considered as follow:

$$RH \rightarrow R\cdot \qquad 2.3.12$$

$$R\cdot + O_2 \rightarrow RO_2\cdot \qquad 2.3.13$$

$$RO_2\cdot + RH \rightarrow ROOH + R\cdot \qquad 2.3.14$$

where RH is denoted as the polymer chain. The reaction 2.3.13 is a fast process so that reaction 2.3.14 determines the rate of whole oxidation of the polymer without antioxidant. The role of antioxidant, that was denoted as IH, in an inhibition process was also discussed:

$$R\cdot + IH \rightarrow RH + I\cdot \qquad 2.3.15$$

$$RO_2\cdot + IH \rightarrow ROOH + I\cdot \qquad 2.3.16$$

For the cured polyethylene the oxidation was reported to occur more rapidly than for the uncured counterpart (Crine and Duval, 1985). According to their oxidation induction time results, the uncrosslinked sample with antioxidant is oxidized after a much longer time than XLPE even with double antioxidant content, indicating that the crosslinking process modifies the oxidation process. The IR absorption peak at $1720cm^{-1}$ also supported this finding. It was thought that the crosslinking hinders the phenolic chain breaking function of the thiobisphenol antioxidant, that had been used in their experiment, reducing the functionality of antioxidant. In their study of the autoxidation of polyethylene, Winslow and co-workers (1966) found that attack of oxygen occurred primarily in the crosslinks within the amorphous region. They also noted that during oxidation, oxygen-induced crystallization occurred, resulting in the increase in density. Oxidative crystallization was thought to result from scission of constrained chains in the amorphous region.

Kato and Miyashita (1987) examined possible chemical reactions at high temperatures above $150^{o}C$. They reported that water was formed in chemically crosslinked polyethylene at a high temperature. The water was considered to be formed from the dehydration reaction of cumylalcohol, one of the main by-products of the DCP crosslinking, in the presence of a certain kind of antioxidants, even though the cumylalcohol itself is quite thermally stable in the normal crosslinking condition. However, it has been also pointed

out that dehydration of cumylalcohol normally occurs under acidic conditions, which can be attained from the presence of a phenolic antioxidant that donates $H^+$. Thus, it was concluded that prevention can be achieved by the use of other types of antioxidant that are very weak $H^+$ donors. In another study of the water formed from the dehydration of cumyl alcohol, it was reported that a large number of voids form under low water diffusion during the cooling process (Miyashita, 1985).

Thermal aging was also reported to cause structural modification for the extrudated XLPE insulation (Vatansever, 1987; Phillips, 1988). Major discernible aging effect on the morphology was noted in their thermal studies as a change from a broad melting curve to a curve showing multiple melting peaks. Their TEM results, however, reveal no major change in morphology, the only difference lying in the generation of short stacks of thicker lamellae on a scale much smaller than the sheaf size when aging was carried out at 107°C. They stated three basic mechanisms for aging - perfection of existing crystals, recrystallization, and sol-gel immiscibility. They also confirmed their early finding of sol-gel separation in the temperature range of 100 -109°C in the form of clusters or microdroplets. The effect of annealing on the electrical properties was reported to depend on the aging temperature. Aging below 98°C was noted to result in a reduction in dielectric strength caused by microvoid generation, whereas the opposite effect was noted for aging at higher temperatures.

2.3.4. Linear Low Density Polyethylene

Linear-low-density polyethylene (LLDPE) is produced by the copolymerization of ethylene with various alpha-olefins at relatively low temperatures and low pressures. Complex Ziegler-Natta type catalysts are used for the polymerization in either gas phase fluidized bed reactors or liquid phase solution reactors. By contrast, conventional LDPE is produced at very high pressures from ethylene alone, using air (oxygen) or other catalysts (Johle, 1986).

Some LLDPE can be produced in a swing facility which can also produce conventional high-density polyethylene with different catalysts. A swing facility usually utilizes a gas phase fluidized bed reactor. The density of the LLDPE (generally 0.916-0.930 $g/cm^3$) is determined by the substance and the amount of alpha-olefin comonomer, which generally ranges from 6 to 9 weight-percent.

LLDPE contains short chain branches, while LDPE contains long chain branches. The length of short chain branches in LLDPE depends upon the alpha-olefin used as a comonomer. The comonomers generally used are butene, hexene, and octene. Octene is often used in the liquid-phase solution process and either butene or hexene in the gas phase fluidized bed reactor.

The length of comonomer, which determines the length of the side chain, also has an effect upon the properties of the end products produced from the resin. Increasing the side chain length by two carbon atoms increases both impact and tear resistance by about 30%. Property improvement using hexene as the comonomer in

place of butene is large. However, property improvement by using octene over hexene is much less.

Films made from LLDPE are known to offer advantages over those made from LDPE through better puncture resistance, higher elongation, and improved tensile properties (Johle, 1986). LLDPE also has a higher melting temperature than LDPE with the same density so that thermal stability improves.

# 3. EXPERIMENTAL

## 3.1. Materials

The materials used in this research are three different grades of crosslinked polyethylene and one grade of linear-low-density polyethylene. All four grades are manufactured by Union Carbide Corp. especially for application as electrical insulation. The three grades of crosslinkable polyethylenes studied are (a) conventional HFDE-4201, (b) super-clean HFDE-4201 EC and (c) tree retardant UCAR TR-4202 EC. One grade of LLDPE is UCAR TR-7521. The manufacturer's specifications and known properties of these polymers are presented in Table 3.1.1.

All three grades of XLPE are low-density polyethylene mixed with two percent by weight of dicumyl peroxide (DCP). One of the three grades of crosslinkable PE (UCAR TR-4202 EC) is claimed to have superior dielectric properties and high resistance to the formation of water trees. This material is an unfilled insulation compound designed to provide improved performance, in power cable rated at 5 kV or higher, in service involving exposure to water. This light tan compound is claimed to have an extremely low level of contamination and bears the designation EC (extra clean).

Super-clean HFDE-4201 EC is also low-density, crosslinkable, unfilled polyethylene designed for high voltage (5kV and higher) power cable insulation. This material is specially designed for

Table 3.1.1 Comparison of polyethylene used in this work.

| | TR-XLPE | EC-XLPE | N XLPE | TR-LLDPE |
|---|---|---|---|---|
| Grade Code | TR-4202 EC | HFDE-4201 EC | HFDE-4201 | TR-7521 |
| Melt Index | | | | 0.7 |
| Density ($g/cm^3$) | 0.92 | 0.92 | 0.92 | 0.92 |
| Tensile Strength (Mpa) | 20.1 | 16.8 | 16.8 | 15.8 |
| Elongation (%) | 620 | 550 | 550 | 700 |
| Dielectric Constant60 Hz | 2.3 | 2.3 | 2.3 | 2.3 |
| Dielectric Strength 50 mils | | | | 1090 |
| Dielectric Strength 125 mils (V/mil) | 660 | 550 | | |

insulation requiring a high degree of cleanliness and has an extremely low level of contamination. HFDE-4201 EC is thought to be essentially the same compound as normal HFDE-4201 except having a low level of contamination. All extra-clean grades of compound were established through a strict standard for cleanliness. Throughout the production process of the pellets of extra-clean grade of polyethylenes which involves totally stainless steel construction, the compound is subject to visual pellet inspection and examination of extruded tape under magnification. A continuous side-stream of the pellet is also viewed by an electronic pellet inspector.

UCAR TR-7521 is a tree-retardant extrusion compound based on linear-low-density polyethylene (LLDPE) manufactured by the UNIPOL process. It is designed to provide extended life to medium voltage cables which might be in contact with water. It contains tree retardant additives as well as a non-staining anti-oxidant. It also has a low level of contamination and is of special importance since production of conventional LDPE for XLPE is much more expensive than LLDPE. There is a possibility that LLDPE having a melting point 10°C higher than XLPE will be able to function well enough without the necessity of crosslinking.

## 3.2. Sample Preparation

### 3.2.1. Molding

Most specimens were prepared by compression molding. Commercial pellets of XLPE obtained from the manufacturer were

placed between two preheated platens at 135°C for about 10 minutes and pressed for a few minutes with an applied force of 20 tons to form initial molded sheets. The sheets were quenched to room temperature by circulating cold water through the pipe within the heating platens. The thickness of the initial molded sample was varied for the specific experiment to be carried out with a given specimen. Specimens for small angle x-ray scattering experiments were molded to have a thickness of ca. 1.5 mm. On the other hand, specimens for infrared spectroscopic study or breakdown strength measurement were prepared to have a thickness of 1 to 5 mils by compression molding. The LLDPE samples were also prepared by compression molding using the above conditions, however a molding temperature of 145°C was used.

Curing of XLPE was performed by holding the sample in a compression mold under the same force used for molding but at 200°C for 5 minutes. The sheets were then quenched to room temperature by circulating cold water inside the platens. During curing, two sheets of polyimide film were placed at the upper and lower boundaries between the molten polymer and the preheated platen to reduce sticking.

### 3.2.2. Annealing Procedures

Annealing is known to take place when a polymer is held at a temperature below its melting point. In a sense, annealing is heat treatment without large-scale melting. Annealing of semi-crystalline polymers is also defined as partial melting and recrystallization.

In that definition annealing occurs within the melting range. This partial melting followed by recrystallization of the melted portion causes structural rearrangement, elimination of stress and production of imperfections within a material.

During normal operation of any electrical equipment, joule heating is generated due to the power loss. Normally, this newly created heat is transferred to the electrical equipment including the insulation. Thus, thermal stability is one of the major functions to be satisfied by any insulation material. It is known that during heavy load periods, the internal temperature of high voltage insulation cables reaches 90$^{o}$C or even higher.

Annealing has been carried out for all grades of sample to look into the effect of the annealing on the structure and the properties. A typical annealing experiment was carried out by placing a small strip of sample in a glass tube. The glass tube was then held in a preadjusted constant high temperature bath controlled to $\pm$0.5 $^{o}$C for a prescribed period of time. Annealing temperature was determined using a digital thermometer having its thermocouple in contact with the sample in the glass tube. After keeping a sample in the high temperature bath for the desired period of time, they were allowed to cool to ambient temperature.

## 3.3. Characterization

### 3.3.1. Infrared Spectroscopy

Infrared spectroscopy involves the twisting, bending, rotating, and vibrational motions of atoms in a molecule. Upon

interaction with infrared radiation, portions of the incident radiation are absorbed at particular wavelengths. The multiplicity of vibrations and other motions simultaneously produces a highly complex absorption spectrum, which is uniquely characteristic of the functional groups comprising the molecule and of the overall configuration of the atoms as well.

The infrared spectrum of a compound is essentially the superposition of absorption (or transmission) bands of specific functional groups. Interactions with surrounding atoms of the molecule impose the individuality of each compound on the spectrum. For qualitative analysis one of the best features of the infrared spectrum is that absorption or the lack of absorption in specific frequency regions can be correlated with specific stretching and bending motions and with the relationship of these groups to the remainder of the molecule. Thus, by the interpretation of the spectrum, is possible to state that certain functional groups are present in the material and that certain others are absent. With these data, the presence of other chemicals within a polymeric system can be recognized and the content can be identified.

In this work, infrared spectroscopy was used to obtain information on the presence of any chemical additive within various polyethylenes, especially the presence of an anti-oxidant or a voltage stabilizer. It is also used to obtain information on the chemical structure of the material. All the infrared spectra were

recorded on either a DIGILAB FTS-40 Fourier Transform Infrared Spectrophotometer or a Perkin-Elmer 1330 Infrared Spectrophotometer.

Fourier transform infrared spectrophotometry utilizes a scanning interferometer instead of using a monochromator, for the analysis of the infrared radiation after passage through the sample. This consists of moving and fixed mirrors and a beam splitter. Radiation from the infrared source is collimated and later divided at the beam splitter. One of the divided beams passes through the sample and later recombines with the other split beam. The recombined beam generates the detector signal at very precise intervals during scanning. The resulting signal is known as an interferogram and contains all the information required to reconstruct the spectrum via a mathematical process known as Fourier transformation. This technique has several distinct advantages over the conventional technique. There is only one moving part required, and dispersion or filtering is not required. This technique also produces high frequency accuracy and high spectral signal-to-noise ratio within a very short time.

Specimens were prepared as thin films of thickness of 2 mils by compression molding. The thin film was then held in a sample holder bracket and placed in the path of the sample beam. All scannings were made in the frequency range of 4000 to 400 $cm^{-1}$. For normal infrared spectrum scanning the samples were scanned with a medium slit. Electrically ruptured samples were also examined by the Fourier transform infrared spectrophotometer using special micro-

scanning involving the microscope attached to the FTS-40 Fourier transform infrared spectrometer. All scans by FTIR were monitored by from 50 to 64 scans with resolution of 8.0 for the accuracy.

### 3.3.2. Thermal Analysis

Differential Scanning Calorimetry (DSC) is based on the principle that the heat flow into or out of a sample relative to a reference can be measured as a function of time or temperature, while keeping the sample and the reference at the same temperature (Figure 3.3.1). The sample and reference are heated separately by individually controlled elements at a programmed heating rate. The power to these heaters is continuously adjusted in response to any temperature difference arising during analysis. As a sample undergoes a transition, the sample heater must supply additional energy to the material in order to keep the sample and reference temperature the same. The power required to achieve this condition is recorded as the ordinate of the recorder with the programmed linear temperature or the time scale as the abscissa.

All thermal analysis in this work was carried out using a Perkin-Elmer Differential Scanning Calorimeter Model 7 attached to the Perkin-Elmer Professional Computer PE 7500, TAC-7 interface between the computer and the DSC-7, and a graphic plotter.

The instrument was calibrated with NBS standard material supplied by NBS. Calibrations were performed using known values of the melting transition of pure indium, whose onset melting temperature and heat of fusion are 156.6$^{o}$C and 28.45 J/g,

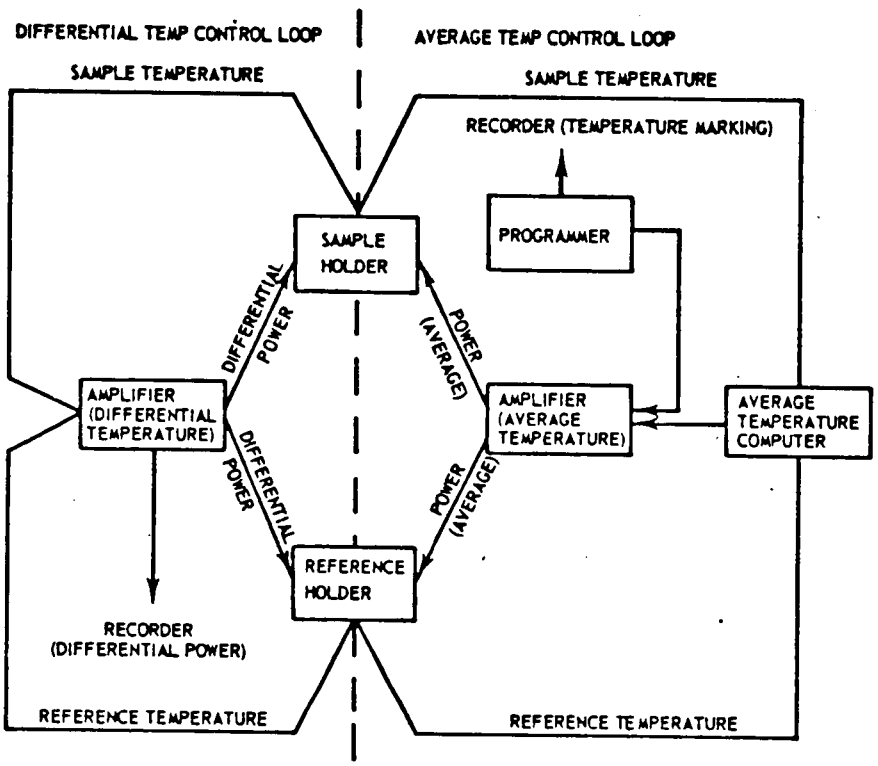



Figure 3.3.1 Schematic representation of a typical DSC system.

respectively. In some occasions, the melting transition of tin ($T_{onset}$ = 231.88°C , Heat of fusion = 60.46 J/g) were also used. Before DSC scanning the sample holder was closely examined to see if there was any residue stuck in the sample holder. If necessary, the sample holder was cleaned out by holding the DSC at 600°C for about 4 minutes. Most carbonaceous or organic materials burn off in the neighborhood of 600°C.

Baseline optimization was also carried out before scanning, either manually or automatically. Manual baseline optimization is done by adjusting two control knobs located behind the DSC front panel so that DSC scan curve plotted in the monitor is visually flat and linear. Automatic baseline optimization is carried out by using an optimization program included in the TAS-7 operating program. First the baseline is run without any sample and is saved in the computer memory. The program uses this baseline to automatically correct sample runs thereafter.

To reduce the experimental error all sample weights were kept in the range of $5 \pm 0.5$ mg. Sample and reference covers were placed in the same manner with the holes aligned in one direction to reduce the effect of the flow rate of purging gas.

DSC was used to measure heats of fusion, onset and peak temperatures of melting, and crystallinities. Typical DSC melting curves are presented in Figure 3.3.2. Initial melting temperatures were determined as the cross point between the base line, which was extended from the base line beyond the melting peak, and the melting

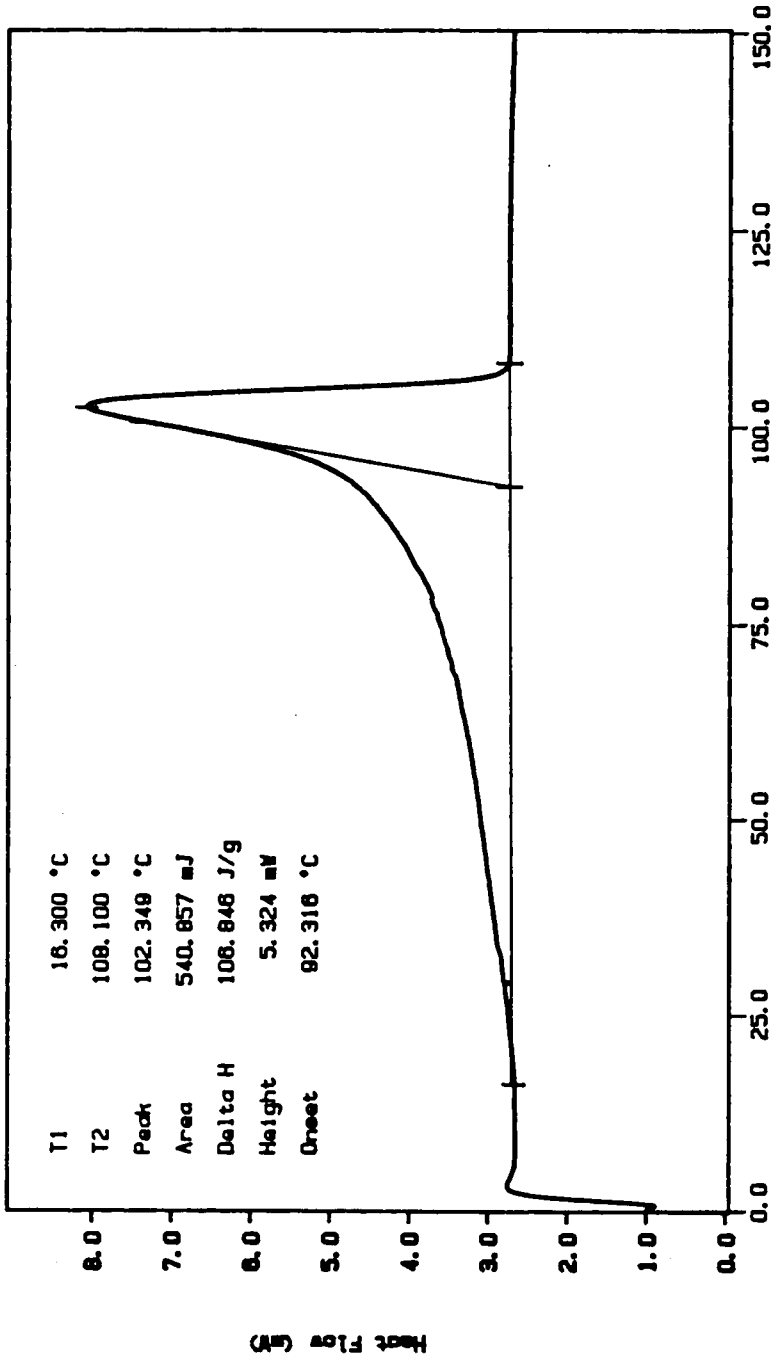



Figure 3.3.2 Typical DSC melting curve of XLPE.

peak. Onset and melting peaks of the material were estimated by the PE 7500 computer attached to the DSC-7. The values obtained from the computer were found to conform to the manner described in the ASTM D 3418-82. The DSC-7 operated with a temperature accuracy of $\pm 0.1^{o}C/min$.

Heat of fusion was used to estimate the crystallinity of the material based on the theory of Dole (1967). A simple two phase structural model was employed with the assumption that the amorphous and crystalline phase have different heat capacities at any particular temperature and that they are additive (Mandelkern, 1968). The degree of crystallinity is given by the following equation:

$$X = (\triangle H_f \; / \; \triangle H^{o}_f \;) \times 100 \; (\%) \qquad 3.3.1$$

where $\triangle H_f$ is the measured heat of fusion of the polymer and $\triangle H^{o}_f$ is the theoretical heat of fusion of 100 % crystalline polymer. The measured heat of fusion of the sample is determined by calculating the area under the melting peak above the baseline. Since normal melting of XLPE, LDPE and LLDPE start near room temperature, most DSC experiments were carried out from $0^{o}C$ to $150^{o}C$.

### 3.3.3. Oxidative Induction Time

The oxidative stability was measured by monitoring copper-induced oxidative induction times using the Perkin Elmer DSC-7. The experimental procedure followed ASTM D 3895-80. Oxidative induction time is a relative measure of the level (or degree) of stabilization

of the material tested. The presence of antioxidant or copper deactivator, or both, can be determined by this method. A typical use of the test is the monitoring of the stabilization level in a raw material as received from the supplier.

Specimens were prepared as thin films by compression molding. Disks of specimens 6.4 mm in diameter were then punched out and placed in a pre-oxidized copper sample pans. The pre-oxidized copper sample pan and cover were prepared by placing them in a 50% solution of concentrated HCl and absolute ethanol for 5 minutes. The copper pan and cover were then rinsed in ethanol, dried in air. The cover were then punctured with sharp metal pin so as to have 10 tiny holes 0.5 mm in diameter. After covering with a punctured copper cover, the sample pan was then crimped in four places so that the cover is maintained in place in good contact with the specimen disk.

The prepared specimen piece and an empty oxidized copper sample pan with oxidized copper cover were placed in the sample and the reference positions of the DSC-7. A special flow-through disk cover was placed on top of the sample and reference holder disk to provide a short exit path for decomposed products. The DSC-7 was purged with prepurified nitrogen gas for 5 minutes at a flow rate of 40 mL/min.

The DSC-7 was heated from 50°C at a constant rate of 20°C/min in a nitrogen environment. When equilibrium was reached at 200°C, the programmed heating was discontinued and the atmosphere was switched to oxygen at the same flow rate of 40 mL/min. The specimen

was then held at a constant temperature and isothermal operation was continued until at least 2 minutes have elapsed after the commencement of the oxidative exotherm as shown in Figure 3.3.3. The oxidative induction time (OIT) is measured from the zero time, where the nitrogen purge was switched to oxygen purge, to the intercept of the extended base line and the slope of the oxidative exotherm (See Figure 3.3.3).

### 3.3.4. Small Angle X-ray Scattering

The small angle x-ray scattering (SAXS) experiments were carried out on the ten-meter small angle x-ray scattering camera at the National Center for Small Angle Scattering Research at the Oak Ridge National Laboratory in Oak Ridge, Tennessee. The ten-meter camera utilizes a rotating anode x-ray source, crystal monochromatization of the incident beam, pin-hole collimation, and a two-dimensional position sensitive counter, as described by Hendricks (Hendricks, 1978) as shown in Figure 3.3.4.

The x-ray source, manufactured by Rigaku-Denki, consists of a power supply, rotating anode, and tungsten filament, being operated at 40 kV and 40 mA with the source to sample distance set at 162 cm. Monochromatization of the incident beam is done by reflecting the characteristic K x-rays emitted by the copper anode off a flat piece of pyrolytic graphite crystal to select the $\alpha$-component of the beam. The collimation is achieved using a pin-hole collimator which consists of two 1 mm diameter pin-holes in a lead sheet having polished tungsten flaps separated by 154 cm.

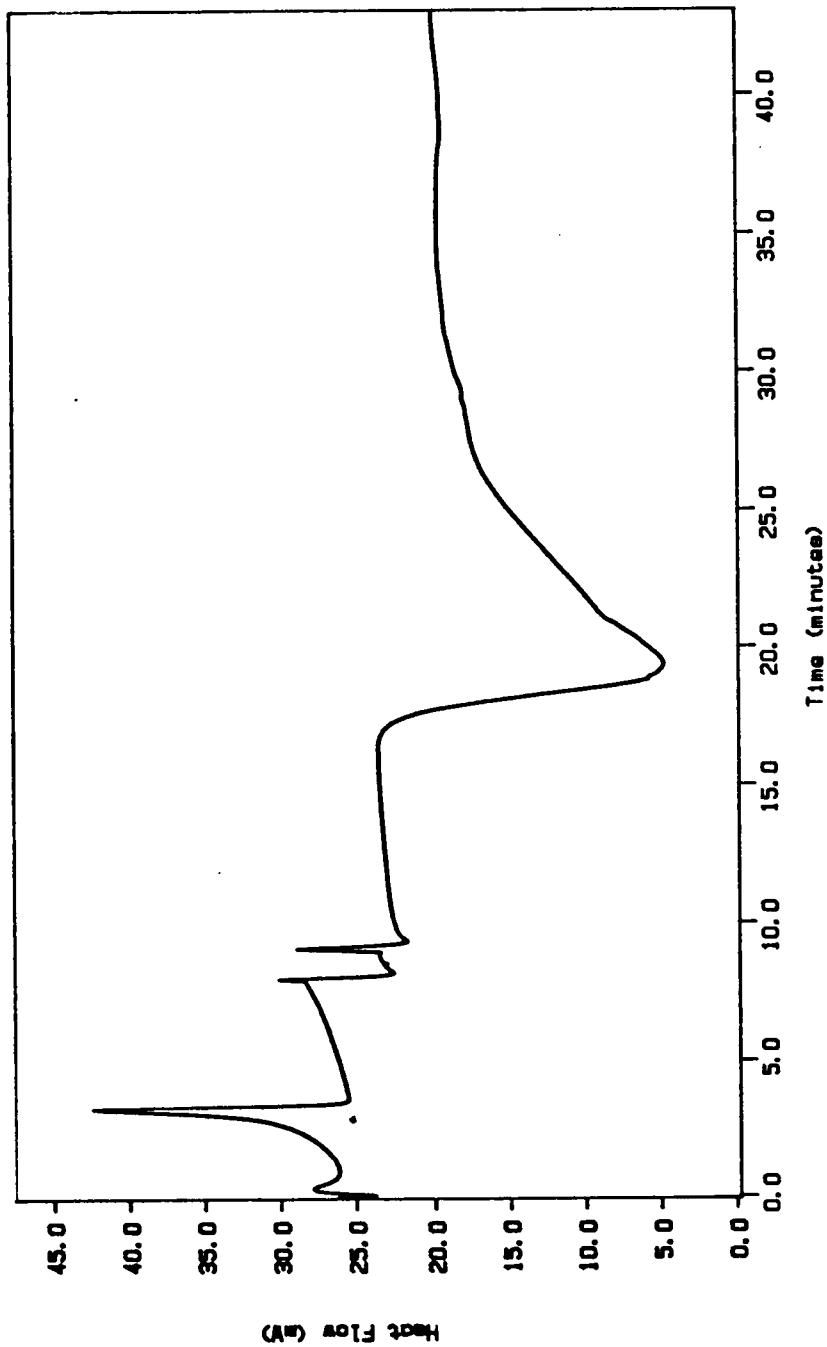



Figure 3.3.3 Typical oxidative exotherm of XLPE.

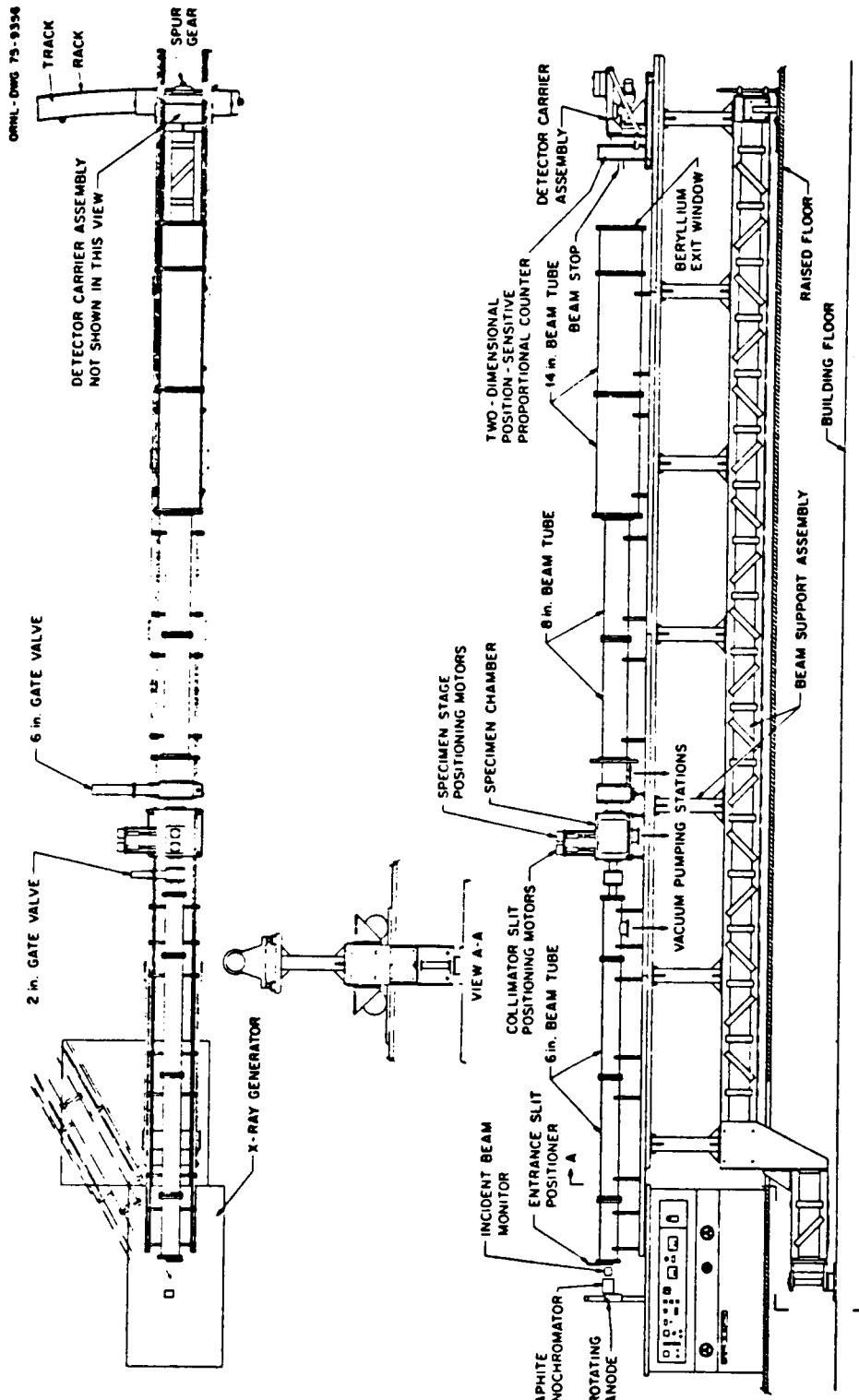



Figure 3.3.4 Schematics of the ORNL ten meter SAXS spectrometer.

The specimen chamber of 30 x 30 x 35 cm contains an externally operated x-y position device for the second pinhole. The position is controlled by two stepping motors which can be manipulated either manually or via computer. Glassy carbon is installed on a sliding mechanism mounted on the second pinhole stage and is moved into or out of the incident beam. The intensity of the x-ray beam scattered by the glassy carbon and the attenuation of intensity by a sample are measured to determined the transmission coefficient of the specimen. The transmission coefficient, (ratio of the intensity transmitted through the specimen to the incident x-ray), is given as,

$$T_S = \frac{I_{gc+sam} - 0.7 \times I_{sam}}{I_{gc} - 0.7 \times I_{dc}} \qquad 3.3.2$$

where $I_{gc+sam}$ is the intensity of the beam with glassy carbon and sample in the path of x-rays, and $I_{sam}$ is the intensity of the x-ray scattering with only the sample in the beam path, and $I_{gc}$ is the x-ray intensity of the beam with the glassy carbon in the path of the incident beam. The coefficient of 0.7 is the transmission coefficient of glassy carbon. $I_{dc}$ is the dark current beam intensity which is measured without anything in the path of the beam.

Samples were mounted in the automatic sample changer which can hold up to 12 different specimens. The movement of the sample changer wheel is controlled by a stepping motor which in turn is manupulated by computer software. The sample holder was rotated

after each running of the experimental run with each specimen. The flight path from the specimen chamber to the detector consists of 0.5 m and 1 m lengths of vacuum pipes of diameters 20 cm or 35 cm. The whole vacuum system consists of three different vacuum sections each of which has its own vacuum pump and electropneumatic gate valves in between. Each of three sections is separately pumped to a vacuum of less than 10 μmHg.

A two-dimensional position sensitive detector is cased in a round aluminium disk of 40 cm in diameter and 10 cm deep, with an active area of 20 x 20 cm having 64 x 64 resolution elements. The data array of the 64 x 64 matrix is recorded in the memory of the minicomputer by a high-speed interface which uses a microprocessor to map the digitized x-y position of incident photons into an allocated minicomputer memory address.

A Modular Computer System ModComp II/220 CP computing system is employed as the on-line computer system for the collection and processing of the data recorded by the position sensitive detector. Tektronix Model 4014-1 Graphics Terminal with a 48 cm display screen is employed for the display of data plots.

These data were plotted as contour maps of intensity as a function of scattering vector K. Since there is no pronounced orientation in the samples, all data were radially averaged to obtain one-dimensional scattering data of intensity versus scattering angle. The specimen-to-detector distance used was 5.126 m. The angular resolution in this case is about 0.5 mrad

corresponding to the scattering vector of 0.004 $Å^{-1}$. The scattering intensity has been corrected for cosmic radiation, unnecessary scattering from collimation slits, and possible nonuniform efficiency of detector.

### 3.3.5. In-situ SAXS

The small angle x-ray study of this material at high temperatures was carried out by in situ experimentation. Figure 3.3.5 shows the schematic diagram outlining an in-situ experiment. The 10-meter SAXS camera located in the Oak Ridge National Lab was used. Specimen was held in a sample mount surrounded by a copper pipe of 5 mm diameter. A temperature oil bath was attached to the x-ray sample chamber, hot ethylene glycol being pumped and circulated to the sample holder in order to control sample temperature during the measurements. The temperature was measured using a thermocouple attached to the sample.

For the analysis of some of the data obtained, the distance distribution function which shows the numbers of distance within the particle was used. This function can be calculated using the fourier transformation of the intensity function. This function is related to the correlation function $\tau(r)$. For the easy comparison the $F(r)$ function, which is simply the function of $P(r)$ divided by the distance r, is normally used.

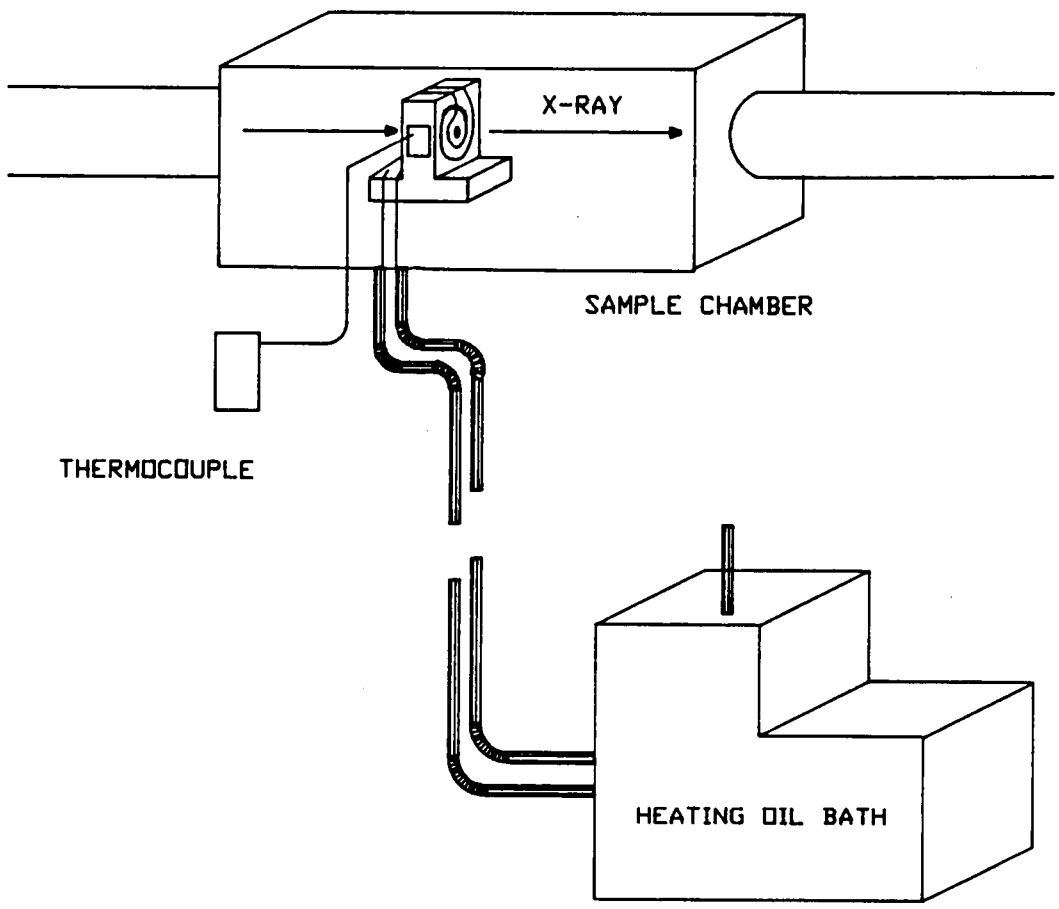



Figure 3.3.5 Schematic of in-situ SAXS experiment.

### 3.3.6. Electrical Breakdown Studies

A comparison of dielectric strength of the series of XLPEs and TR-LLDPE was performed using an ac breakdown strength test. The breakdown strength tests were made using a Biddle AC/DC Breakdown, Leakage and Ionization Tester, RM Z15-L/2, at Oak Ridge National Laboratory. The tester is capable of 12 kV dc and 6 kV ac (rms). The measuring probes consist of two opposing cylindrical brass rods 6.4 mm (0.25 in.) in diameter with edges rounded to 0.8 mm (0.031 in.) radius (electrode type 3 in ASTM D149). The bottom electrode was stationary and the top electrode was movable to permit the insertion of samples. The top electrode was counterbalanced to produce a net force on the specimen of $50 \pm 2$ g.

Failure was evident by actual rupture of the specimen. Breakdown tests were carried out only with unaged samples. For TR LLDPE biaxially stretched samples were also prepared using a T. M. Long stretcher to investigate the influence of biaxial orientation on breakdown strength. Data were then plotted using Weibull distribution functions. Structural observations were made of the breakdown area by means of polarized optical and scanning electron microscopy. To obtain a more detailed view of the ruptured surface, some samples were etched with permanganic acid for 90 minutes (Naylor, 1983) and studied using scanning electron scanning microscopy.

# 4. EXPERIMENTAL RESULTS

There have been many attempts to reduce or eliminate treeing in polymeric insulation ever since the treeing problem was noted in cable insulation. These approaches can be divided into two groups. One is the modification of the cable construction method, and the other is the modification of material or material structure, often with the aid of additives. Commercially, several grades of polyethylene have been introduced. Among these materials there are tree retardant crosslinked polyethylene (UCAR TR-4202) and tree retardant linear-low-density polyethylene (UCAR TR-7521) introduced by Union Carbide Corp. Both of them are claimed to have higher dielectric breakdown strength and to resist or retard the rate of tree growth. Great care has been also taken during preparation of resins (such as UCAR EC 4201) to reduce the contamination level for the electrical insulation application.

In this work, the characterization of these different grades of materials is carried out along with an evaluation of the effects of thermal stress on the structure and properties.

## 4.1. Characterization

### 4.1.1. Crosslinking of XLPE

Three of the four grades of polyethylene samples used in the present work are crosslinkable polyethylenes. These materials utilize thermal crosslinking by means of dicumyl peroxide, which is the major crosslinking agent used in polyolefins. All curing was

performed at 200°C under pressure to reduce formation of bubbles. Improper release of pressure during or before crystallization causes sudden formation of bubbles throughout the whole thickness.

It is known that dicumyl peroxide is consumed by a first order decomposition reaction (Harpell and Walrod, 1973). The time required for 99.9% decomposition of DCP is 3 minutes at the temperature of 200°C (Karakelle, 1986). For the molding of thick specimens, samples were sometimes kept up to 5 minutes at the curing temperature under pressure. The pressure applied during curing was the same as the pressure (20 tons) applied during molding.

To ensure that proper crosslinking had occurred, extraction experiments were carried out. The amount of percent extractables (sol) of the crosslinked polyethylene was determined from the weight loss in boiling xylene, as described in Chapter 3. The sol fraction of TR grade XLPE cured at 190°C for 2 minutes was found to be 38.6%. However, the sol fraction of the sample cured at 200°C for more than 3 minutes was about 18.7% or less. The other grades of crosslinked samples showed similar results. An extractable ratio of 18% is typical of complete decomposition of the dicumyl peroxide level used in these materials.

### 4.1.2. Infrared Analysis

One of the best techniques available for the study of chemical composition is infrared spectroscopy. Analysis of IR spectra gives valuable information regarding the chemical composition, unsaturation and other microstructural chemistry. 1 to 2 mil thick

specimens were prepared by compression molding from all different grades of polyethylenes. Gel fractions of the samples were also prepared from extraction of very thin molded films. Most samples thickened due to swelling during the extraction. Meanwhile, sol fractions were obtained by molding of sol powder, which was collected from the extracted solution.

Figure 4.1.1 shows the infrared spectra produced by a regular infrared spectrometer (Perkin-Elmer 1330) for four materials in the 1800-600 $cm^{-1}$ region. All curves show the three major peaks which are typical of polyethylenes. Close comparison of bands in the 1378 $cm^{-1}$ region, which is known to be directly proportional to the methyl group concentration, reveals a slight difference between LLDPE and the XLPEs. Relatively low intensity of the 1378 $cm^{-1}$ band was observed for the tree-retardant (TR) LLDPE (TR-7501). This result indicates a lower level of short chain branching for this material, consistent with its copolymer structure. The amount of short chain branching is known to affect the melting point substantially (Reding, 1958), a more randomly branched polymer having a lower final melting point and a sharper melting range.

TR-LLDPE also exhibits two medium sized peaks in the range of 1000 to 800 $cm^{-1}$, where the unsaturation of polyethylene can be investigated. These features are more evident in Figure 4.1.2 which shows infrared spectra measured using a Fourier transform infrared spectrophotometer. Three types of unsaturated groups are known to exist in polyethylenes in detectable amounts. These are vinylidene

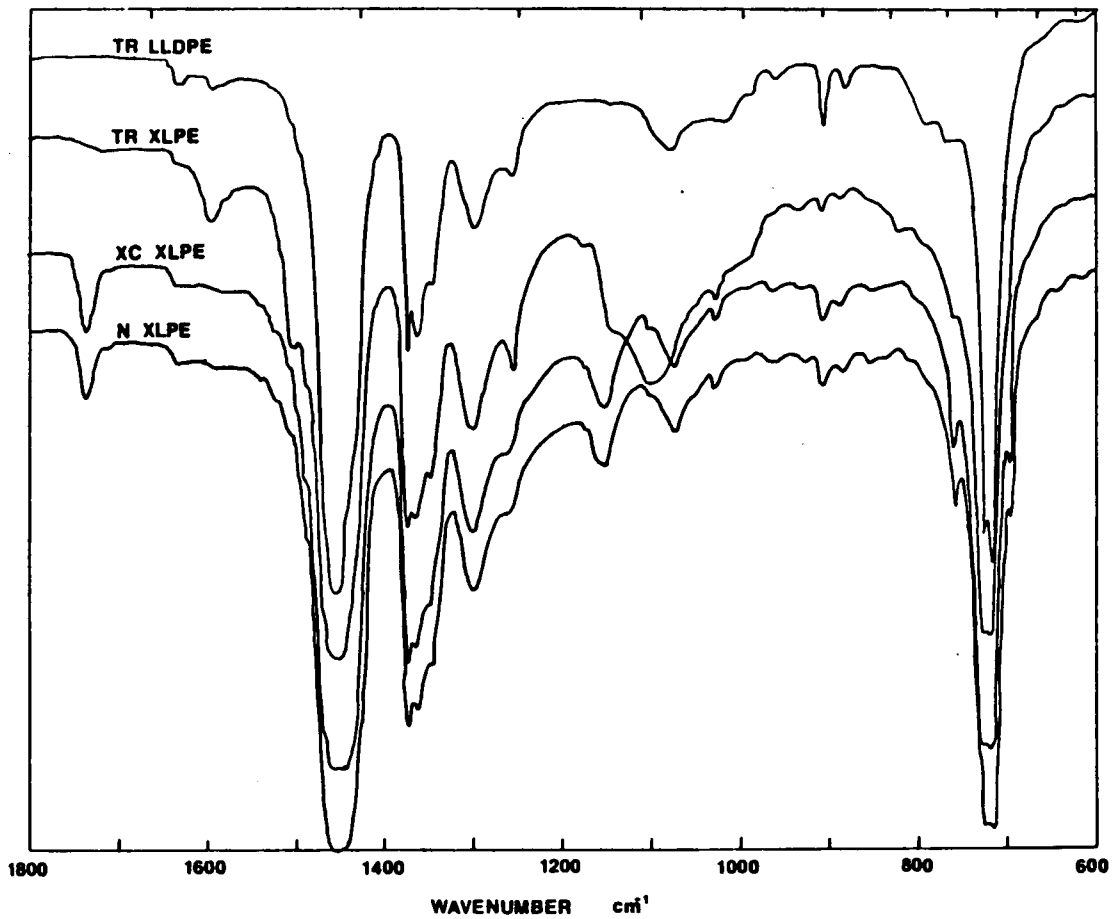



Figure 4.1.1 IR spectra of TR-XLPE, EC-XLPE, PL-XLPE and TR-LLDPE.

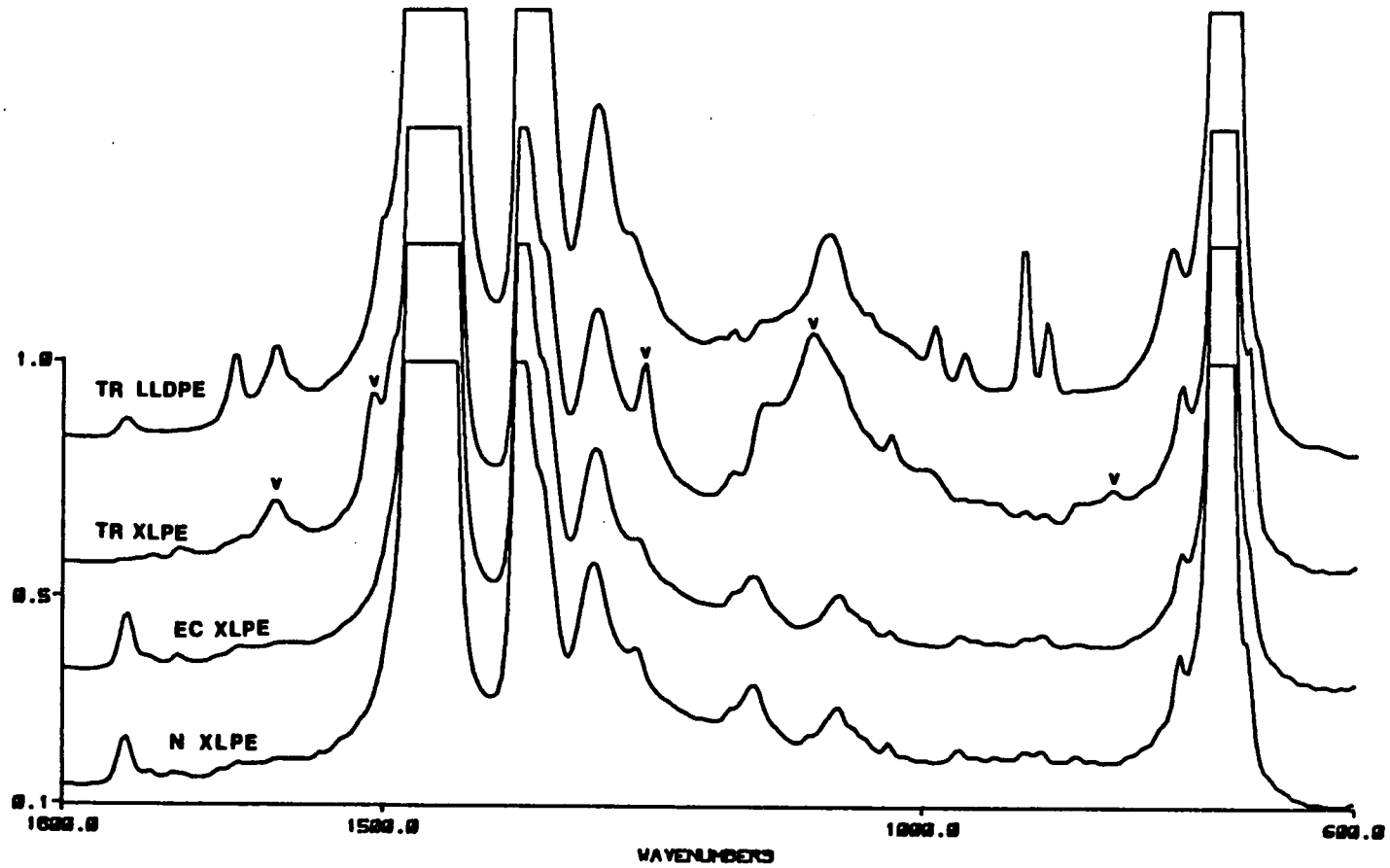



Figure 4.1.2 FTIR spectra of TR-XLPE, EC-XLPE, PL-XLPE and TR-LLDPE.

($R_1R_2C=CH_2$), vinyl ($RCH=CH_2$) and trans-vinylene ($R_1CH=CHR$). These groups will generate bands at 888 $cm^{-1}$, 910 $cm^{-1}$ and 965 $cm^{-1}$ corresponding to vinylidene, vinyl and trans-vinylene absorptions respectively. TR-LLDPE shows a higher degree of vinyl unsaturation (at 908 $cm^{-1}$) than vinylidene (880 $cm^{-1}$) or t-vinylene (963 $cm^{-1}$) unsaturation.

Figures 4.1.1 and 4.1.2 also show IR spectra of all three grades of XLPE. Extra-clean (EC) XLPE (HFDE-4201 EC) exhibits a pattern similar to that of normal (PL) XLPE (HFDE-4201). Both of them show a typical band at ca. 1740 $cm^{-1}$ which arises from the ester group. They also show very low peaks in the range of 1000 $cm^{-1}$ to 800 $cm^{-1}$ in which major unsaturation can be detected. A band at ca. 1693 $cm^{-1}$ was known to be caused by the presence of acetophenone produced from dicumyl peroxide during the cross-linking process. All XLPEs show a small peak at the same location, as expected; confirming that they utilized the same curing agent.

On the other hand, TR-XLPE (TR-4202) exhibited several additional bands at ca. 1604, 1512, 1257, 1103, 1030, and 825 $cm^{-1}$. These bands are more distinguisable on the difference spectra shown in Figure 4.1.3 which was obtained from Perkin-Elmer IR spectrometer with TR-XLPE in the sample side and other XLPE in the reference side. These peaks are thought to arise from the chemical agents added to the TR grade of polymer. Since the manufacturer claims that this grade of polyethylene has a function of retardation of tree

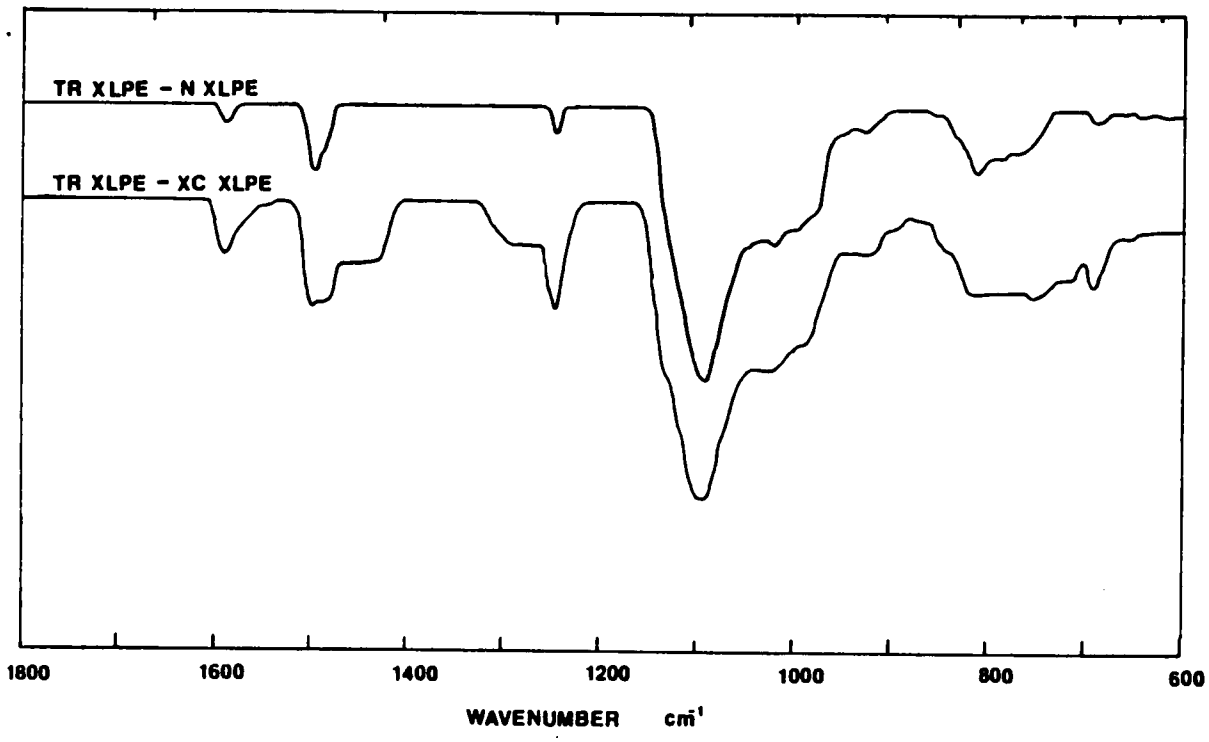



Figure 4.1.3 Difference IR spectra of TR-XLPE (EC-XLPE or PL-XLPE subtracted).

formation and growth, the chemical additives are considered to be the tree retardant.

Comparison of IR spectra of various parts of TR-XLPE will give a glimpse of the way of attaching this chemical agent to the polymer. Infrared spectra of gel and sol fractions as well as uncured and cured TR-XLPE are plotted in Figure 4.1.4 for the wavenumber range of 1800 $cm^{-1}$ to 600 $cm^{-1}$. The additional bands developed by the chemical additive are present in all the sample fractions. These bands are present in the same locations in TR-LDPE. TR-LDPE is virtually same material as the TR-XLPE except that TR-LDPE is just compression molded by melting at 135°C, while XLPE was cured thermally at 200°C. The peaks located at 1103 and 1030 $cm^{-1}$ are sharper and clearer for TR-LDPE than those present in the spectra of cured TR-XLPE. The additional five bands are also seen in the IR spectra of the gel fraction of TR-XLPE. Even though the spectra of the sol fractions show the same bands from the additive, the shape and size is not as noticeable as those obtained from the gel or cured TR-XLPE. The extractable fraction also shows a highly intense band at ca. 1720 $cm^{-1}$.

The change in the degree of unsaturation from olefinic groups for different grades of XLPE will give information on the efficiency and chemistry of peroxide crosslinking. Figure 4.1.5 illustrates infrared spectra of three different grades of XLPE in the range of 1050 $cm^{-1}$ and 800 $cm^{-1}$.

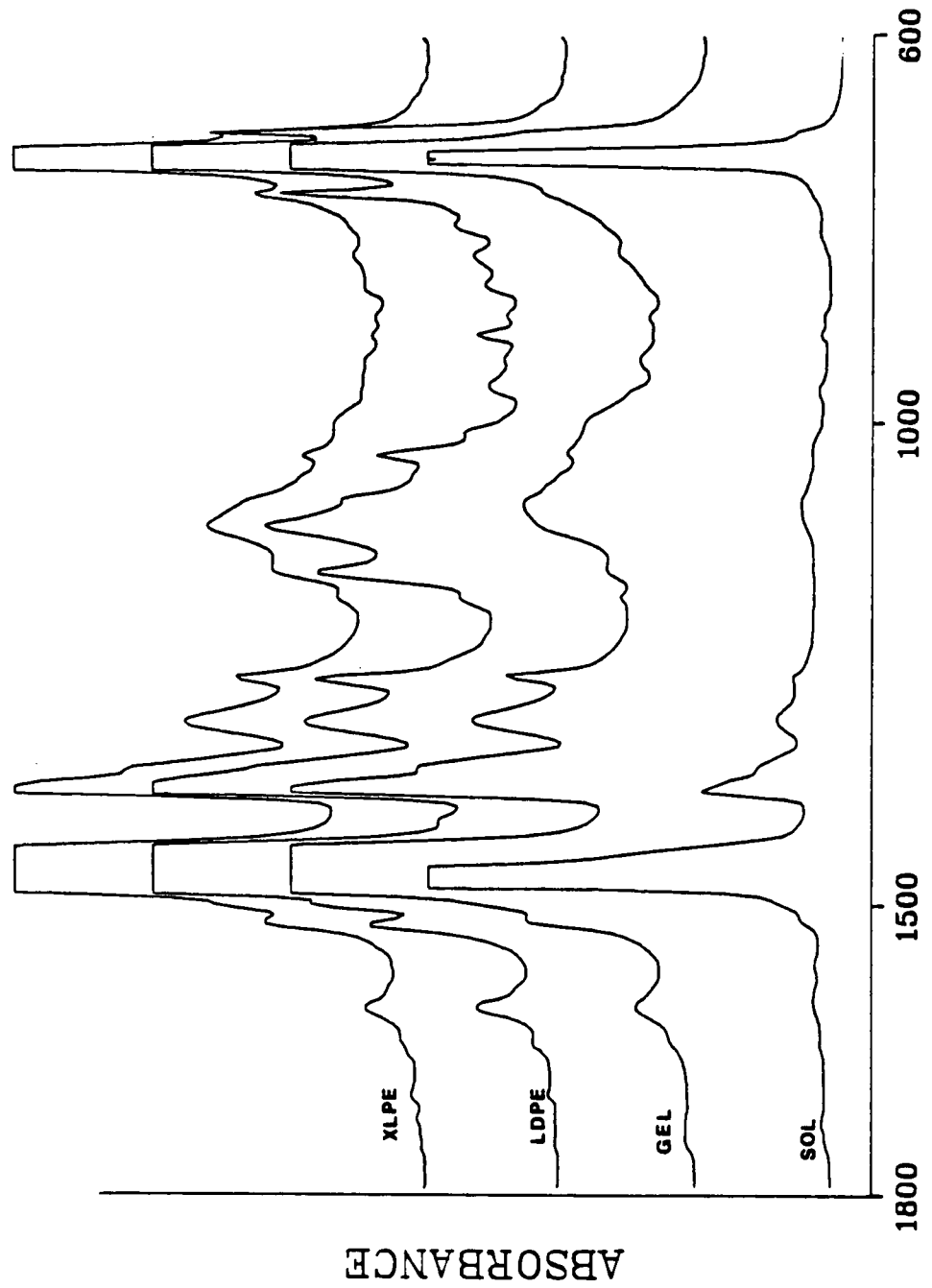



Figure 4.1.4 FTIR spectra of TR-XLPE, TR-LDPE, sol and gel fractions of TR-XLPE.

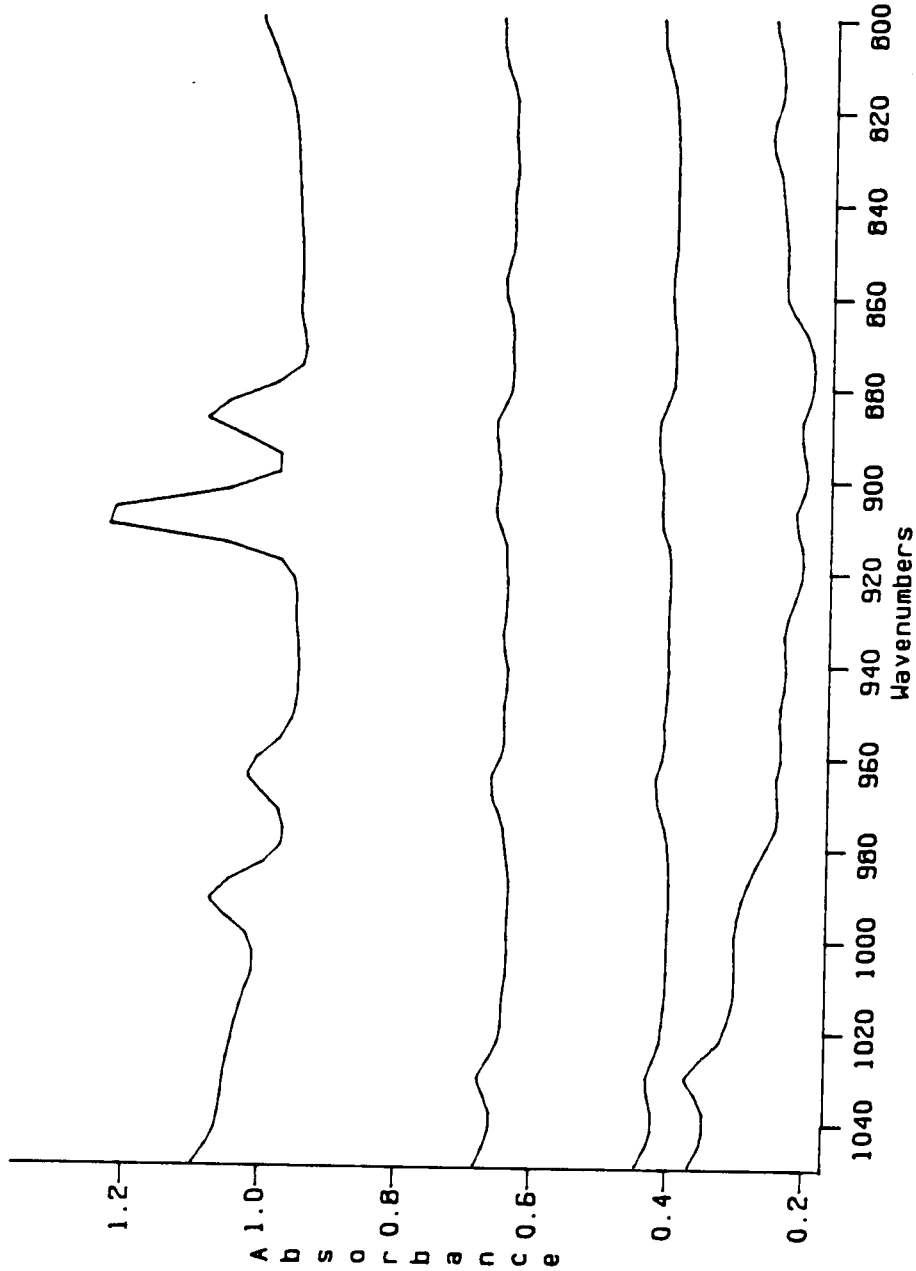



Figure 4.1.5 FTIR spectra of TR-XLPE, EC-XLPE, PL-XLPE and TR-LLDPE in the region of 1050 - 800 $cm^{-1}$.

Figure 4.1.6 gives a comparison of spectra in the range of 1050 $cm^{-1}$ to 800 $cm^{-1}$ of the spectra by extractables, gel fraction, crosslinked, and uncured TR-XLPE. The extractables of TR-XLPE exhibit a higher level of t-vinylene unsaturation and a relatively lower level of methyl and ethyl end group, whereas uncured material shows a higher level of vinyl unsaturation.

4.1.3. DSC Study

Even though differences in chemical additives are indicated in the IR study, all three grades of XLPE show similar melting and annealing behavior. Differential thermal calorimetry experiments were performed for all XLPE samples cured and subsequently quenched by circulating cold water inside the platens of the molding machine. Melting curves of these crosslinked polyethylene samples are compared with TR-LLDPE in Figure 4.1.7. All XLPEs show very similar melting behavior, having the very same melting peak (ca. 104°C).

It is very interesting to note that the determination of the onset of melting is not easy. All XLPE samples were found to have small humps around 45°C. Melting curves of TR-XLPE quenched from the melt to 0°C within the DSC machine did not show similar humps as compared in Figure 4.1.8. Subtraction of the melting curve of the sample quenched within the DSC machine from that of the sample quenched outside the DSC shows that the hump located around 50°C was caused by annealing at room temperature (Figure 4.1.9). Thus, it is clear that actual melting of XLPE begins below room temperature. A subtraction plot shown in Figure 4.1.9 also shows that room

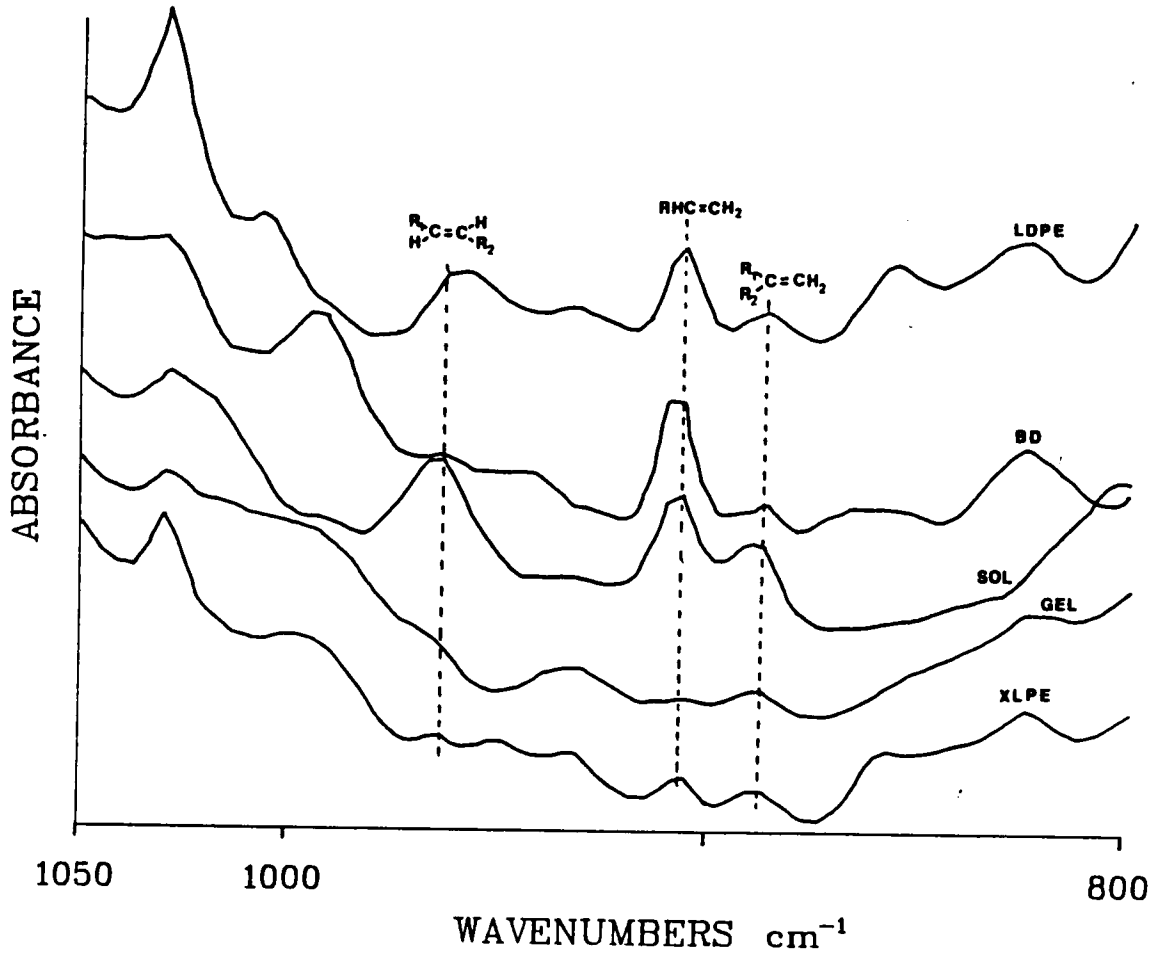



Figure 4.1.6 FTIR spectra of TR-XLPE, TR-LDPE, sol and gel fractions of TR-XLPE in the region of 1050 - 800 $cm^{-1}$.

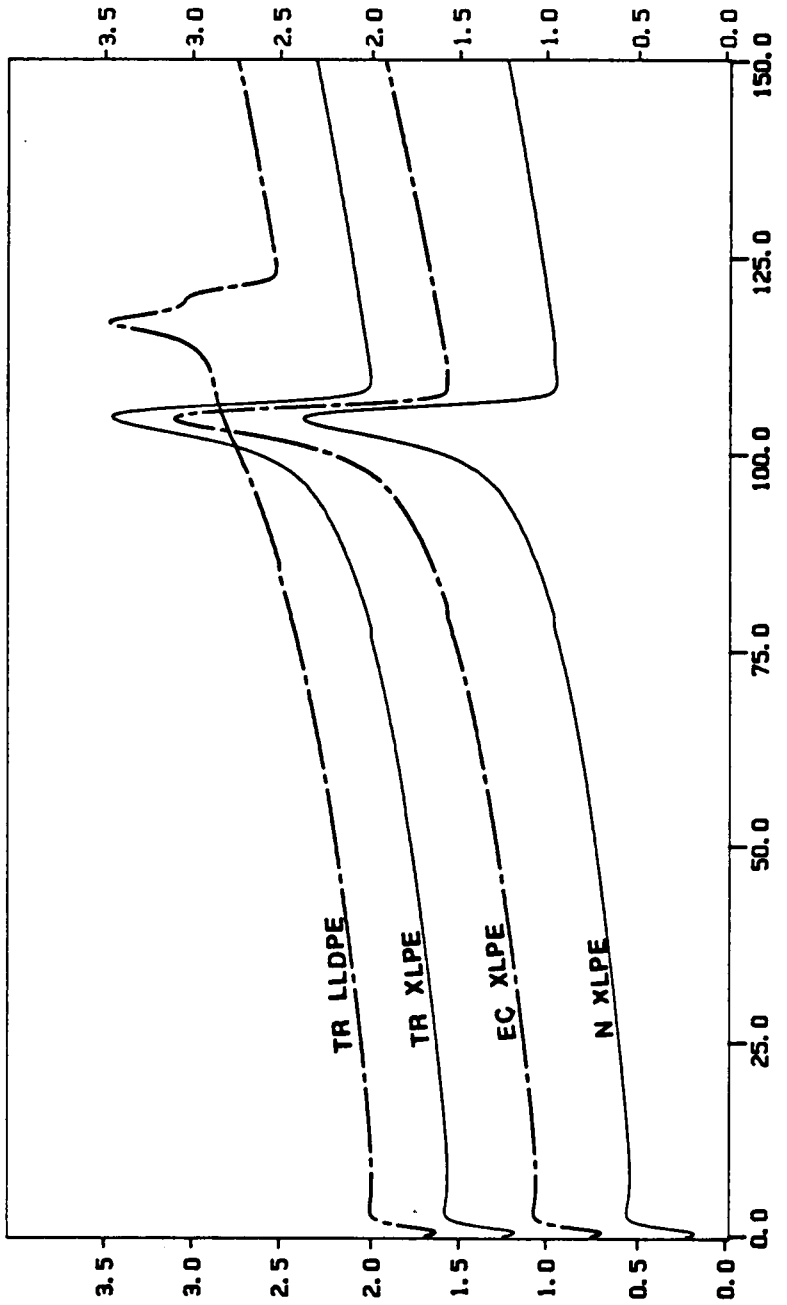



Figure 4.1.7 DSC thermograms of TR-XLPE, EC-XLPE, PL-XLPE and TR-LLDPE.

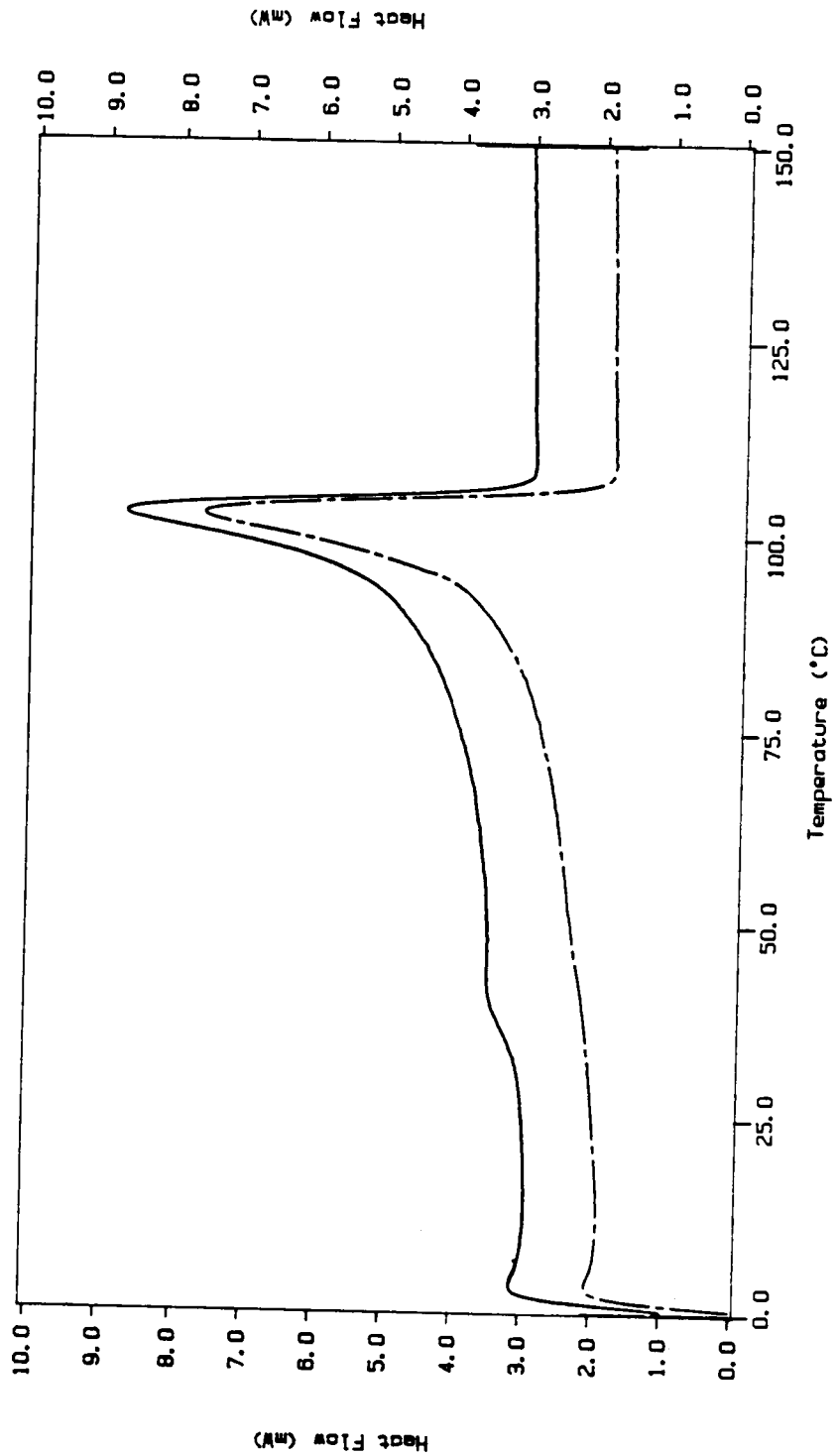



Figure 4.1.8 DSC thermograms of TR-XLPE held at room temperature and quenched in the DSC.

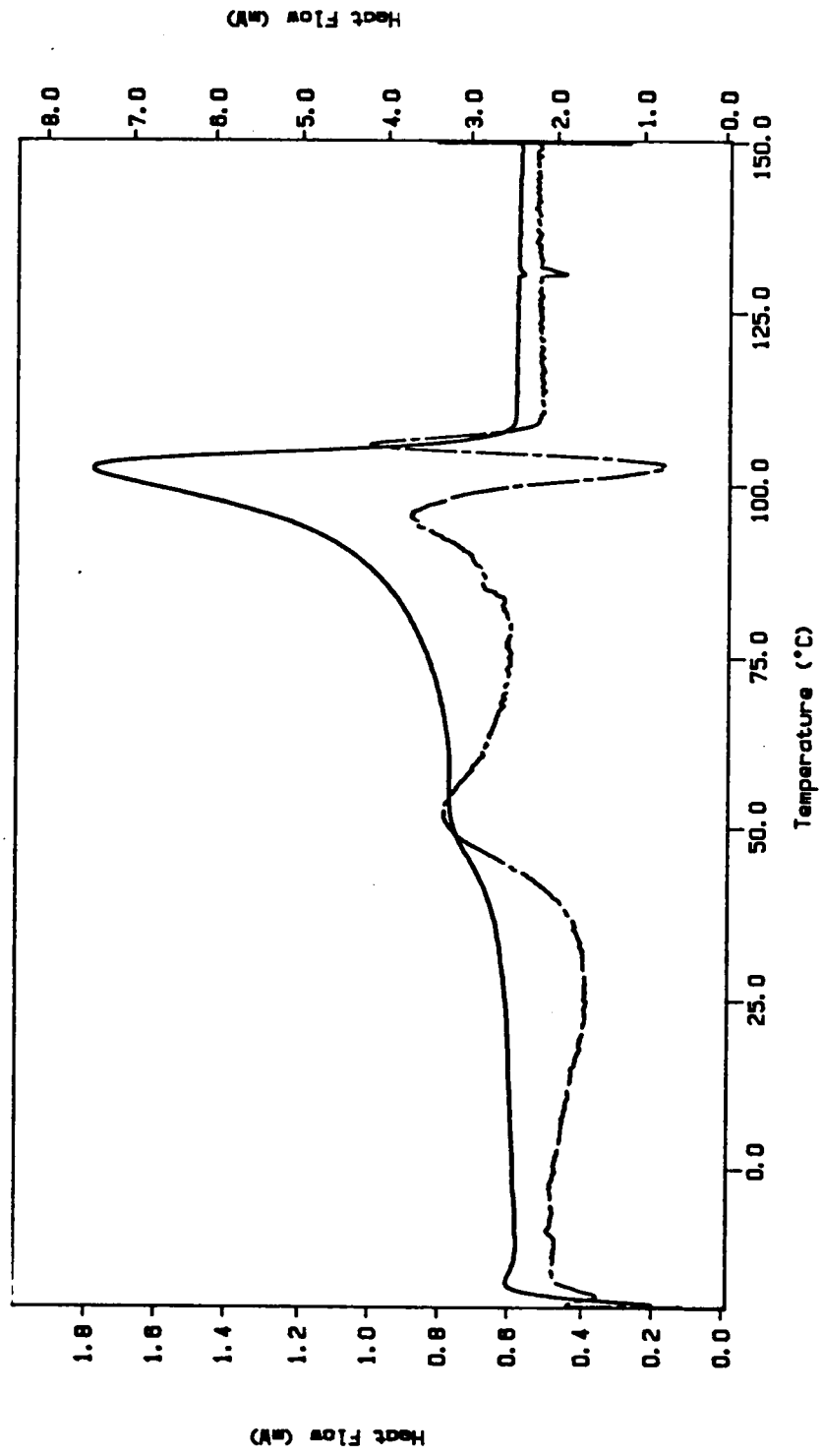



Figure 4.1.9 Difference DSC curve of TR-XLPE held at room temperature having subtracted from it the curve of TR-XLPE quenched in the DSC.

temperature holding creates not only a broad peak at 40 to 50°C but also a sharp peak at the temperature above the melting peak of sample quenched in the DSC.

The room temperature annealing phenomenon is an unavoidable feature of XLPE, because even a short exposure to ambient temperature causes annealing to occur. Similar behavior was noted for all uncured LDPEs and LLDPE. The error caused by the room temperature annealing was noted as a shifting of heats of fusion as well as melting peaks. Possible error was observed not to be negligible, ranging up to 15% of whole heats of fusion. Therefore, all DSC experiments were carried out by raising the temperature from 0°C. Meantime, the error level was reduced by applying the same storage conditions to all samples.

The melting behavior of TR-LLDPE is quite different from those of the XLPEs, as indicated in Figure 4.1.7. The shape of the melting peak is not as simple as for the crosslinked polyethylenes, there being a shoulder before the major melting peak. To induce a single melting peak in the TR-LLDPE sample, the samples were quenched in various ways. Figure 4.1.10 shows melting curves of TR-LLDPE quenched in air, ice-bath and a dry ice-ethanol bath. The room-temperature quenched sample shows shoulders at temperatures above and below the major peak. Quenching in an ice bath as well as a dry ice-ethanol bath did not produce a single peak. The slowly cooled TR-LLDPE, interestingly, shows two completely separated peaks, one being sharper and at a higher temperature than the other. These

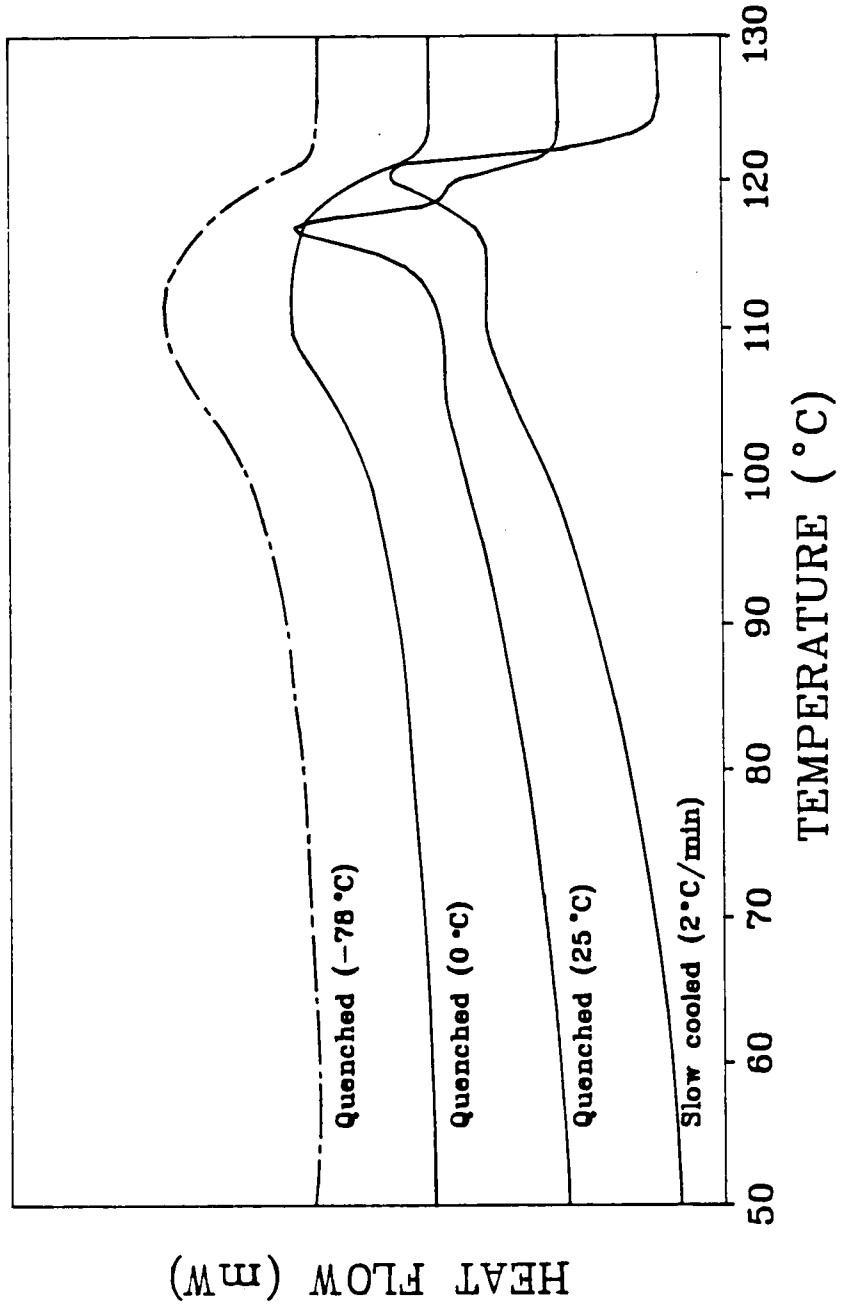



Figure 4.1.10 DSC curves of TR-LLDPE solidified under different conditions.

results are at least as complex as those for XLPE but of different origin. They may be caused by crystals having different levels of branching in their molecules.

The melting behavior of different fractions of XLPE was also investigated in order to understand the effects of gel and sol fractions on the melting behavior of whole XLPE. The melting curves of uncured, crosslinked, gel, and extractable fractions of TR-XLPE are presented in Figure 4.1.11. Uncured material as well as the extractable or sol fraction of TR-XLPE show a higher melting peak (ca. 107°C), whereas the cured sample and gel fraction show peaks around 103°C. This result is consistent with previous results obtained for normal XLPE (Phillips, 1984). All other uncured XLPEs also show higher melting peaks as shown in Figure 4.1.12. This indicates a lowering of the melting point by crosslinking.

Another interesting finding was the change in size of areas under the melting peaks, which are measures of the heats of fusion. Figure 4.1.13 shows the change in heat of fusion upon curing for various XLPE samples. The figure also shows the heats of fusion of gel and sol fractions. Cured samples show lower heats of fusion, revealing the crystallinities are lower than those of the uncured counter-parts. However, the gel fractions show larger values of the heat of fusion. The results of a higher heat of fusion for the gel fraction can be related to the observation that the gel fraction can have a higher crystallinity than whole XLPE sample (see next section).

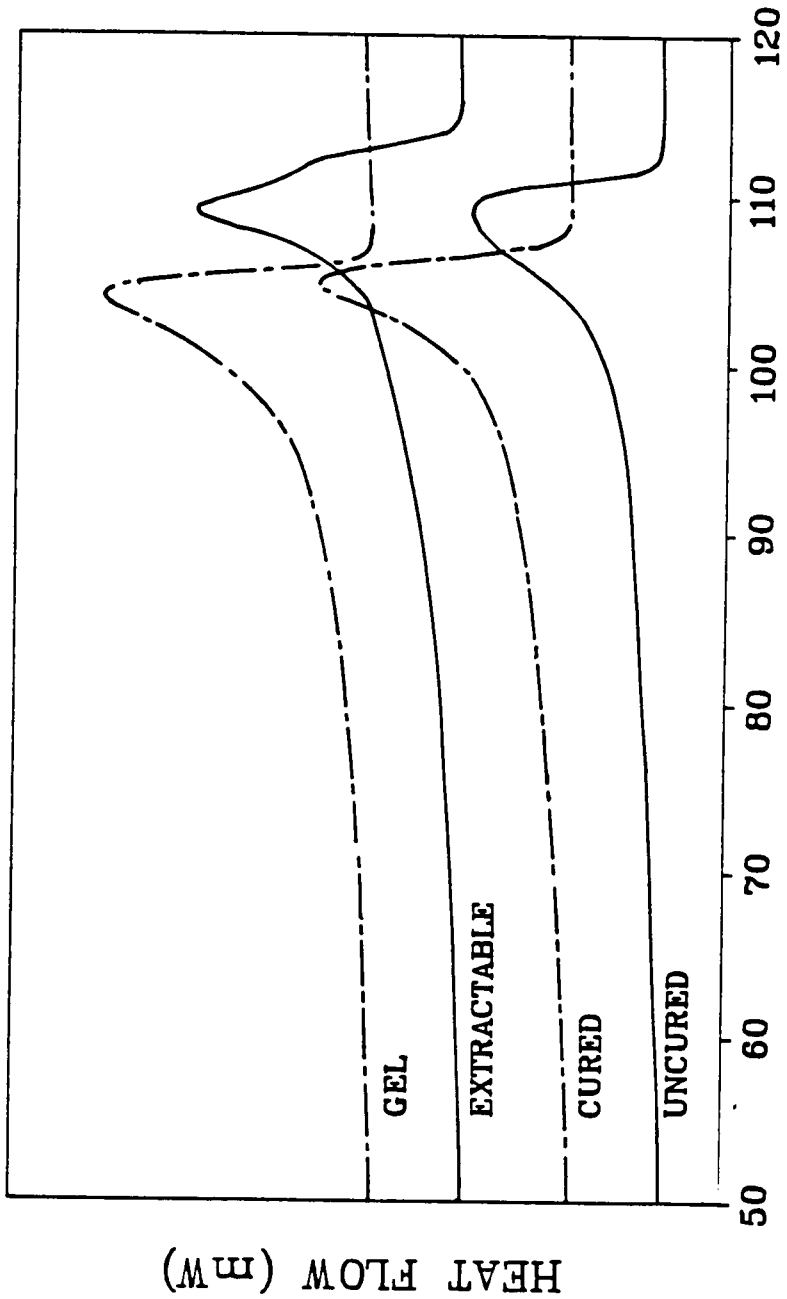



Figure 4.1.11 DSC curves of gel, extractables, cured and uncured TR-XLPE.

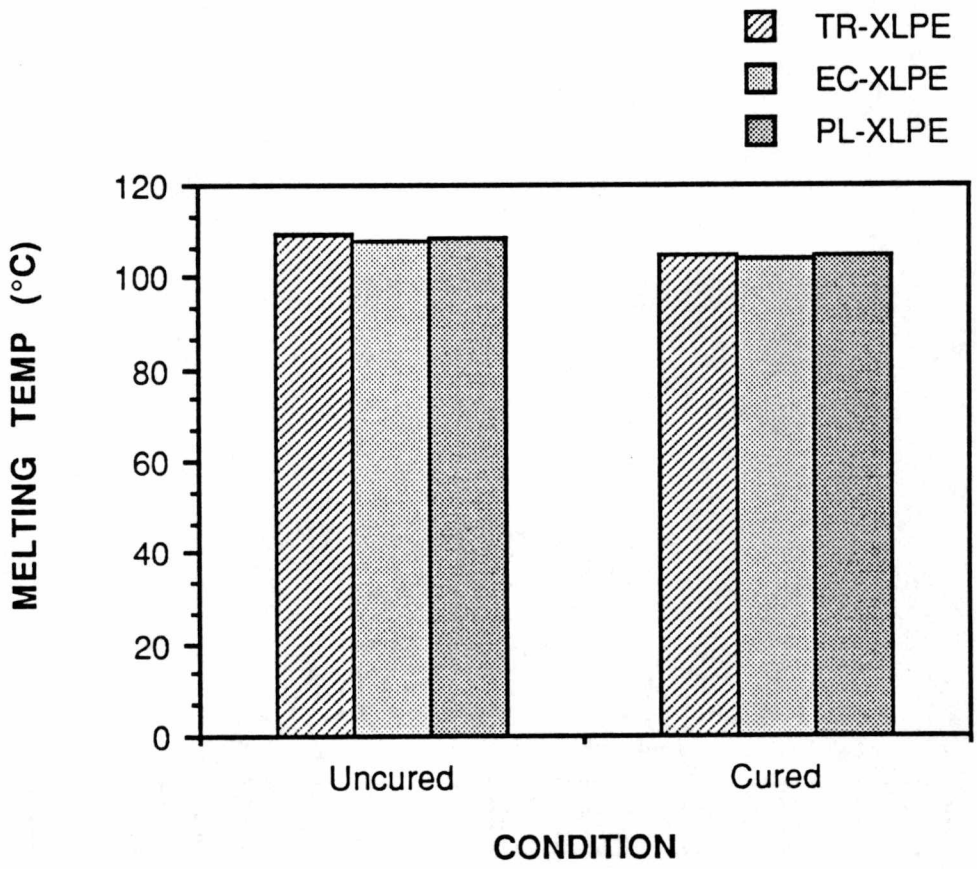



Figure 4.1.12 Variation of melting points with curing for TR-XLPE, EC-XLPE and PL-XLPE.

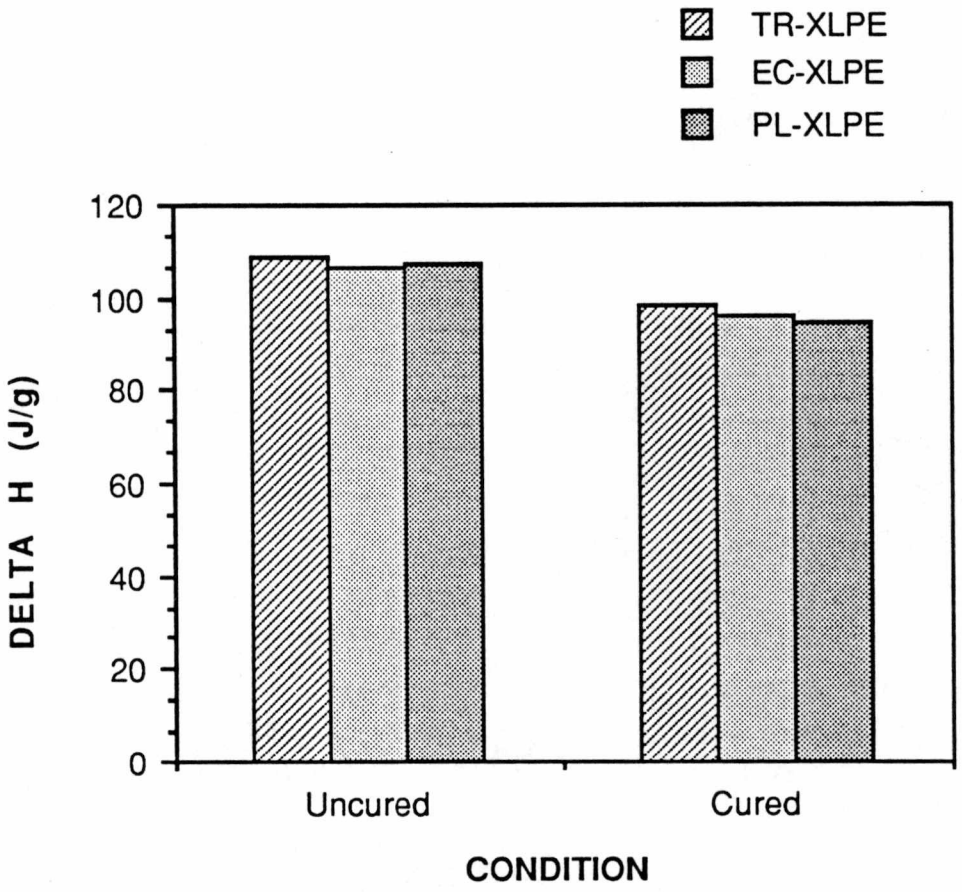



Figure 4.1.13 Variation of heat of fusion with curing for TR-XLPE, EC-XLPE and PL-XLPE.

4.1.4. Density Measurement

The variation of heat of fusion can be related to the change in crystallinity. Another major way of determining crystallinity is density measurement. Densities were measured with the aid of a density gradient column held at room temperature. The column was prepared from a solution of water and isopropanol so that the density in the column ranged from 0.88 to 0.94 $g/cm^3$ in accordance with ASTM-D 1505. There is no observable evidence of swelling or dissolution of the materials in solution.

The density of cured and uncured XLPEs and the gel fractions are presented in Figure 4.1.14. As expected, cured samples show lower densities than the uncured counter-parts. However, the densities of gel fractions were found to be much higher than those of cured and uncured XLPE. Even though these results match exactly with the results of heat of fusion, the higher crystallinities for gel fractions are important results.

Another striking feature is that the overall density of TR-XLPE is higher than that of EC-XLPE or PL-XLPE. Cured and uncured EC-XLPE, however, shows very similar values of densities to those of cured and uncured PL-XLPE within experimental error. The values of crystallinities obtained from the densities range from 49.7% for cured EC-XLPE to 57.5% for the gel fraction of TR-XLPE, based on an amorphous density of 0.85 $g/cm^3$ at 25°C and crystalline density of 1.00 $g/cm^3$ at the same temperature.

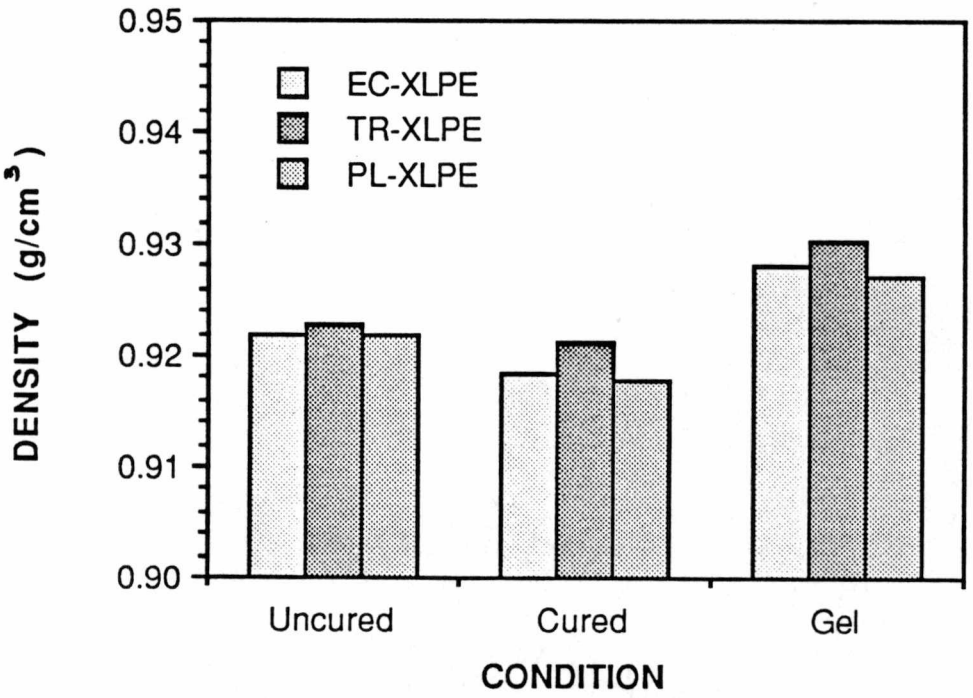



Figure 4.1.14 Densities of uncured, cured and gel fraction of EC-XLPE, TR-XLPE and PL-XLPE.

4.1.5. Wide Angle X-ray Study

To confirm the crystallinity change with curing, wide angle x-ray diffraction patterns were also obtained using the Rigaku$^{TM}$ x-ray diffractometer as described in Chapter 3. The diffractometer is controlled by a microprocessor and can be programmed to measure the integral diffraction intensity from each crystalline peak. The incoherent scattering and air scattering was removed by deducting a background correction from total intensity. 1.5 millimeter thick samples were prepared by compression molding to reduce the effects of deformation or orientation. Figure 4.1.15 shows typical WAXD patterns of gel fraction, cured and uncured TR-XLPE. The x-ray intensity of the gel fraction is lower than those of cured or uncured XLPE even though the thickness of the gel specimen is greater than those of the others. All WAXD patterns show amorphous halos located in the diffraction angles from 14.4° to 19.6° with a maximum at around 18° and two major crystalline peaks produced by the (110) and (200) planes. 110* peaks range from 20.2° to 22.4°, whereas 200* peaks range from 22.7° to 24.4°.

WAXD crystallinities were determined using the following empirical equation.

$$\text{Crystallinity (\%)} = 100 \frac{I_{110} + 1.43\ I_{200}}{0.69\ I_{am} + I_{110} + 1.43\ I_{200}} \qquad 4.1.1$$

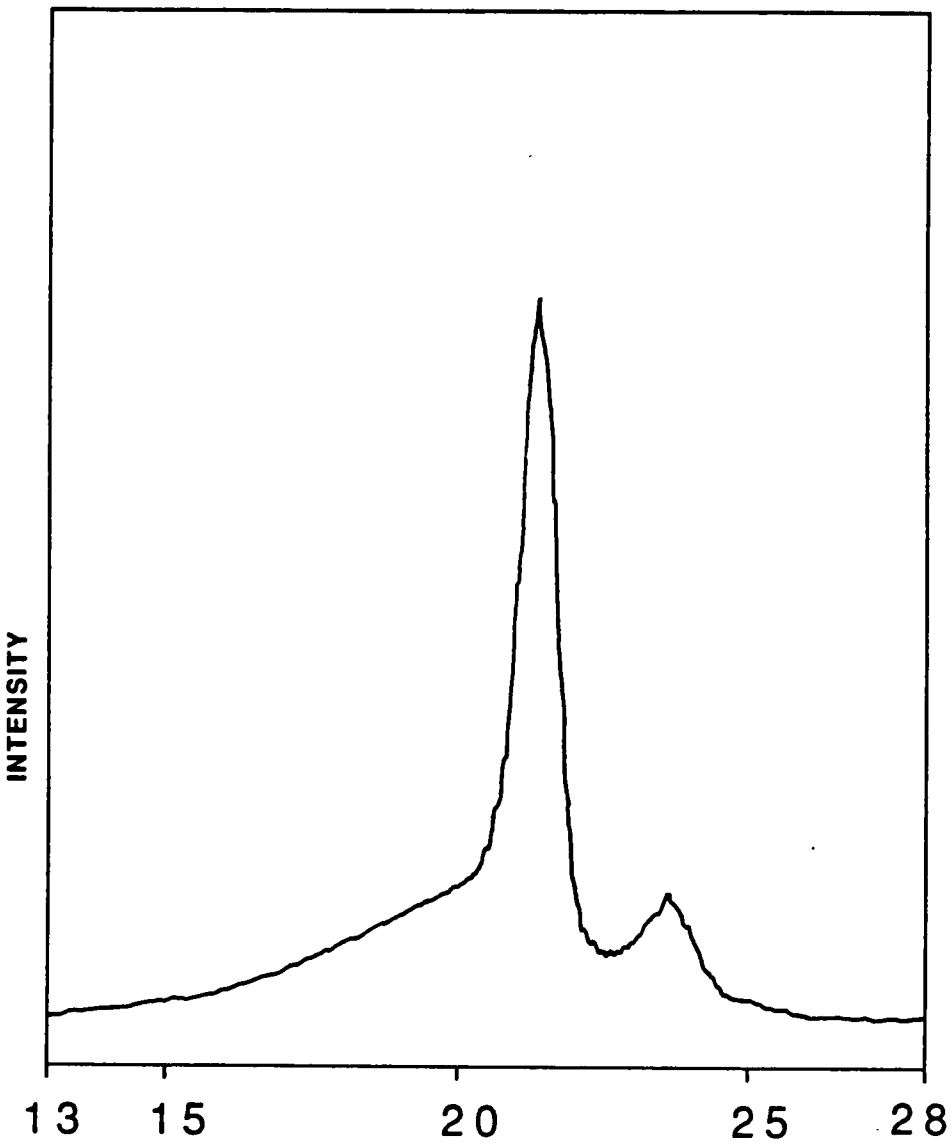



Figure 4.1.15 Wide angle x-ray diffraction curve of TR-XLPE.

where $I_{110}$ and $I_{200}$ indicates integrated area under the peaks of $110^*$ and $200^*$. $I_{am}$ indicates integrated intensity area under the amorphous halo.

The calculated WAXD crystallinities for gel, cured and uncured XLPE are shown in Figure 4.1.16. Uncured XLPE shows higher WAXD crystallinity than the cured counter-part. The gel fraction of TR-XLPE also shows higher crystallinity than even uncured TR-XLPE. Overall crystallinity values of TR-XLPE are larger than those of PL-XLPE.

4.1.6. Oxidative Induction Time Measurement

Oxidative induction time (OIT) is a relative measure of the level of oxidative stabilization of the material tested. OIT was determined for all freshly prepared samples in the presence of oxygen at 200°C. DSC curves were recorded in a plot with the time on the x-axis. The results are presented in Figure 4.1.17. The striking feature is that EC-XLPE and PL-XLPE show instantaneous oxidative exotherms on the introduction of oxygen. On the other hand, TR grade polyethylenes such as TR-XLPE and TR-LLDPE show oxidative induction times of 4.7 and 7.5 minutes, respectively.

The other finding to note is that the oxidation exotherm of XLPE is much larger than that of LLDPE. This may indicate that XLPE will have more damage resulting from the oxidation reaction than LLDPE.

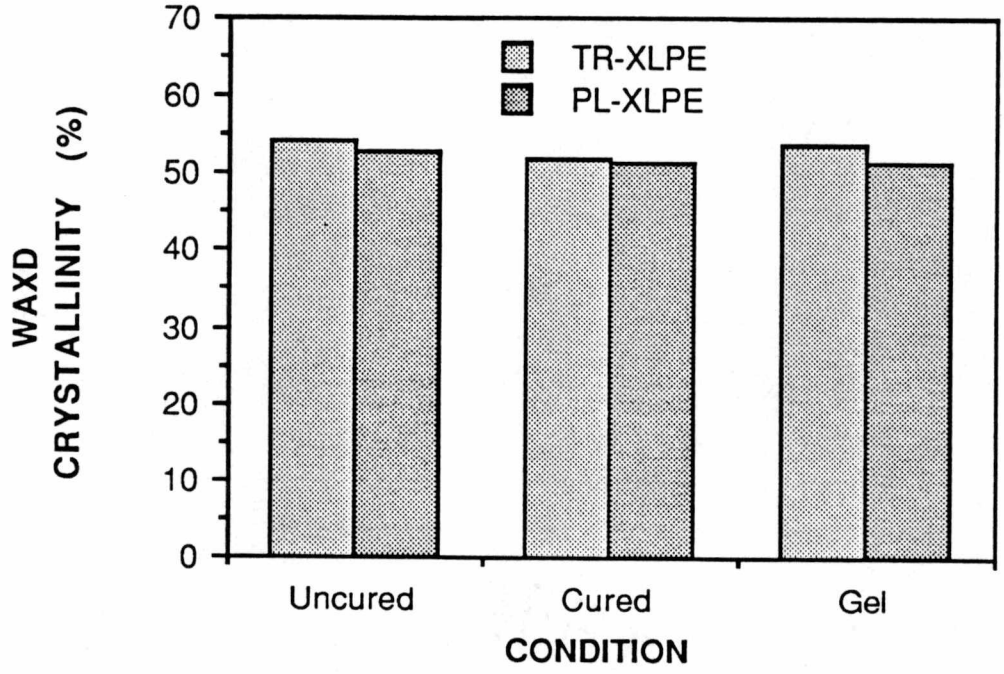



Figure 4.1.16 WAXD crystallinities of uncured, cured and gel fraction of TR-XLPE and PL-XLPE.

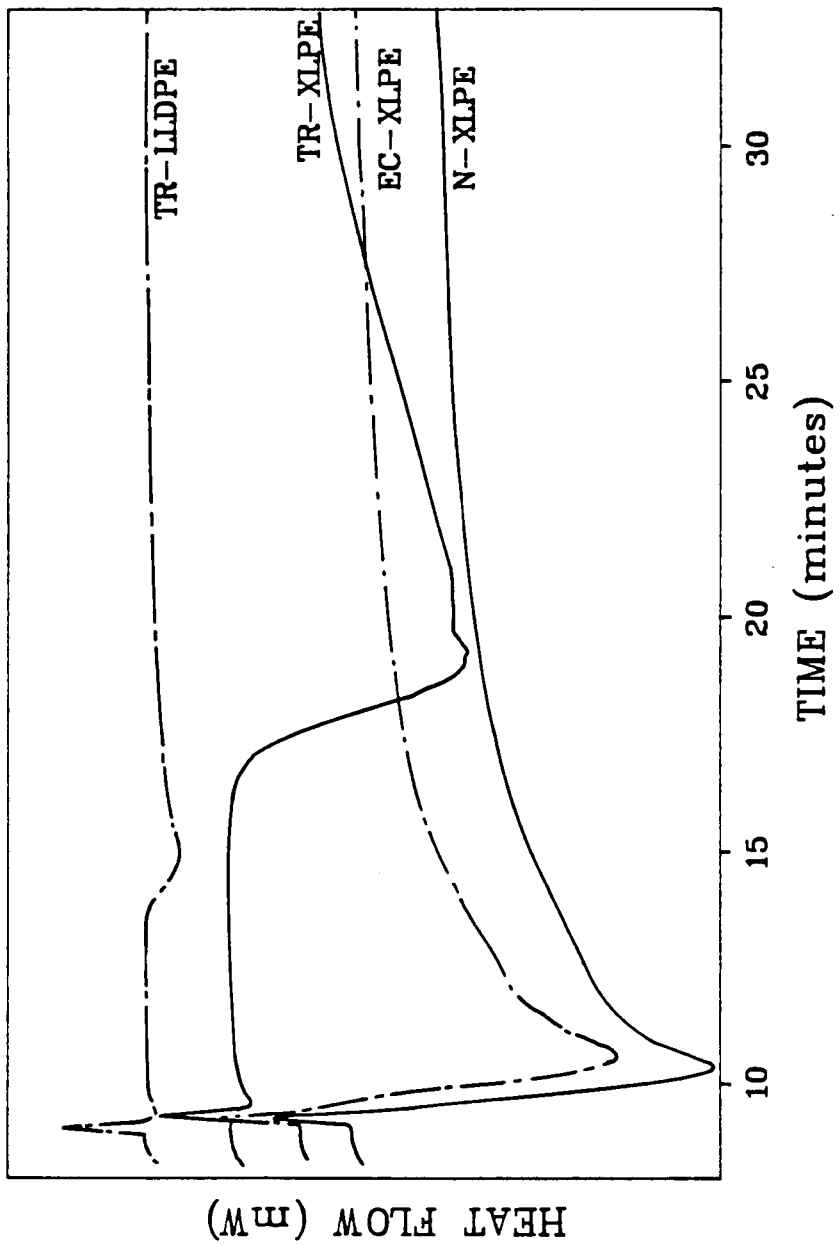



Figure 4.1.17 Oxidative exotherms of TR-XLPE, EC-XLPE, PL-XLPE and TR-LLDPE.

## 4.2. Annealing and Thermal Effects

All polymeric insulators used in transmission and distribution are exposed to high levels of thermal stresses during their normal operations, since electrical power transmission generates heat. Thermal stresses not only change properties of polymeric insulators but they also modify the structure of the materials. It is well understood that morphology of a polymeric insulator is one of the major material parameters that determine the final dielectric properties (Fukuda, 1981; Kolesov, 1980; Ceres, 1984). Therefore, it is extremely important to understand the effects of thermal stresses on the morphology of the polymeric insulators. In this section the annealing behavior and concurrent morphological developments of these recently introduced polyethylenes will be reported.

Annealing was carried out by placing samples in small test tubes, which were then placed in a silicone oil bath in which the temperature was controlled in a predetermined way for a specified time. The samples were cut from the compression molded samples in dimensions of 0.5 cm x 2.5 cm with a thickness of 1.5 mm. It was observed that the color of TR-XLPE was darkened by annealing, while the other samples did not show any noticeable change in color.

Studies of the morphological changes produced by annealing were carried out by the use of various techniques such as differential scanning calorimetry (DSC), density measurement, wide angle and small angle x-ray scattering (SAXS). The small angle x-ray scattering data will be reported in a separate section.

4.2.1. DSC Study

The melting behavior of the three different grades of crosslinked polyethylene are very similar, as discussed in the previous section. Melting curves of annealed crosslinked samples were also noted to be very similar in nature. Figure 4.2.1 shows the changes in the DSC curve of TR-XLPE with increasing annealing temperature. All annealing treatments have been carried out for three hours. At lower annealing temperatures (<100°C), a shoulder-like hump was developed about 3°C higher than the annealing temperature.

On the other hand, at annealing temperatures higher than 100°C the generation of multiple melting peaks occurs. This multiple peak was considered to be due to the phase separation of crosslinked polyethylene during annealing at temperatures from 100°C to 107°C (Phillips, 1984). The melting peak located at lower temperature is believed to be caused by the gel fraction, which has a melting peak at the same temperature. The peak at higher temperature coincides with the melting peak of the sol fraction. This indicates that small fractions with high melting point are present even after curing. Even though supercooling does not allow this fraction to separate from the gel network, annealing gives sufficient time for separation to occur.

For the annealed TR-LLDPE, a complicated melting pattern developed with increasing annealing temperature. Figure 4.2.2 shows

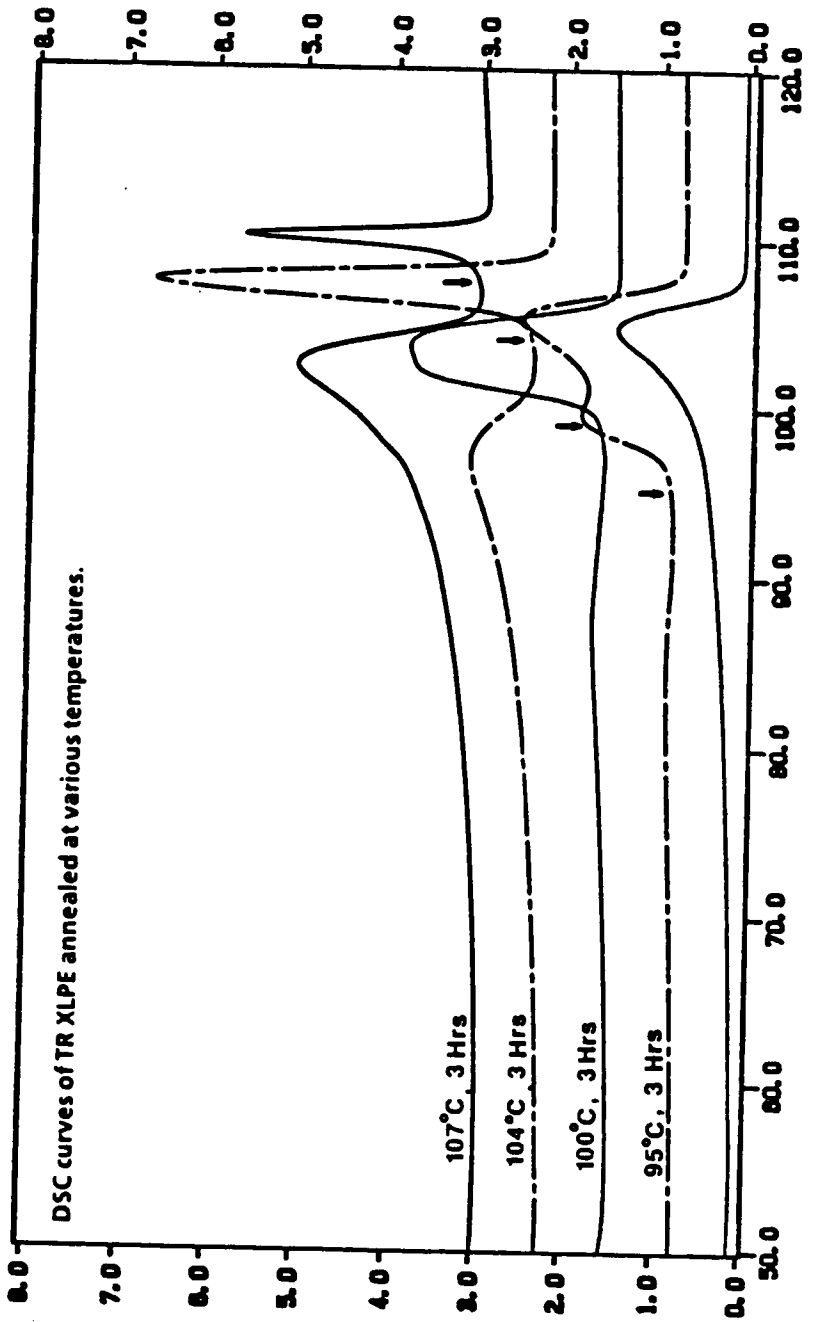



Figure 4.2.1 Variation of DSC curves of TR-XLPE annealed at different temperatures for 3 hours.

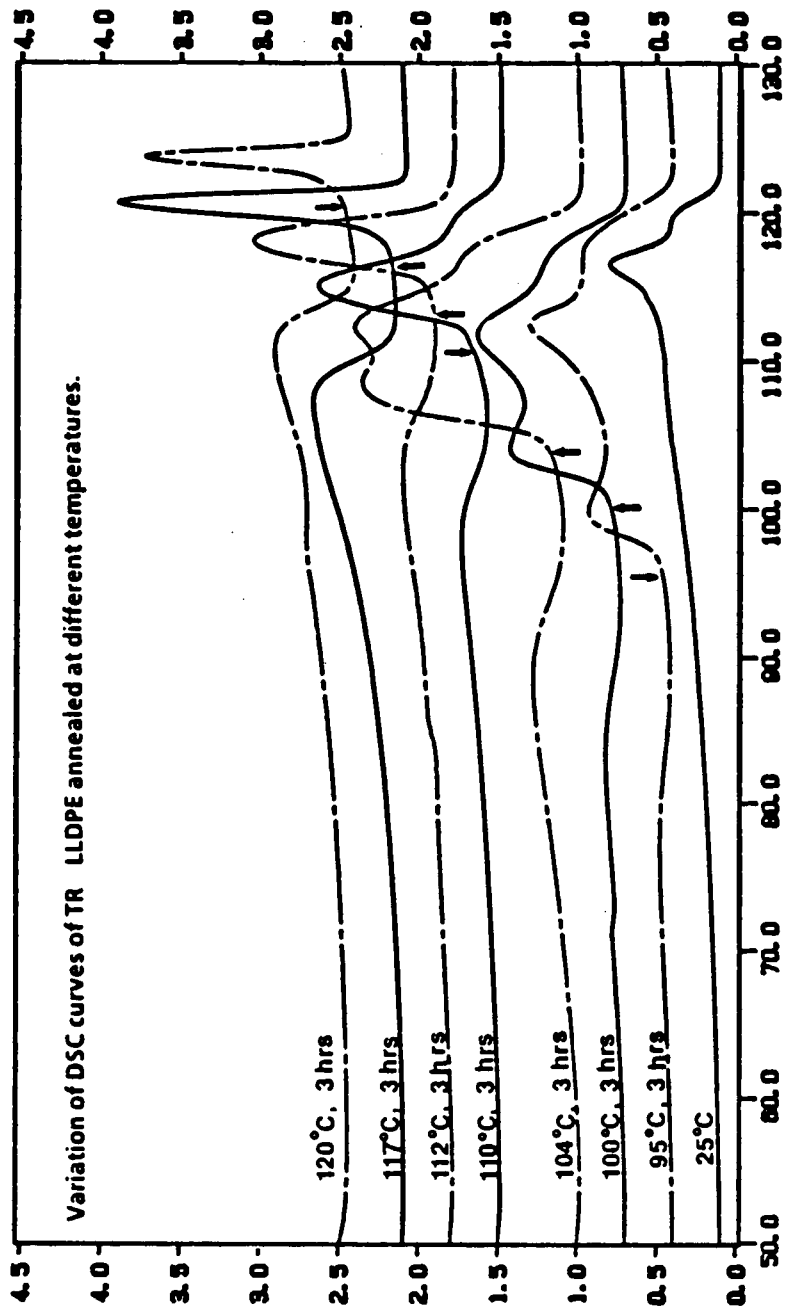



Figure 4.2.2 Variation of DSC curves of TR-LLDPE annealed at different temperatures for 3 hours.

the melting curves of TR-LLDPE annealed at different temperatures. At a lower annealing temperature an abrupt shoulder was developed about 3 degrees higher than the annealing temperature. However, at relatively high annealing temperatures (ca. 112-120°C), TR-LLDPE exhibits major separation of melting peaks. The lower broad peak is thought to be produced by material unable to crystallize at the annealing temperature.

The effect of annealing time on the melting behavior of TR-XLPE is illustrated in Figure 4.2.3. This figure shows change in melting curves with annealing time for TR-XLPE annealed at 107°C. At the annealing temperature where separation occurs, the gap between the two melting peaks increases with annealing time. The first melting peak moves toward lower temperatures, while the higher melting peak increases to higher temperatures. Similar trends were also noted for all polyethylene samples including TR-LLDPE. As shown in Figure 4.2.4, TR-LLDPE annealed at 117°C for various periods of time shows a further increase in the gap between the two melting peaks. The time dependence observed at the annealing temperature of 117°C for TR-LLDPE is considered to be similar in nature to those observed for XLPEs annealed at 107°C.

The increase of second peak temperature with annealing time is illustrated in a semi-log plot at annealing temperatures 107°C as shown in Figures 4.2.5. The increase in melting peak was found to follow linear relationship in a semi-log plot. This feature is not unique, since all time dependences in annealing has been noted to be

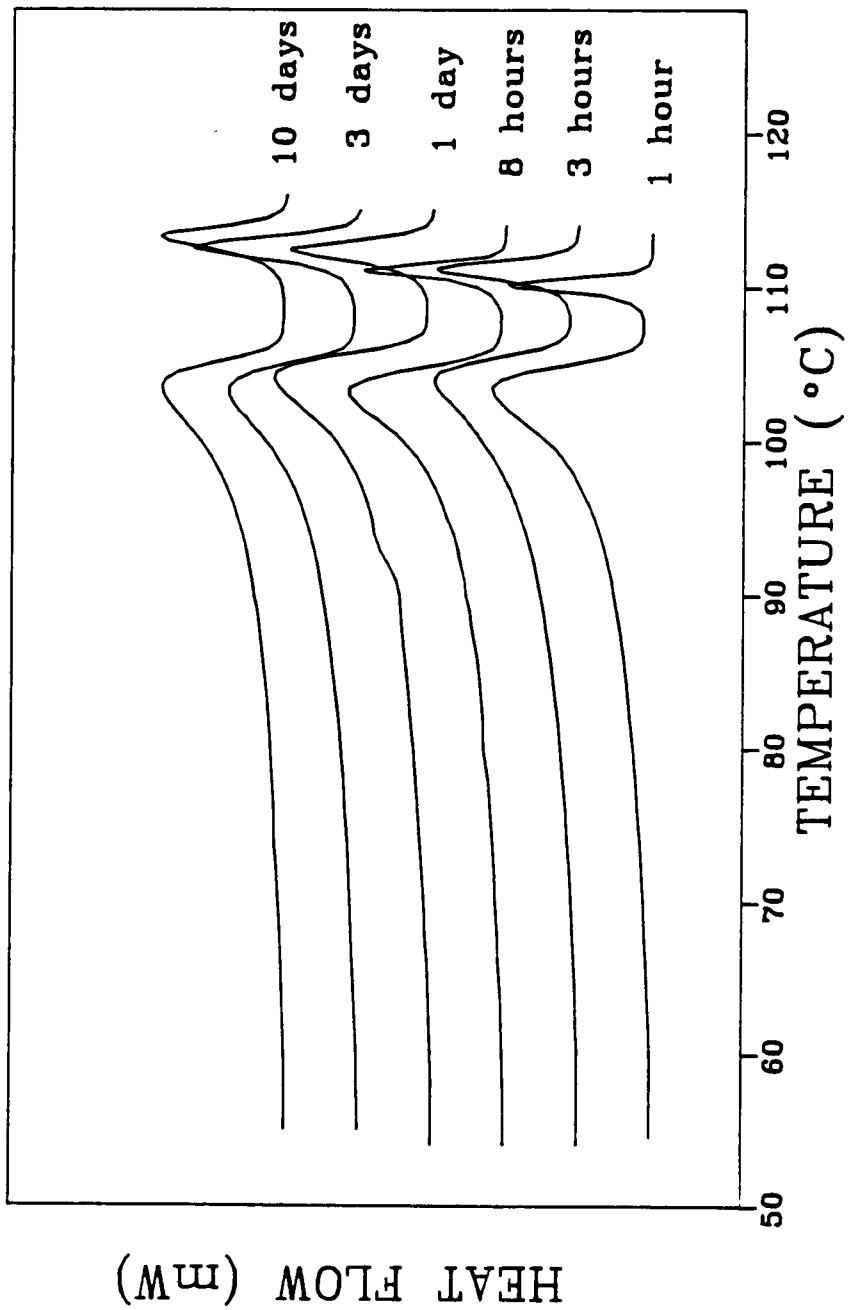



Figure 4.2.3 DSC curves of TR-XLPE annealed at 107°C for various periods of time.

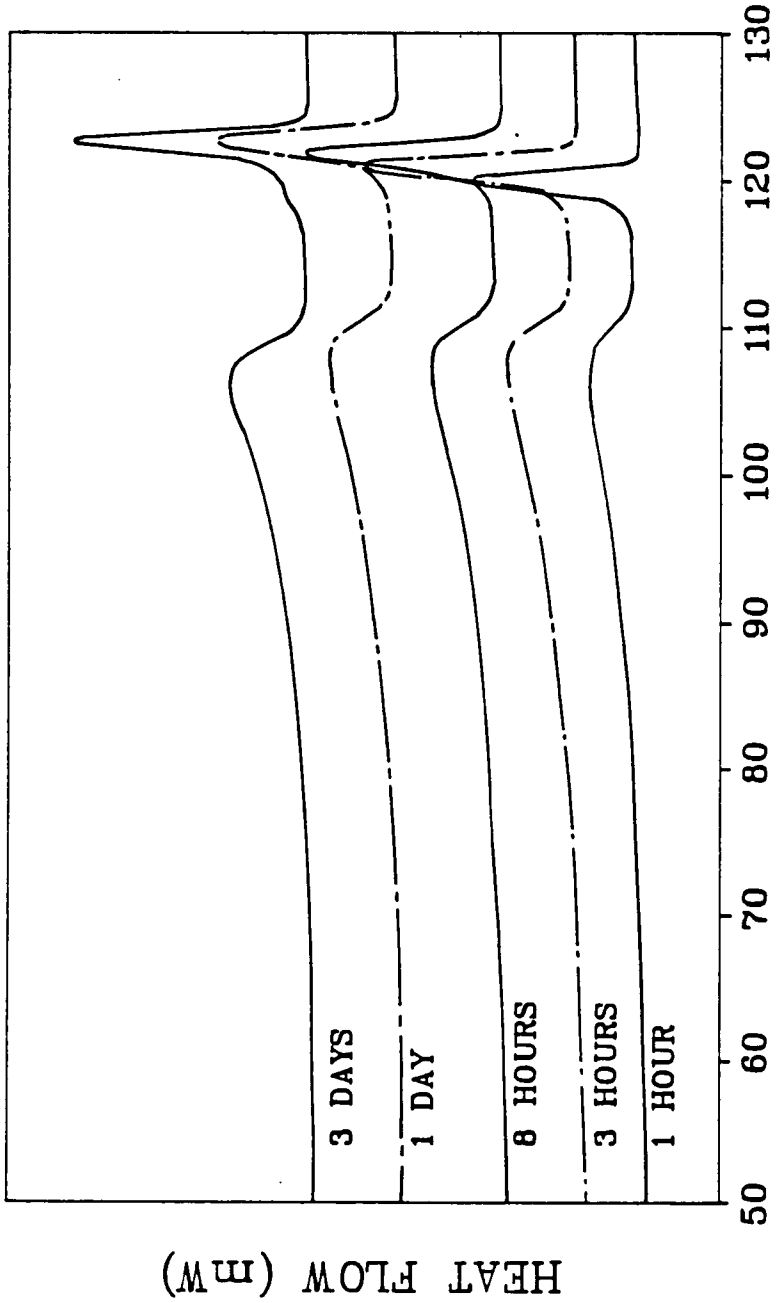



Figure 4.2.4 DSC curves of TR-LLDPE annealed at 117°C for various periods of time.

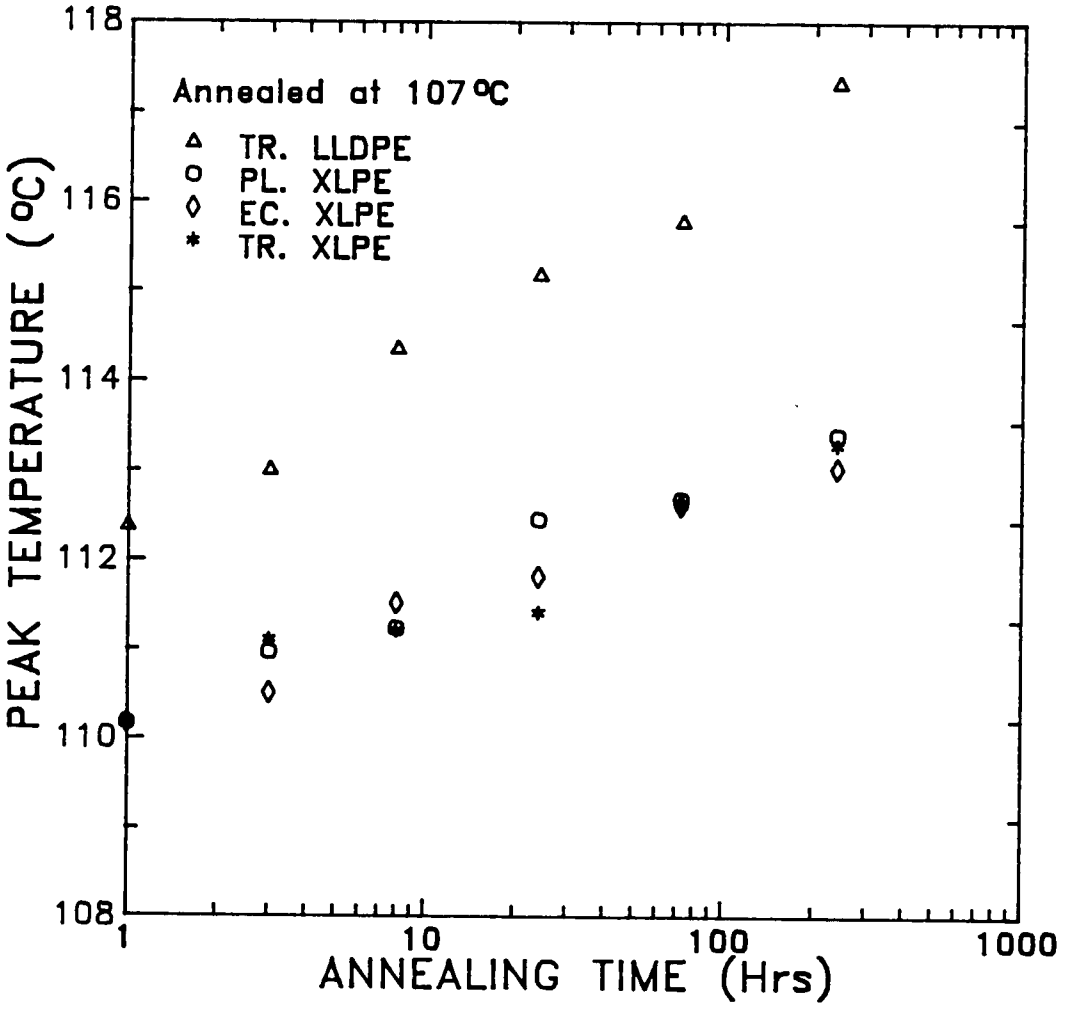



Figure 4.2.5 Plots of second melting peak temperatures of TR-XLPE, EC-XLPE, PL-XLPE and TR-LLDPE as a function of annealing time at 107°C

logarithmic. It is, however, interesting that TR-LLDPE annealed at 107°C shows an increase in melting temperature of the second peak, and that the increment of temperature for TR-LLDPE is much higher than XLPEs. Similar trends are also found for the polyethylene samples annealed at 100°C as shown in the Figure 4.2.6. It was also noted that the increments of second melting peak with the increase of annealing time at the annealing temperature of 100°C are lower than those performed at the annealing temperature of 107°C.

Another feature of the change in the DSC curve with annealing time is the variation of the heats of fusion of each peak. The heat of fusion ($\triangle H_f$) is an indicator of the fraction of crystals melting. Figure 4.2.7 shows changes in the total heat of fusion with annealing time for samples annealed at 107°C. It was noted that all annealed samples show lower values of heat of fusion than fresh samples without annealing. This can be attributed to the separation of two peaks out of one single melting peak. Upon annealing, however, $\triangle H_f$ shows a steady increase. The overall values of heat of fusion of TR-LLDPE annealed at 107°C show higher values than those of XLPE, even though the initial value of TR-LLDPE is almost the same as that of other XLPEs. This can be due also to the more severe separation of melting peaks for XLPE.

Separation of melting peaks was further investigated to evaluate the heat of fusion values of each peak for the sample annealed at 107°C. Figure 4.2.8 shows the variation of heats of fusion of the melting peak located at the lower temperature. Data

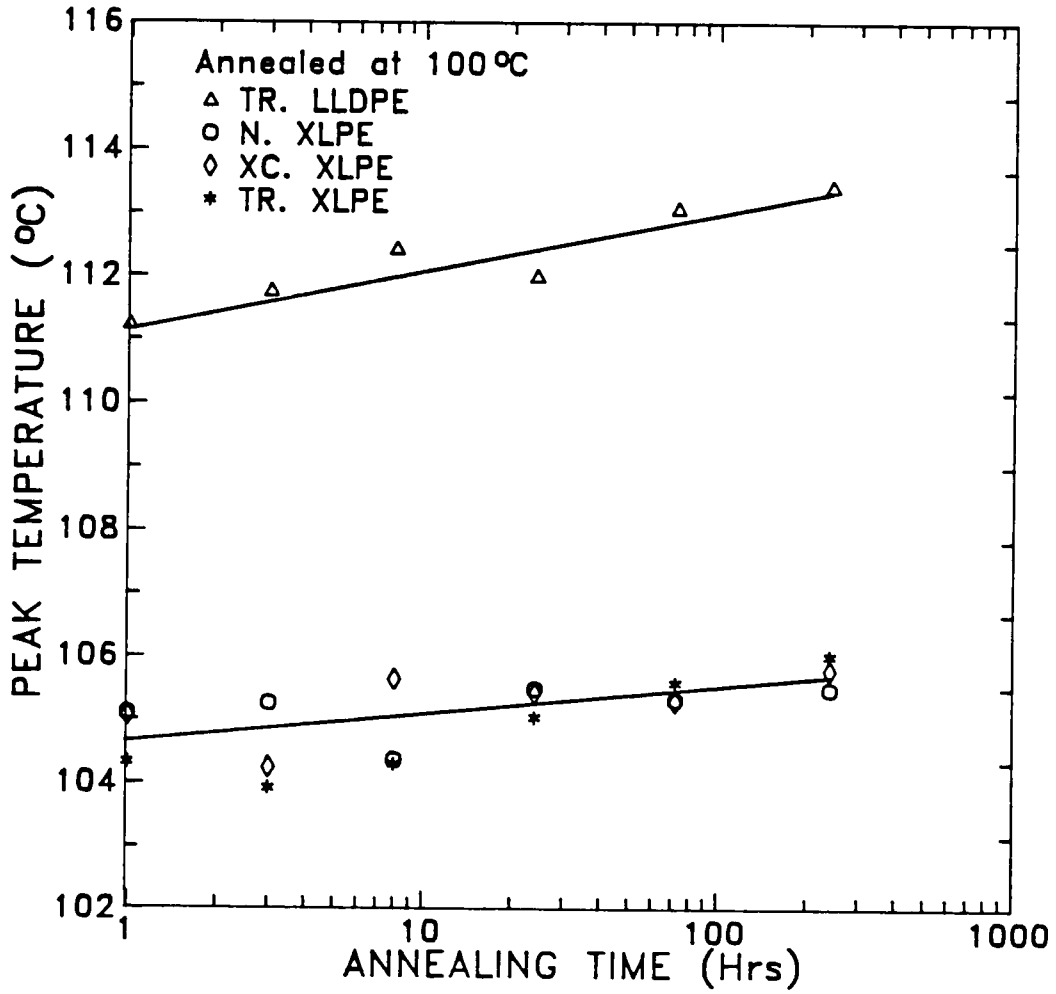



Figure 4.2.6 Plots of second melting peak temperatures of TR-XLPE, EC-XLPE, PL-XLPE and TR-LLDPE as a function of annealing time at 100°C

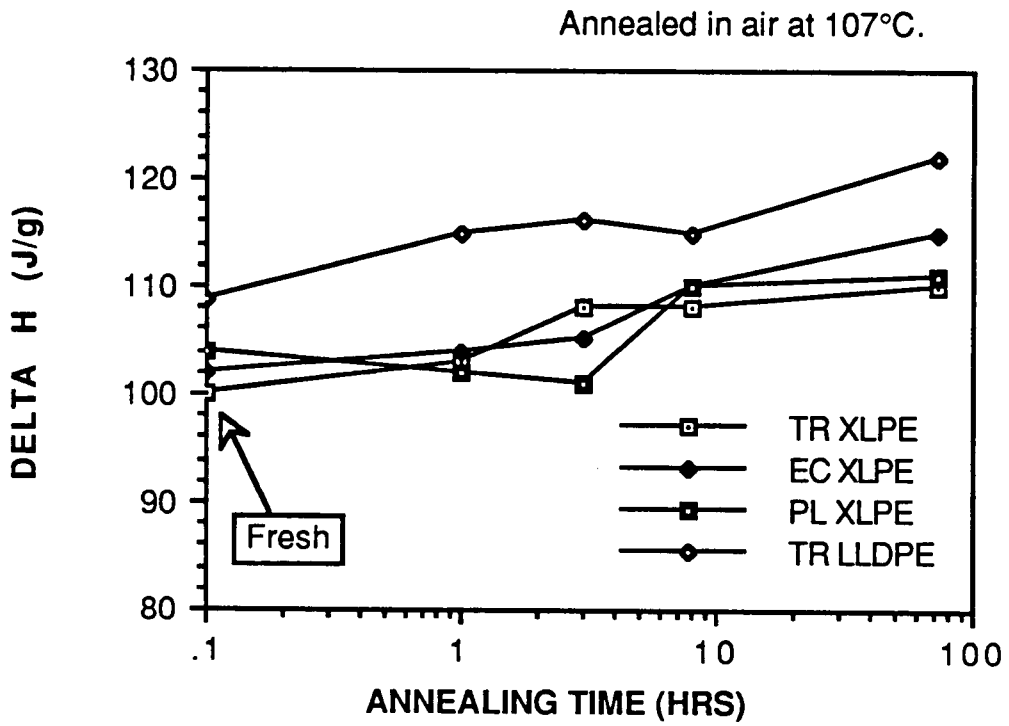



Figure 4.2.7 Variation of heat of fusion of TR-XLPE, EC-XLPE, PL-XLPE and TR-LLDPE with annealing time.

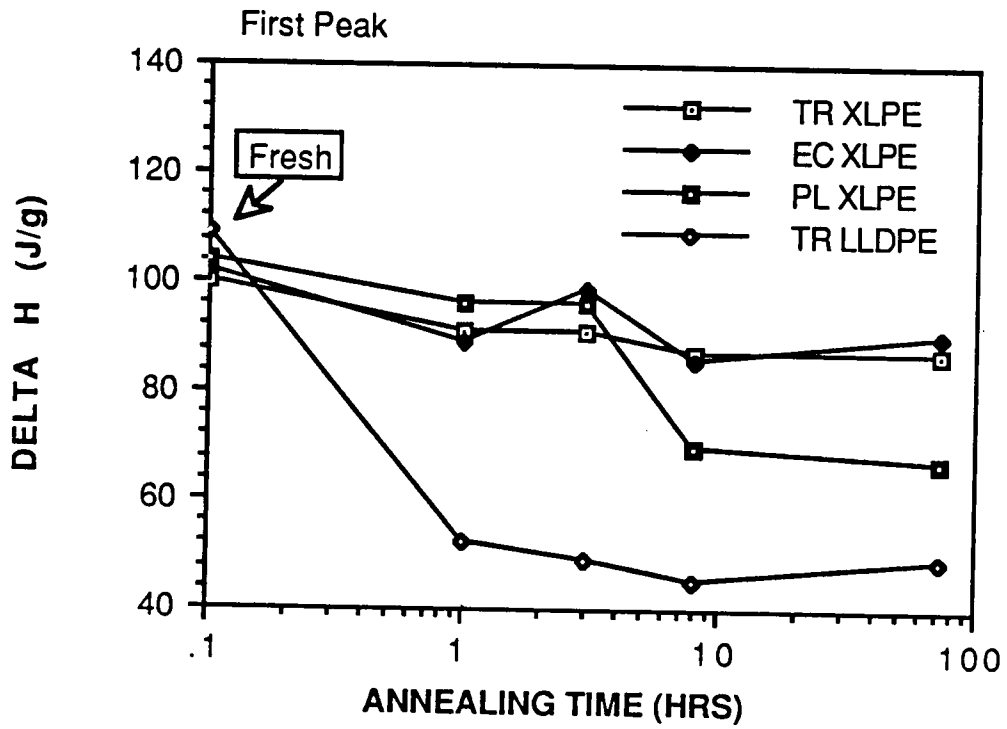



Figure 4.2.8 Variation of heat of fusion of first melting peaks of TR-XLPE, EC-XLPE, PL-XLPE and TR-LLDPE with annealing time.

points located in leftmost position in the plots indicate the total value of heat of fusion for the unannealed samples. As annealing time increases, $\hat{}H_f$ of the peak located at a lower temperature shows a steady decrease.

The variation of the second melting peaks with annealing time is illustrated in Figure 4.2.9. The second melting peak was noted to increase in size with annealing time. It is of interest to note that the incremental values of $\hat{}H_f$ of the second peak are larger than the decrements of $\hat{}H_f$ of first peaks. This finding suggests that the perfection of crystals associated with the second peak occurs at the expense of the crystals melting in first peaks as well as of the amorphous content.

TR-LLDPE follows similar trends with annealing time at 107°C, resulting in decreasing the first peak size and increasing the second peak size. The initial point of TR-LLDPE shown in Figure 4.2.8 indicates the whole heat of fusion of unannealed TR-LLDPE. Relatively small value of the heat of fusion of the first peak of the annealed TR-LLDPE indicates that the amount of crystalline fraction having a lower melting temperature that the annealing temperature is small compared to the cases of XLPEs.

Annealing studies were also performed using different environments. Samples were annealed at 107°C in a silicone bath held in a test tube filled with silicone oil. Annealing with direct contact to the oil can be more effective. During annealing it was observed that some portion of the oil penetrated to the sample,

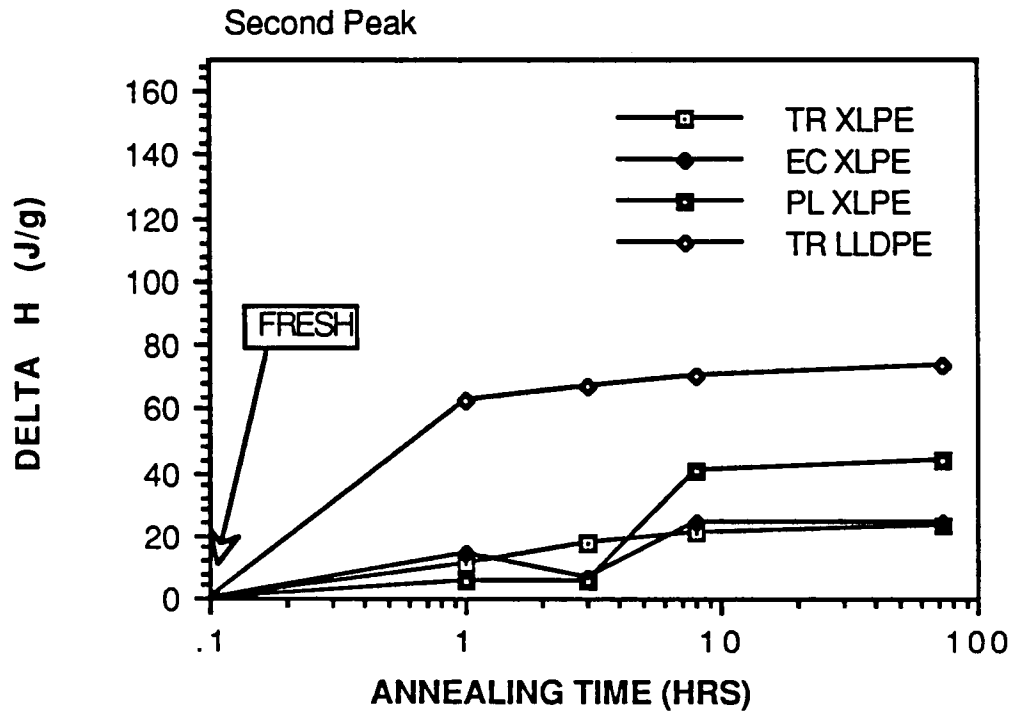



Figure 4.2.9 Variation of heat of fusion of second melting peaks of TR-XLPE, EC-XLPE, PL-XLPE and TR-LLDPE with annealing time.

generating a yellowish tint throughout the samples. Especially, TR-XLPE shows a much darker color than the sample annealed in air. Figure 4.2.10 shows the variation of the second melting peak with annealing time. The second melting peak moves toward higher temperatures with increase of annealing time, as was observed for the samples annealed in air. The values of second melting peaks were also noted to be similar to those of the samples annealed in air. Total heats of fusion of the samples annealed at 107°C in silicone oil were found to change in a similar pattern to those of the samples annealed in air, as illustrated in Figure 4.2.11.

For additional DSC studies, samples were annealed in an electric insulating oil supplied by Exxon Corp having the brand name Univolt™ 60. Annealing of XLPEs and LLDPE was carried out in an insulating oil bath at various temperatures, to investigate the interactions between materials and oils. All samples were annealed for 3 to 8 hours.

Figures 4.2.12 and 4.2.13 show the DSC curves of XLPEs and LLDPE annealed at 107°C for 8 hours. Annealing all grades of XLPEs resulted in drastic changes in the DSC curves, revealing one broad melting peak below the annealing temperature (ca. 89-94°C). This indicates dissolution of the material, especially fractions having higher melting point, and recrystallization of other fractions upon cooling from annealing. Since the fractions of material with high melting point are believed to be short and uncrosslinked, this fraction may be more subjected to chemical damage than other

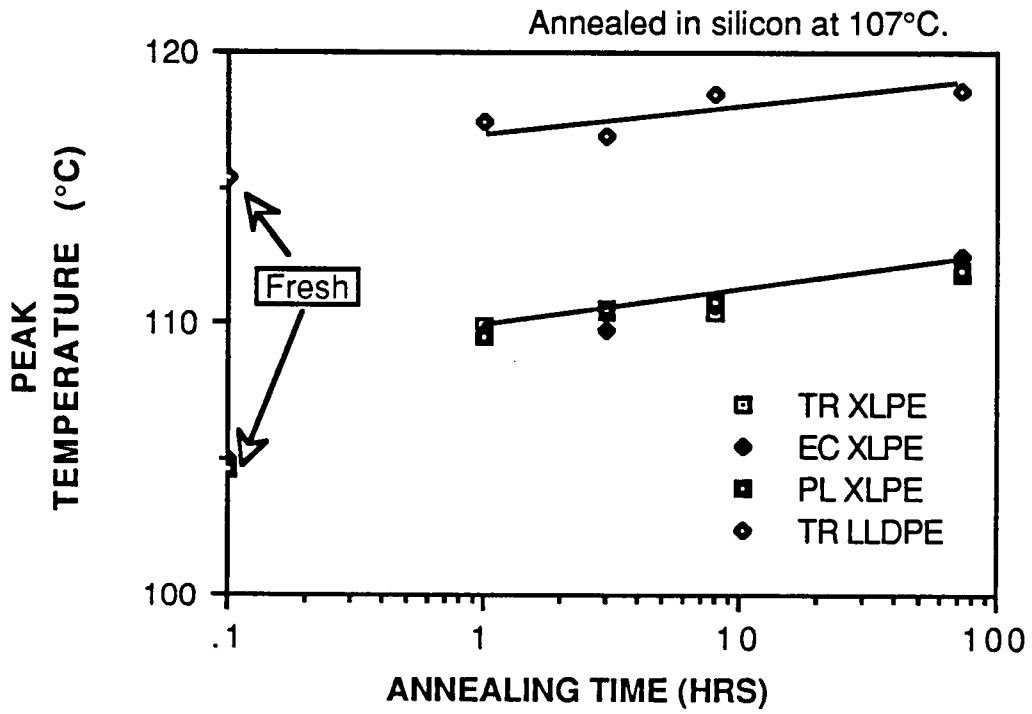



Figure 4.2.10 Variation of second melting peak temperatures of TR-XLPE, EC-XLPE, PL-XLPE and TR-LLDPE as a function of annealing time at 107°C in silicone oil.

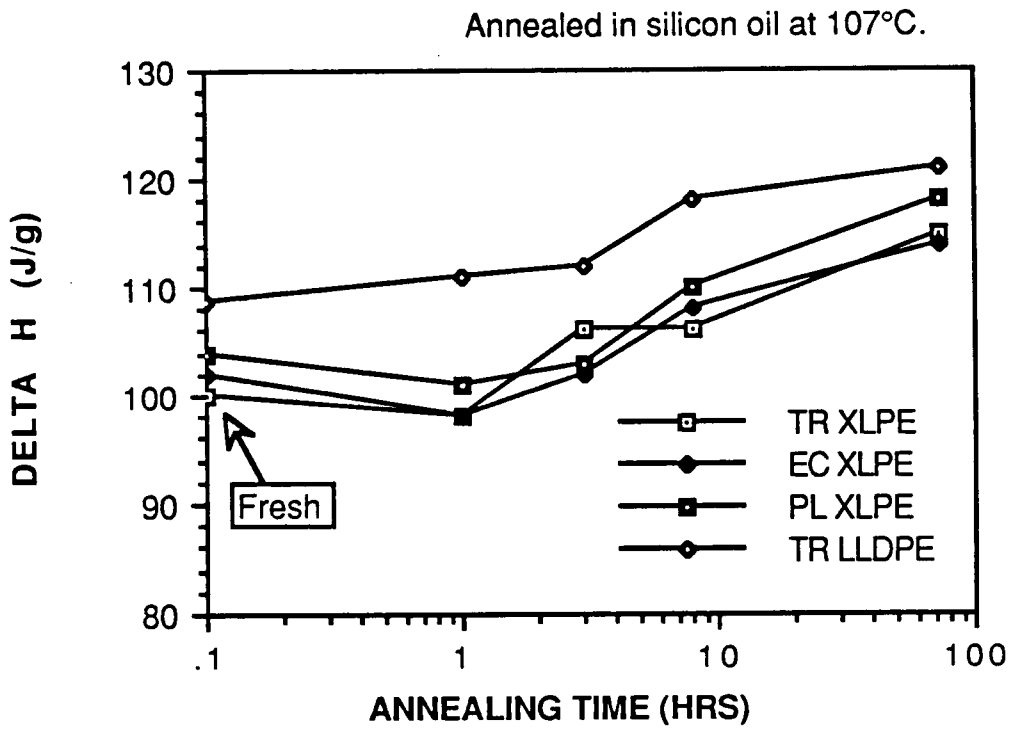



Figure 4.2.11 Variation of heat of fusion of TR-XLPE, EC-XLPE, PL-XLPE and TR-LLDPE with annealing time at 107°C in silicone oil.

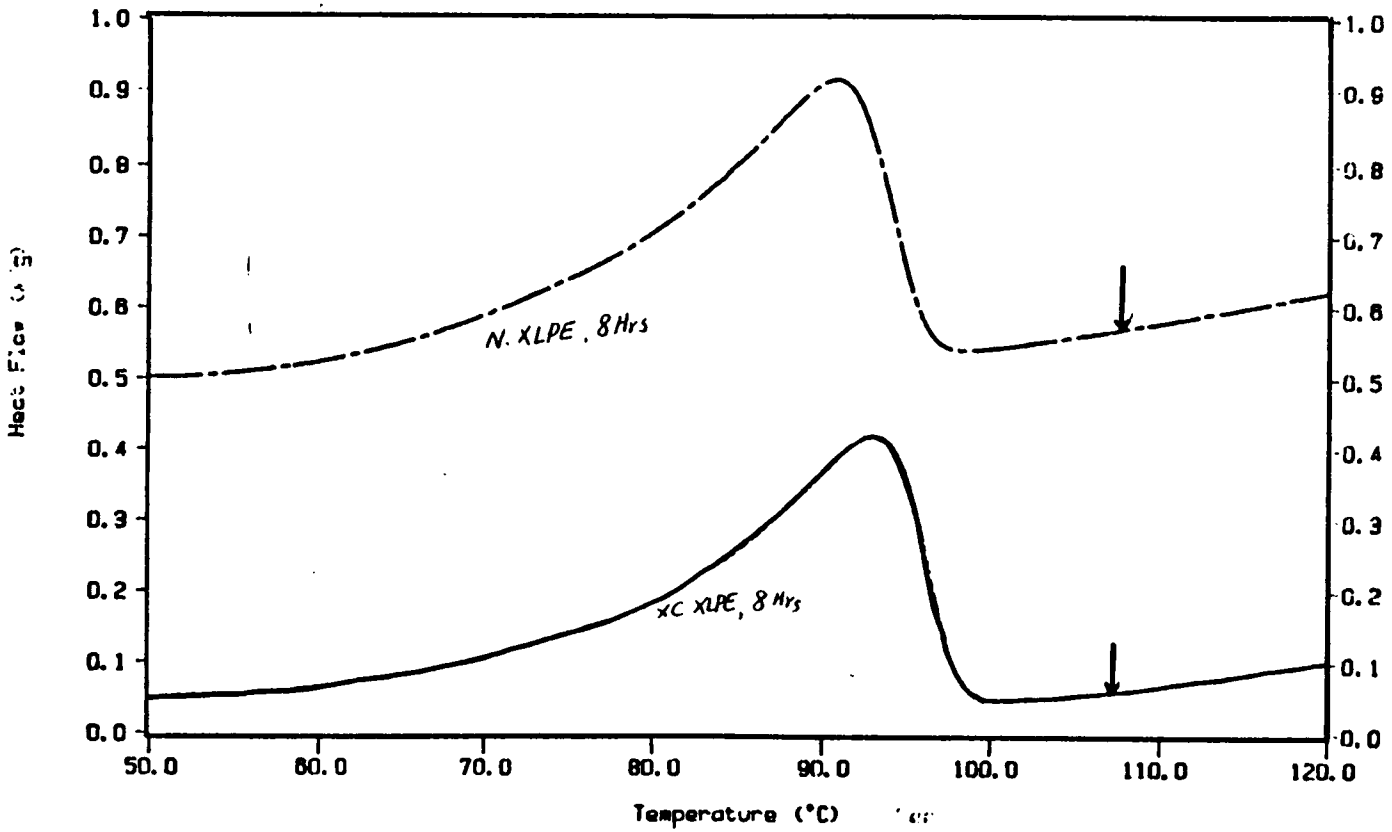



Figure 4.2.12 DSC curves of PL-XLPE and EC-XLPE annealed at 107°C in transformer oil for 8 hours.

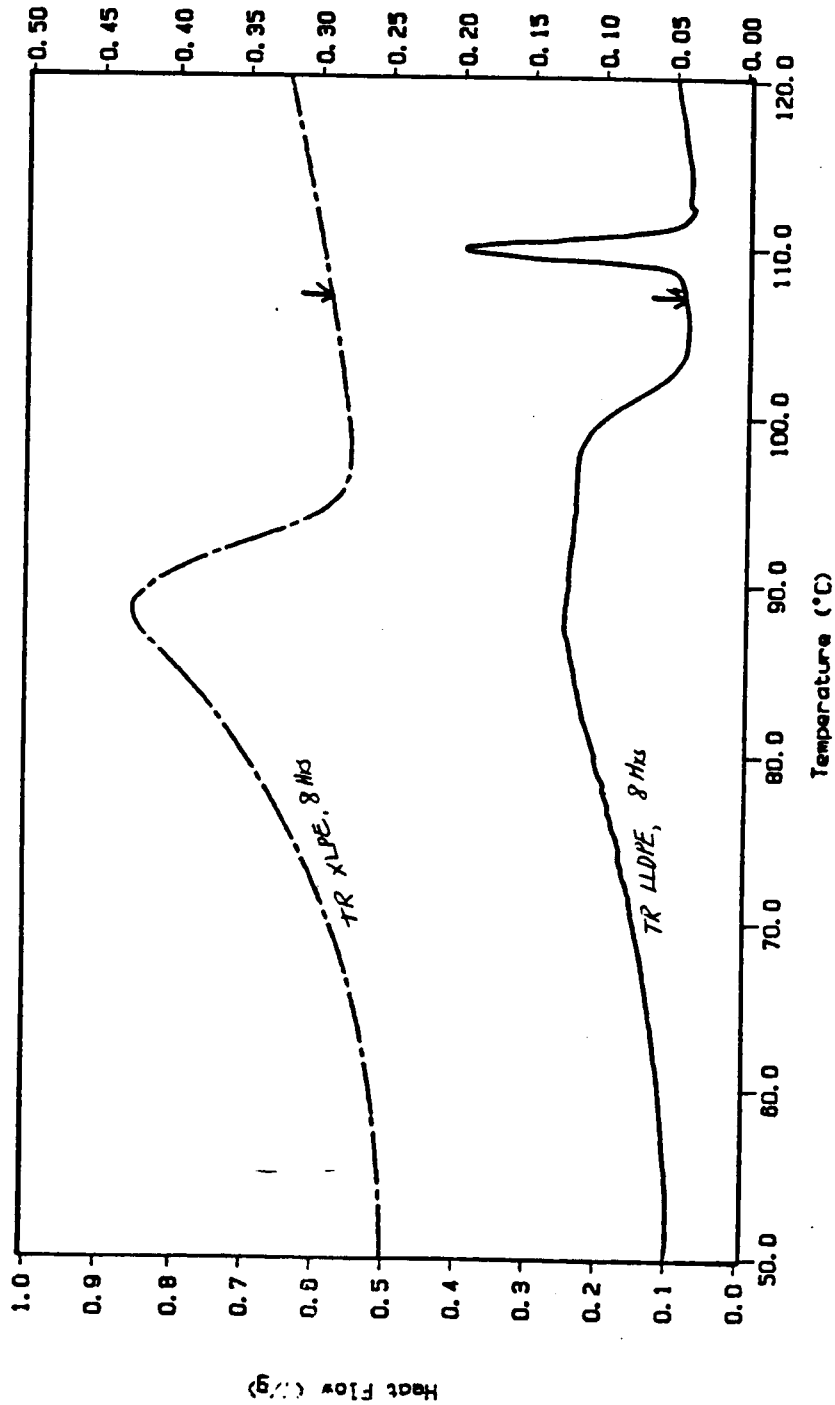



Figure 4.2.13 DSC curves of TR-XLPE and TR-LLDPE annealed at 107°C in transformer oil for 8 hours.

portions. However, data indicate that the actual dissolved fraction is larger than the portion of extractables which is normally believed to be ca. 18%. EC-XLPE shows a relatively higher melting peak (ca. 94°C) than the other grades. TR-XLPE shows the lowest melting peak (ca. 89°C). However, annealing at 78°C did not cause any severe damage to the materials. Their DSC curves are quite similar to those annealed in other media, such as air or silicone oil (Figure 4.2.14).

As illustrated in Figure 4.2.13, the DSC curve of annealed TR-LLDPE is quite different from those of XLPE, exhibiting separation of melting peaks located below and above the annealing temperature. The fraction associated with the lower melting peak was not a crystalline solid at the annealing temperature. This fraction forms a very broad melting peak, indicating a wide range of distribution of copolymer contents.

### 4.2.2. Density Measurement

For the crosslinked polyethylene samples annealed at 107°C in air environment, densities were determined using the density column described in Chapter 3 and the previous section. The variation of densities of the samples are illustrated in Figure 4.2.15. It was found that density increases as the annealing time increases. However, the initial increase in density with short exposure (one hour) to the higher temperature shows an increase higher than the increase for an annealing time of 30 hours.

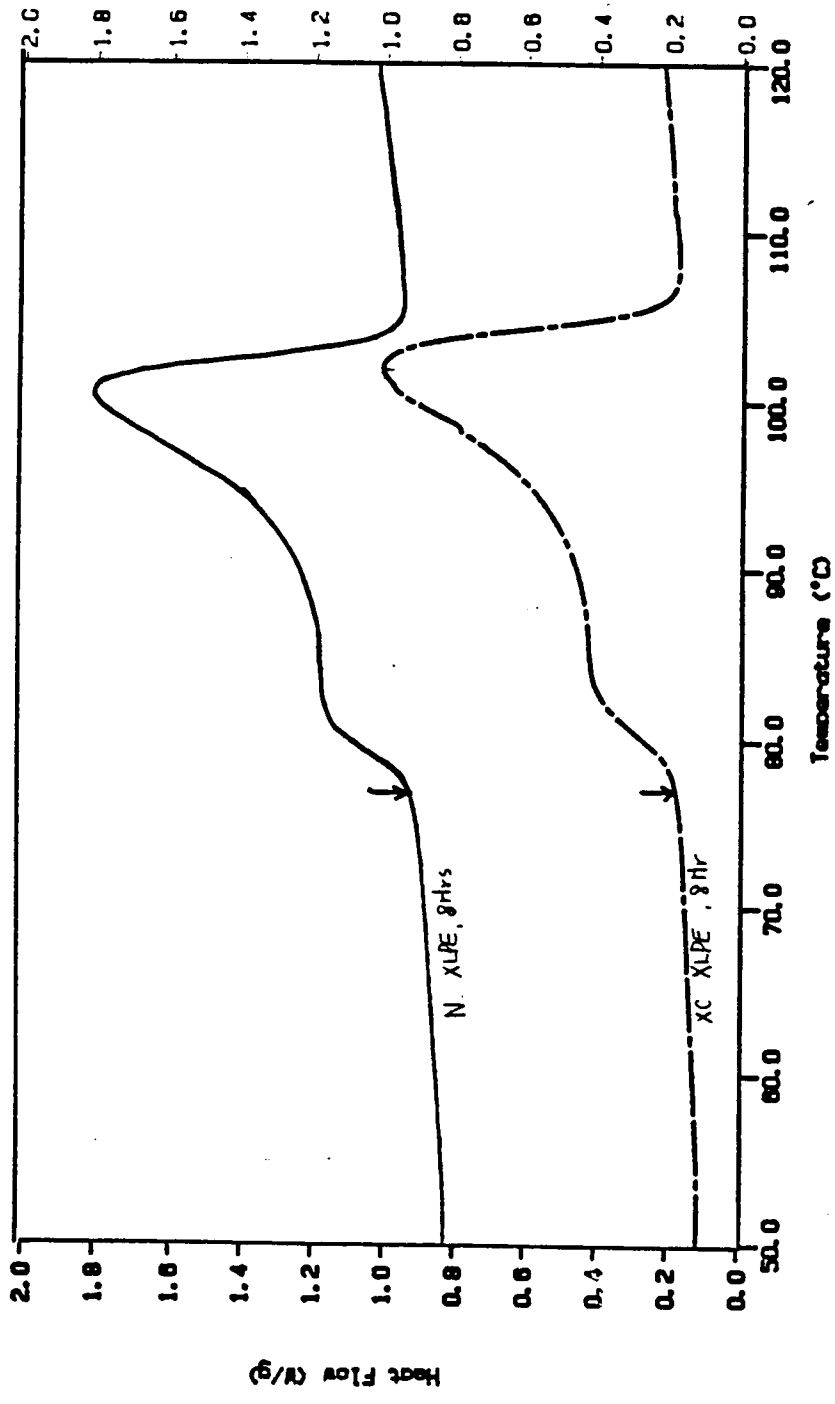



Figure 4.2.14 DSC curves of PL-XLPE and EC-XLPE annealed at 78°C in transformer oil for 8 hours.

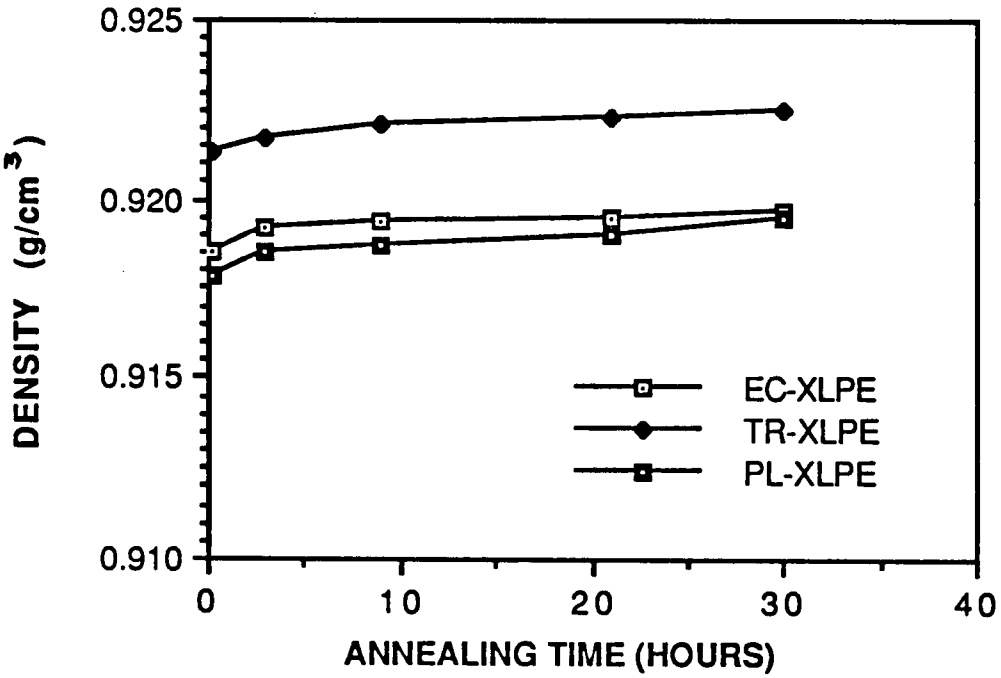



Figure 4.2.15 Variation of densities of TR-XLPE, EC-XLPE and PL-XLPE with annealing time at 107°C.

It is interesting that the densities of annealed TR-XLPE are higher than those of the other XLPEs for the same annealing treatment. The density of fresh TR-XLPE was also higher than those of the other XLPEs. However, the increment in density of TR-XLPE with annealing time was almost the same as those of the other XLPEs.

Crystallinity was also determined from the density using the linear relationship between density and crystallinity as described in the previous section. The density of TR-XLPE shows the variation from 51.5% for the unannealed sample to 52.1% for the sample annealed for 30 hours. On the other hand, the crystallinities of EC-XLPE vary from 49.7% for unannealed sample to 50.5% for the sample annealed for 30 hours.

### 4.2.3. Wide Angle X-ray Diffraction

Crystallinities were also determined from wide-angle x-ray diffraction scans for the crosslinked polyethylene sample annealed at 107$^{o}$C for various periods of time. Figure 4.2.16 shows the variation of crystallinity determined from WAXD data. The increase in crystallinity was noted for all annealed samples compared to the fresh samples. The crystallinity shows an increase with annealing time, varying from 51.1% for unannealed PL-XLPE to 53.7% for fully annealed EC-XLPE. It is interesting to note that unlike the density data, TR-XLPE did not show a higher crystallinity value than the rest of the crosslinked polyethylenes. However, some TR-XLPE samples showed higher crystallinity values within the experimental error.

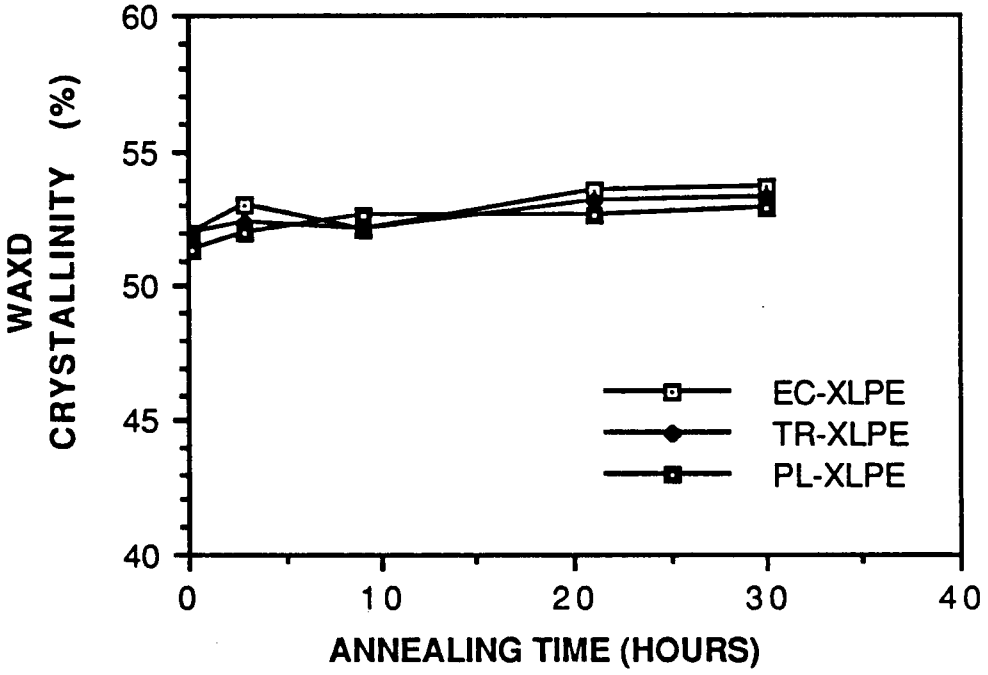



Figure 4.2.16 Variation of WAXD crystallinities of TR-XLPE, EC-XLPE and PL-XLPE with annealing time at 107°C.

## 4.3. Experimental Results of SAXS

### 4.3.1. General Observations

Crosslinked polyethylene, which is the major polymeric insulation for the cable application, can be divided into sol and gel fraction as other elastomers. Lightly crosslinked polyethylene normally contains up to 20 % of uncrosslinked sol fraction within the matrix of the crosslinked gel network. In addition to sol and gel contents, crystalline and amorphous regions also have to be characterized as for regular semi-crystalline polymers. Small angle x-ray scattering (SAXS) was utilized to elucidate the general macrostructure of crosslinked polyethylene.

Small angle x-ray scattering stems from the fluctuation of electron densities of the entities within the materials. Interpretation of SAXS results makes it possible to understand macrostructures ranging up to 1000 Å in size. The SAXS experiments in this work have been carried out using the 10-meter SAXS camera at the NCSASR in Oak Ridge, Tennessee.

SAXS studies were performed for uncured crosslinkable polyethylenes, cured crosslinked polyethylenes and a linear-low-density polyethylene. Major studies were carried out with a long geometry whose actual distance of sample to detector is 5.126 m. SAXS measurements were also performed with short geometry, where sample to detector distance was 2.126 m. SAXS measurement with a short geometry reveals information for a smaller range of macrostructure. Even though the shorter sample-to-detector distance

permits the collection of data over a wide range of scattering vector, SAXS data thus obtained are not very useful in the understanding of macro-structure. Most analyzable features occur near the beam stop in a very small angle region with a scattering vector less than 0.06 $A^{-1}$. The data in the smaller angle region can be more easily obtained using the 5.126 m geometry.

### 4.3.2. Unaged Polyethylenes

SAXS analyses begin with the collection of scattering intensity contour plots. Since all polyethylene samples were prepared by compression molding only, all SAXS patterns are circular in shape as illustrated in Figure 4.3.1. The iso-intensity contour plots were then radially averaged to obtain one-dimensional SAXS intensity plots. Figure 4.3.2 shows the radially averaged SAXS intensity plots against scattering vector K for HDPE, LLDPE, tree-retardant (TR) XLPE, and TR-LDPE. It is of interest to note that whereas the SAXS plot of HDPE shows a relatively sharp peak near the beam-stop, the plots of the other polyethylenes show broad Bragg maxima at higher angles. The general shapes of radially averaged SAXS curves of XLPE are different from those of LLDPE. The SAXS plots of XLPE show well-defined Bragg maxima, indicating the presence of stackings of two entities with different electron densities, presumably amorphous and crystalline layers. On the other hand, the SAXS intensities of LLDPE decrease monotonically with a smaller hump-like Bragg maximum. The SAXS curves corrected by the Lorentz geometric factor are presented in Figure 4.3.3 for the data

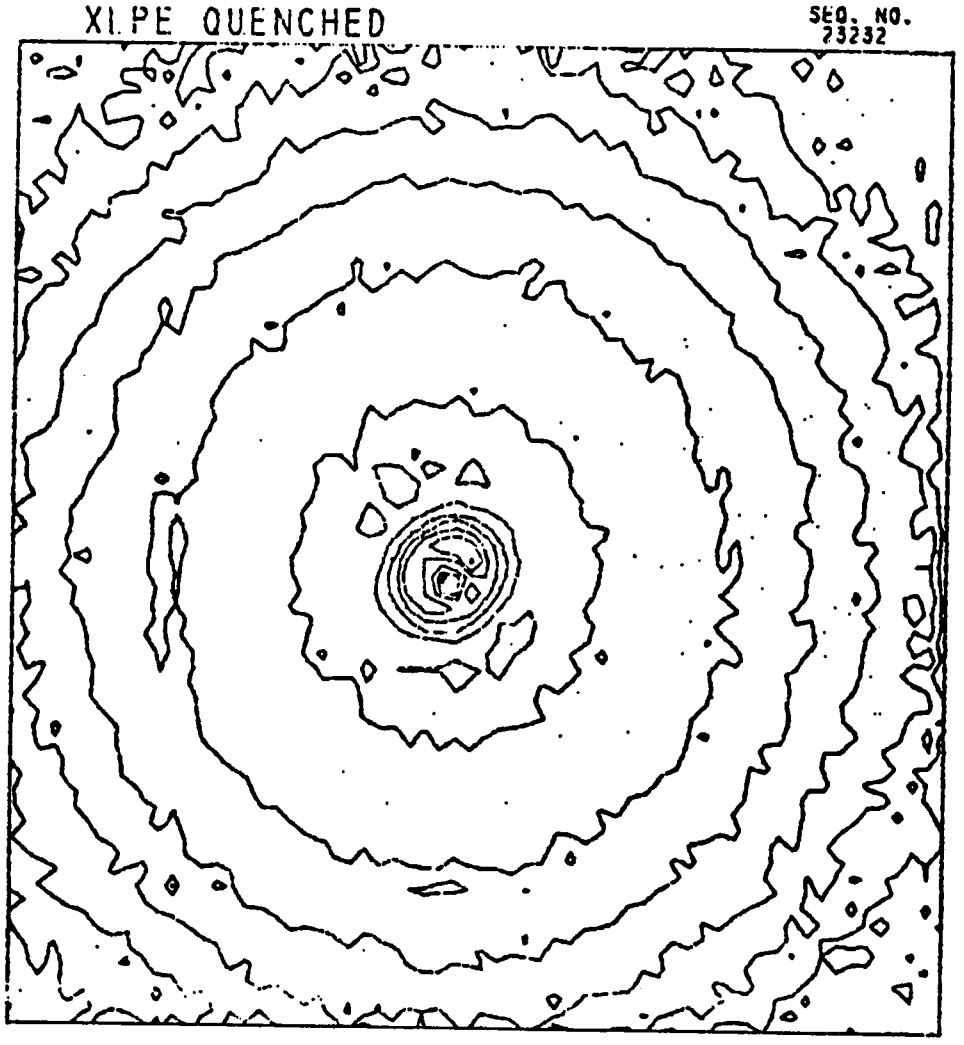



Figure 4.3.1 SAXS contour plot of unannealed TR-XLPE.

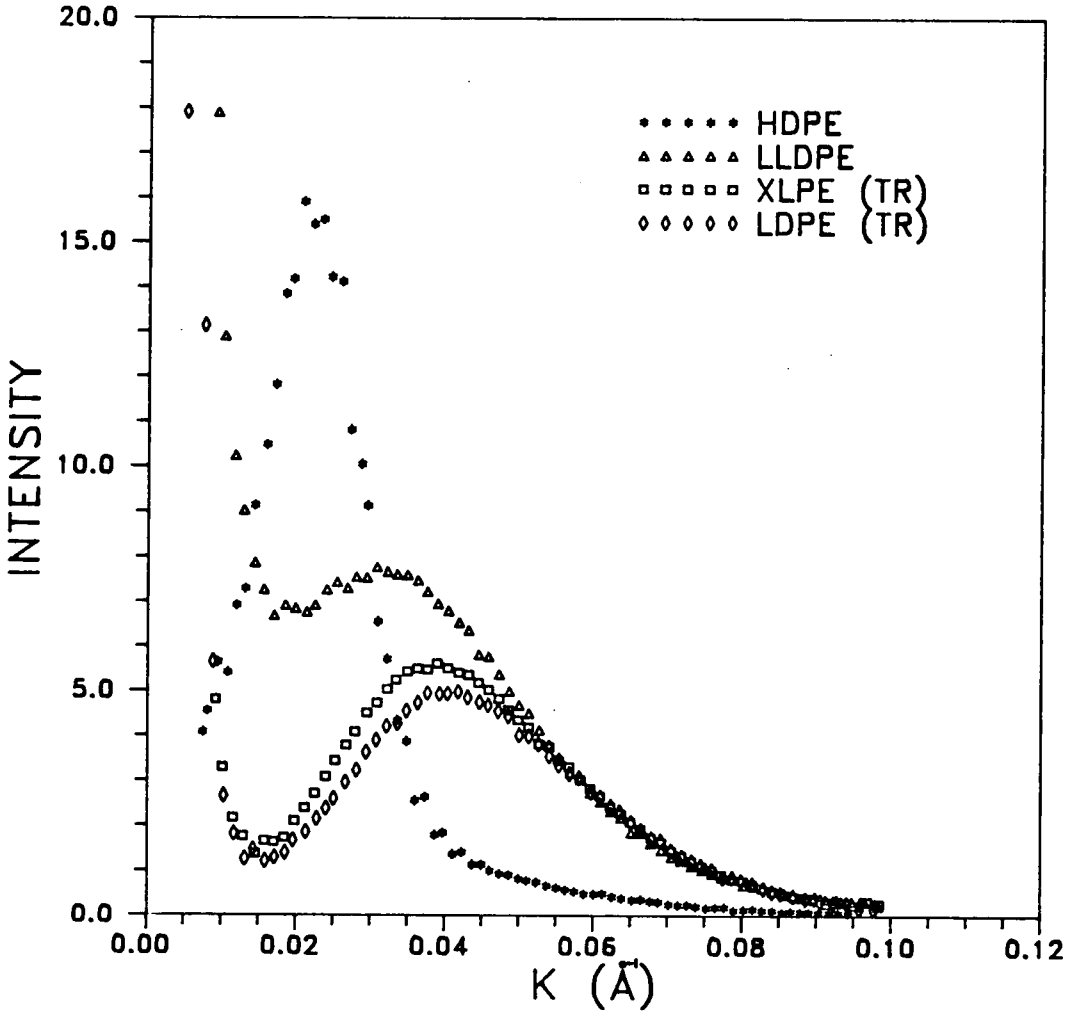



Figure 4.3.2 SAXS intensity curves of HDPE, TR-XLPE, TR-LDPE and TR-LLDPE.

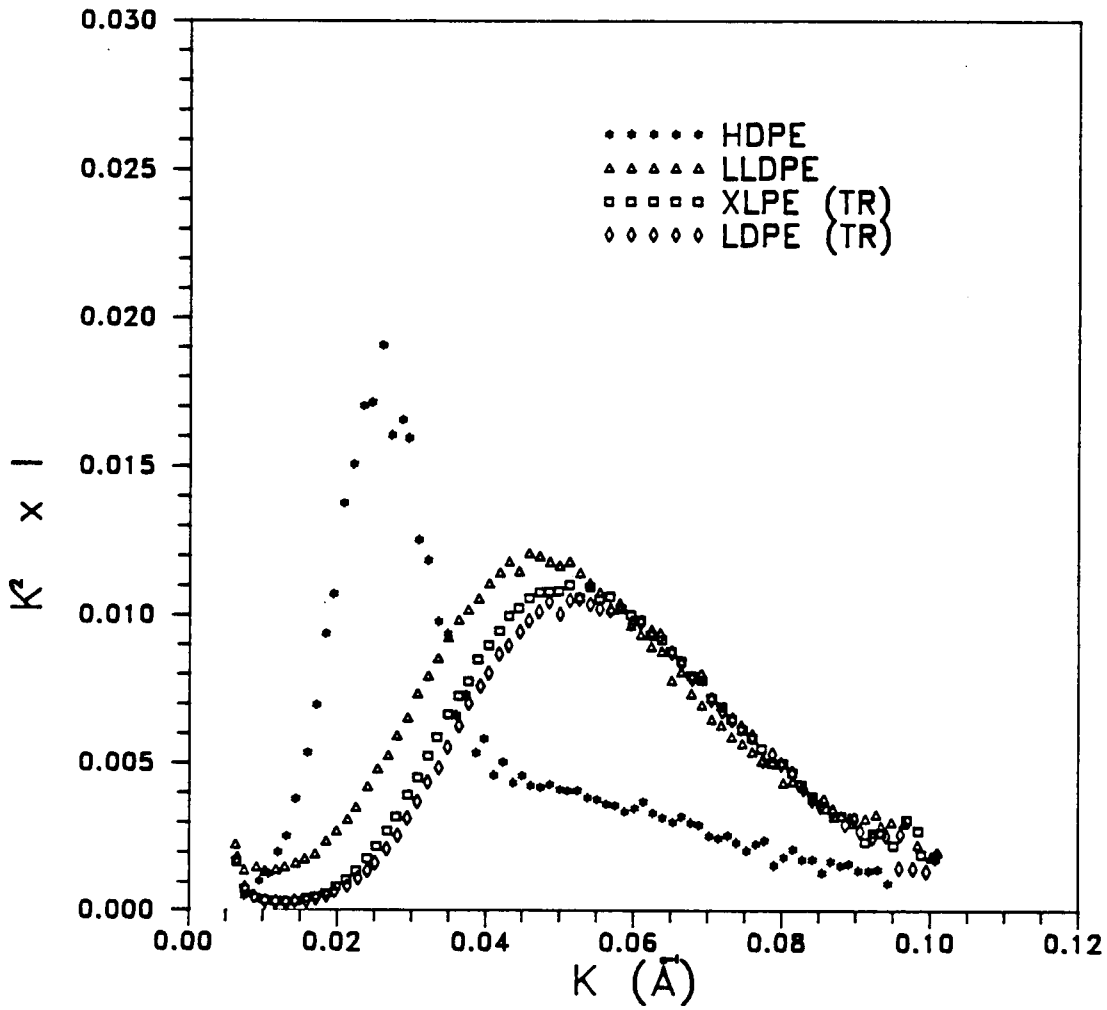



Figure 4.3.3 Lorentz-corrected SAXS intensity curves of HDPE, TR-XLPE, TR-LDPE and TR-LLDPE.

of Figure 4.3.2. The plot of HDPE shows a distinct major peak along with a minor second peak near the Bragg maxima of the other polyethylenes.

The plots of intensity versus scattering vector are different from one another for different fractions from the same TR-XLPE sample. SAXS intensity plots of uncured TR-LDPE, cured TR-XLPE and the gel portion of TR-XLPE are compared in Figure 4.3.4. The scattering invariant for the cured sample was found to be higher than that of uncured LDPE as shown in Figure 4.3.5 in which the Lorentz-correction has been applied. The scattering invariant Q, that can be written as a function of crystallinity and density of each phase, is the area under the Lorentz-corrected SAXS intensity curves. Similar trends are also found between cured and uncured extra-clean (EC) grade polyethylene as shown in Figures 4.3.6 and 4.3.7 that illustrate the unmodified and Lorentz-corrected SAXS intensity curves, respectively.

One-dimensional SAXS curves of all three different grades of XLPE are shown in Figures 4.3.8 and 4.3.9. The tree-retardant XLPE shows relatively lower scattering intensity compared to that of the other XLPEs such as PL-XLPE and EC-XLPE in unmodified SAXS plot (Figure 4.3.8) and corrected SAXS plot (Figure 4.3.9). However, the uncured counterpart of these materials show no major difference in SAXS curves as plotted in Figure 4.3.10.

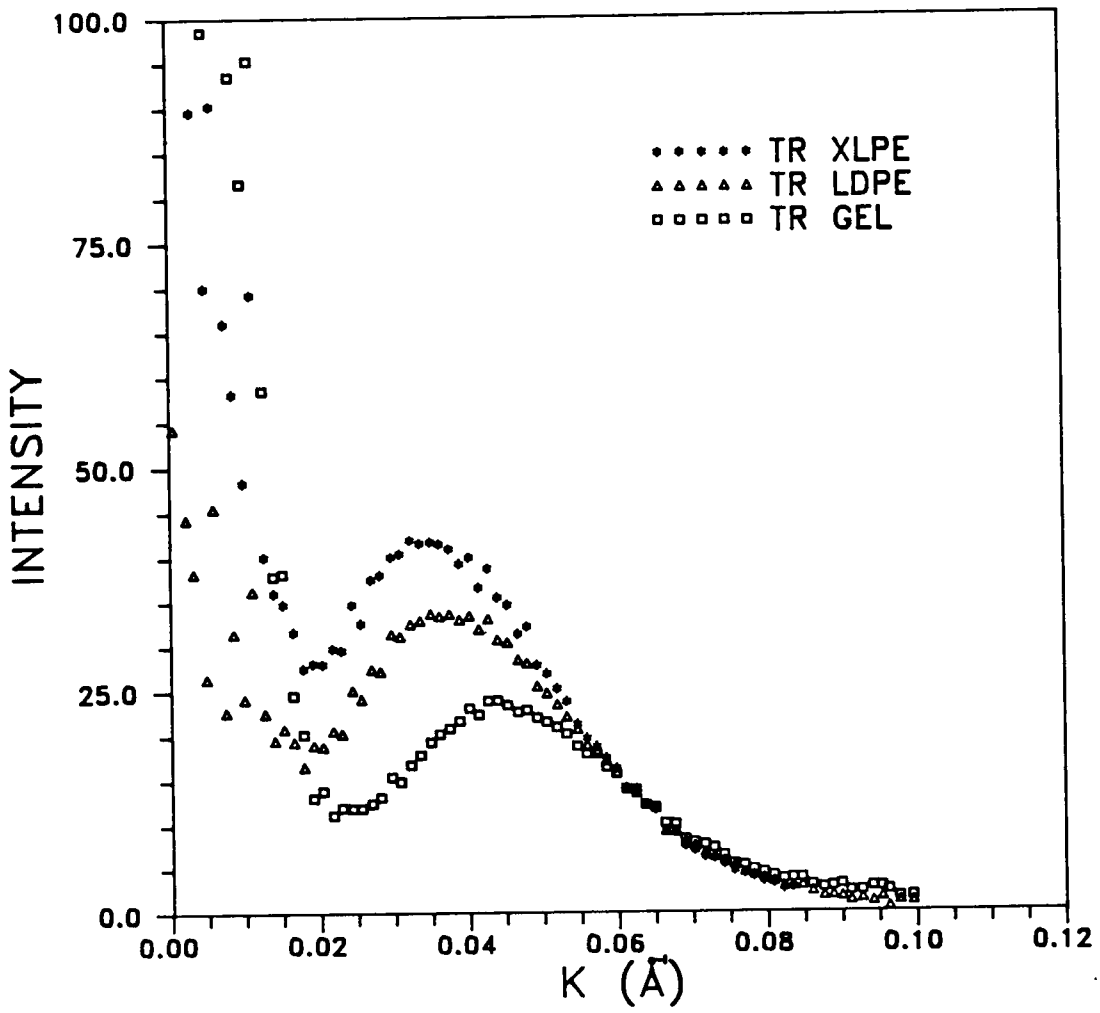



Figure 4.3.4 SAXS intensity curves of TR-XLPE, TR-LDPE and gel fraction of TR-XLPE.

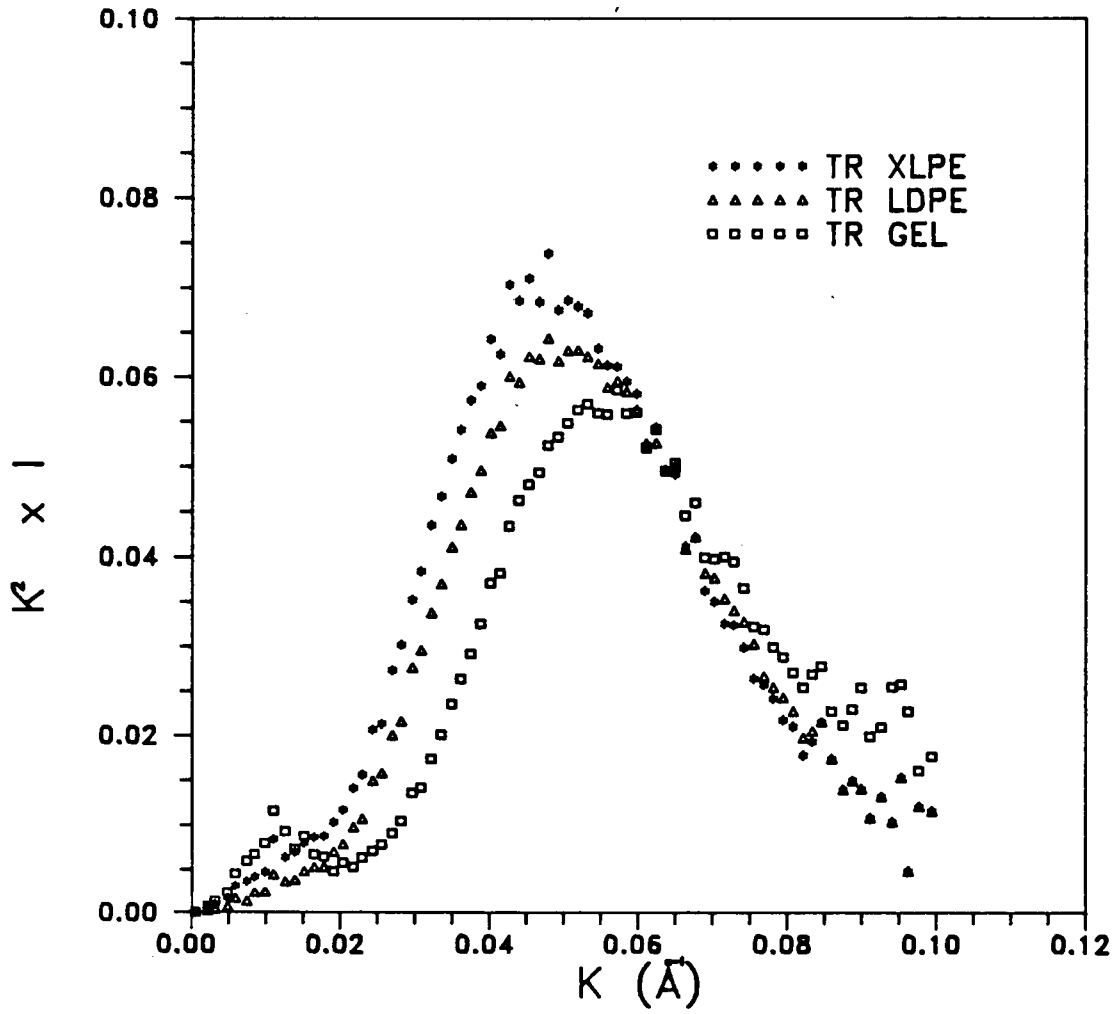



Figure 4.3.5 Lorentz-corrected SAXS intensity curves of TR-XLPE, TR-LDPE and gel fraction of TR-XLPE.

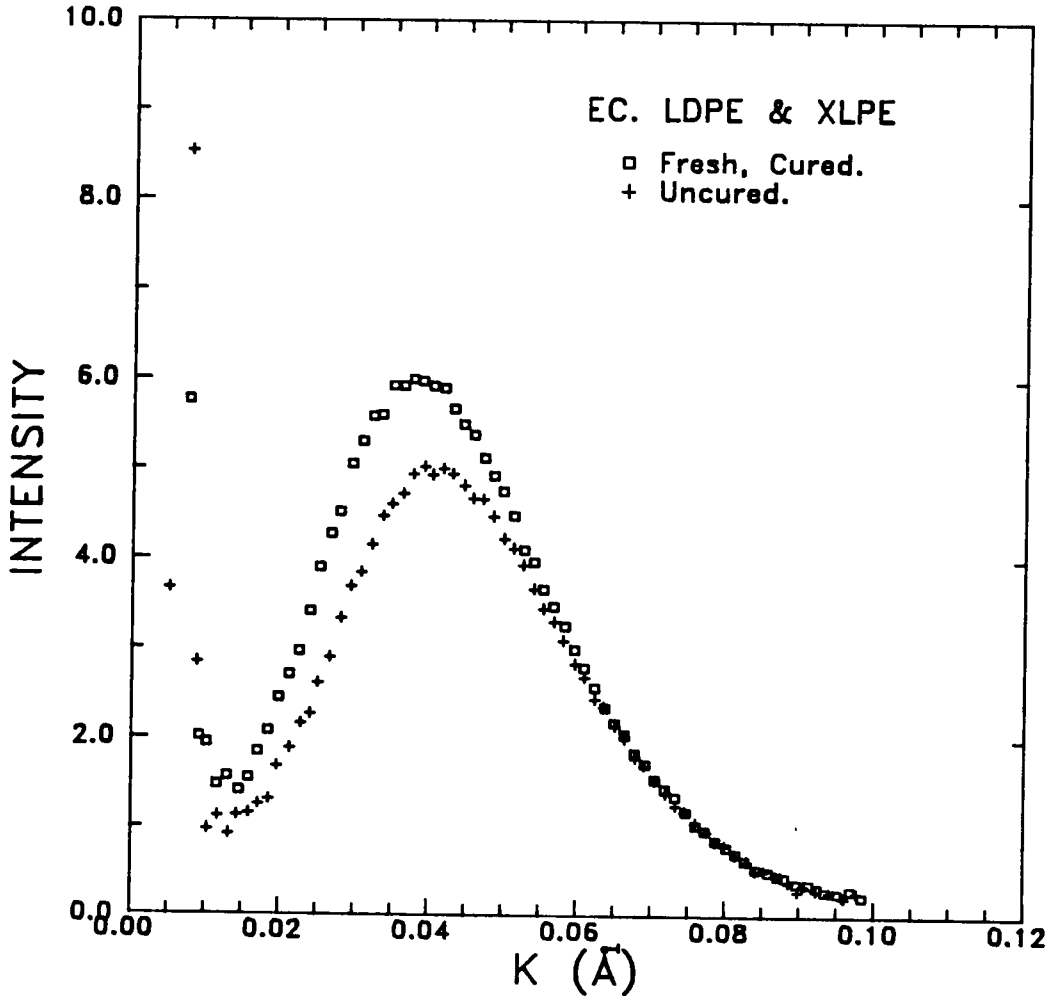



Figure 4.3.6 SAXS intensity curves of EC-XLPE and EC-LDPE.

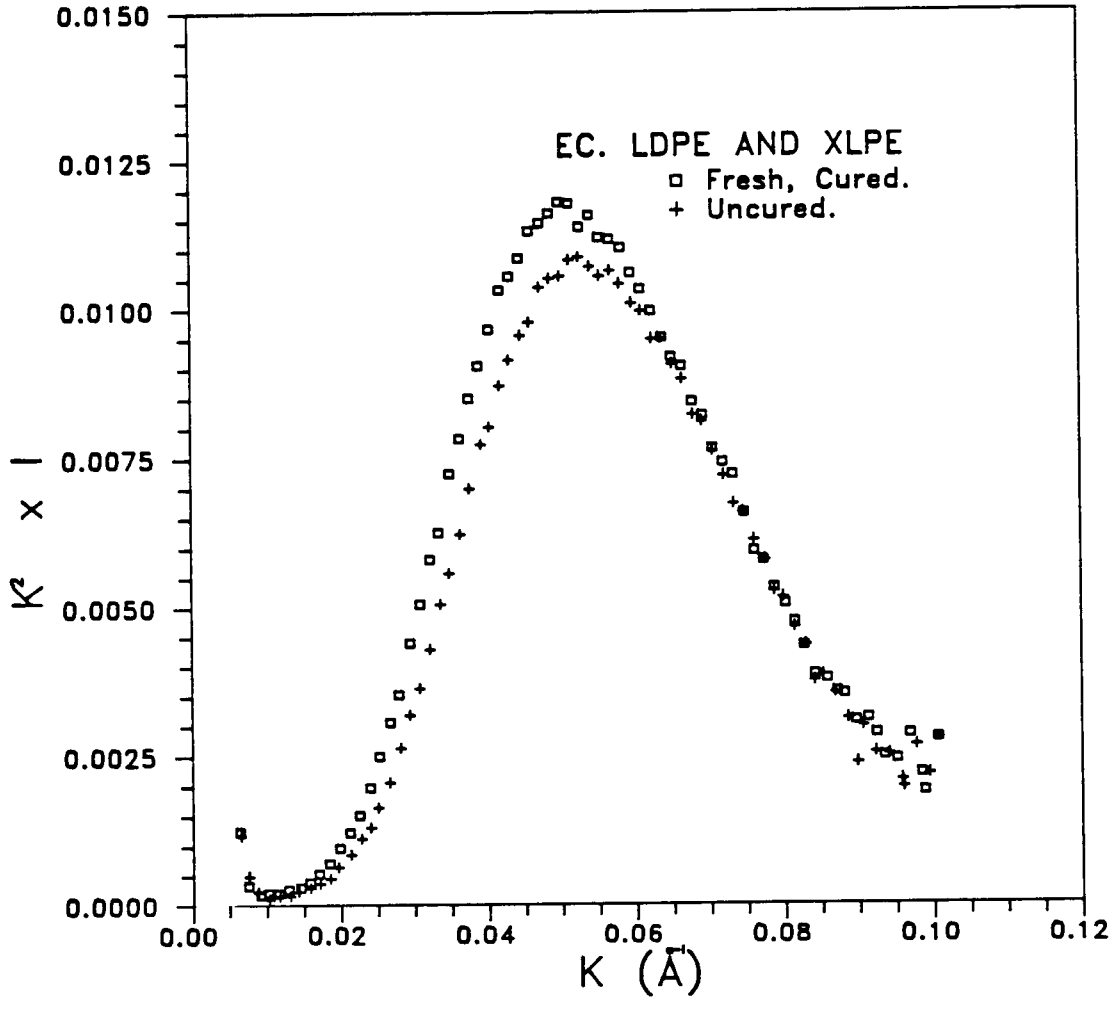



Figure 4.3.7 Lorentz-corrected SAXS intensity curves of EC-XLPE and EC-LDPE.

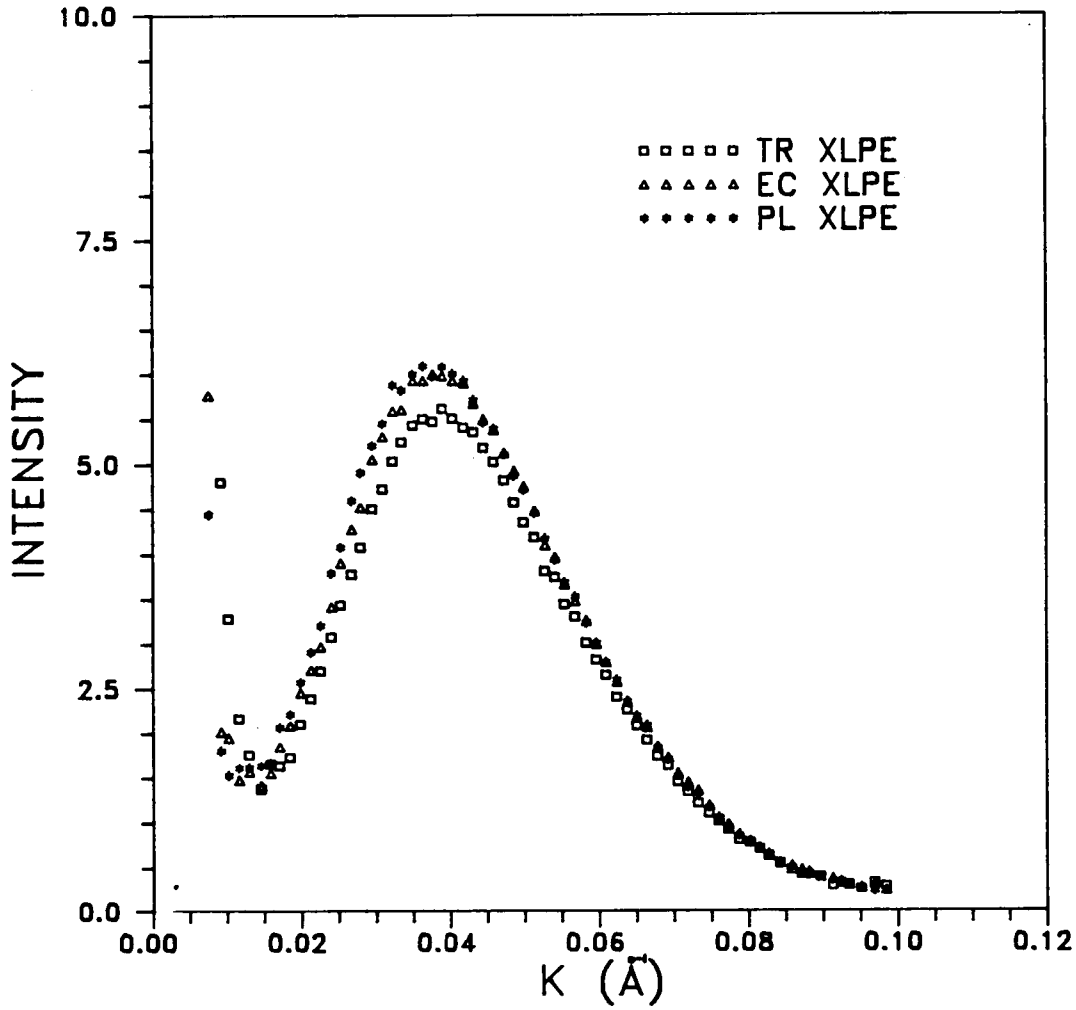



Figure 4.3.8 SAXS intensity curves of TR-XLPE, EC-XLPE and PL-XLPE.

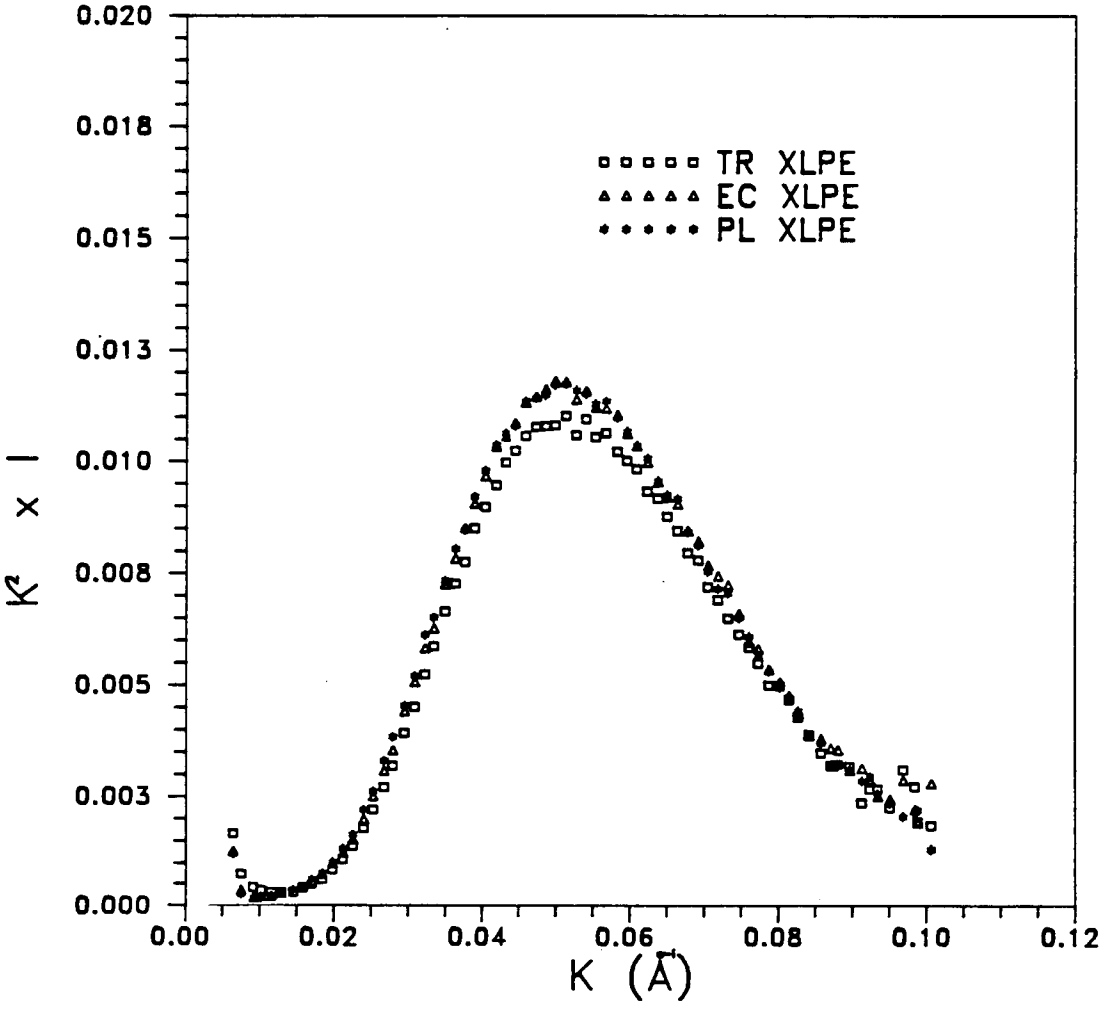



Figure 4.3.9 Lorentz-corrected SAXS intensity curves of TR-XLPE, EC-XLPE and PL-XLPE.

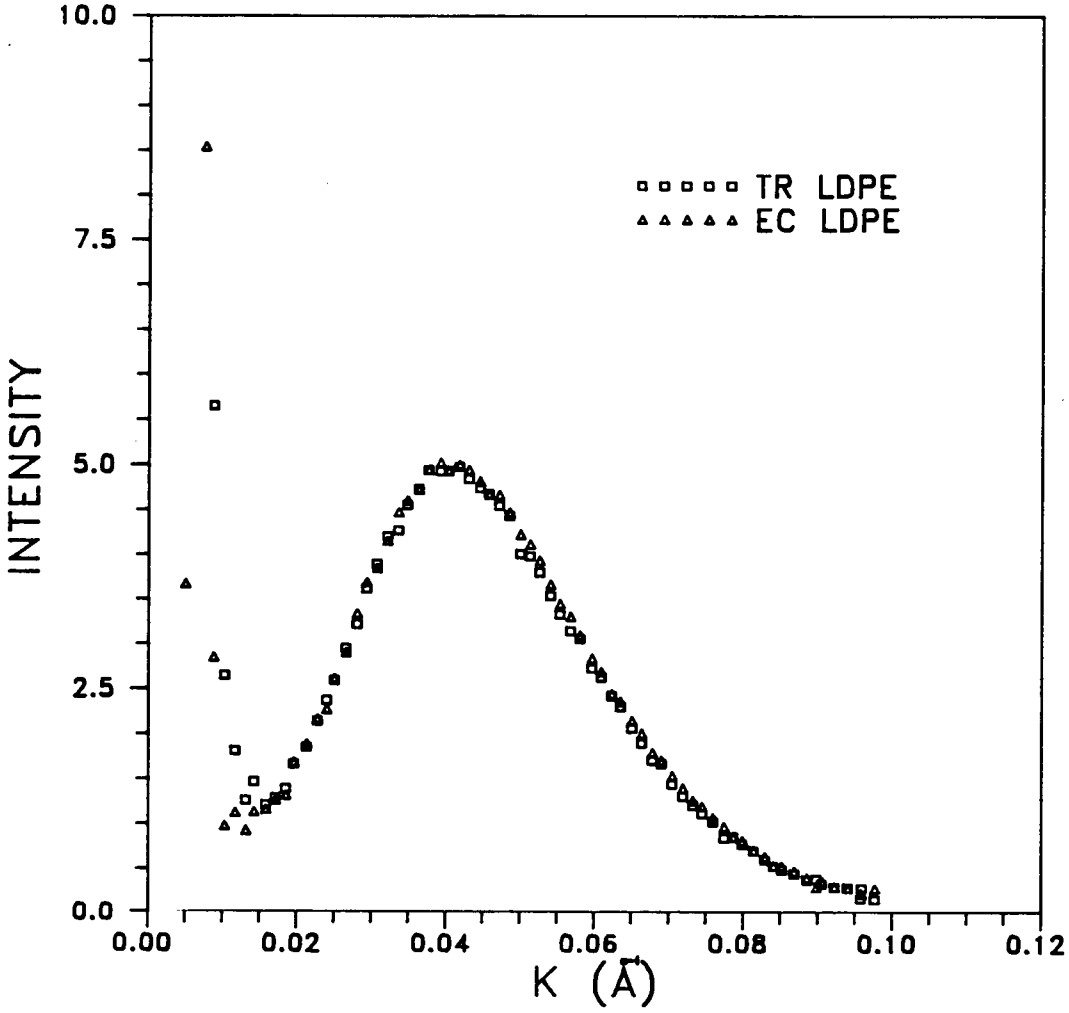



Figure 4.3.10 SAXS intensity curves of TR-LDPE and EC-LDPE.

4.3.3. Annealed Polyethylenes

SAXS data were also collected for annealed polyethylenes. All samples were annealed at 107°C for prescribed periods of time in different environments. Figures 4.3.11, 4.3.12, 4.3.13 and 4.3.14 are radially averaged intensity plots obtained from SAXS intensity contour plots for TR-XLPE, EC-XLPE, PL-XLPE, and TR-LLDPE, respectively, annealed at 107°C in air. The Lorentz-correction was made for all radially averaged data for reasonable comparison and corrected plots are present in Figures 4.3.15, 4.3.16, 4.3.17 and 4.3.18.

The effects of annealing at the same temperature on the uncured crosslinkable polyethylenes and high-density polyethylene were also investigated. Figures 4.2.19, 4.3.20, 4.3.21 and 4.3.22 show the one-dimensional SAXS intensity plots of uncured TR-LDPE, uncured EC-LDPE, uncured PL-LDPE and HDPE respectively. Lorentz-corrected one- dimensional SAXS intensity plots of the data are seen in Figures 4.3.23, 4.3.24, 4.3.25 and 4.3.26. Three major changes in SAXS curves with the increase of annealing time for cured as well as uncured crosslinkable polyethylenes are noted - i.e.,(a) lowering the location of Bragg maximum, (b) increasing general intensities and (c) reducing peak width especially for the uncorrected data. The effects of annealing on modification of SAXS intensity curves for uncured low-density polyethylenes are not as important as for the crosslinked counterparts. Interestingly, it was noted that SAXS curves of high-density polyethylene show virtually no lowering of

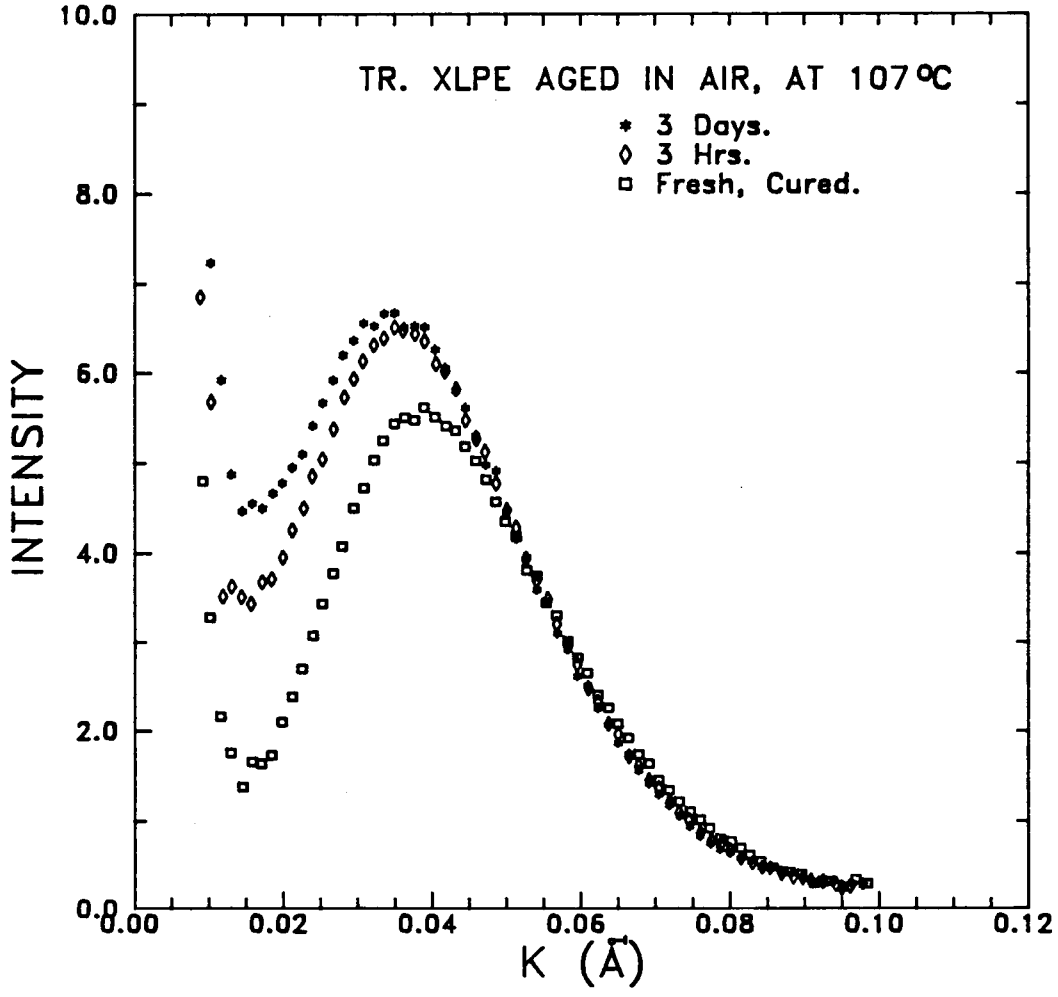



Figure 4.3.11 Variation of SAXS intensity curves of TR-XLPE annealed at 107°C in air with annealing time.

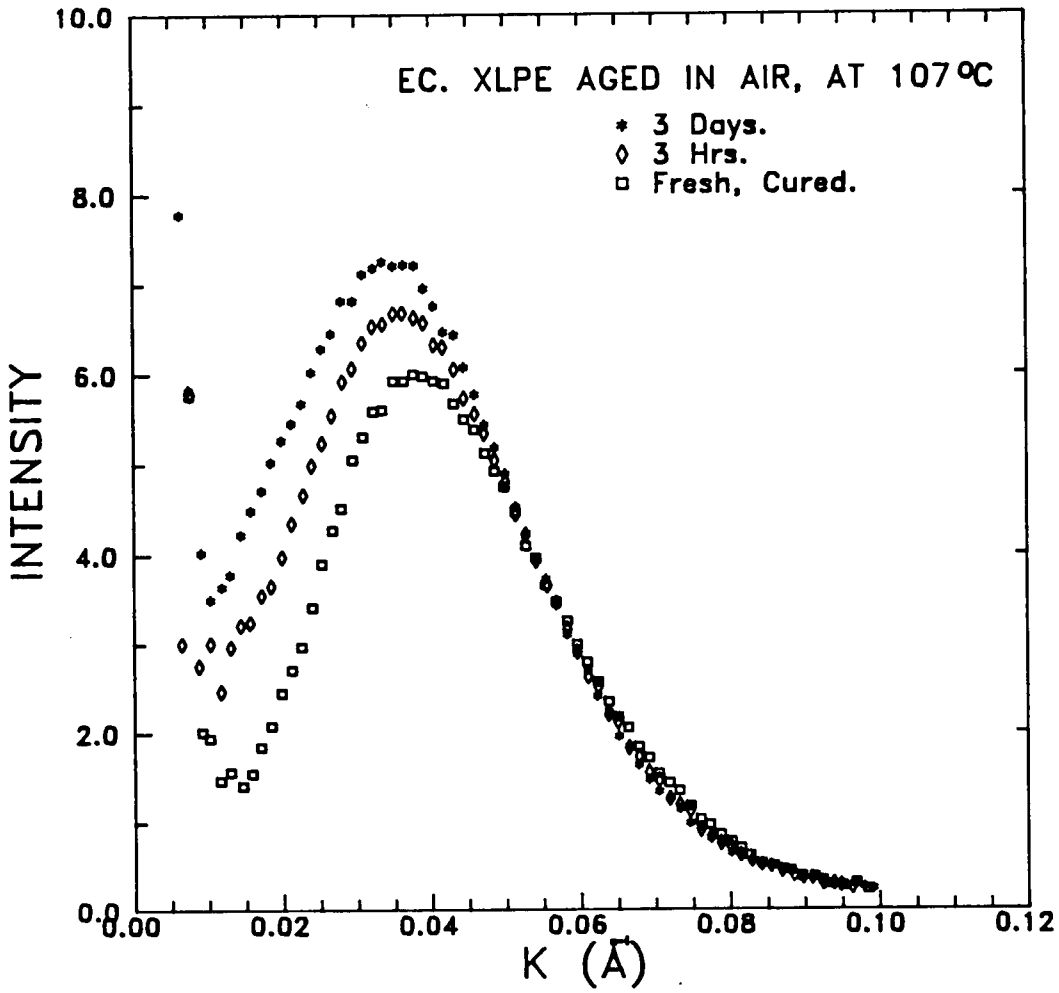



Figure 4.3.12 Variation of SAXS intensity curves of EC-XLPE annealed at 107°C in air with annealing time.

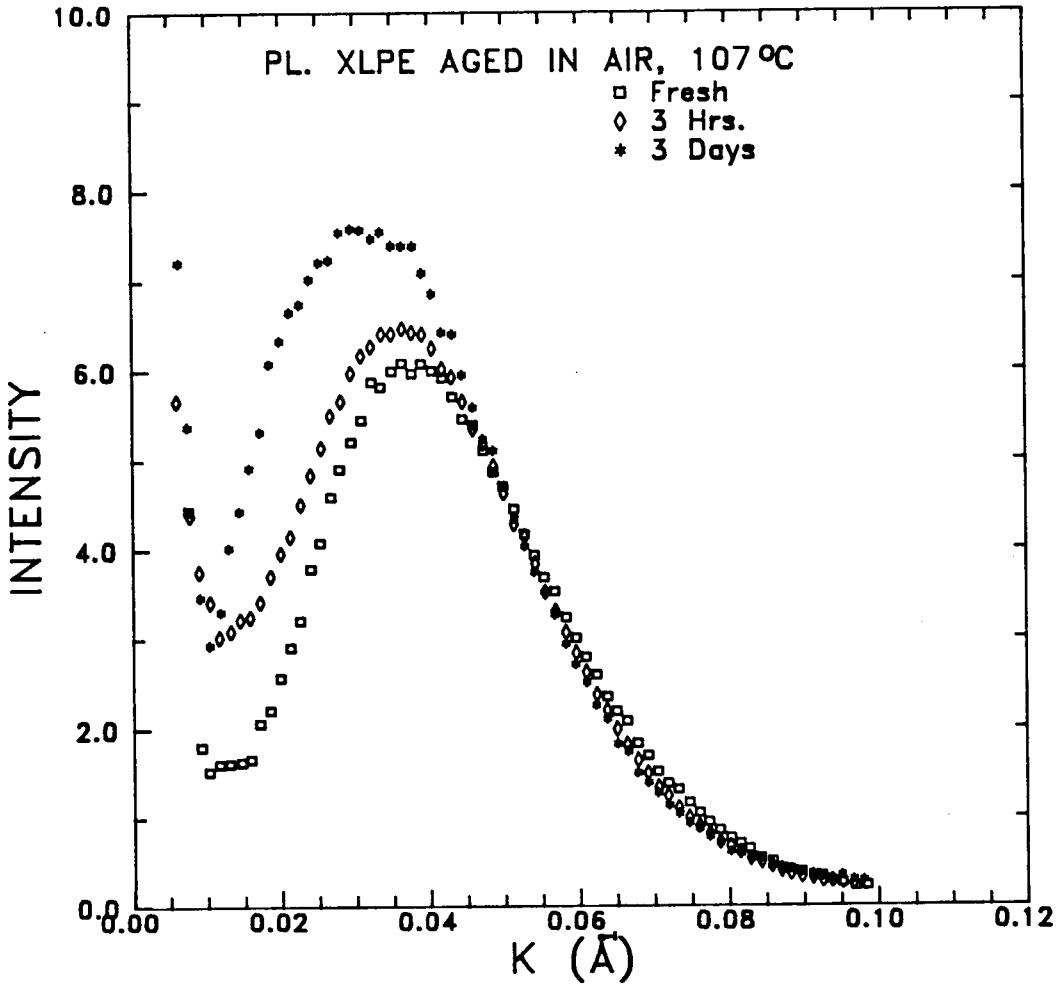



Figure 4.3.13 Variation of SAXS intensity curves of PL-XLPE annealed at 107°C in air with annealing time.

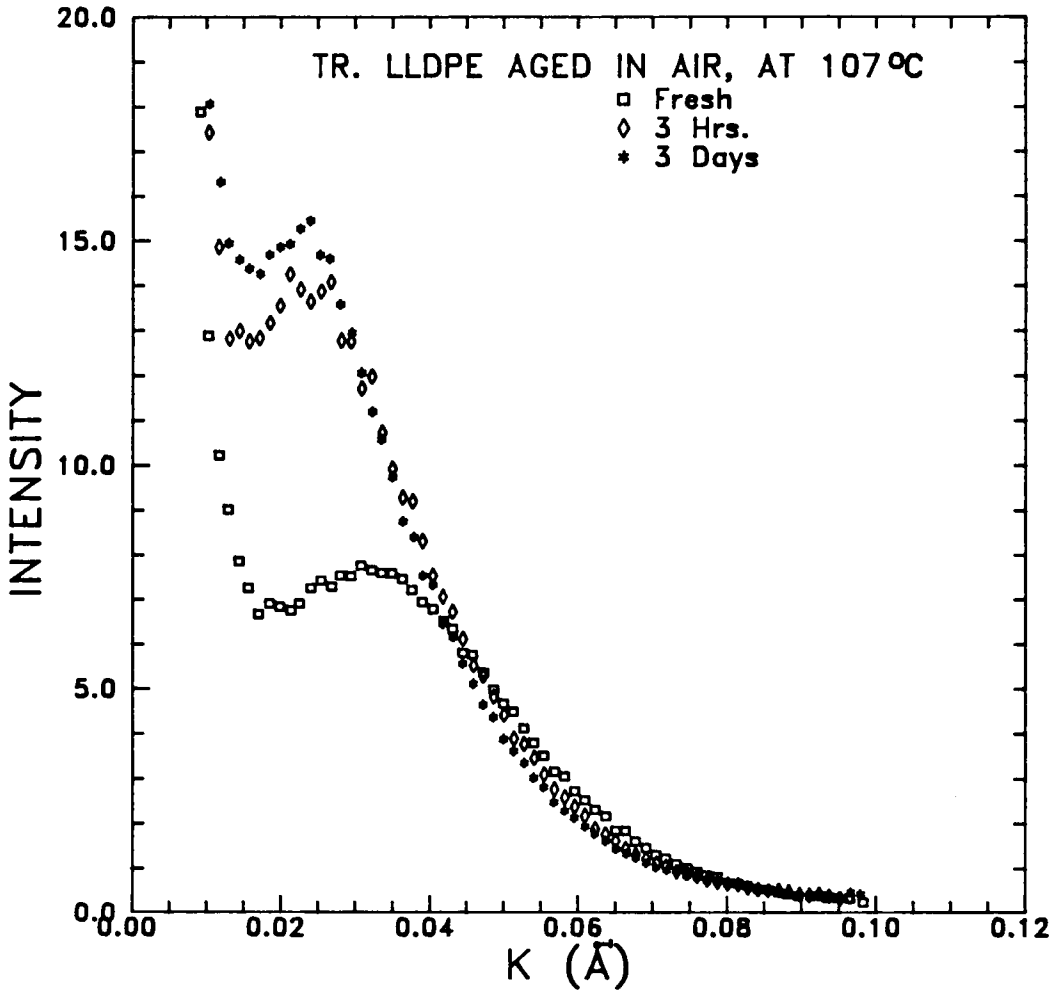



Figure 4.3.14 Variation of SAXS intensity curves of TR-LLDPE annealed at 107°C in air with annealing time.

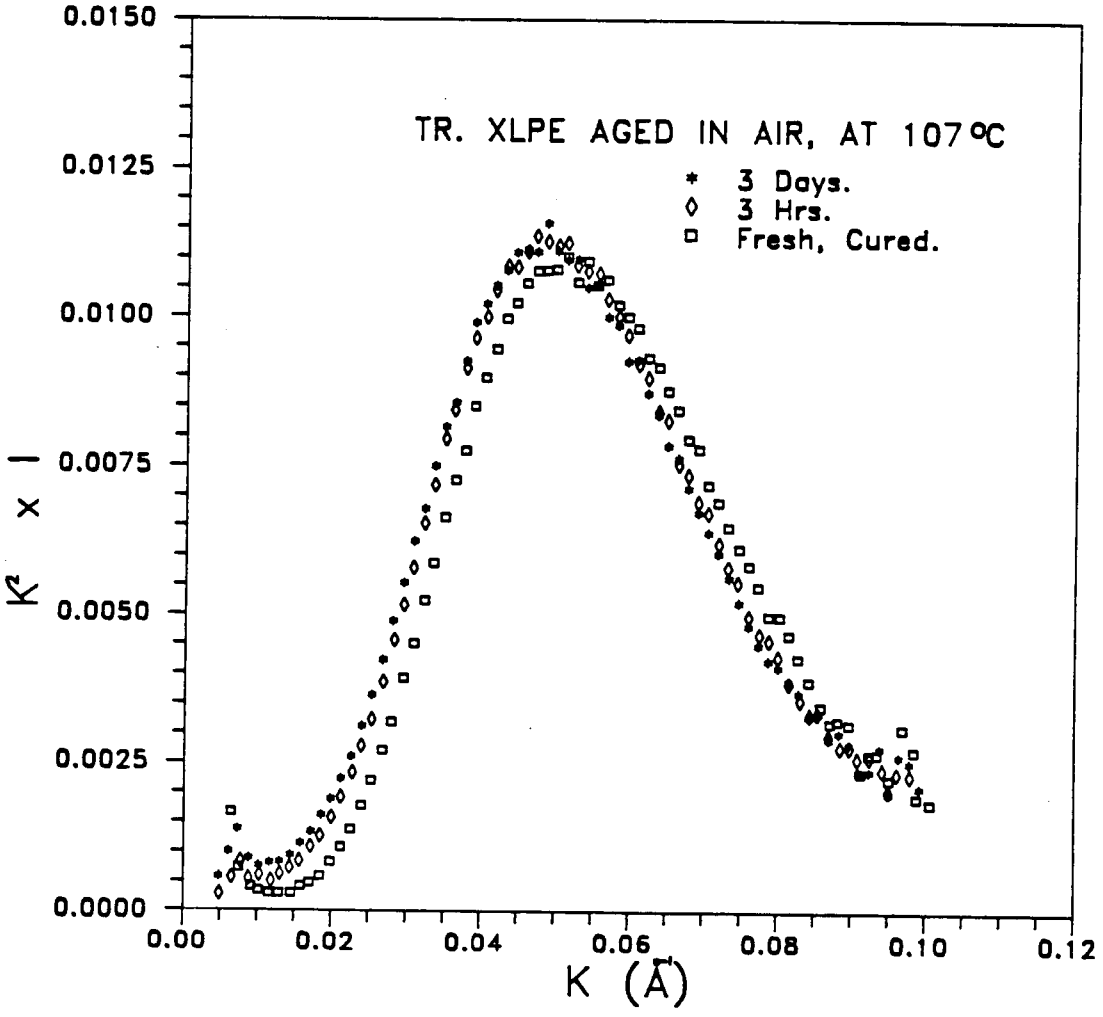



Figure 4.3.15 Variation of Lorentz-corrected SAXS intensity curves of TR-XLPE annealed at 107°C in air with annealing time.

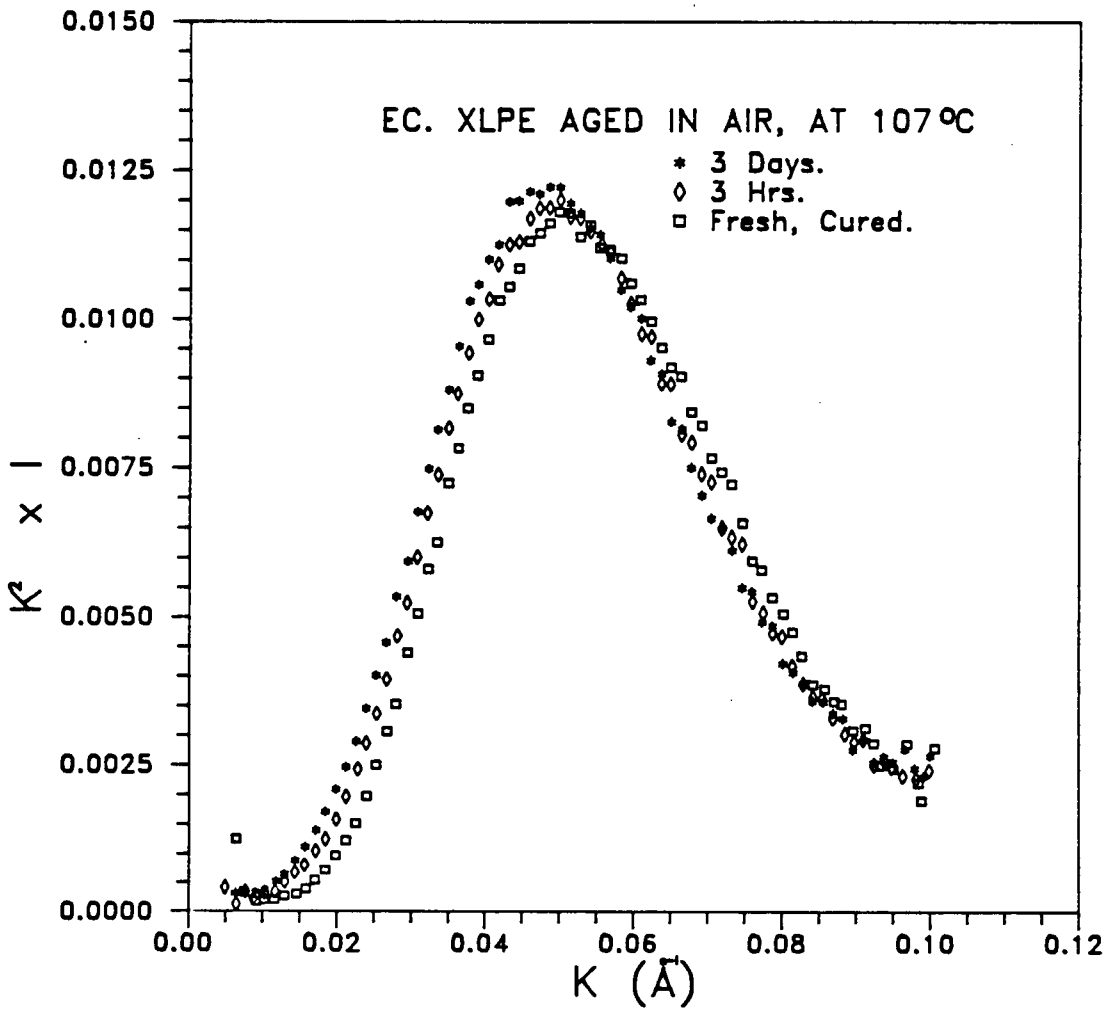



Figure 4.3.16 Variation of Lorentz-corrected SAXS intensity curves of EC-XLPE annealed at 107°C in air with annealing time.

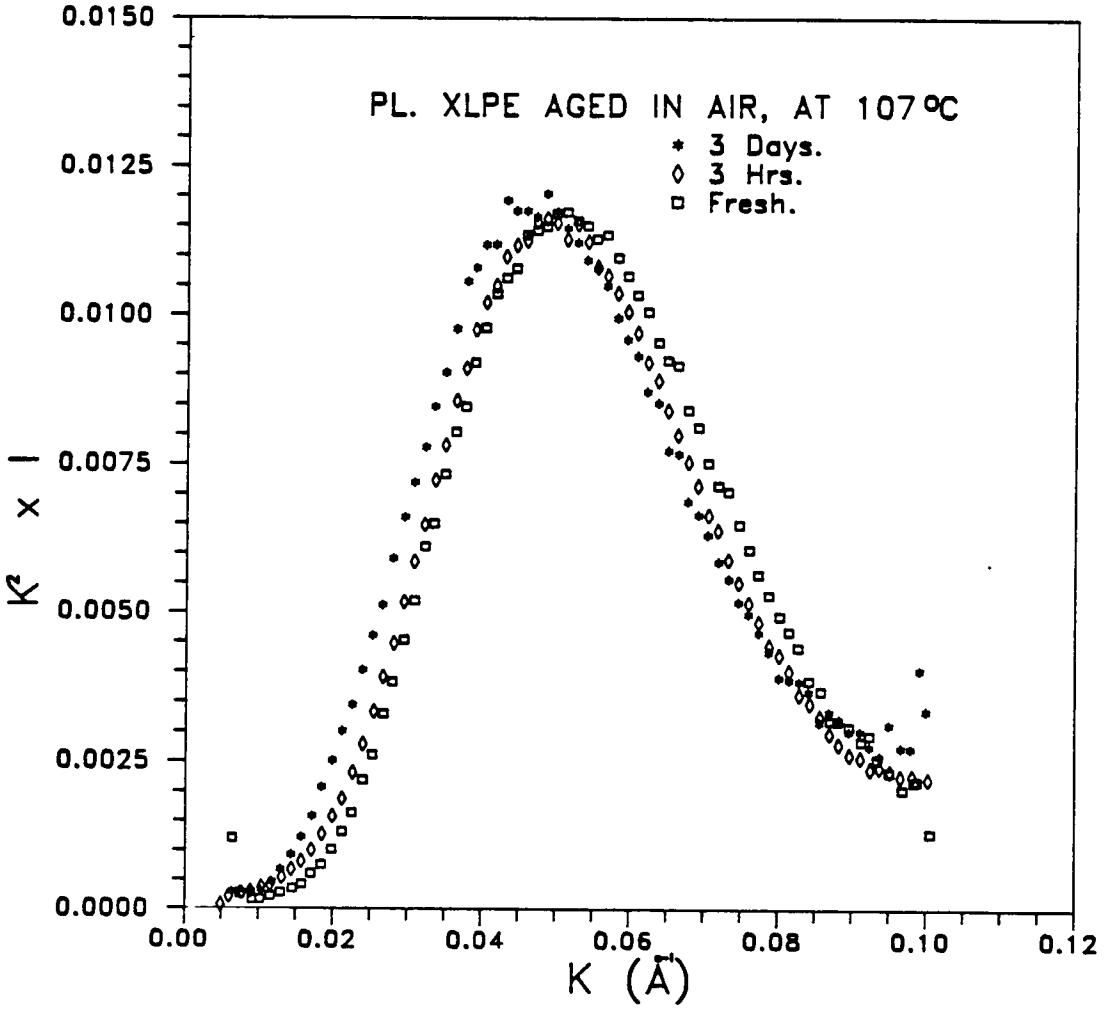



Figure 4.3.17 Variation of Lorentz-corrected SAXS intensity curves of PL-XLPE annealed at 107°C in air with annealing time.

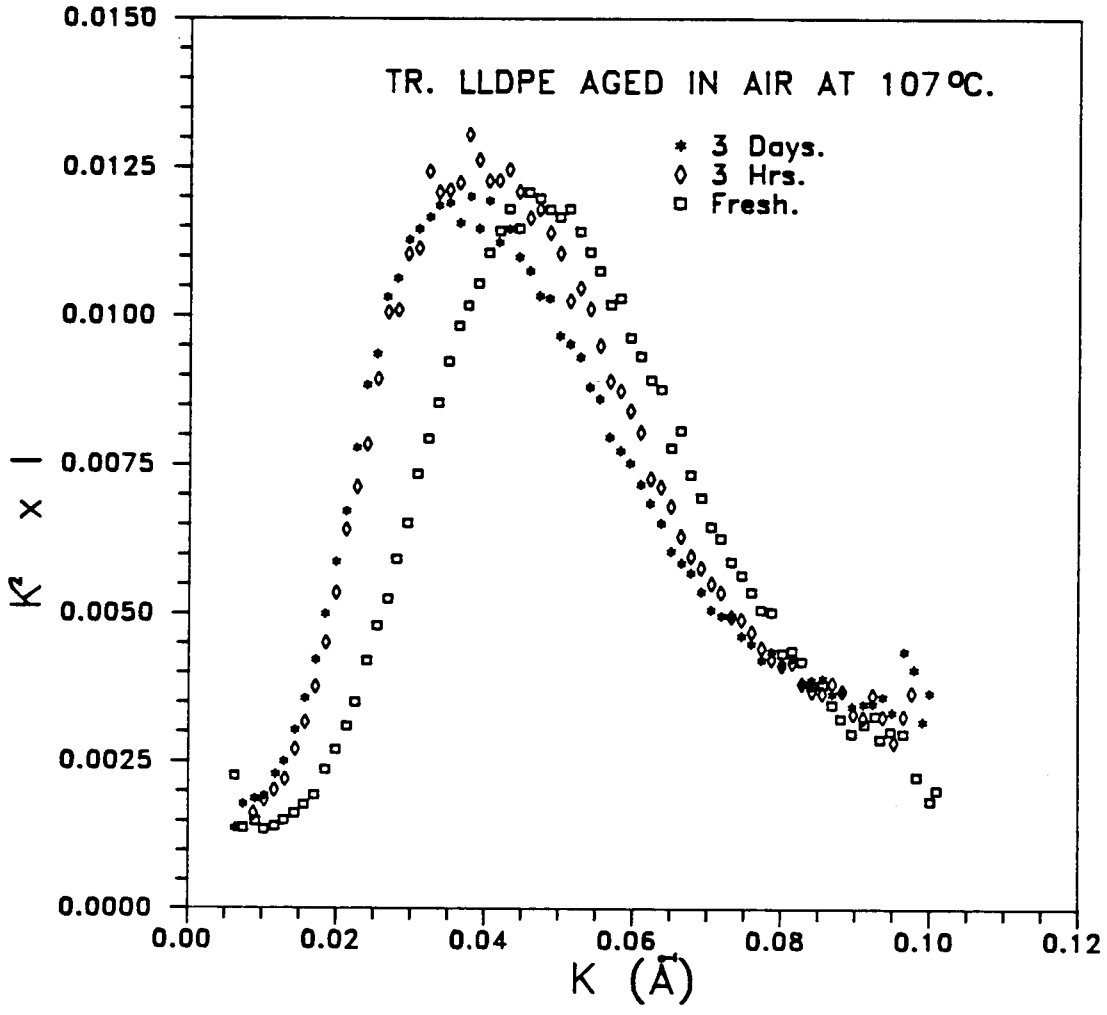



Figure 4.3.18 Variation of Lorentz-corrected SAXS intensity curves of TR-LLDPE annealed at 107°C in air with annealing time.

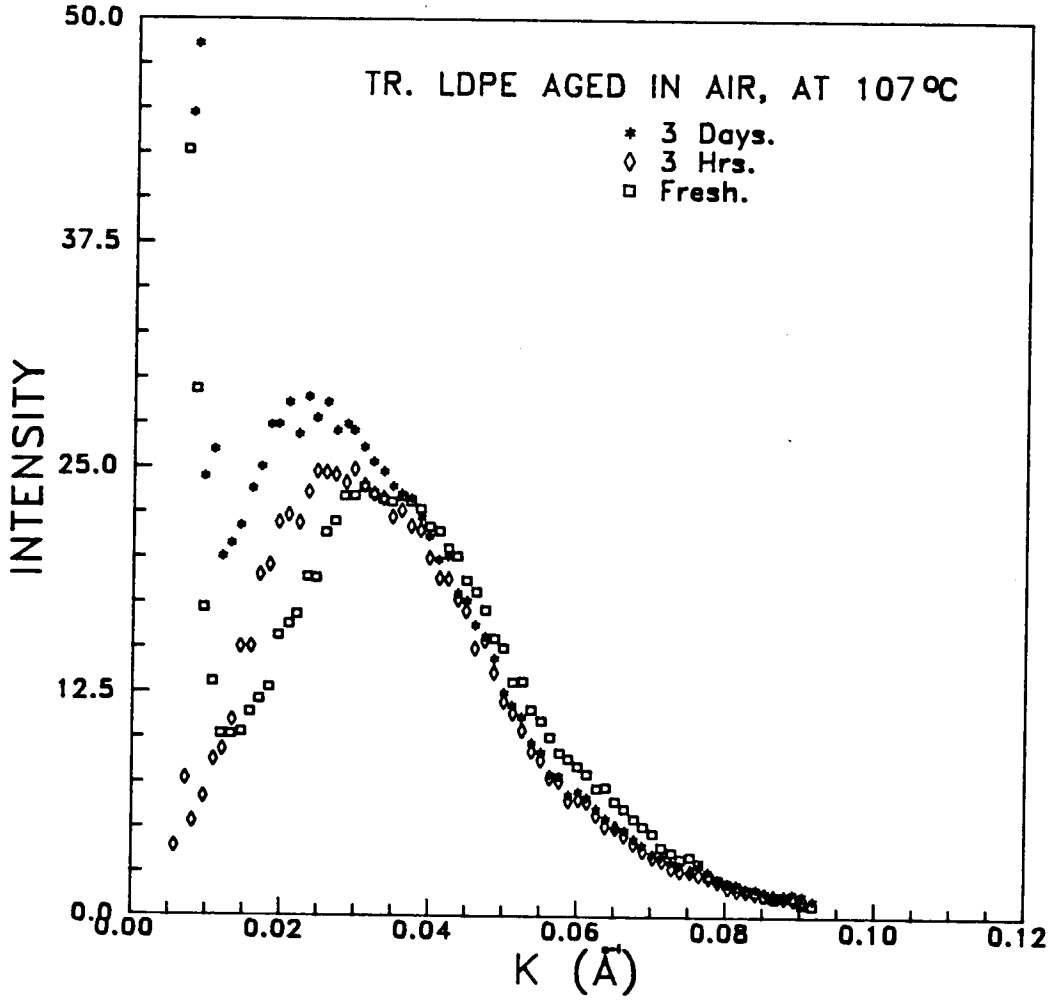



Figure 4.3.19 Variation of SAXS intensity curves of TR-LDPE annealed at 107°C in air with annealing time.

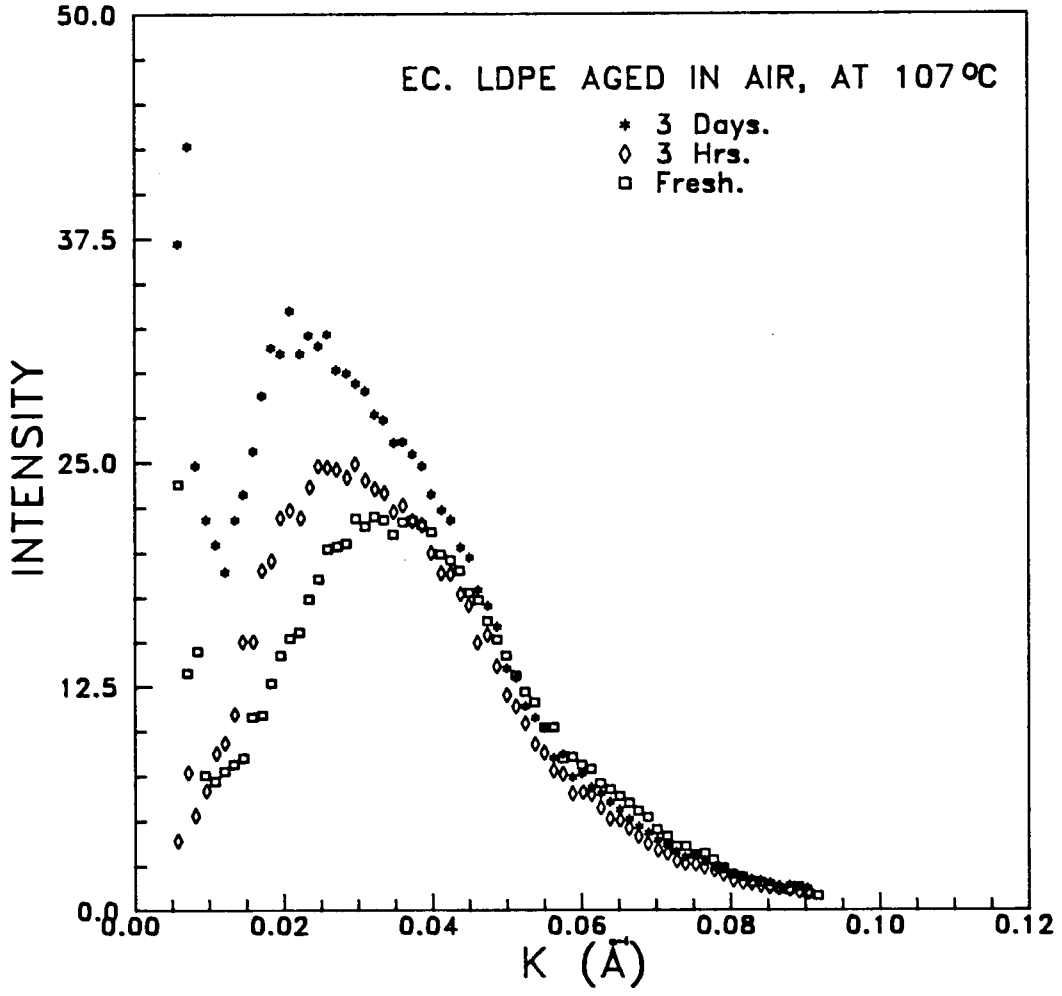



Figure 4.3.20 Variation of SAXS intensity curves of EC-LDPE annealed at 107°C in air with annealing time.

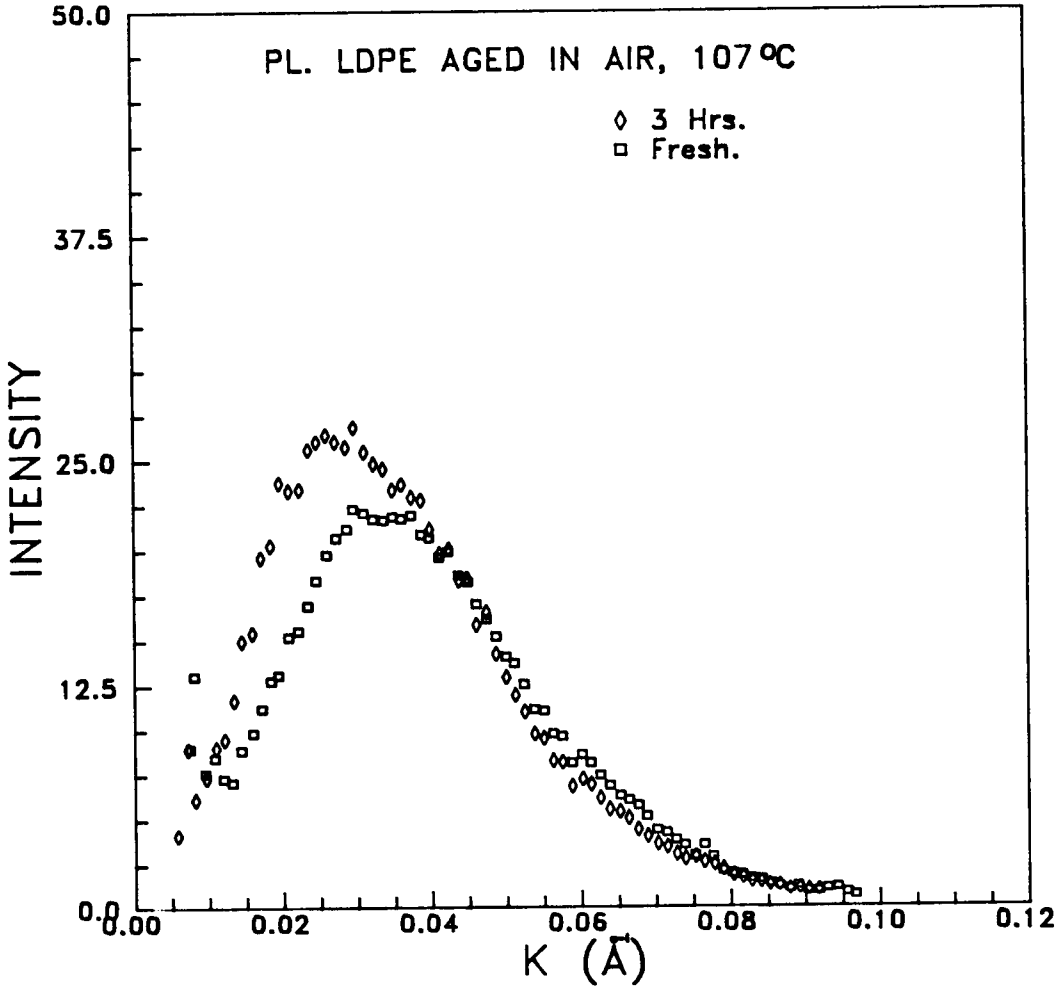



Figure 4.3.21 Variation of SAXS intensity curves of PL-LDPE annealed at 107°C in air with annealing time.

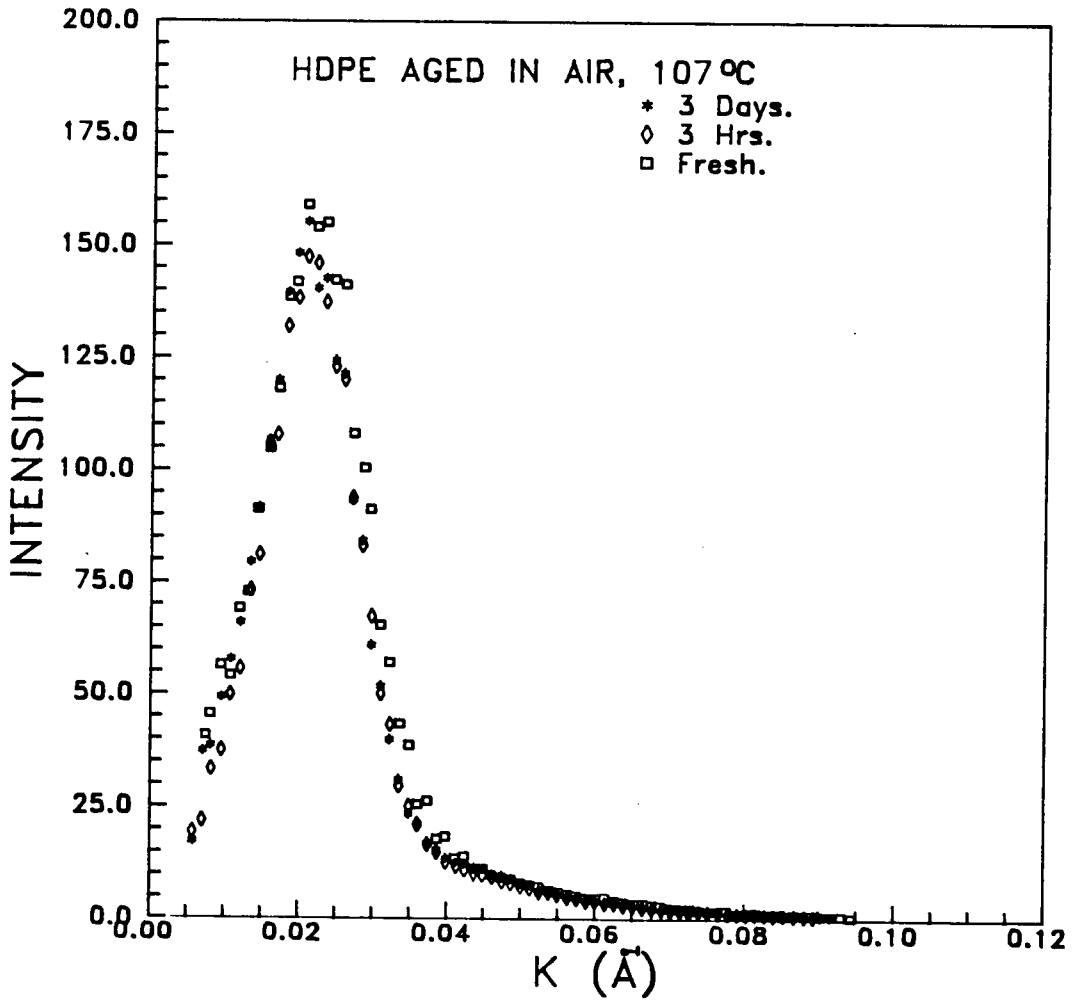



Figure 4.3.22 Variation of SAXS intensity curves of HDPE annealed at 107°C in air with annealing time.

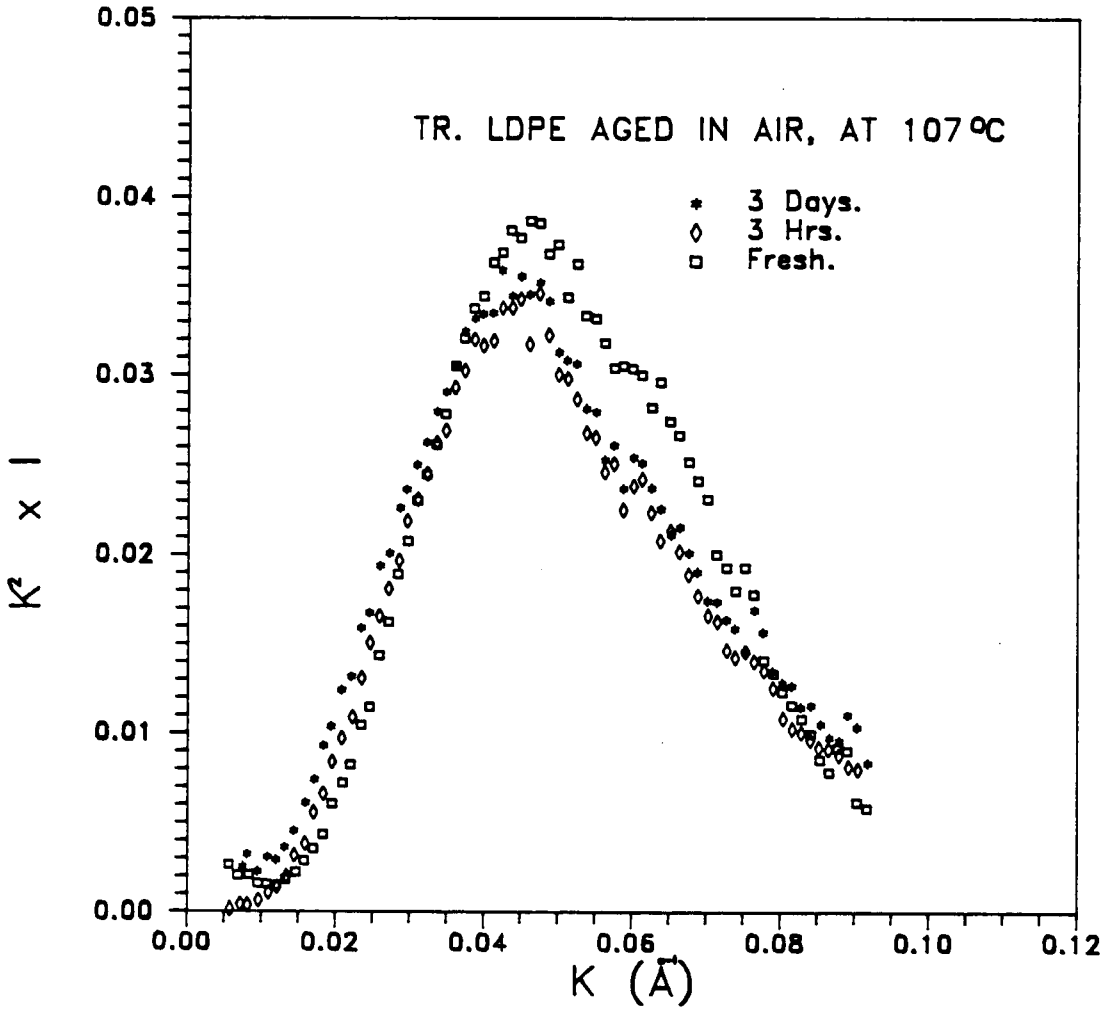



Figure 4.3.23 Variation of Lorentz-corrected SAXS intensity curves of TR-LDPE annealed at 107°C in air with annealing time.

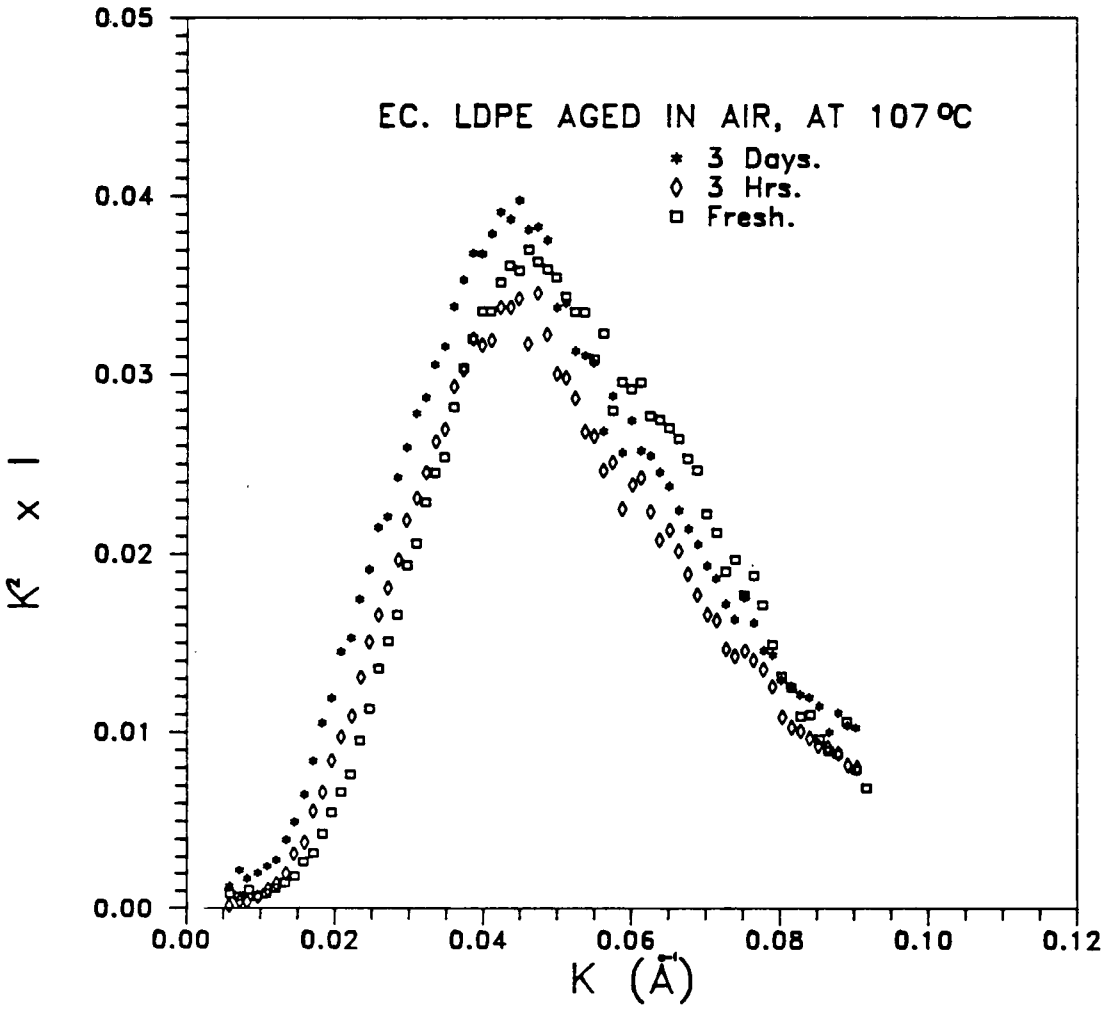



Figure 4.3.24 Variation of Lorentz-corrected SAXS intensity curves of EC-LDPE annealed at 107°C in air with annealing time.

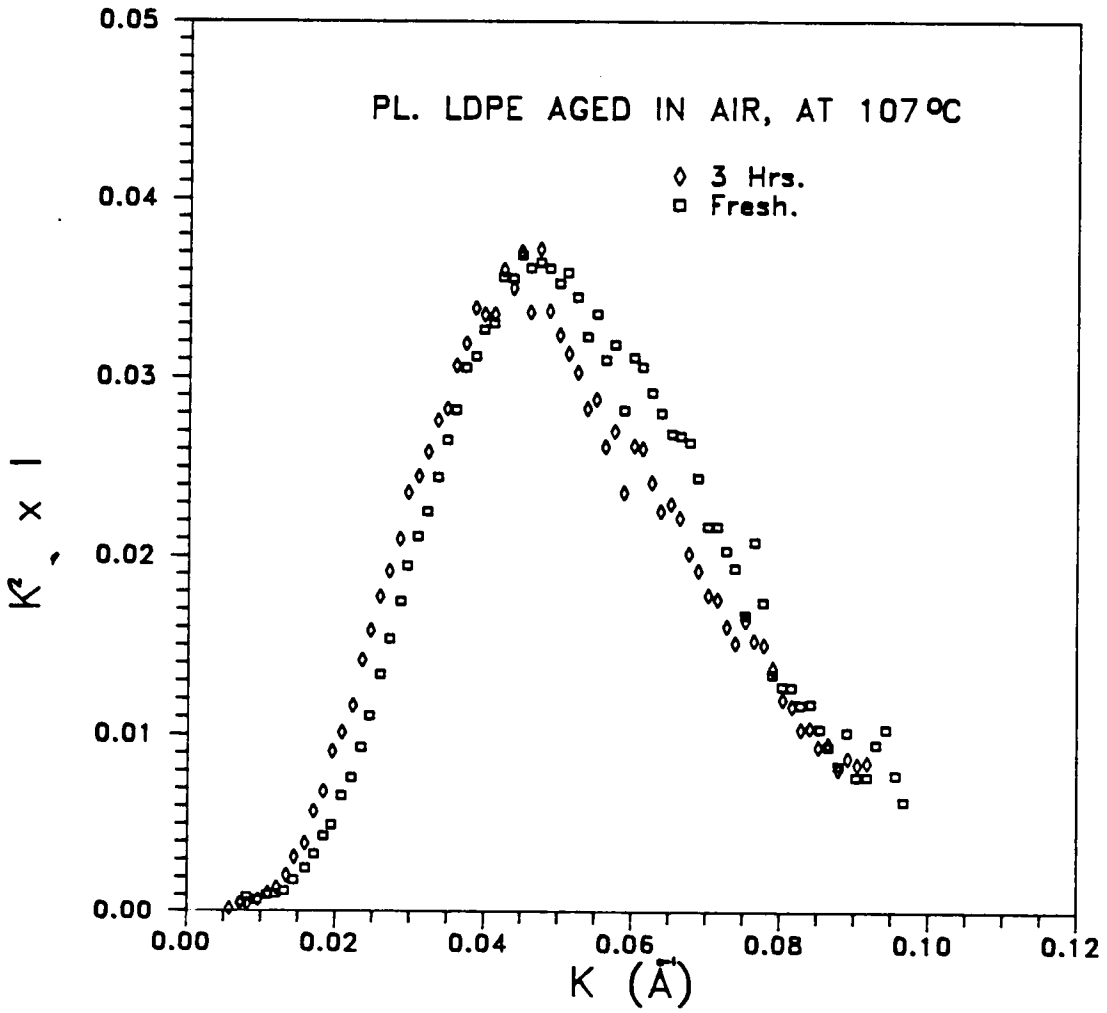



Figure 4.3.25 Variation of Lorentz-corrected SAXS intensity curves of PL-LDPE annealed at 107°C in air with annealing time.

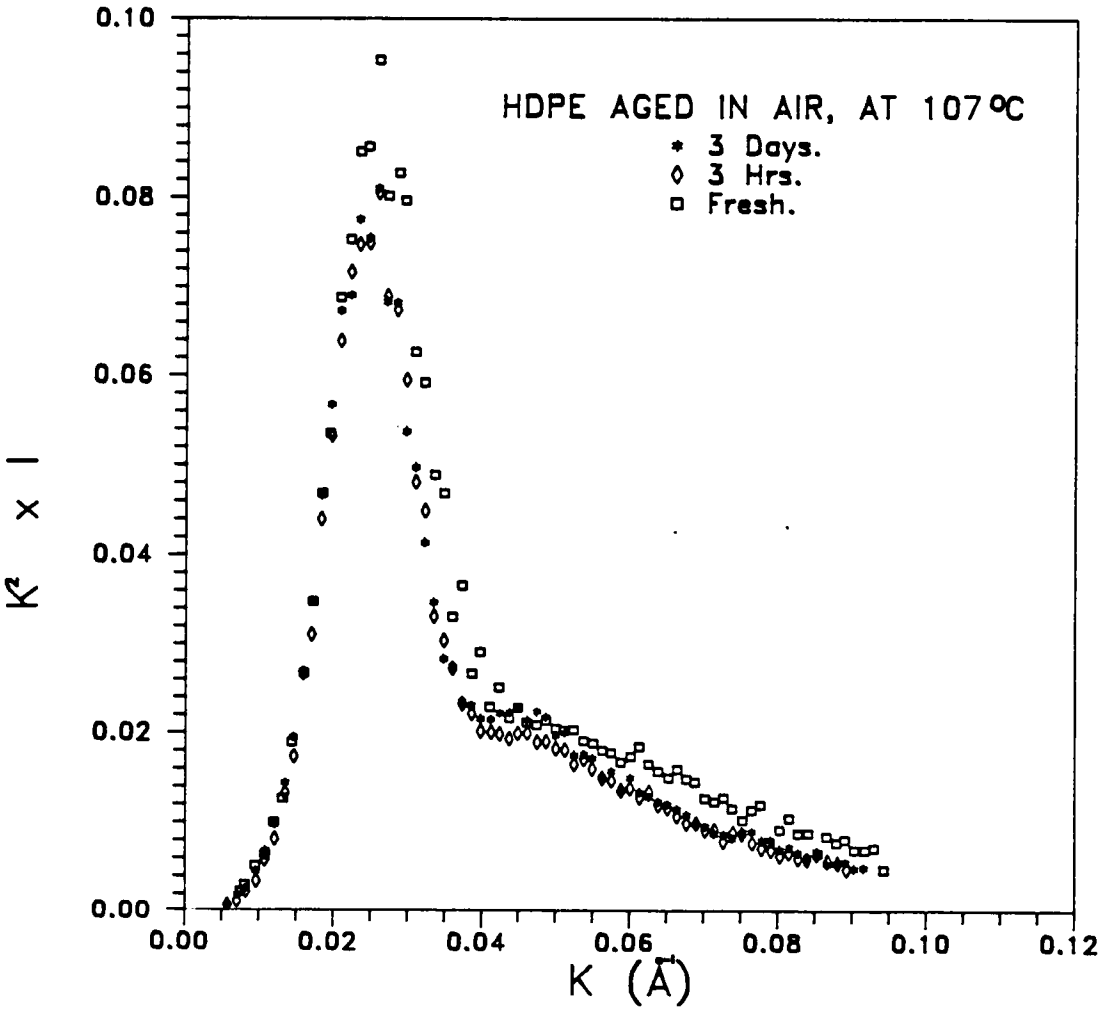



Figure 4.3.26 Variation of Lorentz-corrected SAXS intensity curves of HDPE annealed at 107°C in air with annealing time.

angle of Bragg maxima nor the increase in the overall SAXS intensity with the period of annealing treatment. However, the breath of the peak reduces drastically with annealing. Moreover, annealing enhanced the second Bragg maximum located next to the major Bragg peak especially for the Lorentz-corrected SAXS intensity plot (Figure 4.3.26).

Annealing treatments were also carried out in different environments such as a silicone oil and a transformer oil. Figures 4.3.27, 4.3.28, 4.3.29, and 4.3.30 show the uncorrected radially-averaged SAXS intensity plots of TR-XLPE, EC-XLPE, PL-XLPE, and TR-LLDPE, respectively, annealed in a silicone oil at 107$^{o}$C. Lorentz-factor was also applied for each of these data and the corrected plots are given in Figure 4.3.31, 4.3.32, 4.3.33, and 4.3.34. Even though annealing was performed in a silicone oil, the effects of annealing in a silicone oil on the macro-structure were almost identical to those for annealing in air.

One of the major differences in uncorrected SAXS data was the change in the intensity at a very low scattering angle. Interpretation of data in this region has been very difficult and controversial. Since the angle near the beam-stop corresponds to the large dimension in the range of 250 to 1000 Å, some researchers believed that SAXS intensities in this region are due to the entities of that size- mainly large crystals, microvoids or foreign particles. Vatansever impregnated field-aged XLPE cable insulations with a mineral oil, whose electron density was higher than that of

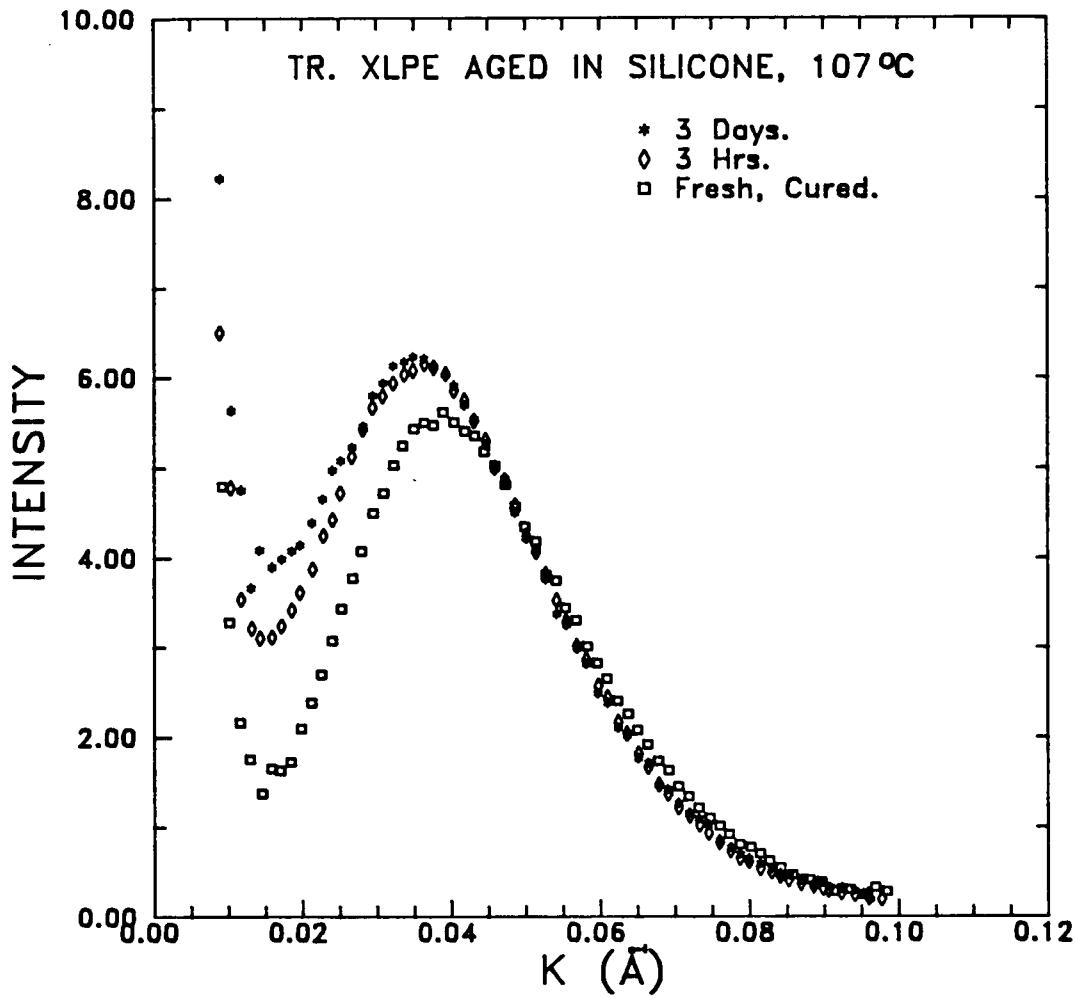



Figure 4.3.27 Variation of SAXS intensity curves of TR-XLPE annealed at 107°C in silicone oil with annealing time.

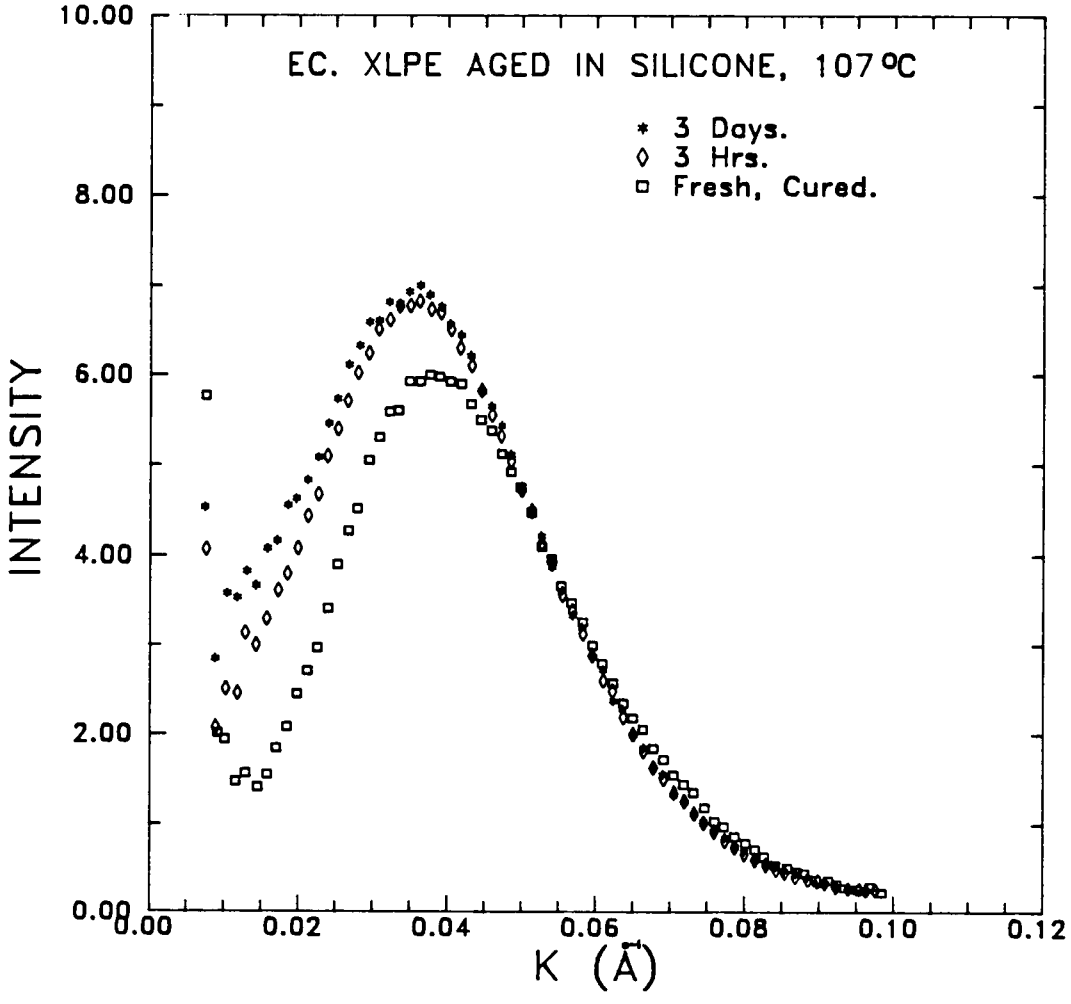



Figure 4.3.28 Variation of SAXS intensity curves of EC-XLPE annealed at 107°C in silicone oil with annealing time.

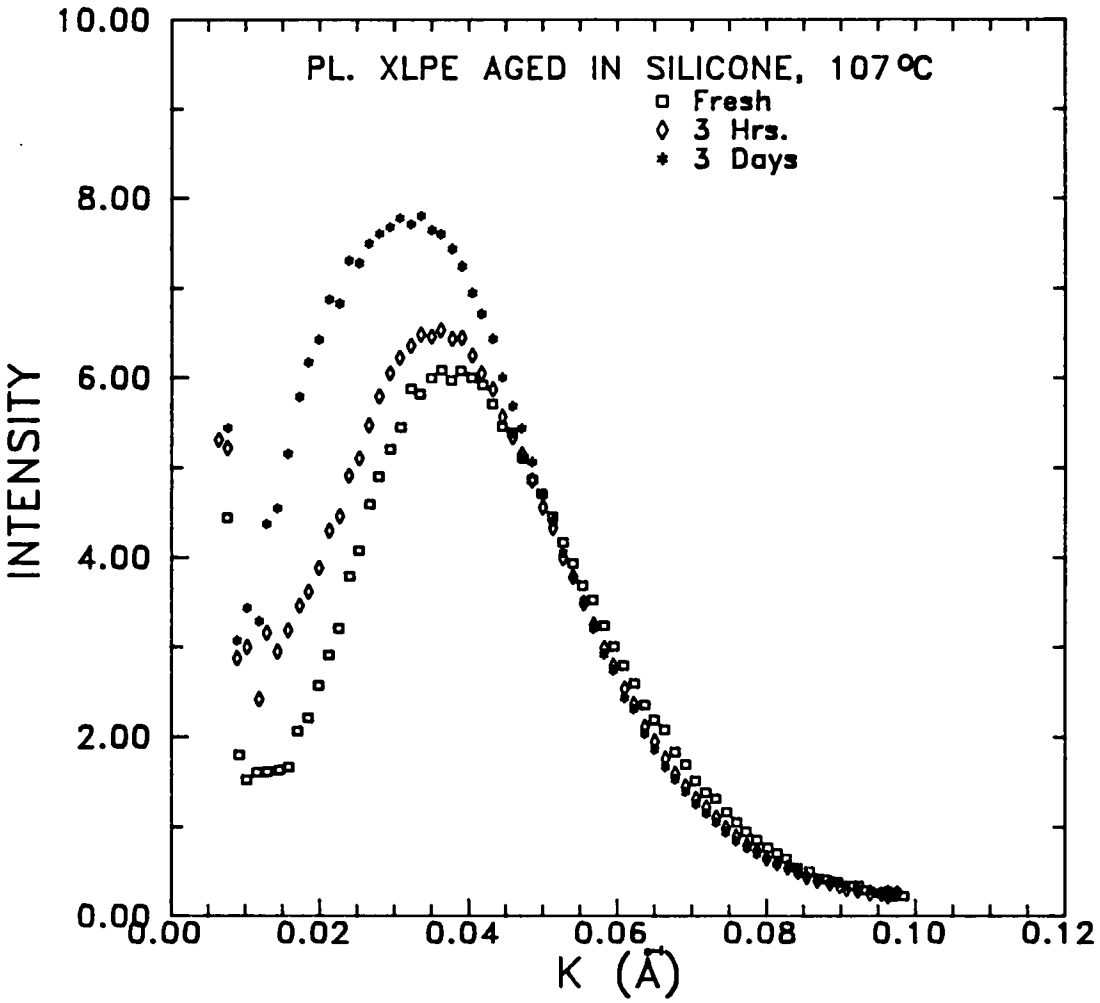



Figure 4.3.29 Variation of SAXS intensity curves of PL-XLPE annealed at 107oC in silicone oil with annealing time.

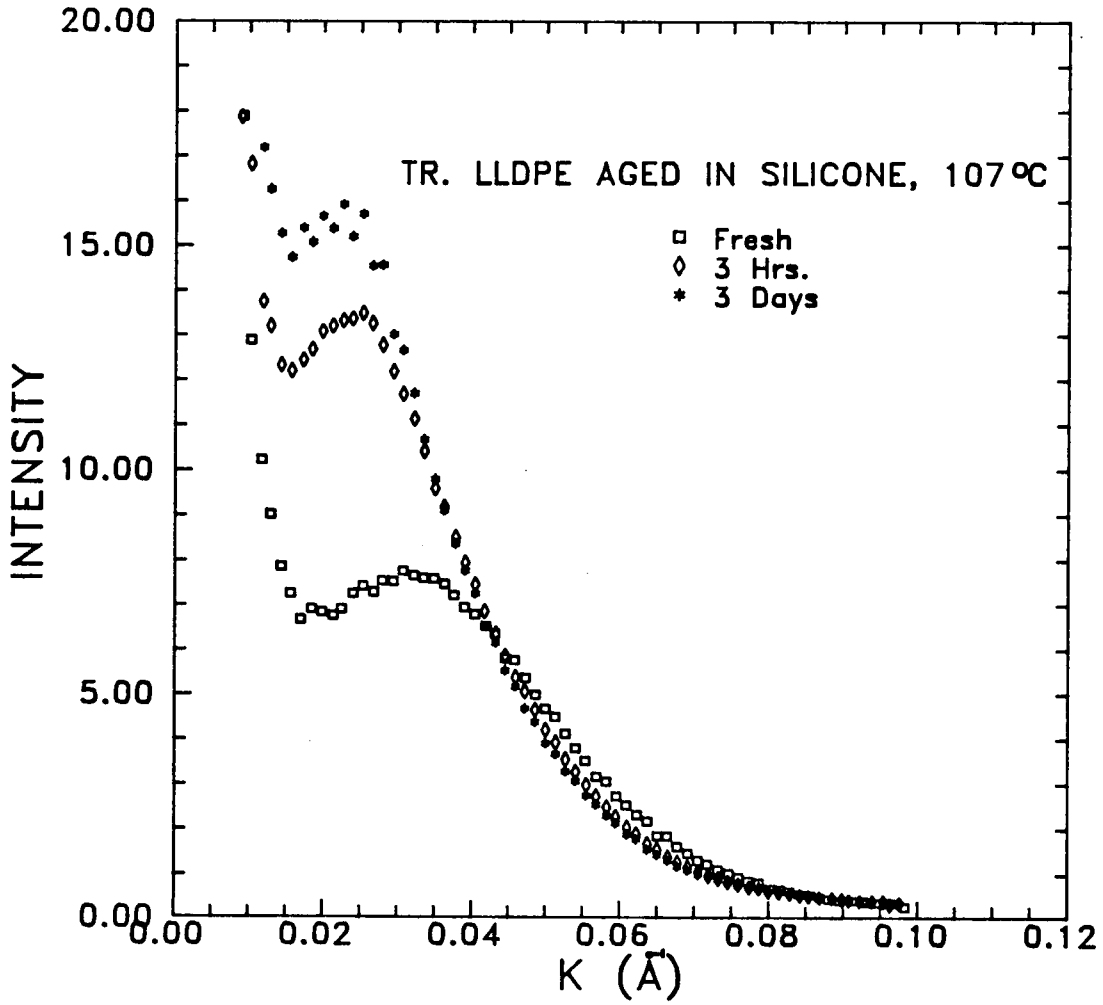



Figure 4.3.30 Variation of SAXS intensity curves of TR-LLDPE annealed at 107°C in silicone oil with annealing time.

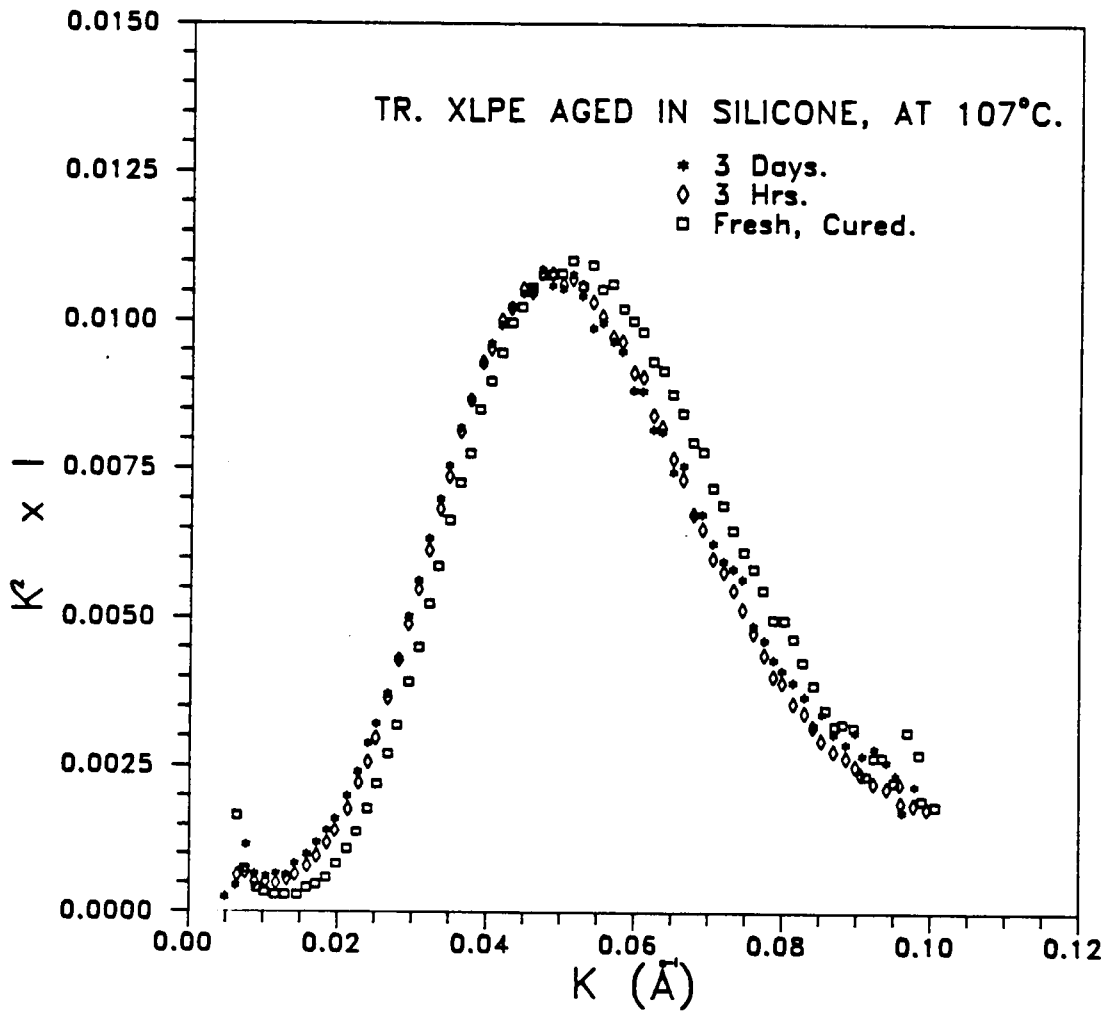



Figure 4.3.31 Variation of Lorentz-corrected SAXS intensity curves of TR-XLPE annealed at 107°C in silicone oil with annealing time.

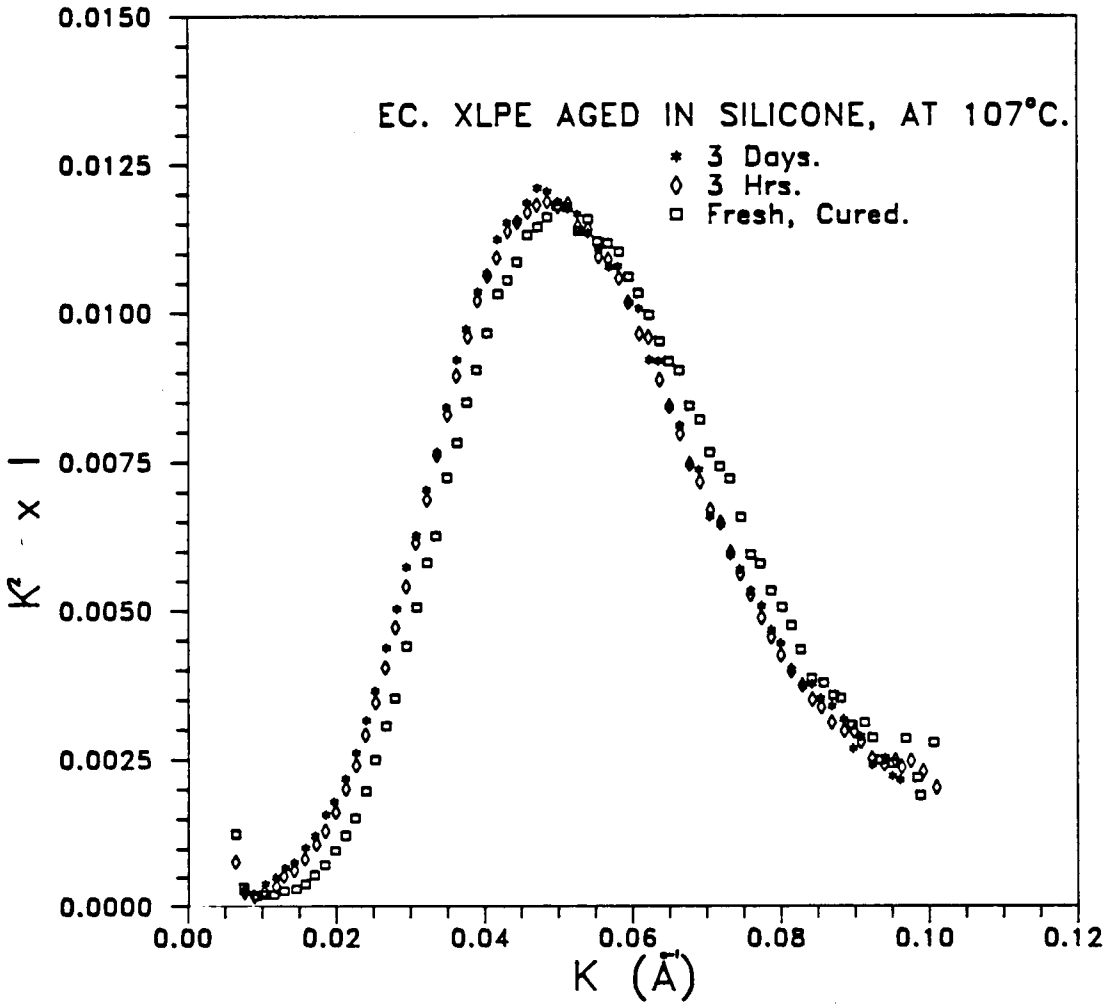



Figure 4.3.32 Variation of Lorentz-corrected SAXS intensity curves of EC-XLPE annealed at 107°C in silicone oil with annealing time.

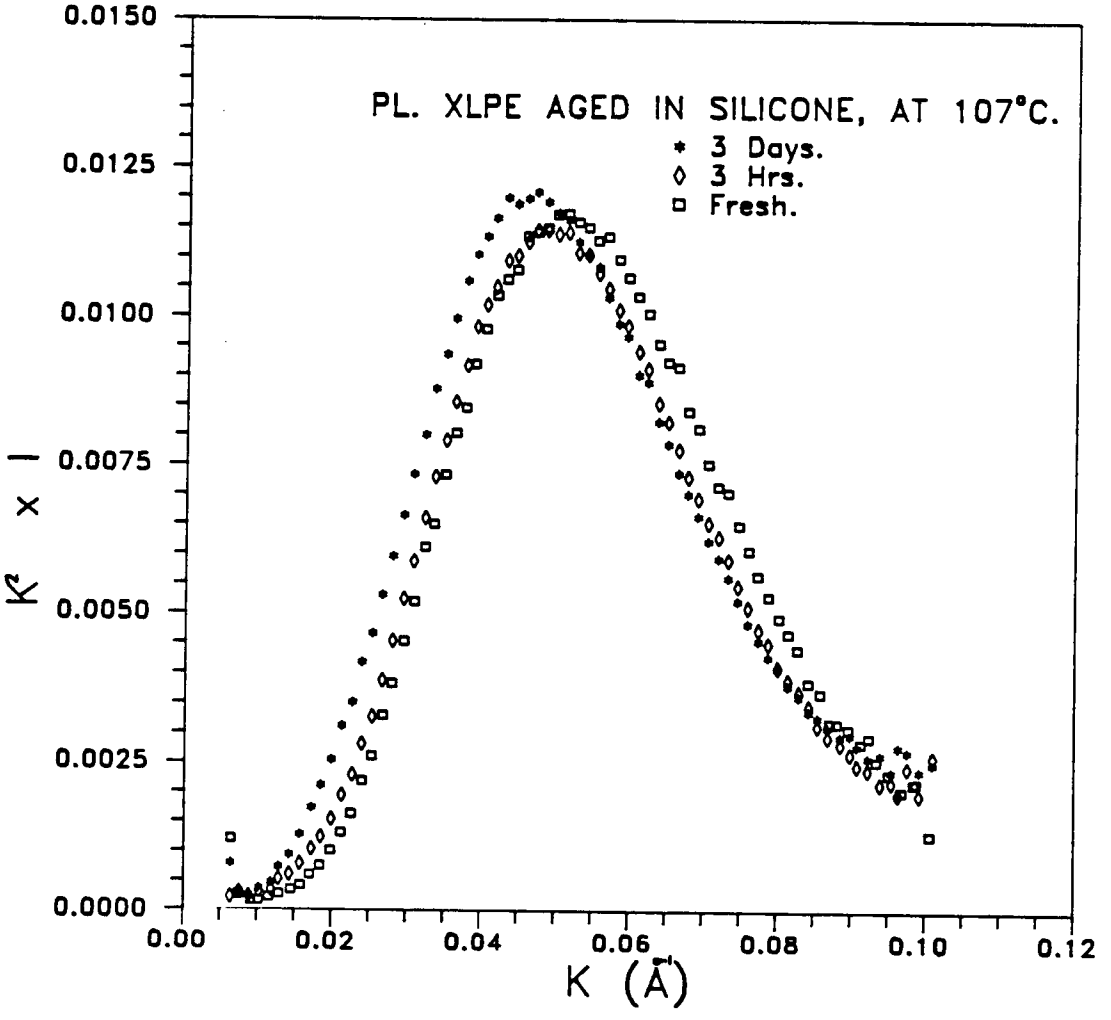



Figure 4.3.33 Variation of Lorentz-corrected SAXS intensity curves of PL-XLPE annealed at 107°C in silicone oil with annealing time.

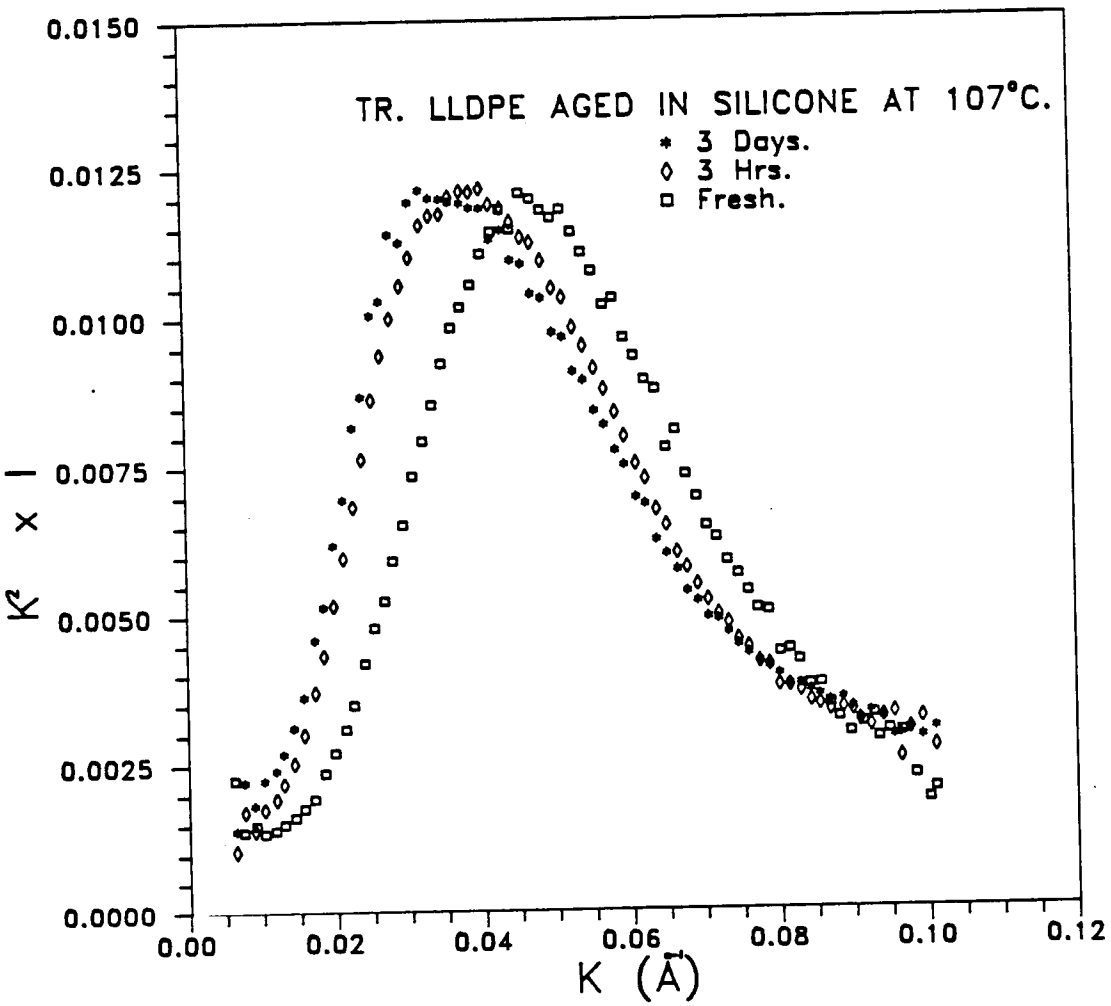



Figure 4.3.34 Variation of Lorentz-corrected SAXS intensity curves of TR-LLDPE annealed at 107°C in silicone oil with annealing time.

the voids but similar to that of polyethylene solid, to fill up the voids caused by bow-tie trees. He found that the impregnated samples did not show the intensity at low angles, and estimated the average size of voids to be 720 Å.

The previously annealed samples were also immersed in the same mineral oil (Univolt$^{tm}$ 60) that was used in Vatansever's experiment. The samples were placed in the mineral oil under vacuum at relatively low temperature (50$^{o}$C). The samples impregnated at temperatures higher than 80$^{o}$C show partial dissolution by the mineral oil of the polymer as reported in the previous section. Figures 4.3.35, 4.3.36, 4.3.37 and 4.3.38 show the radially averaged SAXS intensity curves for TR-XLPE, EC-XLPE, PL-XLPE, and TR-LLDPE impregnated in the transformer oil after being annealed at 107$^{o}$C in air. The SAXS curves of immersed samples do not show any lowering of SAXS intensity near the beam stop, having virtually the same SAXS patterns as the untreated samples. This can be speculated as due to either that the penetration of the mineral oil is impossible, or that the sample studied does not contain the micro-voids with the dimension that correspond to the size in this scattering vector range.

### 4.3.4. SAXS Data at High Temperature

Semicrystalline polymers normally show broad melting peaks, meaning that melting starts well below a quoted melting peak temperature. Partial melting at a temperature below the major

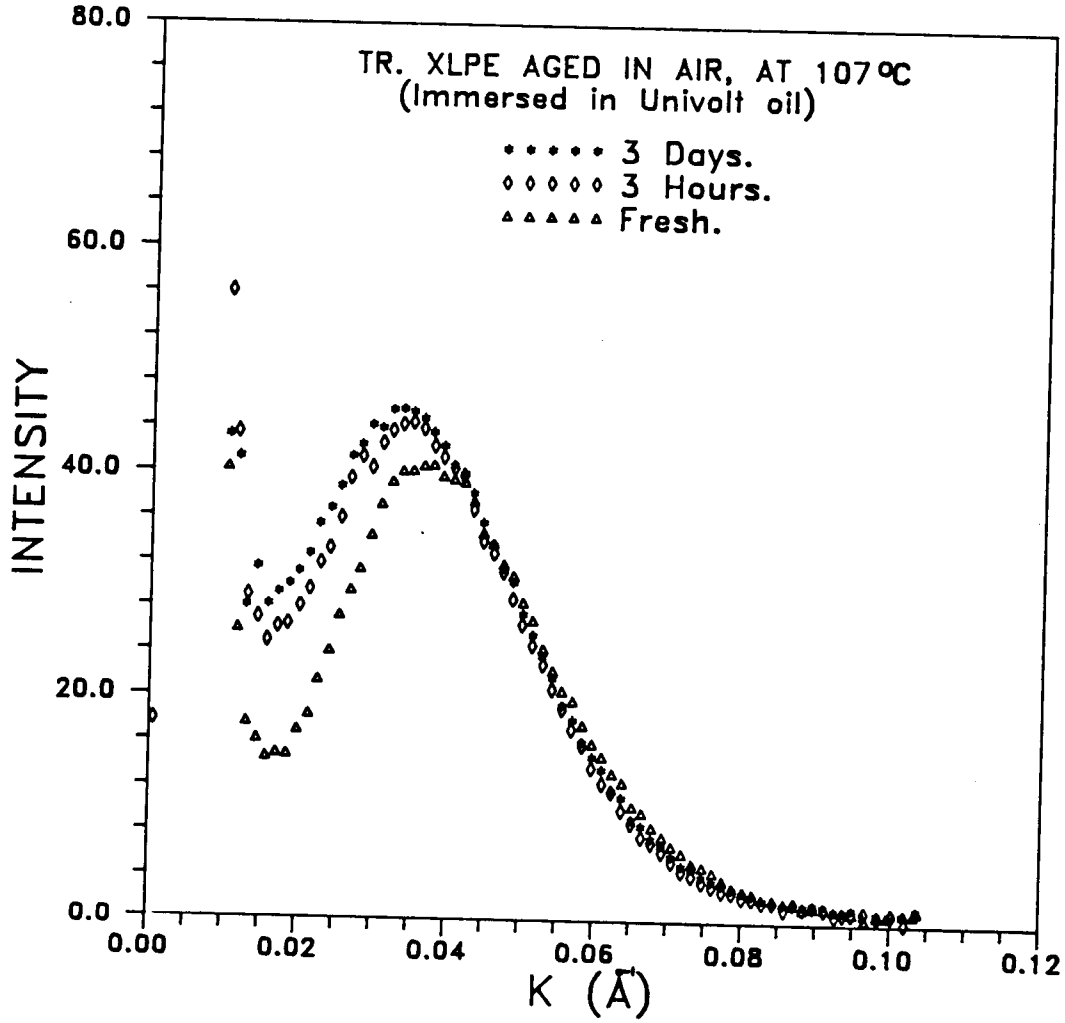



Figure 4.3.35 Variation of SAXS intensity curves of TR-XLPE annealed at 107°C in air with annealing time. (immersed in transformer oil after annealing)

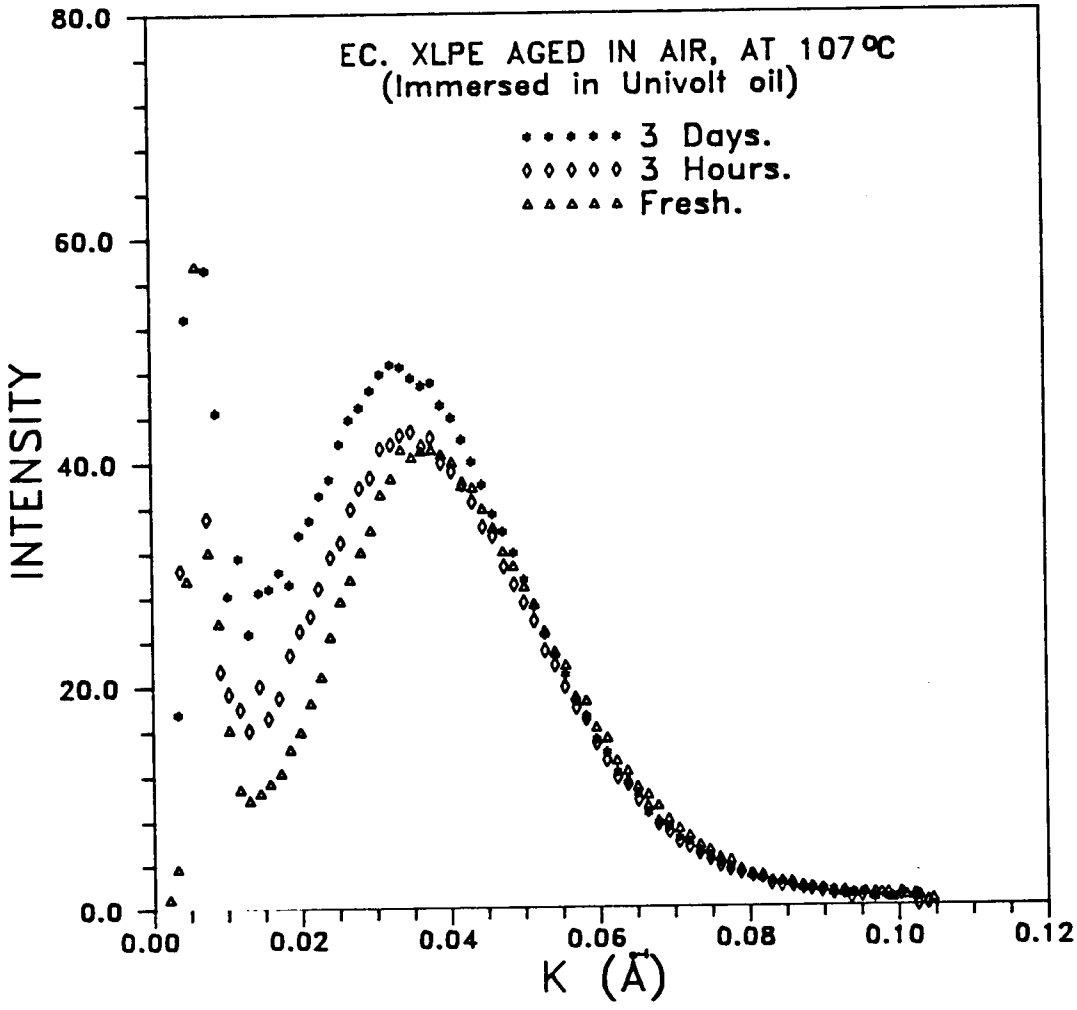



Figure 4.3.36 Variation of SAXS intensity curves of EC-XLPE annealed at 107°C in air with annealing time. (immersed in transformer oil after annealing)

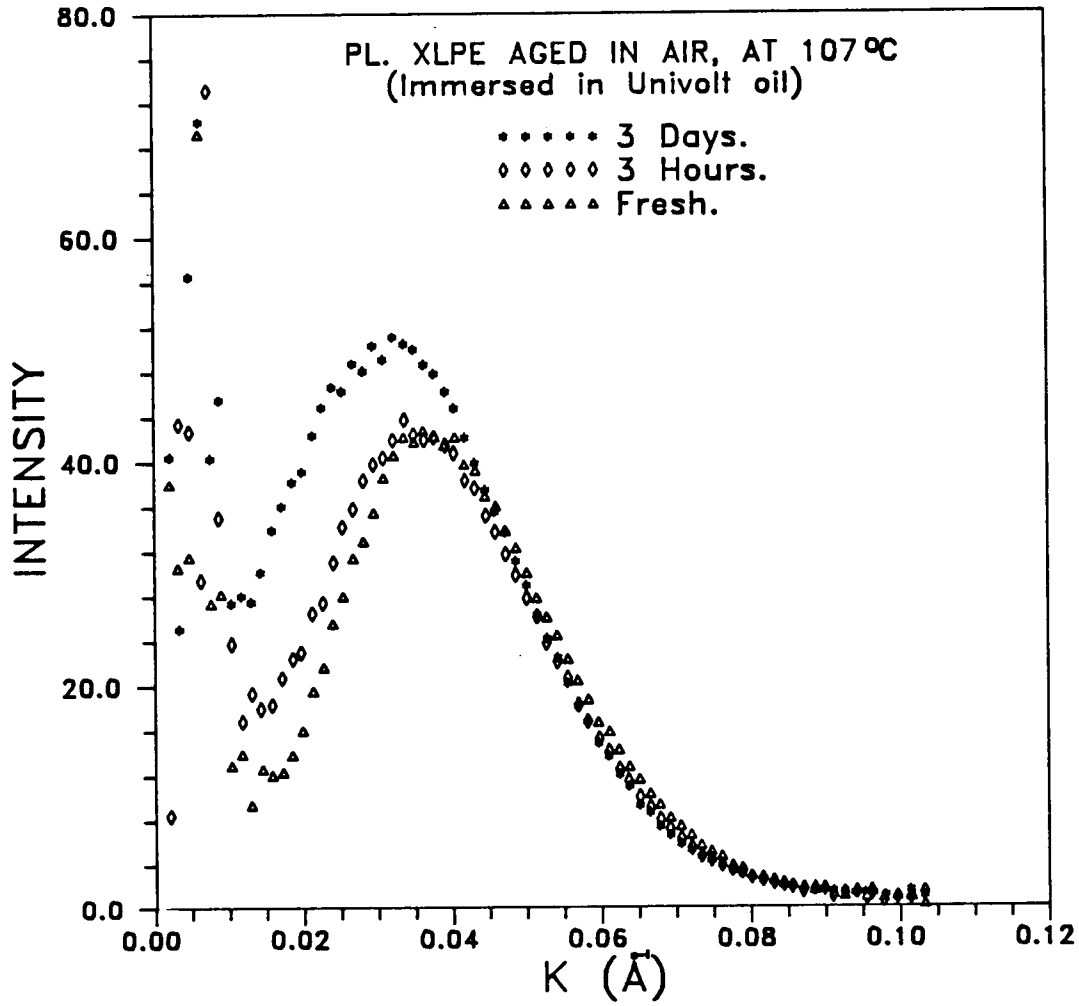



Figure 4.3.37 Variation of SAXS intensity curves of PL-XLPE annealed at 107°C in air with annealing time. (immersed in transformer oil after annealing)

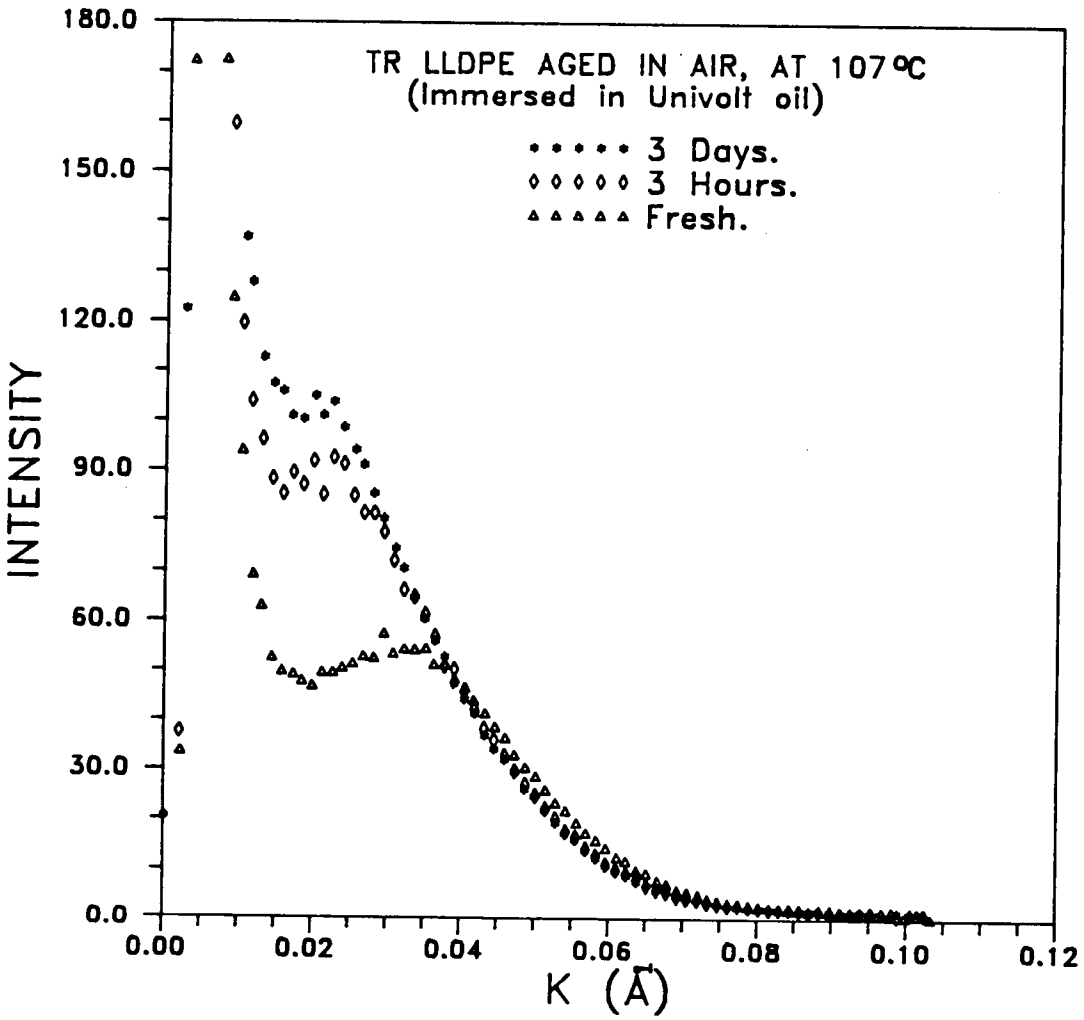



Figure 4.3.38 Variation of SAXS intensity curves of TR-LLDPE annealed at 107°C in air with annealing time. (immersed in transformer oil after annealing)

melting peak is thought to occur preferentially in less perfect or thinner crystals.

All lightly crosslinked polymers including crosslinked polyethylene are known to have an uncrosslinked fraction in their system. Studying micro-structure at higher temperatures can generate information about the shape or quantity of the unmolten fraction, since the molten fraction has a different electron density from the molten fraction.

In-situ SAXS experiments were performed in the 10-meter SAXS camera with a sample chamber equipped with a temperature control unit. The collection and radial averaging of data from in-situ experiments are performed in the same way as at room temperature. The in-situ temperatures were also confirmed through inspection of the DSC curves of the samples after in-situ measurements, since the locations of annealing peaks and onset temperatures reveal the temperatures of treatment.

Figure 4.3.39 displays changes in unmodified SAXS intensity curves of TR-XLPE on a linear scale with variation of in-situ temperature. Changes in SAXS curves of various other crosslinked polyethylenes with various in-situ temperatures are shown in Figure 4.3.40. The data evidently show dramatic change in SAXS curves with variation of in-situ temperatures. Up to the in-situ temperatures of 106$^{o}$C, SAXS curves show Bragg peaks. However, the location of the peak approaches the zero-angle region, indicating an increase of long periodicity. Further increase in in-situ temperature results in

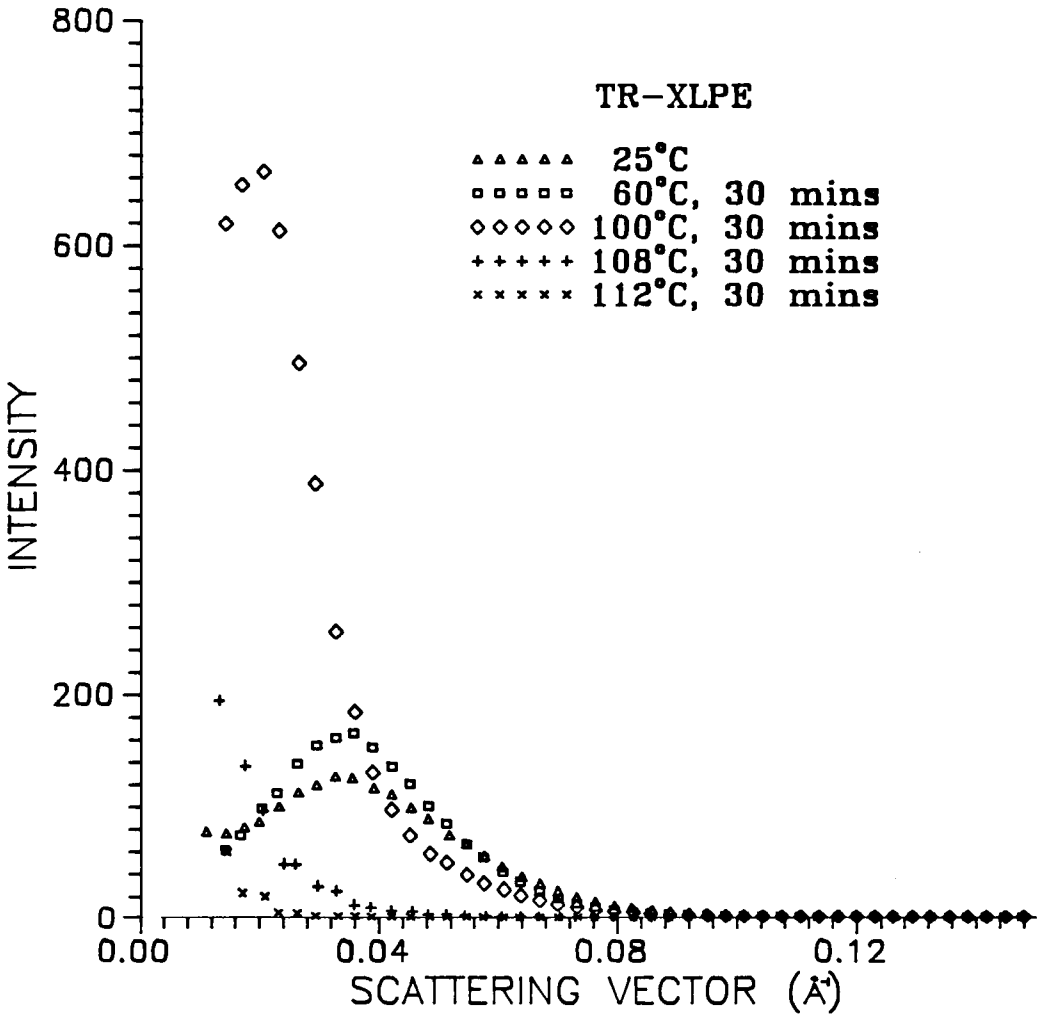



Figure 4.3.39 Variation of SAXS intensity curves of TR-XLPE held at various in-situ temperatures.

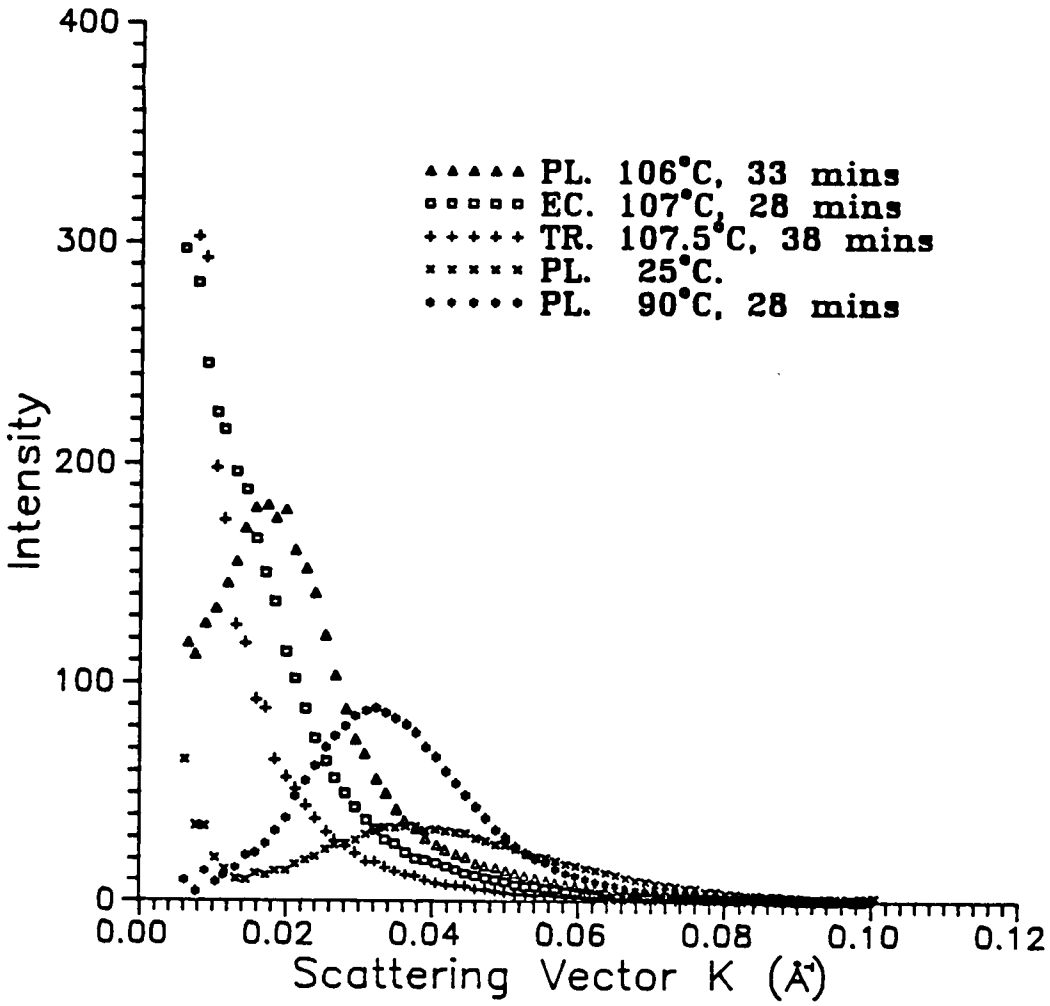



Figure 4.3.40 SAXS intensity curves of various XLPE held at various in-situ temperatures.

loss of the Bragg peak, illustrating that the internal structure is totally different from that at low temperature. The scattering system at higher temperature can be considered to be particle scattering, whereas the one at lower temperature is considered to be dense scattering with long-range interference. The intensity near the beam-stop region also increases dramatically with increasing in-situ temperature.

Lorentz-corrected SAXS intensity curves, however, show peaks for all samples at any in-situ temperature. Figure 4.3.41 shows the variation of Lorentz-corrected SAXS intensity curves with temperature. The intensity at a peak monitored at 90°C is highest, and decreases with increasing in-situ temperature. The position of the peak approaches lower angles with increasing in-situ temperature.

In-situ SAXS intensities were also recorded according to time after the sample was exposed to the condition. Figures 4.3.42 and 4.3.43 show changes in unmodified and Lorentz-corrected SAXS intensity curves, respectively, of TR-XLPE exposed to the in-situ temperature of 107.5°C. In about 8 minutes of exposure, which is the lowest time-interval possible due to the time required for the collection of a reasonable data size, the SAXS curve displays a different shape from those obtained at room temperature, showing no peak in unmodified data. As the exposure time increases, the intensity at low angles increases. The Lorentz corrected curve also shows increase in intensities at low angles (Figure 4.3.43). SAXS

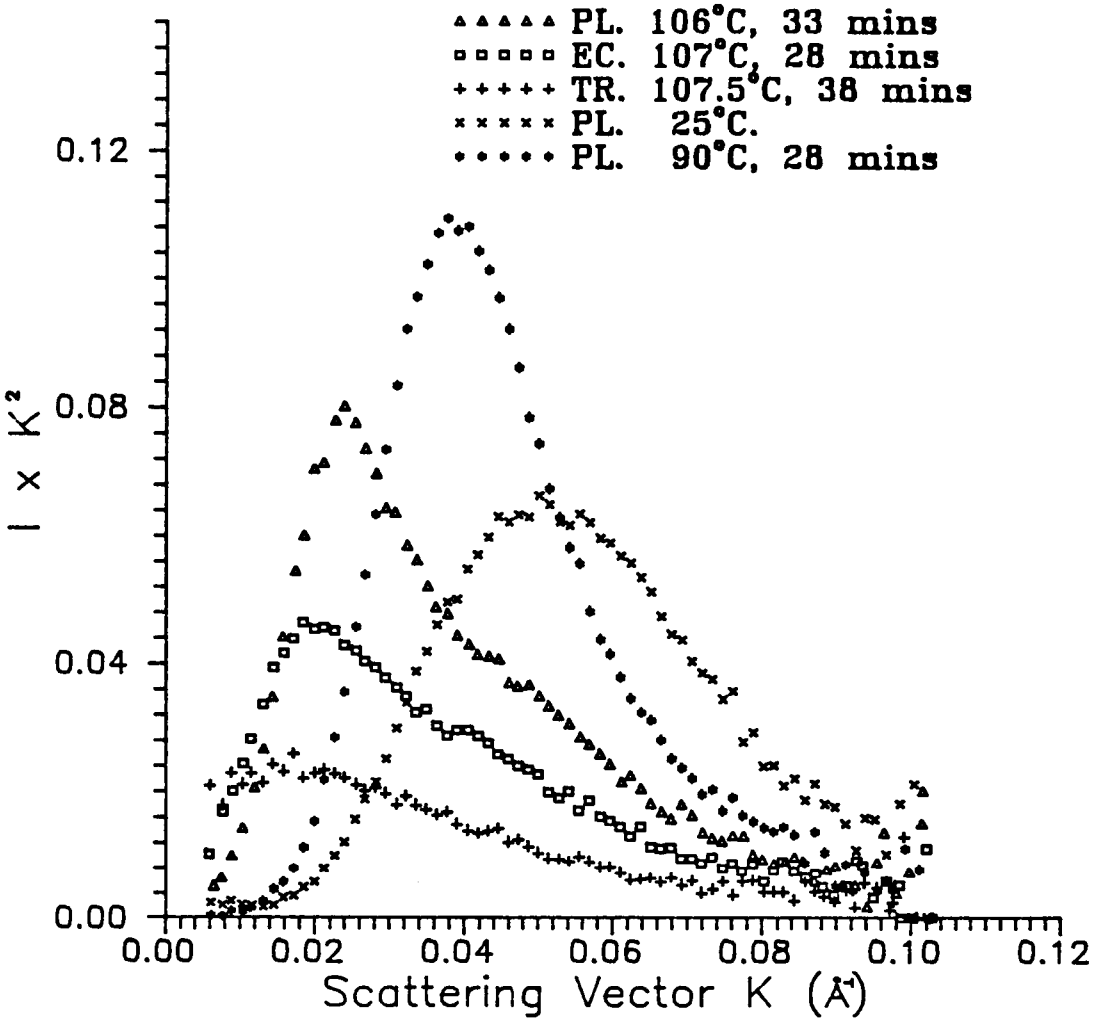



Figure 4.3.41 Lorentz-corrected SAXS intensity curves of various XLPE held at various in-situ temperatures.

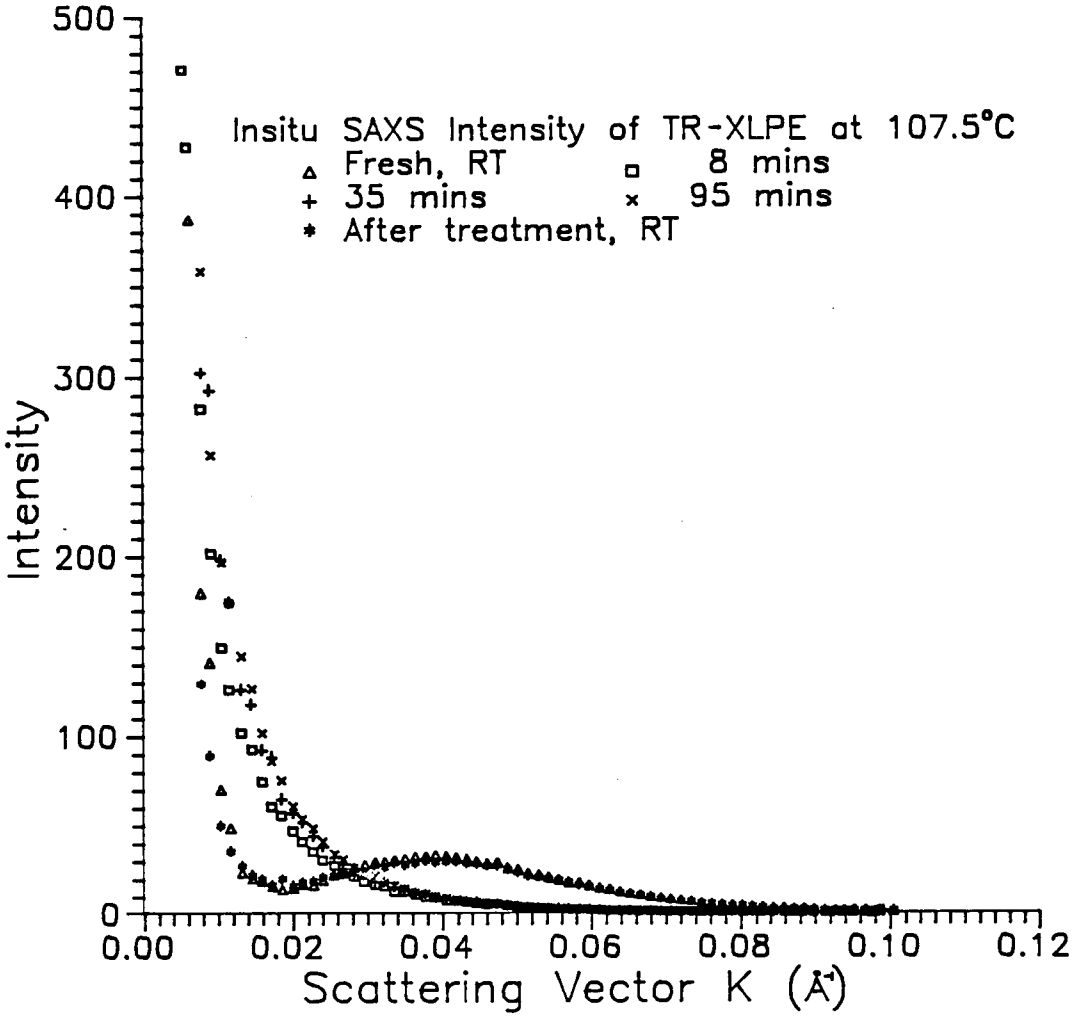



Figure 4.3.42 SAXS intensity curves of TR-XLPE held at in-situ temperature of 107.5°C for various periods of time.

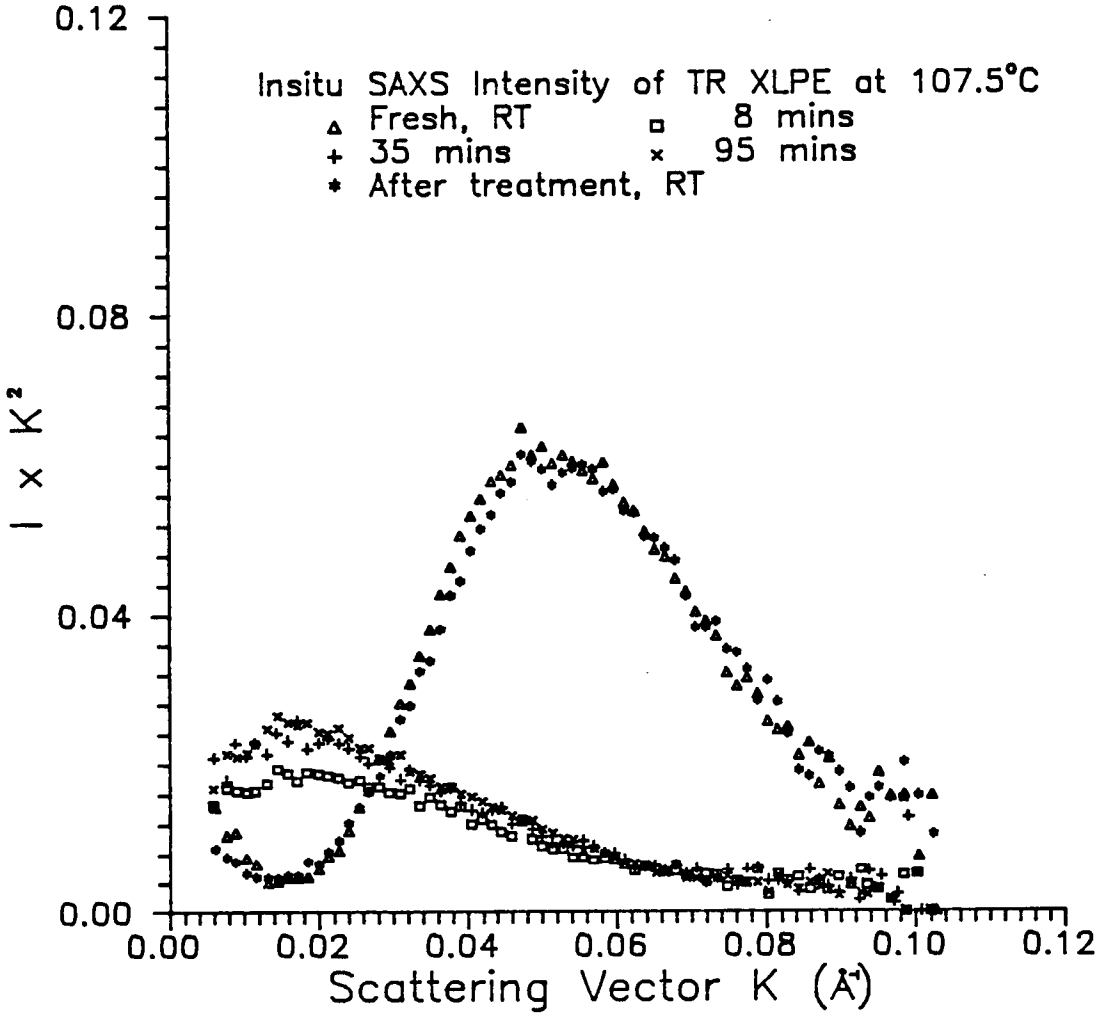



Figure 4.3.43 Lorentz-corrected SAXS intensity curves of TR-XLPE held at in-situ temperature of 107.5°C for various periods of time.

curves after the treatment show similar increases in intensities at low angles.

In-situ SAXS measurement of EC-XLPE was performed at 107°C and plotted in Figures 4.3.44 and 4.3.45. Unmodified SAXS curve (Figure 4.3.44) shows a transitional hump after about 8 minutes of exposure. The hump is considered to be reflection of early formation of a Bragg peak. With longer exposure, however, similar peaks do not appear in that region. However, Lorentz-corrected curves show peaks at lower angles. The intensities at the peak after about 8 minutes of exposure show the highest intensities, and then decrease with exposure time.

SAXS plots of PL-XLPE at 106°C produce peaks near the beam-stop as shown in Figure 4.3.46. The intensities at the peak increase slightly with increasing time. Lorentz corrected intensity curves are plotted in Figure 4.3.47. In-situ experiment was also performed for another temperature (90°C) with PL-XLPE. Results are shown in Figure 4.3.48. After about 28 minutes after exposure to the temperature of 90°C, the SAXS intensity curve exhibits a peak with a higher intensity at the peak than the ones measured at a room temperature. However, the intensities at the peak are lower than the ones measured at the even higher temperature of 106°C. Lorentz-corrected curve displayed in Figure 4.3.49, on the other hand, shows highest peak intensities at the in-situ temperature of 90°C due to the factor of $K^2$ during the correction.

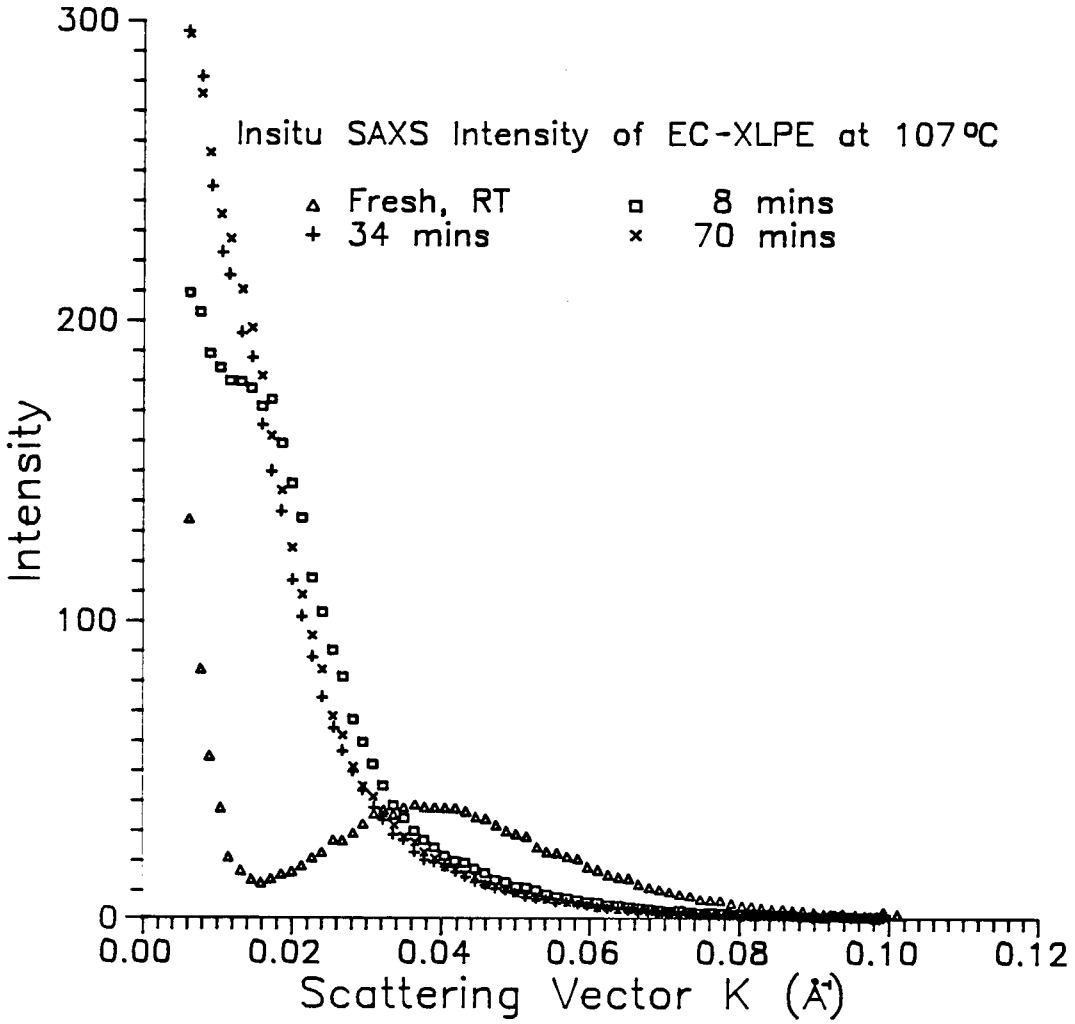



Figure 4.3.44 SAXS intensity curves of EC-XLPE held at in-situ temperature of 107°C for various periods of time.

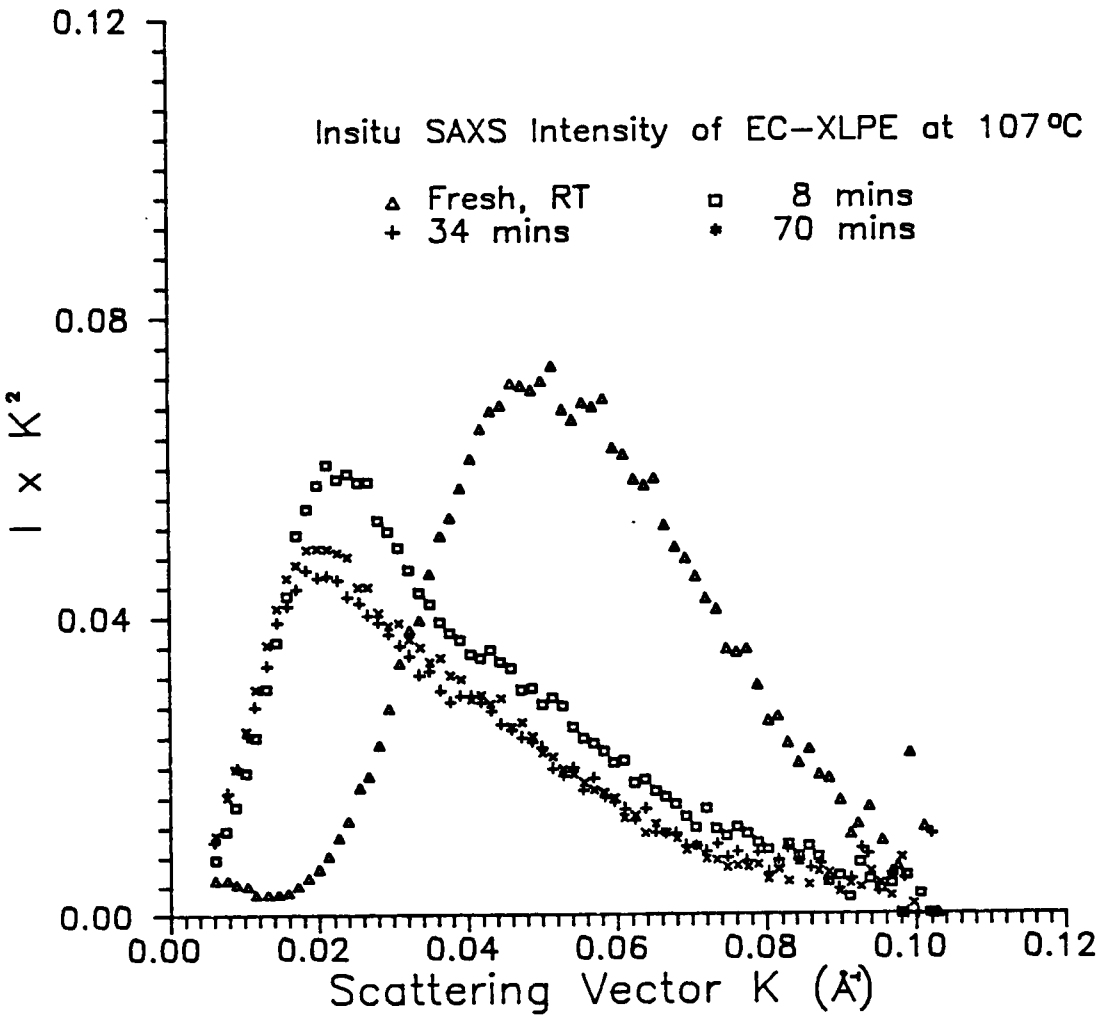



Figure 4.3.45 Lorentz-corrected SAXS intensity curves of EC-XLPE held at in-situ temperature of 107°C for various periods of time.

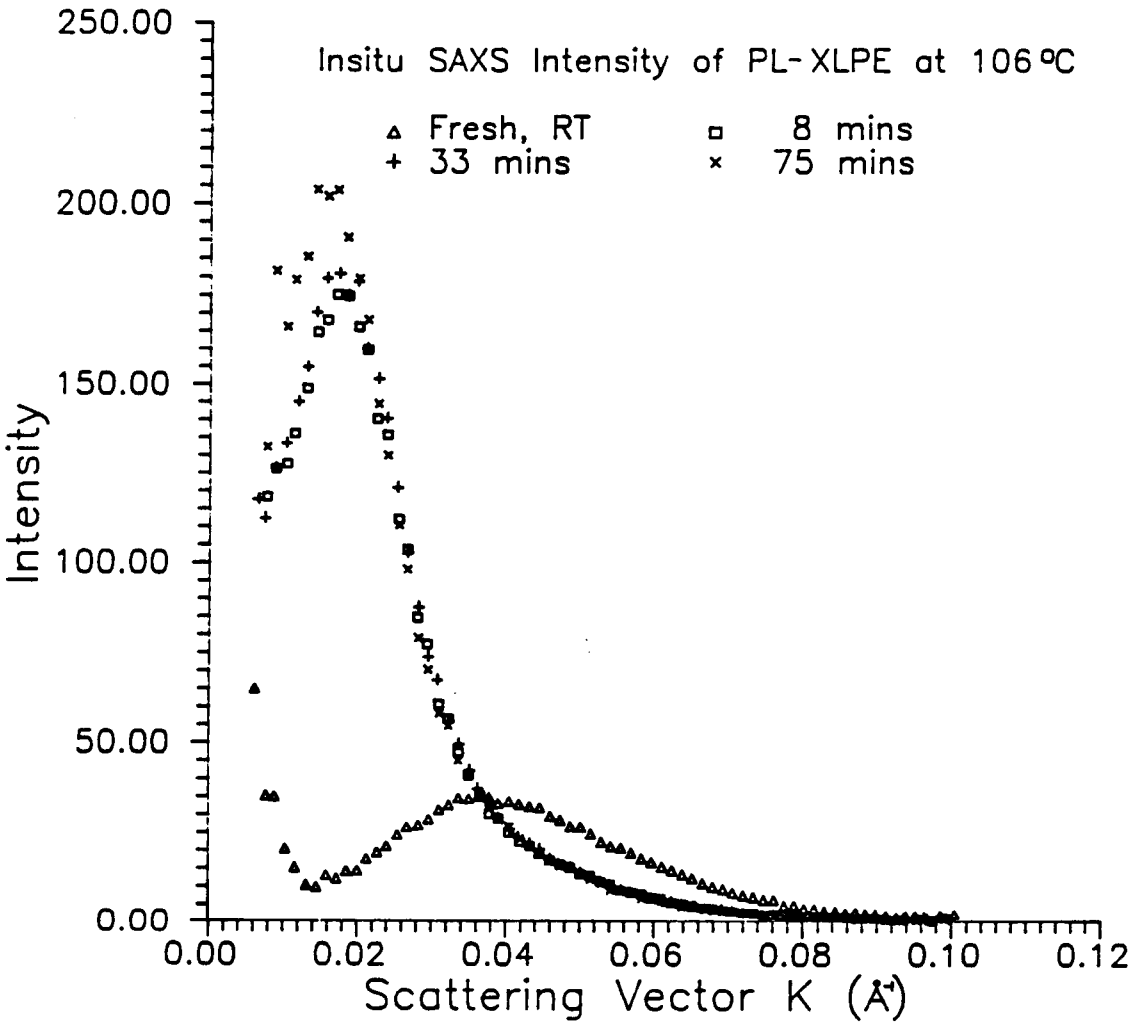



Figure 4.3.46 SAXS intensity curves of PL-XLPE held at in-situ temperature of 106°C for various periods of time.

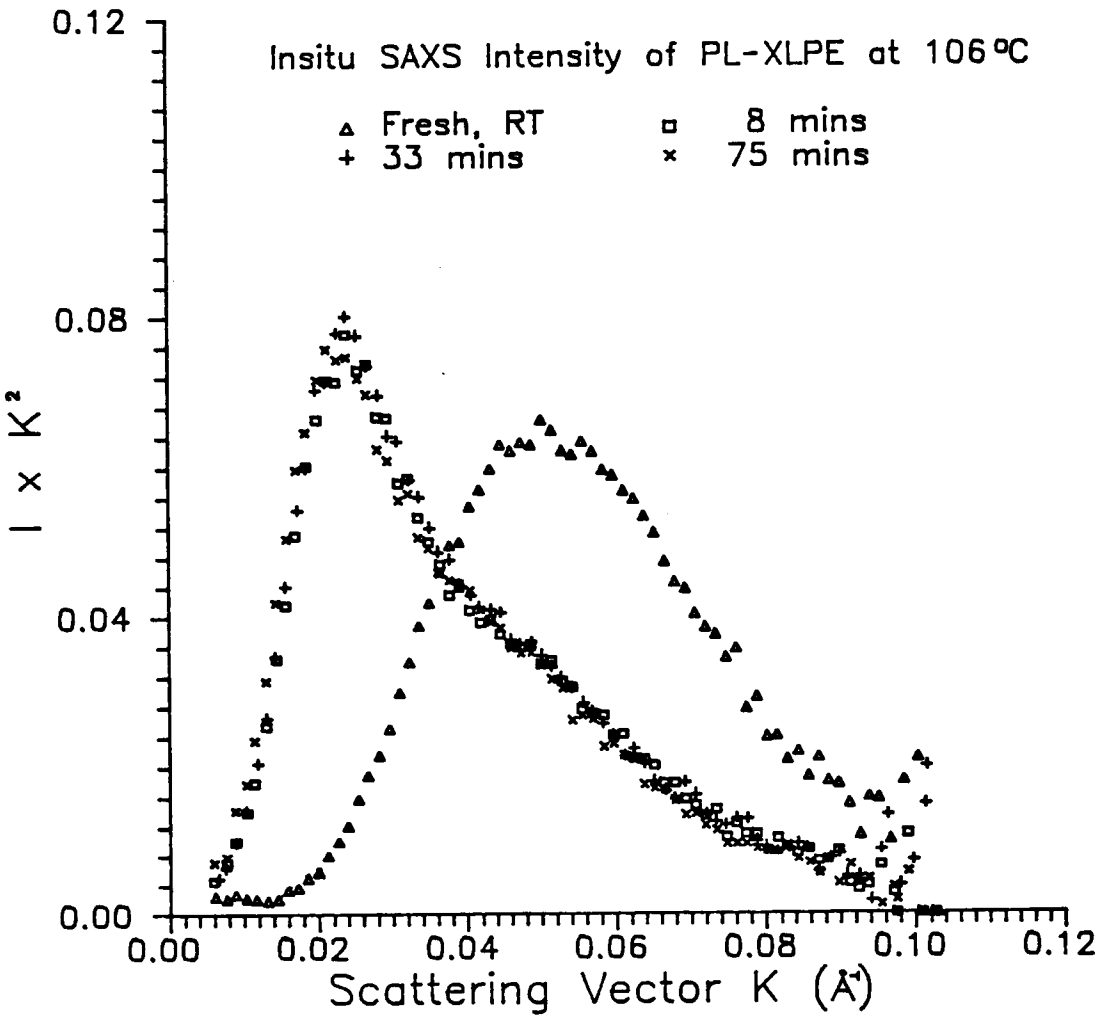



Figure 4.3.47 Lorentz-corrected SAXS intensity curves of PL-XLPE held at in-situ temperature of 106°C for various periods of time.

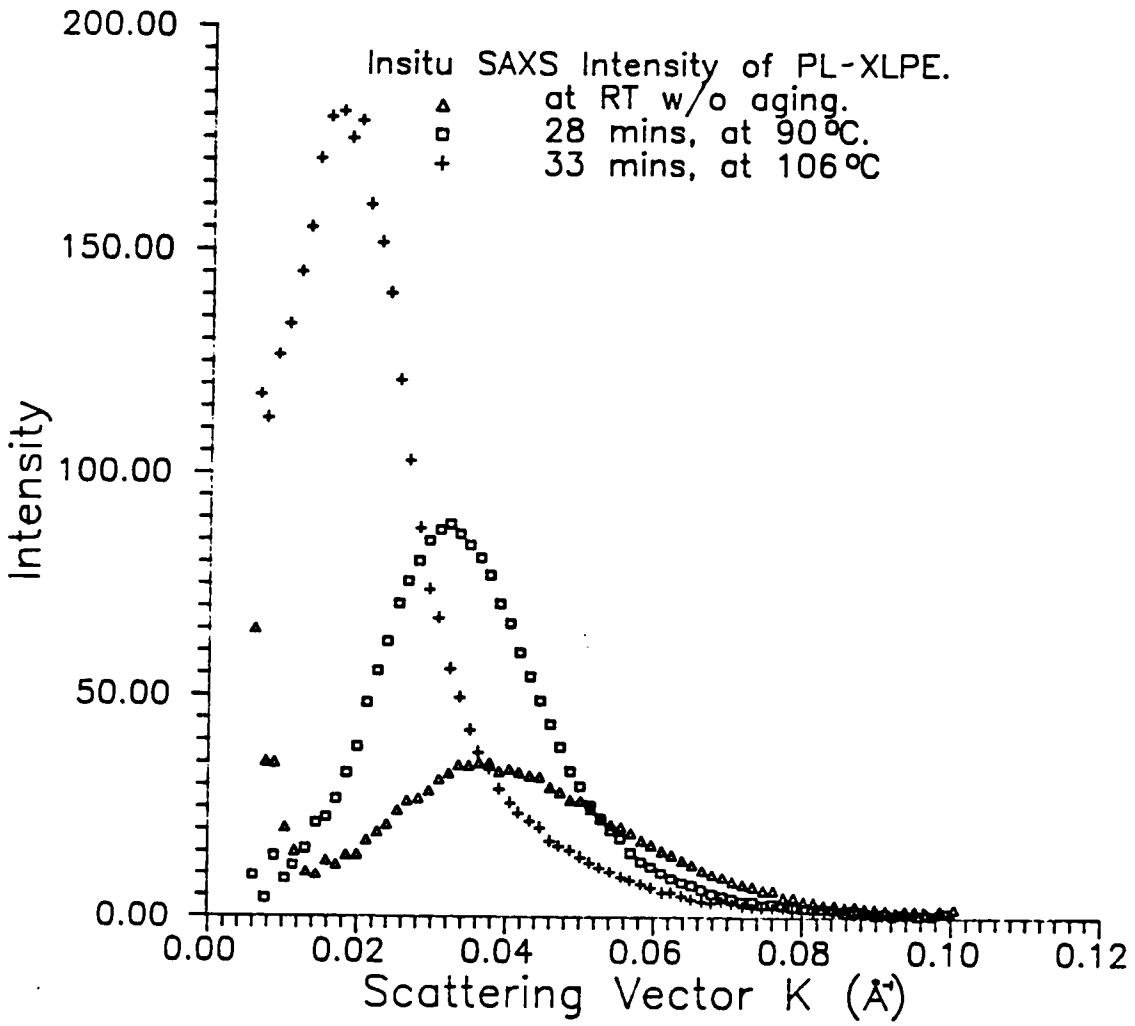



Figure 4.3.48 SAXS intensity curves of PL-XLPE held at in-situ temperature of 25°C, 90°C and 106°C for about 30 minutes.

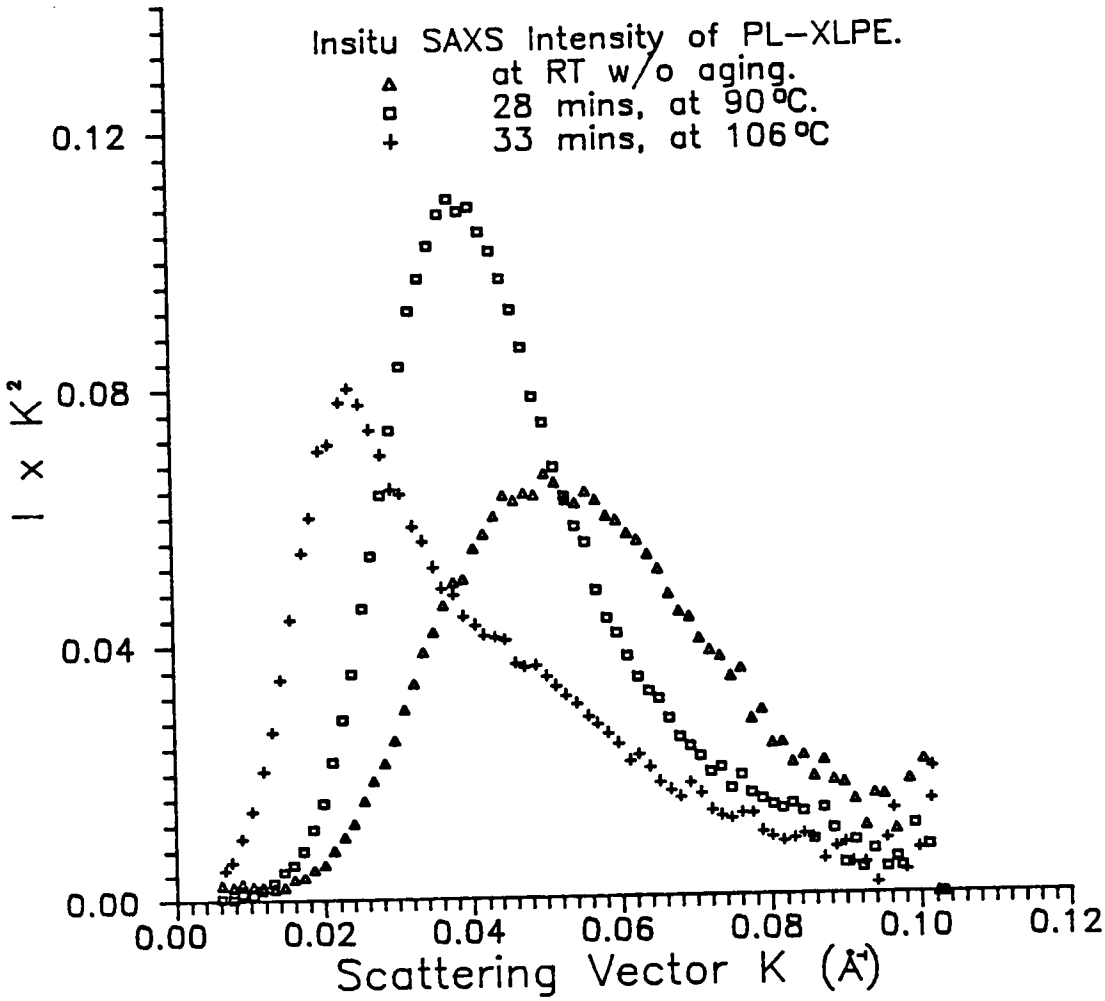



Figure 4.3.49 Lorentz-corrected SAXS intensity curves of PL-XLPE held at in-situ temperature of 25°C, 90°C and 106°C for about 30 minutes.

To illustrate possible separation during annealing at around 107°C, the samples were pre-annealed at 106°C for 3 hours before in-situ experiments. DSC curves after pre-annealing show two melting peaks with the onset temperatures of the second peak at around 108°C. Therefore, it can be expected that the sample at around 108°C melts only the fraction which contributes the lower melting peak. As shown in Figures 4.3.50, 4.3.51 and 4.3.52 for TR-XLPE, EC-XLPE, and PL-XLPE, respectively, all cross-linked samples display smooth curves with high intensities at low angles without Bragg maxima, indicating that the remaining fraction at the in-situ temperature behaves as a dilute system without any long-range interaction among the entities. In fact, the curves are very similar to the curves of unannealed samples at such high in-situ temperatures. Lorentz-corrected curves are plotted in Figures 4.3.53, 4.3.54, and 4.3.55 for TR-XLPE, EC-XLPE, and PL-XLPE, respectively. TR-LLDPE was also preannealed at 106°C before being subjected to the in-situ experiment at 108°C. Figure 4.3.56 shows unmodified SAXS intensity curves of TR-LLDPE at room temperature and at 108°C after pre-annealing. The SAXS curve of pre-annealed TR-LLDPE sample at 108°C shows an unclear hump that can be recognized as the trace of Bragg maximum. It is natural to show a trace of a Bragg peak for LLDPE, since the sample has a higher melting peak than the regular XLPEs.

To investigate any possible fractal behavior of a sample at a high in-situ temperature, the SAXS data were plotted on a log-log scale as shown in Figures 4.3.57 and 4.3.58 for TR-XLPE and PL-XLPE,

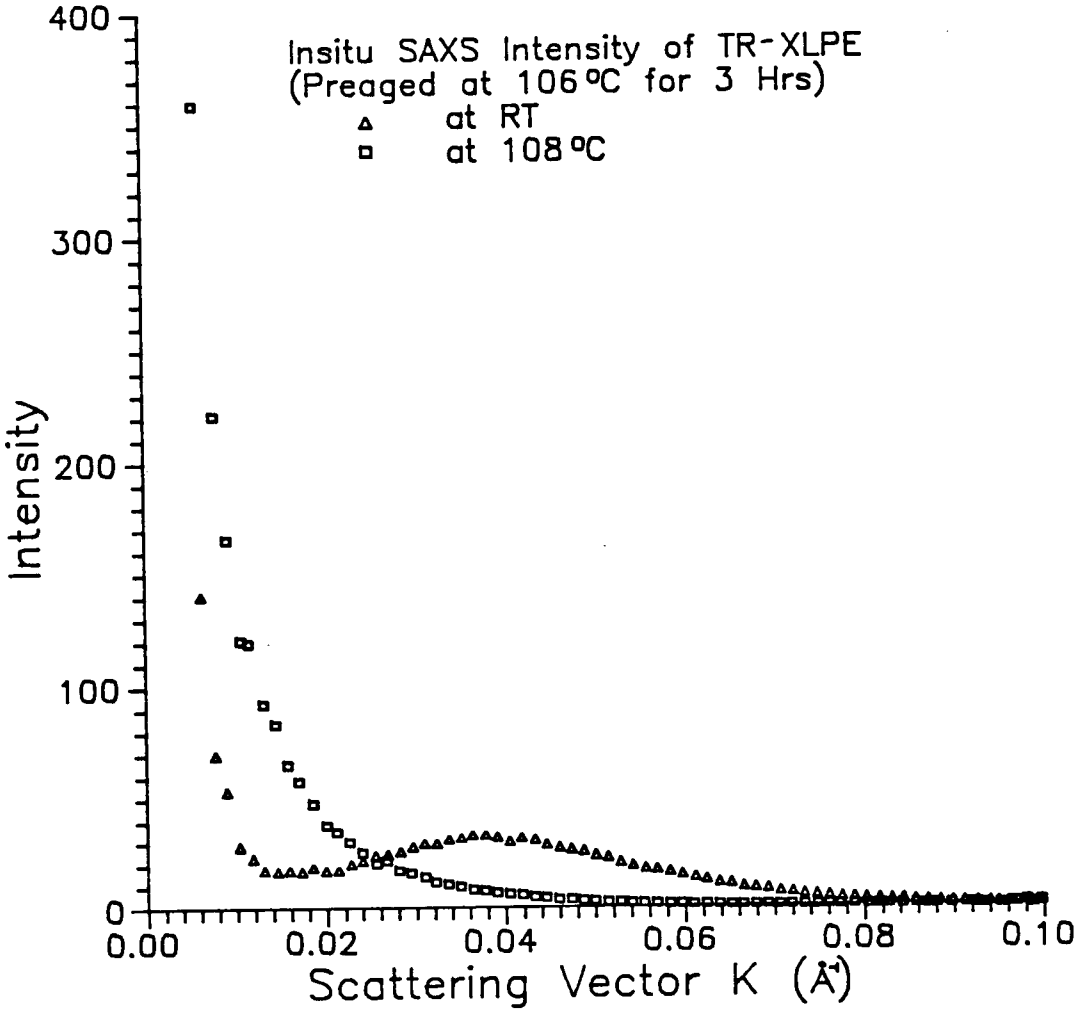



Figure 4.3.50 In-situ SAXS intensity curves of pre-annealed TR-XLPE measured at room temperature and 108°C. (annealed at 106°C prior to the experiment)

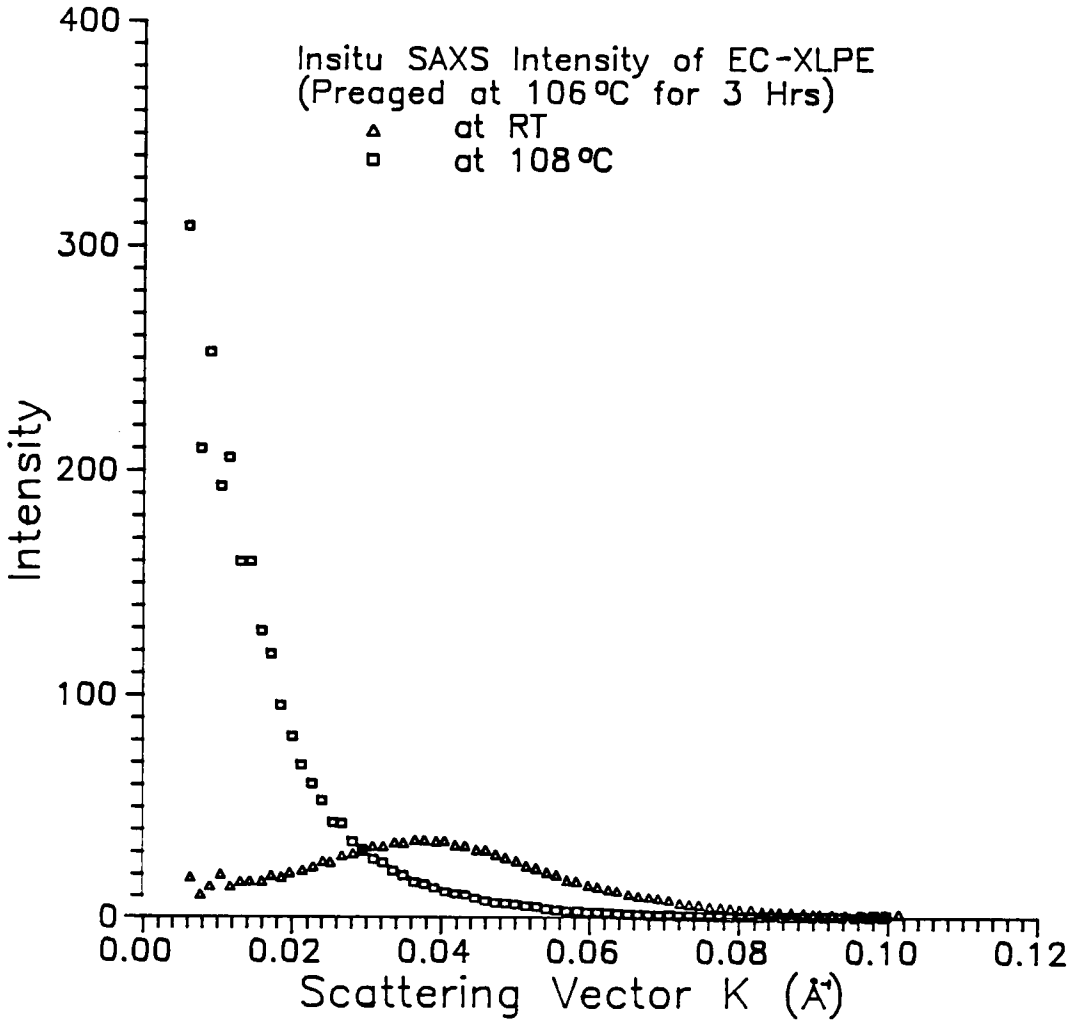



Figure 4.3.51 In-situ SAXS intensity curves of pre-annealed EC-XLPE measured at room temperature and 108°C. (annealed at 106°C prior to the experiment)

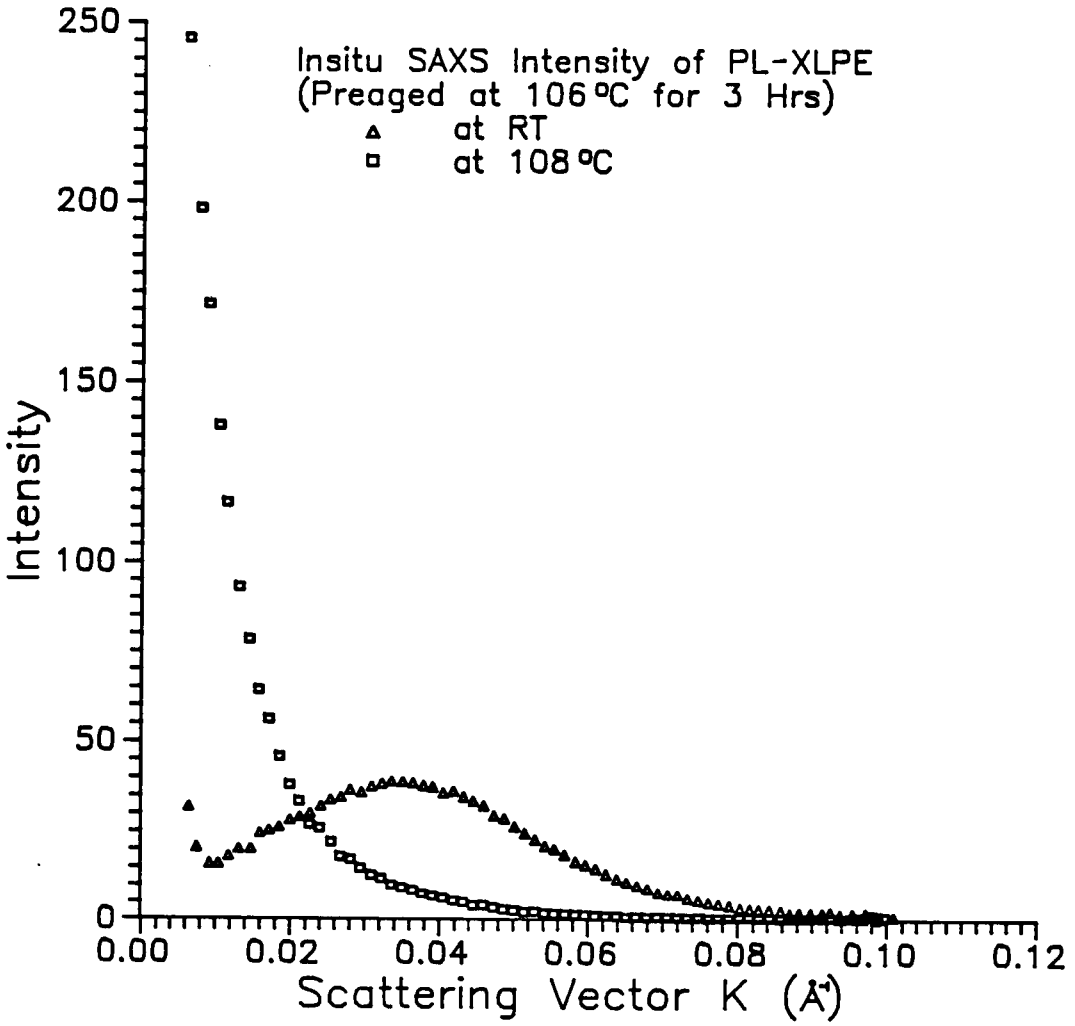



Figure 4.3.52 In-situ SAXS intensity curves of pre-annealed PL-XLPE measured at room temperature and 108°C. (annealed at 106°C prior to the experiment)

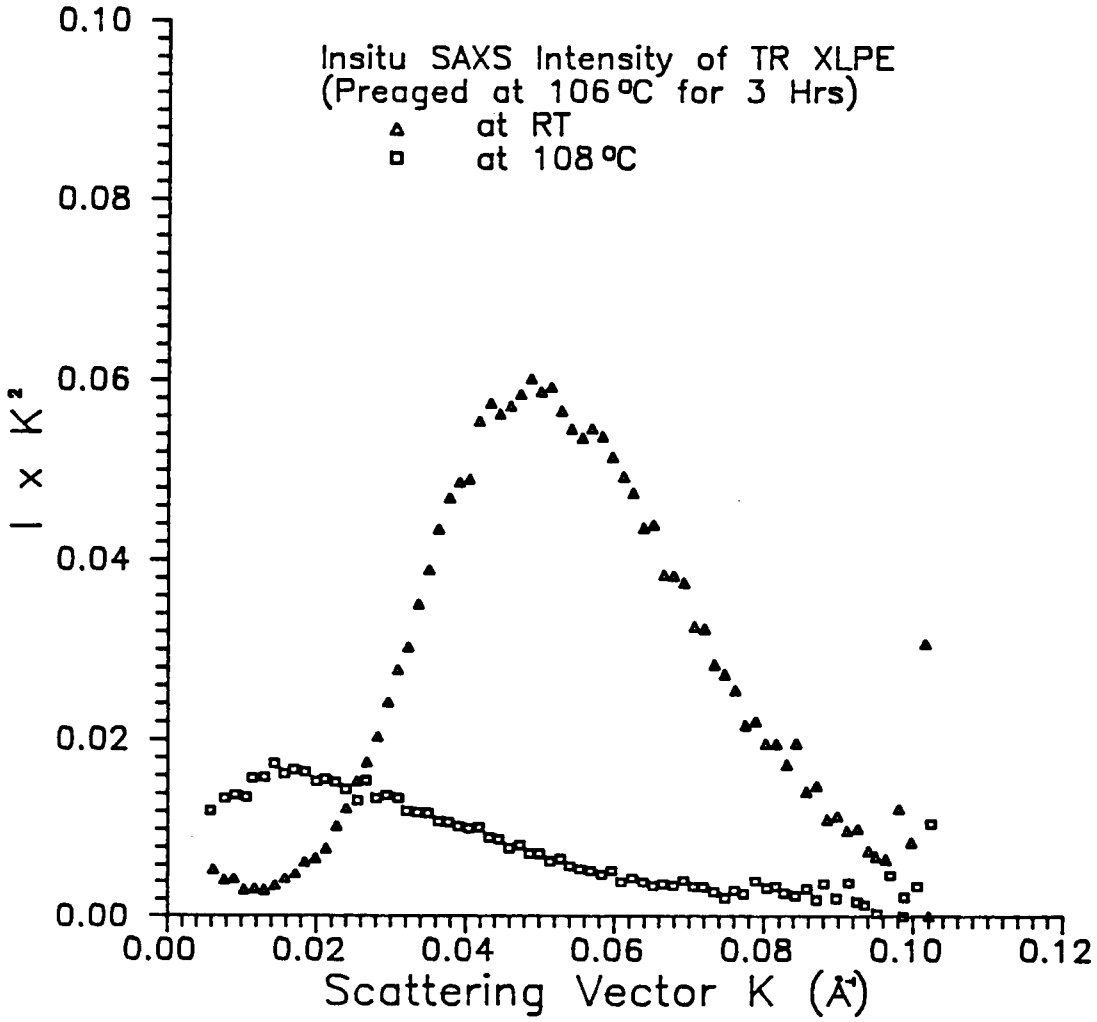



Figure 4.3.53 Lorentz-corrected SAXS intensity curves of pre-annealed TR-XLPE measured at room temperature and 108°C. (annealed at 106°C prior to the experiment)

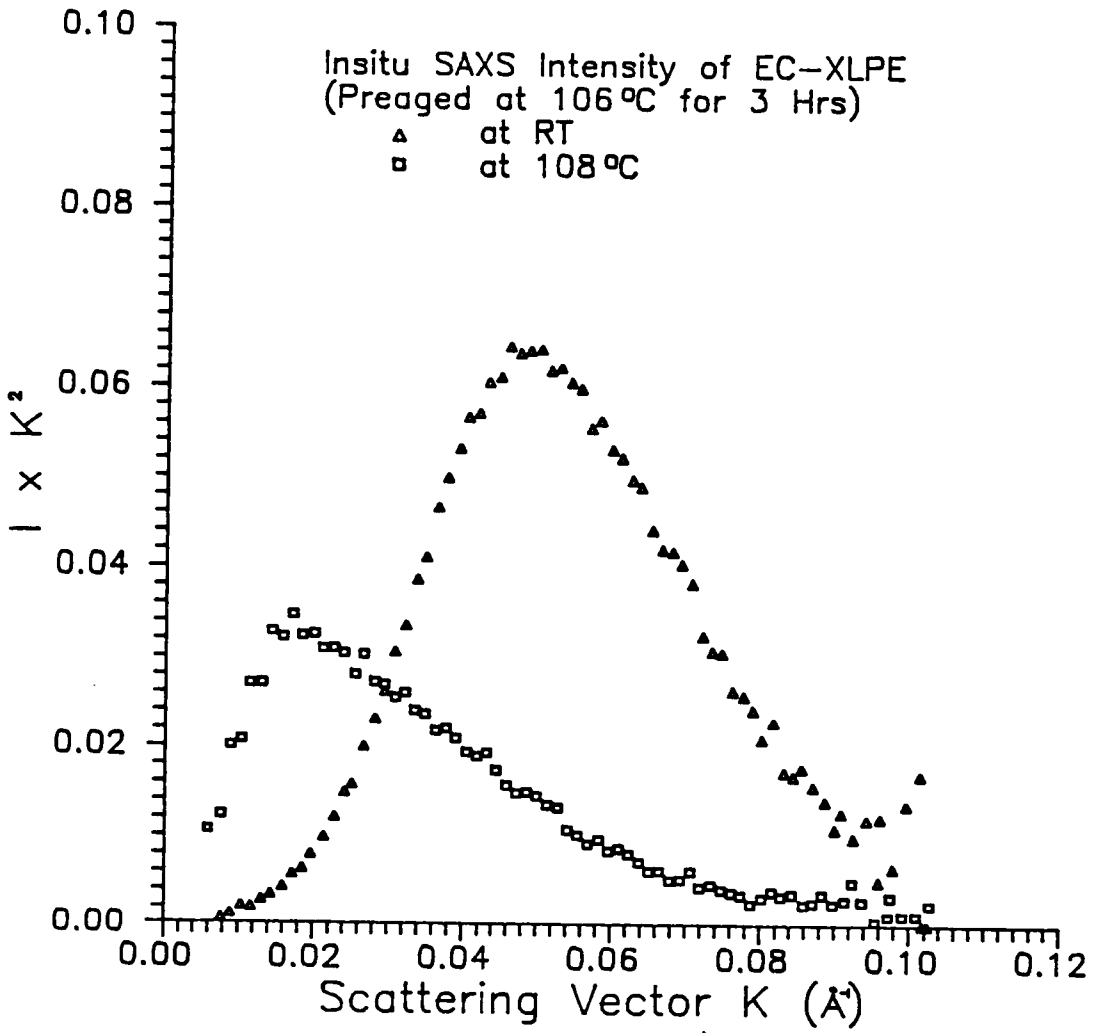



Figure 4.3.54 Lorentz-corrected SAXS intensity curves of pre-annealed EC-XLPE measured at room temperature and 108°C. (annealed at 106°C prior to the experiment)

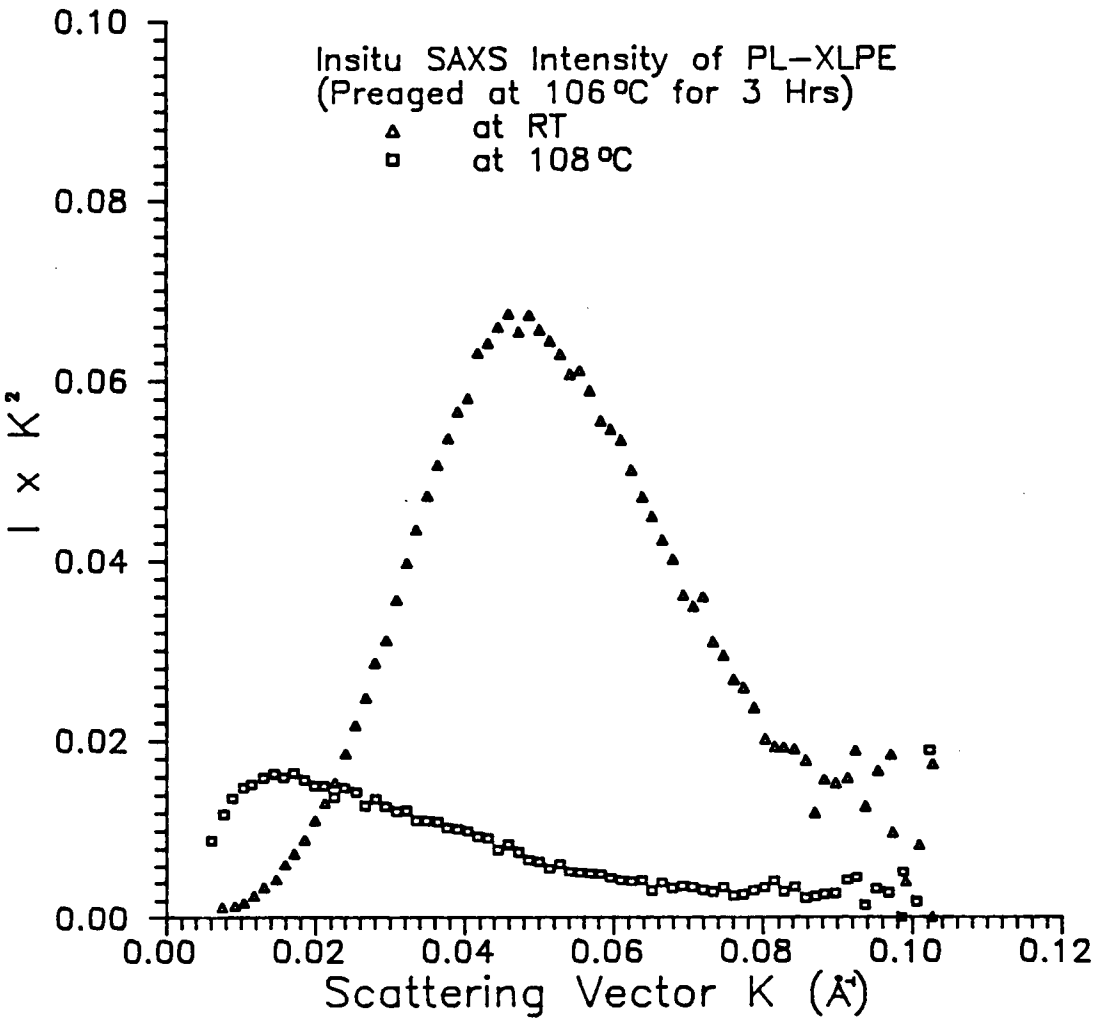



Figure 4.3.55 Lorentz-corrected SAXS intensity curves of pre-annealed PL-XLPE measured at room temperature and 108°C. (annealed at 106°C prior to the experiment)

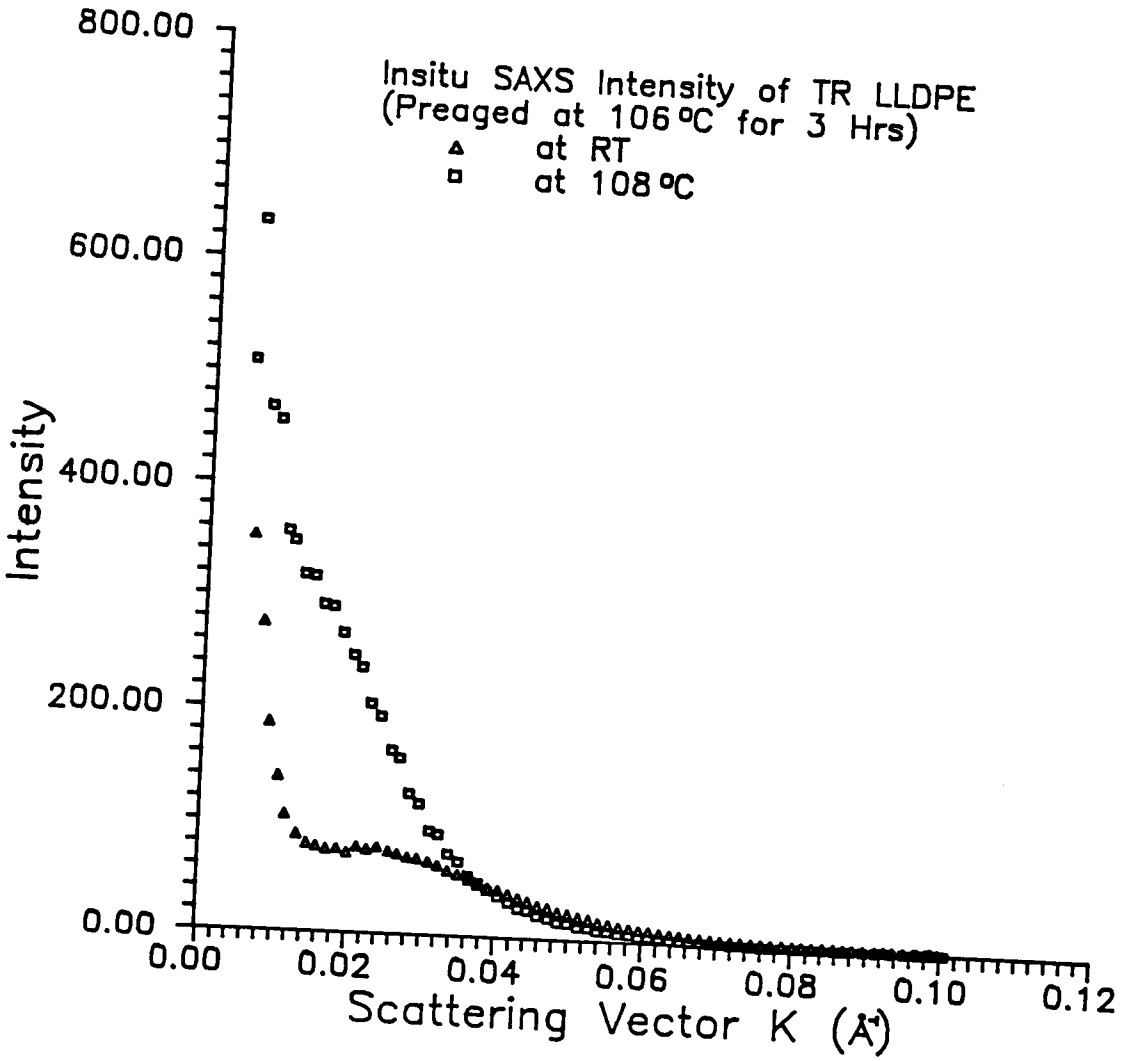



Figure 4.3.56 In-situ SAXS intensity curves of pre-annealed TR-LLDPE measured at room temperature and 108°C. (annealed at 106°C prior to the experiment)

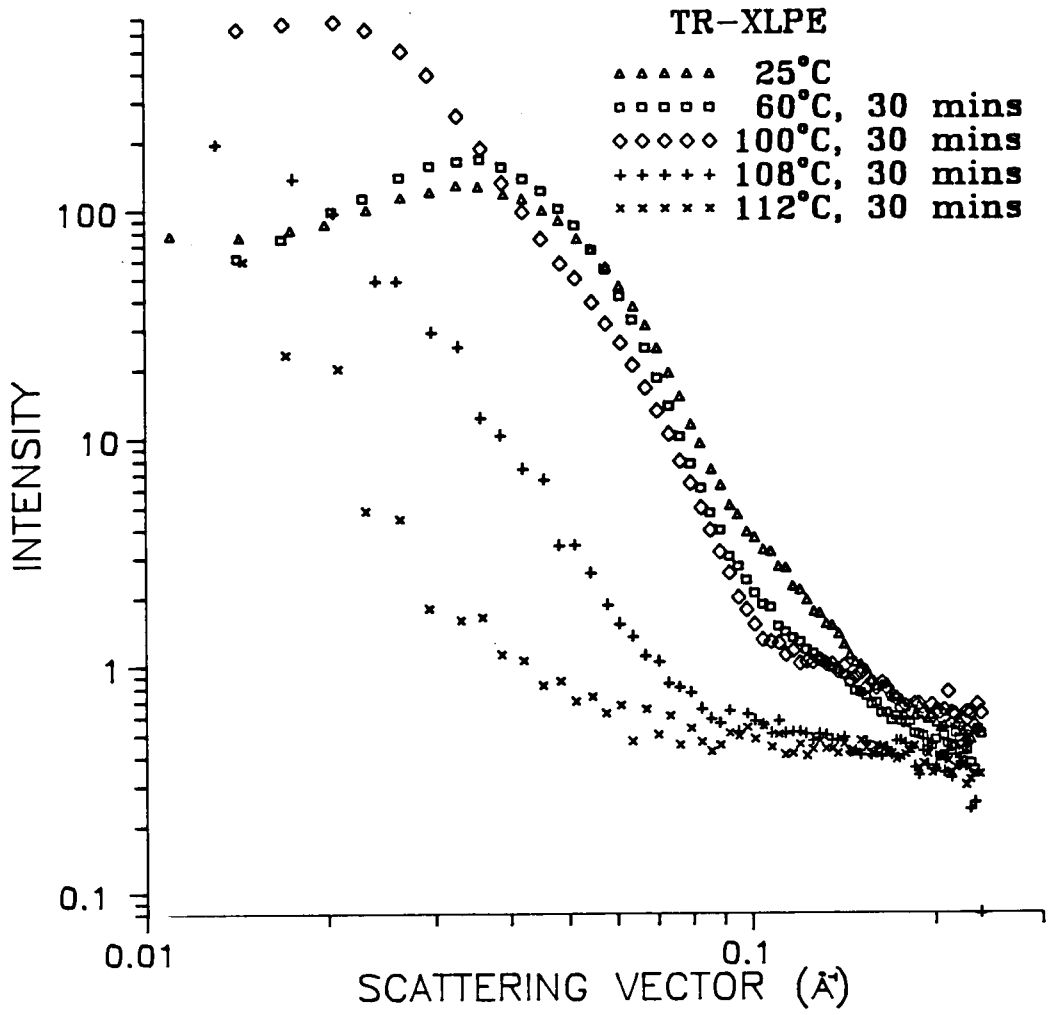



Figure 4.3.57 In-situ SAXS intensities of TR-XLPE for various conditions on a log-log scale.

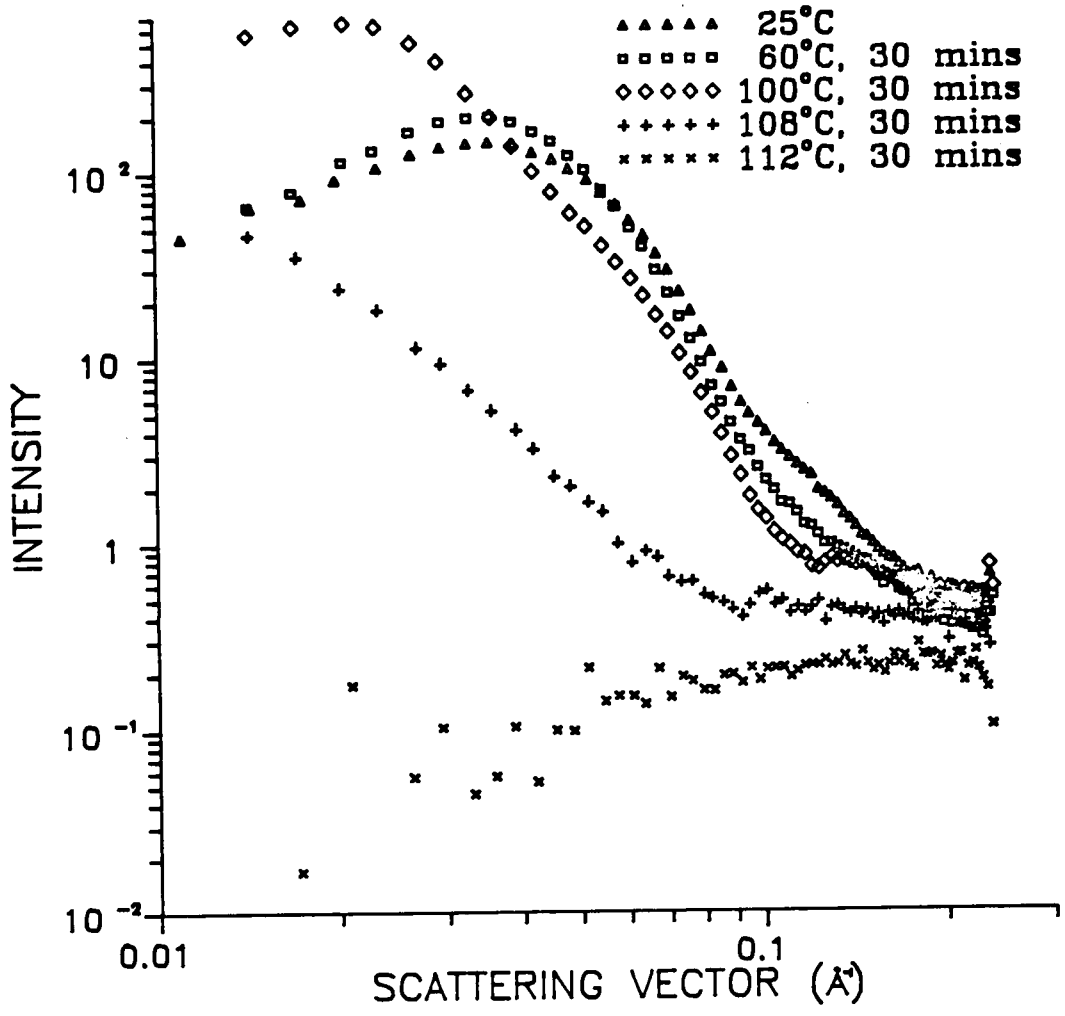



Figure 4.3.58 In-situ SAXS intensities of PL-XLPE for various conditions on a log-log scale.

respectively. The curves monitored at low temperature show very broad peaks at low scattering vectors with a linear decrease afterward. The linear decrease in intensity on the log-log scale has been recognized as one of the typical features of fractal behavior that can be monitored by the SAXS technique. The slope of the linear change was interpreted as the fractal dimension as discussed by some other researchers (Tang, 1984). Even though the SAXS curves monitored at higher temperature (>108$^{o}$C) show a linear decrease in log-log scale at low and medium values of scattering vector, a linear decrease is not seen over the entire range of scattering vector measured. It can be stated that the fractal behavior here is very limited, if present at all.

## 4.4. Theoretical Study of SAXS

### 4.4.1. Introduction

Most semi-crystalline polymers give rise to rather broad diffraction maxima in the small angle range (ca. 1$^{o}$) with diffuse scattering extending to zero angle. The broad peaks have been interpreted frequently in terms of the simplest model of regularly alternating crystalline and amorphous regions. On the other hand the diffuse zero angle intensities have not been interpreted in a quite generalized method. For the broad peaks the angular position of the diffraction maximum can thus be interpreted by Bragg law to yield the average structural period (so called long period) of the polymers.

As discussed in the review chapter, the major difficulty with the simple approach using Bragg law has been recognized as disagreement between SAXS data and direct observation using electron microscopy (Geil, 1966). In a similar way, the case for the interpretation of the diffuse scattering extending to zero degree has not been agreed among investigators. One reason is that the zero angle intensity measured at room temperature is not major. Furthermore, the Lorentz-correction, which is necessary for the interpretation of a non-spherically symmetric system such as solid polymer particles, makes the near-zero-angle scattering intensity negligible. Another reason appears to be due to the fact that there may be particle scattering in solid polymer. These factors made the theoretical interpretation as well as theoretical and quantitative analysis of SAXS data very complicated.

In this section, models for SAXS scattering from highly dispersed lamellae that have been proposed for LDPE will be examined along with other models for the analysis of the data obtained in this experiment. Modelling will make it possible to understand differences among different SAXS data sets as well as establishing a new way for the interpretation and analysis of SAXS data of general melt crystallized polyethylenes and other semi-crystalline polymers.

In the model study, it was assumed that the lamellar stacks are effectively of infinite lateral width, so that only one-dimensional variation of electron densities normal to the lamellar planes accounts for scattering. The statistics of the density

fluctuation were assumed to follow Hosemann's general model (1962) in which the thicknesses of the crystal and amorphous layers vary independently of each other. It was also assumed that the number of layers within a stack is infinite, so that the number of layers does not influence the total scattering. The third assumption will reduce one term (the crystalline component) within the Hosemann's theoretical intensity profile so that the intensity profiles can be given as

$$I(k) = \frac{\Delta d^2}{4\pi^2 k^2 X} \frac{|1-F_y|^2 \cdot (1-|F_z|^2) + |1-F_z|^2 \cdot (1-|F_y|^2)}{|1 - F_y F_z|^2} \qquad 4.4.1.$$

The derivation of this equation was reviewed in Chapter 2. Using these frameworks for an individual stack, two types of models will be examined.

## 4.4.2. Simple Lamellar Stack Model

In the simplest model, the system can be represented by a single stack of lamellae, where the stack is sufficiently large that any stack within the system can be considered to be statistically identical and the scattering profile from one stack can be considered to be the same as the scattering from the whole system. This basic simple model has been extensively used in previous investigations, as reviewed by Crist (1973).

For the distribution of thicknesses within a stack, two major methods have been used: symmetric and exponential distributions. A

typical symmetric distribution of thicknesses can be described by the Gaussian distribution given as

$$H(Y) = \frac{1}{\sigma_y (2\pi)^{1/2}} \exp - \frac{(Y - \bar{Y})^2}{2 \sigma_y^2} \qquad 4.4.2$$

where Y and $\sigma_y$ are the mean and standard deviation.

Figure 4.4.1 shows the Gaussian distribution function for a mean of 0.5 with various standard deviations. A Gaussian distribution function with a standard deviation of 0.05 shows most of the distribution within the range 0.35 to 0.65. Those with the standard deviation of 0.15 spread mainly from 0.1 to 0.9. A standard deviation more than 0.20 is somewhat meaningless because some portion will go beyond the 0 or 1 of variables. The Fourier transforms corresponding to the Gaussian distribution have the form

$$F_y = \exp(-2\pi^2 k^2 \sigma_y^2) \exp(-2\pi i k \bar{Y}) \qquad 4.4.3$$

A similar derivation can be performed for the amorphous thickness variation. Two terms, $F_y$ and $F_z$, can be substituted in equation 4.4.1 to obtain the intensity profile.

The theoretical intensity profiles were calculated by numerical methods using the Fortran program listed in Appendix I. In the numerical calculation the total average thickness (or the long period) was set to be 1. The average crystal thickness was set to be 0.5. For a reasonable approximation and simplicity, the standard

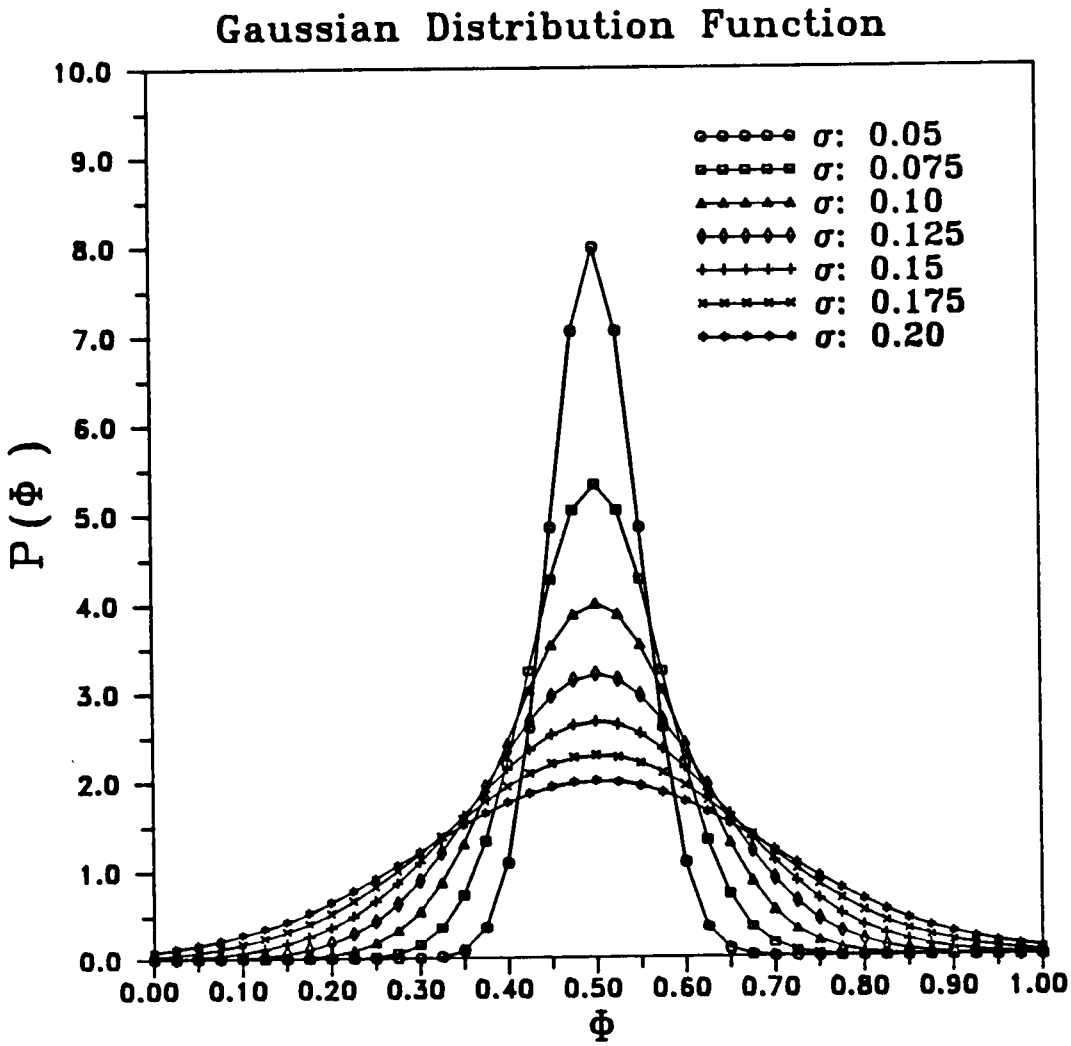



Figure 4.4.1 Gaussian distribution functions with the average of 0.5 and various standard deviations.

deviations of amorphous and crystalline thicknesses are assumed to be equal. The step size of the scattering vector was given as 0.04, with the range from 0.04 to 3.

Figure 4.4.2 shows the calculated SAXS intensity corresponding to the intensity plots observable from the pin-hole geometry. Figure 4.4.3 illustrates the Lorentz-corrected SAXS intensity profiles. Most Bragg peaks were located at the same position of 1.0. The widths of most peaks are very narrow, even though the widths increase with increasing standard deviations.

Asymmetric thickness distributions have been studied in the past to look for effects of asymmetry on the distortion of the diffraction peak. One of the asymmetric distributions studied is the exponential distribution. In the present study SAXS intensity profiles were obtained based on the modified exponential distributions suggested by Blundell (1978). The modified distribution function is given as

$$H(Y) = \frac{1}{\sigma_y} \exp -\left[\frac{(Y - Y_o)}{\sigma_y}\right] \qquad \text{for } Y \geq Y_o \qquad 4.4.4$$

$$= 0 \qquad \text{for } Y < Y_o$$

where $\sigma_y$ is the standard deviation and the number average thickness is given as the sum of $Y_o$ and $\sigma_y$. The distribution function is plotted in Figure 4.4.4 in which the average is 0.5. Fourier transforms of this distribution have the form:

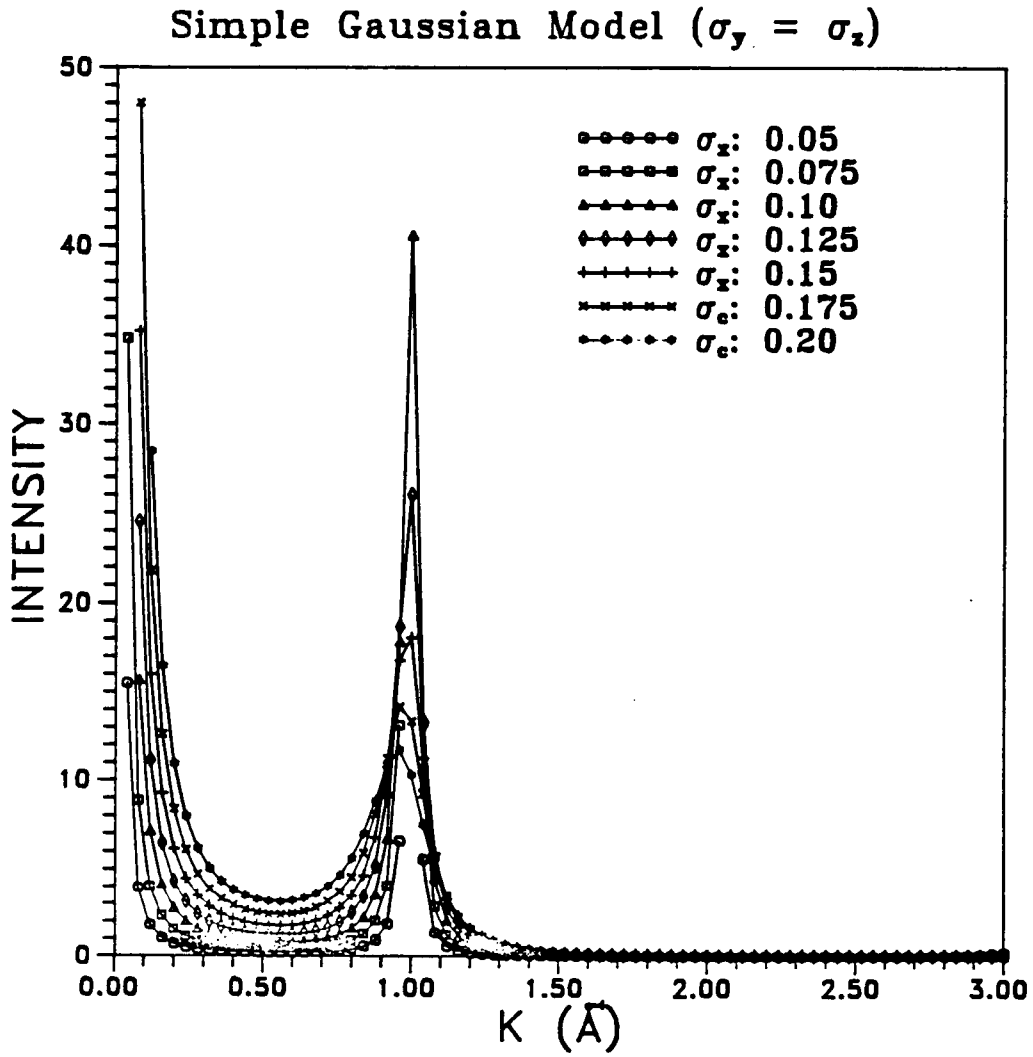



Figure 4.4.2 Calculated SAXS intensity curves based on the simple stack model with Gaussian thickness distributions.

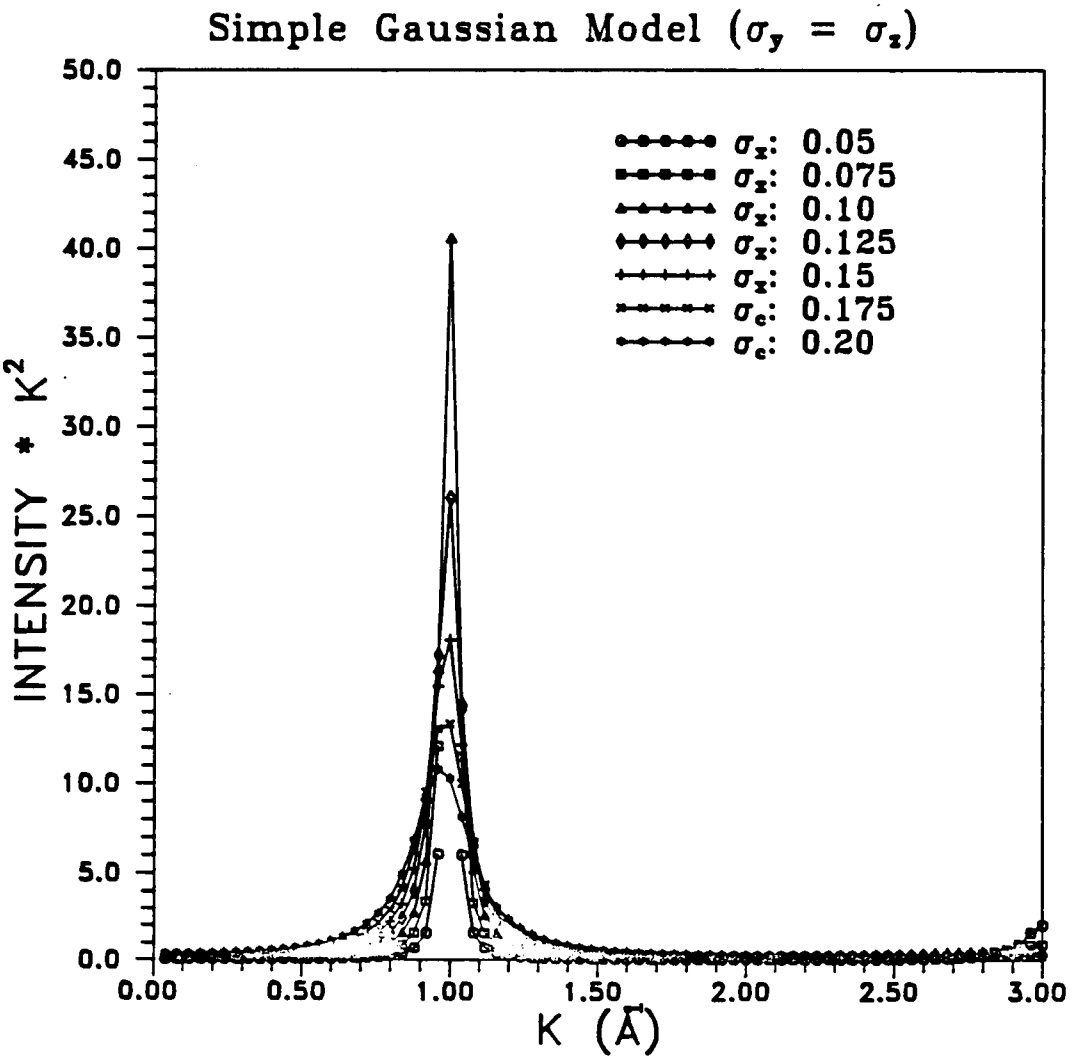



Figure 4.4.3 Calculated one-dimensional SAXS intensity curves based on the simple stack model with Gaussian thickness distributions.

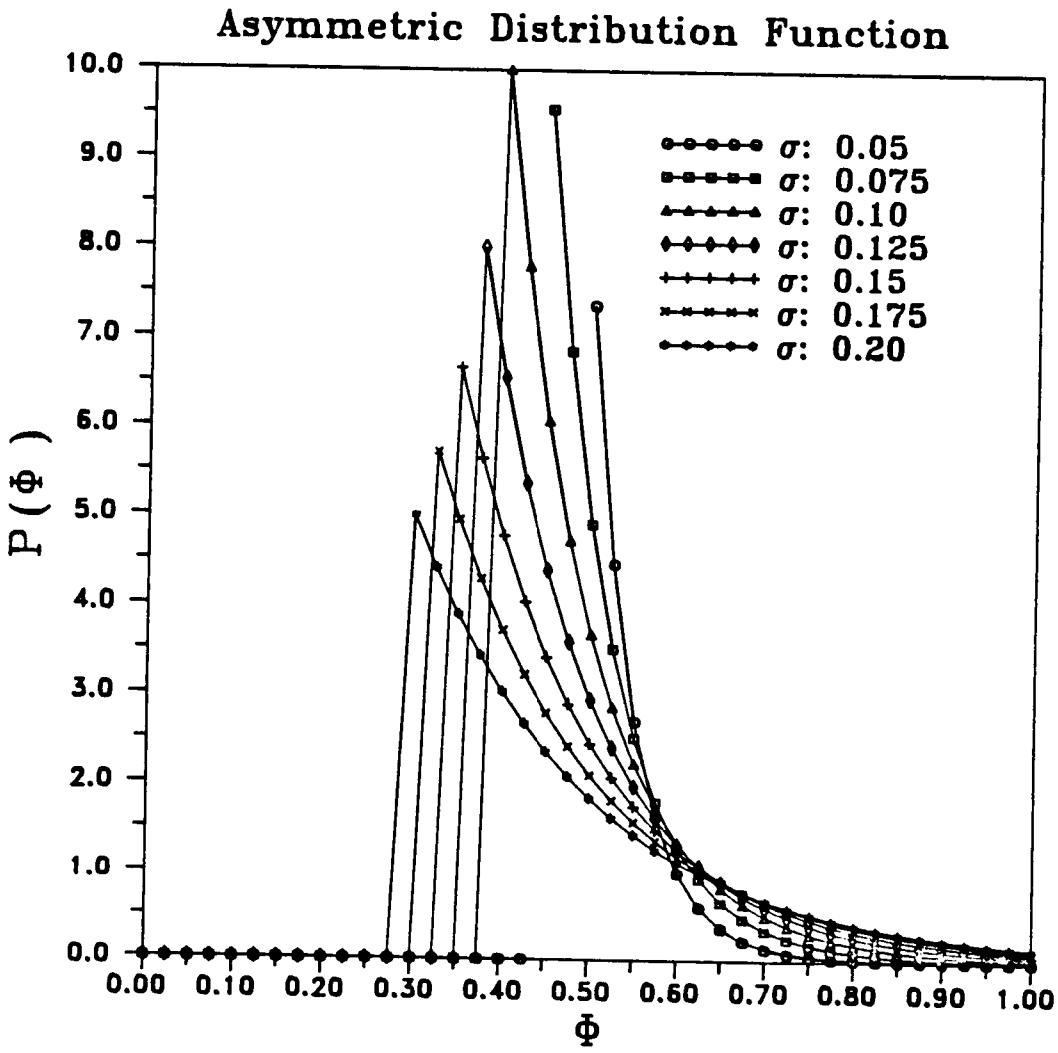



Figure 4.4.4 Modified Exponential distribution functions with the average of 0.5 and various standard deviations.

$$F_y = \frac{1}{1 + 2\pi i k\, \sigma_y} \exp(-\, 2\pi\, i\, k\, Y_o\, ) \qquad 4.4.5$$

Calculated observable SAXS intensity curves and one-dimensional SAXS intensity curves corresponding to the Lorentz corrected curves are plotted in Figures 4.4.5 and 4.4.6 respectively. Calculation was performed by the Fortran program listed in Appendix II. Scattering vectors vary from 0.04 to 3.0 with a step of 0.04, and the $\sigma_y$ and $\sigma_z$ were assumed to be equal. Average amorphous and crystalline thicknesses were fixed to be 0.5 so that total average crystallinity can be 0.5. Calculated intensity curves looks very similar to those appearing in Figures 4.4.2 and 4.4.3 in which thicknesses vary according to the Gaussian distribution function. However, in another extreme case such as higher standard deviation of thickness distribution, the calculated SAXS curves based on the simple model with modified exponential thickness distributions was noted to be different from those based on the simple model with Gaussian thickness distribution. The major difference in the curves is that the apparent Bragg maximum calculated by the modified exponential distribution with higher thickness distributions are located at angles higher than 1.0, while those by Gaussian distribution appear at angles lower than 1.0.

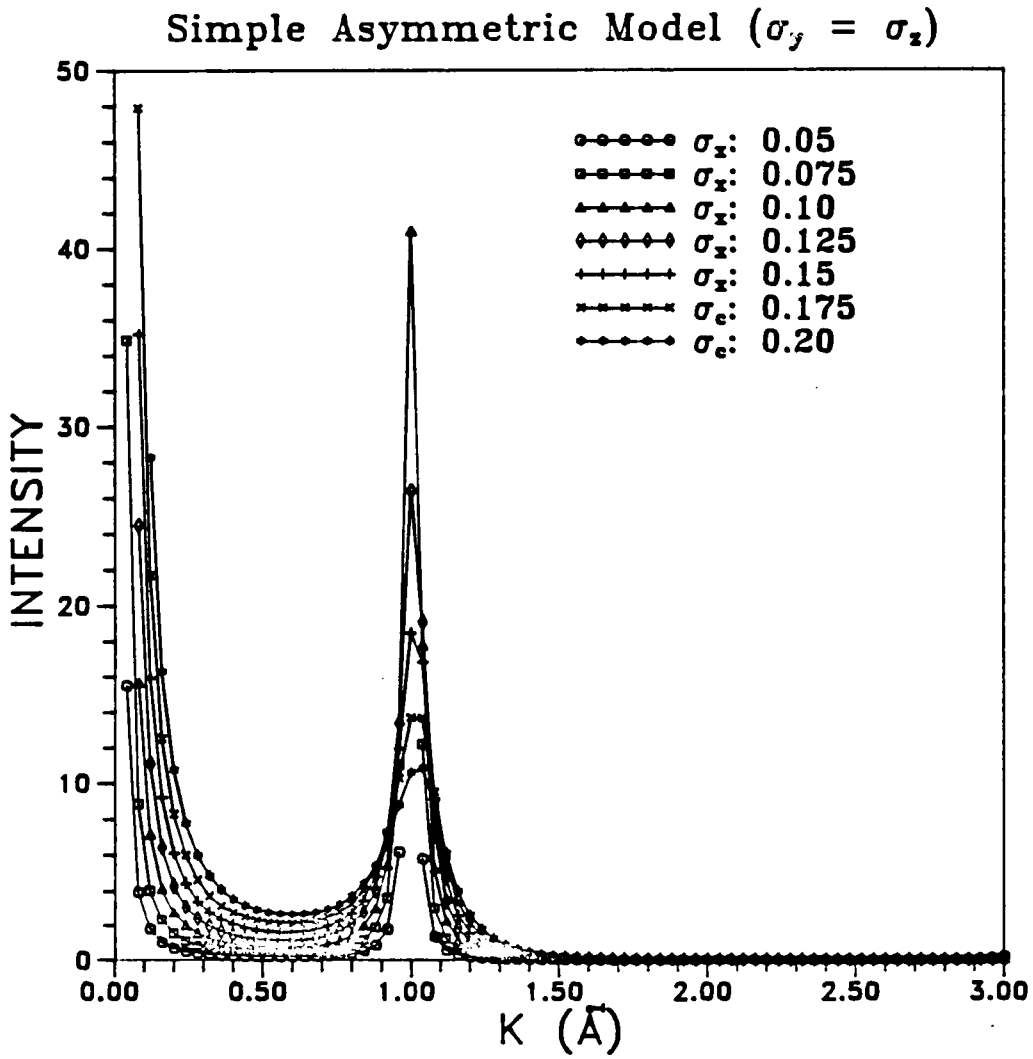



Figure 4.4.5 Calculated SAXS intensity curves based on the simple stack model with modified exponential thickness distributions.

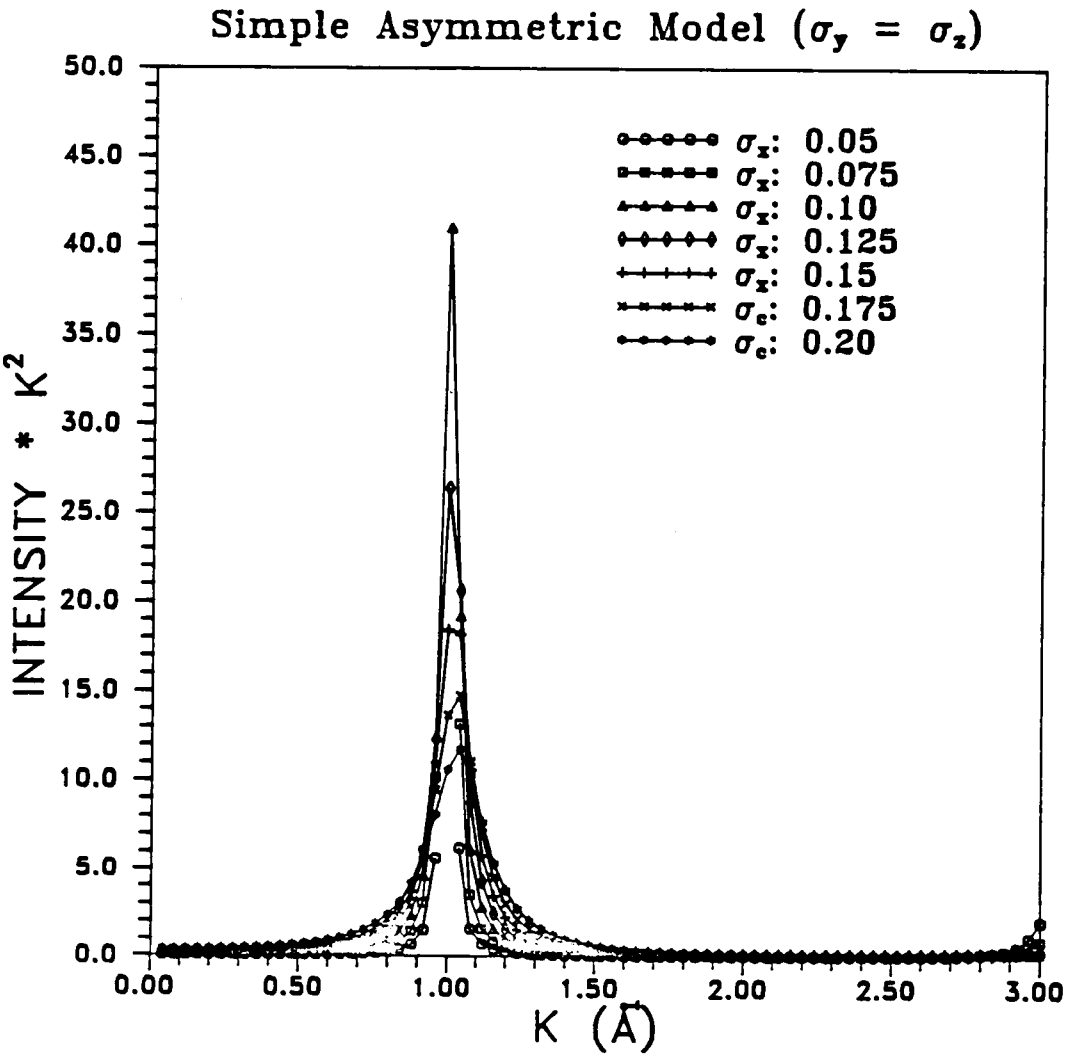



Figure 4.4.6 Calculated one-dimensional SAXS intensity curves based on the simple stack model with modified exponential thickness distributions.

4.4.3. Variable Stack Model

In this model, It was assumed that there is a longer range inhomogeneity in which there are fluctuations among the stacks as well as fluctuations within each stack. The intensity profile will be the weighted average of the intensities of all stacks. This model has been proposed by Strobl (1973) for LDPE and later modified by Blundell (1978). Among many possible stack dispersities as proposed by Strobl, Blundell considered one specific model where local crystallinity varies from stack to stack according to the Gaussian distributions, but where the average amorphous thickness within each stack is kept constant. In the model he also assumed that the average crystalline thicknesses vary according to a Gaussian distributions.

However, Blundell mostly focused on the diffraction peak area without a detailed investigation of the near-zero-angle region. The main reason for this cut-off appears to be due to the limitation of their SAXS experiments in which the near-zero-angle data could not be obtained with a reasonable accuracy.

In this study, the thickness distributions within each stack were assigned according to the Gaussian and modified asymmetric distributions discussed in the previous section. Each stack was assumed to have a different crystallinity in the fashion of a normalized standard distribution so that the whole intensity per unit volume would be the volume-average of the intensity of the system. The whole one-dimensional intensities are given according to

$$I(k) = \int I(k,\varphi) \cdot P(\varphi)\, d\varphi \qquad 4.4.6.$$

where $P(\varphi)$ is assumed to follow a standard distribution similar to equation 4.4.1. For simplicity the following relationship between the standard deviations of the amorphous and crystalline thicknesses was assumed.

$$\sigma_y / \bar{Y} = \sigma_z / \bar{Z} \qquad 4.4.7.$$

In addition, the average amorphous thickness was assumed to be constant (0.5), while the average crystal thickness of each stack was set to follow the distribution determined by $P(\varphi)$. The whole calculated intensity curves based on symmetric thickness distribution were obtained using the Fortran programs listed in Appendix III. $I(k,\varphi)$ term in Equation 4.4.6 was obtained from the simple stack model for a given crystallinity. Crystallinities were set to vary from 0.01 to 0.99. Scattering vector changes from 0.04 to 3.0 for every 0.04.

Figure 4.4.7 shows the calculated intensity curves for the system with $\sigma_x$ of 0.05. The calculated curves for different values of $\sigma_x$ are shown in Figures 4.4.8, 4.4.9, 4.4.10, 4.4.11 and 4.4.12 for $\sigma_x$ of 0.1, 0.125, 0.15, 0.175 and 0.2. With the introduction of fluctuations of crystallinity, the SAXS intensity curves were noted to change drastically. As $\sigma_c$ increases, the Bragg peaks become broader with increase of intensity near the beam-stop region.

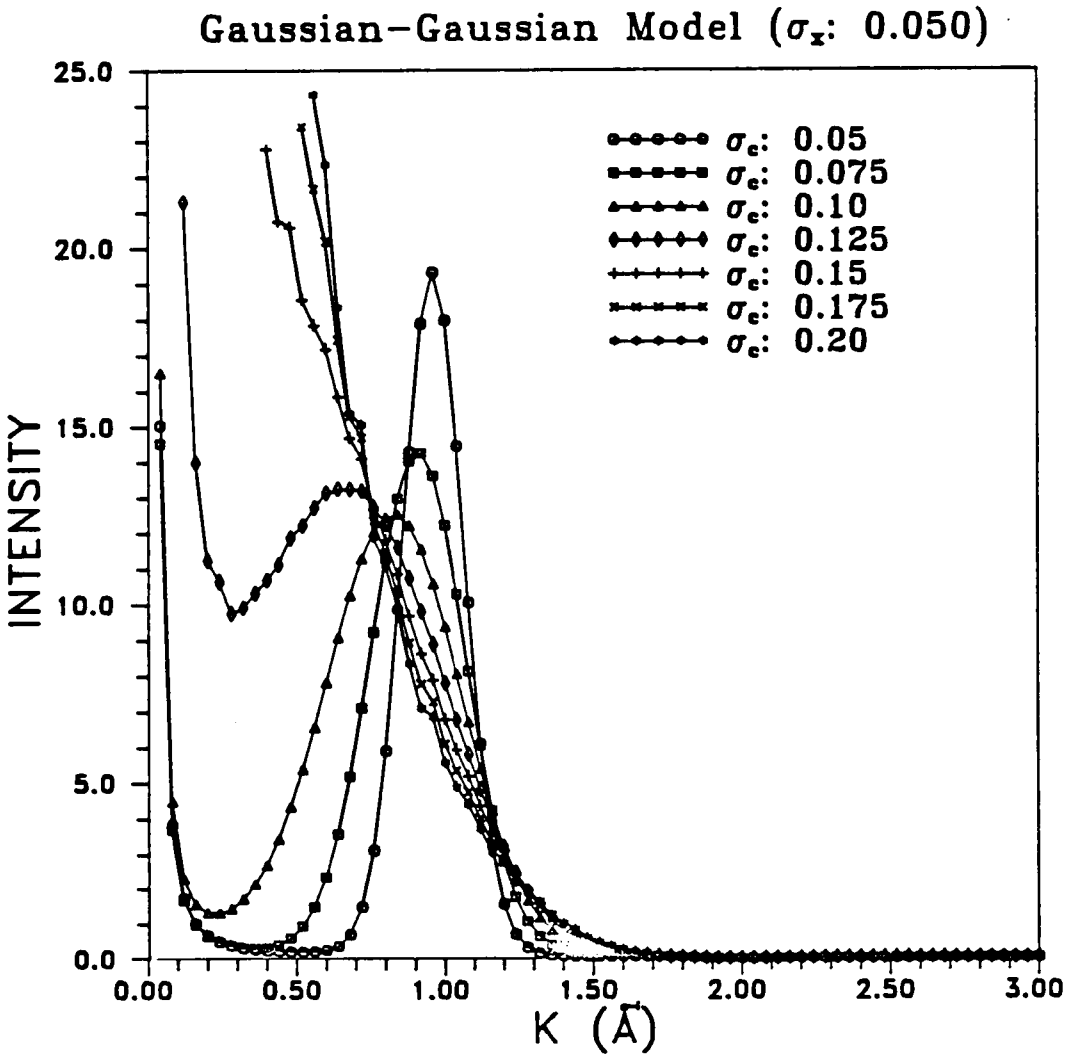



Figure 4.4.7 Calculated SAXS intensity curves based on the variable stack model with Gaussian thickness distributions and Gaussian crystallinity distributions among stacks.
($\sigma_x$ = 0.05)

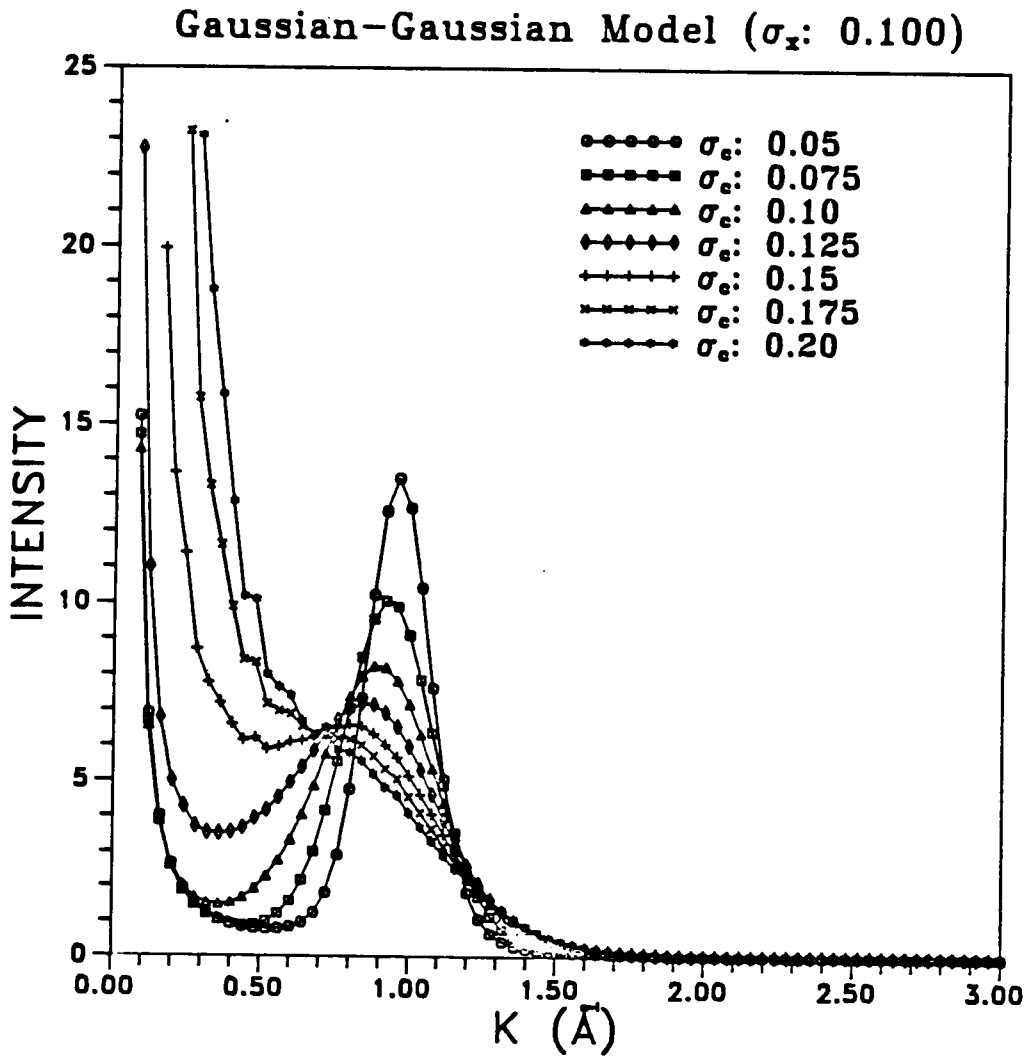



Figure 4.4.8 Calculated SAXS intensity curves based on the variable stack model with Gaussian thickness distributions and Gaussian crystallinity distributions among stacks.
($\sigma_X$ = 0.1)

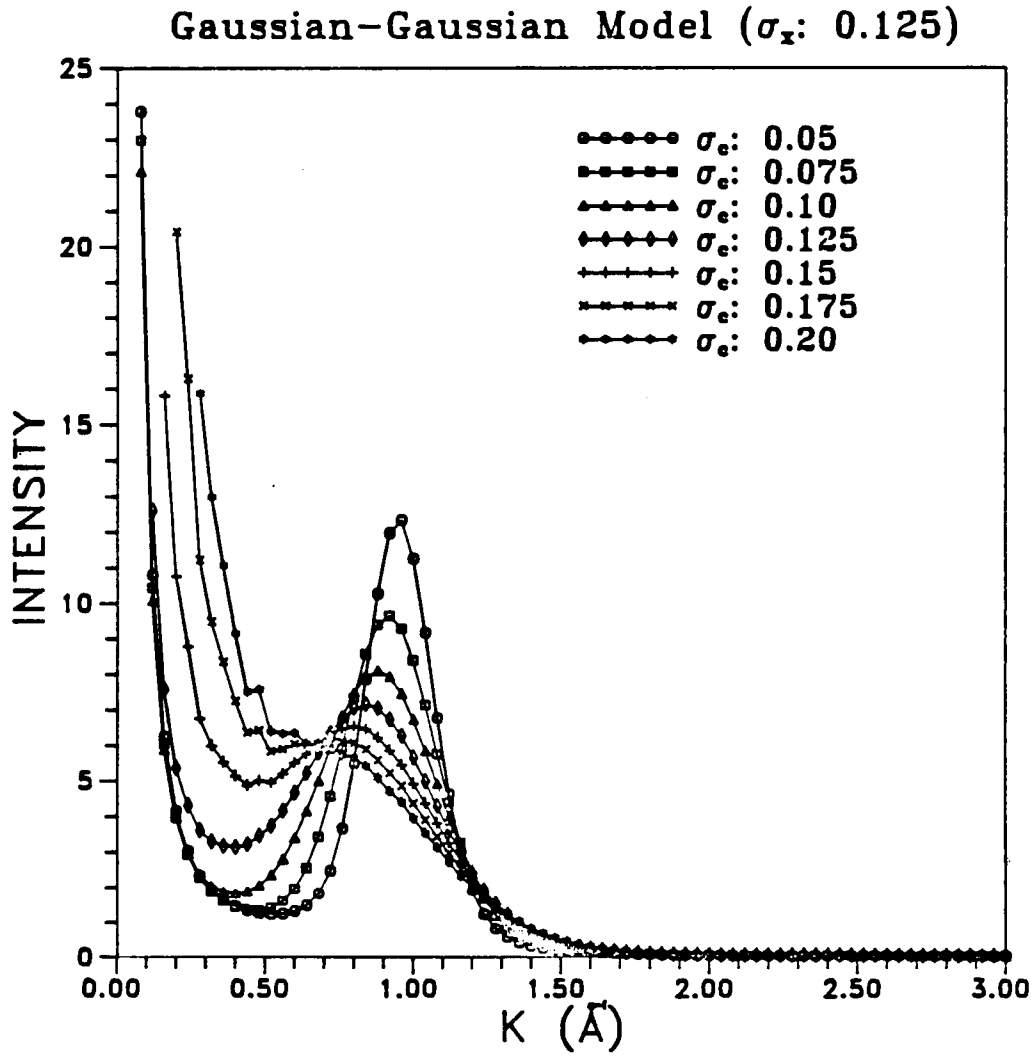



Figure 4.4.9 Calculated SAXS intensity curves based on the variable stack model with Gaussian thickness distributions and Gaussian crystallinity distributions among stacks.
($\sigma_x$ = 0.125)

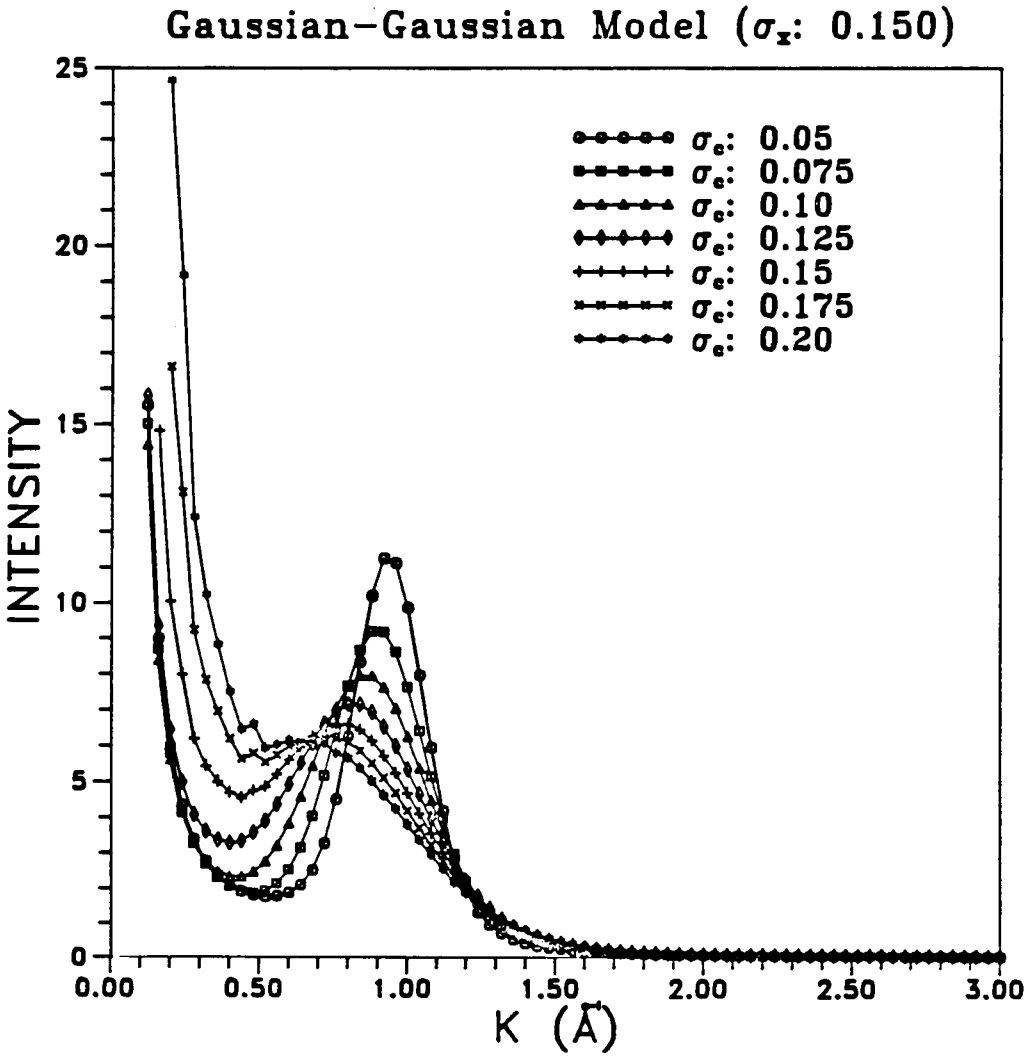



Figure 4.4.10 Calculated SAXS intensity curves based on the variable stack model with Gaussian thickness distributions and Gaussian crystallinity distributions among stacks.
($\sigma_x$ = 0.15)

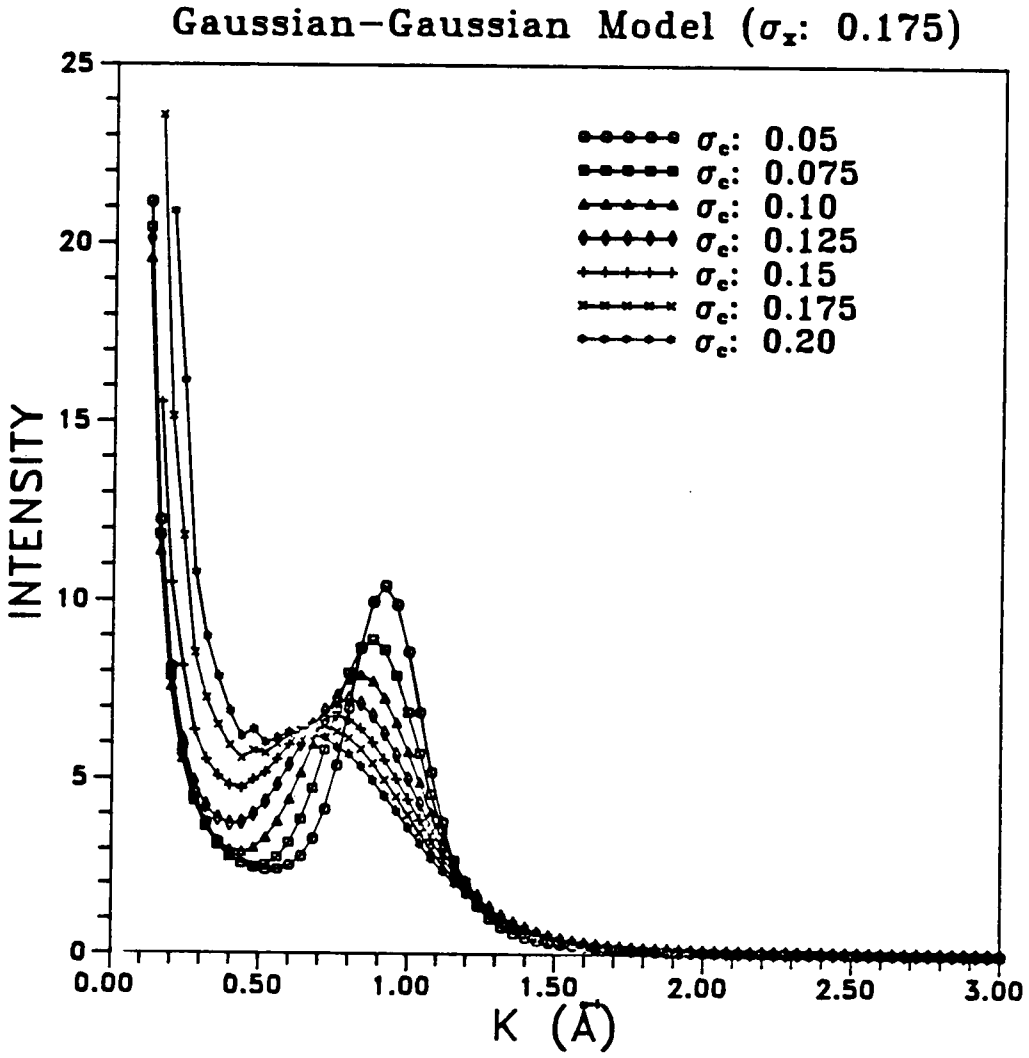



Figure 4.4.11 Calculated SAXS intensity curves based on the variable stack model with Gaussian thickness distributions and Gaussian crystallinity distributions among stacks.
($\sigma_x$ = 0.175)

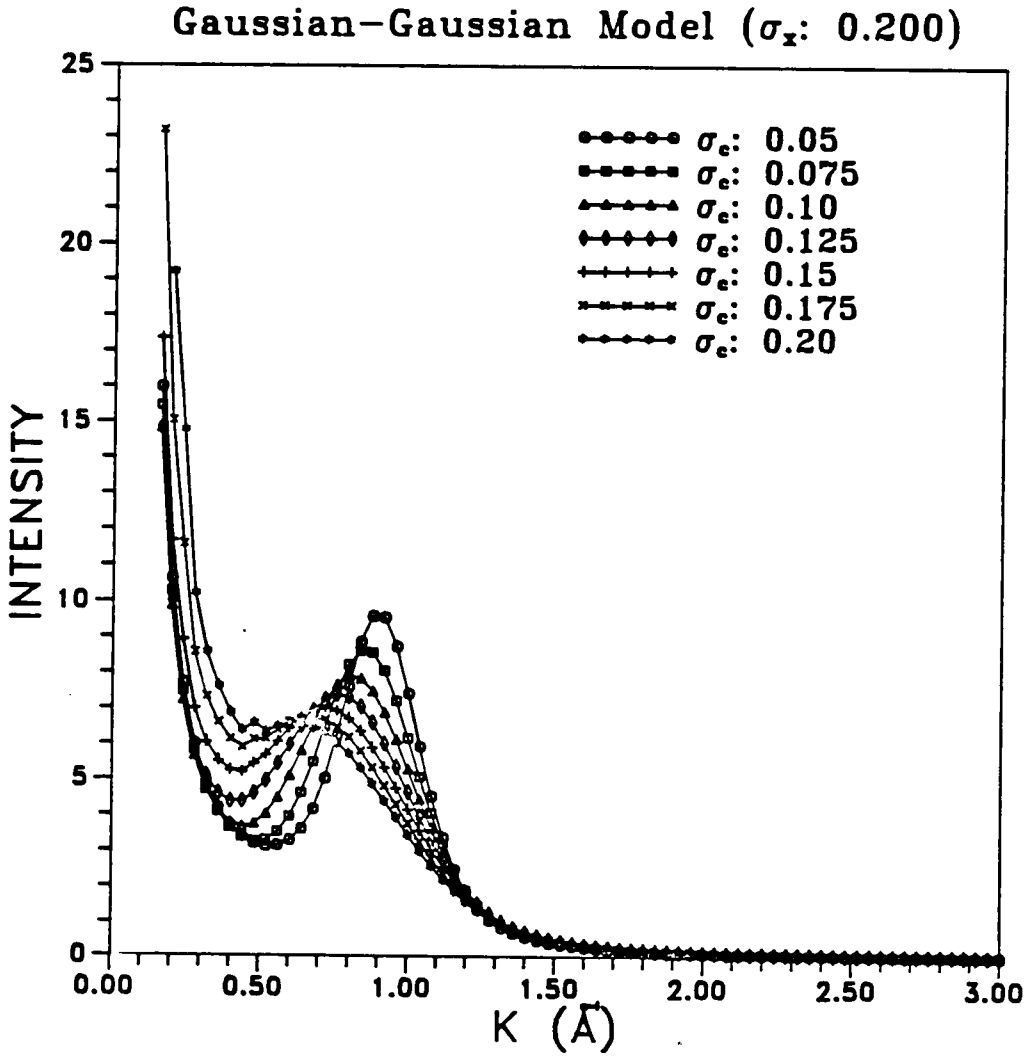



Figure 4.4.12 Calculated SAXS intensity curves based on the variable stack model with Gaussian thickness distributions and Gaussian crystallinity distributions among stacks.
($\sigma_x$ = 0.2)

Extreme cases show no Bragg maxima or a low intensity hump as the Bragg peak. The variations of the curves are more distinctive for small values of $\sigma_x$. Figures 4.4.13 and 4.4.14 show one-dimensional SAXS intensity curves, corresponding the Lorentz-corrected experimental data, for the cases in which $\sigma_x$ was set to be 0.1 and 0.15 respectively.

The other case of the variable stack model studied was for asymmetric thickness distributions within each stack. The whole intensity profiles were obtained with the integration given in Equation 4.4.6 in which $I(k,\varphi)$ term was evaluated using the simple asymmetric model discussed in the previous section. The program listing used for the numerical evaluation of this intensity profile is attached in Appendix IV. Figures 4.4.15, 4.4.16 and 4.4.17 show the intensity curves of the variable stack model with asymmetric thickness distributions having values of $\sigma_x$ of 0.05, 0.15 and 0.2. It was interestingly noted that even though different modes of distribution of crystal and amorphous thicknesses are used, the data obtained for asymmetric thickness distributions are very similar to those for the symmetric thickness distribution case.

## 4.5. Electric Breakdown

### 4.5.1. Electrical Breakdown Strength

Specimens with thickness of 1 to 4 mil (25 to 100 μm) were prepared by compression molding, for electric breakdown testing. All specimens were unaged in order to investigate the differences in as-

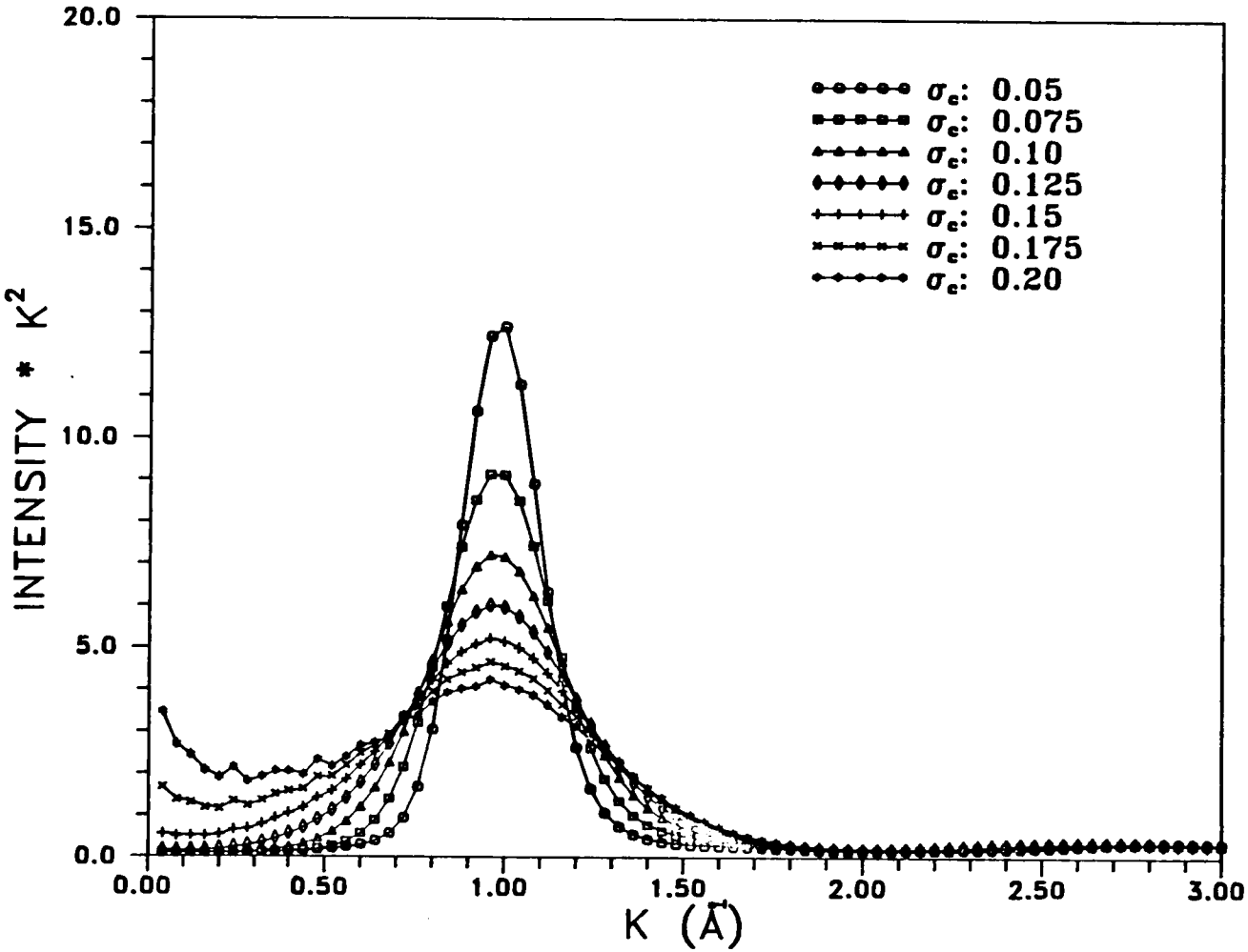



Figure 4.4.13 Calculated one-dimensional SAXS intensity curves based on the variable stack model with Gaussian thickness distributions and Gaussian crystallinity distributions among stacks. ($\sigma_x$ = 0.1)

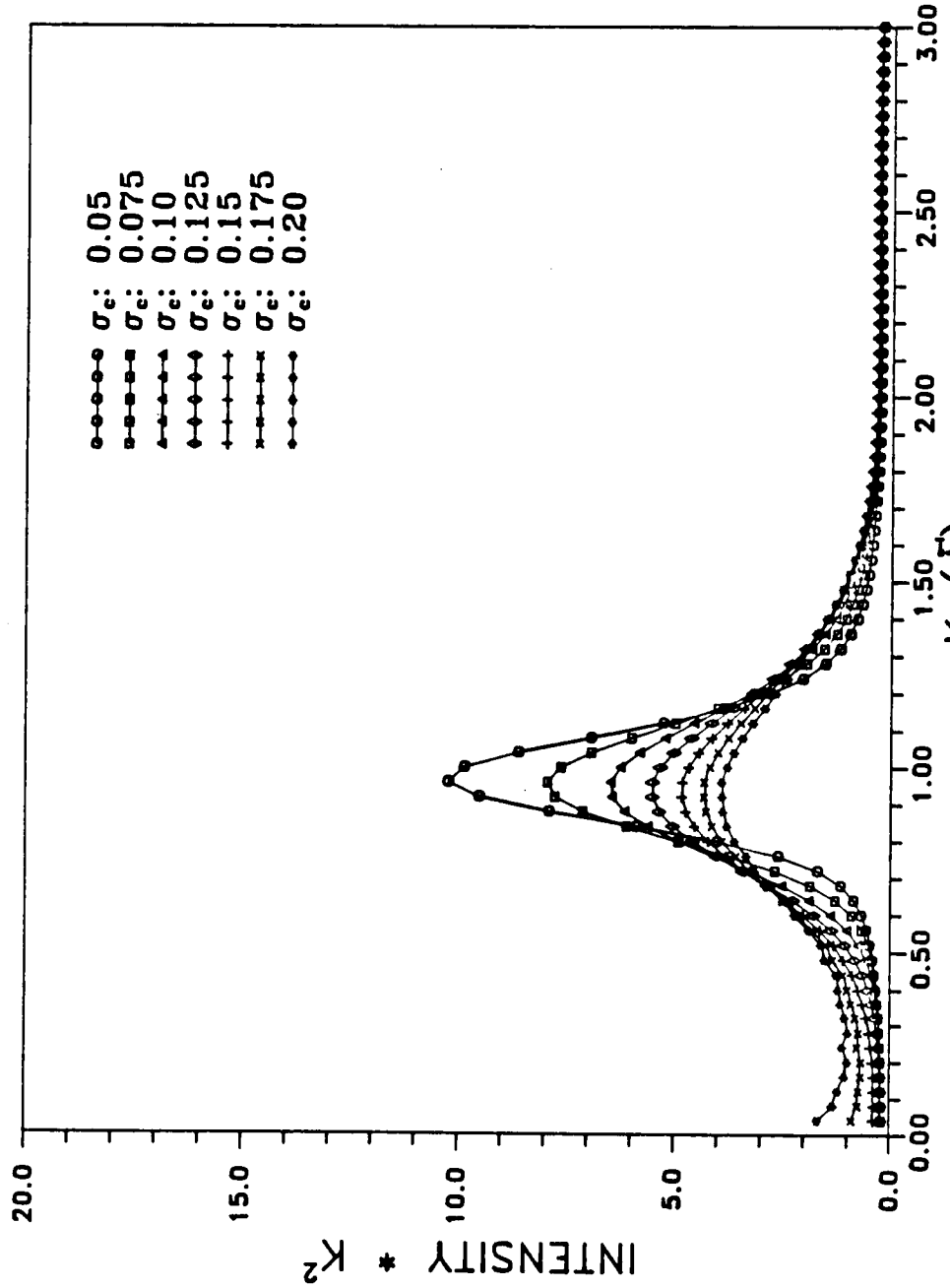



Figure 4.4.14 Calculated one-dimensional SAXS intensity curves based on the variable stack model with Gaussian thickness distributions and Gaussian crystallinity distributions among stacks. ($\sigma_x$ = 0.15)

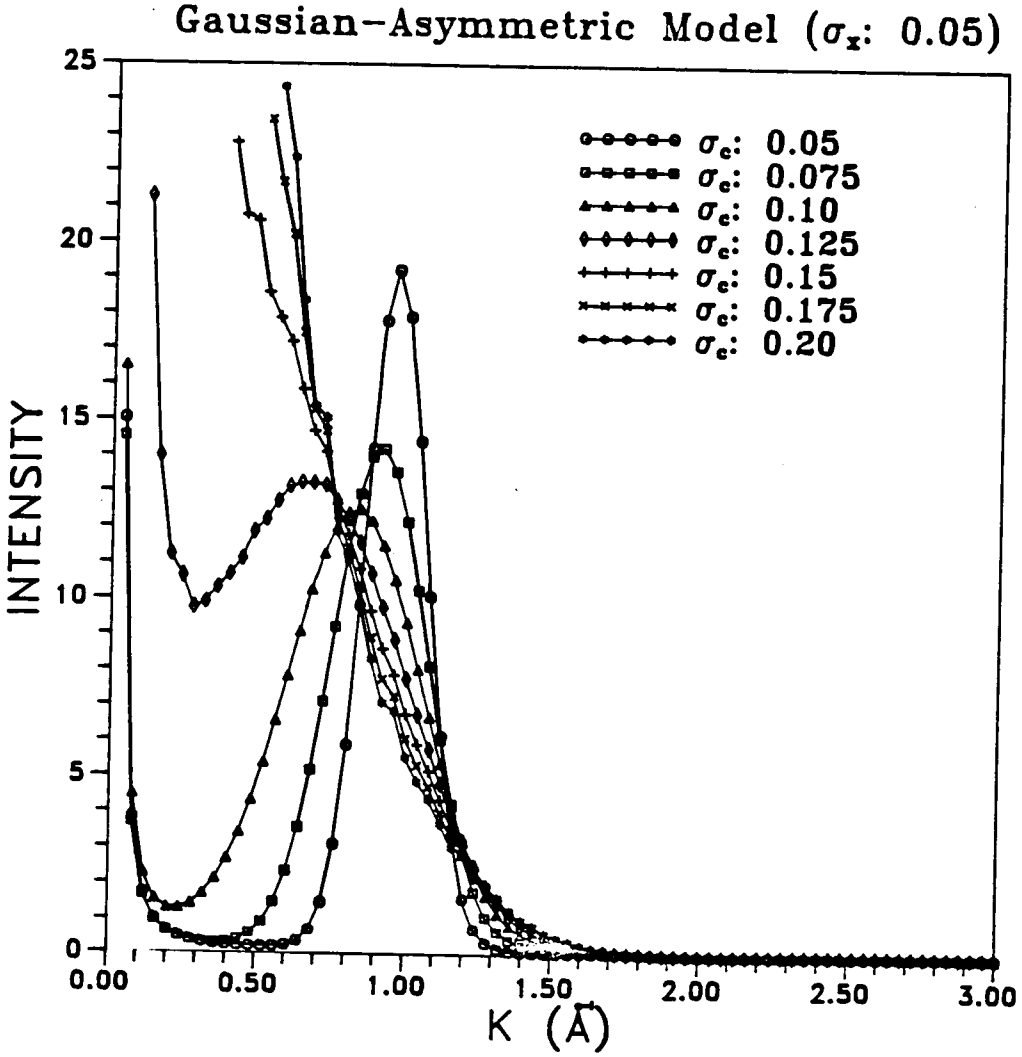



Figure 4.4.15 Calculated SAXS intensity curves based on the variable stack model with modified exponential thickness distributions and Gaussian crystallinity distributions among stacks. ($\sigma_x$ = 0.05)

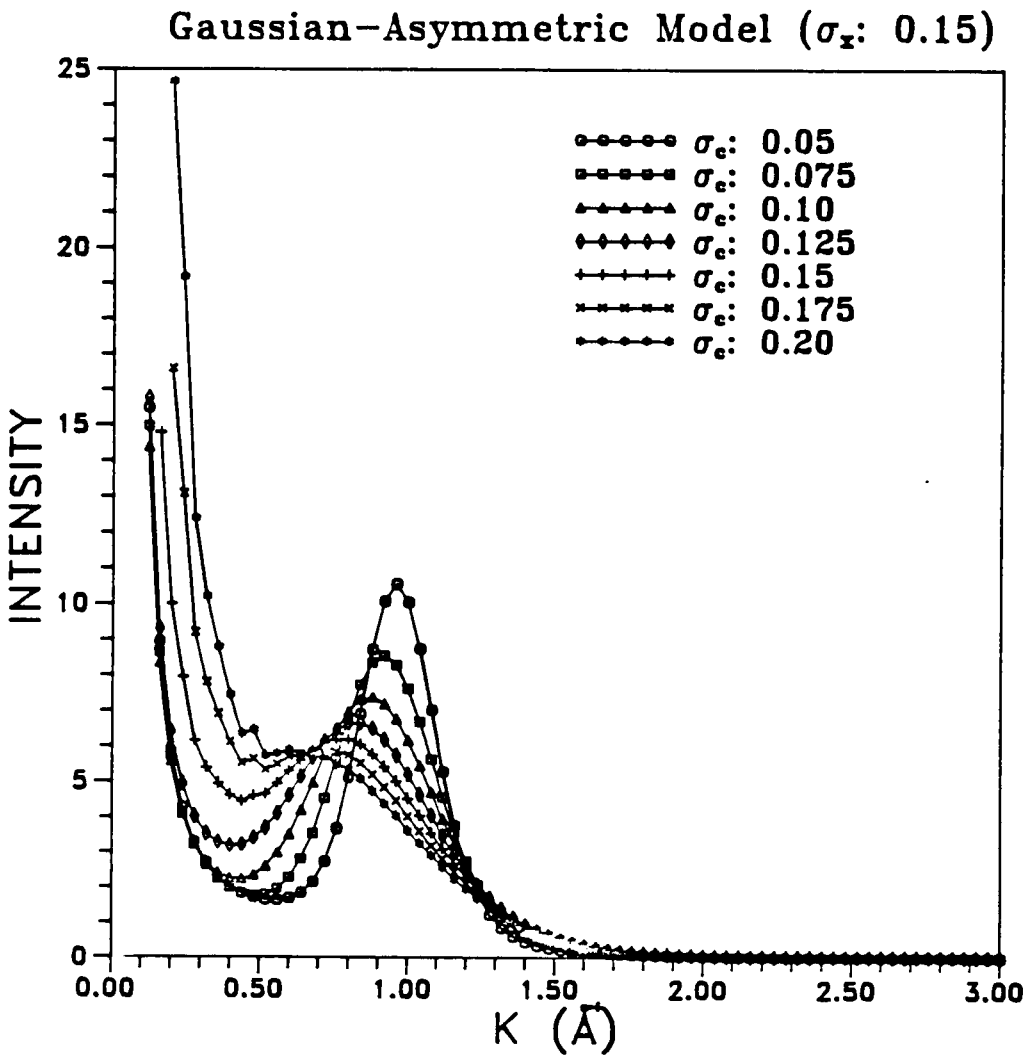



Figure 4.4.16 Calculated SAXS intensity curves based on the variable stack model with modified exponential thickness distributions and Gaussian crystallinity distributions among stacks. ($\sigma_x$ = 0.15)

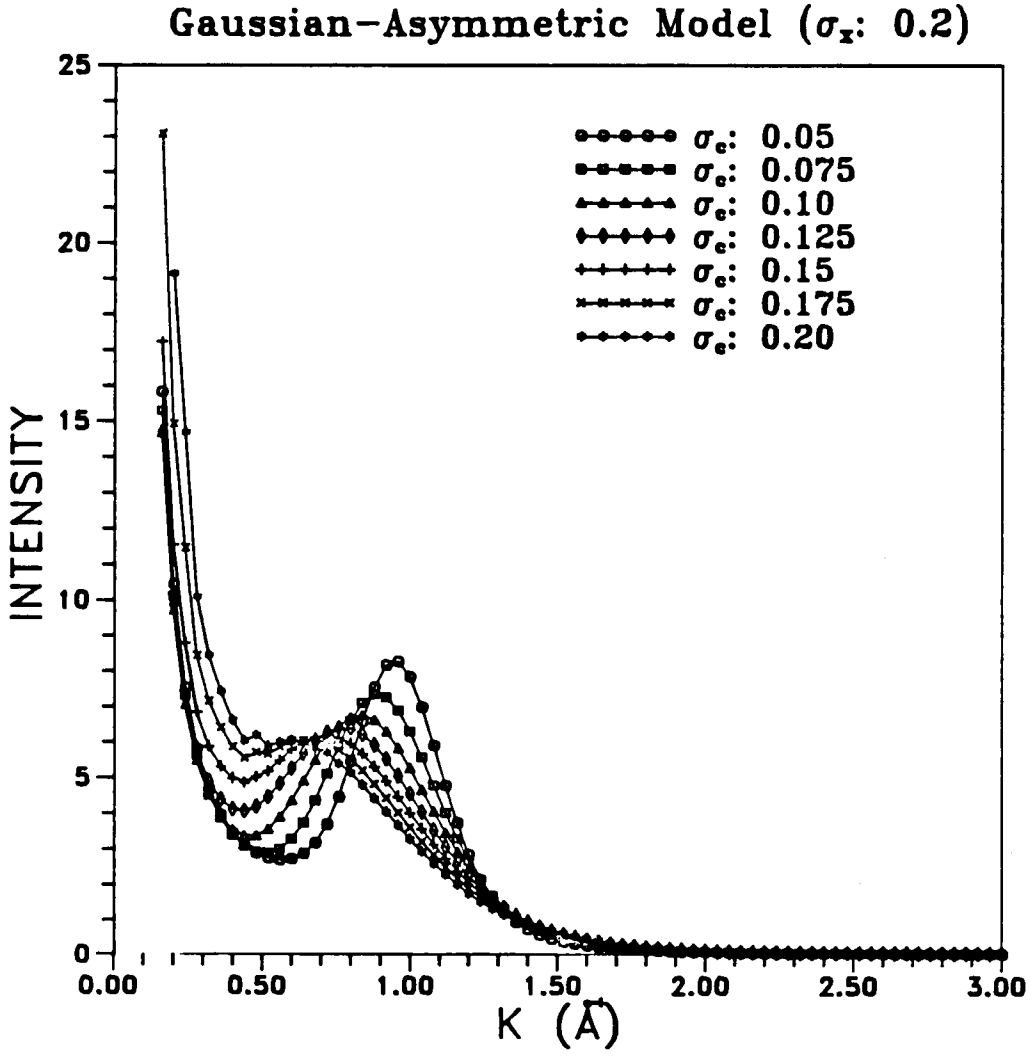



Figure 4.4.17 Calculated SAXS intensity curves based on the variable stack model with modified exponential thickness distributions and Gaussian crystallinity distributions among stacks. ($\sigma_X$ = 0.2)

molded breakdown strength. For TR-LLDPE, biaxially stretched specimens were also prepared using a T. M. Long stretch machine following compression molding. Due to severe problems associated with biaxial stretching, XLPE specimens were not able to be stretched.

The Weibull distribution plots of ac breakdown strength of TR-XLPE, EC-XLPE and TR-LLDPE are compared in Figure 4.5.1. All XLPEs and unstretched TR-LLDPEs show a more or less similar distribution. TR-XLPE shows a higher value of the scale parameter (ca. 3.6 kV/mil), which corresponds to the average value of the standard distribution, than EC-XLPE (3.0 kV/mil). TR-XLPE also shows a significant curvature to the Weibull plot, such as has been seen in studies of XLPE annealed at high temperature (Phillips, 1988). TR-LLDPE also shows a relatively higher value of the scale parameter (ca. 3.3 kV/mil). This finding is matched, to some degree, with the claim of the manufacturer that TR grade shows higher breakdown strengths. It is noteworthy that the biaxially stretched TR-LLDPE has the highest BD strength with a scale parameter of 5.3 kV/mil. This may be due to a thickness effect as well as an orientation effect since the biaxially oriented specimen was half as thin as the other specimens.

### 4.5.2. Morphology of The Breakdown Area

During examination of the breakdown area using an optical microscope the generation of banded spherulites was noticed in almost all specimens. The shapes of the breakdown areas are either

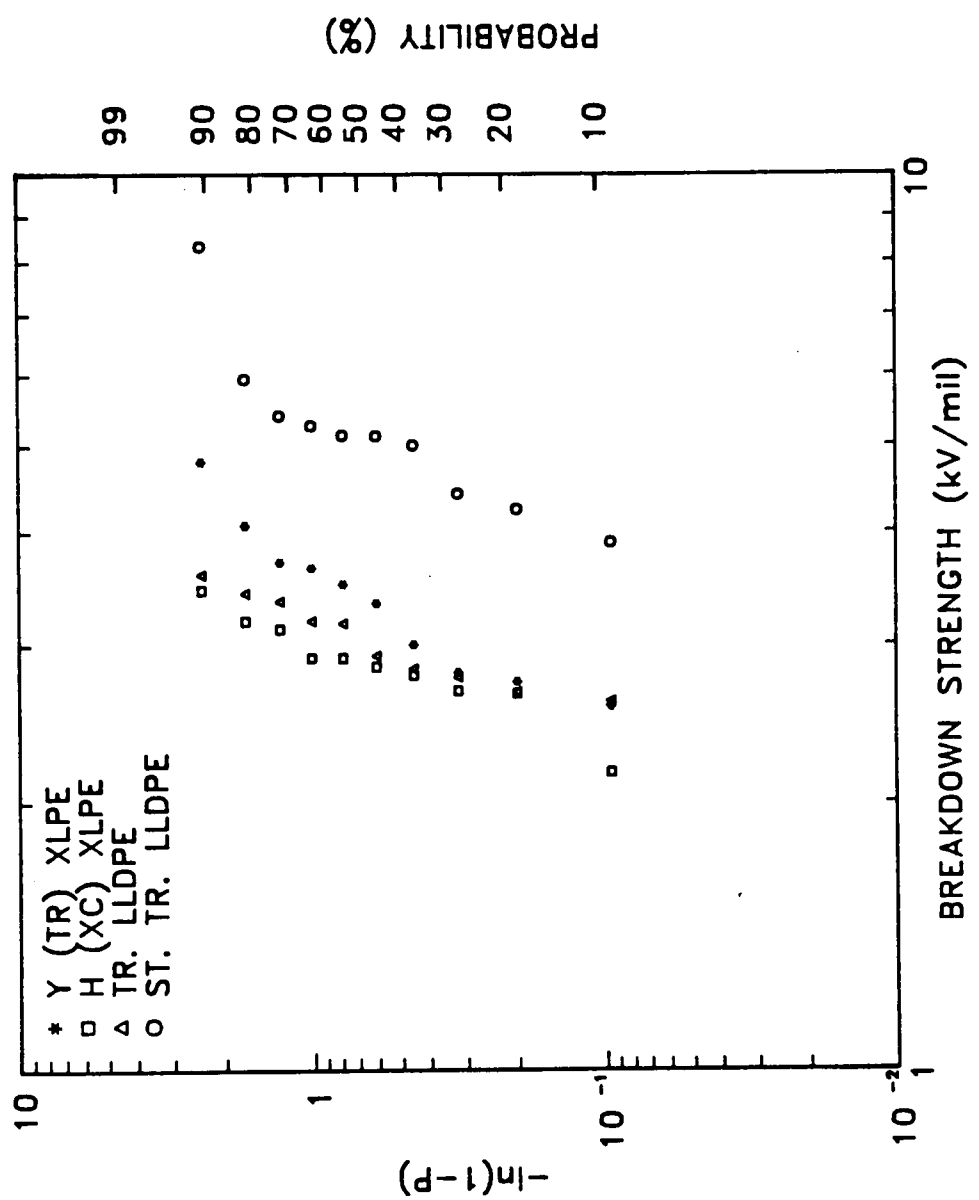



Figure 4.5.1 Weibull distribution plot of breakdown strength of TR-XLPE, EC-XLPE, TR-LLDPE and biaxially stretched TR-LLDPE.

one large major hole surrounded by a spherulitic region (Figure 4.5.2) or one large and many tiny holes embedded in the spherulite region (Figures 4.5.3, 4.5.4, 4.5.5). By close examination of this structure under crossed polars it was observed that there are banded spherulites with Maltese crosses (Figures 4.5.4).

The other remarkable observation was the formation of two kinds of tiny spots which are also filled with spherulites. One kind of spot is thinner than the normal area. On some spots of this kind there were star- or streak-like holes which are connected to the major hole as shown in microphotographs of Figure 4.5.5. The other kind of spot is thicker than other area, presumably formed by material which migrated out of the thinner spot or major hole. This thicker spot is illustrated in Figure 4.5.2. Figure 4.5.6 shows the surface of a thin spot around the ruptured area after etching by permanganic acid for 90 minutes. This picture also shows the presence of banded spherulites.

In order to confirm the spherulitic structure around the ruptured area small angle light scattering (SALS) patterns were obtained. The spherulitic region around the hole produced very clear clover leaf SALS patterns (Stein, 1960) as shown in Figure 4.5.7a. The average diameter of the spherulites in this particular region was observed to be ca. 15 μm. The maximum size of the spherulites observed by the optical microscope was ca. 30 μm. For the comparison of the structure within the ruptured area with the extractable fraction of cured 4202-TR, SALS pattern of the latter quenched to

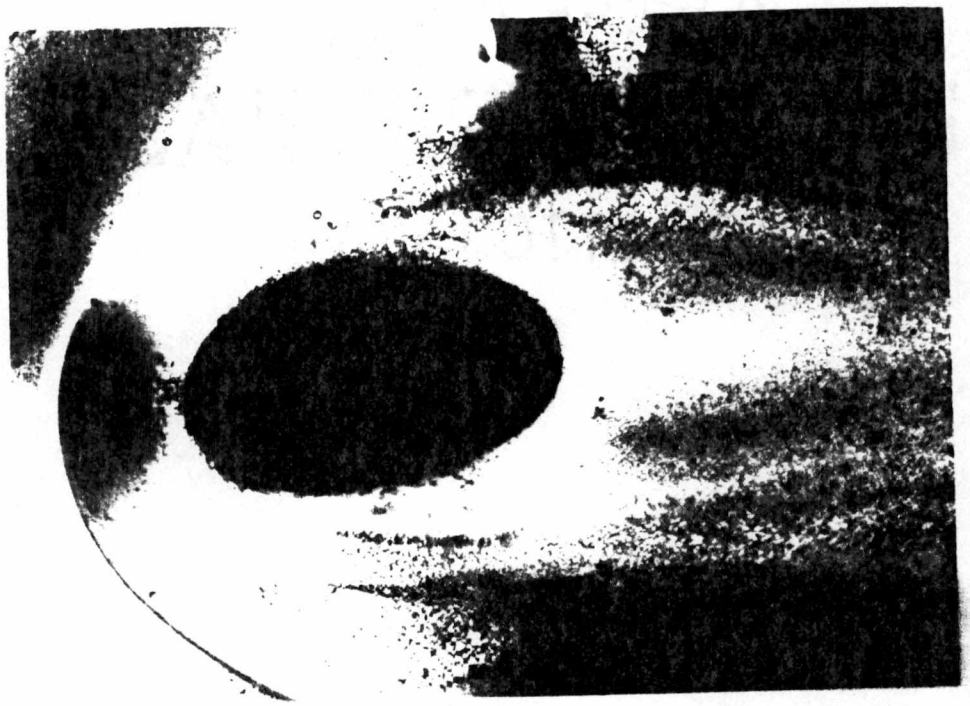


Figure 4.5.2 Overview of the electrically ruptured area of TR-XLPE.

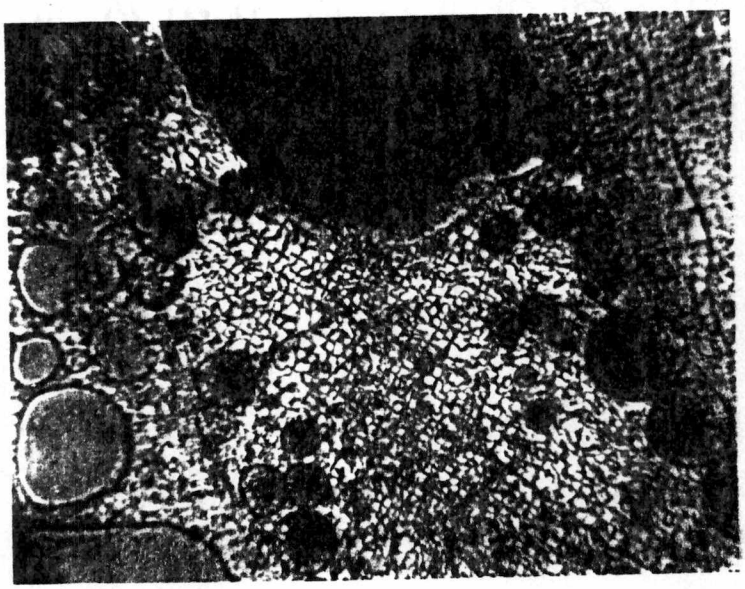


Figure 4.5.3 Microphotograph of the electrically ruptured area of TR-XLPE.

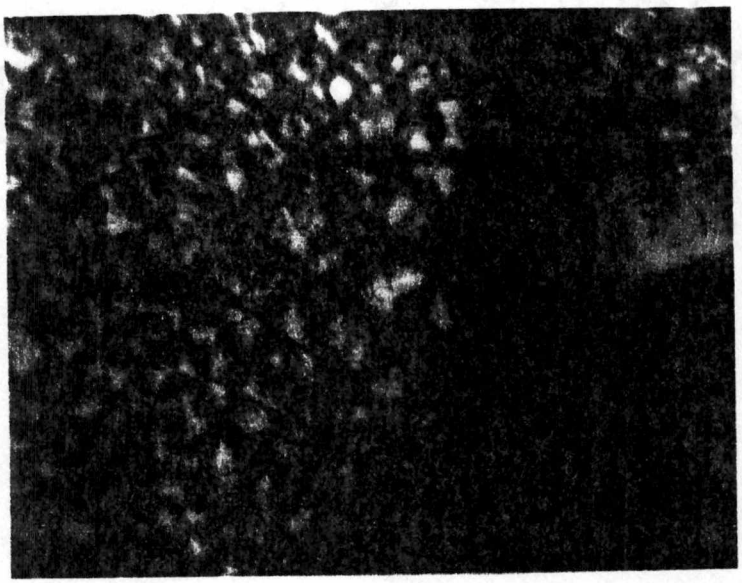


Figure 4.5.4 Microphotograph of spherulites in the electrically ruptured area of TR-XLPE under cross polars.

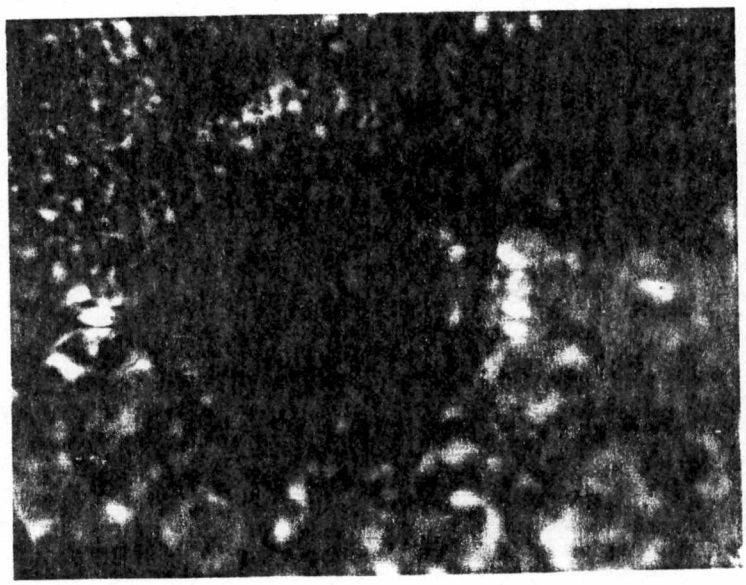


Figure 4.5.5 Microphotograph of star-like breakdown streaks in the electrically ruptured area of TR-XLPE under cross polars.



Figure 4.5.6 Microphotograph of the etched surface of electrically ruptured area of TR-XLPE.

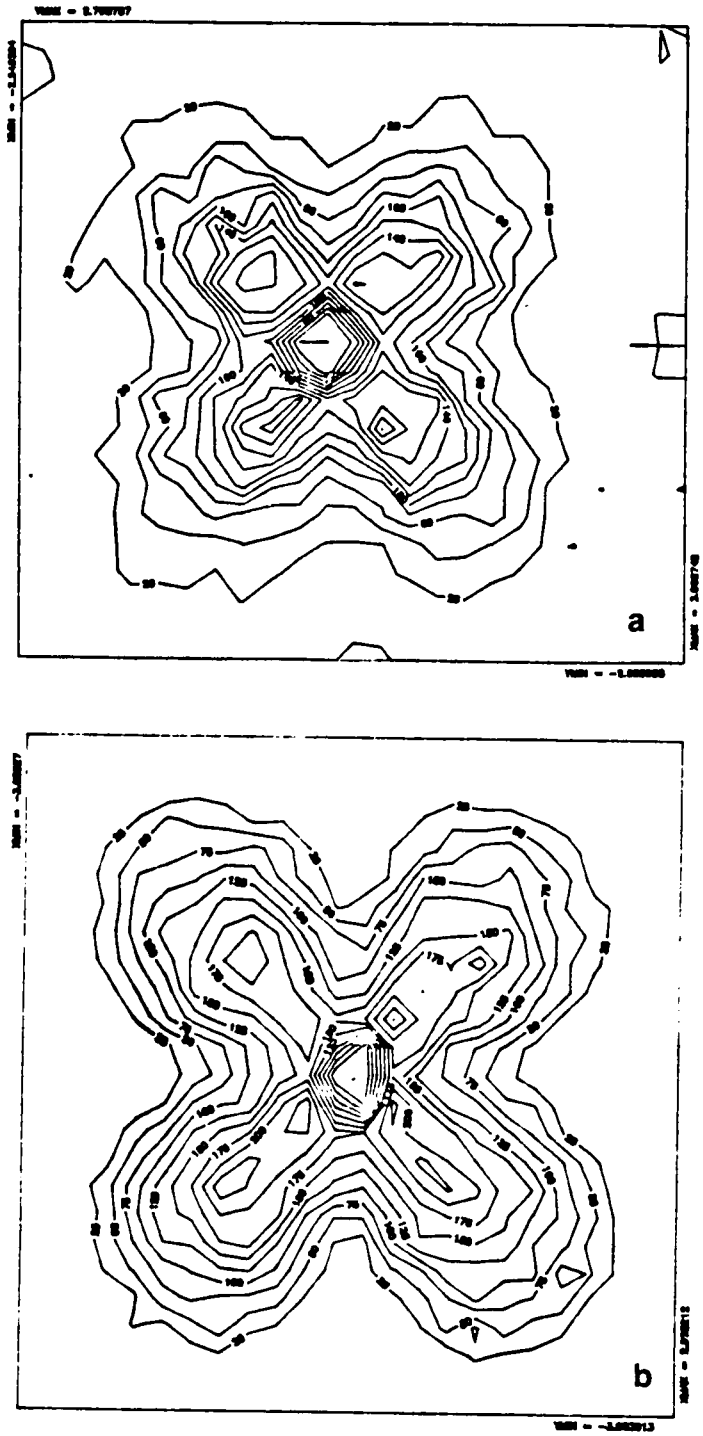



Figure 4.5.7 SALS patterns of the electrically ruptured area of TR-XLPE(a) and extractable portion quenched to room temperature(b).

room temperature was also taken. One is shown in Figure 4.5.7b and also has a typical clover leaf pattern. The average size of the spherulites in extractables was ca. 5 μm in diameter.

4.5.3. Infrared Spectroscopy

Fourier-transform infrared (FTIR) spectroscopy was used to detect any change in chemical structure upon electrical rupture. Due to the small size of the breakdown area within the samples, micro analysis was applied, utilizing an aperture of the diameter of 1 mm. Among three different grades of XLPE, TR-XLPE was studied extensively, since this grade showed a relatively large breakdown region.

The FTIR spectrum of the ruptured area of TR-XLPE in the region of 2000-1500 $cm^{-1}$ is compared with those of uncured and cured TR-XLPE samples in Figure 4.5.8. The major feature of FTIR in this region is the intense band at 1720 $cm^{-1}$ which appears only in the spectrum of the ruptured area. This band is believed to be associated with C=O double bond stretching vibration. It has been noted that a band at ca. 1720 $cm^{-1}$ are the typical band caused by the oxidation of polyethylene (Winslow, 1963).

It is of interest, however, to note that the extractable fraction of TR-XLPE also show the same band at 1720 $cm^{-1}$, while the gel fraction merely show a trace of the band (Figure 4.5.9). This may indicate that the C=O double bond which may be produced by oxidation during curing or extraction, even in small amounts, is attached to the short polymer backbone chains. The important point,

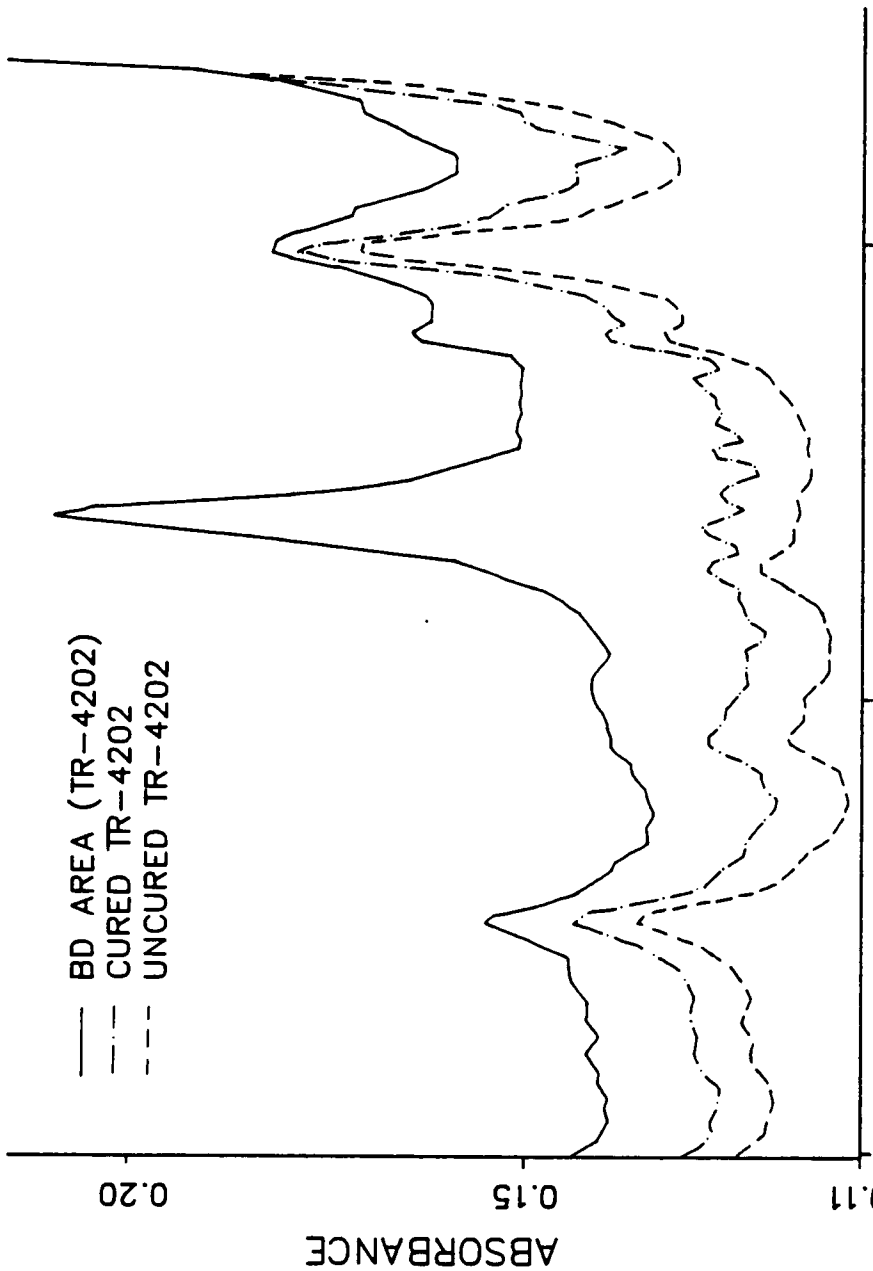



Figure 4.5.8 FTIR spectra of the electrically ruptured area, cured and uncured TR-XLPE in the region of 2000-1500 $cm^{-1}$.

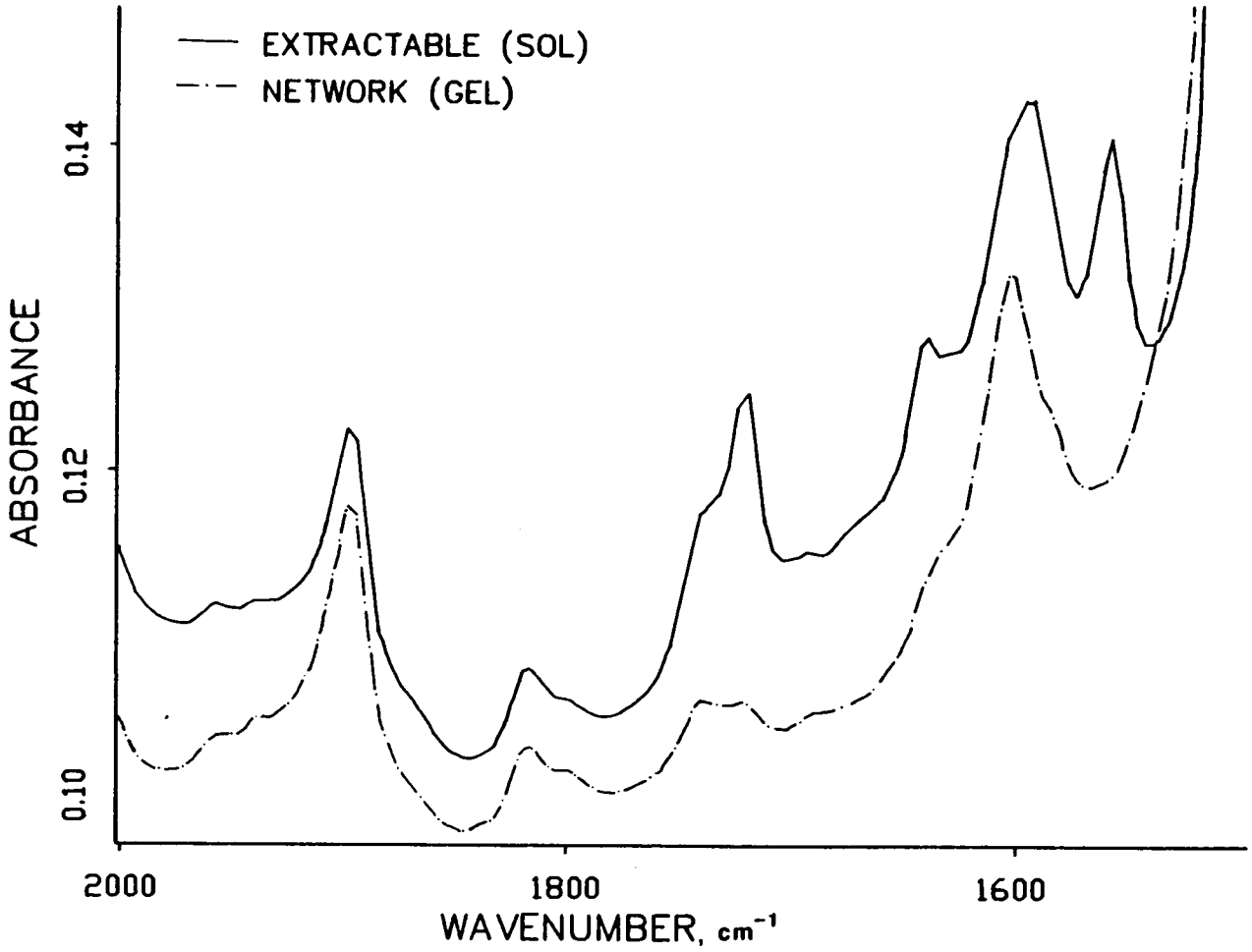



Figure 4.5.9 FTIR spectra of sol and gel fractions of TR-XLPE in the region of 2000-1500 $cm^{-1}$.

here, is that the C=O double bond appears concentrated around the ruptured region, indicating that the ruptured area is full of short polymer chains or even sol fraction of the material.

The degree of unsaturation within the sample was also studied by examining the absorption bands at 910, 888, and 963 $cm^{-1}$ for vinyl end, t-vinylidene and vinylene groups, respectively (de Kock, 1964). Figure 4.5.10 illustrates the IR spectra for cured and uncured TR-XLPE as well as the electrically ruptured area in the region of 1050 $cm^{-1}$ to 800 $cm^{-1}$. Upon curing TR-XLPE shows a reduction of the contents of vinyl end groups (910 $cm^{-1}$) and t-vinylenes (888 $cm^{-1}$) with a negligible change of the contents of vinylidene unsaturation. On the other hand, the electrically ruptured area shows a higher increase of vinyl end group content, with very little change in the other types of unsaturation. These results may imply that depolymerization processes occurred during breakdown process, and suggest a severe chain scission reaction. It is a remarkable result that the three bands associated with chemical unsaturation are very pronounced in the extractable fraction of TR-XLPE as indicated in Figure 4.5.11.

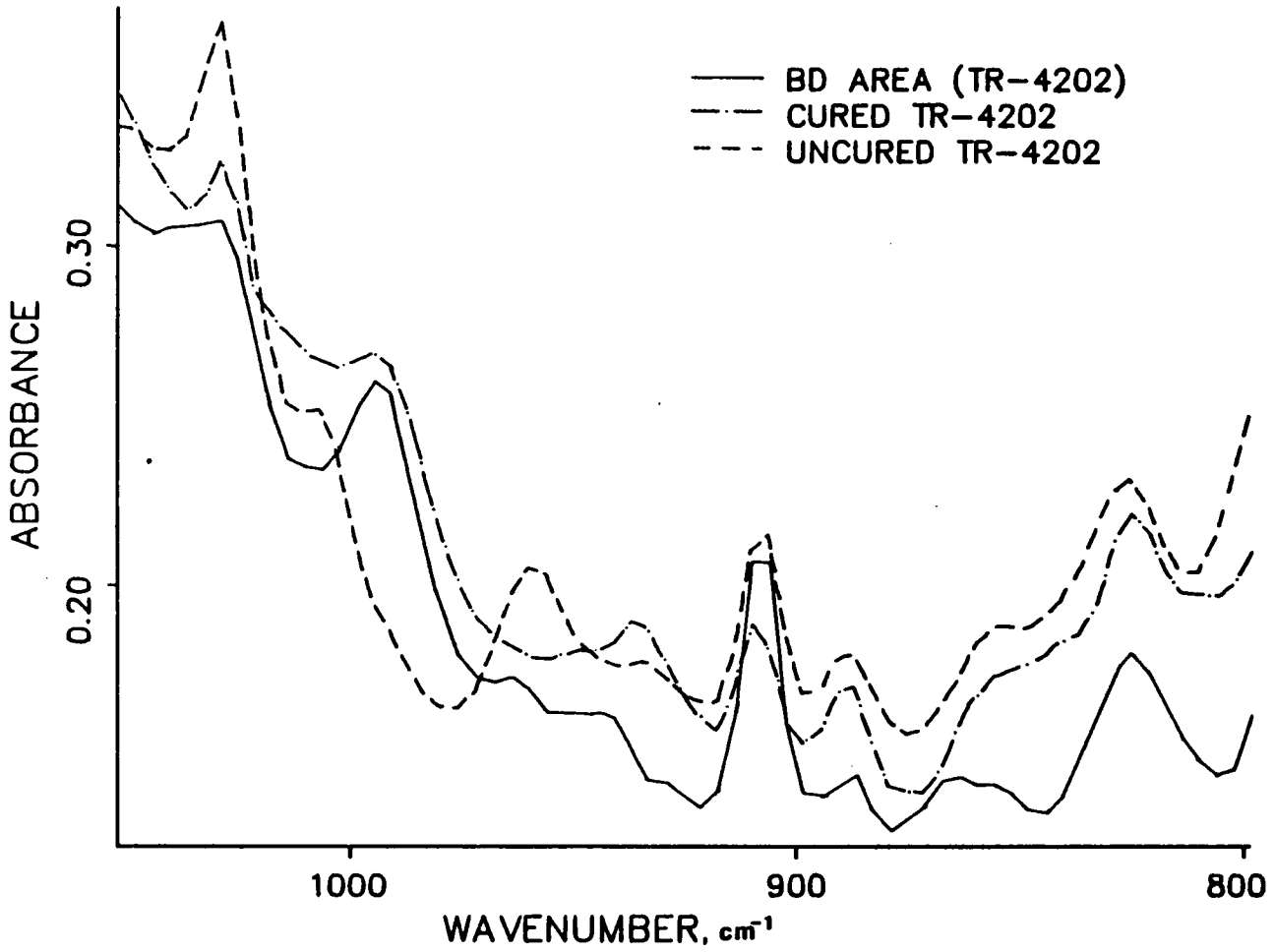



Figure 4.5.10 FTIR spectra of the electrically ruptured area, cured and uncured TR-XLPE in the region of 1050-800 $cm^{-1}$.

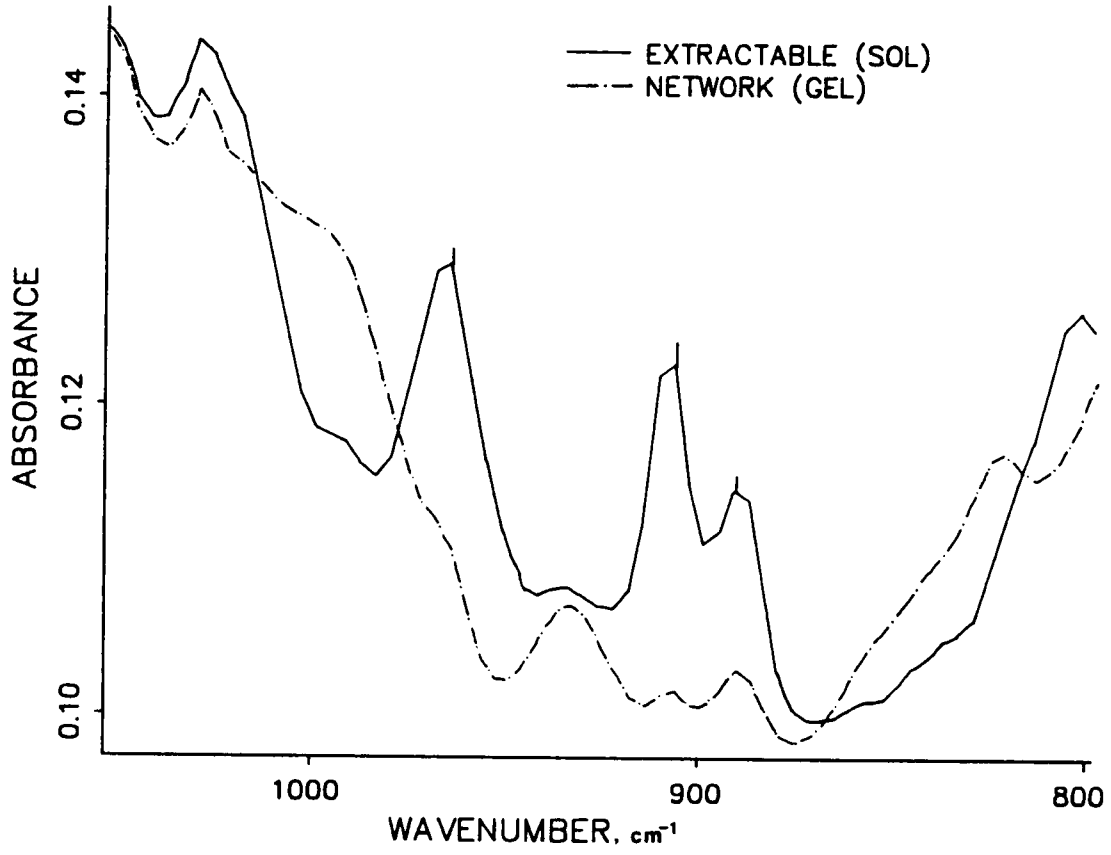



Figure 4.5.11 FTIR spectra of sol and gel fractions of TR-XLPE in the region of 1050-800 $cm^{-1}$.

# CHARACTERISTICS AND ANNEALING BEHAVIOR OF POLYETHYLENE DESIGNED FOR USE AS UNDERGROUND CABLE INSULATION

A Dissertation

Presented for the

Doctor of Philosophy

Degree

The University of Tennessee, Knoxville

Young Dae Lee

August 1989

VOLUME II

# 5. DISCUSSIONS

A major achievement in cable insulation development was the introduction of crosslinked polyethylene as an insulation material. This offered higher temperature service and improved chemical resistance over the uncrosslinked counterparts (Eichhorn, 1981). At first, the improvement of electrical properties and resistance to treeing were attributed to crosslinking. However, several workers suggested that the improvement resulted from the presence of the acetophenone, one of several chemical by-products from the peroxide crosslinking reaction (Braun, 1980). This is a typical example showing that a sound understanding of materials is crucial to the development of better insulation materials along with the understanding of failure mechanisms under electrical stress.

One of the important properties of any insulation material is thermal stability. Many polymeric insulators are exposed to high levels of thermal stresses during normal operation, since electrical power transmission generates heat. Thermal stresses not only change the properties of polymeric insulators but they also modify the structure of the materials. It is recognized that the morphology of a polymeric insulator is one of the major material parameters that determines the final dielectric properties (Fukuda, 1981; Kolesov, 1980; Ceres, 1984). Therefore, it is extremely important to understand the effects of thermal stresses on the morphology of the polymeric insulators.

This chapter begins with a discussion of the SAXS model study for the better interpretation of SAXS data which will be utilized throughout the remainder of this chapter. Later, the characterization of four different cable insulation materials based on the experimental findings will be discussed. The thermal aging behavior and concurrent morphological developments of these recently introduced polyethylenes will be also discussed. The morphological changes produced by annealing will be examined by the use of several techniques including small angle x-ray scattering (SAXS), wide angle x-ray scattering, density measurement and differential scanning calorimetry (DSC). Phase separation of XLPE at higher temperatures, that has been suggested previously (Phillips, 1986), will be reevaluated and compared with the experimental results of an in-situ SAXS study. The mechanisms of electrical breakdown will then be discussed based on findings on the damage caused by breakdown.

## 5.1. Interpretation of SAXS data

### 5.1.1. SAXS Model Study

Observable as well as Lorentz-corrected SAXS intensities were calculated based on the several SAXS models in order to develop an understanding of the nature of SAXS intensity curves. In the calculation the average crystallinities were assumed to be 50%. All the experimental samples have a crystallinity between 48% and 55%. This is the range over which the intensity curves are relatively insensitive to a difference in crystallinity.

The comparison between simple stack model and variable stack model indicates that the simple infinite stack model generates peaks much narrow for those found by experiment. The closest approach of theory to experiment occurs when $\sigma_x$ becomes large (>0.2). Still, the experimental SAXS curves of LLDPE cannot be predicted by the simple stack model. In the simple stack model the distribution mode between symmetric and asymmetric distributions does not cause any significant difference except for the case of a wide distribution in which Bragg peaks of calculated SAXS curves based on asymmetric distribution are located higher than 1.0, whilst those of symmetric distribution are located below 1.0. This behavior is also occurred in the variable stack model where the thickness was assumed to change either symmetrically or asymmetrically.

The variable stack model, however, shows marginally better fitting for the experimental curves. Moreover, the shapes of curves generated by the variable stack model covers those of LLDPE as well as XLPE, ranging from an almost linear dependence without any peak to the typical curve with a distinctive Bragg peak. It is remarkable that the variation of crystallinity distributions among stacks causes a more dramatic change in calculated observable intensity curves than the variation of lamellar thickness distribution in each stack. The variation of the intensity curve shape with change of $\sigma_c$ is more noticeable when $\sigma_x$ is small. In other words, it can be stated that the importance of crystallinity distribution is more

recognizable when the thickness variation within each stack is narrow.

It is interesting to know the effects of crystallinity distribution on the shapes of SAXS intensity curves. Figure 5.1.1 shows the difference SAXS intensity curves calculated using $\sigma_x$ of 0.1. Each curves represents the gains of intensity with increase in the value of $\sigma_c$ from the base intensity value of $\sigma_c$ of 0.05. Similar plots for a value of $\sigma_x$ of 0.15 are shown in Figure 5.1.2. The major changes in the difference curves for unmodified intensity are in the lower angle region and in the peak region for both cases. As the crystallinity distribution becomes wider, the intensity at the peak decreases and the intensity away from the peak increases. Other effect to note is that when $\sigma_x$ is lower (0.1), the increment of intensities with the increase of $\sigma_c$ is higher. This indicates that the system having a narrow distribution of lamellar thickness is subject to change more severely with the change of $\sigma_c$.

It can be speculated that the number of layers with a specific thickness, somehow, is related to the changes in the SAXS intensity curves. With increasing standard deviation of crystallinity distribution, the number of stacks having crystallinity of 0.5 will be reduced, and the number of stacks with higher or lower crystallinity values will be more populated. Due to the symmetric nature of a normalized Gaussian distribution, the increment and decrement of number of stacks having different crystallinity have to be symmetric. However, the SAXS curves indicate that the increment

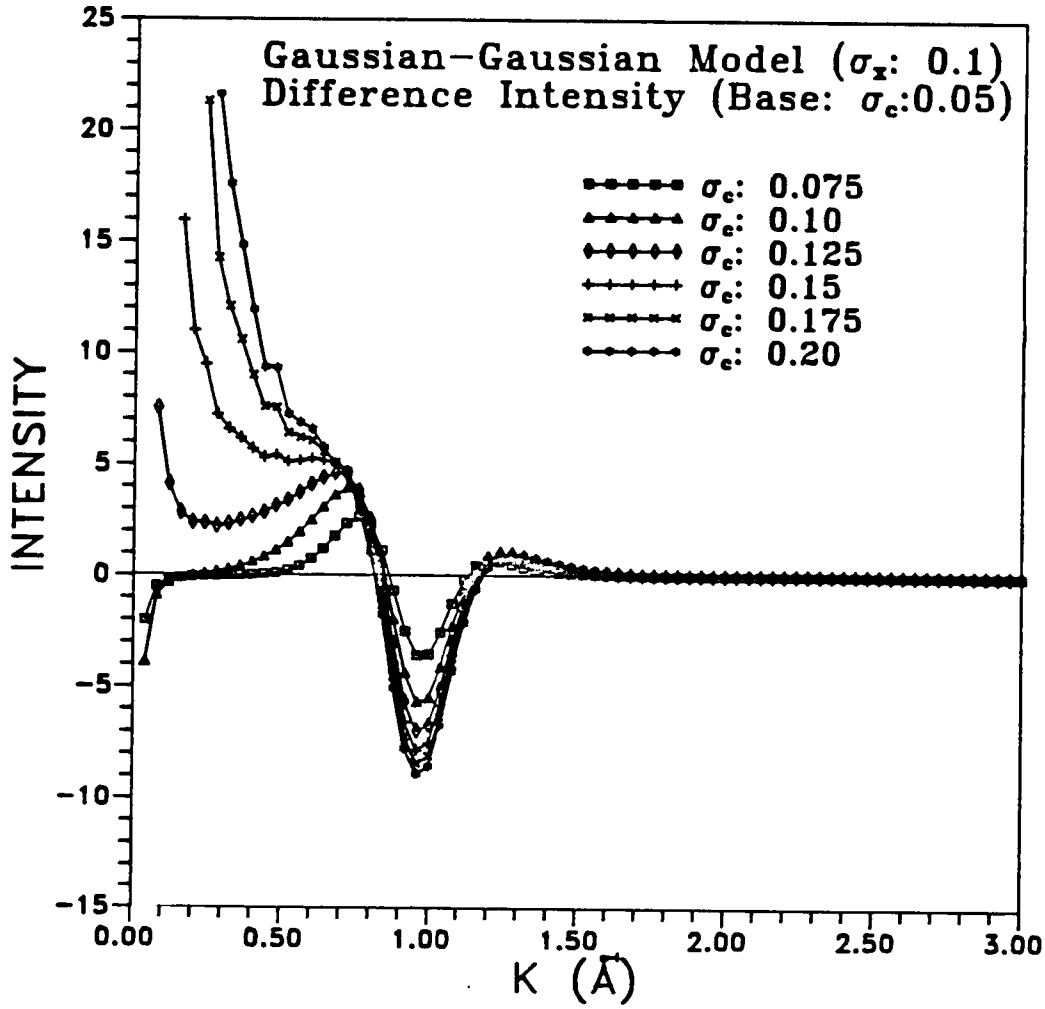



Figure 5.1.1 Calculated difference SAXS intensity curves based on the variable stack model with Gaussian thickness distributions with $\sigma_x$ of 0.10. (Intensities of $\sigma_c$ of 0.05 subtracted)

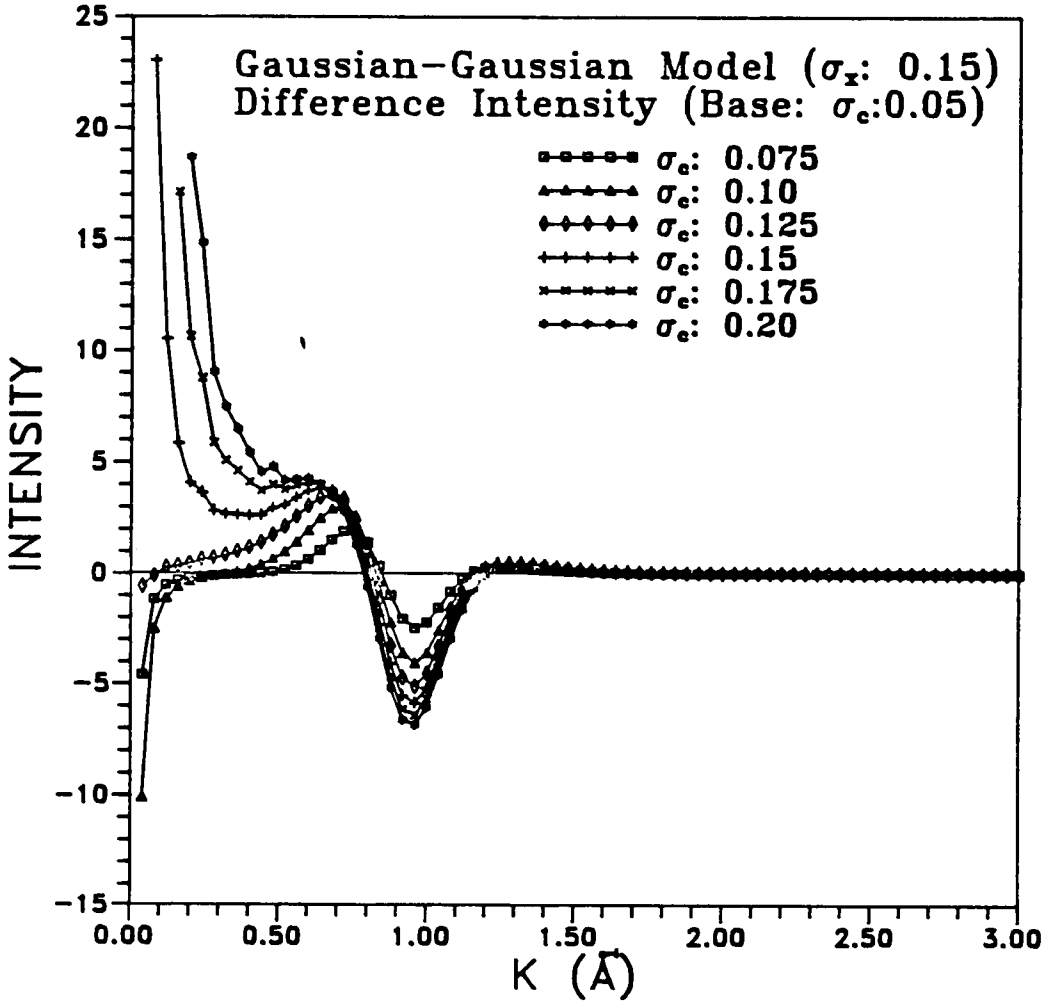



Figure 5.1.2 Calculated difference SAXS intensity curves based on the variable stack model with Gaussian thickness distributions with $\sigma_x$ of 0.15. (Intensities of $\sigma_c$ of 0.05 subtracted)

of layers with thick lamellae have a greater effect than the increment of layer with thin lamellae. Thus, the intensities near the zero-angle are more sensitive to the change of number of layers having dimensions corresponding to the scattering angle.

Table 5.1.1 shows various parameters calculated from the model SAXS intensity curves using the variable stack model with a symmetric thickness distribution. Apparent long periods were obtained from the calculated SAXS intensity curves as a reciprocal of peak locations. It is of interest to note that the peak position, and thus the apparent long periodicity, change with variation in the two distribution parameters, $\sigma_x$ and $\sigma_c$. The shift is more marked in unmodified SAXS intensity curves.

Peak position has been a major concern for most investigators, since the reciprocal of the peak position gives valuable and unique information about the long periodicity. Any long periodicity by nature is a mean value. Moreover, the value of long periodicity has been criticized for not being reasonable compared to the values obtained by direct measurement techniques such as electron microscopy (Geil, 1963). One of the remedies for correct prediction of the mean long periodicity was suggested as the application of the Lorentz-geometric correction to SAXS intensity curves (Crist and Morosoff, 1973, Hosemann and Bagachi, 1962). The Lorentz-correction was originally introduced as an intensity correction for wide angle X-ray rotation photographs. In a randomly oriented sample it should be applied to correct for the different probabilities of planes

Table 5.1.1. Results from variable stack model simulations.

| Sigma X | Sigma C | Lorentz Corrected | | Observable Intensity | | | |
|---|---|---|---|---|---|---|---|
| | | Peak Location | Apparent Long Period | Peak Location | Apparent Long Period | Distance Ratio | Height Ratio |
| 0.1 | 0.1 | 0.97 | 1.03 | 0.90 | 1.11 | 2.42 | 0.18 |
| 0.1 | 0.15 | 0.97 | 1.03 | 0.86 | 1.17 | 2.04 | 0.29 |
| 0.1 | 0.175 | 0.96 | 1.04 | 0.76 | 1.32 | 1.70 | 0.37 |
| 0.1 | 0.2 | 0.96 | 1.04 | 0.73 | 1.37 | 1.59 | 0.47 |
| 0.15 | 0.1 | 0.95 | 1.05 | 0.81 | 1.23 | 1.48 | 0.91 |
| 0.15 | 0.15 | 0.94 | 1.06 | 0.78 | 1.28 | 1.79 | 0.74 |
| 0.15 | 0.175 | 0.94 | 1.06 | 0.76 | 1.32 | 1.73 | 0.67 |
| 0.15 | 0.2 | 0.94 | 1.06 | 0.72 | 1.40 | 1.70 | 0.75 |
| 0.175 | 0.1 | 0.92 | 1.09 | 0.73 | 1.37 | 1.14 | 1.00 |
| 0.175 | 0.15 | 0.91 | 1.10 | 0.72 | 1.40 | 1.48 | 0.87 |
| 0.175 | 0.175 | 0.90 | 1.11 | 0.72 | 1.40 | 1.48 | 0.87 |
| 0.175 | 0.2 | 0.89 | 1.12 | 0.68 | 1.48 | 1.55 | 0.88 |
| 0.2 | 0.1 | 0.90 | 1.11 | | | | |
| 0.2 | 0.15 | 0.88 | 1.14 | 0.65 | 1.53 | 1.27 | 0.94 |
| 0.2 | 0.175 | 0.88 | 1.14 | 0.62 | 1.61 | 1.21 | 0.94 |
| 0.2 | 0.2 | 0.88 | 1.14 | 0.61 | 1.65 | 1.21 | 0.95 |

being in the reflection condition. Crist suggested that at low angles the combined Lorentz-geometric correction takes the form of a $k^2$ multiplication factor for the system when the lateral dimensions of the entities are effectively infinite. The Lorentz-correction was also strongly suggested to avoid the distortion which results from spatially randomizing a scattering pattern that has been laterally broadened.

The results in Table 5.1.1 also support the necessity of the Lorentz-correction as far as mean long periodicity is concern. Apparent long periods determined from the Lorentz-corrected curves range from 1.03 to 1.14. Theory starts with the assumption the mean value of long periodicity is 1.0. However, the apparent long periods determined from the unmodified SAXS intensity curves reach up to 1.65. A major shift was noted for the SAXS intensity curves with small Bragg peaks such as the one obtainable from LLDPE. Such severe distortion is thought be due to the wide distribution of layer thickness.

The distance and the height ratios were also determined from the unmodified SAXS intensity curves, since the noticeable changes with variation of the two distribution parameters is found in the relative positions and heights of the peaks. Schematics illustrating these SAXS parameters and their definitions are given in Figure 5.1.3. Table 5.1.1 tabulates the list of the distance and height ratios for various distributions in the case of the variable stack model with symmetric thickness variation. These two parameters can

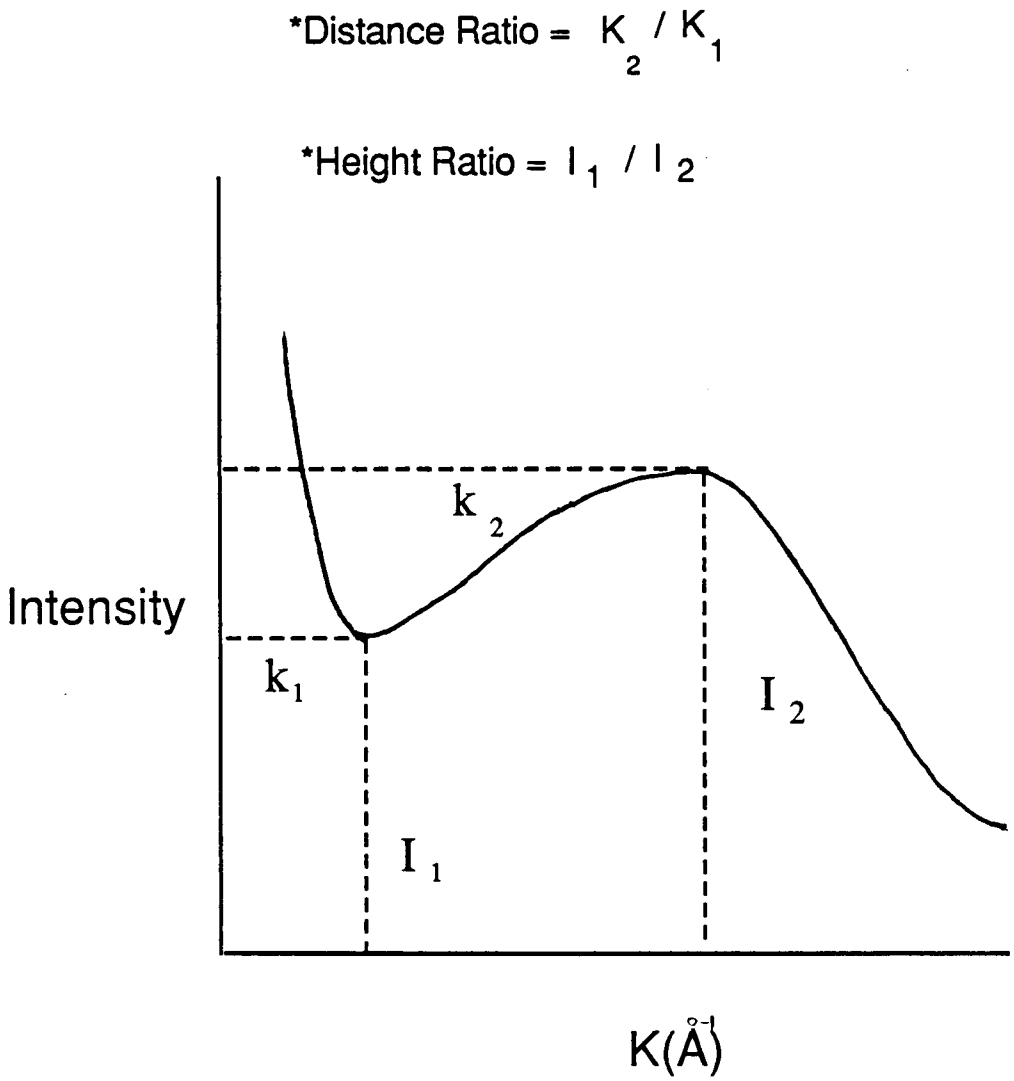



Figure 5.1.3 Schematics of typical SAXS intensity curves and definitions of characteristic parameters.

be regarded as characteristic since they are based on the ratio of the same dimension.

It was noted that the distance and height ratios do not change in a simple way. However, for a given value of $\sigma_c$ the distance ratio decreases with increasing $\sigma_x$ from 1.14 to 2.42. A wide variation of the distance ratio was noted with a small value of $\sigma_c$. On the contrary, the height ratio increases with increasing $\sigma_x$ for a given value of $\sigma_c$, having values from 0.18 to 1.0.

Another remarkable feature was observed in the one-dimensional correlation functions. As discussed in the review chapter, the one-dimensional correlation function can be calculated using the Fourier transform of Lorentz-corrected intensity. The nature of Fourier transform requires integration from zero to infinity, hence any experimental SAXS intensity curves need to be extended to those values using various fitting methods. Since the numerical intensity calculation can be made for any values of scattering vector, the one-dimensional correlation functions obtained from the theoretical calculations are more reliable than those from the experimental data. Figures 5.1.4 and 5.1.5 show one-dimensional correlation functions from the variable stack model with symmetric thickness distributions of 0.15 and 0.175, respectively. The first positive peak is located around the distance of 1.0 with a slight deviation. However, the depth of the first negative peak changes with the variation of standard deviations of thickness.

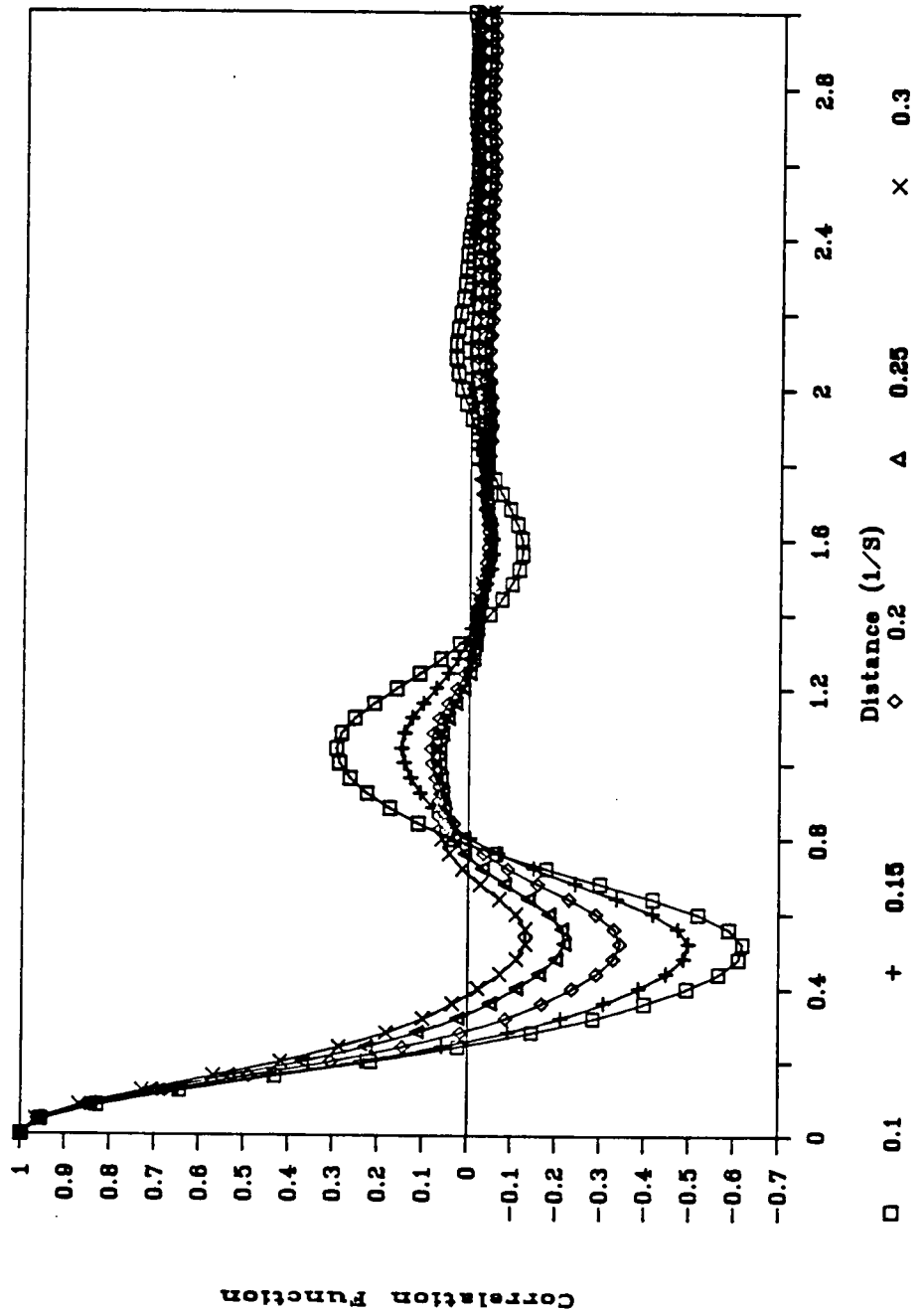



Figure 5.1.4 Calculated one-dimensional correlation function based on the variable stack model ($\sigma_x = 0.15$)

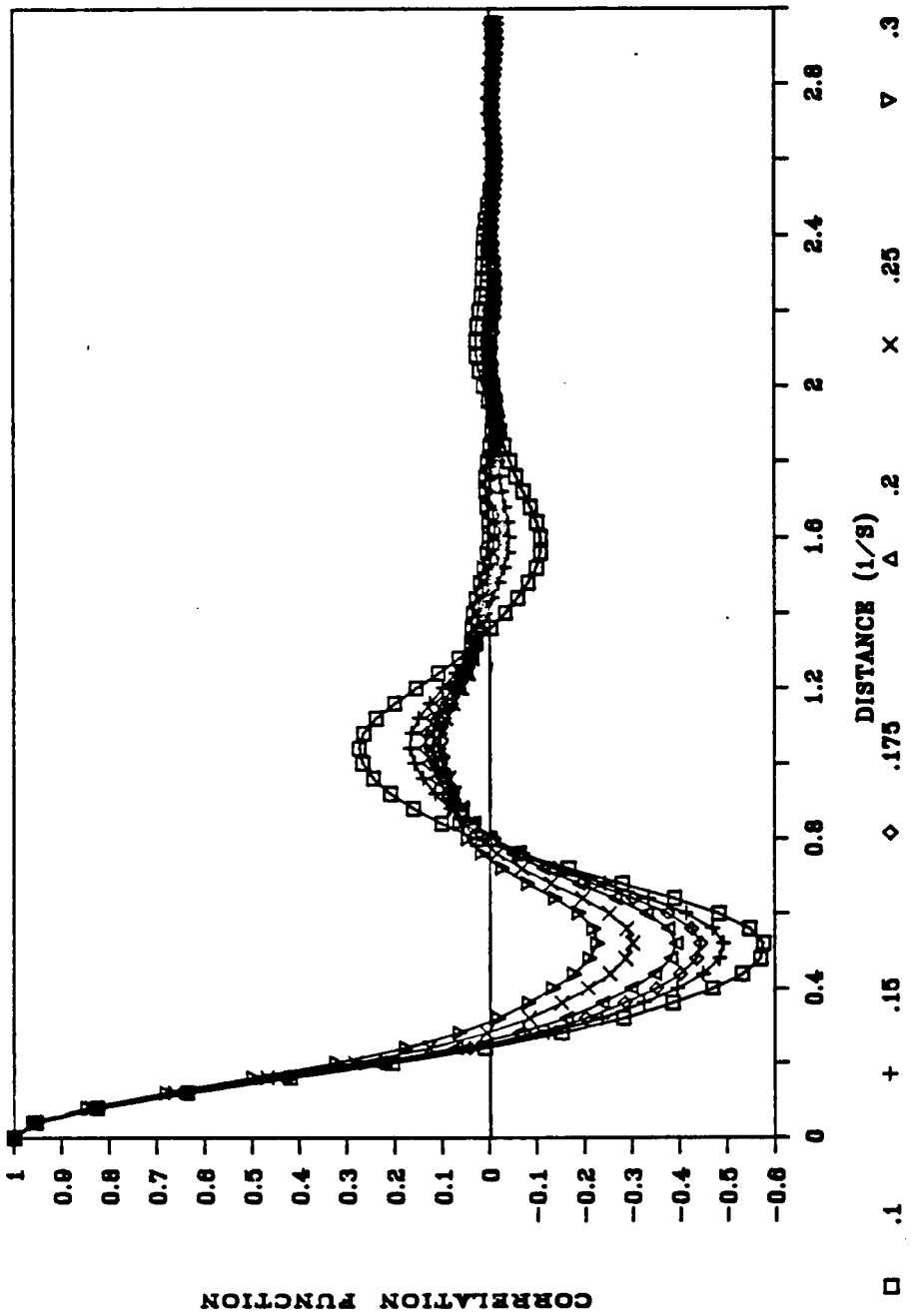



Figure 5.1.5 Calculated one-dimensional correlation function based on the variable stack model ($\sigma_x = 0.175$)

The depth of the peak has been linked to the crystallinity using a formula of $-\phi/(1-\phi)$ for an ideal lamellar structure (see Figure 2.2.1, Page 85) (Vonk, 1985a). The variable stack model does not predict a single value of the depth of the first negative peak in a one-dimensional correlation function, even though all calculations were made with the assumption of a mean crystallinity of 0.5. For the real polymer complex shape of the one-dimensional correlation function is more plausible. Thus, the nature of one-dimensional correlation function need to be studied further.

5.1.2. Physical Meanings of Models

The crystallinity distribution appears to control the general shape of the SAXS intensity curve. Figures 5.1.6 and 5.1.7 show the various observable intensity curves calculated using the model and values of $\sigma_c$ of 0.1 and 0.15, respectively. The intensity curves calculated using $\sigma_c$ of 0.1 are similar to the experimental SAXS curves of LDPE or XLPE (Figure 5.1.6). On the other hand, Figure 5.1.7 shows theoretical curves similar to the experimental SAXS curves of LLDPE.

This finding is expected since the broad distribution of crystallinities in LLDPE is well-known. LLDPE is produced by the copolymerization of ethylene with various alpha olefins. The length of comonomer, which determines the length of the side chain, will have an effect upon crystallization. It is expected that the different copolymer contents will crystallize in a selective way, resulting in molecular segregation. When samples cool, the less

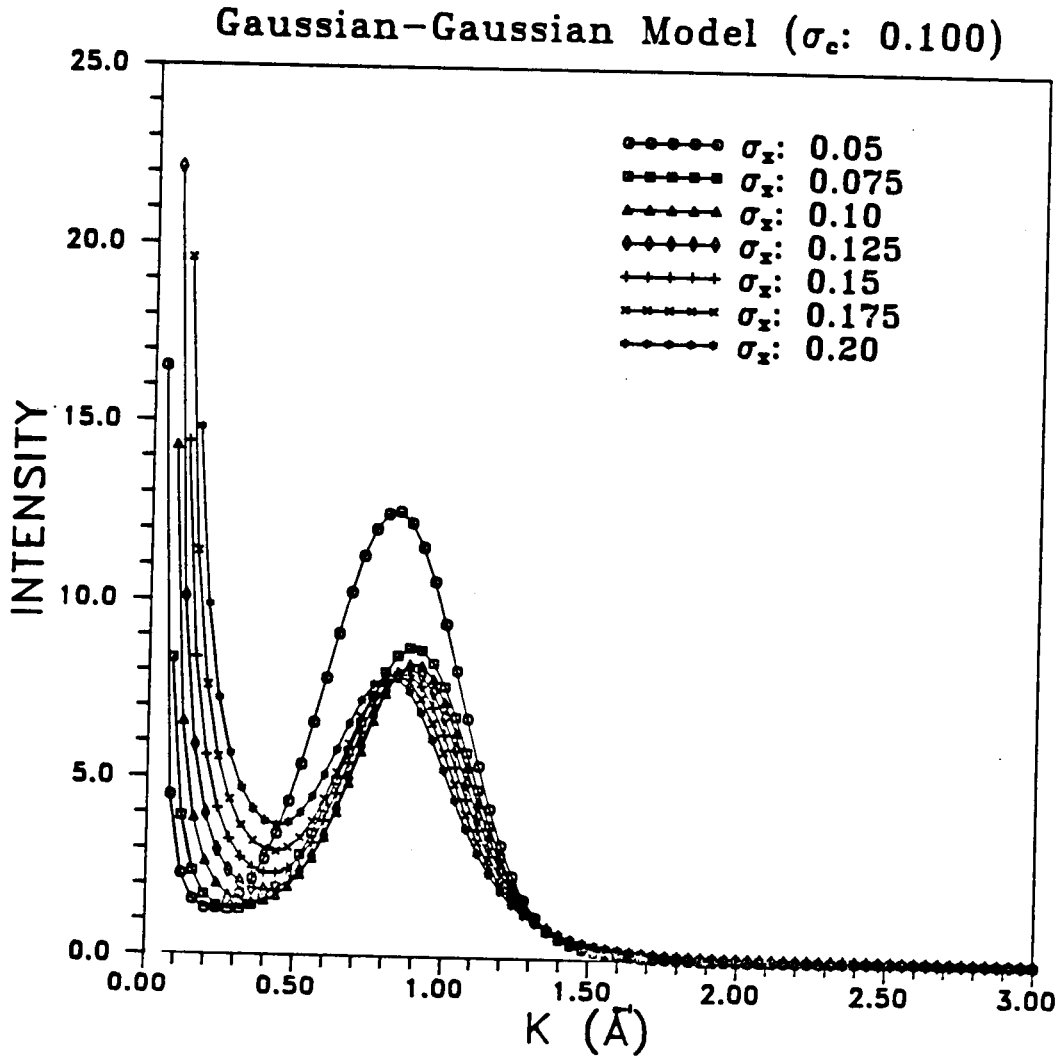



Figure 5.1.6 Calculated SAXS intensity curves based on the variable stack model with Gaussian thickness distributions and Gaussian crystallinity distributions among stacks. ($\sigma_c$ =0.1)

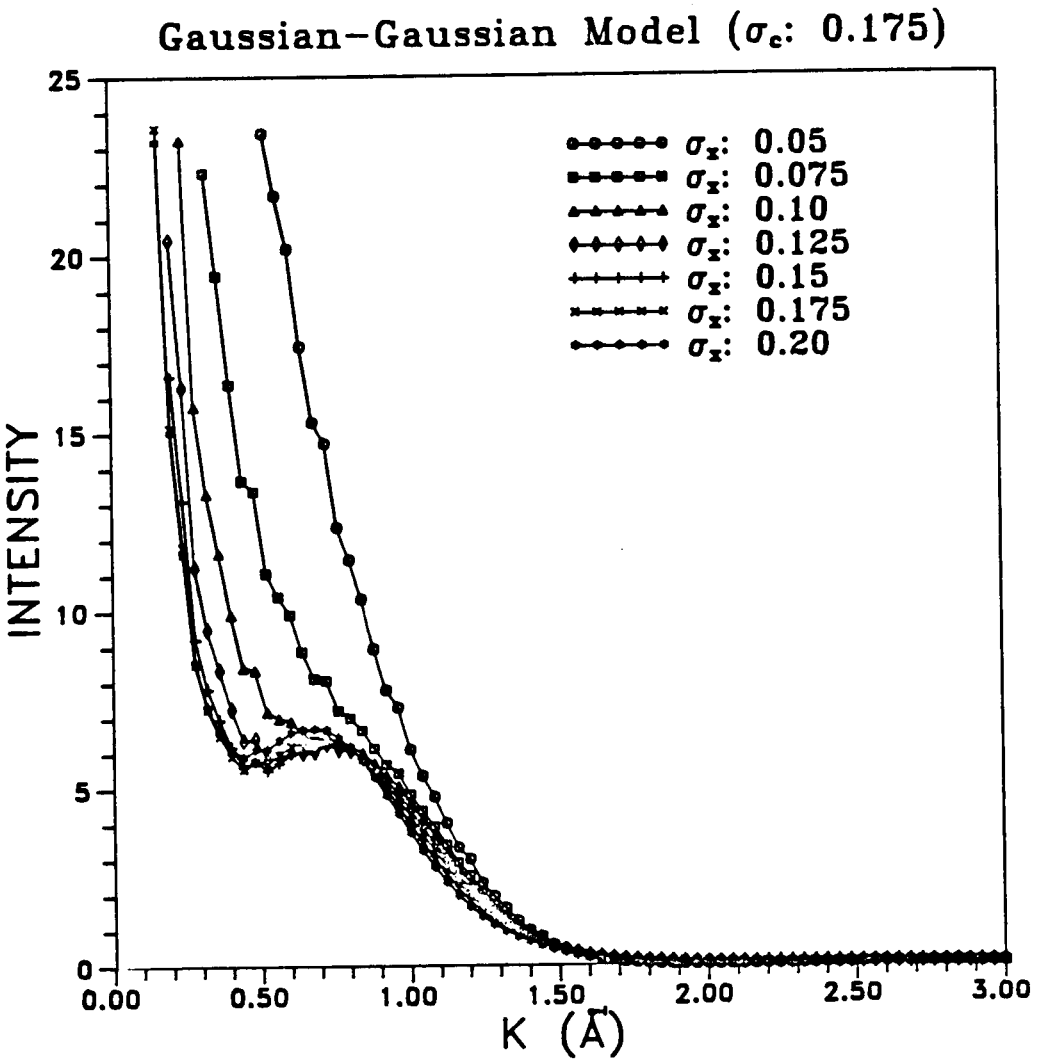



Figure 5.1.7 Calculated SAXS intensity curves based on the variable stack model with Gaussian thickness distributions and Gaussian crystallinity distributions among stacks. ($\sigma_c$ =0.175)

branched molecules will tend to crystallize first giving lamellar stacks of higher crystallinity and high long periodicity. Lamellar stacks containing more highly branched molecules will crystallize at a lower temperature, giving lower local crystallinities and smaller mean long periodicities. Such crystallization behavior has been reported previously (Basset, 1981). In high-pressure crystallization of a polyethylene copolymer, Basset observed lamellae of four different thicknesses corresponding to four populations in the melting endotherm. First were the long, thickest layer then the thick infilling lamellae. These contain the longest and most linear molecules. The third family is repetitively ridged which identifies it as having crystallized as the orthorhombic structure. The last family is the envolving matrix of thinnest lamellae containing the most defective crystallizable molecules.

The SAXS intensity curves obtained for quenched and slow cooled TR-LLDPE support fractionation during crystallization. Figure 5.1.8 shows the SAXS curves of two TR-LLDPEs, one being quenched to room temperature and the other being cooled slowly at 1.5$^{o}$C/min. The curve of the slow-cooled TR-LLDPE shows virtually no peak. This type of intensity curve can be obtained either for low values of thickness distribution in a given value of crystallinity distribution or for higher values of crystallinity distribution. The first possibility is illustrated in Figure 5.1.7. Both cases, however, support required molecular segregation.

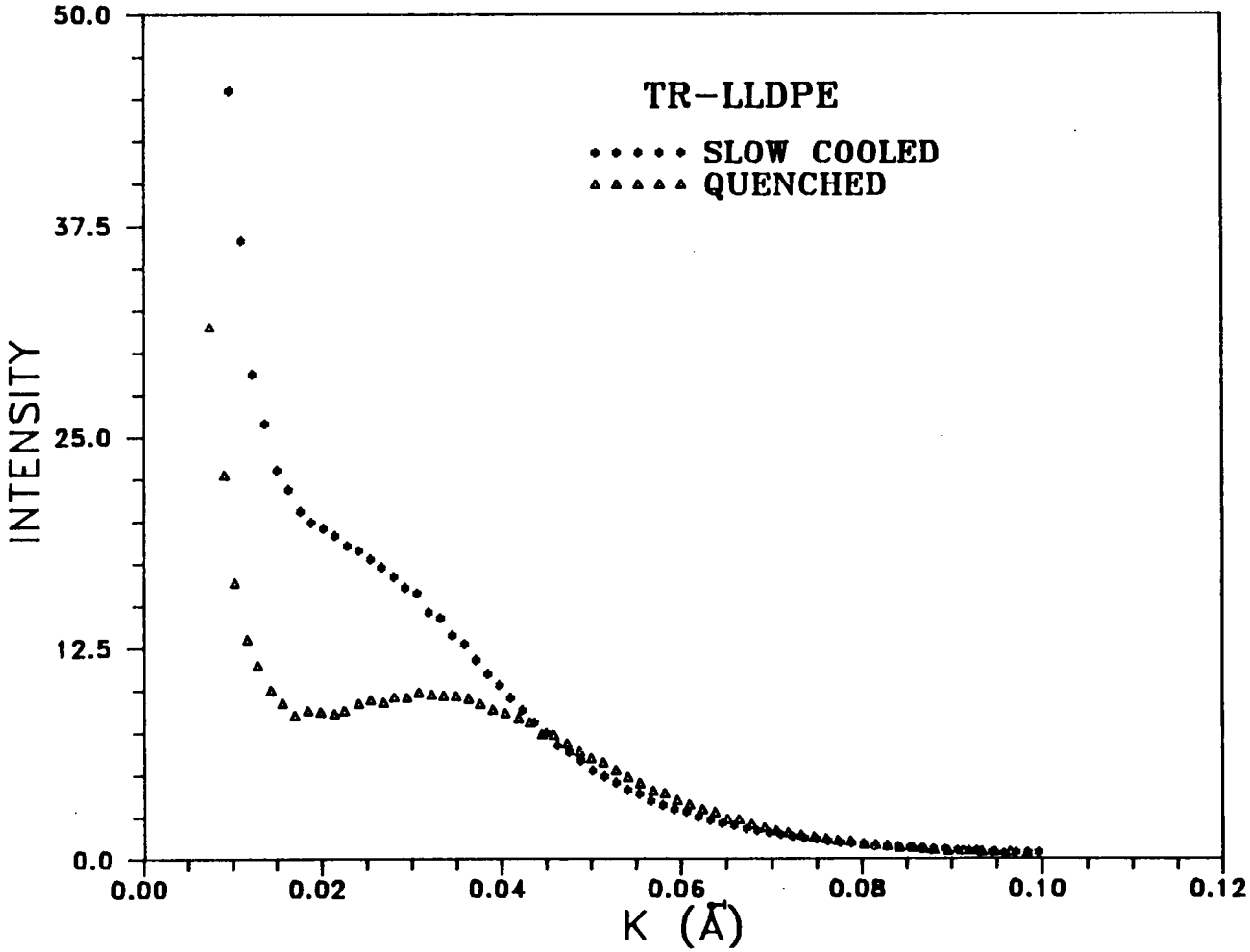



Figure 5.1.8 SAXS intensity curves of slow-cooled (1.5°C/ min) and quenched TR-LLDPE.

The slow-cooled TR-XLPE and TR-LDPE are compared with the quenched counterparts in Figure 5.1.9 and 5.1.10. Quenched TR-XLPE shows height ratio of 0.29 and a distance ratio of 2.58, while the slow-cooled TR-XLPE shows a height ratio of 0.40 and a distance ratio of 2.40. Slow-cooled TR-XLPE shows a greater height ratio than the quenched material, indicating a narrower thickness distribution. The SAXS intensity curve for slow-cooled TR-XLPE shows a Bragg peak at a lower angle. This result appears to be due to a lamellar thickening process during slow-cooling along with the refinement of thickness in each stack. TR-LDPE also shows similar features, reflecting the fact that during slow-cooling the crystallinity distribution become wider along with increase of long periodicity that may be expected due to the slow crystallization process. Another point to be noted is that the TR-XLPE shows relatively smaller shifts of SAXS intensity curves within experimental error. This can be attributed to the recrystallization process being less active during re-melting and crystallization than in TR-LDPE, due to the presence of tie molecules.

Therefore, the basic principles of the variable stack model appear to be plausible on the basis of molecular behavior. The schematics for the variable model are presented in Figure 5.1.11. The round boundary indicates the stack boundary. It has to be sufficiently large so as not to cause any interference among stacks for the SAXS scattering, even though the physical meaning of the actual boundary is not clear. The boundary can be made to correspond

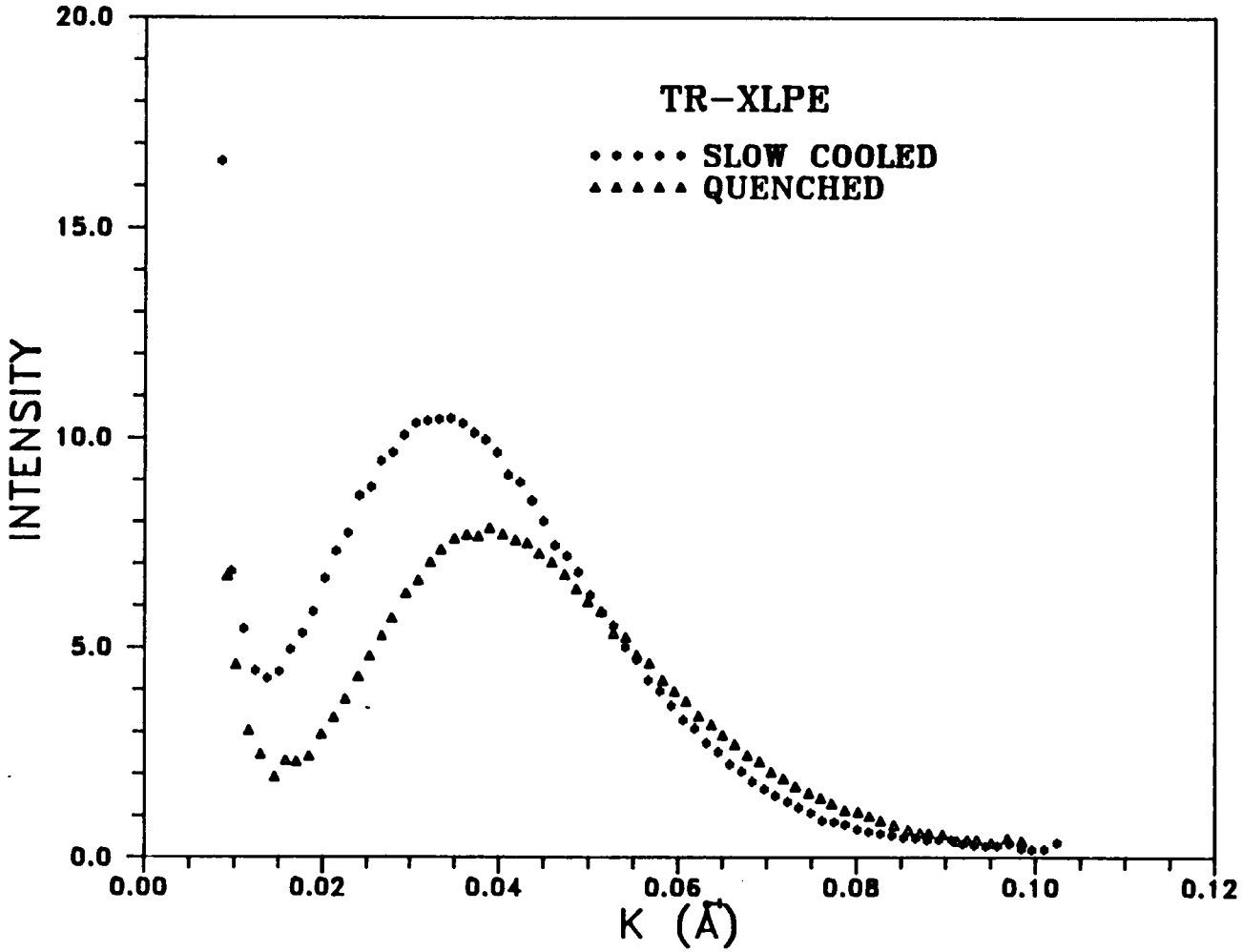



Figure 5.1.9 SAXS intensity curves of slow-cooled (1.5°C/ min) and quenched TR-XLPE.

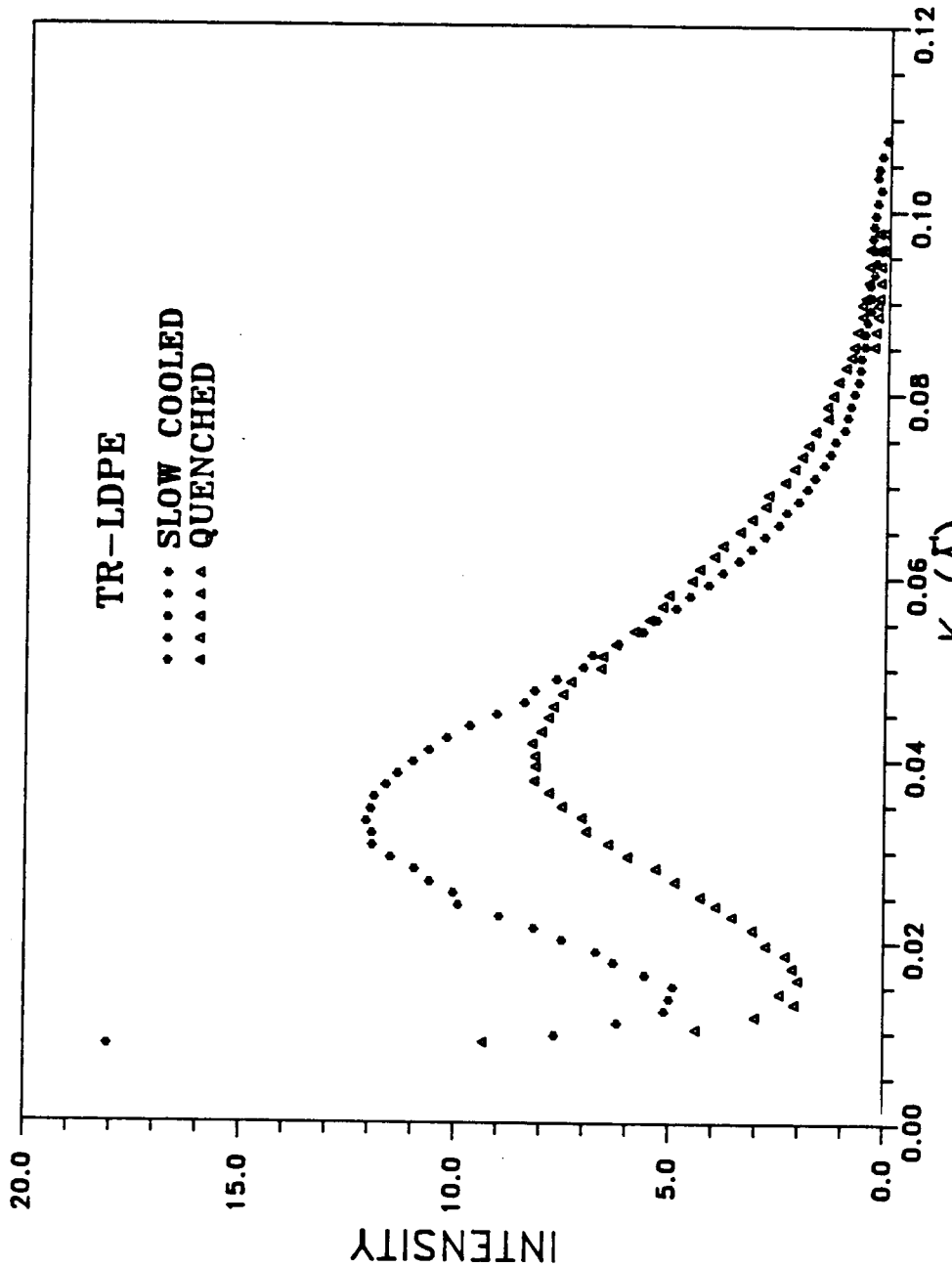



Figure 5.1.10 SAXS intensity curves of slow-cooled (1.5°C/ min) and quenched TR-LDPE.

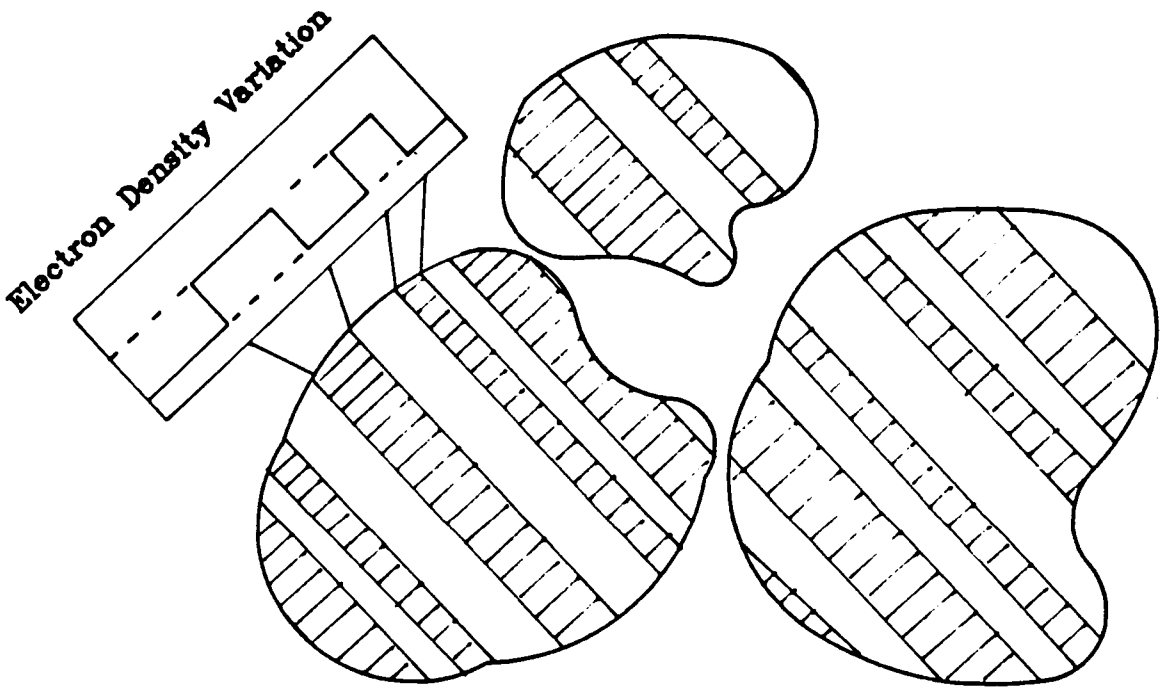



Figure 5.1.11 Schematics of the variable stack model.

to the local region which has a given crystallinity with a similar gathering of layers. For LLDPE the boundary can be assigned to the boundary of groups of molecules that have similar comonomer contents. A similar imaginable boundary can also be made for XLPE or LDPE along with the groups of molecules which have a similar molecular chain configuration.

Each stack has crystalline and amorphous layers alternately stacked in one direction. The electron density variation along the normal to the lamellar plane was assumed to follow the diagram in the graph, having two different electron density values throughout the stacks and an abrupt increase at the boundary. Since this is a one-dimensional model, it can be extended to three dimensional systems by dividing by the Lorentz-geometric factor for the one-dimensional SAXS intensities calculated.

### 5.1.3. Interpretation of Experimental SAXS Data

The broad scattering peaks are known to occur from the scattering profiles for highly dispersed lamellae such as LDPE (Strobl, 1973), ethylene copolymer (Kilian, 1974), and poly(tetramethylene oxide) (Brown, 1973). Such broad scattering peaks are difficult to interpret using the simple stack model. The introduction of crystallinity variation inside the imaginary boundary helps to better fit experimental data to the theoretical scattering curves.

Most investigators including Schultz and his colleagues interpreted their SAXS data for melt-crystallized polyethylene in a

similar way. When they interpreted their data, they generally examined the following five points: (1) shape and slope of zero-angle scattering intensity, (2) location of Bragg maxima, (3) ratio of two intensity maxima, (4) the breadths of the Bragg Peaks and (5) integrated intensity. Major emphasis was put on the location of the Bragg peak which reveals information about the long period, utilizing a simple two phase model consisting of crystalline and amorphous regions. For the zero-angle diffuse scattering intensity, they tried to use Guinier theory, claiming that those intensities were associated with the amorphous gaps (or lamellar thickness) in the lamellar stacking within a spherulite (Schultz, 1977, 1978).

The variable stack model clearly shows that there are other types of information that can be obtained from the SAXS intensity curves. Major concern can be focused on the general shape and on some characteristic dimensions from the unmodified SAXS intensity curve. The characteristic height and the distance ratios help to understand molecular segregation behavior and to determine the quantitative values of distributions. With a highly reliable and accurate SAXS camera, such as the one in NCSASR, Oak Ridge, Tennessee, the scattering intensity curves are quite reproducible, especially near the zero-angle region. The intensity in the region, as well as the general shape, was found to be related to the distribution of crystallinity as well as the thicknesses.

The somewhat unexpected shape of the SAXS intensity curves from TR-LLDPE appears to be due to the wide distribution of

crystallinities among the stacks. Similar shaped intensity curves were also found in LDPE and XLPE at relatively high temperatures (from 60°C to 105°C). Such intensity curves can be explained using the same approach. At a high temperature a crystal fraction with a particular thickness will melt and then isothermally crystallize. The lamellar thickening happens with the aid of the recrystallization process. At the same time, some other fractions will still be molten, and have the electron densities similar to those of amorphous regions at the annealing temperature. These molten crystal fractions will act as an amorphous fraction causing the thickening of the amorphous layers. The whole process is considered to happen in a very localized way due to restrictions of overall chain mobility, resulting in wide distribution of local crystallinity.

However, the model is still crude since it does not consider a smooth boundary between layers, there being a smooth increase of electron density rather than an abrupt increase of electron density. Further tailoring of the model might help to build a better model that can be matched exactly with experimental data. The addition of a third phase such as voids or some other particle to the model calculation can be considered necessary to build a better SAXS model. Especially, a third material having a dimension that corresponds to the near the zero angle would have a significant effect similar to that of a small fraction of thick layers.

The contradiction between structure parameters from the SAXS technique and other direct observations can also be attributed to the wide distributions possible in a polymer system. This nature was fully integrated in the variable stack model. In other words, several direct measurements are necessary to obtain an average value of any structural parameter, while a single SAXS measurement shows an integrated feature of structure.

On the other hand, there is an unavoidable deficiency in the SAXS technique alone, which means SAXS data alone will cause ambiguity because of the nature of scattering, such as the principle of Babinet's reciprocity. Nonetheless, this technique can be utilized more in the elucidation of overall superstructure due to the nature of the measurement of somewhat averaged superstructures.

## 5.2. Characterization of Various Polyethylenes

### 5.2.1. IR Study

Chemical additives have been used for the purpose of reducing treeing by capturing energetic electrons chemically, retarding propagation of trees electrically and interfering physically with tree propagation. The detailed mechanisms of various additives were reviewed by Eichhorn (Eichhorn, 1983). Several commercial grades of polyethylene have been introduced as enhanced products. TR-XLPE and TR-LLDPE, which are used in this work, are among these enhanced materials introduced by Union Carbide Corp. Both of them are claimed

to have higher dielectric breakdown strength and to resist or retard the rate of tree growth.

First, a series of XLPEs will be considered with the main focus being on TR grade of XLPE. It is known that the only difference in production of EC-XLPE compared to PL-XLPE is that great care is taken in the prevention of solid particle contamination. Infrared spectra of these two materials show that there are no special chemical additives present, supporting the manufacturer's claim. A lower level of solid contamination is crucial for the enhancement of electrical properties. As mentioned in the review chapter, the solid contaminants or their boundaries are likely initiation points of treeing or electrical breakdown.

The high peaks in 1740 $cm^{-1}$ observed in EC- and PL-XLPE are considered to be due to the presence of the ester group. This ester group was not generated during the crosslinking process, even though esters are typical oxidation by-products of regular polyethylene (Luongo, 1963). The presence of the same peak was also noted for uncured materials. Not surprisingly, the ester group has been reported for the major cable material (Crine, 1988), being attributed to thioesters (distearyl thiodipropionate or dilauryl thiodipropionate) used as antioxidant synergists.

The situation is quite different for TR-XLPE where a liquid antioxidant has been used together with an additional chemical bonded to the polymer chain. This latter adaptation is designed to function in the same way as acetophenone is believed, by some, to

function in XLPE. It is known that XLPE, once having lost its acetophenone by-product, is much more susceptible to tree initiation than when freshly made. This resistance may be caused by the acetophenone reacting chemically, partially filling voids or acting as a surfactant in trees, incipient or otherwise. The additive, which has a similar chemical function to acetophenone, is bonded to the chain so that it cannot be lost by diffusion to the environment. It is believed to be added as a comonomer during synthesis. As such it might influence the level of chain branching in the polymer as well as the crystallization and annealing behavior.

It will be recalled that the infrared spectra showed that the extractable fraction had higher levels of t-vinylene unsaturation and lower levels of branching than the gel fraction. The uncured material showed a high vinyl content. It is possible that the vinyl group of a major additive reacts and is bonded into the gel network. The major differences in IR spectra between EC-XLPE and TR-XLPE lie in the peaks present at 1103, 1257 and 1604 $cm^{-1}$. Also notable is the low magnitude of the small peak at 1740 $cm^{-1}$, indicating the absence of antioxidant synergists.

Major differences between the gel fraction of TR-XLPE and EC-XLPE/PL-XLPE lie in the presence of the peaks at 800, 1000, 1103, 1257, 1570 and 1604 $cm^{-1}$. The magnitudes of these additional peaks vary from extractable to gel fraction (Figure 4.1.4, page 140). The extractables alone show the 800 and 1720 $cm^{-1}$, while the peaks at 1000, 1103, 1257 and 1570 $cm^{-1}$ are enhanced over the gel. Clearly

one segment of additive is extractable and a second has been attached to the network. The peaks at 1103, 1257 and 1604 $cm^{-1}$ do however appear for both extractable and gel fractions and so some chemical groups, if not entire additives, are present in both components of final product.

The peak at 1720 $cm^{-1}$ shown in sol fraction of TR-XLPE is thought to be induced from the ketones, which are oxidation by-products generated by the high temperature during crosslinking and/or extraction (Crine, 1988), rather than from the acetophenone. Acetophenone, a major by-product in the DCP crosslinking system, was reported to cause the peak at c.a. 1693 $cm^{-1}$. These bands are noted only for all cured materials but are of low intensity. This observation indicates that the same crosslinking system is used, regardless of the material, as expected.

Secondly, the tree retardant LLDPE will be considered. The IR spectra show that the chemical additives present in the LLDPE are similar to those used in the TR-XLPE. Notable, however, is the presence of an enhanced vinyl content at 908 $cm^{-1}$ which is considerably larger than in the uncrosslinked TR-XLPE indicating either a different formulation or an abnormally high vinyl content in the polymer molecules of the LLDPE. LLDPEs are copolymers of ethylene with unsaturated hydrocarbons longer than ethylene. Commonly butene is used along with heptene, hexene, octene etc. It is known that a distribution of copolymer content exists amongst the

molecules, some being essentially linear polyethylene whilst others have a high comonomer content.

5.2.2. DSC Study

The melting behavior of polymers normally reflects their crystallization procedure and their thermal history thereafter. Noticeable differences were observed in the DSC curves of XLPE and LLDPE. However, the melting behaviors of each XLPE were not very different, indicating slight difference in their morphological structures. All XLPEs quenched to room temperature show melting peaks around 104.5°C. Their melting peaks show an onset temperature around 98°C. The heats of fusion of XLPEs were identified at about 92 J/g if measured from the small hump around in 45°C. This value of heat of fusion corresponds to 45% crystallinity based on $\Delta H_f$ of 100% crystalline XLPE of 202.7 J/g (Kao, 1983). However, the heat of fusion measured from the temperature below the hump was found to be around 104 J/g, having a 51% crystallinity. The measurement method of the melting endotherm thus can cause two different results. The presence of the hump around 45°C in their melting curves are unavoidable, once held at room temperature even for a very short period of time.

On the other hand, XLPEs quenched from the melt to 0°C within the DSC machine show different melting curves. These XLPEs show very smooth melting curves without any hump around 45°C. Their melting peaks are a little lower than those of XLPEs quenched to room temperature (ca. 0.3°C), as are the melting onset temperatures.

$\Delta H_f$ of these XLPEs are around 96 J/g that can be related to 47% crystallinity. These finding clearly indicate that the humps were generated by annealing at room temperature. Thus, the melting of XLPE has to be measured from the temperature below the humps so that the humps are included. The values of $\Delta H_f$ of XLPEs quenched to 0°C are lower than those of XLPE quenched to room temperature by 8 J/g that corresponds about 8% of initial crystalline fraction present when the samples were quenched to 0°C. The gain of crystalline fraction was found to be dependent on the period of the room temperature annealing time.

TR-XLPE held at room temperature for two years also shows the room temperature annealing behavior with a reduced modification compared to either gel of sol fractions. Figure 5.2.1 shows the melting curve of the TR-XLPE held at room temperature for two years along with the curve measured from the quenched sample from the melt to 0°C within the DSC machine. The annealed TR-XLPE shows a smooth melting curve with a shoulder generated by room temperature annealing. The TR-XLPE kept at room temperature for 2 years shows up to 127 J/g of $\Delta H_f$. The increment of $\Delta H_f$ by the room temperature annealing is about 31 J/g by the room temperature annealing phenomenon. The room temperature annealed sample also shows enhancement of melting peak to 106.9°C, having a gain of 2.2°C. The major gain in DSC melting curve is at 50°C and 107°C as shown in Figure 5.2.2 in which the difference melting thermogram is seen.

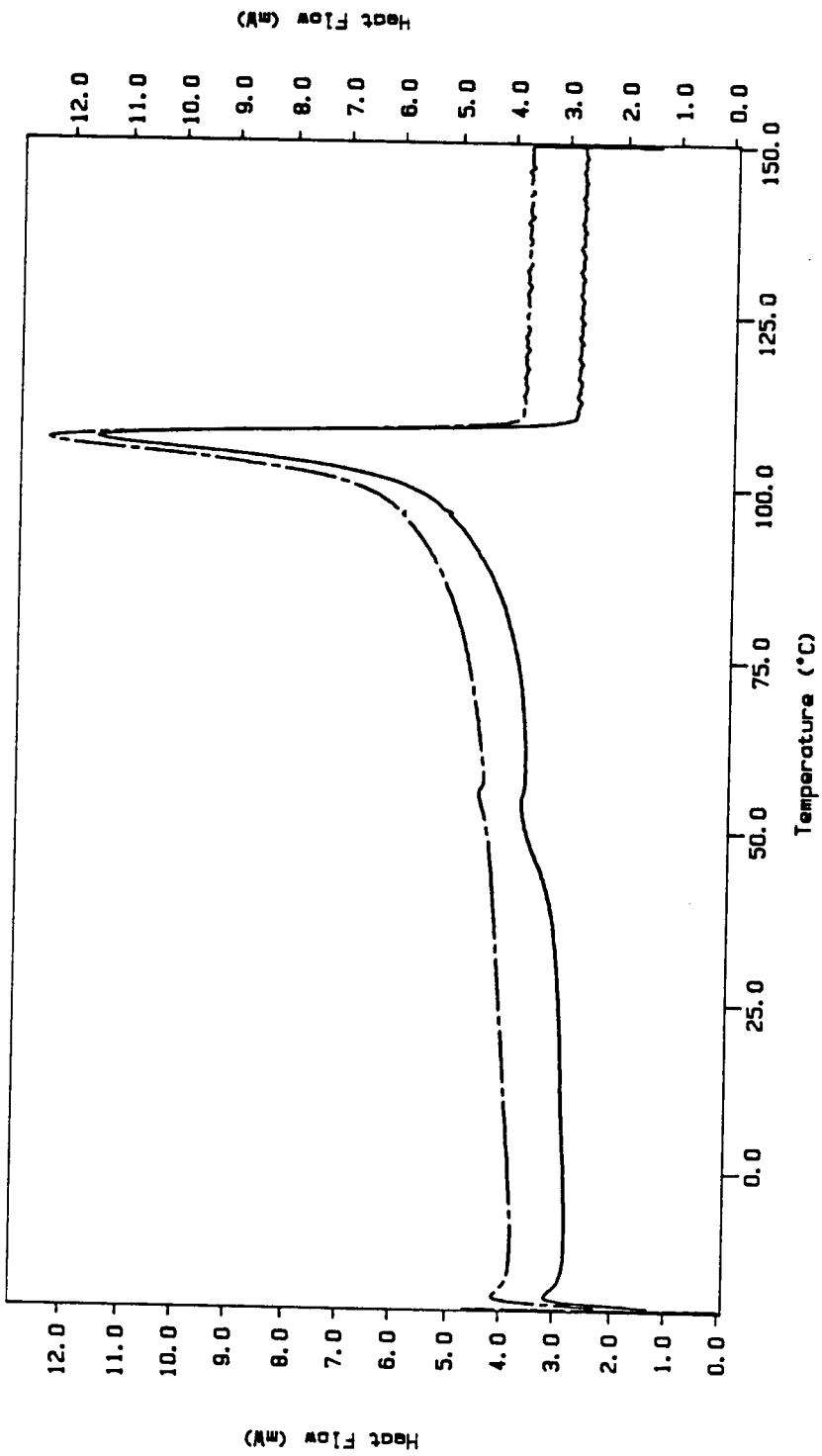



Figure 5.2.1 DSC thermograms of TR-XLPE held at room temperature for two years and quenched in the DSC.

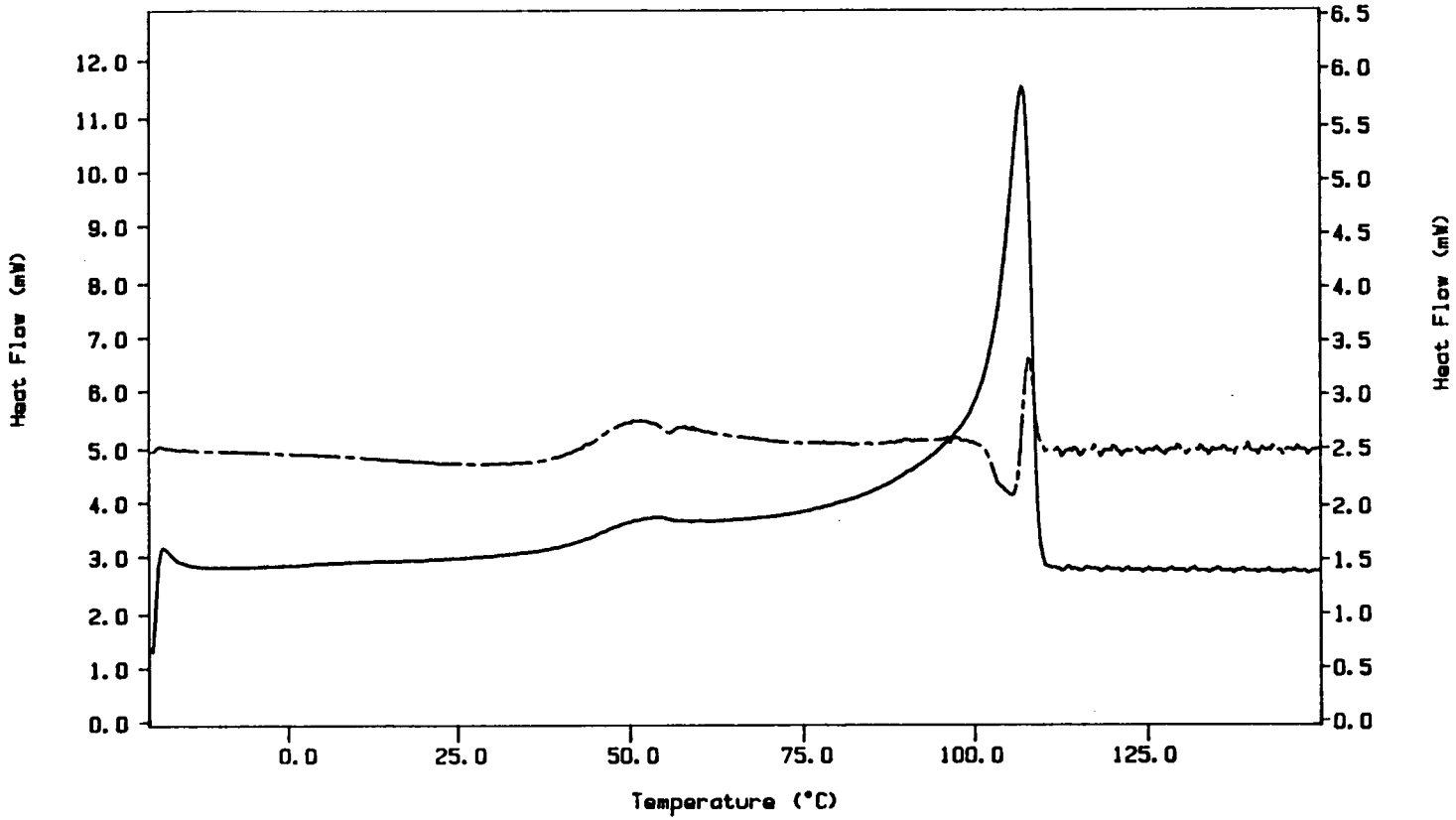



Figure 5.2.2 Difference DSC curve of TR-XLPE held at room temperature having subtracted from it the curve of TR-XLPE quenched in the DSC.

However, either the increment of $\Delta H_f$ or the enhancement of melting peak is not as remarkable as those of the sol or gel fractions.

The gel, as well as the sol fraction, shows the similar features, indicating the crystallites that melt at room temperature did not belong to only one part of XLPE. Figure 5.2.3 shows melting curves of gel quenched within the DSC machine and gel kept at room temperature for nearly 2 years. The smooth melting curve without major humps except one in low temperature range demonstrated that this material was not exposed to any additional high temperatures. However, the unextractable fraction, that is about 82% of whole XLPE, shows a major increase in melting peak up to 107°C, one being kept at room temperature for two years. Quenched network fraction merely shows a melting peak at 104°C. Even more impressive is the increase in heat of fusion, gaining about 37 J/g from 103 J/g to 140 J/g. The increment equals 18% crystallinity, corresponding to a 35% increase in crystallinity from the original quenched network fraction.

The subtracted thermogram presented in Figure 5.2.4 shows the difference in melting curves of the quenched and room temperature annealed gel fraction of TR-XLPE. A major gain was noted in high temperature range beyond melting peak of quenched gel fraction. A minor increase was also noted in the low temperature range that corresponds to the location of low temperature humps (ca. 50°C).

Comparable melting thermograms of the sol fraction of TR-XLPE kept at room temperature for two years are shown in Figures 5.2.5

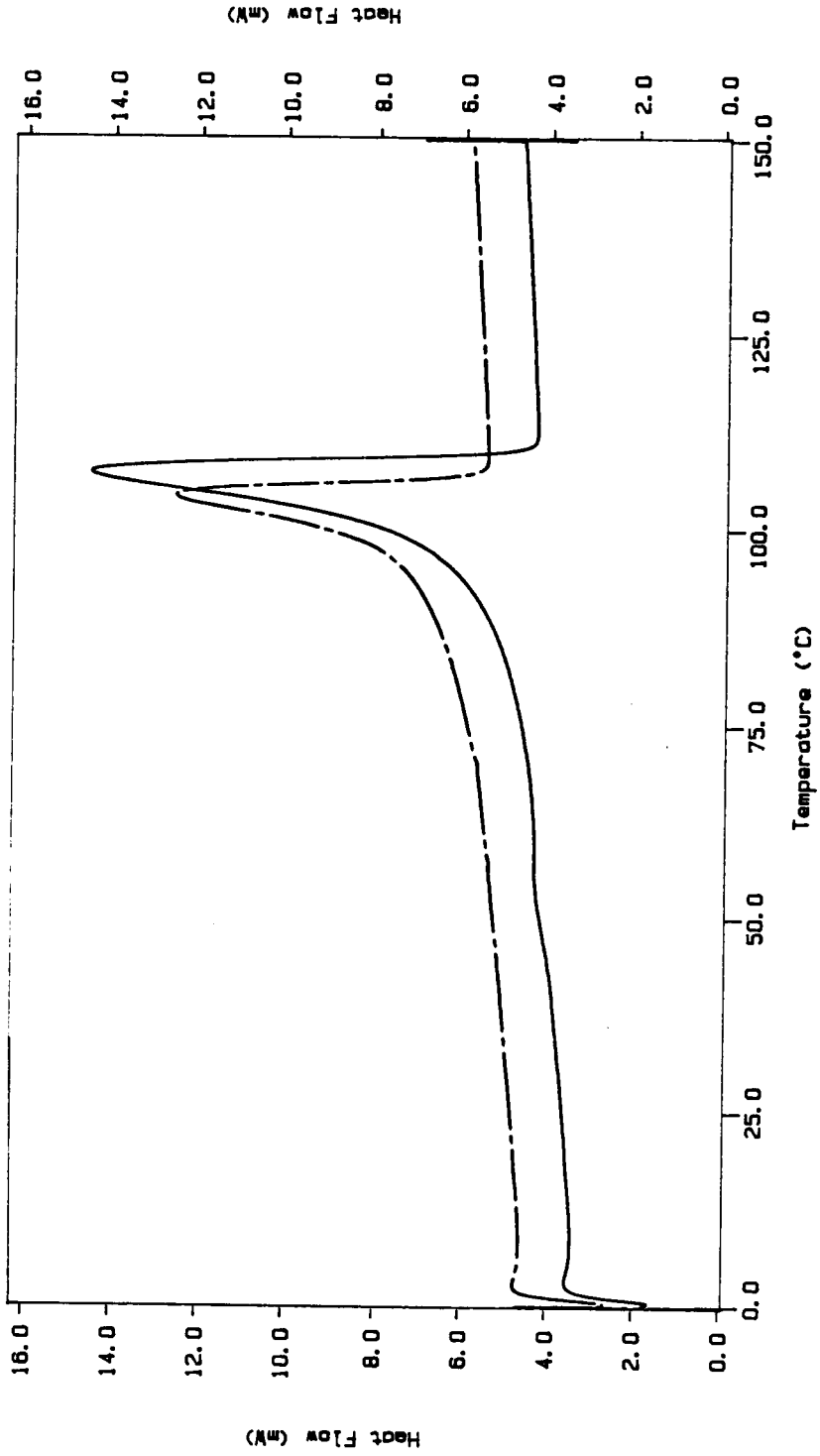



Figure 5.2.3 DSC thermograms of TR-XLPE gel held at room temperature for two years and quenched in the DSC.

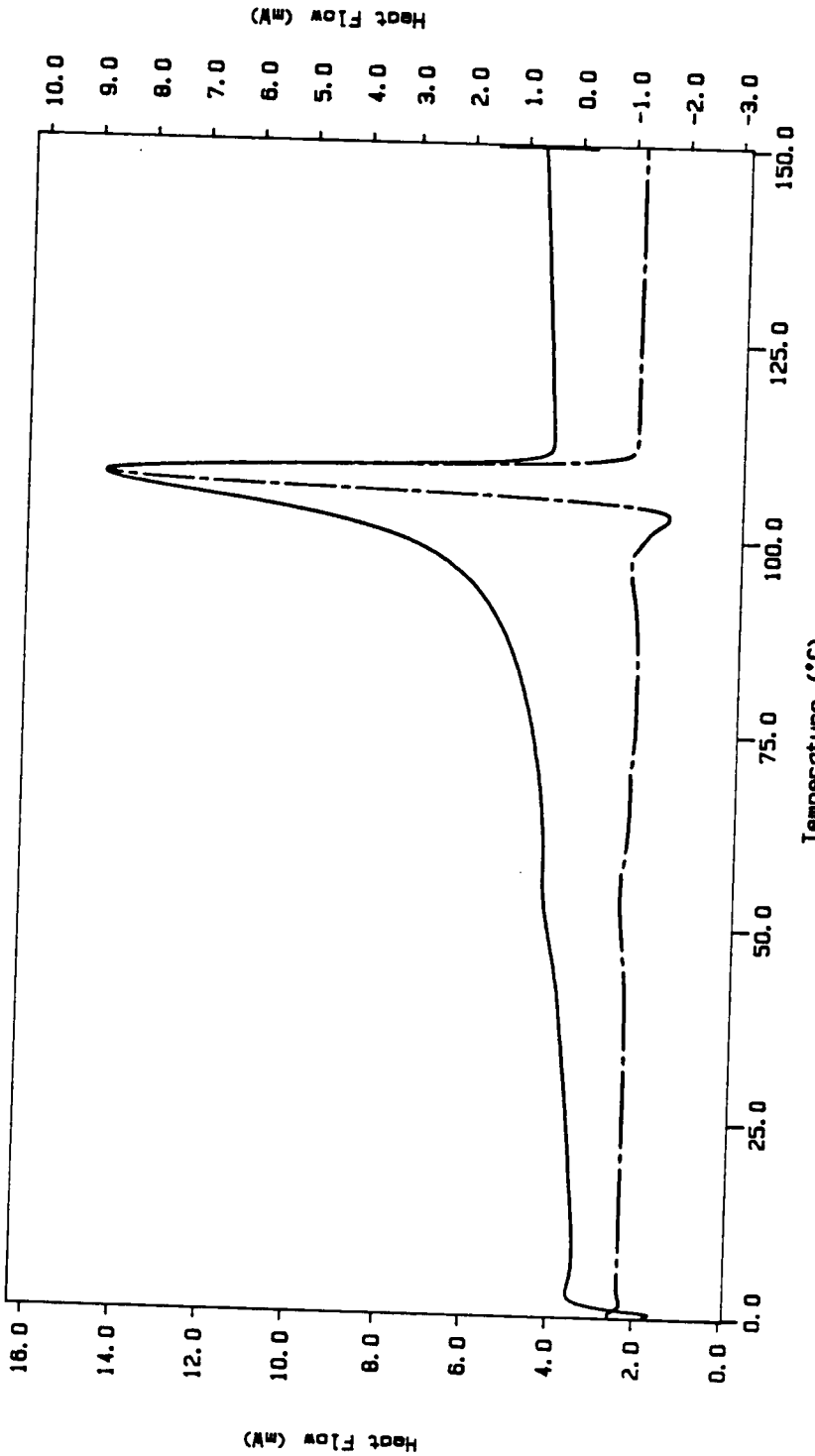



Figure 5.2.4 Difference DSC curve of TR-XLPE gel held at room temperature having subtracted from it the curve of TR-XLPE gel quenched in the DSC.

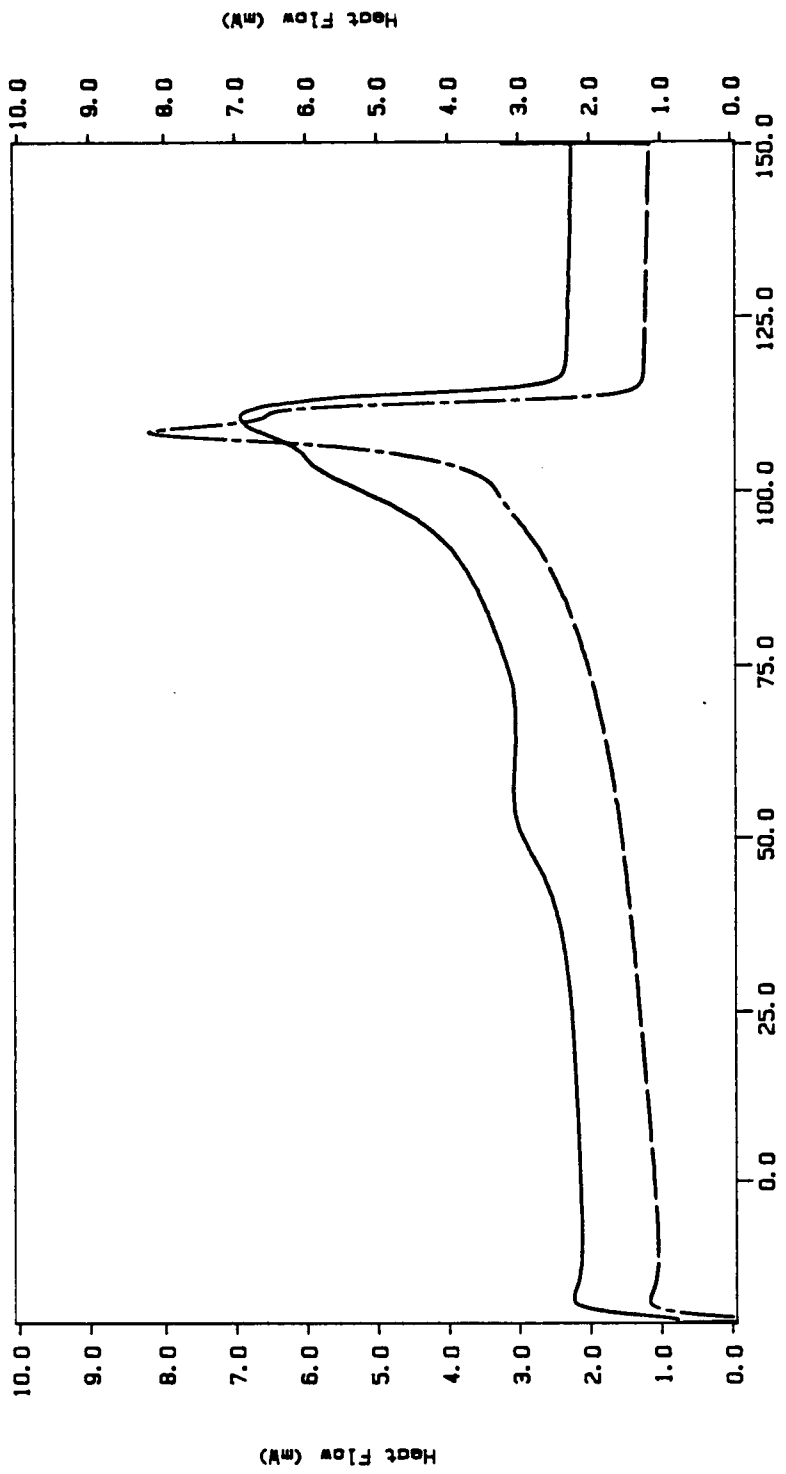



Figure 5.2.5 DSC thermograms of TR-XLPE sol held at room temperature for two years and quenched in the DSC.

and 5.2.6. Opposite to the case of the gel fraction, the melting curves of sol fraction did not show a single peak whether they are for a quenched sample or room temperature held sample. The room temperature annealed sol fraction shows a small peak in 104°C and a major peak at 110°C. The quenched one, however, shows a major peak at 107°C and a small peak at 111°C. The major melting peak of the quenched sample matches the melting peak of the initially prepared sol fraction. The occurrence of a second peak in a quenched sample, that has been kept at room temperature for two years before quenching, clearly suggested that room temperature annealing causes a permanent modification in the morphology. It is of interest to note that the DSC curve of the same sample, measured when it was freshly prepared, showed a slight shoulder in the temperature range of the second peak (see Figure 4.1.11, Page 150).

$\Delta H_f$ for the annealed sol fraction is a little smaller than that of the unextractable fraction, having 134 J/g. The quenched sol fraction, on the other hand, shows 126 J/g of heat of fusion. The difference here is somewhat smaller than that of the unextractable fraction. The subtracted thermogram of these two sol fractions are shown in Figure 5.2.6. A major gain in the difference melting curve by room temperature annealing occurs in two temperature ranges, 104°C and 110°C. These two temperature ranges match well with the two melting peaks which appeared in the annealed sample.

The room temperature annealing phenomenon appears to be due to low temperature melting of submicroscopic crystallites imbedded in a

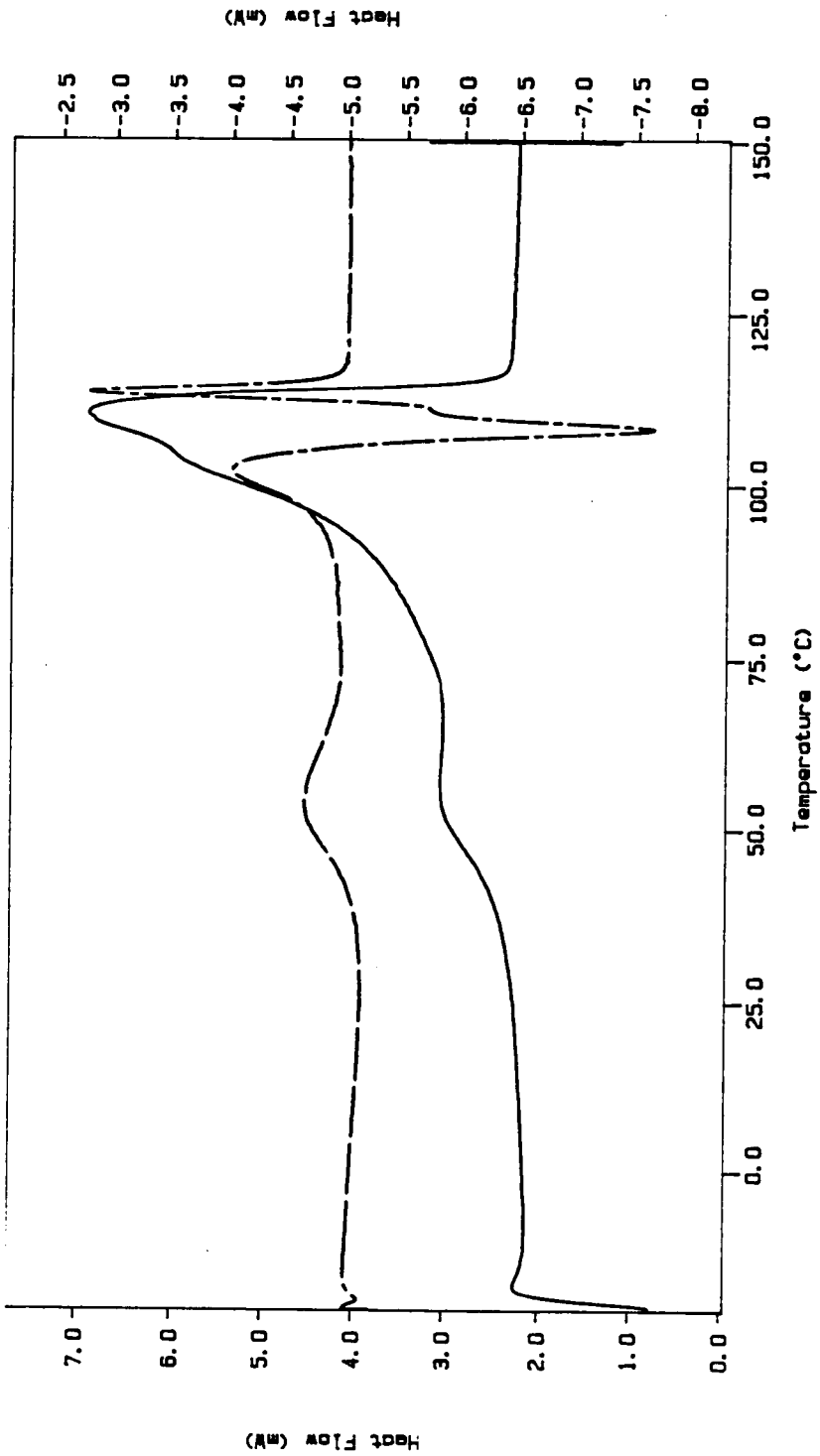



Figure 5.2.6 Difference DSC curve of TR-XLPE sol held at room temperature having subtracted from it the curve of TR-XLPE sol quenched in the DSC.

residual amorphous matrix. Holding XLPE at room temperature may result in melting of these crystallites. Molten submicroscopic crystallites are then recrystallized to form more perfect and larger crystalline regions. Enhancement of melting peak and of the increment of area under the melting curve, beyond the initial melting peak, which appeared in the difference melting curve between quenched and room temperature annealed XLPE, also indicates that the molten small crystallites may be attached to the regular crystalline phase to emerge as more perfect crystalline species.

Even though the detailed mechanism cannot be postulated at this stage, room temperature annealing can be considered to cause a perfecting of crystalline phases embedded in both the extractable and unextractable fractions. The effects of this phenomenon are more noticeable when each fraction is kept separately compared to case of XLPE in which these two fractions are mixed. The major effect of room temperature annealing on the gel fraction excludes the postulate that the submicroscopic crystallites arise only from the short molecules, since most short molecules are extracted in boiling xylene. The overall gain in $\Delta H_f$ indicates that the secondary crystallization or perfection was made not only from the crystalline fraction whose melting peak is below room temperature but also from the amorphous region.

The occurrence of room temperature annealing makes the measurement of genuine melting behavior difficult. Clear evidence of a time effect on this phenomenon requires correct measurement of

holding time at room temperature for the true analysis of melting parameters, in addition to the regular thermal history. Furthermore, annealing was noted even for the sample that was been kept at room temperature for a very short period of time. Finding that the room temperature annealing affects not only the low temperature range but also the higher temperature range of the DSC curves indicates that exclusion of the melting curve below the hump resulting from room temperature annealing behavior is not the only mechanism operating. Thus, direct comparison of melting curves of XLPE can be misleading if the measurement was made without consideration of the room temperature annealing behavior.

The comparison among the melting curves of various XLPE was made for the samples that had been quenched within the DSC machine. There is only a small difference, if any within the limit of experimental error, in the melting thermogram of TR-XLPE from those of the other groups of XLPEs. TR-XLPE shows higher melting peak (104.7°C) than PL-XLPE (104.5°C) or EC-XLPE (104.4°C). TR-XLPE also shows a little higher $\Delta H_f$ (98.2 J/g) than EC-XLPE (96.2 J/g) and PL-XLPE (94.4 J/g). The higher value of heat of fusion of TR XLPE may represent higher crystallinity. The general higher SAXS intensity of this material as well as higher density also support the above measurement. The slightly higher value of heat of fusion of EC-XLPE than that of PL-XLPE appears to be due to the cleanliness of this material. Loss of solid contaminants may reduce the number of nucleation sites.

TR-LLDPE was also noted to show the room temperature annealing behavior. Figure 5.2.7 shows melting curves of a room temperature-quenched sample as well that of material quenched to 0°C within the DSC machine. The sample quenched to room temperature and kept at the temperature shows a higher melting peak (117.6°C) than the one quenched to 0°C (116.7°C). Shifting of the melting peak by room temperature annealing is accompanied by an enhancement of the heat of fusion from 101 J/g to 109 J/g. The two shoulders observed in LLDPE are moved along with the major melting peak by room temperature annealing. The shoulder below the major melting peak moves toward higher temperature and become more noticeable; while the shoulder above the major melting peak becomes weaker by the same phenomenon. This results are more obvious in the subtracted DSC curve shown in Figure 5.2.8.

Chemical structural variations of TR-LLDPE discussed in the previous section can be expected to have a major influence on the crystallization process since molecular segregation, according to comonomer content, is predicted. The difficulty in producing a single broad melting peak on quenching is a symptom of this phenomenon. Only a drastic method such as ethanol- dry ice bath quenching produced a relatively conventional melting peak, however, it was also much broader than is usually observed for LDPEs. Fractionation on crystallization is much more clearly shown in the DSC curve of slow cooled TR LLDPE (cooling rate 2°C/min) (See Figure 4.1.10, Page 148) where one broad peak is located at 109°C along

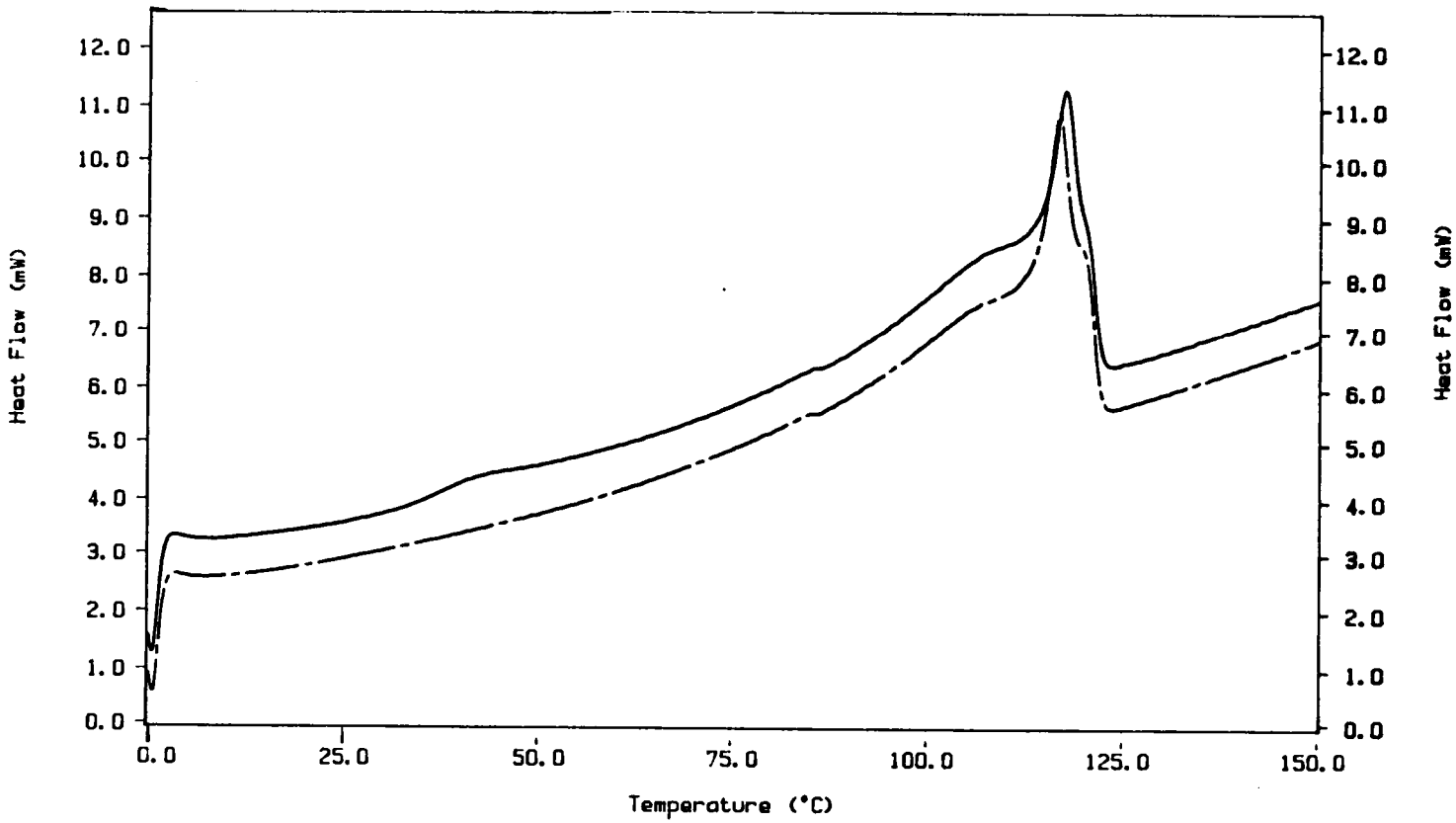



Figure 5.2.7 DSC thermograms of TR-LLDPE held at room temperature for two years and quenched in the DSC.

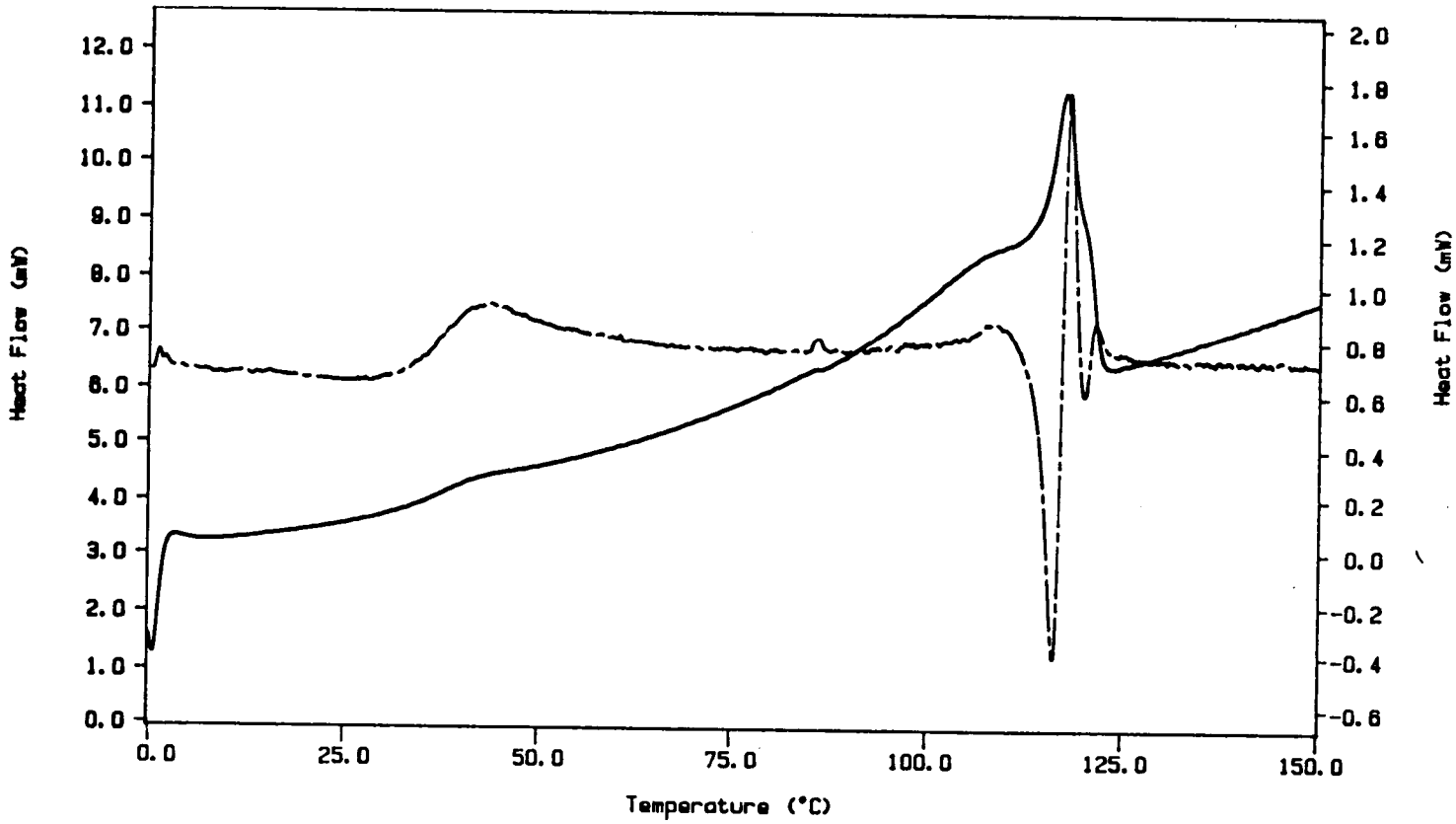



Figure 5.2.8 Difference DSC curve of TR-LLDPE held at room temperature having subtracted from it the curve of TR-LLDPE quenched in the DSC.

with the major sharp peak at 125°C. It is not uncommon, since there is enough time for fractionation during slow cooling. The melting curve of insulation produced from this material is likely to be similar to that produced by a room temperature quenching, i.e. complex. It should therefore show a long tail beginning at room temperature leading to an important shoulder at ca. 105°C, a peak at 115°C and a final end of melting at about 122°C. The consequences of this melting curve are major for thermal aging and perhaps also for useful operating temperature ranges since the insulation is likely to retain its structural integrity up to at least 115°C.

5.2.3. Density Measurement

The density measurement is usually made when the degree of crystallinity by volume needs to be estimated. The solution used in the density column was a mixture of isopropanol and water. There was no observable evidence of swelling or dissolution of the samples. The column was calibrated using the standard beads. The crystallinity by volume calculated from the densities fell into the range of crystallinity determined by the DSC measurement(c.a. 51.3%), ranging from 49.3% to 52.6%.

As shown in Figure 4.1.14, a major apparent feature in density measurement is that the TR grade of XLPE shows the highest density value (0.9213 g/cm$^3$), followed by EC-XLPE (0.9185 g/cm$^3$). PL-XLPE shows the lowest density, being 0.9178 g/cm$^3$. This finding matches well with the heat of fusion measurement by DSC. Similar differences

in density were also seen among uncured LDPEs and the gel fractions of the crosslinked materials.

The high density value of TR-XLPE seems to be due to the presence of chemical additives to the material. For this speculation to be plausible the density of the additive has to be larger than the density of the material. For example, if the additive are 10% of the whole TR-XLPE, then the additive must have a density of 0.953 $g/cm^3$. The other possibility is that the TR grade has fewer voids or the voids, if any, must be filled with other materials. The density measurement is based on the densities of whole material content including voids. However, similar values of crystallinity from density measurement and DSC may mean that void content is not significant, because during the crystallinity calculation the material is assumed to consist of only two fractions, crystalline and amorphous regions, each having a density of 1.0 and 0.85 $g/cm^3$. The finding of a slightly higher crystallinity value for EC-XLPE compared to PL-XLPE may suggest that the cleanliness of the resins does not only affect the solid contamination level but also influence some other material parameters affecting crystallization kinetics to some degree.

### 5.2.4. Wide Angle X-ray Study

Wide angle x-ray diffractometry was also utilized for the evaluation of crystallinity. The degrees of crystallinity calculated from the WAXD intensity peaks are the crystalline fractions by

weight. WAXD scans did not show any shift of Bragg peaks among the XLPEs, having 110 and 200 crystalline peaks and an amorphous halo.

The degrees of crystallinity obtained by WAXD show that TR-XLPE has higher crystallinity than the PL-XLPE as shown in Figure 4.1.16 (Page 158). This finding also matches the findings made by DSC and density measurement. TR-XLPE shows 52.3% crystallinity, while the degree of crystallinity of PL-XLPE was 51.9%. The difference in crystallinity measured by WAXD techniques for these two materials is smaller than those measured by DSC or density measurement. However, the value of crystallinity here is found in a similar range to that obtained by the other methods.

Without knowing the exact chemical formula of the additive, it is rather difficult to describe the mechanism behind the effects. However, the larger density may be attributed to the filling-up mechanism of the chemical additives or some part of them into voids generated during curing process. The other mechanism that cannot be excluded is that the polymer chains that have been pre-bonded to the chemical additives play a role as nucleation sites, leading to additional crystallization.

5.2.5. Small Angle X-ray Study

The comparison of SAXS plots from four different polyethylenes illustrated in Figures 4.3.2 (see Page 187) and 4.3.3 (see Page 188) discloses the different nature of the morphologies in these four polyethylenes. LLDPE, XLPE or LDPE did not show the second order Bragg maxima present in HDPE. This finding caused by the

crystallinity of this material being very near to 50%, since the second maximum is present when the volume fraction of one entity is either larger or smaller than 0.5 (Schultz, 1978).

The SAXS plots of XLPE and LDPE are characterized by well-defined broad Bragg maxima, indicating the presence of stacking of two entities with different electron densities, presumably amorphous and crystalline layers. Roughly speaking, the broadness of the Bragg peaks of XLPE or LDPE compared to HDPE tells us that these materials have wide distributions of crystalline and amorphous layers. As described in Sections 4.4. and 5.1, this broadness cannot be described by a single distribution within the system, contrary to the case of HDPE. The SAXS model study clearly shows that the double range distribution is necessary for better understanding of this type of scattering curve. The double range distribution can be considered to be a distribution of layers within a stack combined with a distribution of crystallinity among the stacks consisting of crystalline and amorphous layers. The intensities for a scattering vector of 0.02 $Å^{-1}$ and lower are also related to these double range distributions.

The results of room temperature annealing can be noted by the SAXS measurement. Figure 5.2.9 shows the SAXS intensity curves of two TR-XLPEs, one being measured after 2 years of holding at room temperature. Since the intensity level depends on experimental parameters such as voltage and current of the x-ray generator, exposure time, alignment of sample within X-ray beam path, thickness

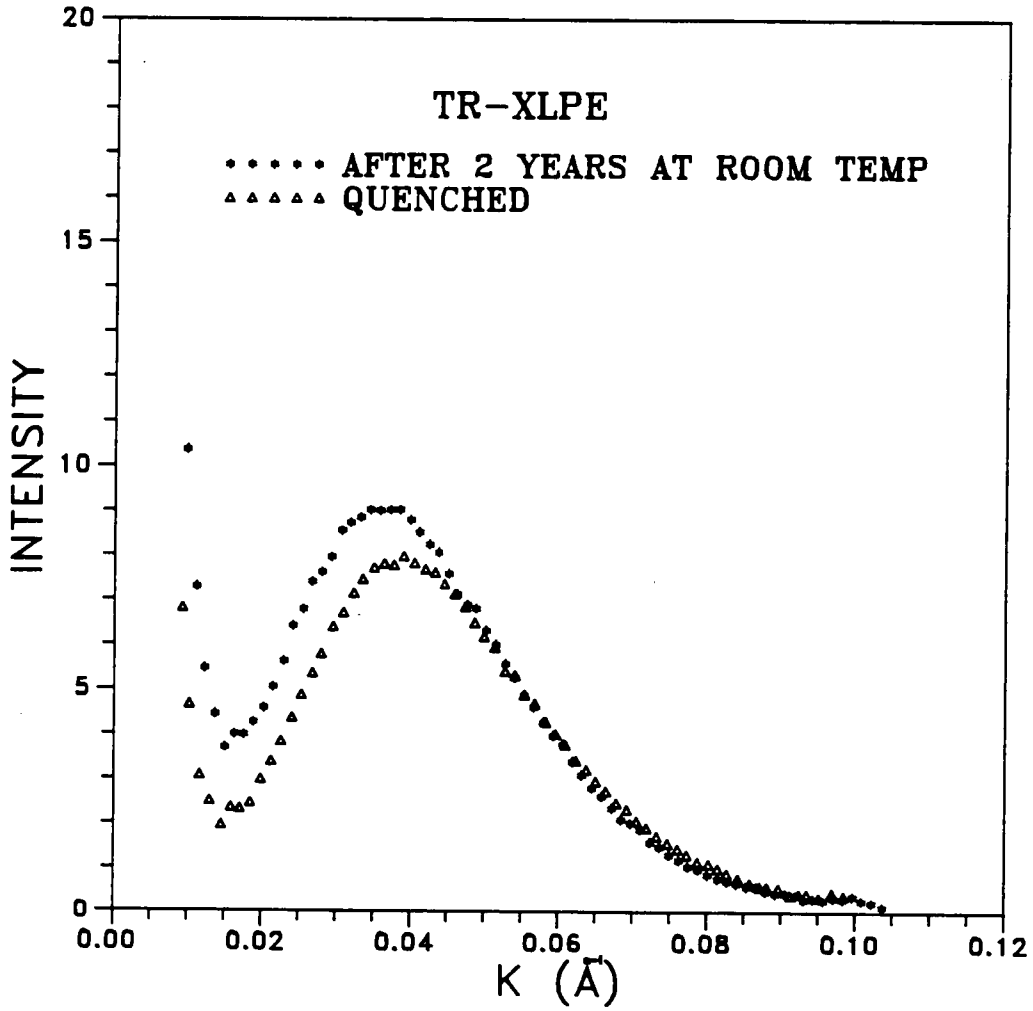



Figure 5.2.9 SAXS intensity curves of TR-XLPE held at room temperature for two years and quenched in the DSC.

of sample, direct comparison can contain errors. Nonetheless, with the proven information that the tails of the SAXS intensity curves are not very sensitive to any degree of annealing, an approximate modification is possible. The SAXS intensity curves from the room temperature annealed sample show higher intensity in the lower angle region. Moreover, the location of peak moves toward a lower scattering angle, indicating an increase in long periodicity. This can be interpreted using two possible mechanisms: (a) the increase of crystallinity variation between stacks and/or (b) the refinement of layer thickness variation within each stack. Further theoretical consideration of the point can be found in Section 5.3.

The difference between SAXS intensity curves of the different XLPEs is minimal, except for the level of scattered intensity especially at the peak as noted in Figure 4.3.8 (Page 194). The TR-XLPE shows a relatively lower intensity than the other XLPEs. This difference is directly related to difference of SAXS invariant that, in turn, is related to crystallinity. Other experimental results strongly suggest that the TR grade of XLPE have has crystallinity than the others. The lower level of intensity also can be attributed to higher crystallinity. However, the decrement here also can be correlated with the decrease of crystallinity because of the nature of the SAXS technique (i.e., The Babinet principle). The invariant equation shows that the integrated SAXS intensity is a function of the square of the density difference and the volume fraction of one phase. When the value of crystallinity is 0.5, the difference of

integrated SAXS intensity, therefore, can be interpreted as either an increase or a decrease of the volume fractional ratio of one phase.

SAXS curves of LLDPE can be easily distinguished from the rest of polyethylenes. LLDPE shows relatively higher intensities near the zero-angle region, and its Bragg maximum is not as easily distinguished as in the others. The overall SAXS intensity curve of LLDPE appears like a monotonically decreasing slope with a small hump-like Bragg maximum. However, the Lorentz corrected curves are similar to those of LDPE or XLPE, having a distinct major single peak without high intensities near the zero-angle.

Such patterns as the ones in the unmodified SAXS curves of LLDPE can considered to be due to the presence of poorly defined stacking structures, heavy contribution of particle scattering or the presence of a very wide distribution. The first consideration can be ruled out because of the stacking nature of LLDPE crystallites that must be better stacked than those of LDPEs or XLPEs due to the presence of a greater number of linear molecules. The second possibility is implausible. XLPEs must have more causes of particle scattering than LLDPE due to the necessary step of crosslinking. Crosslinking, if done without pressure, forms a large amount of visible bubble-like defects throughout the sample due to the generation of gaseous by-products. Therefore, the main cause of the not-so-well defined Bragg maxima and high intensities near the

zero-angle region appears to be due to the wide distribution of morphological parameters within the system.

In facts, the SAXS model study, as discussed in Section 5.1, clearly shows that a wide distribution of crystallinity among the stacks can cause such a scattering curve. Such a feature is more prominent when the distribution of layer thickness become more narrow while the crystallinity distribution remains constant. This speculation is not at variance with the nature of LLDPE morphology, since LLDPE is a copolymer having a wide range of copolymer contents according to the branch levels. Crystallites having similar contents of comonomer units will be assembled together during the crystallization process, because of differences in the melting and crystallization temperatures. The fractions with more linear chain will crystallize at higher temperatures, while those with more branched molecules will crystallize at lower temperatures. The group of stacks that crystallize first will have thicker crystals, leading to a high crystallinity. Other fractions will crystallize with thinner crystals. The separate crystallization mechanism will help the formation of a somewhat narrower distribution of thicknesses within each stack.

Thus, it is quite natural that the stacks with higher crystallinity will have a larger long periodicity. This postulate leads to definite wide distributions of long periodicities. Normally, the mean long periodicity obtained from unmodified SAXS curves can be misleading, as discussed in Section 5.1. The mean long

periodicity calculated from the unmodified SAXS curve is 212 Å, while that from the Lorentz corrected data was 137 Å. On the other hand, HDPE shows a long periodicity of 287 Å from the uncorrected curve, and 244 Å from the Lorentz corrected curve. From now on, most dimensional measurement will be based on the Lorentz-corrected SAXS intensity, since all material dealt with in this study can be considered to have non-symmetric entities, mainly lamellar structures.

Room temperature annealing was also affected SAXS results for the TR-XLPE sample. The SAXS intensity curves of freshly prepared sample and the sample kept at room temperature for more than two years are seen in Figure 5.2.10. The each curve has been modified by multiplying factor so that the tail slope is almost matched. The annealed sample clearly shows a better developed Bragg peak at lower scattering angles. This finding can be correlated well with the DSC finding of room temperature annealing leading to a better refined morphology.

5.2.6. Dielectric Property and OIT Measurements

It has been claimed that TR-XLPE is more resistance to electrical aging than the EC-XLPE by Turbitt (1985) and Chan (1984). They also reported that TR-XLPE has a higher breakdown strength in its original state. The summary of Chan's experimental results are shown in Figures 5.2.11 and 5.2.12. TR-XLPE has a 6% higher initial breakdown strength than EC-XLPE (Figure 5.2.11). As shown in the preceding chapter, results of electrical breakdown strength tests

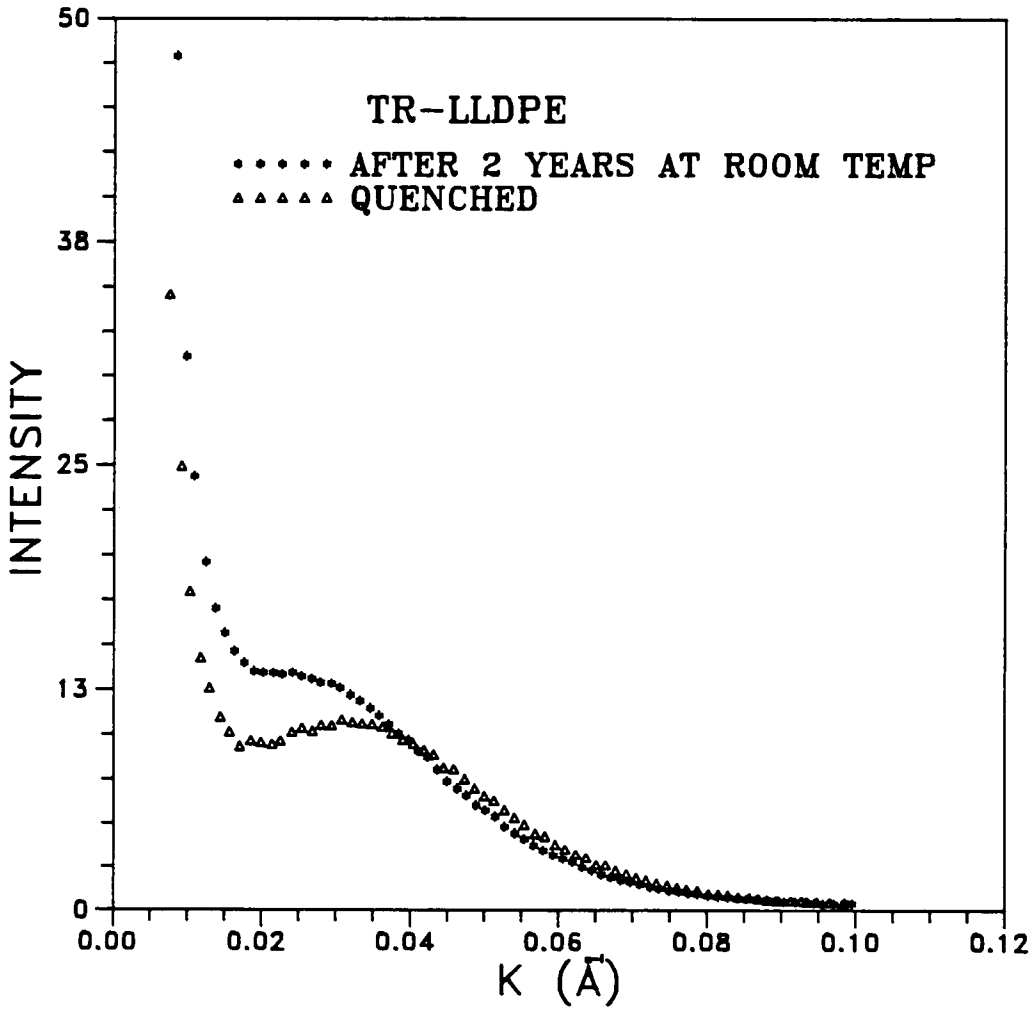



Figure 5.2.10 SAXS intensity curves of TR-LLDPE held at room temperature for two years and quenched in the DSC.

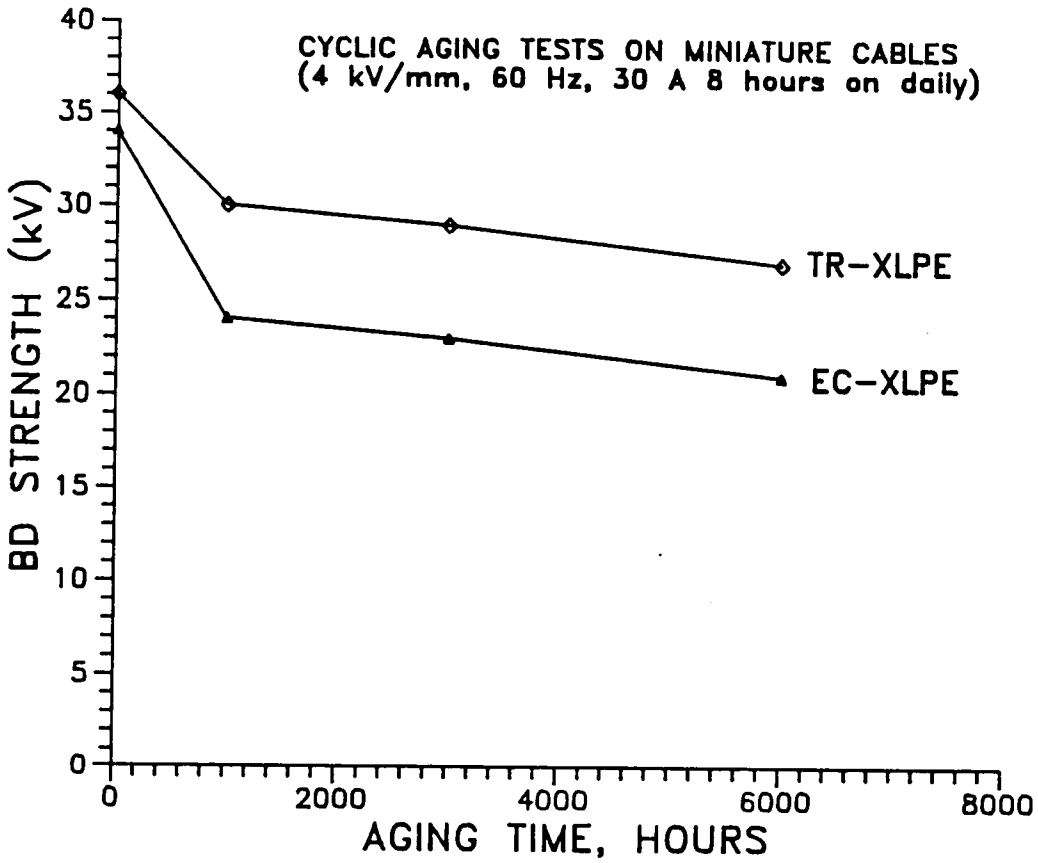



Figure 5.2.11 Variation of BD strength of TR-XLPE and EC-XLPE with aging time. (Source: Chan, 1985)

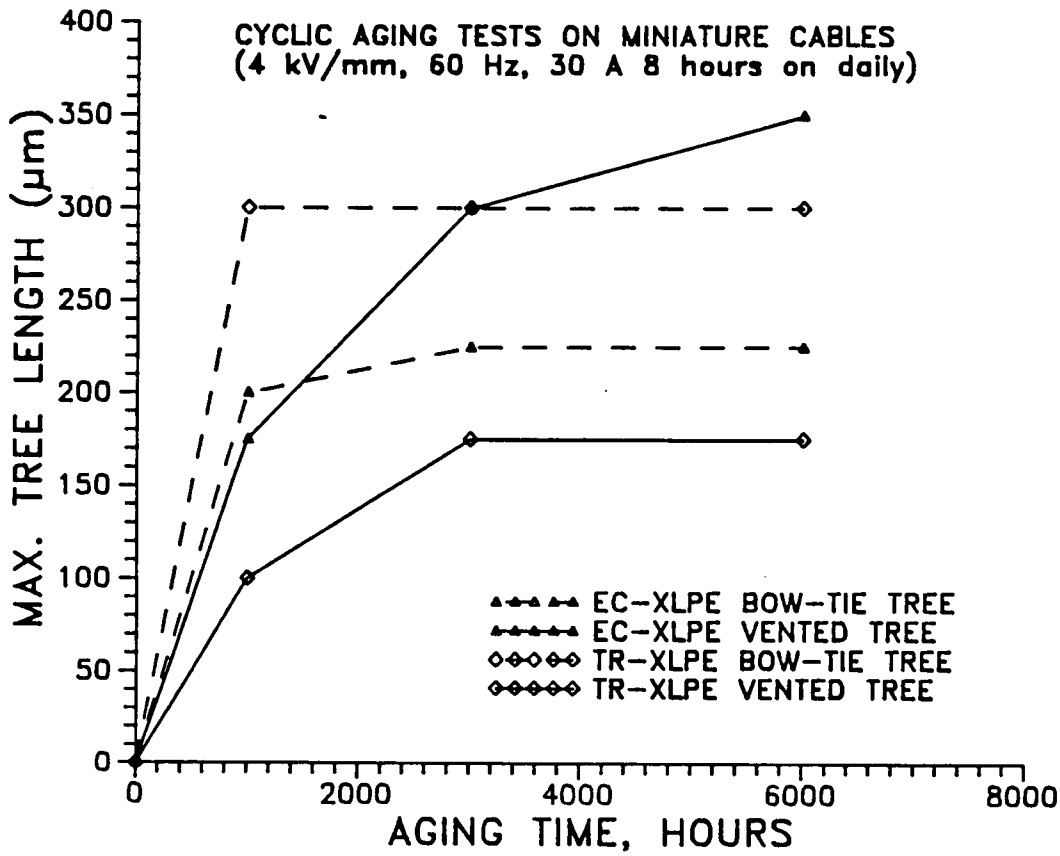



Figure 5.2.12 Variation of maximum tree length of TR-XLPE and EC-XLPE with aging time. (Source: Chan, 1985)

(see Figure 4.5.1, Page 279) also agree with their results. Since the major difference between TR XLPE and normal XLPE is the presence of the chemical additives, the enhancement of the electrical properties is due to the additive. Moreover, the OIT analysis shows that TR grade polymer exhibit a longer OIT. Therefore, it can be concluded that the chemical additive has dual functions- antioxidant and tree retardant. Effective antioxidant, in fact, can increase the breakdown strength, since at least part of the damage by electrical breakdown is considered to be generated by oxidation. Detailed discussion of this point is found in Section 5.5. The yellowish tint of TR-XLPE indicates that the chemical additive has a tan color. This color darkens when the material is annealed.

It is also known that electrical rupture and associated damage can be characterized as a thermo-oxidative degradation process (Gorton, 1987, Shimizu, 1988). Since antioxidant normally works as an electron acceptor, it provide some voltage stabilizing activity in addition to its normal role of retarding polymer oxidative degradation. Some part of this additive may also fill up any voids formed during the curing process, as indicated in higher crystallinity of TR-XLPE by density and other crystallinity measurement.

Another striking feature to note is that the additives are strongly bonded to the polymer chain, as demonstrated by the presence of the same absorption bands in the spectra of uncured LDPE, cured XLPE, sol and gel. Sol-gel separation is carried out at

the boiling temperature (139°C) of xylene. This indicates that the chemicals bonded to the polymer chains are still intact at such a high temperature. This strongly bonded chemical will not diffuse at high temperatures or under other conditions unless it breaks off the chain. Thus, TR-XLPE will retain higher dielectric properties and tree resistance.

It is not known how the different thermal behavior of TR-LLDPE will influence dielectric breakdown and tree resistance. Studies on XLPE showed that annealing below the melting peak resulted in considerably reduced tree resistance and dielectric breakdown strength (Phillips, 1988). Annealing above the melting peak produced an enhanced breakdown strength. If such a situation recurs here, the breakdown strength might be reduced for annealing temperatures up to 115°C, whereas for XLPE improved properties resulted for annealing at 100°C and above. Conversely, annealing at 90°C and below may have little effect on LLDPE. Only additional experimentation can resolve the issue.

### 5.2.7. Effect of Crosslinking

Two of the prime effects of thermal crosslinking are known to be the suppression of melting point and reduction of crystallinity. DSC results show that XLPE has a lower melting temperature (ca. 104°C) than uncured LDPE (107°C). It was also revealed that XLPE has a lower heat of fusion (ca. 96 J/g) than LDPE (ca. 104 J/g). These findings conform well to the earlier findings by Kao and Phillips (1986). The values of crystallinity determined by other methods such

as density measurement and WAXD also shows that once cured, the material shows lower values of crystallinity. These results may support assumption that the peroxide curing is a homogeneous process, resulting in uniform crosslinking throughout the material. The crosslinks act as defects within the crystallizable melt and result in smaller crystals. Eventually, the crosslinking tie molecules reduce the mobility of the molecular chains within the melt and hinder the crystallization process, leading to a lower crystallinity.

However, it is of interest to note that curing and subsequent cooling in the compression molder with circulating cold water inside the platen results in similar effects to those of annealing, as shown by the SAXS study. Once cured, the sample shows an increase in long periodicity and overall intensity as well as a sharpening of the Bragg peak compared to the uncured one with subsequent quenching.

The long periodicity obtained from the Lorentz-corrected SAXS curves falls in the range of 120-126 Å. The long period spacing is known to be an average value of total thickness of crystallites and amorphous portions, provided that a model consisting of alternating crystalline and amorphous regions in the direction of lamellar axis is appropriate. Uncured LDPE shows a smaller value of long period spacing than the cured one. For example, he Lorentz-corrected long periodicity of TR-XLPE was found to be 126 Å, while that of uncured TR-LDPE was 120 Å. It is known that the Lorentz correction is

necessary for scattering entities of anisotropic geometry such as lamellar structure (Crist, 1973).

With the aid of crystallinity measured using the DSC, the average thicknesses of crystalline and amorphous layers can be calculated. Uncured TR-LDPE which has been exposed to room temperature shows a typical value of heat of fusion of 112 J/g, leading to a crystallinity of 55%. Typical TR-XLPE having a similar thermal history, on the other hand, has 51% crystallinity. Based on these numbers of crystallinity and long periodicity from the Lorentz corrected SAXS data, crosslinking leads to a decrease in crystalline thickness from 66 Å to 64 Å and increase in amorphous thickness from 54 Å to 61 Å. The crystalline thickness is considerably smaller than the lamellar thickness (140±20Å) for similar material that has been crystallized at 103-5°C reported elsewhere, utilizing TEM (Gohil and Phillips, 1986). The measurement by direct observation does not necessary lead to the dimension of lamellar perpendicular to the lamellar surface.

Figure 4.3.4 (Page 190) also reveals some additional information about the macro-structure of the samples. The area under the scattering intensity curve within the range of up to 0.02 $Å^{-1}$ of scattering vector represents weight fractions of large entities in the size range of 250 to 1500 Å, such as thick crystalline fractions, microvoids or impurities embedded inside the material. As was discussed in the previous section, even small concentration of entities in this range will affect intensity. The intensities of the

cured samples in this region are higher than that of the uncured sample, indicating increased contents of such entities.

Another note to be made is that the levels of SAXS intensity of the cured samples are higher than the counterparts of the uncured LDPE samples. The scattering invariant for the cured sample was found to be also higher than that of uncured LDPE as shown in Figure 4.3.5 (Page 191). However, increase of intensity level or invariant alone is not adequate for the estimation of crystallinity. The invariant simply reflects the fractional ratio of one phase and the difference of electron densities of the two phases, due to the Babinet principle.

The major increase of amorphous thickness by crosslinking may be due to the reduced mobility of molecular chains. During the cooling process, the introduction of 80% gel fraction will increase nucleation sites and pre-existent tie molecules which are an inherent feature of the crosslinked system and restrict the attainment of full crystallization as occurred in LDPE. Thus, crystal fractions that crystallize at lower temperatures may more likely be trapped in the amorphous layer rather than being attached to the surface of existing crystals compared to the uncured system.

These trapped crystallites are not necessarily from low molecular weight materials. In fact, sol fractions, which are known to be a short molecules, are crystallized much more quickly than networks. It is possible that these submicroscopic crystallites are more highly branched than the other part of the XLPE, since branch

level, especially short chain branching, is known to be one of main parameters that governs the melting point as well as crystallinity regardless of the molecular weight (Wild, 1982). It is also possible that a fraction of these branched chains are involved in crosslinking. The branching level is much greater than the crosslinking level in XLPE with 20% extractable ratio (Kao and Phillips, 1986). An easier attack of crosslinking agent on the branch points also supports the idea that the gel fraction has more branched material than the sol fraction. At least some of these highly branched polymer chains will be excluded to the amorphous region even though they enter submicroscopic crystallites trapped in the amorphous region.

In the solid state, some of these embedded submicroscopic crystallites will melt even at room temperature. Partial melting will increase the mobility of the neighboring. Highly mobile chains will reorganize to form either higher crystalline fraction or to be added to neighboring crystallites having high melting temperatures.

These speculations can be extended to other systems such as LLDPE and LDPE, where a noticeable distribution of short chain branching has been reported (Wild, 1982). Having a wide distribution of short chain branching, there is always some fraction which forms submicroscopic crystallites trapped in amorphous region. They may be locally segregated during crystallization, part of the molecules forming amorphous regions. Thus, secondary crystallization can easily happen even at room temperature.

There is another possible explanation for the effects of curing on SAXS results being similar to the effects of room temperature annealing. Unavoidable exposure to room temperature after molding or curing might affect the SAXS results. It was noted that XLPE is more susceptible to room temperature annealing than LDPE, mainly because of the larger fraction of low melting crystals that originates from the gel fraction. A higher susceptibility to room temperature annealing means that for a given time the XLPE will encounter more annealing. The DSC data indicate that the room temperature annealing affects not only low melting temperature region but also the crystal fraction having higher melting temperature. Thus, even room temperature can cause annealing effects in high melting fractions.

Another interesting point is regarding the material parameters of the gel fraction. In the literature, it has been noted that the gel fraction has lower crystallinity than the crosslinked material (Kao and Phillips, 1986). On the other hand, Vatansever (1987) reported that gel fractions of original and field aged XLPE cable have up to 14.6% more crystallinity (53.8% crystallinity) than XLPE cables (39.2% crystallinity) that has about 80% of gel fraction. These contradictory results are not surprising, since the gel fraction is most susceptible to the room temperature annealing phenomenon. The gel fraction of TR-XLPE that has been at room temperature for more than two years has a heat of fusion of 140.4 J/g, corresponding to 69% crystallinity. Once quenched from

the melt to 0°C within the DSC, the gel fraction however shows 103 J/g and 50.8% crystallinity. Thus, without knowledge of the room temperature annealing time, the comparison of the number may be unreal. To make things worse, most former investigators studied melting ranges using the DSC only beyond 50°C, excluding the humps caused by the room temperature annealing phenomenon. This factor may be the reason for difficulties associated with measurement of crystallization temperature dependence of the melting point of the gel fraction reported by Kao and Phillips (1986).

The value of crystallinity of gel fraction by DSC is slightly higher than that of XLPE itself, which has 48% crystallinity for a quenched sample. Other experimental data also support this finding, except for one material, with WAXD where the accuracy is not so high due to the small size of the small crystalline peaks and amorphous halo. High crystallinity indicates easier crystallization of gel fraction in the absence of extractables. The sol fraction may act as a barrier to the crystallization of gel fractions, since the sol fraction starts to crystallize first. Meantime, the network may be self-crystallized by itself acting as nucleation site. Thus, the crystallization of XLPE can be characterized as co-crystallization of two fractions having different crystallization kinetics (Phillips and Kao, 1986).

## 5.3. Annealing of Polyethylene

### 5.3.1. DSC Study

It was noted that most annealed samples generate either another peak or a shoulder at a temperature just above the annealing temperature (Karakelle, 1986). The DSC data shown in Figures 4.2.1 (Page 162) and 4.2.2 (Page 163) support these findings. At the annealing temperature the crystalline fractions having lower melting temperatures than the annealing temperature will melt, while the fraction having a higher melting peaks will remain as a crystalline state. The molten fraction can be considered as two different fractions. Some fractions can isothermally crystallize at the annealing temperature but, other fractions will stay molten and re-crystallize upon cooling. The fraction which isothermally crystallizes at the annealing temperature will change the shape of the melting curve. Shifting melting peak and changing mode of melting curve shapes, however, suggests that the isothermally crystallized fraction can be added to the crystalline fraction having a melting temperature slightly higher than the annealing temperature, thus generating a shoulder or a peak. It is also possible that the isothermally crystallized fraction can be added to the already existent crystals.

In this discussion, attention will be paid to annealing at the temperature of 107$^{o}$C, in which most of the network structure will be a molten state as indicated in Figure 4.1.11 (Page 150) and some other works (Phillips, 1984; Karakelle, 1987). Annealing at this

temperature is also known to affect the treeing phenomenon (Phillips, 1984). Even though the gel fraction of XLPE is thought to be completely molten at this temperature, annealing for as little as 30 minutes generates a second melting peak at about 110oC. The main mechanism for this behavior has been proposed as melt separation, presumably separation of sol fraction from the network, followed by separate crystallization on cooling.

Interestingly, the size of the new peak increases logarithmically with annealing time. On the other hand, the peak located below the annealing temperature reduces its size and the peak location temperature. This time effect suggests that the crystal fraction having a higher melting temperature can grow at the expense of the crystalline fractions located below the melting temperature. However, the increase of the total heat of fusion also suggest that secondary crystallization from the amorphous area is also happening. Further discussion regarding the origin and procedure of possible melt separation will be given in Sections 5.3.4 and 5.4.

A minor difference between the crosslinked polyethylenes lies in the magnitude of the high temperature peak produced by high temperature annealing (e.g., 107oC) of the tree-retardant material compared to normal XLPE. It is, reproducibly, of slightly higher magnitude suggesting that it is slightly easier for sol-gel separation to take place in the melt than in EC-XLPE. The chemical

differences between the sol and gel phases might provide the extra driving force in free energy difference needed (Phillips, 1989).

Annealing causes major changes for TR-LLDPE (see Figure 4.2.2, Page 163). Although a low temperature hump appears, symptomatic of material that cannot isothermally crystallize at the annealing temperature, it is not of major significance unless the temperature is greater than ca. 115°C. Hence most of the material re-crystallizes during annealing, in contrast to XLPE. The production of the hump coincides with the emergence of a sharp high melting peak. The temperature of this peak is very sensitive to the annealing temperature, generally being located ca. 3°C above the annealing temperature.

The LLDPE annealed at 120°C, where a complete melt can be expected, shows a sharp melting around 124°C. TR-LLDPE however is not a blend of sol and gel as is the case of XLPE. Nonetheless, it is similar in appearance to the peak observed in XLPE annealed at ca. 107°C. In all likelihood it is produced by the most linear molecules present and indicative of fractionation according to branching. Since the temperature of the peak is sensitive to annealing time (Figure 4.2.4, Page 166), it is likely that the crystals are able to thicken appreciably. The SAXS data show this effect very clearly, but will be discussed later.

### 5.3.2. Density measurement and Wide Angle X-ray Study

Crystallinities of the four polyethylenes annealed at 107°C in air were determined from density measurement and wide angle x-ray

diffraction pattern. The density variation shown in Figure 4.2.5 (Page 167) corresponds to a variation of crystallinity from 49.3% to 51.8%. Interestingly enough, the variation of crystallinity based on density of each annealed sample has a quite narrow range compared to the variation of crystallinity from DSC. For example, EC-XLPE shows 49.7% crystallinity for a fresh sample and 50.5% crystallinity for the sample aged for 30 hours. Even TR-XLPE shows a variation from 51.6% crystallinity to 52.2% crystallinity. All crystallinity was determined based on the theoretical density of 100% crystal (1.0 g/cm3) and 100% amorphous regions (0.85 g/cm3 at room temperature).

Such narrow variations of crystallinity may indicate that during the annealing process voids are generated within the system. Increase in void volume fraction has been considered to be one of the main effect of annealing in HDPE (McHugh, 1971) for XLPE (Namiki, 1980). However, these investigators also reported the filling of voids with thickened portions of adjacent crystals, thus forming sharp-crack like defects. Another possibility is a change in the intrinsic densities of the amorphous and the crystalline regions. For this speculation to be plausible the density of the amorphous region has be little smaller. For example, the density value of 0.8419 $g/cm^3$ for the 100% amorphous phase and the crystalline density of 1.0 $g/cm^3$ will give a reasonable range of crystallinities comparable to the DSC crystallinities.

The results from WAXD measurement also suggest that annealing at 107$^oC$ increases crystallinity. The variation of crystallinity by

WAXD is somewhat larger than that by density determination, ranging from 51.1% for unannealed PL-XLPE to 53.7% for fully annealed EC-XLPE. However, the range of the crystallinity values is slightly smaller than that of DSC measurement, even though the values are vary similar. The WAXD crystallinity is based on the volume fraction of the crystal phase, while that of DSC is based on the weight fraction of crystal fraction.

Another point to be noted is that TR-XLPE shows a much higher density than all the other XLPEs for any level of annealing. Even the highest obtainable density of annealed EC-XLPE is lower than the value of unannealed TR-XLPE. As discussed in Section 5.2.3, the chemical additives appear to play a major role. The additive may have a higher density than that of the material or may be found in voids.

5.3.3. Small Angle X-ray Study

The general shape of the SAXS curves of annealed XLPE are similar to that of the unannealed sample, having well-defined broad Bragg peaks (Figures 4.3.11-13, Pages 198-200). The annealed LLDPE sample shows hump-like peaks similar to the untreated LLDPE sample (Figure 4.3.14, Page 201). The non-radical change of SAXS curve shape may indicate that the annealing process does not modify the basic morphology of the samples. Even though the shapes of the intensity curves of the XLPEs are different from that of TR LLDPE, the effects of annealing time on these two polyethylenes are similar. One sees three principal effects.

First, with increasing annealing time the Bragg maximum moves towards lower angles, indicating an increase in long period spacing. Such an effect is known to be common in annealing of polymers (Alexander, 1969). Figure 5.3.1 shows the variation of long periodicity calculated from the Lorentz-corrected SAXS curves with annealing time for three XLPEs and one LLDPE annealed at 107°C in air. All samples show a logarithmic increase of long periodicity. Such results have been considered to be a major effect of annealing (Schultz, 1974). XLPE shows an increase of long periodicity from 122 Å to 133 Å. Uncured polyethylene also shows a shift of Bragg maximum with annealing towards lower angles, as shown in Figures 4.3.19-4.3.21 (Pages 206-208). However, the mean long periodicity calculated from the one-dimensional SAXS curves shows negligible increase, compared to the cured polyethylenes. Especially, high density polyethylene shows no major thickening with annealing at 107°C. The reason for this is considered to be an annealing temperature to low compared to the normal melting temperature (135°C). Figure 5.3.2 shows the variation of long period for uncured materials, including HDPE, with annealing time.

A second effect is a general increase of intensity as annealing time increases. This effect is more clearly shown in the subtracted plots where the intensity values of the unannealed sample were subtracted from those of annealed samples, as exemplified in Figures 5.3.3 and 5.3.4 for TR-XLPE and TR-LLDPE, respectively. One can see clearly that the major enhancement of intensity with

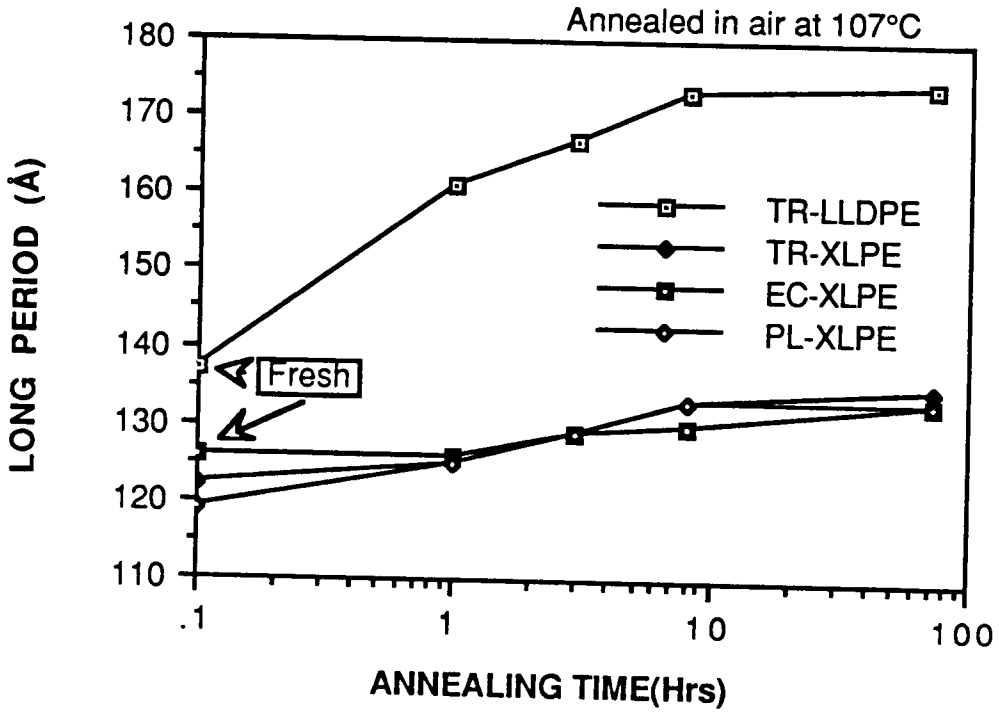



Figure 5.3.1 Variation of long period of TR-XLPE, EC-XLPE, PL-XLPE and TR-LLDPE with annealing time at 107°C in air.

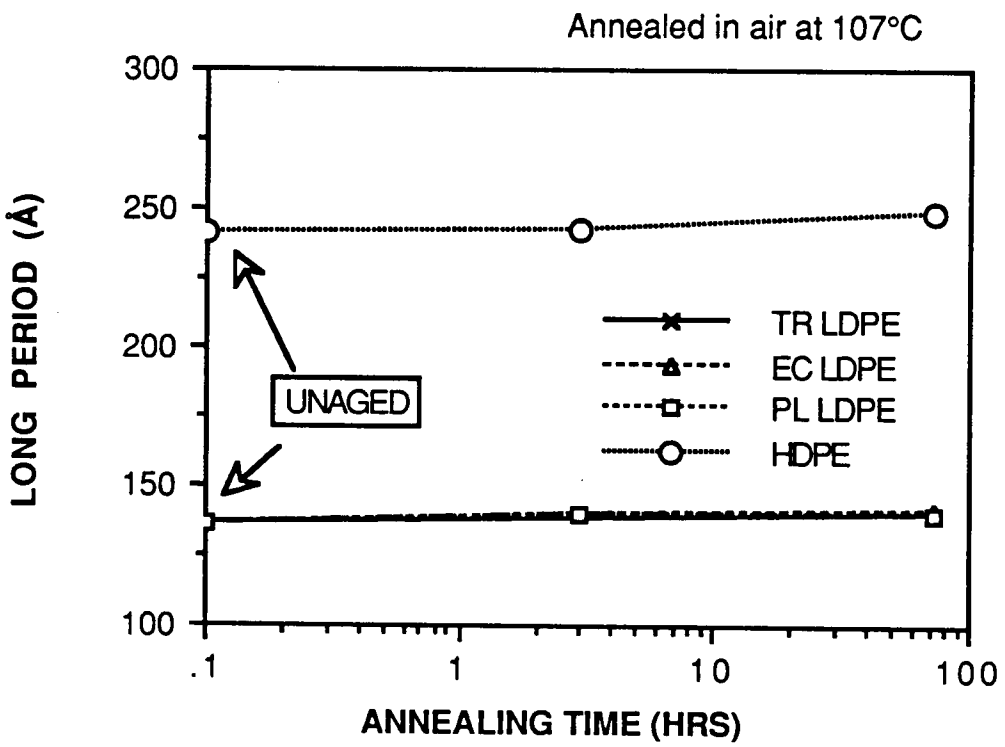



Figure 5.3.2 Variation of long period of uncured TR-LDPE, EC-LDPE, PL-LDPE and HDPE with annealing time at 107°C in air.

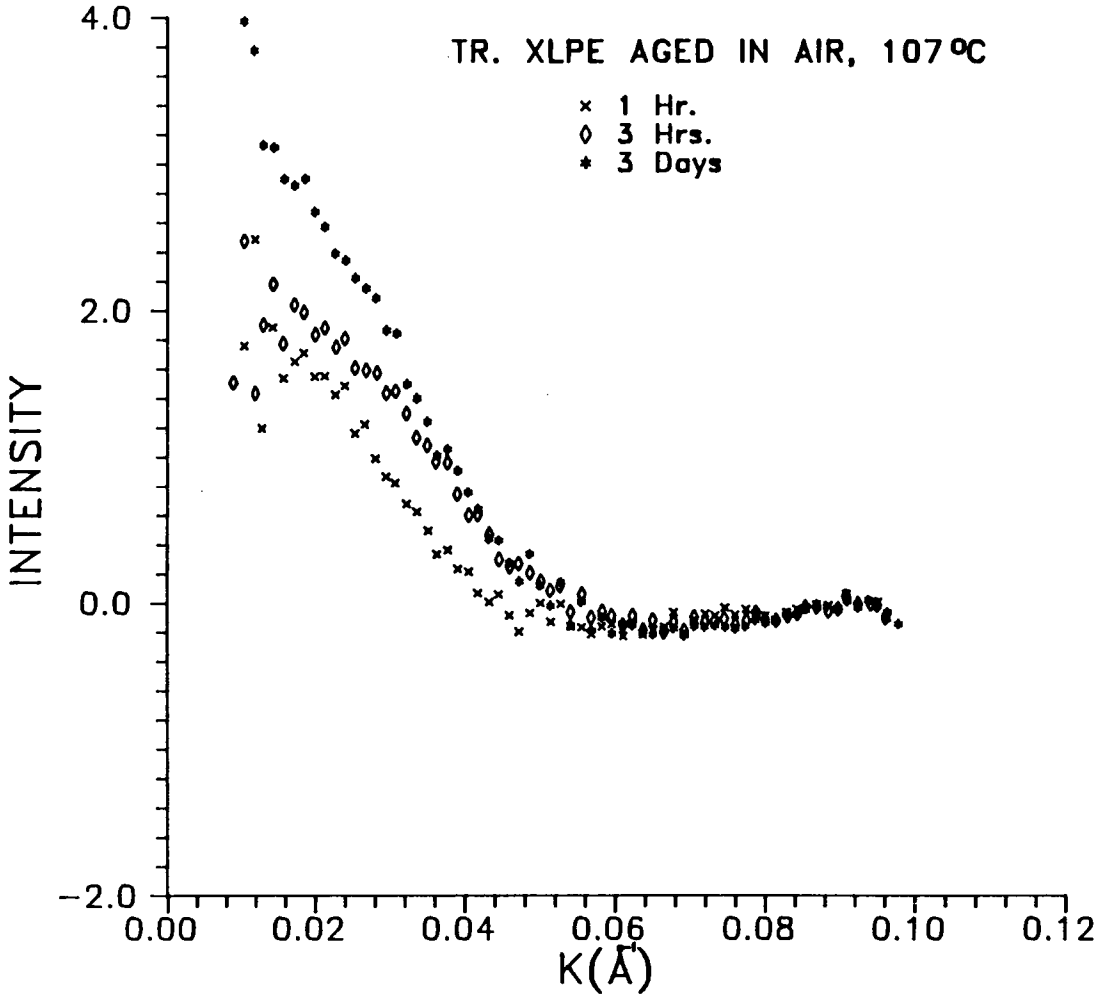



Figure 5.3.3 Difference SAXS intensity curves of TR-XLPE annealed at 107°C for various period of time in air (Fresh TR-XLPE subtracted)

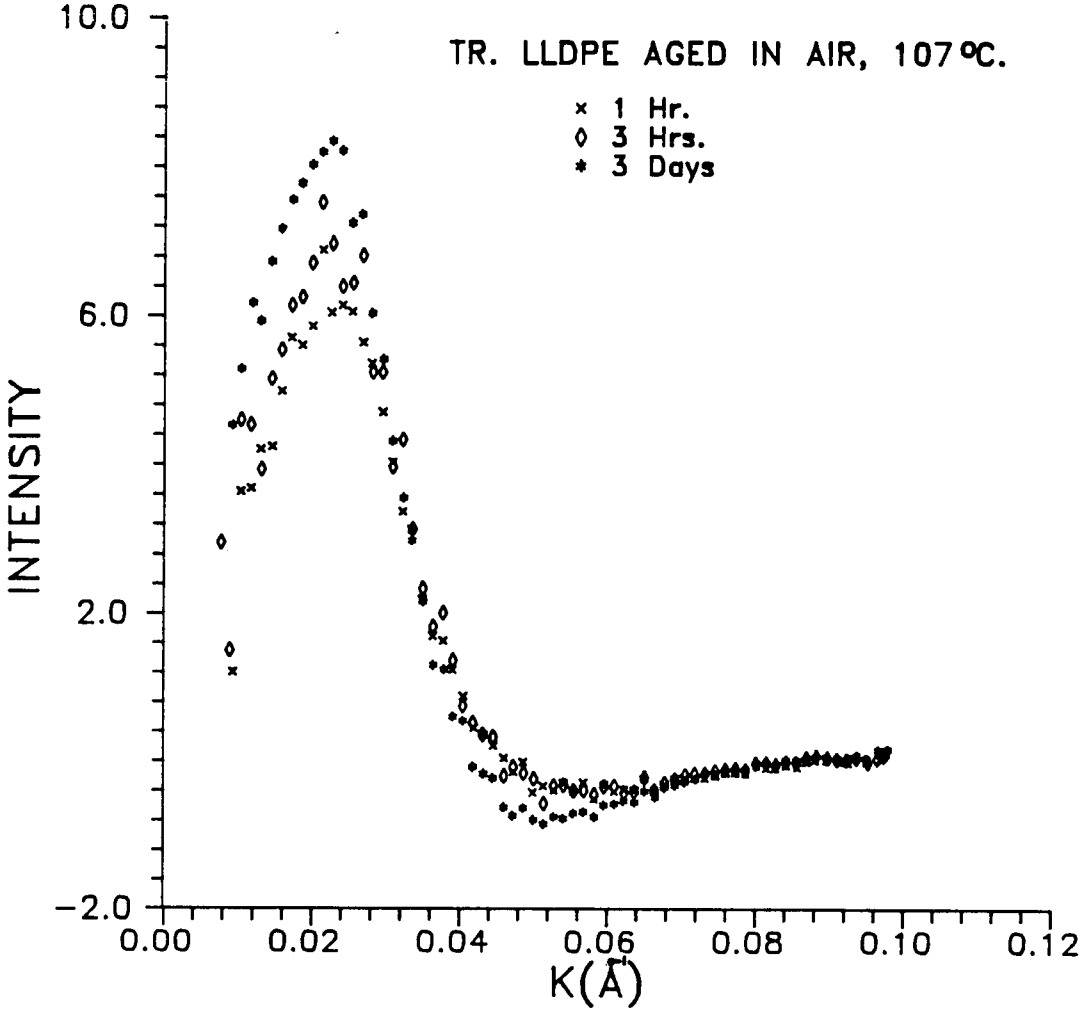



Figure 5.3.4 Difference SAXS intensity curves of TR-LLDPE annealed at 107°C for various period of time in air (Fresh TR-LLDPE subtracted)

annealing occurs at the lower angles near the beam stop, with the maximum of subtracted intensity being at an angle just below the Bragg maximum.

In the literature, it has been proposed that the intensity near the beam stop, referred to as zero-angle diffused intensity, is associated with amorphous gaps in the lamellar stacking (Schultz, 1976; Schultz, 1978; McCready, 1979). It also has been speculated that the scattering intensity up to 0.015 $Å^{-1}$ of scattering vector arises from particles, such as microvoids (Kawaguchi, 1984), impurities or trapped small crystallites. For linear polyethylene, however, it was reported that the zero-angle intensity showed a slight decrease with increasing crystallization time. The diminishing of zero-angle intensity with crystallization time was asserted to be due to the growth of new crystallites within the amorphous gap (Schultz, 1978). If this assertion is true for crystallization of polyethylene, then the slight increase of near zero-angle intensity observed in annealing in XLPE suggests that the growth mechanism of crystallites during annealing of XLPE is different from that of linear polyethylene.

On the other hand, the speculation of void generation cannot be excluded in annealing of XLPE, since the density measurement variation with annealing does not follow a similar pattern to that of DSC crystallinity. Particle scattering theory is based on a dilute system without long range interference among the entities. In the particle scattering system, the size of the particle is not

directly related to the scattering vector, since the value is calculated from the slope rather than the absolute location of scattering. If voids are formed, the crystallinity increase based on density measurement may be slower than those deduced by DSC measurement with increasing annealing time, as discussed in the preceding section. However, a sudden increase of intensity near the zero-angle on exposure to the annealing temperature of 107°C cannot be considered to be caused by the formation of impurities. IR study of the annealed sample indicated no major change of chemical composition with annealing at that temperature.

It is however very plausible that the intensity increase at smaller angles can be a result of small crystallites embedded inside the material, provided that the trapped crystallites have no long range interference. For LLDPE these entities can be possible, since the system is considered to be segregated, according to the branch level. The remaining speculation is that the high zero-th order peak intensity may be generated from the presence of small number of super-thick lamellae. This consideration is not based on the dilute system, but the dense system with long range interference. Thus, the dimension of entities is directly related to the reciprocal of the location of the scattering, following the Bragg's law. The SAXS model study clearly proves that the presence of very small amount of such lamellae can cause a higher intensity to result in the smaller angle regions.

Close examination of difference SAXS curves reveals the differences between TR-XLPE and TR-LLDPE. The former shows a continuously decreasing slope, while TR-LLDPE shows a peak indicating a maximum. This difference might indicate that the annealing mechanisms may be slightly different, even though these mechanisms are of the same origin. The difference curves calculated from the variable model, as illustrated in Figures 5.1.1 and 5.1.2 (Pages 297, 298), show two types of difference curves. One type has maximum and minimum peaks, while the other only shows a minimum peak near the location of the original Bragg peak. The type having a negative and a positive difference peak was generated through a smaller difference in crystallinity distribution among stacks having a similar crystallinity variation. On the other hand, the difference curve from two SAXS curves having a wider gap in the standard deviation of crystallinities shows only one negative peak and a small shoulder. This visual match may indicate that the TR-XLPE undergoes more severe change in crystallinity distribution among the stacks than the TR-LLDPE.

The third effect is that the breadths of the peaks become narrower with annealing. The narrow peak arises from an increase in the regularity of lamellar stacking. So the distribution of stack size becomes narrow. Not surprisingly, this effect has been reported for the crystallization of high-density polyethylene (Schultz, 1978, McCready, 1979).

Based on the SAXS model study given in Sections 4.4 and 5.1, further clarification of evenness can be made. Major noticeable changes in unmodified SAXS curves are the change in peak ratio and the distance ratio that were defined in Figure 5.1.5. The peak ratio increases and the distance ratio decreases with the increase of annealing time. These results clearly indicate that the thickness distribution within a stack become narrower, and at the same time the variation of crystallinity among the stack increase.

This can be achieved through melt segregation during the annealing process. It is more reasonable that at least part of the void generation is incorporated into the effects of annealing on the material. The voids are not necessary in the range of dimension that can be detected by the SAXS techniques. If the void size is in that range, the SAXS intensity near the zero angle region would be boosted. However, without the aid of void formation the increase in intensity in the range can be achieved, at least qualitatively, as described previously.

However, the Lorentz-correction for the SAXS data diminished the magnitude second and third effects in regular plots as presented in Figures 4.3.15-4.3.18 (Pages 202-205). All Lorentz-corrected SAXS data of XLPE show less-distinguishing trends of the above-stated behavior. Such features are not strange, since the Lorentz-correction reduces the effects of variations in material parameters on the SAXS curves shape, especially near the beam stop region, due to the factor of $k^2$.

The major difference in the modification of the Lorentz-corrected SAXS curves by annealing is that the location of the Bragg maximum approaches the beam-stop as the level of annealing increases. Shortening the location of Bragg peak reflects the increase in long periodicity. In fact, it has been proven that mean values of long periodicity from the Lorentz-corrected SAXS curves are more reliable than those from the unmodified curve, especially for the scattering from non-symmetric entities.

5.3.4. Morphological Influence

Other information that can be obtained from the SAXS experiment are the quantitative values of the sizes associated with the microstructure. The location of the Bragg angle in an one-dimensional SAXS curve reveals the value of the long period. The crystallinity can be calculated from the DSC results as the ratio of a heat of fusion of a specific sample to that of theoretically 100 % crystalline polyethylene. With these two parameters one can evaluate the average thicknesses of the crystalline and amorphous layers. In this quantitative analysis, however, the simple one-dimensional variation of electron density has to be assumed. The material has to be assumed also to have only two different entities, presumably amorphous and crystalline regions. The variation of amorphous and crystalline thicknesses for the samples annealed at 107°C in air are tabulated in Table 5.3.1.

The major response to thermal aging treatments of all XLPEs is thickening of the crystal with a minor change in the amorphous

Table 5.3.1 Variation of crystalline and amorphous thickness of TR-XLPE, EC-XLPE, PL-XLPE and TR-LLDPE annealed at 107°C in air.

| | Condition | SAXS Long Period (Å) | Crystal-linity (%) | Crystal Thickness (Å) | Amorphous Thickness (Å) |
|---|---|---|---|---|---|
| TR-XLPE | Fresh | 122 | 49.8% | 61 | 61 |
| | 107°C/1 hr | 125 | 50.5% | 63 | 62 |
| | 107°C/3 hrs | 129 | 53.0% | 68 | 61 |
| | 107°C/8 hrs | 133 | 53.1% | 71 | 62 |
| | 107°C/3 days | 135 | 54.0% | 73 | 62 |
| EC-XLPE | Fresh | 126 | 50.3% | 63 | 63 |
| | 107°C/1 hr | 126 | 51.1% | 64 | 62 |
| | 107°C/3 hrs | 129 | 51.9% | 67 | 62 |
| | 107°C/8 hrs | 130 | 54.2% | 70 | 60 |
| | 107°C/3 days | 133 | 56.5% | 75 | 58 |
| PL-XLPE | Fresh | 119 | 51.3% | 61 | 58 |
| | 107°C/1 hr | 125 | 50.1% | 63 | 62 |
| | 107°C/3 hrs | 129 | 49.9% | 64 | 65 |
| | 107°C/8 hrs | 133 | 54.5% | 72 | 61 |
| | 107°C/3 days | 133 | 54.8% | 73 | 60 |
| TR-LLDPE | Fresh | 137 | 53.7% | 74 | 63 |
| | 107°C/1 hr | 161 | 56.5% | 91 | 70 |
| | 107°C/3 hrs | 167 | 57.3% | 96 | 71 |
| | 107°C/8 hrs | 173 | 56.9% | 98 | 75 |
| | 107°C/3 days | 174 | 60.2% | 105 | 69 |

layer. When cured at a temperature of 200°C, all grades of XLPE show a sudden increase of amorphous thickness of about 7 Å, with a slight decrease of crystalline thickness (c.a. 2 Å). However, as annealing time at 107°C increases from 1 hour to 3 days, the amorphous layer shows little or no change in thickness. Some samples even show a slight decrease in amorphous thickness. On the other hand, the average thickness of he crystal layer of XLPE increases steadily with annealing time from ca. 61 to ca. 75 Å.

TR-LLDPE also shows similar trends with annealing except for the initial sudden increase of amorphous thickness. Once annealed, the amorphous layer thickens by 7 Å. The variation in amorphous thickness thereafter is not significant. Meantime, the crystalline thickness increases by as much as 17Å for even short annealings, and thickening of the crystalline layer of TR-LLDPE occurs continuously with increasing annealing time, reaching 105 Å. Calculation of crystalline and amorphous thickness with the aid of DSC crystallinity data reveals that all annealed XLPEs show a thicker amorphous layer (ca. 70-75 Å) than the unannealed specimen (ca. 63 Å).

It is of interest to note that even one hour of annealing results in a drastic thickening of the crystals of TR-LLDPE as much as 17 Å (see Table 5.3.1) which is quite intense compared to the XLPE. Crystal thickening also occurs along with the increase of mean long periodicity. This initial sudden increase of crystal thickness is followed by a steady increase. This variation mode is in good

agreement with the results previously reported for polyethylene single crystal (Kawaguchi, 1984). Similar results were also reported for the melt crystallized linear polyethylene using the synchrotron x-ray technique (Martinez-Salazar, 1985. The drastic thickening of LLDPE can be also inferred from the DSC melting curves of annealed samples as shown in Figure 4.2.4 (Page 166). Even with little annealing, LLDPE shows a much wider gap between the two melting peaks than XLPE. The melting point of linear polyethylene fraction of LLDPE is usually in the range 130-135$^{o}$C whereas that of the branched polyethylene fraction is ca. 105$^{o}$C.

Based on the findings made so far, one can postulate mechanisms for cooling and annealing of LLDPE from the viewpoint of variation of distribution mode. Upon cooling, LLDPE can crystallize selectively according to the branch levels, leading to the wide distribution of crystallinity among stacks. This speculation has been already made in Section 5.2 using DSC and SAXS data. When annealed at 107$^{o}$C, most branched fractions, whose melting temperature is ca. 105$^{o}$C, will melt. Among the molten fractions, the more linear molecular fraction will be gradually incorporated into the unmolten linear fraction, whose melting temperature is ca. 130$^{o}$C, resulting in crystal growth. The recrystallization can be considered to be very local mainly due to the presence of the unmolten fraction. Thus, in the process the crystallinity variation become wider but on a reduced scale. Meanwhile, the thickness distributions within a stack will change in a more complicated

manner, depending on the initial distribution. If LLDPE has been fully segregated, the unmolten crystal fraction at the annealing temperature can be a form of cluster, or stack. In such a system, only the surface or outer area of the stack will be a recrystallization site, leading to a wider thickness distribution within the stack. However, if the system was not fully segregated, most unmolten fraction will be in the form of a crystal layer. The thin crystal layer can be consider to have more branches and a lower melting temperature. In this system the thickness distribution will be narrower, since each layer can be a site of crystal growth. In either process, part of the amorphous layer will also become crystalline through secondary crystallization.

On the other hand, TR-XLPE shows a steady but smaller increase in crystal thickness with annealing at 107°C, resulting in a total increase of 12 Å for 3 days of annealing. This clearly shows that XLPE shows a much smaller thickening effect on annealing, indicating less favorable isothermal recrystallization. In fact, XLPE at such a high temperature is considered to be in the molten state with very little trace of crystal, as previously reported, and indicated in DSC data (Figure 4.1.11, Page 150). Even though SAXS and other experimental data support possible melt separation, more accurate speculation can be made with understanding of in-situ behavior of the material at 107°C. Thus, a complete interpretation will be given later in Section 5.4.3.

Another interesting result is in the variation of amorphous thickness; XLPE shows an almost constant value of amorphous thickness. LLDPE also shows a very small variation of average amorphous thickness compared to the average crystalline thickness. This result may indicate the presence of a certain characteristic amorphous thickness regardless of annealing or crystallization conditions. This speculation also makes it possible for the average amorphous thickness to be the same throughout the entire stack. Such a speculation has been made previously (Korteleve, 1968). This also supports the assumption of a constant average amorphous thickness made for the variable SAXS model.

5.3.5. Effects of Annealing Environment

Major changes in the SAXS pattern of the sample annealed in the silicone oil bath are three-fold as was the case for the sample annealed in air. The three major changes occurring in the uncorrected SAXS patterns with annealing time are (a) a lowering of the angle of the Bragg maximum, (b) a general increase of SAXS intensity with annealing time, and (c) a reduction of the half-width of the Bragg peaks. However, the third effect is not as pronounced as the other changes, especially for XLPEs. On the other hand, annealed LLDPE shows a better-developed Bragg maximum. For Lorentz-corrected SAXS intensity curves, the annealed samples show lower values of the location of the Bragg maximum. The long periodicities calculated from the Lorentz-corrected SAXS curves are plotted in Figure 5.3.5. The amorphous and crystalline thicknesses were also

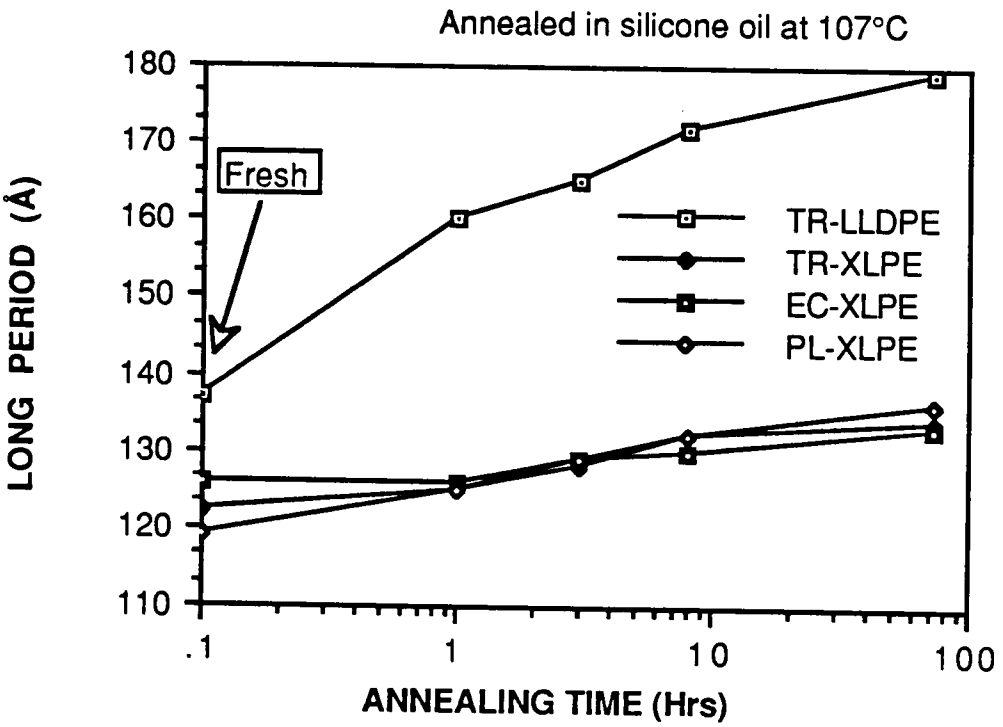



Figure 5.3.5 Variation of long period of TR-XLPE, EC-XLPE, PL-XLPE and TR-LLDPE with annealing time at 107°C in silicone oil.

estimated using the crystallinity values calculated from the DSC measurement. The results are listed in Table 5.3.2. In general, the variation of thickness, as well as the long periodicity, with annealing time in silicone oil is quite similar to that of the sample annealed in air.

The remaining annealing environment was the transformer oil with a trade name of Univolt$^{TM}$ 60. This system is of particular interest, because the same oil was used by Vatansever for the filling of voids in the field aged XLPE cables. The SAXS data from the immersed XLPE cable showed little or no intensity near zero angle but there was a single well-developed Bragg maximum. However, the experimental SAXS results from the sample annealed at 107$^{o}$C and immersed in the Univolt oil at 50$^{o}$C does not show similar results, as shown in Figures 4.3.35-4.3.38 (Pages 224-227). The reason for the discrepancy may be the difference in immersion condition and/or the difference in the nature of voids within the samples. Unfortunately, he did not describe the immersion conditions. The immersion temperature was seen to be very important, since a high immersion temperature will dissolve the material. The DSC melting curve for the material immersed in oil at 107$^{o}$C shows a major loss of crystal fractions having high melting temperatures (Figures 4.2.12-4.2.13, Pages 177,178). The XLPE sample immersed at 78$^{o}$C shows a lower melting peak at around 100$^{o}$C (Figure 4.2.14, Page 180).

Table 5.3.2 Variation of crystalline and amorphous thickness of TR-XLPE, EC-XLPE, PL-XLPE and TR-LLDPE annealed at 107°C in silicone oil.

| | Condition | SAXS Long Period (Å) | Crystal-linity (%) | Crystal Thickness (Å) | Amorphous Thickness (Å) |
|---|---|---|---|---|---|
| TR-XLPE | Fresh | 122 | 49.8% | 61 | 61 |
| | 107°C/1 hr | 125 | 48.5% | 61 | 64 |
| | 107°C/3 hrs | 128 | 52.4% | 67 | 61 |
| | 107°C/8 hrs | 132 | 52.1% | 69 | 63 |
| | 107°C/3 days | 134 | 56.0% | 75 | 59 |
| EC-XLPE | Fresh | 126 | 50.3% | 63 | 63 |
| | 107°C/1 hr | 126 | 48.6% | 61 | 65 |
| | 107°C/3 hrs | 129 | 50.4% | 65 | 64 |
| | 107°C/8 hrs | 130 | 53.1% | 69 | 61 |
| | 107°C/3 days | 133 | 56.1% | 75 | 58 |
| PL-XLPE | Fresh | 119 | 51.3% | 61 | 58 |
| | 107°C/1 hr | 125 | 49.3% | 62 | 63 |
| | 107°C/3 hrs | 129 | 50.5% | 65 | 64 |
| | 107°C/8 hrs | 132 | 54.2% | 72 | 60 |
| | 107°C/3 days | 136 | 58.1% | 79 | 57 |
| TR-LLDPE | Fresh | 137 | 53.7% | 74 | 63 |
| | 107°C/1 hr | 160 | 50.0% | 80 | 80 |
| | 107°C/3 hrs | 165 | 55.4% | 91 | 74 |
| | 107°C/8 hrs | 172 | 58.4% | 100 | 72 |
| | 107°C/3 days | 179 | 59.9% | 107 | 72 |

It is interesting to look at the SAXS curve from the XLPE annealed in the mineral oil at 107°C for 3 hours (Figure 5.3.6 shows the TR-XLPE). The radially averaged SAXS intensity curve does not show any Bragg maximum, but the intensity changes almost linearly with the scattering vector in a semi-log plot. The system clearly appears to be a dilute system with no evidence of lamellar structure, resulting in particle scattering. Similar results were also noted for TR-LLDPE annealed at 117°C as shown in Figure 5.3.7. In fact, a total change of external structure was clearly seen. The whole material looks like wax, having a slippery surface. This evidence clearly suggests that, during immersion at such a high temperature, most linear molecular fractions are extracted. Thus, only highly branched fractions, which definitely have lower melting points, recrystallized during cooling. The loss of the high temperature melting fraction by immersion at 78°C may also be due to the same reason. The loss of linear molecular fraction may also indicate the loss of thick crystallites, which would have a high melting peak.

The same field aged XLPE insulation used in Vatansever's study was also immersed in the same oil at the relatively lower temperature of 60°C for 3 hours. At such a temperature the loss of high temperature melting fractions is not considered to be major. Figures 5.3.8 and 5.3.9 show unmodified and Lorentz-corrected SAXS curves of the XLPE cables used in Vatansever's work. The effect of oil immersion on the unmodified SAXS curve shape is not remarkable

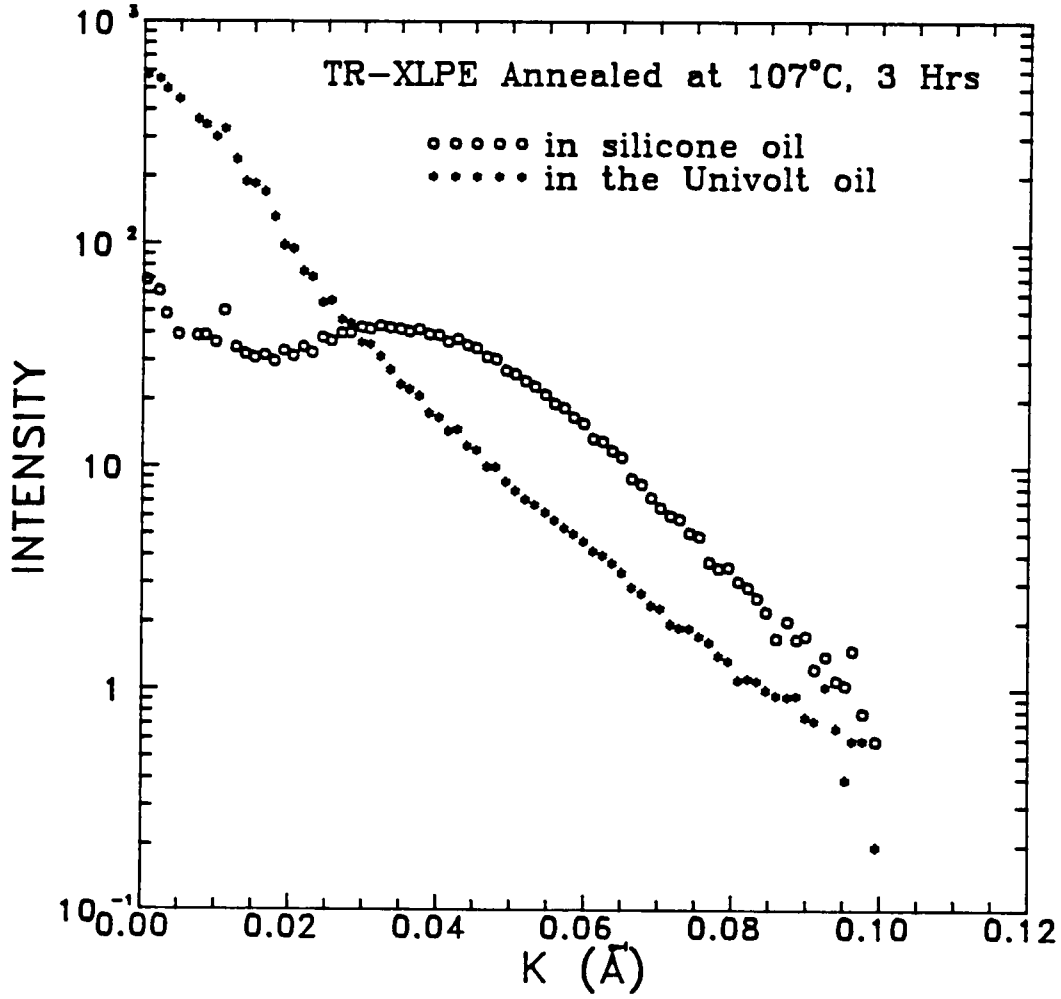



Figure 5.3.6 SAXS intensity curves of TR-XLPE annealed at 107°C for 3 hours in the Univolt oil and in air.

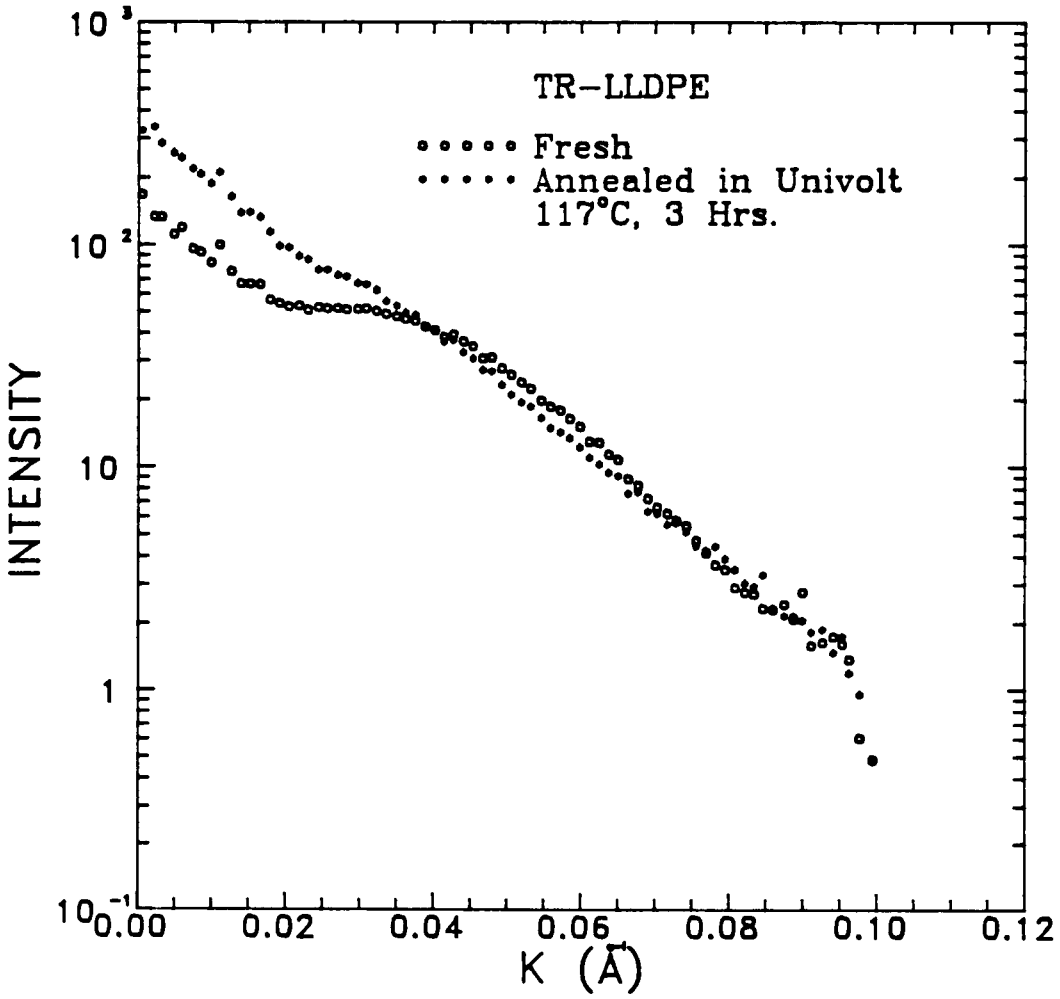



Figure 5.3.7 SAXS intensity curves of TR-LLDPE annealed at 117°C for 3 hours in the Univolt oil and fresh TR-LLDPE.

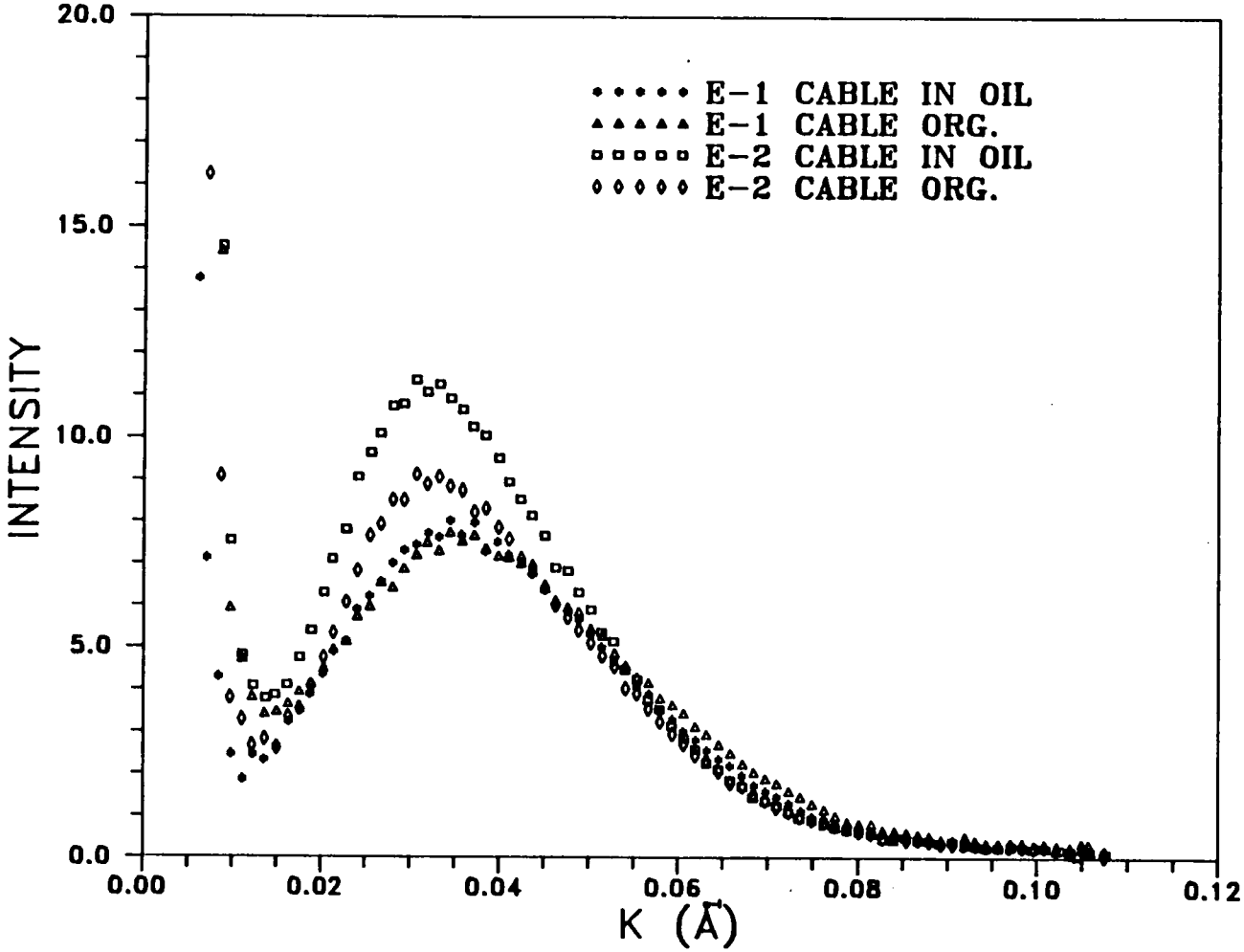



Figure 5.3.8 SAXS intensity curves of E-1 and E-2 cables immersed in the Univolt oil at 60°C for 3 hours prior to the measurement and without treatment.

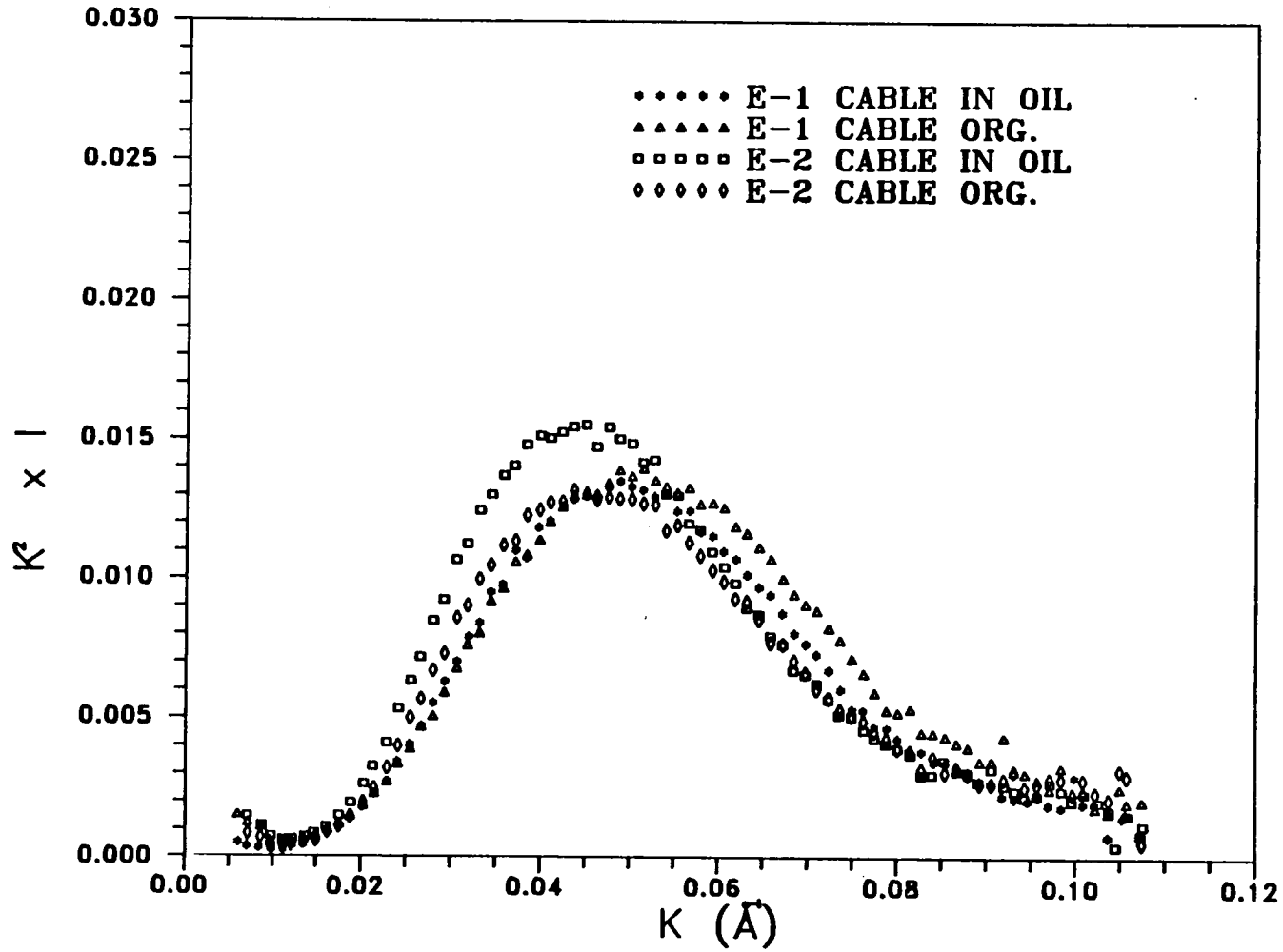



Figure 5.3.9 Lorentz-corrected SAXS intensity curves of E-1 and E-2 cables immersed in the Univolt oil at 60°C for 3 hours prior to the measurement and without treatment.

compared the one reported by Vatansever. However, immersion makes a difference in the SAXS patterns. Unaged cable (E-1) shows a clear decrease in intensities at the lower angles. This effect is more clearly shown in the difference SAXS pattern, where the intensity of the immersed sample was subtracted from that of the untreated sample (Figure 5.3.10). The decrease of SAXS intensity near the zero angle can be attributed to the partial loss of thick crystals and/or the loss of voids within the specimen. The minor loss of thick crystals could be considered to be due to the partial extraction of linear molecules, leading to a narrower distribution of crystallinity variation. However, the possibility of void loss due to the diffusion of the oil cannot be excluded, since the cable was considered to contain a large amount of voids within the system due to its curing system (the steam-cured).

However, the field aged cable, E-2, shows a substantial increase in intensity at the peak by immersion in the transformer oil. There is even a small increase in the lower angle region. The difference SAXS curve is seen in Figure 5.3.10 where the SAXS intensity of the the immersed sample was subtracted from that of untreated sample. In order to understand the effect of the oil on the field aged cable (E-2 cable), another type of subtraction was made. Difference SAXS curves described in Figure 5.3.11 are obtained by subtraction of E-1 cable from the E-2 for each of the immersed and untreated samples. The diamond shaped data points indicate the difference between the difference SAXS curves of the immersed

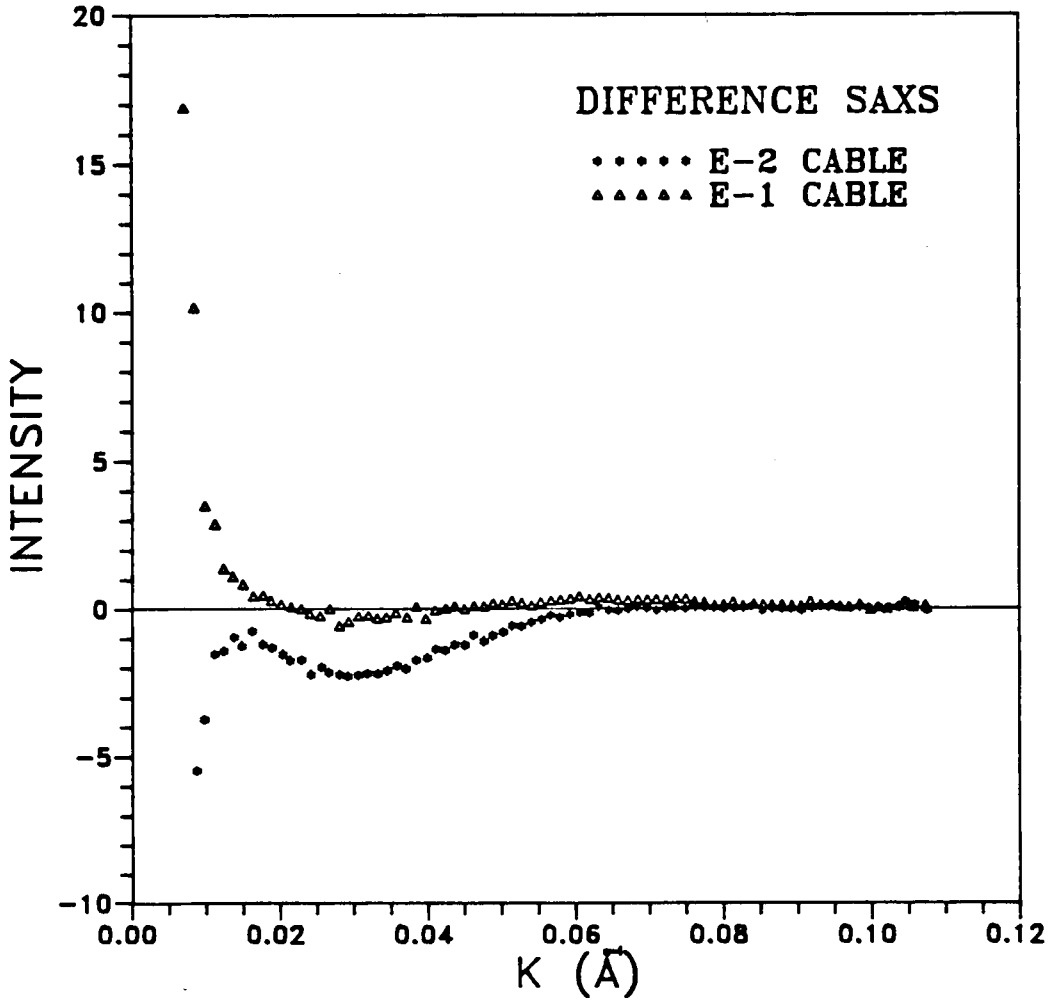



Figure 5.3.10 Difference SAXS curves of E-1 and E-2 cables immersed in the transformer oil subtracted from them the curves of the untreated cables.

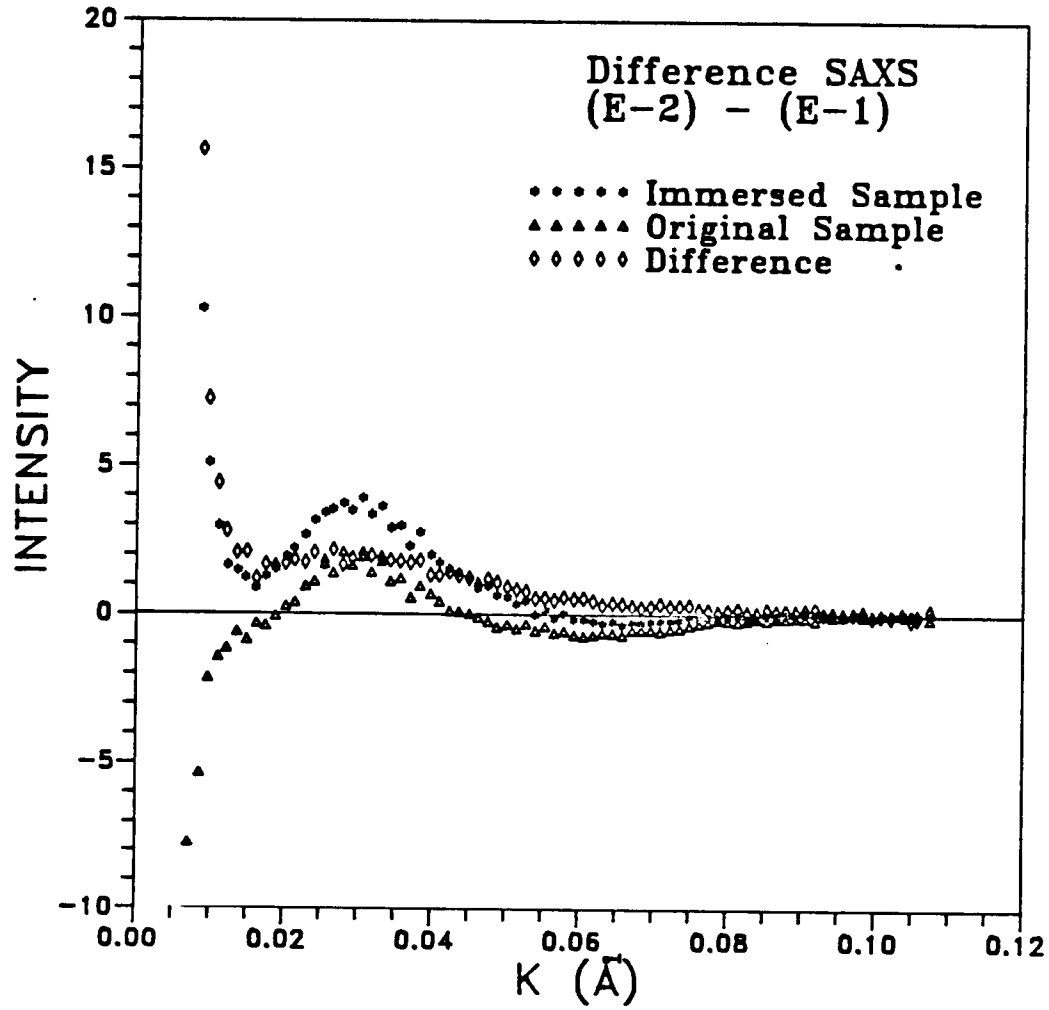



Figure 5.3.11 Difference SAXS curves of immersed and untreated cables (E-1 was subtracted from E-2).

samples and the untreated samples, presumably factoring out all structural changes at the lamellar level within the E-1 and E-2 samples. The final difference SAXS curve is considered to be caused only by the diffusion of oil into the additional void or true structures of E-2. It is interesting to note that the final difference curve shows a gain of intensity near the beam-stop region as well as the peak region, indicating increased contribution of both diffuse and discrete scattering.

This finding appears to be due to the clustering of tiny microvoids into large structures. During clustering, some voids form a false lamellar structure, causing long range interference among the clustered voids. On the other hand, some voids may still cause diffuse scattering, resulting in the increase in the intensity near the zero angle region. This hypothesis could lead to the conclusion that the field aged cable (E-2) is more susceptable to damage by transformer oil diffusion, perhaps involving partial expansion of the void structure. E-2 cable was noted to contain a large amount of bow-tie water trees, which are believed to form as clusters of small voids.

The final difference SAXS curve plotted on a log-log scale also supports the presence of the clustered voids, as presented in Figure 5.3.12. The difference SAXS curve shows two regions with linear slopes, indicative of fractal behavior. The slope in the lower angle region was obtained to be -3.84, leading to a fractal dimension of 2.16 based on the fractal relationship of SAXS

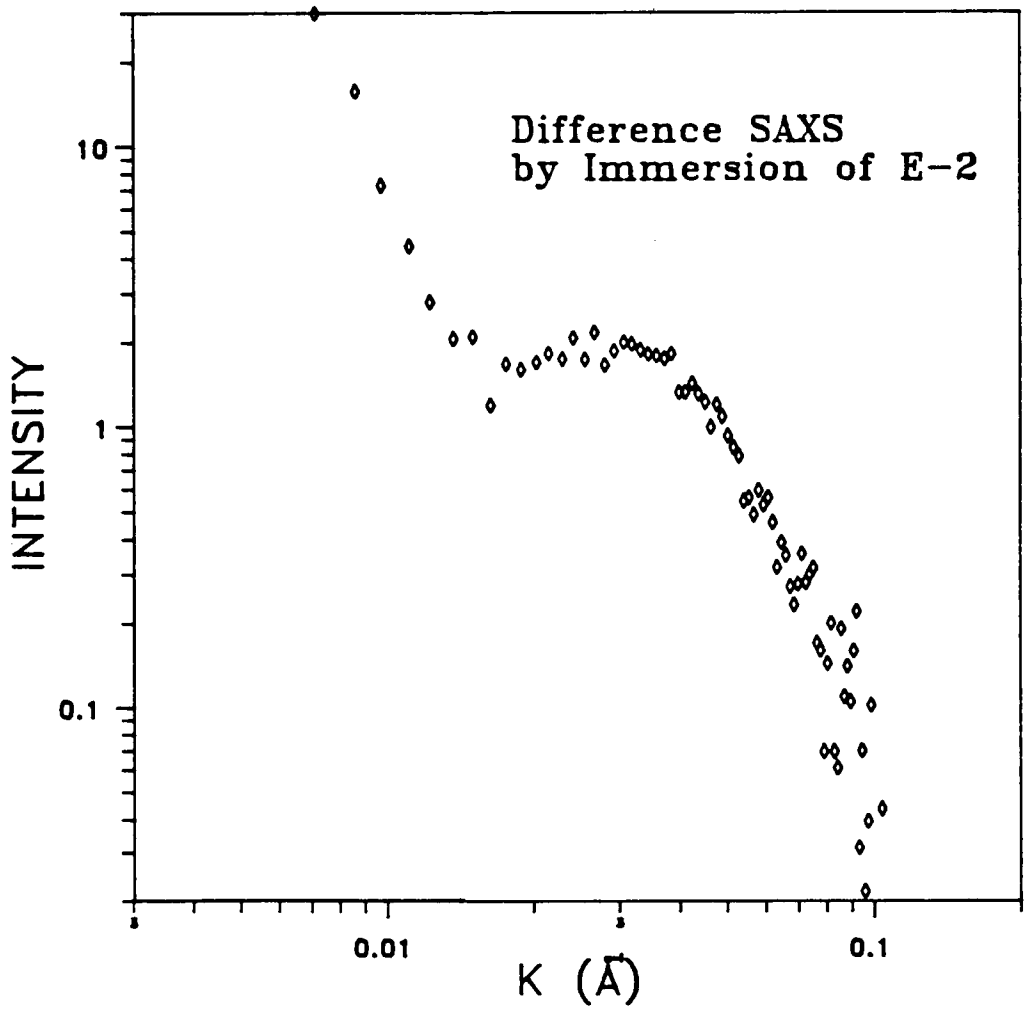



Figure 5.3.12 Difference SAXS curve caused by oil diffusion into additional E-2 structure on a log-log scale.

intensity and scattering vector from the porous materials, $I(k) = C\ k^{-(6-D)}$ (Bale and Schmidt, 1984). For a smooth pore-boundary surface, the fractal dimension D should be 2.0. Bale and Schmidt reported that the fractal dimension of the boundary surface of the pores in lignite coal was $2.56 \pm 0.03$. Even though the fractal behavior of diffused oil within E-2 is considered to be partial, the estimated dimension is not unreal. The partial presence of fractal behavior is considered to be due to the presence of discrete scattering.

Another interesting point to note is that E-2 cable shows similar effects of thermal annealing on the SAXS curves compared to E-1 cable. Field aged cable shows a lower Bragg maximum, higher intensity and narrower width than the original cable. These findings are in good agreement with Vatansever's findings (1987). Vatansever's DSC results showed that the field aged cable had been subjected to a complicated thermal history, revealing multiple melting peaks up to 114°C. In fact, the field aged cable E-2 was aged in the Waltz Mill aging facilities under severe experimental conditions. Immersion in the Univolt™ oil further increased intensities only at the peak. It was shown that annealing increased the intensities in the lower angle region including the near-zero-angle region. This appears to be due to annealing effects combined with the effects of the loss of thick crystals.

## 5.4. Phase Separation of XLPE

### 5.4.1. Physical Evidence of Phase Separation

It is known that most elastomers usually have a significant sol fraction, which is a non-crosslinked material. For example, XLPE used in this example has about 20% sol. However, most investigators do not usually extract the sol fraction prior to experiment of so called network structure, or ignore the sol fraction for the speculation of their physical behavior. Recent studies of crosslinked low density polyethylene suggest an incompatible temperature range where sol fraction separates from the gel network (Phillips, 1984).

After annealing at 107°C even for a short period of time, the DSC melting curve of the annealed XLPE clearly indicates generation of a new melting peak located in 110°C as exemplified in Figure 4.2.1 (Page 162). Phillips et al. (1984) concluded that extractables have been separated from the crosslinked material at 107°C, after the observation that the gel fraction annealed at the same temperature did not generate such a peak. The XLPE is molten at that temperature. In-situ WAXD reported by Vatansever (1987) reveals that at 107°C less than 1% of the initial crystalline fraction remains.

In-situ DSC measurement shows similar results. In in-situ experiment, the XLPE sample was held at temperature for a certain period of time and a further melt scan starting from the in-situ temperature was conducted. Figure 5.4.1 shows the in-situ DSC melting curves from various in-situ temperatures. Each scan was

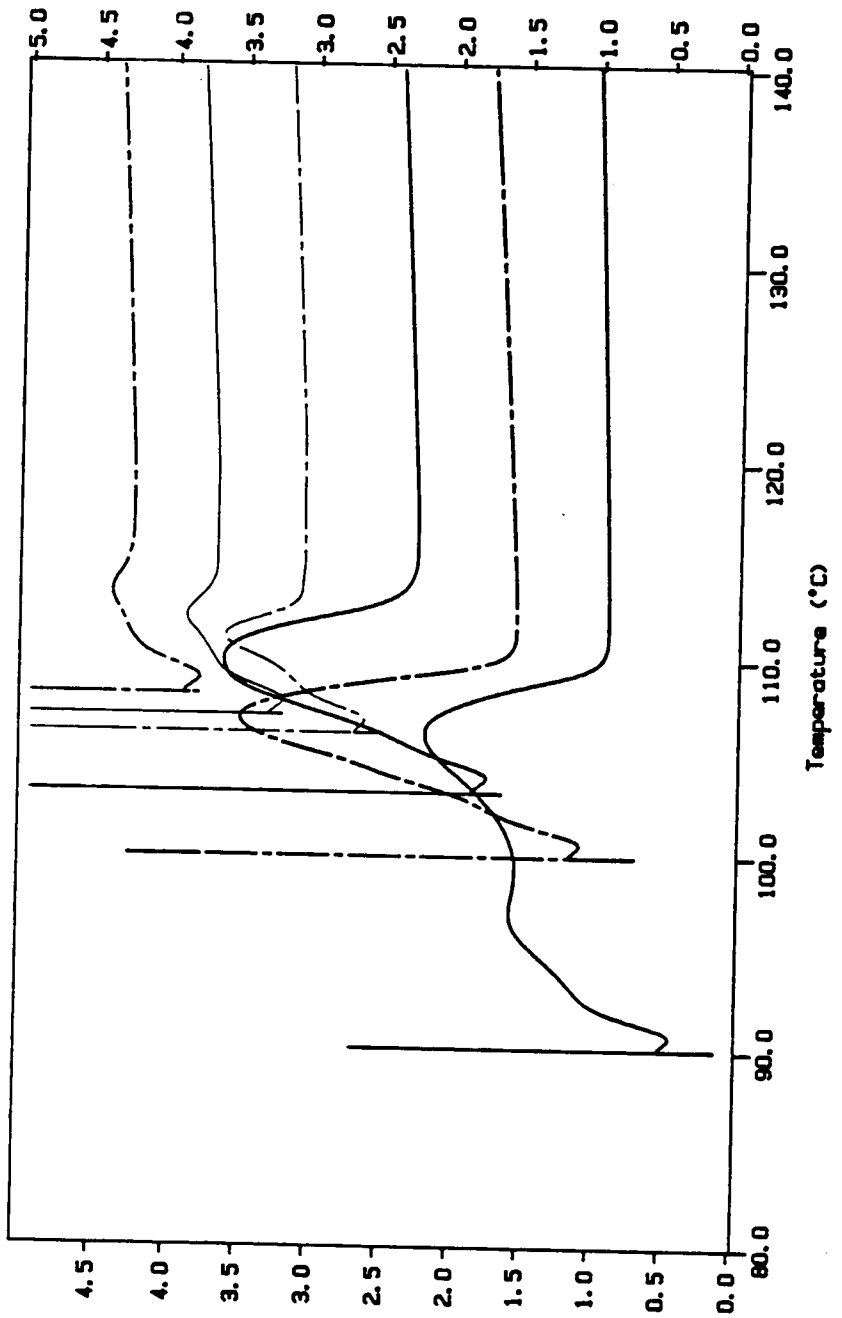



Figure 5.4.1 DSC melting curves of TR-XLPE after holding at various temperatures for 30 minutes.

measured after 30 minutes of in-situ time. The area of the melting peak was measured above the baseline that was extended from the baseline after the additional melting peaks. Table 5.4.1 shows the changes in crystallinity as well as the percent crystalline fraction present at the in-situ temperatures determined by in-situ WAXD and in-situ DSC measurements. As the annealing temperature is increased up to 108°C, the crystallinity and the percent crystalline fraction present decreases up to 1% of crystallinity which is roughly the same as 2.2% of crystalline fraction of the quenched sample. This result is not surprising since most end points of melting (return-to-baseline temperatures) are higher than 108°C. Therefore, the peaks in the in-situ DSC melting curves are thought to be the remaining crystalline fraction rather than newly crystallized fraction out of melt. It should also be remembered that in scanning experiments, such as DSC, there is a superheating and crystallinity may appear to be present at a given temperature, where it would not be detected by other methods such as x-ray techniques.

The above evidence clearly shows negligible crystallinity at temperatures of 107°C and higher. Thus, the formation of a second peak after annealing even for 30 minutes at that temperature may indicate separation of sol from gel. However, based on the findings made so far it is not clear whether the separation is melt separation producing two melts or is a result of recrystallization at 107°C. In-situ SAXS study was utilized primarily for the

Table 5.4.1 Variation of material parameters of TR-XLPE at various in-situ temperatures.

| In-situ Temp ($^{o}$C) | $\Delta H_f$ (J/g) | Crystal-linity (%) | % Crystalline Present DSC (%) | WAXD (%) |
|---|---|---|---|---|
| 25 | 105.6 | 52.1 | 100.0 | 100.0 |
| 90 | 75.4 | 37.2 | 71.4 | 74.0 |
| 100 | 55.6 | 27.4 | 52.6 | 33.0 |
| 103 | 41.6 | 20.5 | 39.4 | 26.0 |
| 106 | 8.0 | 3.9 | 7.6 | |
| 107 | 3.5 | 1.7 | 3.3 | 1.0 |
| 108 | 2.2 | 1.1 | 2.1 | |

understanding of the phenomenon by estimating the shape and the size of the entities at those temperatures.

5.4.2. In-situ SAXS Analysis

First of all, the occurrence of SAXS intensity at high temperature is very remarkable. As shown in Figure 4.3.39 (Page 229), SAXS intensity has been detected at temperatures (up to 109°C) higher than the melting peak of XLPE. Theoretically, the isotropic melt should not generate any scattering, since there is no electron density difference among the entities. Experimentally, no scattering was detected at 134°C for HDPE which has a optical melting temperature at 134°C (Martinez-Salazar, 1985). For XLPE, the exposure taken at 112°C showed a very small level of intensity that is more or less similar to that of the regular background scattering (Figures 4.3.57 -4.3.58, Pages 250-251). This indicates that even the crosslinked material can behave like an isotropic melt at a sufficiently high temperature.

However, the sample held at 109°C or above, which is about 5°C higher than the melting peak, for about 30 minutes showed a reasonable intensity level that can be detected by the two dimensional position sensitive detector (Figure 4.3.39, Page 229). The scattering curves decrease monotonically from zero angle, which is typical of diffuse scattering. Such a scattering pattern has been noted for particle systems where the long range scattering interference is negligible. This finding clearly indicates that even

at such a high temperature the XLPE melt is not fully isotropic, but contains particular species.

The source of the scattering may be the presence of a particle-like melt having a different density than that of rubbery matrix. This particle-like entity must have a higher density than the melt matrix. The polymer molecules within the entities must be packed more densely than the molecules in the rubbery phase. This embedded particle-like melt could be embryo nuclei. The other possible cause may be due to the presence of a small crystalline fraction. However, this speculation for the system at higher temperatures (109$^{o}$C or above) is groundless, since DSC and WAXD results show no evidence of crystallinity. However, the scattering monitored below 109$^{o}$C appears to be due to crystals remaining in the rubbery matrix.

The real identity of these entities needs to be investigated further, however it is possible that the particle-like melt consists of linear molecules not connected to the major crosslinked fraction. These entities may be extracted from the melt matrix due to higher mobility. Furthermore, these entities can act as a nuclei for the crystallization of the fraction having a high melting temperature. These results may be in agreement with the memory effect of the melt, one concept for the initiation of crystallization. The increase of intensity near the zero angle region may indicate the growth of such entities (Figure 4.3.42, Page 233).

It is interesting to note that at the shortest in-situ time (8 minutes) at 107°C EC-XLPE shows a trace of a Bragg peak, indicating the presence of lamellar structures (Figure 4.3.44, Page 236). With increasing in-situ time, the shoulder disappears. This feature is followed by a decrease and then an increase of intensity above a scattering vector of 0.02 $Å^{-1}$. The presence of the shoulder at the initial stage of annealing suggests that the system is changing from one of dense scattering to a dilute one. The pre-existent crystal lamellae definitely start to melt first. Later, the remaining crystals apparently restart growing by adding linear molecules.

At the in-situ temperature of 106°C all XLPEs show Bragg peaks, indicating the presence of lamellar structure. However, the crystallinity measured by other methods is too low for the system to be considered as a dense system (<4%). According to the work by Vonk (1985), the first order peak was generated about 5°C below the melting temperature (135°C) for HDPE, at which point the crystallinity was noted to be more than 7%. This may have resulted from the high thermal stability of XLPE mainly due to the crosslinks reducing the mobility of molecular chains.

The variation of the SAXS intensity pattern with decreasing of in-situ temperature below 106°C can be characterized as a shift of Bragg peak away from the zero angle together with an overall decrease of intensity, especially in the lower angle region. Such a shift may be a reflection of the decreasing contribution of particle scattering with an increasing contribution of discrete scattering.

The major source of particle scattering seems to remain same as that at higher in-situ temperatures, where only particle scattering is present. This means that the source may be the small crystallites embedded away from the lamellae rather than voids. Nonetheless, the change of distribution mode within the system, as discussed in Section 5.1, may also play a partial role.

Even though most scattering was initiated by particles at higher in-situ temperatures, the Lorentz-corrected curves show the peak. The presence of the peak in the Lorentz-corrected SAXS curves at most in-situ temperatures permits the estimation of long periodicity. Application of the Lorentz geometric factor is necessary because of the non-isotropic geometry of the entities. This point will be discussed further in the following section. The major SAXS parameters, such as long periodicity as well as crystal thickness will be discussed later also.

### 5.4.3. Distance Distribution Curves

For the quantitative analysis of structure at the in-situ temperature, distance distribution functions were obtained by numerical calculation using computer program listed in Appendix V. The PASCAL program uses the input of unmodified raw data from the mini-computer attached to the 10-meter SAXS camera. The codes were programmed to fit the data at the initial and final part of actual raw data as well as the Lorentz corrected curves according to the exponential law and Porod's law for the initial and final parts, respectively; since the ideal Fourier transformation has to be

carried out for the entire scattering curve. The fitting, however, was programmed to be selected by a user. The fitted scattering data was then transformed to real domain data by the Fourier transformation scheme developed by the Boland Corporation. Figure 5.4.2 shows typically fitted data applied to the curve at scattering vector values less than 0.012 $Å^{-1}$ and larger than 0.12 $Å^{-1}$.

Distance distribution function gives an estimate of frequency of distance that can be placed within the same types of entities within the particle. This function has a relationship with the other function $\tau(r)$ which is the correlation function. The intensity function also can be obtained by the reverse transformation of the distance distribution function, as discussed in literature review section.

Figure 5.4.3 shows theoretical plots of distance distribution functions for some ideal situations. Easy estimation of structure can be made with the aid of the F(r) function shown in Figure 5.4.4, which is simply the function of P(r) divided by the distance r. For the sphere, the curve is almost symmetric, having a maximum at the distance corresponding almost to the radius of the sphere. The limiting value of the x axis corresponds to the maximum dimension of the sphere, which is the diameter. On the other hand, the distance distribution curve of the rod-like particle is linear in shape after a distance corresponding to the diameter of the cross-section of the rod. For the disk-like material, the P(r) function is hyperbolic shaped so that the F(r) function is linear in shape. The thickness

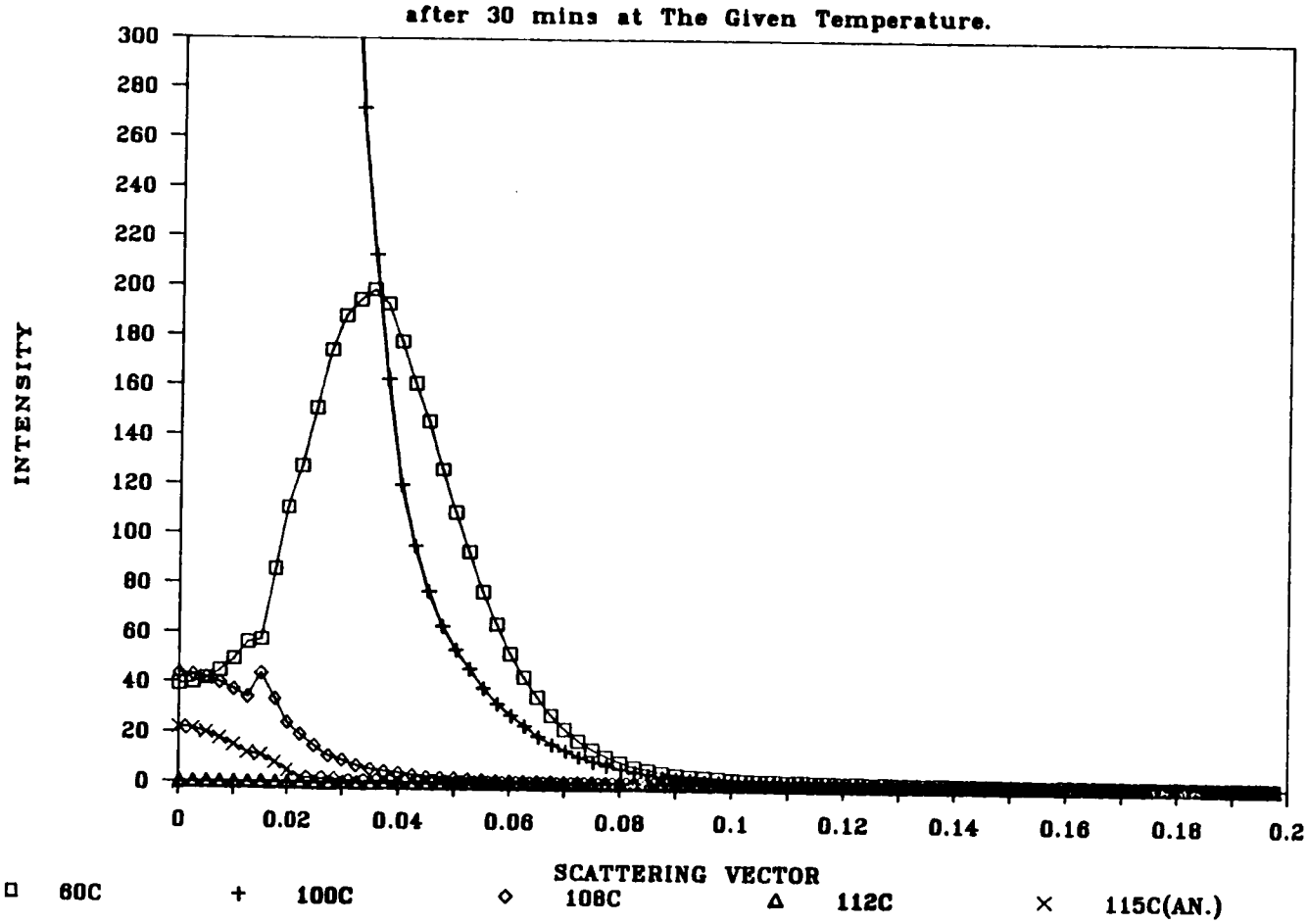



Figure 5.4.2 Typical fitted SAXS intensity curves of TR-XLPE held at the various in-situ temperatures for 30 minutes for the evaluation of the distance distribution function.

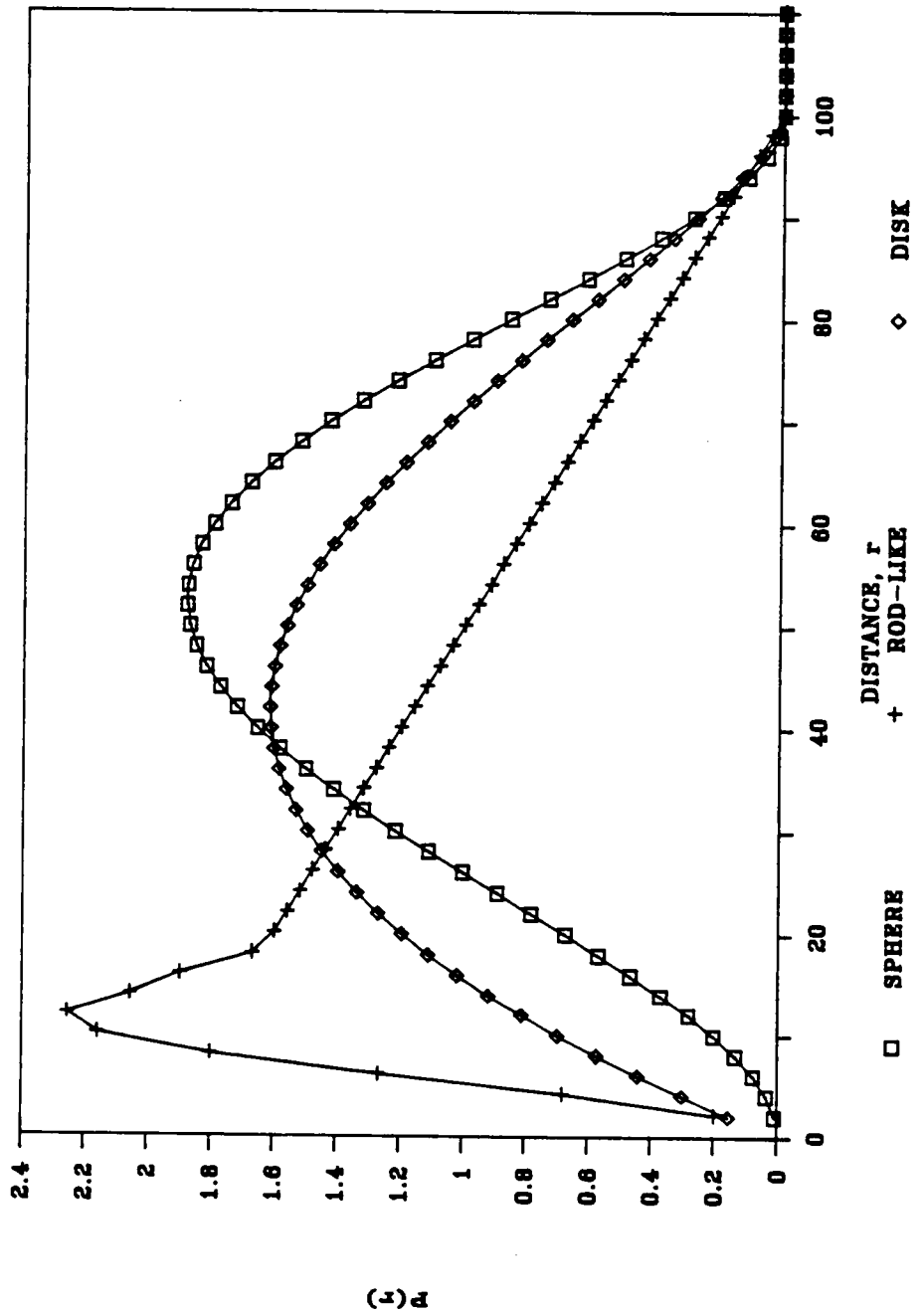



Figure 5.4.3 Theoretical distance distribution curves of spheres, rod-like particles and disk-shape particles.

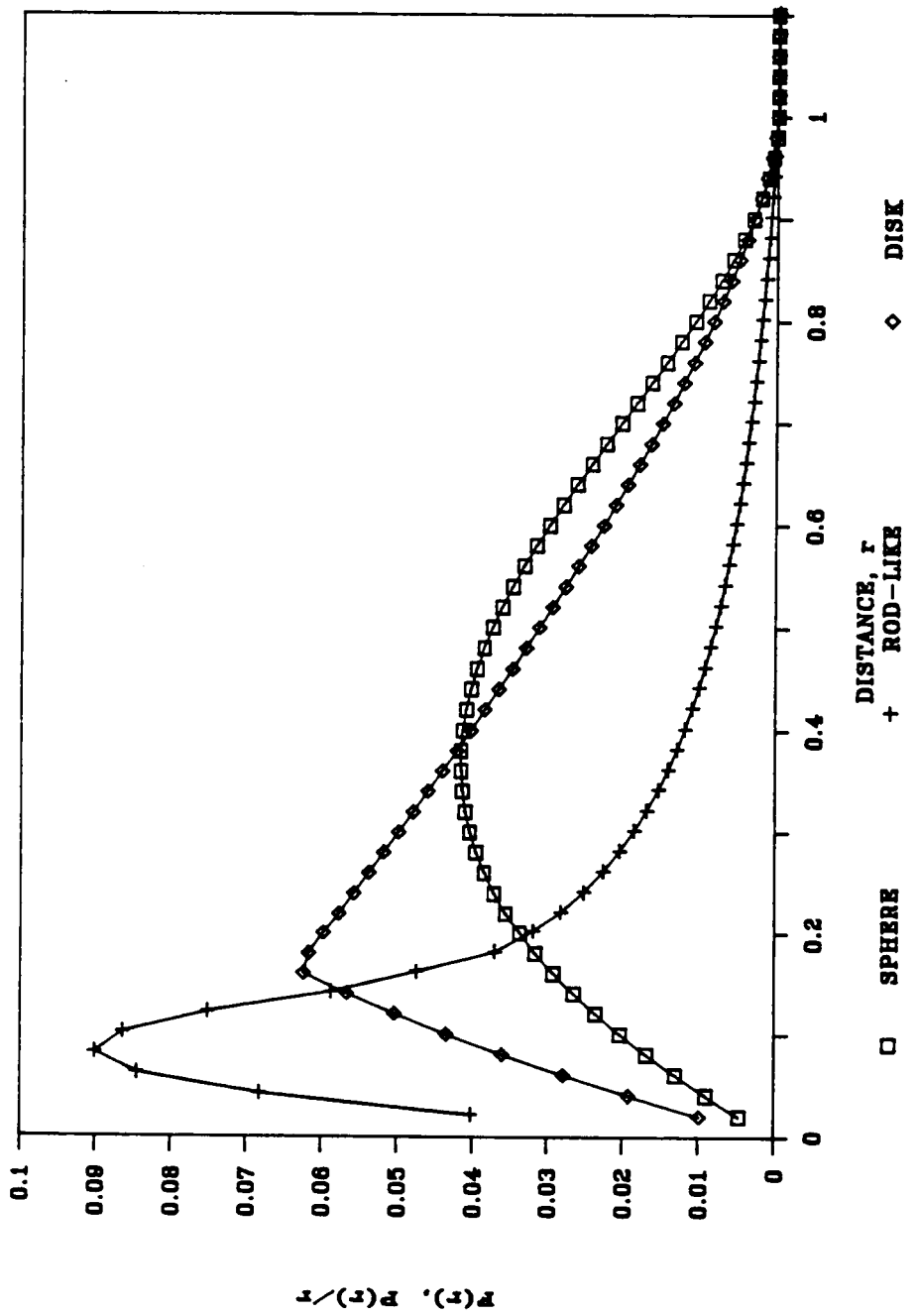



Figure 5.4.4 Theoretical F(r) function curves of spheres, rod-like particles and disk-shape particles.

of the disk-shape particles is the location of the maximum of the F(r) function. The limiting value of the x-axis is also the maximum distance within the particle.

Figure 5.4.5 shows distance distribution functions, P(r) of various XLPEs under different in-situ conditions. Distance distribution functions obtained at low temperature (>106°C) show a minimum with a negative frequency, indicating the distance distribution curve is not based on the dilute system, but has interference among the entities within the system. However, the curves obtained at higher temperatures approach to zero value with increasing the distance.

The F(r) function, that was obtained as the P(r) divided by the distance r, is shown in Figure 5.4.6. The plots obtained at above 107°C of in-situ temperature exhibit similar features to that of the simple ideal structures described in Figure 5.4.4. The plot obtained at 107.5°C is similar to the curve of disk-shape particles. The curve at 109°C is similar to that of sphere but a little shifted. The curve at 112C is not easy to calculate. F(r) plots of the same samples were shown before. Clearly, the curve for 107.5°C is similar to the disk shape having a linear slope at this point. The curve at 109°C shows that the entities look like the oblate spheroids. Interesting here is that the locations of the maxima in the F(r) function are very similar. However, the maximum distance within the entities was reduced to half of the value at 107°C (from about 400 to 200 Å).

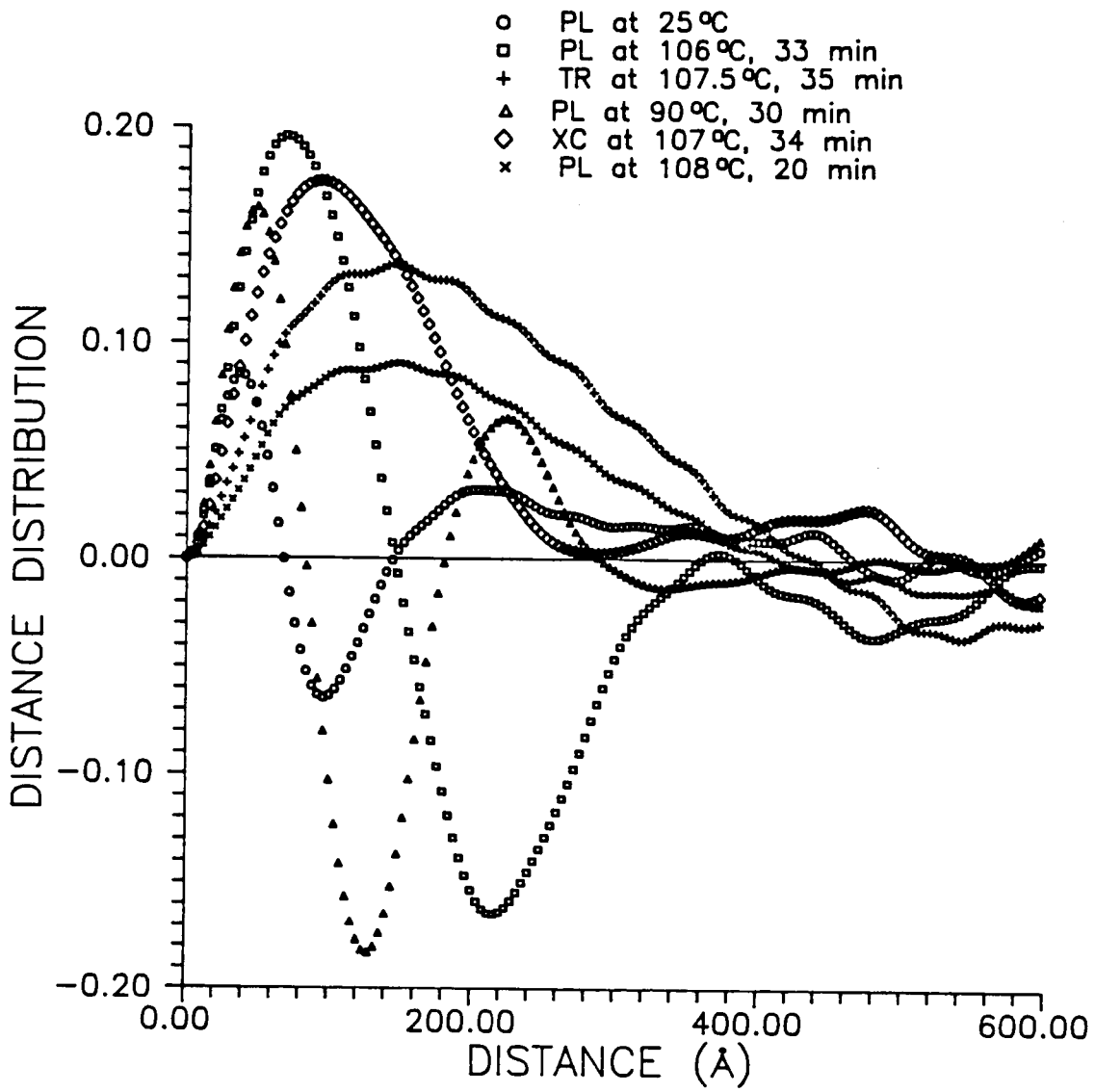



Figure 5.4.5 The distance distribution curves of various polyethylenes at various in-situ conditions.

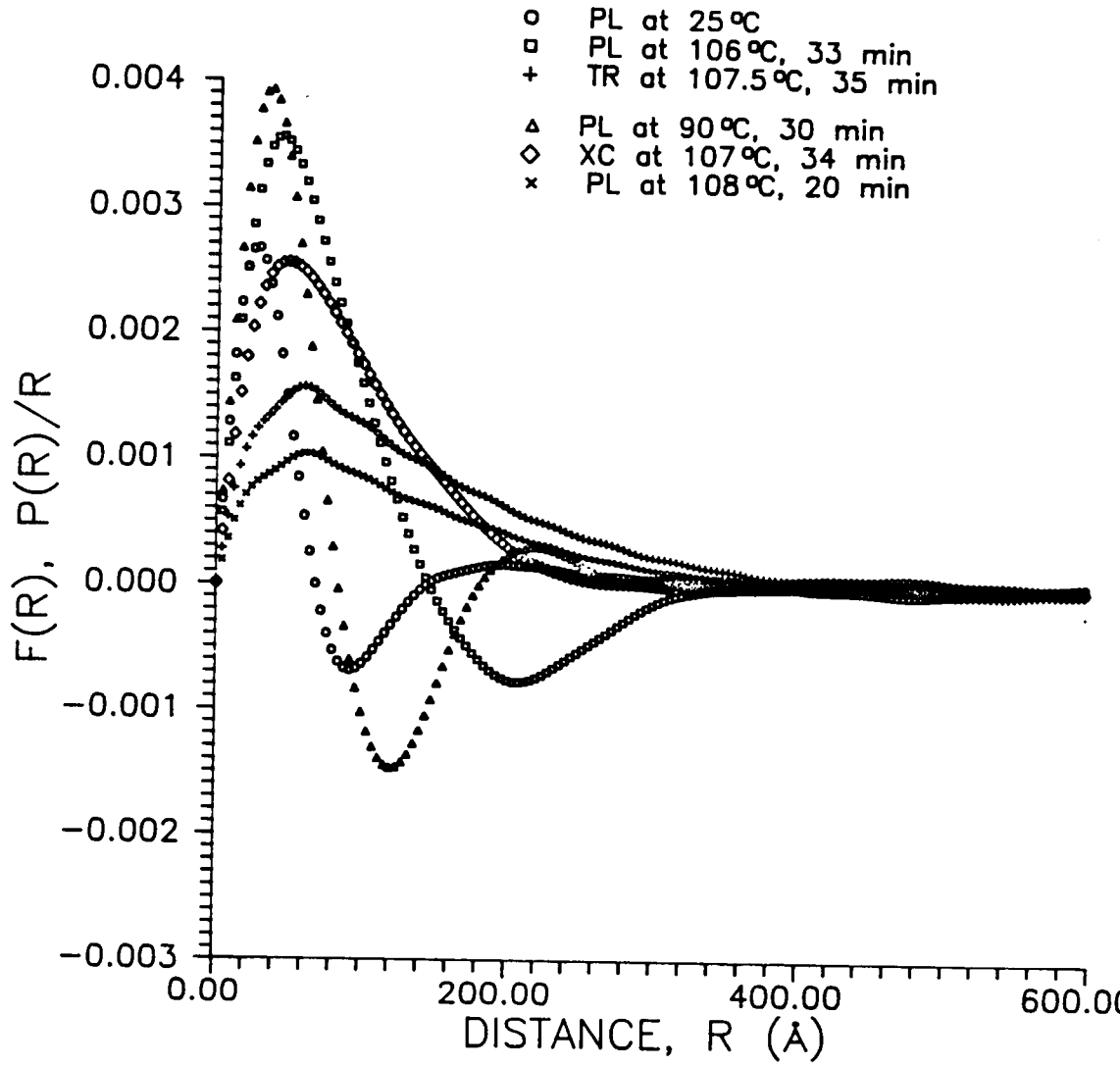



Figure 5.4.6 The F(r) function curves of various polyethylenes at various in-situ conditions.

The distance distribution function and the F(r) function of TR-XLPE at the in-situ temperature of 107.5°C are illustrated in Figures 5.4.7 and 5.4.8, respectively. The shapes of the distance distribution functions resemble disk particles. EC-XLPE shows a similar dependence of the shape of these two functions at in-situ temperature of 107°C as described in Figures 5.4.9 and 5.4.10. The F(r) function from the SAXS curve monitored after 8 minutes shows a negative peak, indicating the presence of non-particle scattering. This peak causes a major change in the limiting value of the x-axis, the measure of maximum distance. However, the location of the positive peak does not vary much from the values of other data. Corresponding P(r) and F(r) curves for the PL-XLPE at the temperature of 106°C are shown in Figures 5.4.11 and 5.4.12. All F(r) curves show a negative peak (Figure 5.4.12).

PL- XLPE that has been pre-annealed at 107°C for 3 hours was exposed to an in-situ temperatures of 108°C. The P(r) and F(r) function are plotted along with those of freshly prepared sample at other in-situ temperatures (Figures 5.4.13, 5.4.14). The only curve monitored at the temperature of 108°C shows a shape characteristic of the dilute system. These observations can be matched with the finding of a loss of Bragg maxima at such a high temperature (Figure 4.3.52). The basic shape of the distance distribution curves of PL-XLPE measured at 106°C is quite similar to the curves measured at room temperature or 90°C, having a minimum with distance frequency. These trends did not change with time elapsed up to 75 minutes.

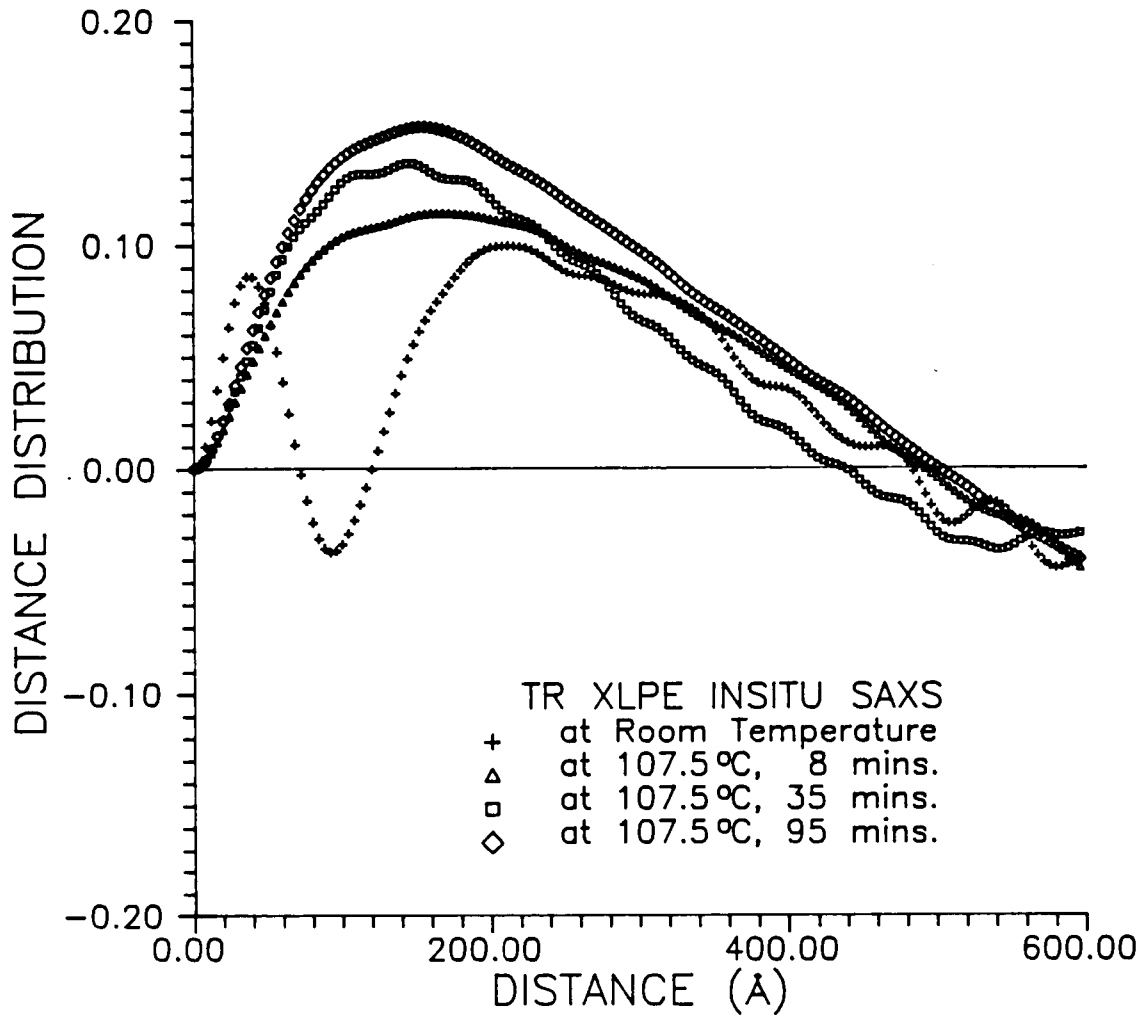



Figure 5.4.7 Variation of the distance distribution curves of TR-XLPE held at 107.5°C with in-situ time.

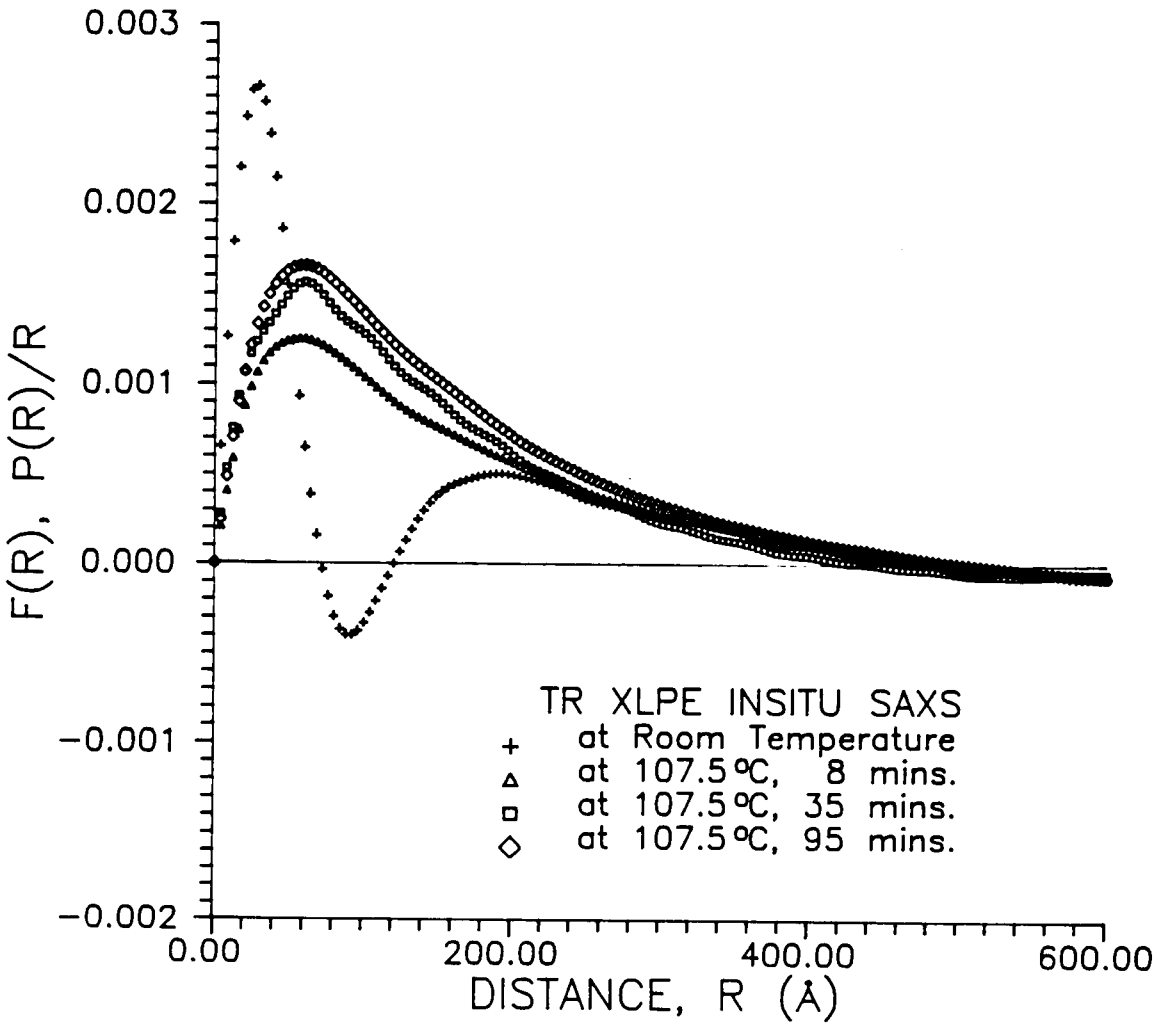



Figure 5.4.8 Variation of the F(r) curves of TR-XLPE held at 107.5°C with in-situ time.

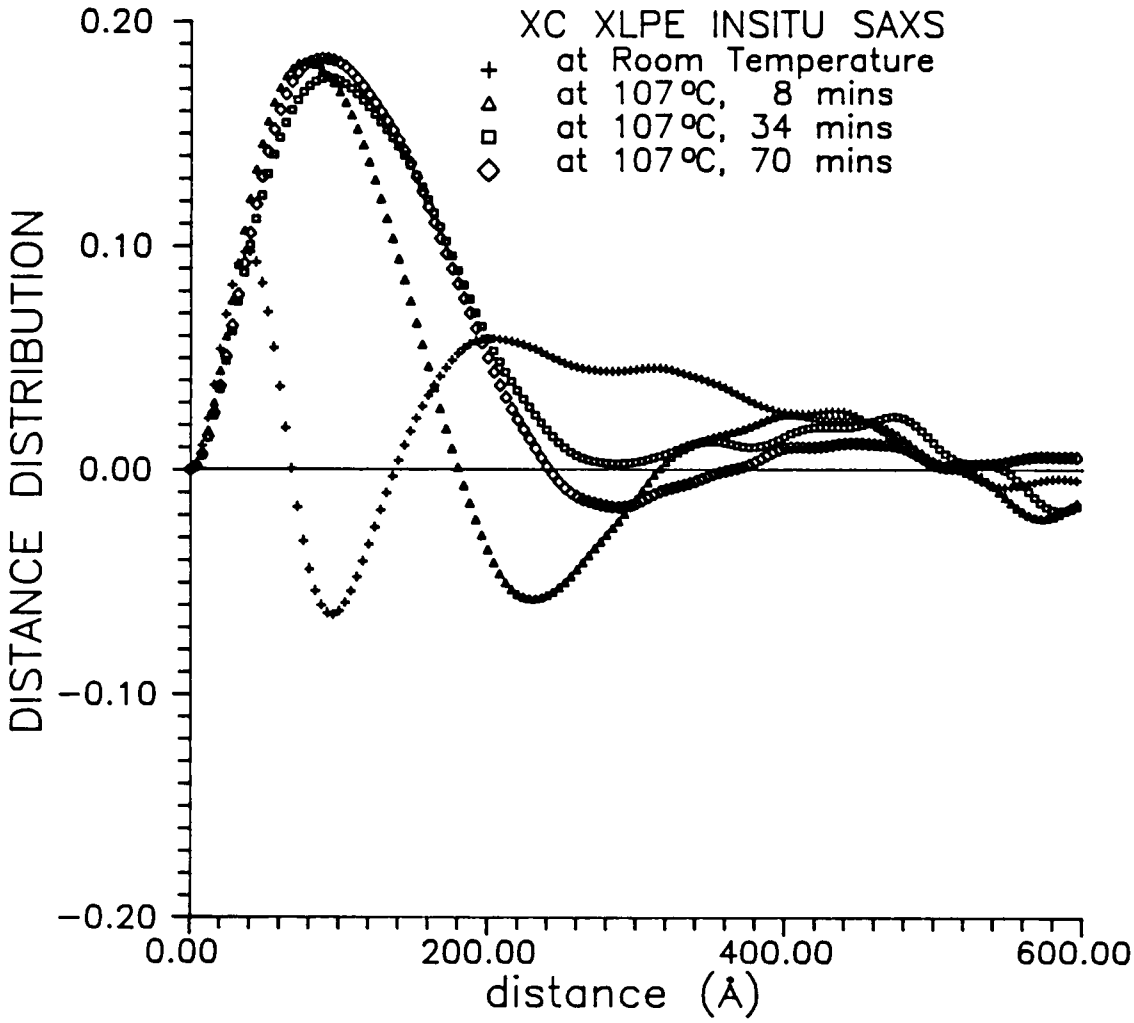



Figure 5.4.9 Variation of the distance distribution curves of EC-XLPE held at 107°C with in-situ time.

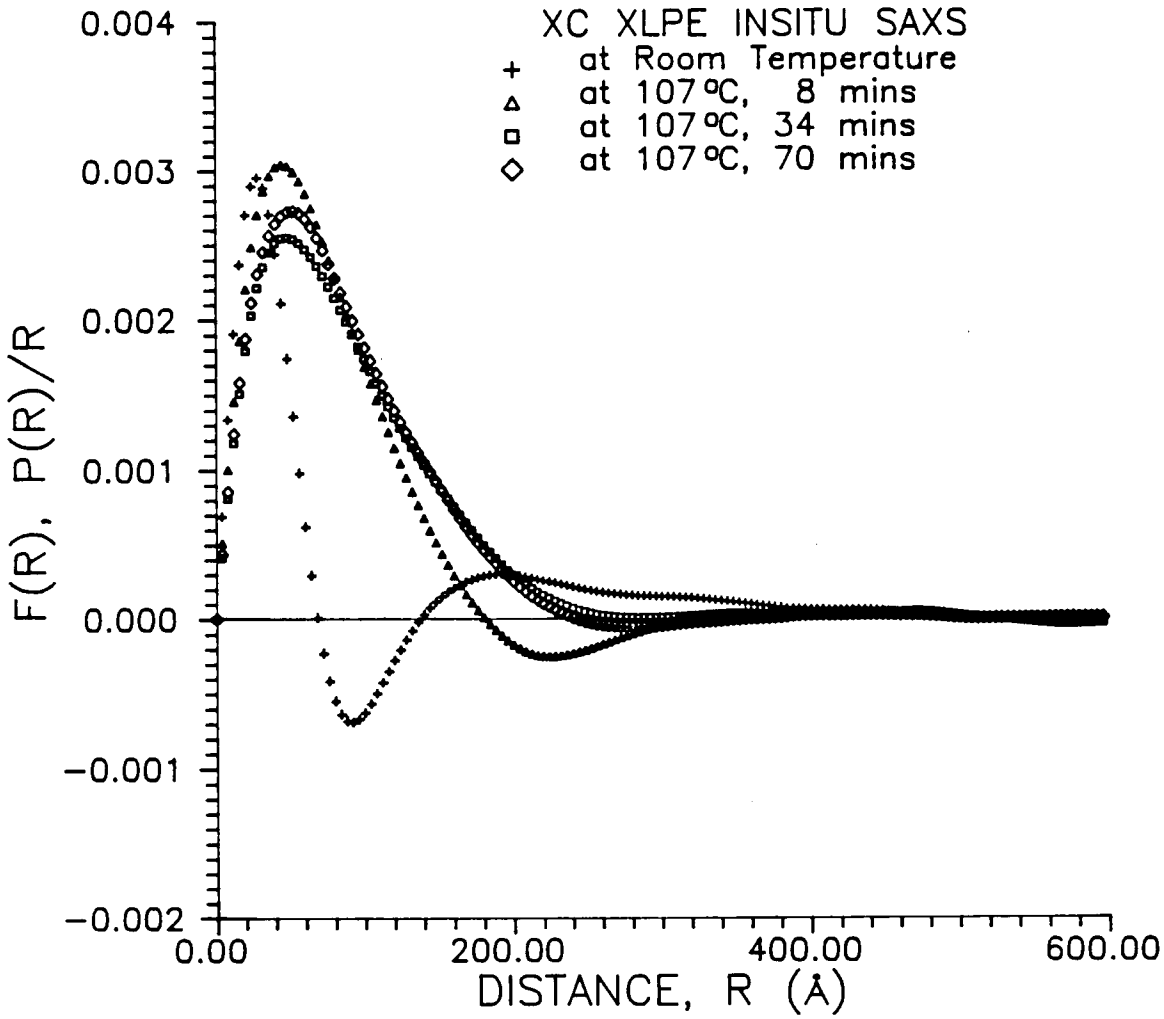



Figure 5.4.10 Variation of the F(r) curves of EC-XLPE held at 107°C with in-situ time.

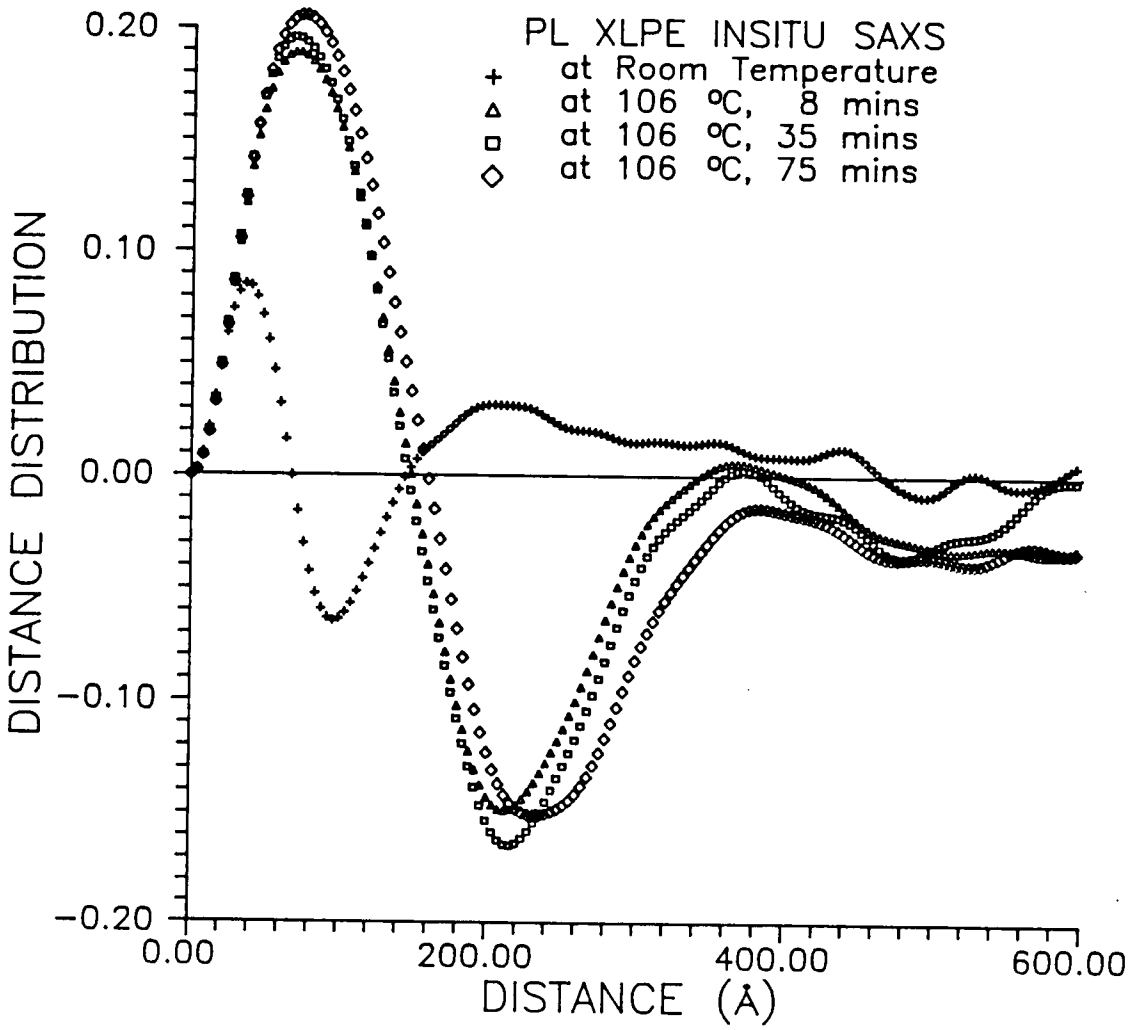



Figure 5.4.11 Variation of the distance distribution curves of PL-XLPE held at 106$^{O}$C with in-situ time.

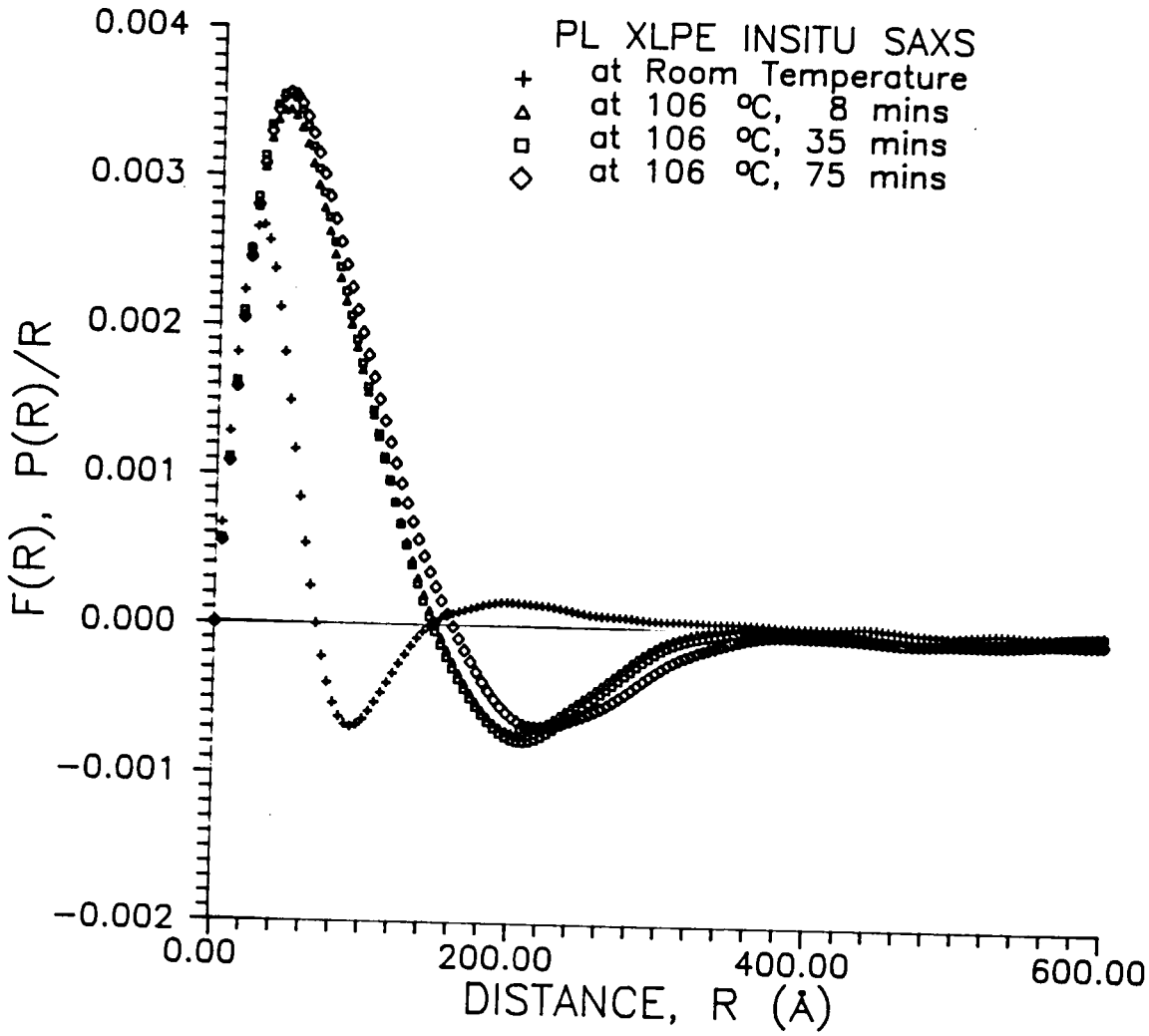



Figure 5.4.12 Variation of the F(r) curves of PL-XLPE held at 106$^{o}$C with in-situ time.

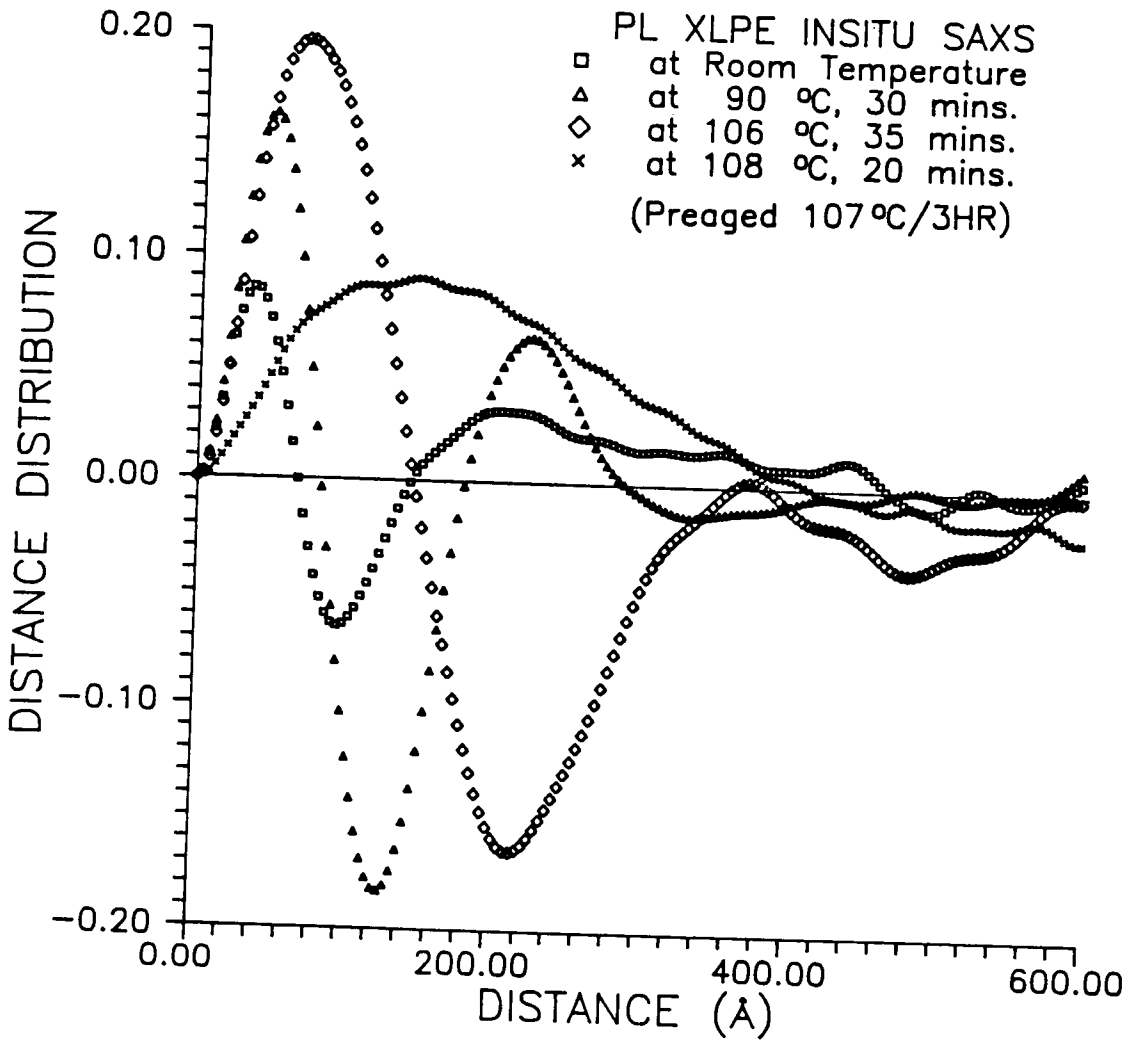



Figure 5.4.13 Variation of the distance distribution curves of PL-XLPE with various in-situ temperature and time.

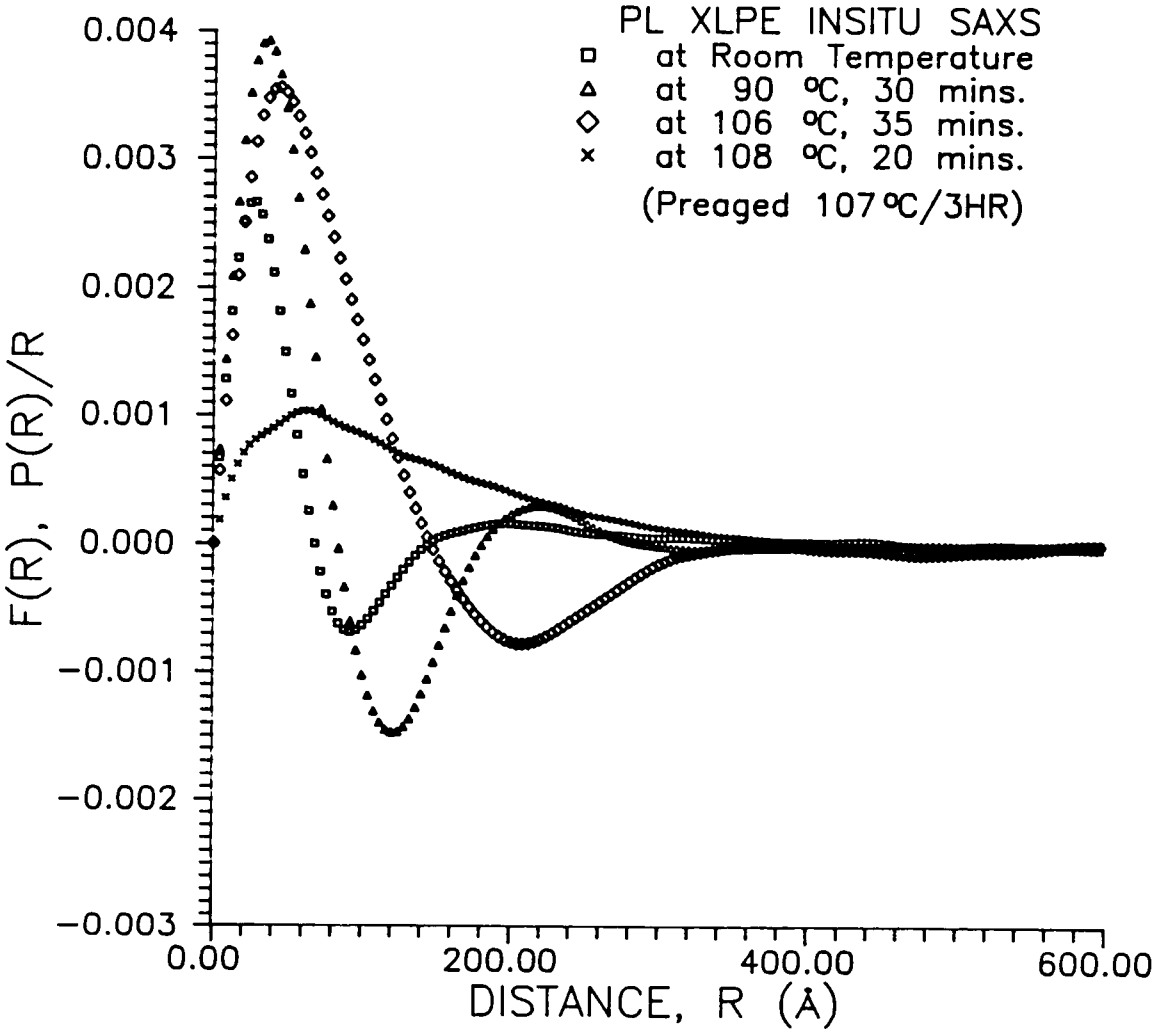



Figure 5.4.14 Variation of the F(r) curves of PL-XLPE with various in-situ temperature and time.

5.4.4. Proposed Mechanisms of Melt Separation and Annealing

A summary of the structural features at various in-situ temperature are shown in Table 5.4.2. It is of interest to note that the most frequent dimension in the entities at temperatures above 107°C is very close to the crystal thickness at lower in-situ temperatures. The most frequent dimension must be a thickness, since the shape of the entities at higher temperatures are either oblate spheroids or disk-like platelets. The coincidence of dimension of thickness at various in-situ temperatures may indicate that there is a characteristic dimension in the crystals of branched LDPE or XLPE. This results in good agreement with the results reported by Vonk and Koga (1985). They measured crystal thickness by two different SAXS analysis methods that are different from the one used in this work. The dimension was reported as c.a. 65 Å, very close to the one obtained in this work. A similar invariance of crystal thickness with temperature in branched polyethylene was also observed by Strobl et al. (1983).

It can be stated that the SAXS intensity at temperatures above 109°C was mainly generated by a particle-like melt. DSC and WAXD show no crystallinity at those temperatures. In fact, samples that have been annealed at those temperature do not generate a second peaks in their melting curves. The general shape of the particle at this stage seems to be an oblate spheroid. Major molecules in these particle-like melts must be relatively linear in shape, leading to higher density than the rest of the matrix.

Table 5.4.2 Dimensions of major entities of TR-XLPE for various in-situ conditions.

| In-situ Temp ($^{o}$C) | Crystal-linity (%) | Long Period (Å) | Cryst. Thickness (Å) | Shape |
|---|---|---|---|---|
| 25 | 52.1 | 122 | 64 | Lamellar |
| 60 | 40.4 | 148 | 60 | Lamellar |
| 90 | 37.2 | 166 | 62 | Lamellar |
| 100 | 27.4 | 220 | 60 | Lamellar |
| 107 | 1.7 | na | 58 | Platelet |
| 109 | 1.1 | na | 58 | Oblate Spheroid |

On the other hand, at lower temperatures (ca. 107°C), the remaining crystals left in the melt cause scattering, in spite of their small content (<3%). At the initial annealing stage, the lamellar structure starts to disappear. More linear molecules with relatively small size start to reorganize and are added to the remaining crystals along their lateral dimension, changing the shape of entities from oblate spheroids to platelets. At this stage, the high mobility of these newly added chains plays a major role for the reorganization. Such chains are considered to be sol fraction, not connected to networks. In fact, no sol fraction was reported to crystallized at this temperature (Kao, 1984; Phillips, 1986). These entities will grow in population with time by the consumption of less linear sol molecules. At the same time, at least some sol fraction is still in the melt state. The molten sol fraction is considered to be more branched than the sol fraction that has been added to the remaining crystals. The presence of such sol fractions is mainly due to the higher branch level than the level of crosslinking. Therefore, all sol molecules are not necessarily separated from the network. However, most molecules in the crystals at the annealing temperature (ca. 107°C) are considered to be sol fraction free from the networks.

Meantime, major crosslinked molecules are still in the melt state. The crosslinked melt will co-crystallize with the rest of the sol fractions, around the sol crystals, as temperature decrease,

leading to a lamellar structure. Thus, the sol separation from the network matrix at the melt state has been verified.

With increasing annealing time, more sol crystals are formed within the melt matrix. These sol crystals are believed to be assembled together, forming loosely stacked lamellae away from the network. This feature results in the higher crystallinity variation among stacks developed in the SAXS pattern of the annealed sample. The increasing crystallinity variation with annealing time is also due to this nature. Similar melt segregation was proposed as the form of lamellar diffusion during heat treatment in LDPE (Rueda, 1984).

## 5.5. Electrical Breakdown

### 5.5.1. IR Analysis

Major differences between IR spectra of the undamaged and the ruptured region of TR-XLPE lie in the presence of a strong band at 1720 $cm^{-1}$ and the variation of peaks in the region of 1050-800 $cm^{-1}$, where most unsaturation feature can be determined. The former band was thought to be caused by the C=O double bond stretching vibration.

First of all, a clarification of the bands in the range of 1675-1800 $cm^{-1}$ is necessary. Most bands in this range are caused by various type of carbonyl and they are typical oxidation bands for polyethylene, (Luongo, 1963). The main carbonyl oxidation product is

known to involve the ketonic carbonyl group (1720 $cm^{-1}$) with a smaller contribution from ester groups (1740 $cm^{-1}$).

The peak at 1720 $cm^{-1}$ shown in the sol fraction as well as in the breakdown region of TR-XLPE is thought to be induced from the stretching of ketones (>C=O), being clear evidence of oxidation. Similar considerations have been published for cable material (Crine, 1988). It is interesting to note that the size of the peak in the BD region is much higher than that in the sol fraction, indicating severe oxidation. A lower level of oxidation has been reported for water tree initiation (Gorton, 1987), and for electrical treeing (Shimizu, 1987).

The band in the sol fraction, however, is thought to be generated by the high temperatures during crosslinking and/or extraction. In fact, heating of polyethylene above 200°C was noted to cause thermo-oxidation (Igarashi, 1964). The higher presence of ketone in sol fraction than in the gel may indicate that the crosslinks or branched tertiary carbons have been attacked by oxidation.

Another interesting point to note is the higher vinyl end group concentration in the breakdown region. Even though oxidation at below or above the melting temperature results in chain scission, the vinyl type double bond contents of polyethylene was reported to decrease with oxidation (Igarashi, 1964). If their finding is true, then the actual surge of vinyl and other double bonds may be much

higher than those appearing in the results. It is the oxidation reaction that may consume some of the double bonds.

It can be deduced also that the formation of vinyl end groups is not a result of the oxidation reaction but from chemical chain scission. The chain scission may be initiated by the temperature rise above the ceiling temperature of the polymer, primarily due to thermal stress build-up by electron bombardment under electrical stress. Even though the temperature rise may be a very local and short-period phenomenon, it can be considered to be very effective in inducing chain scission. Outgassing during a breakdown test associated with local decomposition of material has been observed and provides evidence for a local temperature increase beyond the ceiling temperature. The phenomenological aspects of chemical chain scission have been noted during electrical treeing, but without full explanation (Shimizu, 1987).

### 5.5.2. Morphological Effects

The generation of spherulites in the electrically ruptured XLPE is remarkable. The observation that the breakdown holes are surrounded by a highly dense spherulitic region and that the walls of the holes are composed of closely compact spherulites suggests that the formation of spherulites is closely related to the breakdown of the network. The comparison of the infrared spectra of the electrically ruptured area and the extractables of TR-XLPE polyethylene strongly suggests the possibility of a breakdown of the network.

It is clearly understood that banded spherulites are typical of uncrosslinked polyethylenes, chemically crosslinked polyethylene forming spherulitic structures with great difficulty (Phillips, 1984). In fact, the spherulites observed around the breakdown area are larger (up to 35 μm in diameter) than those of extractable portions of TR XLPE which were prepared by quenching (average 5 μm diameter). This indicates that the breakage of the crosslinks alone cannot generate such large spherulites.

The formation of large spherulites is usually caused by very slow cooling with a lower population of nucleation sites, however, in this case the specimen was effectively quench cooled after breakdown and so the spherulite size is probably a reflection of low molecular weight species with linear chains caused by the breakdown process.

It is hard to believe that any factor other than oxidation and heating due to electric breakdown can have caused these unusual structures. Oxidation of polyethylene is known to result in an increase in density and crystallinity (Winslow, 1965). The increase in density and crystallinity was attributed to the scission of constrained chains in the amorphous region and oxygen-induced crystallization. For oxidized HDPE, near 100% WAXD crystallinity values have been reported. Moreover, the crosslink is listed as the most vulnerable point for oxygen attack (Winslow, 1963). Branched molecules were also noted to a lower resistance to oxygen attack

compared to linear chains, due to the instability of tertiary carbons.

Therefore, it is plausible that the formation of densely packed large spherulites is caused by chain scission at the crosslinks and branch points. The additional chain scission may assist the formation of small molecular weight chains which are linearity in shape. Thus, the remaining chain segments are crystallized to form large spherullites by oxidative crystallization.

5.5.3. Breakdown Mechanisms

There have been several mechanisms proposed for electrical breakdown as reviewed in Chapter 2. Traditional understanding of the thermal breakdown mechanism does not explain chemical chain scission nor oxidation during breakdown, since this postulate relies only on thermal stability. Simple melting cannot break chemical bonds and cannot produce spherulites in XLPE. Similar speculation can be made for the mechanical breakdown theory, since this theory only considered mechanical balance without consideration of molecular level effects. Therefore, these suggested breakdown mechanisms have to be modified.

The most reasonable explanation is the electron breakdown mechanism. However, this mechanism in general considers intrinsic breakdown features without explanation of phenomenological observations (Nelson, 1983). One possible explanation may begin with electron injection for initiation of breakdown (Eichhorn,

1983). After emission into the polymer, some electrons may be trapped and others may return to the electrode. During this return, the electrons are thought to be passing into a very high field and hence accumulate energy. After absorption of sufficient energy for ionization, the oxidation reaction starts with the aid of oxygen from the surroundings.

This severe oxidation reaction must occur primarily at the crosslink and branch points in the amorphous region due to their high vulnerability for oxygen attack (Winslow, 1963). A high electrical stress concentration in the amorphous region due to the low value of dielectric constant may accelerate severe damage in the amorphous region. Oxidation then results in scission of the constrained chains. Definite additional chain scission, as proved by the increase of vinyl content, also assists the further breakup of crosslinks as well as branch points. The resulting chain segments are considered to be very small in size and very linear in shape. Thus, they are able to crystallize easily to form very large spherulites even under rapid cooling. Thermal stress build-up during the breakdown process also increases the temperature of the specimen and enhances the mobility of remaining segments for easy crystallization. Observation of 100% crystallinity for polyethylene under oxidation (Winslow, 1963) can prove the possibility of formation of highly compacted large spherulites, even without consideration of the temperature effect.

Since the electrical breakdown mechanism involves severe breakage of network structure, the properties of materials like XLPE can be enhanced by preventing or reducing the likelihood of breakage of networks. It also suggests that in pre-breakdown phenomena such as partial discharge a volume of material in the vicinity of the discharge will now be composed of spherulites of relatively low molecular weight molecules. Further partial discharge will therefore take place into a preconditioned weak material. If this is true, then the only part of a failure process that occurs within the crosslinked material is the first partial discharge. The rate of progress of a tree may therefore be dependent only on the temperature reached during partial discharge i.e. how far above the ceiling temperature.

# 6. CONCLUSION

## 6.1. SAXS Model Study

It has been shown that the variable stack model better fits the SAXS intensity curves from highly dispersed lamellar systems such as LDPE, XLPE, and LLDPE. The introduction of crystallinity distribution amongst the stacks changes the shape of the unmodified SAXS intensity curve as well as the one-dimensional correlation function. With a given thickness distribution, the peaks become smaller and the intensities near the zero angle become higher as the crystallinity distribution become higher. The unusual shape of the SAXS intensity curves from LLDPE has been simulated with a higher value of crystallinity distribution. Even though the specific details of the model need to be investigated further, the implications and the coincidence with experimental results indicate that fluctuation of local crystallinity and thickness within each stack are characteristic of highly dispersed lamellar systems.

The Lorentz correction is found to be necessary for reasonable prediction of long periodicity. However, unmodified SAXS intensity curves contain more information on the nature of crystallinity distribution as well as thickness distribution. The SAXS model study proves that SAXS intensities near the zero angle can be generated by the presence of extra-thick crystal layers in the system.

## 6.2. Characterization of Various Polyethylenes

The IR investigation has shown that TR-XLPE contains additional chemical additives compared to other polyethylenes. Even though the additives cannot be identified, the basic functions are thought to be antioxidant and voltage stabilization on the basis of the indications of higher oxidative induction time (OIT) and higher breakdown strength of TR-XLPE. The additives are found to be bonded to the chain so that they cannot be lost by diffusion to the environment. The density of TR-XLPE was also found to be higher than other XLPE, presumably from the presence of the additive. IR spectra of EC-XLPE and PL-XLPE show no major differences, as expected. It was also shown that the chemical additives present in TR-LLDPE are similar to those used in TR-XLPE. TR-LLDPE shows the highest unsaturated vinyl content.

DSC results, however, do not show any clear difference between the XLPEs except for the slightly higher heat of fusion of TR-XLPE. The higher crystallinity value for TR-XLPE was also confirmed by WAXD technique. In the DSC study clear evidence of room temperature annealing was observed for all XLPEs and LLDPE. All the polyethylenes attain higher melting temperatures and heats of fusion during storage at room temperature. Thus, during measurement of crystallinity and other physical properties, room temperature annealing of the material has to be considered along with other factors. It was noted that in the precise measurement of melting behavior scanning has to be made from below room temperature.

The SAXS intensity plots of XLPE and LDPE can be characterized by well-defined broad Bragg maxima, indicative of the presence of stacking of amorphous and crystalline layers. The only difference among the SAXS intensity curves of the three XLPEs is that there is a generally lower intensity level for TR-XLPE. On the other hand, TR-LLDPE did not show a definite Bragg maximum, but a hump at much lower angle than the peaks of XLPEs with higher intensity. The scant presence of the peak was interpreted as due to high local crystallinity distribution due to fractionated crystallization caused by branch levels. The room temperature annealing features were also revealed in SAXS experiments, leading to lower angle of Bragg maximum location and higher intensity at the peaks.

## 6.3. Annealing of Polyethylene

DSC experiments have shown that isothermal annealing of polyethylene results in the generation of a new peak or a shoulder next to the annealing temperature. With increasing annealing time at 107$^{o}$C, the second melting peak and its size were noted to increase on a logarithmic scale. The crystallinity determined from the heats of fusion was found to increase with annealing time. Density measurement and WAXD also show similar results, on a reduced scale.

Even though the shapes of the SAXS intensity curves of XLPEs are different from that of TR-LLDPE, effects of annealing time on these two polyethylenes are similar, e.g, lowering of Bragg maxima, general increase of intensity level at lower angles, reducing

breadth of the peak. On the basis of the variable stack SAXS model, the effects were noted as (a) large increase of crystallinity distribution among stacks, (b) a small decrease of thickness distribution within each stack and (c) an increase of mean long periodicity. Increasing of long periodicity of XLPE and LLDPE upon annealing was found to be due to a major increase of crystal thickness as expected. These results may indicate a selective melting-crystallization process leading to partial molecular segregation. It is also noted that curing produces similar trends in SAXS pattern to annealing. However, the increase in long periodicity during curing was attributed to an increase of amorphous thickness.

The effect of the annealing medium was also investigated. Silicone oil was found to cause no major difference compared to annealing in air. However, the mineral oil, Univolt$^{tm}$ 60 causes severe damage especially at higher annealing temperatures. DSC results have shown that most linear molecules had been extracted during annealing at 107oC, resulting in loss of heats of fusion and destruction of lamellar structure. Annealing even at lower temperature resulted in a loss of linear molecules that would have formed thick crystals, affecting the SAXS intensity at lower angles.

## 6.4. Phase Separation of XLPE

The origin of the double melting peak in XLPE annealed at 107$^{o}$C was investigated using in-situ DSC and in-situ SAXS. For the initial stage of annealing at 107$^{o}$C most branched crystalline

fractions with low melting points start to melt. At the intermediate stage, the molten sol with linear molecules crystallizing to platelets. Later, these crystallites are believed to thicken on a long time scale.

Distance distribution functions were found to be very useful for the analysis of SAXS from particle structure, giving information on the shape and the major dimension of the particles. At in-situ temperatures of 109oC or higher, most entities were found to be particle-like having a different density to the melt matrix. These entities are believed to be molten sol having an oblate spheroidal shape with a thickness of 58 Å. At in-situ temperatures around 107oC, the entities causing SAXS appears to be sol crystalline fractions having a platelet shape with a mean thickness of 58 Å. Results and analysis clearly suggest the possibility of melt separation at higher temperature.

Lamellar structure was found at temperatures of 106$^{o}$C and below. The average crystalline thickness after 30 minute of annealing was found to be 60 Å regardless of in-situ temperature. This thickness is believed to increase with in-situ time.

## 6.5. Electrical Breakdown

The formation of large spherulites was observed in the electrically ruptured regions of all polyethylenes. These large spherulites clustered in a dense pattern suggest the major breakup of crosslinks and branches within the system. IR spectra of the

ruptured region shows evidence of severe oxidation and chain scission during breakdown. Molecular chain scission appears to occur chemically by oxidation as well as thermally due to the temperature rise caused by the electrical stress during breakdown. Most chain scission is considered to occur at crosslinks and branches within the amorphous region due to their instability compared to linear chains, resulting in a lowering the number of constrained molecules. The resulting chain segments are considered to crystallize to form large spherulites consisting of very small molecular-weight material with linear chains. Oxidation and chemical chain scission may be initiated by the interaction between trapped electrons and returning electrons to the electrode within the material.

# 7. SUGGESTIONS FOR FURTHER WORK

## 7.1. SAXS Model

In order to understand the SAXS patterns, the model studied here need to be better tailored. One suggested modification is the adaptation of other distribution function for crystallinity distribution as well as thickness distribution. The modification of thickness distribution that has been attempted here was not optimal, since it is known that the short chain branching is major factor affecting crystallinity distribution (Wild, 1982). Most short branching was reported to follow the either bi-modal or exponential distribution. Thus, application of such distribution functions is suggested for better fitting.

## 7.2. Direct Observation

The physical meaning of a stack boundary having a similar crystallinity has been a major problem for understanding of the variable stack model. The observation of such features using electron microscopy is strongly suggested. Slowly cooled or highly annealed LLDPE appears to be the best material for identifying such features.

## 7.3. The Effects of Annealing Time and Temperature

The variation of annealing time at 107°C was found to influence the DSC melting thermograms. Similar behavior is expected for any annealing temperature. It is suggested that similar relationship be established for various annealing temperature for better estimation of annealing damage than just by scanning the material using DSC.

## 7.4. The Room Temperature Annealing Effect

Most polyethylenes having a high branch level were found to change at room temperature. Annealing at room temperature causes a hump around 45°C. Annealing at even lower temperatures is expected, since such polyethylene has a glass transition temperature of -40°C. The estimation of the effects of this feature, especially the time effect, on the structure and properties is recommended. It would be appropriate to publicize this feature so that data can be compared with a full understanding of experimental conditions. Furthermore, all heats of fusion should be measured from at least 0°C.

## 7.5. Visco-Elasticity of XLPE Melt

The possibility of particle-like melt entities in the melt that cannot be measured by DSC nor WAXD, but can be seen in SAXS was noted in this work. It is expected that the presence of such particles may influence the visco-elasticity of the XLPE melt. Analysis of visco-elasticity of XLPE is recommended, since the

presence of a particulate melt may be confirmed. In unpublished results, the XLPE melts show no major deformation above the melting temperature. The cause of such behavior may be of interest.

## 7.6. Thermo-Oxidative Degradation

Thermo-oxidative degradation was suspected as one of the prime causes of the damage during the electrical breakdown. The observation of near 100% WAXD crystallinity has been published for HDPE degraded by oxidation (Winslow, 1963). The simulation of similar results of XLPE using oxidative degradation at high temperature may confirm the findings related to the electrically ruptured region made in this work. The small size of the electrically ruptured region was a major obstacle for the evaluation of the breakdown area. If thermo-oxidative research simulates electrically rupture, more extensive examinations can be made because of the larger material sample.

## 7.7. Mechanisms for Water treeing

Thermo-oxidative degradation is expected to initiate all damage of insulation caused by electrical stress. The presence of moisture, one of the major requirements for water treeing, may be the accelerating factor for the oxidation as well as the chain scission. Close inspection of treed regions using micro-infrared spectroscopy and other micro analysis techniques is strongly

suggested for the elucidation of the cause of the water treeing phenomenon.

# REFERENCES

Alexander, L. E. (1969), " X-ray Diffraction Methods in Polymer Science," Wiley Interscience, New York.

Ambrosio, J. D., G. R. Almeida, and R. E. S. Bretas (1987), IEEE 1987 CEIDP, 401-406.

Andreopoulos, A. G. and E. M. Kampouris (1986). J. Appl. Polym. Sci., 31, 1061-1068.

Ashcraft, A. C. and R.M. Eichhorn (1978), IEEE EI-13, 198-199.

Ashcraft, A. C. (1979), "Treeing Update-Part III," Kabelitem, No 152, Union Carbide Corp., N.Y.

Auckland, D. W., A. B. Borishade, and R. Cooper. (1977), CEIDP 1976, 318.

Bahder, G. and C. Katz. (1973), CEIDP 1972, 190.

Bahder, G., G. S. Eager, and R. G. Lukac. (1975), CEIDP 1974, 289-302.

Bahder, G., G. S. Eager, D. A. Silver, and R.G. Lukac (1976), IEEE PAS-95, 1552-1560.

Bahder, G., T. Garrity, M. Sosnowski, R. Eaton, and C. Katz. (1982), IEEE PAS-101, 1379-1388.

Bale, H. D. and P. W. Schmidt (1984), Phys. Rev. Lett., 53, 596.

Bamji, S. S., A. Bulinski, J. Densley, and A. Garton (1983), IEEE EI-18, 22-41.

Bamji, S. S., A. Bulinski, J. Densley, A. Garton, and N. Shimizu (1984). IEEE 1984 CEIDP, 141- 146.

Bamji, S. S., A. T. Bulinski and R. J. Densley (1984), IEEE 1984 CREI 37-40.

Bamji, S. S., A. T. Bulinski and R. J. Densley (1986a), IEEE 1986 CEIDP, 391- 397.

Bamji, S. S., A. T. Bulinski and R. J. Densley (1986b), IEEE EI-21, 639- 644.

Barlow. A, L. A. Hill, and M. F. Haringer (1983), IEEE PAS-102, 1921-1926.

Basset, D. C. (1981), "Principles of Polymer Morphology," Section 5.2, Cambridge University Press, London.

Bernstein, B. S., N. Srinivas, and P. N. Lee (1978), CEIDP 1975, 296-302.

Bernstein, B. S. (1984), IEEE 1984 CREI, 11-21.

Billing, J. W. and D. J. Groves. (1974), Proc. IEE., 121, 1451-1456.

Blundell, D. J. (1970), Acta Cryst., A26, 472.

Blundell, D. J. (1978), Polym, 19, 1258.

Bolton, B., R. Cooper, and K. G. Gupta. (1965), Proc. IEE., 112, 1215-1220.

Bradwell, A., R. Cooper, and B. Varlow. (1971), Proc. IEE., 118, 247.

Braun, J. M. (1980), IEEE EI-15, 120-123.

Brown, D. S., K. U. Fulcher and R. E. Wetton (1973), Polym., 14, 379.

Buchanan, D. R. (1971), J. Polym. Sci., Pt A-2, 9, 645.

Bulinski, A. T., and R.J. Densley. (1981), IEEE EI-16, 319-326.

Bulinski, A. T., S. S. Bamji, and R. J. Densley (1988), IEEE 1987 CEIDP, 440-447.

Cartier, E. and P. Pfluger (1987), IEEE EI-22, 123-127.

Ceres, B. V. and J. M. Schultz (1984), J. Appl. Polym. Sci., 29, 4183-4197.

Chan, J. C. (1978), IEEE EI-13, 444-447.

Chan, J. C. (1984), CEIDP 1984, 296-301.

Chen, J. L., J. C. Filippini, and Y. Poggi (1986), IEEE 1985 CREI, 366-369.

Clark, F.M. (1962), "Insulating Materials for Design and Engineering Practice," Wiley Interscience, N.Y.

Cooper, R., B. R. Varlow, and J. P. White. (1976), Proc. IEE., 123, 187.

Cooper, R., B. R. Varlow, and J .P. White. (1977), J. Phys., D-10, 1521-1529. (1977),

Crine, J. -P., and M. Duval (1984). IEEE 1984 CREI, 68-71.

Crine, J. -P., S. Haridoss and K. C. Cole (1988), Polym. Eng. Sci., 28, 1445.

Crist, B. (1973), J. Polym. Sci. Phys. Ed., 11, 463.

Crist, B. (1973), J. Polym. Sci., Phys. Ed., 11, 635.

Crist, B. and N. Morosoff (1973), J. Polym. Sci., Polym. Phys. Edn., 11, 1023.

Cross, J. D. and J. Y. Koo (1984), IEEE EI-19, 303-306.

Dakin, D. W. (1975) IEEE 1974 CEIDP, 197-206.

de Bellet, J. J., G. Matey, L. Rose, V. Rose, J. C. Filippini, Y. Poggi, and V. Raharimalala (1987), IEEE EI-22, 211-217.

de Kock R. J. and P. A. H. M. Hol (1964), Polym. Lettr., Vol. 2, pp. 339-341

DeBoer, A. P. and A. J. Pennings (1976). J. Polym. Sci., Polym. Phys. Ed., 14, 187.

Debye, P. (1915), Ann. Physik 46, 809.

Densley, R. J., A. Bulinski, and T. Sudarshan (1980), CEIDP 1979, 469-479.

Dissado, L. A., J. C. Fothergill, and S. V. Wolfe (1980), Elec. Comm., 57, 87-90.

Dissado, L. A., J. C. Fothergill, and S. V. Wolfe (1982), CEIDP 1981, 264-277.

Dissado, L. A., S. V. Wolfe, and J. C. Fothergill (1983), IEEE EI-18, 565-585.

Dole, M. (1967), J. Polym. Sci., Part C, 18, 57.

Eichhorn, R. M. (1974), CEIDP 1973, 289-298.

Eichhorn, R. M.(1976), IEEE EI-12, 2-18.

Eichhorn, R. M. and R. J. Turbett (1979), IEEE PAS-98, 2215-2222.

Eichhorn, R. M. (1981), Kabelitems, No 157, Union Carbide Corp.

Eichhorn, R. M. (1983), "Engineering Dielectrics," Vol IIA, ASTM, STP 783, 355-444.

Favrie, E. and H. Auclair (1980), IEEE PAS-99, 1225-1234.

Filippini, J. C. and C. T. Meyer (1982), IEEE EI-17, 554-559.

Filippini, J. C., C. T. Meyer, and M. E. Kahel (1983), CEIDP 1982, 629-637.

Filippini, J. C., C. Laurent, and C. Mayoux (1986), IEEE EI-21, 65-67.

Filippini, J. C., Y. Poggi, and V. Raharimalala (1986), IEEE 1985 CR PADM, 388- 390.

Fischer, P. and K. W. Nissen. (1976), IEEE EI-11, 37-40.

Fischer, P. (1982), "Electrical Properties of Polymer," Edited by D.A. Seanor, Academic Press.

Franke, E.A. and E. Czekaj (1978a), CEIDP 1975, 287-295.

Franke, E.A. and E. Czekaj (1978b), CEIDP 1976, 403-410.

Frohlich, H. (1947), Proc. Roy. Soc., A188, 521-532.

Fujisawa, Y., T. Yasui, Y. Kawasaki, and H. Matsumura (1968), IEEE PAS-87, 1899-1907.

Fukuda, T., S. Suzuki, M. Goto, and Y. Nitta (1973), CEIDP 1972, 211-215.

Fukuda, T., K. Nakano, T. Tanabe, A. Sudo, and T. Kuhara (1975), CEIDP 1974, 218-228.

Fukuda, T., S. Irie, Y. Asada, M. Maeda, H. Nakagawa, and N. Yamada (1981), IEEE 1980 Conf. Rec. of Electr. Ins., 118-121

Gamez-Garcia, M., R. Bartnikas, and M. R. Wertheimer (1984) IEEE 1984 CREI, 9-11.

Gamez-Garcia, M., R. Bartnikas, and M. R. Wertheimer (1987) IEEE EI-22, 199-205.

Garton, A., S. S. Bamji, A. Bulinski, and J. Densley (1986), IEEE 1986 CEIDP, 404-410.

Geil, P. H. (1963), "Polymer Single Crystals," Interscience, New York.

Geil, P. H. (1966), J. Polym. Sci., Pt C, 13, 149.

Given, M. J., R. A. Fouracre, and B. H. Crichton (1987), IEEE EI-22, 151-156.

Glatter, O. (1977), J. Appl. Cryst. 10, 415-421.

Glatter, O. (1979), J. Appl. Cryst. 12, 166-175.

Glatter, O. and O. Kratky. (1982), "Small Angle X-ray Scattering," Academic Press, New York.

Glover, H. R. (1986). Modern Plastic Encyclopedia, McGraw-Hill Inc., 63, 52-60.

Gohil, R. M. and P. J. Phillips (1986a). Polym., 27, 1687-1695.

Gohil, R. M. and P. J. Phillips (1986b). Polym., 27, 1696-1704.

Gordon, G. F. and M. T. Shaw (1986) IEEE 1986 CEIDP, 426- 431.

Gorton, A., S. S. Bamji, A. Bulinski and J. Densley (1987), 1986 CEIDP, 404.

Graneua, P. (1979), "Underground Power Transmission," Wiley Interscience, N.Y.

Gryzybowski, S., R. Dobroswewski, J. Brzostowski, and E. Grzegorski (1978), CEIDP 1976, 372-379.

Gryzybowski, S., P. Zabielik, and E. Kuffu. (1980), IEEE 1980 CREI, 200-203.

Gryzybowski, S., E. Robles, and O. Dorlanne (1982), IEEE 1982 CREI, 287-289.

Guinier, A. (1939), Ann. Phys., 33, 1275

Guinier, A. and G. Fournet (1955), "Small Angle Scattering of X-rays," New York, John Wiley.

Harpell, G. A. and D. H. Walrod (1973), Rubber Chem. and Tech., 46, No. 4 .

Hayami, T. and Y. Yamada (1973), CEIDP 1972, 239-246.

Henkel, H. -J. and H. Müller (1985), IEEE 1985 CEIDP, 281-289.

Henkel, H. -J., N. Müller, J. Nordmann, W. Rogler, and W. Rose (1987), IEEE EI-22, 157-161.

Hermans, P. H., D. Heikens, and A. Weidinger (1959), J. Polym. Sci., 35, 145.

Hosemann R. and S. N. Bagachi (1962), "Direct Analysis of Diffraction by Matter," North-Holland, Amsterdam, p408.

Hossam-Eldin, A. A. and A. El Shazli (1983), CEIDP 1982, 638-643.

Ieda, M. and M. Nawata. (1973), CEIDP 1972, 143-150.

Ieda, M. (1980), IEEE EI-15, 206-224.

Ieda, M. (1983), "Memoirs of The Faculty of Engineering," Vol 35, No 2, 205, Nagoya University. Nagoya, Japan.

Igarashi, S. and H. Kambe (1964a), Bull. Chem. Soc. Japan, 37, 176.

Igarashi, S., O. Yamamoto and H. Kambe (1964b), Kolloid-Z., 199, 97.

Isshiki, S., M. Yamamoto, S. Chabata, T. Mizoguchi, and M. Ono (1974), IEEE PAS-93, 1419-1429.

Iwata, Z., T. Fukuda, and K. Kikuchi (1973), CEIDP 1972, 200-210.

Johle, R. J. (1986). Modern Plastic Encyclopedia, McGraw-Hill Inc., 63, 62.

Jonscher, A. K., and R. Lacoste. (1984) IEEE EI-19, 567-577.

Kaminaga, K., K. Hirato, S. Irie, H. Kimura, I. Ishino, H. Nakagawa (1986) IEEE 1986 CREI, 170-174.

Kao, Y. H. and P. J. Phillips (1986). Polym., 27, 1669-1678.

Karakelle, M. (1986), Ph.D. Dissertation, University of Utah.

Kato H. and Y. Miyashita (1987). IEEE 1987 CEIDP, 391-400.

Katz, C. and B. S. Bernstein (1974), CEIDP 1973, 307-316.

Katz, C., N. Srinivas, and B. S. Bernstein (1975), CEIDP 1974, 279-288.

Kavesh, S. and J. M. Schultz (1970), J. Polym. Sci., Pt A-2, 8, 234

Kavesh, S. and J. M. Schultz (1971), J. Polym. Sci., Pt A-2, 9, 85.

Kawaguchi, A., T. Ichida, S. Murakami, and K. Katayama (1984), Colliod & Polym. Sci., 262, 597.

Kilian, H. G. and W. J. Wenig (1974), J. Macromol. Sci. (B), 9, 463.

Kim, B and K. Lim (1986) IEEE 1986 CEIDP, 398-403.

Kirkland, J. W., R. S. Thieda, and R. A. Reitz (1982), IEEE PAS-101, 2128-2136.

Kitagawa, K., G. Sawa, and M. Ieda. (1980), Jap. J. Appl. Phys., 19, 389-390.

Kitagawa, K., G. Sawa, and M. Ieda. (1981), Jap. J. Appl. Phys., 20, 87-94.

Kitchin, D. W. and O. S. Pratt. (1958), IEEE PAS-77, 180-186.

Kitchin, D. W. and O. S. Pratt. (1962), IEEE PAS-81, 112-121.

Kolesov, S. V. (1980), IEEE EI-15, 382-388

Koo, J. Y., J. D. Cross, M. El Kahel, C. T. Meyer, and J.C. Filippini. (1984), CEIDP 1983, 301-305.

Korteleve G. and C. G. Vonk (1968), Kolloid Z. Z. Polym., 225, 124.

Kothe, R., S. Bamji, A. Bulinski, and J. Densley (1986), IEEE 1986 CREI, 37-40.

Lanctoe, T. C., J. H. Lawson, and W. L. Mcvey. (1979), IEEE PAS-98, 912-925.

Laurent, C., C. Mayoux and S. Noel (1983), J. Appl. Phys., Vol 54, 1532-1539.

Lawson, J. H. and W. Vahlstron (1973), IEEE PAS-92, 824-835.

Lawson, J. H. and W. A. Thue (1980), IEEE 1980 CREI, 100-104.

Lu, W., D. Du and Q. Liu (1986) IEEE 1985 CR PADM, 705-708.

Luongo, J. P. (1963), J. Polym. Sci., B1, 141.

Mandelkern, L., A. L Allou, and M. R. Gopalan, (1968), J. Phys. Chem., 72, 309.

Manley, T. R. and M. N. Qayyum (1971). Polym., 12, 176.

Martinez-Salazar, J., P. J. Barham, A. Keller (1985), J. Mater. Sci., 20, 1616.

Mason, J. H. (1959), "Progress in Dielectric," Vol 1, 1-58, Edited by J.S. Birks and J.H. Schulman, Heywood and Co., London.

Matsubara, H. and S. Yamanouchi (1975), CEIDP 1974, 270-278.

McCready, M. J., J. M. Schultz, J. S. Lin, and R. W. Hendricks (1979), J. Polym. Sci., Phys. Ed., 17, 725.

McHugh, A. J. and J. M. Schultz (1971), Phil. mag., 24, 155.

Mckean, M. C. (1976), IEEE PAS-95, 253.

Mcmahon, E.J. and J.R. Perkins. (1964), IEEE PAS-82, 1253-1261.

McMahon, E. J. (1968), IEEE EI-3, 3-10.

Mcmahon, E. J. (1981), IEEE EI-16, 304-318.

Meyer, C. T., J. C. Filippini, and N. Felici (1979), CEIDP 1978, 374-381.

Michel, M. C. and J. C. Bobo (1979), J. Appl. Polym. Sci., Symp., 35, 581-587.

Milton, D. and J. 1. Wentz. (1966), Insul. (May 1966), 71-76.

Miyashita, Y., H, Itoh and T. Shimimura (1985). IEEE 1985 CR PADM, 670- 674.

Miyauchi, H. and K. Yahagi. (1972), Trans. Elect. Comm. Engr. Jap., 92-A, 36-45.

Mizukami, T., S. Kuma, and K. Soma (1978), CEIDP 1977, 316-322.

Morita, M., M. Hannai, and H. Shimanuki (1974), CEIDP 1973, 299-306

Morita, M., M. Hannai, H. Shimanuki, and F. Aioa (1978), CEIDP 1975, 335-343.

Nakasaki, S., H. Matsbara, Y. Yamanouchi, M. Yamada, T. Matsuike, and S. Fukunaga (1983), IEEE/PES 1983 Power Summer Mtg., 6.

Namiki, Y., Y. Shimanuki, F. Aida, and M. Morita (1980), CEIDP 1979, 490-499.

Narkis, M., I. Raiter, S. Shkolnik, A. Seigmann, and P. Eyerer (1987). J. Macromol. Sci.-Phys., B26, 37-58.

Naybour, R. D. (1983), CEIDP 1982, 620-628.

Naylor, K. L. and P. J. Phillips (1983), J. Polym. Sci., Polym. Phys. Ed., Vol 21, pp. 2011-2026.

Nelson, J. K. (1983), "Engineering Dielectrics," Vol IIA, ASTM, STP 783, 445-520, ASTM.

Nitta, Y. (1974), IEEE EI-9, 109-112.

Noto, F. (1980), IEEE EI-15, 251-258.

Nunes, S. L. and M. T. Shaw (1984), CEIDP 1983, 312-317.

Nunes, S. L., M. T. Shaw, S. H. Shaw, and R. A. Weiss (1982), CEIDP 1982, 615-619.

O'Tooles, J. L. (1984), "Modern Plastic Encyclopedia," 1984-1985, 437-440, McGraw-Hill.

Olyphant, M. (1963), IEEE PAS-82, 1106-1112.

Orton, H., K. Abdollall, S. Bamji, A. Bulinski, R. J. Densley, and A. Garton (1982), CEIDP 1981, 306-313.

Phillips, P.J. (1983), "Engineering Dielectrics," Vol IIA, ASTM STP 783, 119-237, ASTM.

Phillips, P. J., M. Karakelle and A. Vatansever (1984), Polym. Comm. 25, 204-206.

Phillips, P. J. and Y. H. Kao (1986). Polym., 27, 1679-1686.

Phillips, P. J. (1988) "Morphology of Extruded Dielectric Cable Insulation," EPRI EL-5921 Final Report, EPRI, July 1988

Phillips, P. J. and A. Vatansever (1989), submitted for publication.

Porod, G. (1948), Acta Phys. Austr. 3, 255-292.

Porod, G. (1951), Kolloid-Z, 124, 83.

Prigent, M., J. Bobo, and E. Eyrand. (1975), IEEE Conf. Publ., 129, 32.

R. W. Hendricks (1978), J. Appl. Cryst., 11, 15.

Raman, R., B. L. Deopura, D. D. Varma and V. D. Gupta (1977), Polym. J., 9, 115.

Rayleigh, Lord (1911), Proc. Roy. Soc. (London), A-84, 25.

Reding, F. P. (1958), J. Polym. Sci. 32, 487

Reinhold, C., E. W. Fischer, and A. Peterlin (1964), J. Appl. Phys., 35, 71.

Ren, J., J. Wu, and G. Lui (1986), IEEE 1985 CR PADM, 695-697.

Roe, R. J. (1982), J. Appl. Crystallogr., 15, 182.

Rohl, P. and B. Andreß (1985). IEEE 1985 CEIDP, 290-295.

Rueda, D. R., J. Martinez-Salazar, and F. J. Balta Calleja (1984), J. Polym. Sci., Polym. Phys. Ed., 22, 1811.

Sabuni, H. and J. K. Nelson. (1976), J. Mater. Sci., 11, 1574-1576.

Salyer, I. O. and J. E. Davison (1983) J. Appl. polym. Sci., 28, 2903.

Saums, H. L. and W. W. Pendleton (1973), "Materials for Electrical Insulating and Dielectric Functions," Hyden Book Co. Inc., New Jersey.

Schultz, J. M., (1974), "Polymer Material Science," Prentice-Hall Inc., New Jersey.

Schultz, J. M., (1976). J. Polym. Sci. Polym. Phys. Ed. 14, 2291-2311.

Schultz, J. M., J. S. Lin, R. W. Hendricks (1978), J. Appl. Cryst. 11, 551.

Shah, V. (1984), "Handbook of Plastics Testing Technology," Wiley Interscience, N.Y.

Shaw, M.T. and S.H. Shaw. (1984) IEEE EI-19, 419.

Shimizu, N. and K. Horii (1985). IEEE EI-20, 561-566.

Shimizu, N., K. Uchida and K. Horii (1987). IEEE 1987 CEIDP, 419-424.

Shimizu N., K. Uchida, K. Horii (1988), 1987 CEIDP, 419.

Sillar, R.W. (1973), "Electrical Insulating Materials and Their Application," Peter Peregrinus Ltd., London,

Sletbak, J. and A. Botne (1977), IEEE EI-12, 383-389.

Sletbak, J. (1979), IEEE PAS-98, 1358-1365.

Sletbak, J. and E. Ilstad (1983), IEEE PAS-102, 2069-2076.

Soma, K. and S. Kuma (1980), IEEE 1980 CREI, 212-215.

Song, H. H., R. S. Stein, D. -Q. Wu, M. Ree, J. C. Phillips, A. LeGrand, and B. Chu (1988), Macromol., 21, 1180.

Srinivas, N.N. and H.C. Doepken, Jr. (1978), IEEE 1978 CREI, 106-109.

Stark, K.H. and Garton, C.G. (1955), Nature, 176, 1225-1226.

Statton, W. O. (1962), J. Polym. Sci., 58, 205.

Statton, W. O. (1965), "Newer Methods of Polymer Characterization," Edited by B. Ke, Ch 6, 231 John Wiley, New York.

Stein R. S. and M. B. Rhodes (1960), J. Appl. Phys., Vol. 31, pp. 1873-1884

Strobl, G. R. and N. Muller (1973), J. Polym. Sci, 11, 1219.

Strobl, G. R., T. Engelke, E. Madarek, and G. Urban, Polymere (1983), 24, 1585.

Tabata, T., T. Fukuda, and Z. Iwata (1972), IEEE PAS-91, 1361-1370.

Tanaka, T., Y. Nitta, and T. Fukuda (1973), CEIDP 1972, 216-222.

Tanaka, T. and T. Fukuda (1975), CEIDP 1974, 239-249.

Tanaka, T., T. Fukuda, and S. Suzuki (1976), IEEE PAS-95, 1892-1900.

Tanaka, T. and A. Greenwood. (1978), CEIDP 1977, 309-315.

Tang, M. (1984), Ph.D. Dissertation, The University of Tennessee.

Timpe, N. B. (1979), "Engineering Dielectrics," Vol I, ASTM STP 669, ASTM.

Tsvankin, D. Ya. (1964), Polym. Sci. USSR, 6, 2304.

Tu, D. M. and K. C. Koe (1984), CEIDP 1983, 301-311.

Turbitt, R. J. (1984), "New Long Life Insulation compound for URD Cables," Kabelitems No. 158, Union Carbide.

Varlow, B. R. (1980), "Methods of Experimental Physics," Vol 16, Pt C, Edited by R.F. Fava, 443, Academic Press, N.Y.

Vatansever, A. (1987). Ph.D. Dissertation, The University of Tennessee.

Vonk, C. G. (1973), J. Appl. Crystallogr., 6, 81.

Vonk, C. G. and A. P. Pijpers (1985a), J. Polym. Sci. Phys. Ed., 23, 2517.

Vonk, C. G. and Y. Koga (1985b), J. Polym. Sci. Phys. Ed., 23, 2539.

Wagner, H. (1975), CEIDP 1974, 62-70.

Wagner, H. and J. Wartusch (1977). IEEE EI-12, 6, 395-401.

Wild, L., T. R. Ryle, D. C. Knobeloch, and I. R. Peat (1982), J. Polym. Sci., Polym. Phys. Ed., 20, 441.

Winslow, F. H., C. J. Aloisio, W. L. Hawkins, W. Matreyek, and S. Matsuoka (1963), Chem. Ind. (London), 533.

Winslow, F. H., M. Y. Hellman, W. Matreyek, and S. M. Stills (1966), Polym. Eng. Sci., 6, 273.

Wolter, K. D., J. Tanaka, and J. F. Johnson (1982), IEEE EI-17, 248-252.

Yahagi, K. and Y. Maeda. (1977), Jap. J. Appl. Phys., 16, 1259-1260.

Yahagi, K. (1980), IEEE EI-15, 241-250.

Yamada, Y., S. Yamanouchi, and S. Miyamoto (1979), CEIDP 1979, 500-510.

Yamanouchi, S., T. Shiga, and H. Matsubara (1978), CEIDP 1976, 386-393.

Yoshimitsu, T. and T. Nakukita (1978), IEEE 1978 CREI, 116-121.

Yoshimura, N. and F. Noto (1982), IEEE EI-17, 363-367.

Zubov, U. A., V. I. Selikhova, D. Ya. Tsvankin, and G. S. Markova, and V. A. Kargin (1967), J. Polym. Sci., Pt C, 16, 2215.

# APPENDICES

# APPENDIX I

## LISTING OF FORTRAN PROGRAM FOR SIMPLE SAXS MODEL

## WITH GAUSSIAN THICKNESS DISTRIBUTION

```
C*************************************************************************
C*                                                                       *
C*              P R O G R A M  :  S A X S I M 1. F O R                   *
C*                        B Y    Y. D. L E E                             *
C*                          JANUARY 14, 1988                             *
C*                       (REV.)                                          *
C*************************************************************************
C  Theoretical evaluation of SAXS intensity of the INFINITE STACK MODEL 1.
C
C     MODEL 9: Variable stck with Symmetric distribution of lammellar
C              thickness.
C
C     [1] Theory
C
C       1) Thickness Variation
C
C                              1                              -(Y-Ybar)^2
C           H(Y) = ----------------------  * EXP( --------------)
C                  sigmaY * (2* Pi)^(1/2)          2* sigmaY^2
C
C          where sigmaY : standard deviation of Y.
C                sigmaZ : standard deviation of Z.
C                Y      : layer thickness( Y for crystalline).
C                Ybar   : Average of Y value.
C                Z      : layer thickness (Z for amorphous).
C
C       2) Fourier Transform of the Gaussian Distribution Function.
C
C          Fy(q) = exp(-2 * (Pi * q * sigmaY)^2) * exp (-2* Pi * q * i * Ybar)
C
C          Fz(q) = exp(-2 * (Pi * q * sigmaZ)^2) * exp (-2* Pi * q * i * Zbar)
C
C           where sigmaY : standard deviation of Y.
C                 sigmaZ : standard deviation of Z.
C                 q      : scattering vector.
C                 i      : imaginary number unit.
C                 Ybar   : Average of Y value.
C                 Z      : layer thickness (Z for amorphous).
C
C       3) Crystallinity Variation
C            NO CRYSTALLINITY VARIATION.
```

```
C
C       4) SAXS intensity of a given stack
C
C                                (abs(1-Fy))^2 * (1-(abs(Fz))^2) +
C                                        (abs(1-Fz))^2 * (1-(abs(Fy))^2)
C             Inten(q) = Const * ----------------------------------------
C                                     Xbar * q^2 * (abs(1-Fy*Fz)^2)
C
C             where Const : (rhoCr- rhoAm)^2 / (4* Pi^2)
C                   rhoCr : crystalline density
C                   rhoAm : amorphous density
C                   Xbar  : average of Total thickness (Ybar + Zbar)
C
C        5) Total SAXS intensity
C
C             Totinten(q) = integration of I(q,C) * P(C) dC
C
C                             over C = from 0.01 to 0.99 EVERY 0.01
C
C        6) Assumption: sigmaY / Ybar = sigmaZ / Zbar
C                  .        .
C                   Zbar : const (0.5)
C                                  sigmaX^2
C                   sigmaY^2 = -------------------
C                                (1/C - 1)^2 + 1
C
C    [2] Calculation
C
C        1) Variables :
C                        CRYST         : crystallinity (C) ( 0.5)
C                        YBAR          : average crystallinie thickness (0.5)
C                        FYVAL         : FY values of given QR and PHI
C                        FZVAL         : FZ values of given QR and PHI
C                        SIGMAYSQ      : sigmaY ^2
C                        SIGMAZSQ      : sigmaZ ^2
C
C                        QR            : scattering vector (0.05, 0.075 .. 3.0)
C                        TOTINTEN      : total intensity of each QR
C
C
C        2) Constants : CONST     = 1.0
C                        ZBAR      = 0.5 (average thickness of amorphous layer)
C                        SIGMAX    = GIVEN
C
C    [3] OUTPUT VALUES:
C                      SigmaX, SigmaC
C                      QR VS Totinten on various values of SigmaX and SigmaC.
C
C          ** No. of QR's 75 from 0 to 3 (every 0.024)
```

```
C
C    [4] SUBROUTINES USED:
C                INTENCAL(QR, ZBAR, SIGMAX, CRYST(I), TEMINTEN)
C                FOURGAUS(QR, CRYST(I), ZBAR, FZVAL)
C                CXEXPN(FINCMFX, TEMCMFX)
C                CXARTH(A,B,R,N)--------complex arithmath
C                REAL FUNCTION DSTSQ(X)
C***********************************************************************
C
C
      PROGRAM SAXSAM1
      DIMENSION SIGX(7)
      INTEGER I, K, NUMPHI
      REAL ZBAR, CRYST, QR, SEGINTEN, SIGMAX
      CHARACTER*12 OUTFILE
      DATA SIGX/0.05,0.075,0.1,0.125,0.15,0.175,0.2/
C
C     SET CONSTANTS
C
      ZBAR = 0.5
      CRYST = 0.5
C
C     DO LOOP FOR WHOLE -- CHANGING SIGMAX VALUE (INDEX K)
C
      DO 14 K=1, 7, 1
      SIGMAX = SIGX(K)
      RPHI = 1./CRYST -1.
      SIGMAY = SIGMAX  / SQRT(RPHI**2 + 1.)
      SIGMAZ = SIGMAY * RPHI
C
C INITIALIZATION
        SEGINTEN = 1.0
C
        OUTFILE = 'OSAXM1'//CHAR(48+K)//CHAR(48+J)//'.PRN'
        OPEN (UNIT=30,FILE=OUTFILE,STATUS='NEW')
        WRITE(30,*)'"FILENAME: " "',OUTFILE,'"'
        WRITE(*,*)'"FILENAME: " "',OUTFILE,'"'
C
        WRITE(30,1001)'"SIGMA X: "', SIGMAX
        WRITE(30,1001)'"SIGMA Y: "', SIGMAY
        WRITE(30,1001)'"SIGMA Z: "', SIGMAZ

C
        WRITE(*,1001)'"SIGMA X: "', SIGMAX
        WRITE(*,1001)'"SIGMA Y: "', SIGMAY
        WRITE(*,1001)'"SIGMA Z: "', SIGMAZ
1001    FORMAT(A30,F8.4)
        WRITE(30,*)'"SAXS INF. MODEL 1A"'
        WRITE(*,*)'"SAXS INF. MODEL 1A"'
```

```
 1002     FORMAT(A35)
          WRITE(30,1000)'"-------------"','"------------"'
          WRITE(30,1000)'"    QR       "','" OBS INTEN"'
          WRITE(*,1000)'"-------------"','"------------"'
          WRITE(*,1000)'"    QR       "','" OBS INTEN"'
 1000     FORMAT(2A16)
C
C
            DO 18 QR=0.04, 3.0, 0.04
C
             CALL INTENCAL(QR, ZBAR,SIGMAY,SIGMAZ,CRYST,SEGINTEN)
C
C     INTEGRATION SEGINTEN OVER CRYST VALUE FOR GETTING TOTINTEN
C
            SEGINTEN = SEGINTEN/(QR*QR)
            WRITE (30,1100) QR, SEGINTEN
            WRITE (*,1100) QR, SEGINTEN
 1100       FORMAT(2G16.6)
  18        CONTINUE
C
         CLOSE(UNIT=30)
C
C END OF THE LOOP FOR K VALUE (CHANGING SIGMAX)
  14     CONTINUE
C
         STOP
         END
C
C*******************************************************************************
C #1
C     CALL INTENCAL(QR, ZBAR, SIGMAY, SIGMAZ, CRYST, SEGINTEN)
C
      SUBROUTINE INTENCAL(Q, ZB, SGY, SGZ, XPHI, SITEN)
C
C       [THEORY] SAXS intensity of a given stack
C
C                                (abs(1-Fy))^2 * (1-(abs(Fz))^2) +
C                                        (abs(1-Fz))^2 * (1-(abs(Fy))^2)
C            Inten(q) = Const * ----------------------------------------
C                                     Xbar * q^2 * (abs(1-Fy*Fz)^2)
C
C            where Const : (rhoCr- rhoAm)^2 / (4* Pi^2)
C                  rhoCr : crystalline density
C                  rhoAm : amorphous density
C                  Xbar  : average of Total thickness (Ybar + Zbar)
C
C *   VARIABLE WITH DIMENSION OF 2 IS COMPLEX NUMBER.
C     (RLONE: REAL NUMBER ONE)
C
```

```
C  SUBROUTINES CALLED:
C     CALL FOURGAUS(Q, SIGZSQ, ZB, FZ)
C     CALL CXARTH(FY, FZ, TMCMFX1, 3)
C
      DIMENSION FY(2), FZ(2), TMCMFX1(2), TMCMFX2(2), RLONE(2)
C
      REAL SINTUP, SINUP1, SNTDWN, YB, SIGYSQ, SIGZSQ, RPHI, SITEN, Q
      DATA RLONE/1.,0./
C
C INITIALLIZATION
      FY(1) = 0.0
      FY(2) = 0.0
      FZ(1) = 0.0
      FZ(2) = 0.0
      TMCMFX1(1) = 0.0
      TMCMFX1(2) = 0.0
      TMCMFX2(1) = 0.0
      TMCMFX2(2) = 0.0
      SINTUP = 0.0
      SINUP1 = 0.0
      SNTDWN = 0.0
C
      RPHI = 1./XPHI -1.
      YB = ZB / RPHI
      SIGYSQ = SGY * SGY
      SIGZSQ = SGZ * SGZ
C
C
      CALL FOURGAUS(Q, SIGYSQ, YB, FY)
      CALL FOURGAUS(Q, SIGZSQ, ZB, FZ)
C
      CALL CXARTH(RLONE, FY, TMCMFX1, 2)
      CALL CXARTH(RLONE, FZ, TMCMFX2, 2)
C
      SINTUP = DSTSQ(TMCMFX1)*(1-DSTSQ(FZ))
      SINUP1= DSTSQ(TMCMFX2)*(1-DSTSQ(FY))
      SINTUP = SINTUP+ SINUP1
C
      CALL CXARTH(FY, FZ, TMCMFX1, 3)
      CALL CXARTH(RLONE, TMCMFX1, TMCMFX2, 2)
      SNTDWN = DSTSQ(TMCMFX2) * Q * Q * (YB + ZB)
C
      SITEN = SINTUP / SNTDWN
C
      RETURN
      END
C
C*******************************************************************************
C #2
```

```
C     CALL FOURGAUS(Q, SIGYSQ, YB, FY)
C
      SUBROUTINE FOURGAUS(XQ, SGSQ, BAR, FVAL)
C
C    CALCULATE THE FOURIER TRANSFORM OF THE GAUSSIAN DISTRIBUTION FUNCTION
C
C    Fy(q) = exp(-2 * (Pi * q * sigmaY)^2) * exp (-2* Pi * q * i * Ybar)
C
C    Fz(q) = exp(-2 * (Pi * q * sigmaZ)^2) * exp (-2* Pi * q * i * Zbar)
C
C          where sigmaY : standard deviation of Y.
C                sigmaZ : standard deviation of Z.
C                q      : scattering vector.
C                i      : imaginary number unit.
C                Ybar   : Average of Y value.
C                Z      : layer thickness (Z for amorphous).
C
C
C SUBROUTINES CALLED:
C     CALL CXEXPN(FINCMFX, TEMCMFX)
C     CALL CXARTH(INICMFX, TEMCMFX, FVAL, 3)
C
      DIMENSION FVAL(2), FL(2), TEMCMFX(2), BINCMFX(2), FINCMFX(2)
      REAL CONSTA, CONSTB
C
C    CONSTA = -2* PI, CONSTB = -2* PI* PI
C
      CONSTA = -6.283185307
      CONSTB = -19.7392088
C INITIALLIZATION
      BINCMFX(1) = 0.0
      BINCMFX(2) = 0.0
      FINCMFX(1) = 0.0
      FINCMFX(2) = 0.0
      TEMCMFX(1) = 0.0
      TEMCMFX(2) = 0.0
      FVAL(1) = 0.0
      FVAL(2) = 0.0
C
      BINCMFX(1) = EXP(CONSTB * XQ * XQ * SGSQ)
      FINCMFX(2) = CONSTA * XQ * BAR
      CALL CXEXPN(FINCMFX, TEMCMFX)
      CALL CXARTH(BINCMFX, TEMCMFX, FL, 3)
      FVAL(1) = FL(1)
      FVAL(2) = FL(2)
C
      RETURN
      END
C
```

```
C*******************************************************************************
C #3
C     CALL CXEXPN(FINCMFX, TEMCMFX)
C
      SUBROUTINE CXEXPN(A,R)
C
C     SUBROUTINE CXEXPN EVALUATES THE EXPONENTIAL OF A COMPLEX
C     ARGUMENT
C
C     EXP(A1+ A2 i) = EXP(A1) * ( COS(A2) + i SIN(A1))
C
      DIMENSION A(2), R(2)
C
      B = EXP (A(1))
      R(1) = B*COS(A(2))
      R(2) = B*SIN(A(2))
      RETURN
      END
C
C
C*******************************************************************************
C #4
C     CALL CXARTH(FY, FZ, TMCMFX1, 3)
C
      SUBROUTINE CXARTH(A,B,C,N)
C
C     THIS SUBROUTINE CXARTH DOES COMPLEX ARITHMETIC INVOLVING
C     TWO COMPLEX NUMBERS.
C
C         N=1 FOR ADDITION
C         N=2 FOR SUBTRACTION
C         N=3 FOR MULTIPLICATION
C         N=4 FOR DIVISION
C
      DIMENSION A(2), B(2), C(2)
C
      X = B(1)
      Y = A(1)
      GO TO (1,2,3,4),N
 1    C(1) = X + Y
      C(2) = A(2) + B(2)
      RETURN
 2    C(1) = Y - X
      C(2) = A(2) - B(2)
      RETURN
 3    C(1) = Y*X - A(2)*B(2)
      C(2) = A(2)*X + Y*B(2)
      RETURN
 4    G = X*X + B(2)*B(2)
```

```
      C(1) = (Y*X + A(2)*B(2))/G
      C(2) = (A(2)*X - Y*B(2))/G
      RETURN
      END
C*******************************************************************************
C #6
C     INTDOWN = DSTSQ(TMCMFX2) * XQ * (YB + ZB)
C
      REAL FUNCTION DSTSQ(X)
C
C     CALCULATE SQUARE OF ABSOLUTE VALUE OF COMPLEX NUMBER.
C
      DIMENSION X(2)
      REAL YR, YI
C
      YR = X(1)
      YI = X(2)
      DSTSQ = YR * YR + YI * YI
      RETURN
      END
```

# APPENDIX II

## LISTING OF FORTRAN PROGRAM FOR SIMPLE SAXS MODEL

## WITH ASYMMETRIC THICKNESS DISTRIBUTION

```
C*************************************************************************
C*                                                                       *
C*              P R O G R A M  :  S A X S I M 3. F O R                   *
C*                        B Y    Y. D. L E E                             *
C*                          JANUARY 14, 1988                             *
C*                       (REV.)                                          *
C*************************************************************************
C  Theoretical evaluation of SAXS intensity of the INFINITE STACK MODEL 3.
C
C     MODEL 3: Variable stck with EXPONENTIAL distribution of lammellar
C              thickness.
C              (thickness varies by Modified Tsvankin model)
C
C     [1] Theory
C
C       1) Thickness Variation
C
C                            1                          -(Y-Ybar)^2
C            H(Y) = ----------------------  * EXP( --------------)
C                   sigmaY * (2* Pi)^(1/2)             2* sigmaY^2
C
C           where sigmaY : standard deviation of Y.
C                 sigmaZ : standard deviation of Z.
C                 Y      : layer thickness( Y for crystalline).
C                 Ybar   : Average of Y value.
C                 Z      : layer thickness (Z for amorphous).
C
C       2) Fourier Transform of the Exponential Distribution Function.
C                           (Modified Tzvankin Model)
C
C                    exp(-2 * Pi * i * q * (Ybar - sigmaY))    (Ybar > sigmaY)
C          Fy(q) =  ----------------------------------------
C                         (2 * Pi * i * sigmaY * q) + 1
C
C                    exp(-2 * Pi * i * q * (Zbar - sigmaZ))
C          Fz(q) =  ----------------------------------------
C                         (2 * Pi * i * sigmaZ * q) + 1
C
C                                  1                        ( Ybar < sigmaY)
C          Fy(q) =  ----------------------------------------
C                         (2 * Pi * i * sigmaY * q) + 1
```

```
C
C                                1                          ( Zbar < sigmaZ)
C          Fz(q) =  ---------------------------------------
C                     (2 * Pi * i * sigmaZ * q) + 1
C
C           where sigmaY : standard deviation of Y.
C                 sigmaZ : standard deviation of Z.
C                 q      : scattering vector.
C                 i      : imaginary number unit.
C                 Ybar   : Average of Y value.
C                 Z      : layer thickness (Z for amorphous).
C
C
C       3) Crystallinity Variation
C            NO CRYSTALLINITY VARIATION.
C
C       4) SAXS intensity of a given stack
C
C                               (abs(1-Fy))^2 * (1-(abs(Fz))^2) +
C                                       (abs(1-Fz))^2 * (1-(abs(Fy))^2)
C             Inten(q) = Const * ----------------------------------------
C                                    Xbar * q^2 * (abs(1-Fy*Fz)^2)
C
C             where Const : (rhoCr- rhoAm)^2 / (4* Pi^2)
C                   rhoCr : crystalline density
C                   rhoAm : amorphous density
C                   Xbar  : average of Total thickness (Ybar + Zbar)
C
C        5) Total SAXS intensity
C
C             Totinten(q) = integration of I(q,C) * P(C) dC
C
C                              over C = from 0.01 to 0.99 EVERY 0.01
C
C       6) Assumption: sigmaY / Ybar = sigmaZ / Zbar
C
C                   Zbar : const (0.5)
C                                 sigmaX^2
C                   sigmaY^2 = -------------------
C                                (1/C - 1)^2 + 1
C
C    [2] Calculation
C
C        1) Variables :
C                        CRYST         : crystallinity (C) ( 0.5)
C                        YBAR          : average crystallinie thickness (0.5)
C                        FYVAL         : FY values of given QR and PHI
C                        FZVAL         : FZ values of given QR and PHI
C                        SIGMAYSQ      : sigmaY ^2
```

```
C                       SIGMAZSQ      : sigmaZ ^2
C
C                       QR            : scattering vector (0.05, 0.075 .. 3.0)
C                       TOTINTEN      : total intensity of each QR
C
C
C        2) Constants : CONST      = 1.0
C                       ZBAR       = 0.5 (average thickness of amorphous layer)
C                       SIGMAX     = GIVEN
C
C    [3] OUTPUT VALUES:
C                      SigmaX, SigmaC
C                      QR VS Totinten on various values of SigmaX and SigmaC.
C
C          ** No. of QR's 75 from 0 to 3 (every 0.024)
C
C    [4] SUBROUTINES USED:
C                  INTENCAL(QR, ZBAR, SIGMAX, CRYST(I), TEMINTEN)
C                  FOURTSVN(QR, CRYST(I), ZBAR, FZVAL)
C                  CXEXPN(FINCMFX, TEMCMFX)
C                  CXARTH(A,B,R,N)--------complex arithmath
C                  REAL FUNCTION DSTSQ(X)
C*************************************************************************
C
C
       PROGRAM SAXSIM3
       DIMENSION SIGX(7)
       INTEGER I, K, NUMPHI
       REAL ZBAR, CRYST, QR, SEGINTEN, SIGMAX
       CHARACTER*12 OUTFILE
       DATA SIGX/0.05,0.075,0.1,0.125,0.15,0.175,0.2/
C
C      SET CONSTANTS
C
       ZBAR = 0.5
       CRYST = 0.5
C
C      DO LOOP FOR WHOLE -- CHANGING SIGMAX VALUE (INDEX K)
C
       DO 14 K=1, 7, 1
       SIGMAX = SIGX(K)
       RPHI = 1./CRYST -1.
       SIGMAY = SIGMAX  / SQRT(RPHI**2 + 1.)
       SIGMAZ = SIGMAY * RPHI
C
C INITIALIZATION
         SEGINTEN = 1.0
C
         OUTFILE = 'OSAXM3'//CHAR(48+K)//CHAR(48+J)//'.PRN'
```

```
          OPEN (UNIT=30,FILE=OUTFILE,STATUS='NEW')
          WRITE(30,*)'"FILENAME: " "',OUTFILE,'"'
          WRITE(*,*)'"FILENAME: " "',OUTFILE,'"'
C
          WRITE(30,1001)'"SIGMA X: "', SIGMAX
          WRITE(30,1001)'"SIGMA Y: "', SIGMAY
          WRITE(30,1001)'"SIGMA Z: "', SIGMAZ

C
          WRITE(*,1001)'"SIGMA X: "', SIGMAX
          WRITE(*,1001)'"SIGMA Y: "', SIGMAY
          WRITE(*,1001)'"SIGMA Z: "', SIGMAZ
 1001     FORMAT(A30,F8.4)
          WRITE(30,*)'"SAXS INF. MODEL 1A"'
          WRITE(*,*)'"SAXS INF. MODEL 1A"'
 1002     FORMAT(A35)
          WRITE(30,1000)'"-------------"','"------------"'
          WRITE(30,1000)'"    QR       "','" OBS INTEN"'
          WRITE(*,1000)'"-------------"','"------------"'
          WRITE(*,1000)'"    QR       "','" OBS INTEN"'
 1000     FORMAT(2A16)
C
C
             DO 18 QR=0.04, 3.0, 0.04
C
              CALL INTENCAL(QR, ZBAR,SIGMAY,SIGMAZ,CRYST,SEGINTEN)
C
C     INTEGRATION SEGINTEN OVER CRYST VALUE FOR GETTING TOTINTEN
C
             SEGINTEN = SEGINTEN/(QR*QR)
             WRITE (30,1100) QR, SEGINTEN
             WRITE (*,1100) QR, SEGINTEN
 1100        FORMAT(2G16.6)
  18         CONTINUE
C
          CLOSE(UNIT=30)
C
C END OF THE LOOP FOR K VALUE (CHANGING SIGMAX)
  14      CONTINUE
C
          STOP
          END
C
C*******************************************************************************
C
C
C*******************************************************************************
C #1
C     CALL INTENCAL(QR, ZBAR, SIGMAY, SIGMAZ, CRYST, SEGINTEN)
```

```
C
      SUBROUTINE INTENCAL(Q, ZB, SGY, SGZ, XPHI, SITEN)
C
C       [THEORY] SAXS intensity of a given stack
C
C                                (abs(1-Fy))^2 * (1-(abs(Fz))^2) +
C                                        (abs(1-Fz))^2 * (1-(abs(Fy))^2)
C             Inten(q) = Const * ----------------------------------------
C                                     Xbar * q^2 * (abs(1-Fy*Fz)^2)
C
C             where Const : (rhoCr- rhoAm)^2 / (4* Pi^2)
C                   rhoCr : crystalline density
C                   rhoAm : amorphous density
C                   Xbar  : average of Total thickness (Ybar + Zbar)
C
C *   VARIABLE WITH DIMENSION OF 2 IS COMPLEX NUMBER.
C     (RLONE: REAL NUMBER ONE)
C
C  SUBROUTINES CALLED:
C     CALL FOURTSVN(Q, SIGZSQ, ZB, FZ)
C     CALL CXARTH(FY, FZ, TMCMFX1, 3)
C
      DIMENSION FY(2), FZ(2), TMCMFX1(2), TMCMFX2(2), RLONE(2)
C
      REAL SINTUP, SINUP1, SNTDWN, YB, SIGYSQ, SIGZSQ, RPHI, SITEN, Q
      DATA RLONE/1.,0./
C
C INITIALLIZATION
      FY(1) = 0.0
      FY(2) = 0.0
      FZ(1) = 0.0
      FZ(2) = 0.0
      TMCMFX1(1) = 0.0
      TMCMFX1(2) = 0.0
      TMCMFX2(1) = 0.0
      TMCMFX2(2) = 0.0
      SINTUP = 0.0
      SINUP1 = 0.0
      SNTDWN = 0.0
C
      RPHI = 1./XPHI -1.
      YB = ZB / RPHI
      SIGYSQ = SGY * SGY
      SIGZSQ = SGZ * SGZ
C
C
C
      CALL FOURTSVN(Q, SIGYSQ, YB, FY)
      CALL FOURTSVN(Q, SIGZSQ, ZB, FZ)
```

```
C
      CALL CXARTH(RLONE, FY, TMCMFX1, 2)
      CALL CXARTH(RLONE, FZ, TMCMFX2, 2)
C
      SINTUP = DSTSQ(TMCMFX1)*(1-DSTSQ(FZ))
      SINUP1= DSTSQ(TMCMFX2)*(1-DSTSQ(FY))
      SINTUP = SINTUP+ SINUP1
C
      CALL CXARTH(FY, FZ, TMCMFX1, 3)
      CALL CXARTH(RLONE, TMCMFX1, TMCMFX2, 2)
      SNTDWN = DSTSQ(TMCMFX2) * Q * Q * (YB + ZB)
C
      SITEN = SINTUP / SNTDWN
C
      RETURN
      END
C
C*******************************************************************************
C #2
C     CALL FOURTSVN(Q, SIGYSQ, YB, FY)
C
      SUBROUTINE FOURTSVN(XQ, SGSQ, BAR, FVAL)
C
C    Fourier Transform of the Exponential Distribution Function.
C                          (Modified Tzvankin Model)
C
C                  exp(-2 * Pi * i * q * (Ybar - sigmaY))    (Ybar > sigmaY)
C         Fy(q) =  ---------------------------------------
C                       (2 * Pi * i * sigmaY * q) + 1
C
C                  exp(-2 * Pi * i * q * (Zbar - sigmaZ))
C         Fz(q) =  ---------------------------------------
C                       (2 * Pi * i * sigmaZ * q) + 1
C
C                              1                          ( Ybar < sigmaY)
C         Fy(q) =  ---------------------------------------
C                       (2 * Pi * i * sigmaY * q) + 1
C
C                              1                          ( Zbar < sigmaZ)
C         Fz(q) =  ---------------------------------------
C                       (2 * Pi * i * sigmaZ * q) + 1
C
C
C          where sigmaY : standard deviation of Y.
C                sigmaZ : standard deviation of Z.
C                q      : scattering vector.
C                i      : imaginary number unit.
C                Ybar   : Average of Y value.
C                Z      : layer thickness (Z for amorphous).
```

```
C
C
C SUBROUTINES CALLED:
C     CALL CXEXPN(FINCMFX, TEMCMFX)
C     CALL CXARTH(INICMFX, TEMCMFX, FVAL, 3)
C
      DIMENSION FVAL(2), FL(2), TEMCMFX(2), BINCMFX(2), FINCMFX(2)
      REAL CONSTA, SIG
C
C    CONSTA = 2* PI
C
      CONSTA = 6.283185307
C
C INITIALLIZATION
      BINCMFX(1) = 1.0
      BINCMFX(2) = 0.0
      FINCMFX(1) = 0.0
      FINCMFX(2) = 0.0
      TEMCMFX(1) = 0.0
      TEMCMFX(2) = 0.0
      FVAL(1) = 0.0
      FVAL(2) = 0.0
C
      SIG = SQRT(SGSQ)
      BINCMFX(2) = CONSTA * XQ * SIG
      IF (BAR .GT. SIG) GO TO 340
      FINCMFX(2) = 0.0
      GO TO 360
  340 FINCMFX(2) = -1. * CONSTA * XQ * (BAR-SIG)
  360 CALL CXEXPN(FINCMFX, TEMCMFX)
      CALL CXARTH(TEMCMFX, BINCMFX, FL, 4)
      FVAL(1) = FL(1)
      FVAL(2) = FL(2)
C
      RETURN
      END
C*******************************************************************************
C #3
C     CALL CXEXPN(FINCMFX, TEMCMFX)
C
      SUBROUTINE CXEXPN(A,R)
C
C     SUBROUTINE CXEXPN EVALUATES THE EXPONENTIAL OF A COMPLEX
C     ARGUMENT
C
C     EXP(A1+ A2 i) = EXP(A1) * ( COS(A2) + i SIN(A1))
C
      DIMENSION A(2), R(2)
C
```

```
      B = EXP (A(1))
      R(1) = B*COS(A(2))
      R(2) = B*SIN(A(2))
      RETURN
      END
C
C
C*************************************************************************
C #4
C     CALL CXARTH(FY, FZ, TMCMFX1, 3)
C
      SUBROUTINE CXARTH(A,B,C,N)
C
C     THIS SUBROUTINE CXARTH DOES COMPLEX ARITHMETIC INVOLVING
C     TWO COMPLEX NUMBERS.
C
C         N=1 FOR ADDITION
C         N=2 FOR SUBTRACTION
C         N=3 FOR MULTIPLICATION
C         N=4 FOR DIVISION
C
      DIMENSION A(2), B(2), C(2)
C
      X = B(1)
      Y = A(1)
      GO TO (1,2,3,4),N
 1    C(1) = X + Y
      C(2) = A(2) + B(2)
      RETURN
 2    C(1) = Y - X
      C(2) = A(2) - B(2)
      RETURN
 3    C(1) = Y*X - A(2)*B(2)
      C(2) = A(2)*X + Y*B(2)
      RETURN
 4    G = X*X + B(2)*B(2)
      C(1) = (Y*X + A(2)*B(2))/G
      C(2) = (A(2)*X - Y*B(2))/G
      RETURN
      END
C*************************************************************************
C #6
C     INTDOWN = DSTSQ(TMCMFX2) * XQ * (YB + ZB)
C
      REAL FUNCTION DSTSQ(X)
C
C     CALCULATE SQUARE OF ABSOLUTE VALUE OF COMPLEX NUMBER.
C
      DIMENSION X(2)
```

```
      REAL YR, YI
C
      YR = X(1)
      YI = X(2)
      DSTSQ = YR * YR + YI * YI
      RETURN
      END
```

# APPENDIX III

## LISTING OF FORTRAN PROGRAM FOR VARIABLE SAXS MODEL WITH GAUSSIAN THICKNESS DISTRIBUTION AND GAUSSIAN CRYSTALLINITY DISTRIBUTION

```
C*************************************************************************
C*                                                                       *
C*              P R O G R A M  :  S A X S V M 9. F O R                   *
C*                        B Y    Y. D. L E E                             *
C*                          JANUARY 4, 1988                              *
C*                       (REV.)                                          *
C*************************************************************************
C  Theoretical evaluation of SAXS intensity of the VARIABLE STACK MODEL 9.
C
C     MODEL 9: Variable stck with Symmetric distribution of lammellar
C              thickness. Symmetric distribution of stack composition
C              of different crystallinity value.
C
C     [1] Theory
C
C       1) Thickness Variation
C
C                              1                          -(Y-Ybar)^2
C           H(Y) = ----------------------  * EXP( --------------)
C                  sigmaY * (2* Pi)^(1/2)          2* sigmaY^2
C
C          where sigmaY : standard deviation of Y.
C                sigmaZ : standard deviation of Z.
C                Y      : layer thickness( Y for crystalline).
C                Ybar   : Average of Y value.
C                Z      : layer thickness (Z for amorphous).
C
C       2) Fourier Transform of the Gaussian Distribution Function.
C
C          Fy(q) = exp(-2 * (Pi * q * sigmaY)^2) * exp (-2* Pi * q * i * Ybar)
C
C          Fz(q) = exp(-2 * (Pi * q * sigmaZ)^2) * exp (-2* Pi * q * i * Zbar)
C
C           where sigmaY : standard deviation of Y.
C                 sigmaZ : standard deviation of Z.
C                 q      : scattering vector.
C                 i      : imaginary number unit.
C                 Ybar   : Average of Y value.
C                 Z      : layer thickness (Z for amorphous).
```

```
C
C       3) Crystallinity Variation
C
C                            1                          -(C-Cbar)^2
C            H(C) = ----------------------  * EXP( --------------)
C                    sigmaC * (2* PI)^(1/2)              2* sigmaC^2
C
C          where sigmaC : standard deviation.
C                C      : Crystallinity of stack.
C                Cbar   : Average of C value.
C
C
C       4) SAXS intensity of a given stack
C
C                                (abs(1-Fy))^2 * (1-(abs(Fz))^2) +
C                                        (abs(1-Fz))^2 * (1-(abs(Fy))^2)
C             Inten(q) = Const * ----------------------------------------
C                                     Xbar * q^2 * (abs(1-Fy*Fz)^2)
C
C             where Const : (rhoCr- rhoAm)^2 / (4* Pi^2)
C                   rhoCr : crystalline density
C                   rhoAm : amorphous density
C                   Xbar  : average of Total thickness (Ybar + Zbar)
C
C        5) Total SAXS intensity
C
C             Totinten(q) = integration of I(q,C) * P(C) dC
C
C                             over C = from 0.01 to 0.99 EVERY 0.01
C
C        6) Assumption: sigmaY / Ybar = sigmaZ / Zbar
C
C                   Zbar : const (0.5)
C                                  sigmaX^2
C                   sigmaY^2 = -------------------
C                                (1/C - 1)^2 + 1
C
C    [2] Calculation
C
C        1) Variables :
C                        CRYST(100)    : crystallinity (C) ( 0.01, 0.02 .. 0.99)
C                        SEGINTEN(100) : segment intensity of given QR and PHI
C                        CRYPROB       : probability of phi (P(C))
C                        YBAR          : average crystallinie thickness
C                        FYVAL         : FY values of given QR and PHI
C                        FZVAL         : FZ values of given QR and PHI
C                        SIGMAYSQ      : sigmaY ^2
C                        SIGMAZSQ      : sigmaZ ^2
C
```

```
C                       QR          : scattering vector (0.05, 0.075 .. 3.0)
C                       TOTINTEN    : total intensity of each QR
C
C
C       2) Constants : CONST     = 1.0
C                       ZBAR      = 0.5 (average thickness of amorphous layer)
C                       CBAR      = 0.5 (Total average crystallinity)
C                       SIGMAX    = GIVEN
C                       SIGMAC    = GIVEN
C
C    [3] OUTPUT VALUES:
C                      SigmaX, SigmaC
C                      QR VS Totinten on various values of SigmaX and SigmaC.
C
C          ** No. of QR's 75 from 0 to 3 (every 0.024)
C
C    [4] SUBROUTINES USED:
C                  INTENCAL(QR, ZBAR, SIGMAX, CRYST(I), TEMINTEN)
C                  FOURGAUS(QR, CRYST(I), ZBAR, FZVAL)
C                  CXEXPN(FINCMFX, TEMCMFX)
C                  CXARTH(A,B,R,N)--------complex arithmath
C                  REAL FUNCTION DSTSQ(X)
C*************************************************************************
C
C
       PROGRAM SAXSVM9
       DIMENSION CRYST(100), SEGINTEN(100)
       DIMENSION SIGX(7), SIGC(7)
       INTEGER I, J, K, NUMPHI, NUMSIG
       REAL ZBAR, CBAR, CRYPROB, TMINTEN, QR, TOTINTEN,
     &      SIGMAX, SIGMAC, SIGCON1, SIGCON2
       CHARACTER*12 OUTFILE
       DATA SIGC/0.05,0.075,0.1,0.125,0.15,0.175,0.2/
       DATA SIGX/0.05,0.075,0.1,0.125,0.15,0.175,0.2/
C
C      SET CONSTANTS
C
       ZBAR = 0.5
       CBAR = 0.5
       NUMPHI = 99
C   NUMSIG: NUMBER OF SIGMA
       NUMSIG = 7
C
C      DO LOOP FOR WHOLE -- CHANGING SIGMAX VALUE (INDEX K)
C
       DO 14 K=1, NUMSIG, 1
C*     K = 1
       SIGMAX = SIGX(K)
C*     SIGMAX = 0.175
```

```
C
C         DO LOOP --- CHANGING SIGMAC VALUE (INDEX J)
          DO 16 J=1, NUMSIG, 1
C*        J = 1
          SIGMAC = SIGC(J)
C*        SIGMAC = 0.3
C
C CONSTANTS FOR INTENSITY CALCULATION.
C 2.506628275 = SQRT(2*PI)
          SIGCON1 = 2.506628275 * SIGMAC
          SIGCON2 = -2 * SIGMAC * SIGMAC
C INITIALIZATION
          CRYPROB = 1.0
          TMINTEN = 1.0
          TOTINTEN = 1.0
C
          OUTFILE = 'ASXVM9'//CHAR(48+K)//CHAR(48+J)//'.PRN'
          OPEN (UNIT=30,FILE=OUTFILE,STATUS='NEW')
          WRITE(30,*)'"FILENAME: " "',OUTFILE,'"'
          WRITE(*,*)'"FILENAME: " "',OUTFILE,'"'
C
          WRITE(30,1001)'"SIGMA X: "', SIGMAX
          WRITE(30,1001)'"SIGMA C: "', SIGMAC
C
          WRITE(*,1001)'"SIGMA X: "', SIGMAX
          WRITE(*,1001)'"SIGMA C: "', SIGMAC
 1001     FORMAT(A30,F8.4)
          WRITE(30,*)'"SAXS VAR. MODEL 9:OBS INTEN"'
          WRITE(*,*)'"SAXS VAR. MODEL 9;OBS INTEN"'
 1002     FORMAT(A35)
          WRITE(30,1000)'"-------------"','"------------"'
          WRITE(30,1000)'"    QR       "','" OBS. INTEN"'
          WRITE(*,1000)'"-------------"','"------------"'
          WRITE(*,1000)'"    QR       "','" OBS. INTEN"'
 1000     FORMAT(2A16)
C
C
             DO 18 QR=0.04, 3.0, 0.04
C
                DO 22 I=1,NUMPHI,1
                  CRYST(I)= 0.01 * I
                  CRYPROB = EXP((CRYST(I)-CBAR)**2 / SIGCON2) / SIGCON1
                  CALL INTENCAL(QR, ZBAR, SIGMAX, CRYST(I), TMINTEN)
                  SEGINTEN(I) = TMINTEN * CRYPROB
  22             CONTINUE
C
C     INTEGRATION SEGINTEN OVER CRYST VALUE FOR GETTING TOTINTEN
C
             CALL TPZOD(NUMPHI,CRYST(1),CRYST(NUMPHI),SEGINTEN,TOTINTEN)
```

```
C OBSERVABLE INTENSITY.
            TOTINTEN = TOTINTEN/(QR*QR)
            WRITE (30,1100) QR, TOTINTEN
            WRITE (*,1100) QR, TOTINTEN
 1100       FORMAT(2G16.6)
  18        CONTINUE
C
         CLOSE(UNIT=30)
C
C END OF THE LOOP FOR J VALUE (CHANGING SIGMAC)
  16     CONTINUE
C
C END OF THE LOOP FOR K VALUE (CHANGING SIGMAX)
  14     CONTINUE
C
         STOP
         END
C
C*******************************************************************************
C #1
C     CALL INTENCAL(QR, ZBAR, SIGMAX, CRYST(I), TEMINTEN)
C
      SUBROUTINE INTENCAL(Q, ZB, SGX, XPHI, SITEN)
C
C       [THEORY] SAXS intensity of a given stack
C
C                                (abs(1-Fy))^2 * (1-(abs(Fz))^2) +
C                                        (abs(1-Fz))^2 * (1-(abs(Fy))^2)
C             Inten(q) = Const * ----------------------------------------
C                                     Xbar * q^2 * (abs(1-Fy*Fz)^2)
C
C             where Const : (rhoCr- rhoAm)^2 / (4* Pi^2)
C                   rhoCr : crystalline density
C                   rhoAm : amorphous density
C                   Xbar  : average of Total thickness (Ybar + Zbar)
C
C *   VARIABLE WITH DIMENSION OF 2 IS COMPLEX NUMBER.
C     (RLONE: REAL NUMBER ONE)
C
C  SUBROUTINES CALLED:
C     CALL FOURGAUS(Q, SIGZSQ, ZB, FZ)
C     CALL CXARTH(FY, FZ, TMCMFX1, 3)
C
      DIMENSION FY(2), FZ(2), TMCMFX1(2), TMCMFX2(2), RLONE(2)
C
      REAL SINTUP, SINUP1, SNTDWN, YB, SIGYSQ, SIGZSQ, RPHI, SITEN, Q
      DATA RLONE/1.,0./
C
C INITIALLIZATION
```

```
      FY(1) = 0.0
      FY(2) = 0.0
      FZ(1) = 0.0
      FZ(2) = 0.0
      TMCMFX1(1) = 0.0
      TMCMFX1(2) = 0.0
      TMCMFX2(1) = 0.0
      TMCMFX2(2) = 0.0
      SINTUP = 0.0
      SINUP1 = 0.0
      SNTDWN = 0.0
C
      RPHI = 1./XPHI -1.
      YB = ZB / RPHI
C
      SIGYSQ = SGX * SGX / (RPHI**2 + 1.)
      SIGZSQ = SIGYSQ * RPHI**2
C
      CALL FOURGAUS(Q, SIGYSQ, YB, FY)
      CALL FOURGAUS(Q, SIGZSQ, ZB, FZ)
C
      CALL CXARTH(RLONE, FY, TMCMFX1, 2)
      CALL CXARTH(RLONE, FZ, TMCMFX2, 2)
C
      SINTUP = DSTSQ(TMCMFX1)*(1-DSTSQ(FZ))
      SINUP1= DSTSQ(TMCMFX2)*(1-DSTSQ(FY))
      SINTUP = SINTUP+ SINUP1
C
      CALL CXARTH(FY, FZ, TMCMFX1, 3)
      CALL CXARTH(RLONE, TMCMFX1, TMCMFX2, 2)
      SNTDWN = DSTSQ(TMCMFX2) * Q * Q * (YB + ZB)
C
      SITEN = SINTUP / SNTDWN
C
      RETURN
      END
C
C*******************************************************************************
C #2
C     CALL FOURGAUS(Q, SIGYSQ, YB, FY)
C
      SUBROUTINE FOURGAUS(XQ, SGSQ, BAR, FVAL)
C
C    CALCULATE THE FOURIER TRANSFORM OF THE GAUSSIAN DISTRIBUTION FUNCTION
C
C    Fy(q) = exp(-2 * (Pi * q * sigmaY)^2) * exp (-2* Pi * q * i * Ybar)
C
C    Fz(q) = exp(-2 * (Pi * q * sigmaZ)^2) * exp (-2* Pi * q * i * Zbar)
C
```

```
C           where sigmaY : standard deviation of Y.
C                 sigmaZ : standard deviation of Z.
C                 q      : scattering vector.
C                 i      : imaginary number unit.
C                 Ybar   : Average of Y value.
C                 Z      : layer thickness (Z for amorphous).
C
C
C SUBROUTINES CALLED:
C     CALL CXEXPN(FINCMFX, TEMCMFX)
C     CALL CXARTH(INICMFX, TEMCMFX, FVAL, 3)
C
      DIMENSION FVAL(2), FL(2), TEMCMFX(2), BINCMFX(2), FINCMFX(2)
      REAL CONSTA, CONSTB
C
C    CONSTA = -2* PI, CONSTB = -2* PI* PI
C
      CONSTA = -6.283185307
      CONSTB = -19.7392088
C INITIALLIZATION
      BINCMFX(1) = 0.0
      BINCMFX(2) = 0.0
      FINCMFX(1) = 0.0
      FINCMFX(2) = 0.0
      TEMCMFX(1) = 0.0
      TEMCMFX(2) = 0.0
      FVAL(1) = 0.0
      FVAL(2) = 0.0
C
      BINCMFX(1) = EXP(CONSTB * XQ * XQ * SGSQ)
      FINCMFX(2) = CONSTA * XQ * BAR
      CALL CXEXPN(FINCMFX, TEMCMFX)
      CALL CXARTH(BINCMFX, TEMCMFX, FL, 3)
      FVAL(1) = FL(1)
      FVAL(2) = FL(2)
C
      RETURN
      END
C
C*******************************************************************************
C #3
C     CALL CXEXPN(FINCMFX, TEMCMFX)
C
      SUBROUTINE CXEXPN(A,R)
C
C     SUBROUTINE CXEXPN EVALUATES THE EXPONENTIAL OF A COMPLEX
C     ARGUMENT
C
C     EXP(A1+ A2 i) = EXP(A1) * ( COS(A2) + i SIN(A1))
```

```
C
      DIMENSION A(2), R(2)
C
      B = EXP (A(1))
      R(1) = B*COS(A(2))
      R(2) = B*SIN(A(2))
      RETURN
      END
C
C
C*************************************************************************
C #4
C     CALL CXARTH(FY, FZ, TMCMFX1, 3)
C
      SUBROUTINE CXARTH(A,B,C,N)
C
C     THIS SUBROUTINE CXARTH DOES COMPLEX ARITHMETIC INVOLVING
C     TWO COMPLEX NUMBERS.
C
C         N=1 FOR ADDITION
C         N=2 FOR SUBTRACTION
C         N=3 FOR MULTIPLICATION
C         N=4 FOR DIVISION
C
      DIMENSION A(2), B(2), C(2)
C
      X = B(1)
      Y = A(1)
      GO TO (1,2,3,4),N
 1    C(1) = X + Y
      C(2) = A(2) + B(2)
      RETURN
 2    C(1) = Y - X
      C(2) = A(2) - B(2)
      RETURN
 3    C(1) = Y*X - A(2)*B(2)
      C(2) = A(2)*X + Y*B(2)
      RETURN
 4    G = X*X + B(2)*B(2)
      C(1) = (Y*X + A(2)*B(2))/G
      C(2) = (A(2)*X - Y*B(2))/G
      RETURN
      END
C
C*************************************************************************
C #5
C     CALL TPZOD(NUMPHI,CRYST(1),CRYST(NUMPHI),SEGINTEN,TOTINTEN)
C
      SUBROUTINE TPZOD (M,XO,XH,Y,TPA)
```

```
C
C     TO EVALUATE THE DEFINITE OF A FUNCTION
C     USING THE TRAPEZOIDAL RULE.
C
      DIMENSION Y(1)
      TM = M - 1
      MM = TM
      DI = (XH - XO)/(TM*2.)
      TPA = 0.
      DO 15 I = 1,MM
      AR = Y(I) + Y (I + 1)
      AR = DI*AR
   15 TPA = TPA + AR
      RETURN
      END
C*******************************************************************************
C #6
C     INTDOWN = DSTSQ(TMCMFX2) * XQ * (YB + ZB)
C
      REAL FUNCTION DSTSQ(X)
C
C     CALCULATE SQUARE OF ABSOLUTE VALUE OF COMPLEX NUMBER.
C
      DIMENSION X(2)
      REAL YR, YI
C
      YR = X(1)
      YI = X(2)
      DSTSQ = YR * YR + YI * YI
      RETURN
      END
C
```

# APPENDIX IV

## LISTING OF FORTRAN PROGRAM FOR VARIABLE SAXS MODEL WITH ASYMMETRIC THICKNESS DISTRIBUTION AND GAUSSIAN CRYSTALLINITY DISTRIBUTION

```
C*************************************************************************
C*                                                                       *
C*              P R O G R A M  :  F S A X S V M 7 . F O R                *
C*                        B Y    Y. D. L E E                             *
C*                          JANUARY 6, 1988                              *
C*                      (REV. MODIFIED TZVANKIN MODEL)                   *
C*************************************************************************
C  Theoretical evaluation of SAXS intensity of the VARIABLE STACK MODEL 7.
C
C     MODEL 7: Variable stck with EXPONENTIAL distribution of lammellar
C              thickness. Symmetric distribution of stack composition
C              of different crystallinity value.
C              (thickness varies by Modified Tsvankin model)
C
C     [1] Theory
C
C       1) Thickness Variation
C
C                              1                          -(Y-Ybar)^2
C            H(Y) = ----------------------  * EXP( --------------)
C                   sigmaY * (2* Pi)^(1/2)          2* sigmaY^2
C
C           where sigmaY : standard deviation of Y.
C                 sigmaZ : standard deviation of Z.
C                 Y      : layer thickness( Y for crystalline).
C                 Ybar   : Average of Y value.
C                 Z      : layer thickness (Z for amorphous).
C
C       2) Fourier Transform of the Exponential Distribution Function.
C                           (Modified Tzvankin Model)
C
C                    exp(-2 * Pi * i * q * (Ybar - sigmaY))    (Ybar > sigmaY)
C          Fy(q) = ----------------------------------------
C                         (2 * Pi * i * sigmaY * q) + 1
C
C                    exp(-2 * Pi * i * q * (Zbar - sigmaZ))
C          Fz(q) = ----------------------------------------
C                         (2 * Pi * i * sigmaZ * q) + 1
C
```

```
C                                1                          ( Ybar < sigmaY)
C        Fy(q) =  ----------------------------------------
C                      (2 * Pi * i * sigmaY * q) + 1
C
C                                1                          ( Zbar < sigmaZ)
C        Fz(q) =  ----------------------------------------
C                      (2 * Pi * i * sigmaZ * q) + 1
C
C         where sigmaY : standard deviation of Y.
C               sigmaZ : standard deviation of Z.
C               q      : scattering vector.
C               i      : imaginary number unit.
C               Ybar   : Average of Y value.
C               Z      : layer thickness (Z for amorphous).
C
C      3) Crystallinity Variation
C
C                          1                        -(C-Cbar)^2
C           H(C) = ----------------------  * EXP( --------------)
C                  sigmaC * (2* PI)^(1/2)           2* sigmaC^2
C
C         where sigmaC : standard deviation.
C               C      : Crystallinity of stack.
C               Cbar   : Average of C value.
C
C
C      4) SAXS intensity of a given stack
C
C                              (abs(1-Fy))^2 * (1-(abs(Fz))^2) +
C                                      (abs(1-Fz))^2 * (1-(abs(Fy))^2)
C           Inten(q) = Const * ----------------------------------------
C                                   Xbar * q^2 * (abs(1-Fy*Fz)^2)
C
C           where Const : (rhoCr- rhoAm)^2 / (4* Pi^2)
C                 rhoCr : crystalline density
C                 rhoAm : amorphous density
C                 Xbar  : average of Total thickness (Ybar + Zbar)
C
C       5) Total SAXS intensity
C
C           Totinten(q) = integration of I(q,C) * P(C) dC
C
C                           over C = from 0.01 to 0.99 EVERY 0.01
C
C       6) Assumption: sigmaY / Ybar = sigmaZ / Zbar
C
C                 Zbar : const (0.5)
C                              sigmaX^2
C                 sigmaY^2 = -------------------
```

```
C                              (1/C - 1)^2 + 1
C
C    [2] Calculation
C
C        1) Variables :
C                        CRYST(100)    : crystallinity (C) ( 0.01, 0.02 .. 0.99)
C                        SEGINTEN(100) : segment intensity of given QR and PHI
C                        CRYPROB       : probability of phi (P(C))
C                        YBAR          : average crystallinie thickness
C                        FYVAL         : FY values of given QR and PHI
C                        FZVAL         : FZ values of given QR and PHI
C                        SIGMAYSQ      : sigmaY ^2
C                        SIGMAZSQ      : sigmaZ ^2
C
C                        QR            : scattering vector (0.05, 0.075 .. 3.0)
C                        TOTINTEN      : total intensity of each QR
C
C
C        2) Constants : CONST      = 1.0
C                        ZBAR       = 0.5 (average thickness of amorphous layer)
C                        CBAR       = 0.5 (Total average crystallinity)
C                        SIGMAX     = GIVEN
C                        SIGMAC     = GIVEN
C
C    [3] OUTPUT VALUES:
C                      SigmaX, SigmaC
C                      QR VS Totinten on various values of SigmaX and SigmaC.
C
C          ** No. of QR's 75 from 0 to 3 (every 0.024)
C
C    [4] SUBROUTINES USED:
C                  INTENCAL(QR, ZBAR, SIGMAX, CRYST(I), TEMINTEN)
C                  FOURTSVN(QR, CRYST(I), ZBAR, FZVAL)
C                  CXEXPN(FINCMFX, TEMCMFX)
C                  CXARTH(A,B,R,N)--------complex arithmath
C                  TPZOD(NUMPHI,CRYST(1),CRYST(NUMPHI),SEGINTEN,TOTINTEN)
C                  REAL FUNCTION DSTSQ(X)
C*************************************************************************
C
C
      PROGRAM FSAXSVM7
      DIMENSION CRYST(100), SEGINTEN(100)
C  LOOK! NUMBER.
      DIMENSION SIGX(7), SIGC(7)
      INTEGER I, J, K, NUMPHI, NUMSIG
C NUMSIG---NUMBER OF SIGMAS FOR REPEATING
      REAL ZBAR, CBAR, CRYPROB, TMINTEN, QR, TOTINTEN,
     &     SIGMAX, SIGMAC, SIGCON1, SIGCON2
      CHARACTER*12 OUTFILE
```

```
C>>ORI:       DATA SIGC/0.1,0.15,0.175,0.2,0.25,0.3/
C>>ORI:       DATA SIGX/0.1,0.15,0.175,0.2,0.25,0.3/
      DATA SIGC/0.05,0.075,0.1,0.125,0.15,0.175,0.2/
      DATA SIGX/0.05,0.075,0.1,0.125,0.15,0.175,0.2/
C
C     SET CONSTANTS
C
      ZBAR = 0.5
      CBAR = 0.5
      NUMPHI = 99
      NUMSIG = 7
C
C     DO LOOP FOR WHOLE -- CHANGING SIGMAX VALUE (INDEX K)
C
      DO 14 K=1, NUMSIG, 1
      SIGMAX = SIGX(K)
C
C        DO LOOP --- CHANGING SIGMAC VALUE (INDEX J)
         DO 16 J=1, NUMSIG, 1
C*       J = 1
         SIGMAC = SIGC(J)
C*       SIGMAC = 0.3
C
C CONSTANTS FOR INTENSITY CALCULATION.
C 2.506628275 = SQRT(2*PI)
         SIGCON1 = 2.506628275 * SIGMAC
         SIGCON2 = -2 * SIGMAC * SIGMAC
C INITIALIZATION
         CRYPROB = 1.0
         TMINTEN = 1.0
         TOTINTEN = 1.0
C
         OUTFILE = 'ASXVM7'//CHAR(48+K)//CHAR(48+J)//'.PRN'
         OPEN (UNIT=30,FILE=OUTFILE,STATUS='NEW')
         WRITE(30,*)'"FILENAME: " "',OUTFILE,'"'
         WRITE(*,*)'"FILENAME: " "',OUTFILE,'"'
C
         WRITE(30,1001)'"SIGMA X: "', SIGMAX
         WRITE(30,1001)'"SIGMA C: "', SIGMAC
C
         WRITE(*,1001)'"SIGMA X: "', SIGMAX
         WRITE(*,1001)'"SIGMA C: "', SIGMAC
 1001    FORMAT(A30,F8.4)
         WRITE(30,*)'"SAXS VAR. MODEL 7"'
         WRITE(*,*)'"SAXS VAR. MODEL 7"'
 1002    FORMAT(A35)
         WRITE(30,1000)'"-------------"','"------------"'
         WRITE(30,1000)'"    QR       "','" INTENSITY"'
         WRITE(*,1000)'"-------------"','"------------"'
```

```
          WRITE(*,1000)'"    QR       "','" INTENSITY"'
 1000     FORMAT(2A16)
C
C
            DO 18 QR=0.04, 3.0, 0.04
C
               DO 22 I=1,NUMPHI,1
                 CRYST(I)= 0.01 * I
                 CRYPROB = EXP((CRYST(I)-CBAR)**2 / SIGCON2) / SIGCON1
                 CALL INTENCAL(QR, ZBAR, SIGMAX, CRYST(I), TMINTEN)
                 SEGINTEN(I) = TMINTEN * CRYPROB
  22             CONTINUE
C
C     INTEGRATION SEGINTEN OVER CRYST VALUE FOR GETTING TOTINTEN
C
             CALL TPZOD(NUMPHI,CRYST(1),CRYST(NUMPHI),SEGINTEN,TOTINTEN)
C  UNCORRECTION OF LORENTZ FACTOR FOR DIRECT COMPARISON OF X-RAY
C  EXPERIMENT.
             TOTINTEN = TOTINTEN/(QR*QR)
             WRITE (30,1100) QR, TOTINTEN
             WRITE (*,1100) QR, TOTINTEN
 1100        FORMAT(2G16.6)
  18         CONTINUE
C
          CLOSE(UNIT=30)
C
C END OF THE LOOP FOR J VALUE (CHANGING SIGMAC)
  16      CONTINUE
C
C END OF THE LOOP FOR K VALUE (CHANGING SIGMAX)
  14      CONTINUE
C
          STOP
          END
C
C*******************************************************************************
C #1
C     CALL INTENCAL(QR, ZBAR, SIGMAX, CRYST(I), TEMINTEN)
C
      SUBROUTINE INTENCAL(Q, ZB, SGX, XPHI, SITEN)
C
C       [THEORY] SAXS intensity of a given stack
C
C                                (abs(1-Fy))^2 * (1-(abs(Fz))^2) +
C                                        (abs(1-Fz))^2 * (1-(abs(Fy))^2)
C             Inten(q) = Const * ----------------------------------------
C                                     Xbar * q^2 * (abs(1-Fy*Fz)^2)
C
C             where Const : (rhoCr- rhoAm)^2 / (4* Pi^2)
```

```
C                   rhoCr : crystalline density
C                   rhoAm : amorphous density
C                   Xbar  : average of Total thickness (Ybar + Zbar)
C
C *   VARIABLE WITH DIMENSION OF 2 IS COMPLEX NUMBER.
C     (RLONE: REAL NUMBER ONE)
C
C  SUBROUTINES CALLED:
C     CALL FOURTSVN(Q, SIGZSQ, ZB, FZ)
C     CALL CXARTH(FY, FZ, TMCMFX1, 3)
C
      DIMENSION FY(2), FZ(2), TMCMFX1(2), TMCMFX2(2), RLONE(2)
C
      REAL SINTUP, SINUP1, SNTDWN, YB, SIGYSQ, SIGZSQ, RPHI, SITEN, Q
      DATA RLONE/1.,0./
C
C INITIALLIZATION
      FY(1) = 0.0
      FY(2) = 0.0
      FZ(1) = 0.0
      FZ(2) = 0.0
      TMCMFX1(1) = 0.0
      TMCMFX1(2) = 0.0
      TMCMFX2(1) = 0.0
      TMCMFX2(2) = 0.0
      SINTUP = 0.0
      SINUP1 = 0.0
      SNTDWN = 0.0
C
      RPHI = 1./XPHI -1.
      YB = ZB / RPHI
C
      SIGYSQ = SGX * SGX / (RPHI**2 + 1.)
      SIGZSQ = SIGYSQ * RPHI**2
C
      CALL FOURTSVN(Q, SIGYSQ, YB, FY)
      CALL FOURTSVN(Q, SIGZSQ, ZB, FZ)
C
      CALL CXARTH(RLONE, FY, TMCMFX1, 2)
      CALL CXARTH(RLONE, FZ, TMCMFX2, 2)
C
      SINTUP = DSTSQ(TMCMFX1)*(1-DSTSQ(FZ))
      SINUP1= DSTSQ(TMCMFX2)*(1-DSTSQ(FY))
      SINTUP = SINTUP + SINUP1
C
      CALL CXARTH(FY, FZ, TMCMFX1, 3)
      CALL CXARTH(RLONE, TMCMFX1, TMCMFX2, 2)
      SNTDWN = DSTSQ(TMCMFX2) * Q * Q * (YB + ZB)
C
```

```
      SITEN = SINTUP / SNTDWN
C
      RETURN
      END
C
C*************************************************************************
C #2
C     CALL FOURTSVN(Q, SIGYSQ, YB, FY)
C
      SUBROUTINE FOURTSVN(XQ, SGSQ, BAR, FVAL)
C
C    Fourier Transform of the Exponential Distribution Function.
C                          (Modified Tzvankin Model)
C
C                  exp(-2 * Pi * i * q * (Ybar - sigmaY))    (Ybar > sigmaY)
C         Fy(q) =  ---------------------------------------
C                       (2 * Pi * i * sigmaY * q) + 1
C
C                  exp(-2 * Pi * i * q * (Zbar - sigmaZ))
C         Fz(q) =  ---------------------------------------
C                       (2 * Pi * i * sigmaZ * q) + 1
C
C                                1                         ( Ybar < sigmaY)
C         Fy(q) =  ---------------------------------------
C                       (2 * Pi * i * sigmaY * q) + 1
C
C                                1                         ( Zbar < sigmaZ)
C         Fz(q) =  ---------------------------------------
C                       (2 * Pi * i * sigmaZ * q) + 1
C
C
C          where sigmaY : standard deviation of Y.
C                sigmaZ : standard deviation of Z.
C                q      : scattering vector.
C                i      : imaginary number unit.
C                Ybar   : Average of Y value.
C                Z      : layer thickness (Z for amorphous).
C
C
C SUBROUTINES CALLED:
C     CALL CXEXPN(FINCMFX, TEMCMFX)
C     CALL CXARTH(INICMFX, TEMCMFX, FVAL, 3)
C
      DIMENSION FVAL(2), FL(2), TEMCMFX(2), BINCMFX(2), FINCMFX(2)
      REAL CONSTA, SIG
C
C    CONSTA = 2* PI
C
      CONSTA = 6.283185307
```

```
C
C INITIALLIZATION
      BINCMFX(1) = 1.0
      BINCMFX(2) = 0.0
      FINCMFX(1) = 0.0
      FINCMFX(2) = 0.0
      TEMCMFX(1) = 0.0
      TEMCMFX(2) = 0.0
      FVAL(1) = 0.0
      FVAL(2) = 0.0
C
      SIG = SQRT(SGSQ)
      BINCMFX(2) = CONSTA * XQ * SIG
      IF (BAR .GT. SIG) GO TO 340
      FINCMFX(2) = 0.0
      GO TO 360
  340 FINCMFX(2) = -1. * CONSTA * XQ * (BAR-SIG)
  360 CALL CXEXPN(FINCMFX, TEMCMFX)
      CALL CXARTH(TEMCMFX, BINCMFX, FL, 4)
      FVAL(1) = FL(1)
      FVAL(2) = FL(2)
C
      RETURN
      END
C
C*******************************************************************************
C #3
C     CALL CXEXPN(FINCMFX, TEMCMFX)
C
      SUBROUTINE CXEXPN(A,R)
C
C     SUBROUTINE CXEXPN EVALUATES THE EXPONENTIAL OF A COMPLEX
C     ARGUMENT
C
C     EXP(A1+ A2 i) = EXP(A1) * ( COS(A2) + i SIN(A1))
C
      DIMENSION A(2), R(2)
C
      B = EXP (A(1))
      R(1) = B*COS(A(2))
      R(2) = B*SIN(A(2))
      RETURN
      END
C
C
C*******************************************************************************
C #4
C     CALL CXARTH(FY, FZ, TMCMFX1, 3)
C
```

```
      SUBROUTINE CXARTH(A,B,C,N)
C
C     THIS SUBROUTINE CXARTH DOES COMPLEX ARITHMETIC INVOLVING
C     TWO COMPLEX NUMBERS.
C
C         N=1 FOR ADDITION
C         N=2 FOR SUBTRACTION
C         N=3 FOR MULTIPLICATION
C         N=4 FOR DIVISION
C
      DIMENSION A(2), B(2), C(2)
C
      X = B(1)
      Y = A(1)
      GO TO (1,2,3,4),N
 1    C(1) = X + Y
      C(2) = A(2) + B(2)
      RETURN
 2    C(1) = Y - X
      C(2) = A(2) - B(2)
      RETURN
 3    C(1) = Y*X - A(2)*B(2)
      C(2) = A(2)*X + Y*B(2)
      RETURN
 4    G = X*X + B(2)*B(2)
      C(1) = (Y*X + A(2)*B(2))/G
      C(2) = (A(2)*X - Y*B(2))/G
      RETURN
      END
C
C*******************************************************************************
C #5
C     CALL TPZOD(NUMPHI,CRYST(1),CRYST(NUMPHI),SEGINTEN,TOTINTEN)
C
      SUBROUTINE TPZOD (M,XO,XH,Y,TPA)
C
C     TO EVALUATE THE DEFINITE OF A FUNCTION
C     USING THE TRAPEZOIDAL RULE.
C
      DIMENSION Y(1)
      TM = M - 1
      MM = TM
      DI = (XH - XO)/(TM*2.)
      TPA = 0.
      DO 15 I = 1,MM
      AR = Y(I) + Y (I + 1)
      AR = DI*AR
 15   TPA = TPA + AR
      RETURN
```

```
      END
C*************************************************************************
C #6
C     INTDOWN = DSTSQ(TMCMFX2) * XQ * (YB + ZB)
C
      REAL FUNCTION DSTSQ(X)
C     CALCULATE SQUARE OF ABSOLUTE VALUE OF COMPLEX NUMBER.
C
      DIMENSION X(2)
      REAL YR, YI
C
      YR = X(1)
      YI = X(2)
      DSTSQ = YR * YR + YI * YI
      RETURN
      END
C
```

# APPENDIX V

## LISTING OF PASCAL PROGRAM FOR IN-SITU SAXS DATA TREATMENT

```
program DistantTotal;

{  íëëë
```

```
                    Attr     : byte;
                    Time, Date, Sizelo, SizeHi : integer;
                  end;

var
        Inifile,Lastfile        : String12;
        MainIndic,indicate      : char;
        GuinierYes              : Boolean;   {For Guinier fitting}
        TimeStr, DateStr        : String12;
        Hr1, Min1, Sec1         : Byte;
        Hr2, Min2, Sec2         : Byte;
        SecDif, MinDif          : real;

(*************************************************************)
(*               Show  Date  Module                          *)
(*                  July 22, 1987                            *)
(*************************************************************)
Procedure ShowDate(Var DStr:String12);
var
   Yr, Mon, Day   :String[2];
   Reg            :Reglist;

begin
   Reg.AX :=$2A00;
   msdos(reg);
   Reg.Cx := Reg.CX -1900;
   if Reg.CX >99 then
      Reg.CX := Reg.CX-100;
   str(Reg.CX:2, Yr);
   Str(hi(Reg.DX):2, mon);
   Str(Lo(Reg.DX):2, Day);
   if Yr[1] =' ' then Yr[1] := '0';
   if Mon[1] =' ' then Mon[1] := '0';
   if Day[1] =' ' then Day[1] := '0';
   DStr := Mon+'-'+Day+'-'+Yr;
end;           {Show Date}

(*************************************************************)
(*               Show  Time  Module                          *)
(*                  July 22, 1987                            *)
(*************************************************************)
Procedure Showtime(Var TStr: String12);
var
   HrS, MinS, SecS :String[2];
   Reg             :Reglist;
begin
   Reg.AX := $2C00;
   msdos(reg);
   Str(hi(Reg.CX):2, Hrs);
```

```
   Str(Lo(Reg.CX):2, Mins);
   Str(Hi(Reg.DX):2, Secs);
   if Hrs[1] =' ' then Hrs[1] := '0';
   if Mins[1] =' ' then Mins[1] := '0';
   if Secs[1] =' ' then Secs[1] := '0';
   TStr := HrS+':'+MinS+':'+SecS;
end;               {Showtime}


(*************************************************************)
(*                 Get  Time  Module                         *)
(*                   July 22, 1987                           *)
(*************************************************************)
Procedure Getime(var Hr, Min, Sec  :Byte);
var
   Reg            :Reglist;
begin
   Reg.AX := $2C00;
   msdos(reg);
   Hr  := Hi(Reg.Cx);
   Min := Lo(Reg.CX);
   Sec := Hi(Reg.DX);
end;

(*************************************************************)
(*                 Show Directory Module                     *)
(*                   July 16, 1987                           *)
(*************************************************************)
Procedure ShowDir(FileSpec:String80);

Const
   Columns = 4;
   Attrbt  = $16;              {Attribute of files > $0 : normal files
                                                  $10: add subdir
                                                  $16: add hidden and all.}

Var
   ByteCluster, ByteFree, ByteCapacity : real;
   J, Colsize : integer;
   Reg        : Reglist;
   DTA        : Array[1..43] of byte;
   FileSize   : real;
   FD         : FileData Absolute DTA;

begin
   Writeln('  * Directory Listing for ', FileSpec);

   Reg.Dx  := 0;                              {Default Disk Space checking}
   Reg.Ax  := $3600;
```

```
MsDos(Reg);
if Reg.Ax = $FFFF then
   Writeln('              Error in Checking Disk Space.')
else
   begin
      ByteCluster  := 1.0* Reg.AX * Reg.CX;
      ByteFree     := ByteCluster * Reg.BX;
      ByteCapacity := ByteCluster * Reg.DX;
      Writeln('             * ',ByteFree:9:0,' Bytes Free.');
      writeln('             * ',ByteCapacity:9:0,' Bytes Capacity   * ',
                  ByteCluster:6:0,' Bytes /Cluster');
   end;

ColSize := 80 div Columns;                {Directory Scan}
Reg.DX  := Ofs(DTA);
Reg.DS  := seg(DTA);
Reg.AX  := $1A00;
Msdos(Reg);
FileSpec:= Filespec + chr(0);
Reg.DX  := Ofs(FileSpec[1]);
Reg.DS  := Seg(Filespec[1]);
Reg.CX  := Attrbt;
Reg.AX  := $4e00;
Msdos(Reg);
if Lo(Reg.AX) <> 0 then
   Begin
     Writeln('  ** No Filenames Found. **');
     exit
   end;
if DTA[22] and $10 <> 0 then write('[Dir]');
J := 31;
while DTA[J] <>0 do
   begin
     write(Chr(DTA[J]));
     J := J + 1;
   end;
Filesize := lo(FD.sizelo) + 256.0 * hi(FD.SizeLo) +
            65536.0 * lo(FD.SizeHi) +
            16777216.0 * hi(FD.SizeHi);
while(WhereX mod Colsize) <> 13 do write(' ');        {Move to next column}
write(FileSize:7:0);                                  {Writing File Size}

repeat
   Reg.DX  := ofs(DTA);
   Reg.DS  := Seg(DTA);
   Reg.AX  := $4F00;
   MSDOS(Reg);
   if Lo(Reg.AX) =0 then
      begin
```

```
            if WhereX > (Columns-1) * Colsize + 1 then writeln;
            while(WhereX mod Colsize) <> 1 do write(' ');   {Move to next col}
            If DTA[22] and $10 <> 0 then write('[Dir]');    {It's SubDir}
            j := 31;
            while DTA[J] <> 0 do
               begin
                 write(Chr(DTA[j]));
                 J := J + 1;
               end;
            Filesize := lo(FD.sizelo) + 256.0 * hi(FD.SizeLo) +
                        65536.0 * lo(FD.SizeHi) +
                        16777216.0 * hi(FD.SizeHi);
            while(WhereX mod Colsize) <> 13 do write(' ');  {Move to next col}
            write(FileSize:7:0);                            {Write file size}
         end;
   until Lo(Reg.AX) <> 0;
   writeln;
   writeln('  * End of Directory Listing. *' );writeln;
end;  {Show Dir}


(*************************************************************)
(*                Write Line in Monitor and Printer          *)
(*                   June 1, 1987                            *)
(*************************************************************)
Procedure wrtln(strng:string80);
                                                {WRITELN for whole procedure}
var
   TemX, TemY :integer;

begin
   writeln(strng);
   writeln(lst,strng);
   temX := whereX;
   temY := whereY;
   gotoXY(1,1); clrEol;
   gotoXY(5,1);writeln('Íëëëëëëëëëëëëëëëëëëëëëëëëë< SAXS DATA ANALYSIS
>ëëëëëëëëëëëëëëëëëëëëëëëëë¸');
   gotoXY(1,2); clrEol;
   gotoXY(5,2);writeln('°  CORELATION FUNCTION                    Initial File : ',inifile,'
°');
   gotoXY(1,3); clrEol;
   gotoXY(5,3);writeln('°                                        Final   File : ',lastfile,'
°');
   gotoXY(1,4); clreol;
   showtime(TimeStr);

gotoXY(5,4);writeln('°ÉÉÉ
```

```
   gotoxy(44,4);Writeln('[Time> ', TimeStr,']');
   gotoXY(1,5);clrEol;
   gotoXY(5,5);writeln('Åëëë
```

```
        Slope    := 0.0;
        Intercept:= 0.0;
        CorrCoeff:= -15.0;
        WrtLn (#7+'     >>Error: All identical data sets in Regression.(Demon = 0)');
        exit
      end
   else
      Slope     :=(SumXY - SumX * SumY / Numdatapr)/Denom;
   Intercept :=(SumY  - Slope* SumX)/ Numdatapr;
   Denom     := SumYSq - SumY* SumY / Numdatapr;
   if Denom = 0.0 then
      CorrCoeff := 1.0
   else
      CorrCoeff := Sqrt(Slope * (SumXY - SumX * SumY /NumDataPr)/Denom);
end;



(*************************************************************)
(*                   Cubic spline module                     *)
(*                  Copyright (C) 1985 by                    *)
(*                  BORLAND International                    *)
(*************************************************************)

procedure MakeSpline(A:PlotArray;          {Input array}
                N:integer;                 {Number of input data}
                X1,XM:real;                {initial and final x value}
                var B:PlotArray;           {output array}
                M:integer);                {No of data of output}

  type Vector = array [1..MaxSpline] of real;
  var x,y,z:Vector;
      i:integer;
      DeltaX:real;

  procedure stg(Vector1,Vector2,Vector3:Vector;
                var Vector4:Vector;
                NPts:integer);
    var i:integer;
        Factor:real;

    begin
      for i:=2 to NPts do
       begin
        Factor:=Vector1[i-1]/Vector2[i-1];
        Vector2[i]:=Vector2[i]-Factor*Vector3[i-1];
        Vector4[i]:=Vector4[i]-Factor*Vector4[i-1];
       end;
      Vector4[NPts]:=Vector4[NPts]/Vector2[NPts];
```

```
    for i:=1 to NPts-1 do
      Vector4[NPts-i]:=(Vector4[NPts-i]-Vector3[NPts-i]*Vector4[NPts-i+1]) /
                       Vector2[NPts-i];
  end;

procedure sc(X,Y:Vector;
             var Z:Vector;
             NPts:integer);
  var i:integer;
      D,C:Vector;

  begin
    D[1]:=1.0;
    C[1]:=0.5;
    Z[1]:=0.5;
    for i:=2 to NPts-1 do
     begin
      D[i]:=2.0*(X[i+1]-X[i-1]);
      C[i]:=X[i+1]-X[i];
      Z[i]:=6.0*((Y[i+1]-Y[i])/(X[i+1]-X[i])-(Y[i]-Y[i-1])/(X[i]-X[i-1]));
     end;
    D[NPts]:=1.0;
    C[NPts-1]:=0.0;
    C[NPts]:=0.0;
    Z[NPts]:=0.0;
    stg(C,D,C,Z,NPts);
  end;

function si(V:real;
            X,Y,Z:Vector;
            NPts:integer):real;
  var i,j:integer;
      dummy,ai,hi:real;

  begin
    if (V>X[1]) and (V<X[NPts]) then
     begin
      j:=1;
      repeat
        j:=j+1;
        i:=NPts-j;
        dummy:=V-X[i];
      until (dummy>=0.0) or (i=2);
      hi:=X[i+1]-X[i];
      ai:=dummy*(Z[i+1]-Z[i])/(6.0*hi)+0.5*Z[i];
      ai:=dummy*ai+(Y[i+1]-Y[i])/hi-hi*(2.0*Z[i]+Z[i+1])/6.0;
      si:=dummy*ai+Y[i];
     end
    else if V=X[1] then si:=Y[1]
```

```
    else si:=Y[NPts];
  end;

procedure sia(X,Y:Vector;
              NPts:integer;
              XInt:Vector;
              var YInt:Vector;
              N:integer);
  var i:integer;
      V3:Vector;

  begin
    sc(X,Y,V3,NPts);
    for i:=1 to N do YInt[i]:=si(XInt[i],X,Y,V3,NPts);
  end;

begin { MakeSpline }
  if (abs(N)>=2) and (abs(M)>=2) then            {error N and M should be}
   begin                                         {Larger than 2}
    if ((X1>=A[1,1]) and (XM<=A[N,1])) and (M>=2) then
     begin
      DeltaX:=(XM-X1)/(M-1);
      for i:=1 to N do
       begin
        X[i]:=A[i,1];
        Y[i]:=A[i,2];
       end;
      for i:=2 to M-1 do Z[i]:=X1+(i-1)*DeltaX;
      Z[1]:=X1;
      Z[M]:=XM;
      sia(X,Y,N,Z,Y,M);
      for i:=1 to M do
       begin
        B[i,1]:=Z[i];
        B[i,2]:=Y[i];
       end;
     end
    else WrtLn(#7+'     >>Error[Spline]: Limits of new data are out of range.');
   end
  else WrtLn(#7+'     >>Error[Spline]: Number of data set is less than 2.');
end; {MakeSpline}


(*************************************************************)
(*        Get Data from Diskette (Form of PRN file)          *)
(*                    June 1, 1987                           *)
(*************************************************************)
procedure get_data(FileName: String12; var OrgXY:PlotArray;
                   var n: integer);
```

```
                                        { get values for n and arrays x,y }
                                        { from filename }

Label
  2exit;                                {exit for error}
var
     j                 : integer;
     DumData, message  : String80;
     InFile            : text;
     Dumkappa,temconst : real;
     numstr            : String12;

begin
   Assign(InFile,FileName) ;
   {$I-} Reset(InFile) {$I+} ;                {Locate specific file}
   If IOResult <> 0 Then
   Begin
      message :=#7+'     >>Error: File '+FileName+' Can Not Be Located.' ;
      Wrtln(message) ;
      n := 0;
      Exit ;
   End ; { If IOResult <> 0 }
   J:=1;
   Repeat
      { $I-} Readln(InFile,Dumdata) {$I+} ;
      j := j + 1 ;
   Until j = 9;          {SKIP 8 Line of headings}
   temconst := InitialK- SpResol;    {set to be 0.005 so that data start with
                                        0.006 or larger}
   Repeat
      { $I-} Readln(InFile,Dumkappa,Dumdata) {$I+} ;
      j := j + 1 ;
   Until Dumkappa >= TemConst;
   J :=1;

   While not(eof(InFile)) do     {actual collecting data}
      Begin
        {$I-} Readln(InFile, OrgXY[J,1], OrgXY[J,2] ) {$I+} ;
        if OrgXY[J,2] <= 0.0 then
           {$I-} Readln(InFile, OrgXY[J,1], OrgXY[J,2] ) {$I+} ;
        If IOResult <> 0 Then
          Begin
             str(j:3, Numstr);
             message :=#7+'     >>Error>in data file <'+filename+'> in row '+Numstr+' .' ;
             Wrtln(message) ;
             GoTo 2Exit ;
          End ; { If IOResult <> 0 }
         J := J + 1;
      End ;                 { While J }
```

```
     Goto 2Exit;
2Exit:
   Close(InFile);
   n := J-2;              {Take out last data point from actual data}
End ; { Get_data }


(*************************************************************)
(*      Write Data to Diskette (Form of PRN file)            *)
(*                   June 1, 1987                            *)
(*************************************************************)

procedure write_data(Filename:String12; outxy:plotarray; n:integer);
{ Make output file and write the answers }

var     P       : integer;
        OutFile : Text;

begin

  assign(OutFile, FileName);
  rewrite(OutFile);
  for P:=1 to n do
    writeln(OutFile,outxy[P,1]:20:7,outxy[P,2]:20:7);
  close(outFile);
end;            { write_data }


(*************************************************************)
(*        Lorentz Correction to Raw Data                     *)
(*                   June 1, 1987                            *)
(*************************************************************)
Procedure Lorentz(KapInten : Plotarray; m:integer;            {Input}
                  var LorInten:Plotarray);                    {Output}

{Lorenz correction calculation it will import Kappa and
 intensity as X and Y respectively. It will make output only LorY which is
 (K^2*I).  It also has to get number of data set(m) }

var K : integer;
begin
   for K := 1 to m do
     begin
       LorInten[k,1] := KapInten[K,1];
       LorInten[k,2] := KapInten[K,1] * KapInten[K,1] * KapInten[K,2];
     end;
end;  {Lorentz}
```

```
(*************************************************************)
(*        Traperzoidal Integration Module                    *)
(*                   June 1, 1987                            *)
(*************************************************************)
Function Trap_Integr( intxy      :Plotarray;
                      pieces     :integer) : real;
{ integration for randomly devided values. }
{ with number of regions equal to PIECES }
{ Not fixed number and size of pieces and answer is SUM }

var     i         : integer;
        Psum      : real;
begin

  psum:=0.0;
  for i:=2 to pieces do
     Psum := Psum+(intXY[i,2]+intXY[i-1,2])*(intXY[I,1]-intXY[I-1,1]) * 0.5;
  Trap_integr := Psum;
end;            { Integration }


(*************************************************************)
(*     Distance Distribution Funtion Calculation             *)
(*                   June 6, 1987                            *)
(*************************************************************)
Procedure DistDist( Kval  : PlotArray;                    {Input X and Y value}
                var DistXY:PlotArray;                    {Output corrected X,Y}
                n      : integer;                       {number of kappa}
                NewNo : integer);          { Number of new DistDist data point}

{  DistDist is the procedure for the calculation of corelation function
                     Integration( I(h)*(h*x)*Sin(x*h)dh )
          P(x) = ----------------------------------------
                       2* Pi^2
where I can be normalintensity or Lorentz corrected intensity.
      Integration is carried from K=0 to infinity.    }

var
   UpSum          : Ary;
   DownSum        : Real;
   i, L           : integer;
   KValUp         : Plotarray;

begin       {DistDist}
   DownSum := 19.7392088; {for dividuend: 2* pi^2 }
   DistXY[1,1] :=0.0;
   For L := 1 to NewNo do
      begin
        if L > 1 then
```

```
          DistXY[L,1] := DistXY[L-1,1] + LimitGam/NewNo;
        for i := 1 to n do
          begin
            KvalUp[i,1] := Kval[i,1];
            KvalUp[i,2] :=Kval[i,2] * (DistXY[L,1]*Kval[i,1])
                          * Sin(DistXY[L,1]*Kval[i,1]);
          end;
        upsum[L] := Trap_integr(Kvalup, n);
        DistXY[L,2] := UpSum[L]/DownSum;
      end;
end;     {DistDist}

(*************************************************************)
(*              Finding Minimum Module                       *)
(*                   July 17, 1987                           *)
(*************************************************************)
Function MinIndex(InAry : Plotarray; Numini, NumLimit : Integer) : Integer;
{Getting index for the minimum value of Y}
var
   MinY      : real;
   I, MinTem : integer;

begin
   MinY := InAry[NumIni,2];
   MinTem := 1;
   for I := NumIni to NumLimit do
      begin
         If InAry[I,2] <= MinY then
            begin
               MinTem := I;
               MinY := InAry[I,2];
            end;
      end;
   MinIndex := MinTem;
end;                                    {MinIndex}


(*************************************************************)
(*              Extrapolation  Module                        *)
(*                  July 16, 1987                            *)
(*************************************************************)

Procedure Extrapol(InputAry:plotarray;  NofIndata:integer;
                   var OutputAry:plotarray; var NofOutData:integer);

{This module will complete SAXS data by fitting extra data set
 beyond actual data range. Extrapolation of data set will be done
 by Gunier approximation in the initial portion of the data.
 For the tail part of data, Modified Porod approximation will
```

```
 be applied, where the exponent of q is not -4 but a certain
 value. This exponent value is actually obtained by linear
 regression method.

 Eqns.  Gunier methods: Ln I = Ln I(0) - G * K^2
              where G = Rg^3/3 for isotropic spherical structure
        Porod  Method : Ln I = A -P (Ln(K))
              where A = constant, P: Porod exponent}

Label
   3exit;
const
   PorodLmt   = 15;   {Number of data set for Porod Approximation regression}
Var
   AConst, Pcoef, LnInt0             : real ;        {constants needed}
   Gcoef, CorelCf                    : real ;        {in above eqs}
   IniVal                            : Plotarray;    {for regression}
   J, temint, temcount1, Temcount2   : integer;
   AconstStr, PcoefStr, LnInt0Str    : String12;     {For displaying in}
   GcoefStr, CorelCfStr, numstr      : String12;     { monitor }
   NumGuinier, NumPorod              : integer; {Number of data after fitting}
   GuinierLmt                        : Integer; {# of data for regression}

begin;
   GuinierLmt := MinIndex(InputAry,1,15)-2;
   If GuinierLmt < 5 then GuinierLmt := 5;
   for J := 1 to GuinierLmt do                        {Guiner approximation}
      begin
        if GuinierYes then                             {Guinier Approximation}
           IniVal[J,1] := InputAry[J,1]*InputAry[J,1]
           else                                        {Power Law Approximation}
           IniVal[J,1] := Ln(InputAry[J,1]);
        if InputAry[J,2] <= 0.0 then
           begin
             wrtln(#7+'     >>Error [Guinier Fitting] : Y value is less than 0. No
logarithm.');
             goto 3exit;
           end;
        iniVal[J,2] := Ln(InputAry[J,2]);
      end;
   LinReg(IniVal, GuinierLmt, LnInt0, Gcoef, CorelCf);
   Str(Lnint0:10,Lnint0Str);
   Str(Gcoef:10, Gcoefstr);
   str(GuinierLmt:4,NumStr);
   Str(CorelCf:10:6, CorelCfStr);
   If GuinierYes then
      WrtLn('         *Guinier Region was fitted by Guinier Approximation Law.')
   else
      wrtln('         *Guinier Region was fitted by Simple Power Law.');
```

```
wrtln('              *Intercept : '+Lnint0str+'    *Slope: '+Gcoefstr);
wrtln('              *No of Data: '+NumStr+'    *Correl.Coef: '+CorelCFstr);
if (CorelCf < 0.0) or (CorelCf > 1.0) then
   begin
    wrtln(#7+'     >>Error [Guinier Fitting] : Correlation Coeff is out of Range.');
    goto 3exit;
   end;

NumGuinier := Trunc(InputAry[1,1]/Spresol);
for J := 1 to Numguinier do                {Guinier Approximation Fitting}
   begin
     if GuinierYes then
        OutPutary[J,1] := SpResol * (J-1.0)
     else if J > 1 then
        Outputary[j,1] := SpResol * (J-1.0)
     else
        Outputary[J,1] := SpResol * (J-0.95);    {Only for 0 of kappa}

     if GuinierYes then
        Outputary[J,2] := exp(LnInt0+Gcoef*OutPutary[J,1]*OutPutary[J,1])
     else                                        {PowerLaw approximation}
        Outputary[J,2] := exp(LnInt0) * exp(Gcoef*Ln(Outputary[J,1]));
   end;

Temcount1 := NumGuinier +1;
Temcount2 := NofInData + NumGuinier;
for J := TemCount1 to Temcount2 do              {Collecting original data}
   begin
     Temint := J-NumGuinier;
     OutputAry[J,1] := InputAry[Temint,1];
     OutputAry[J,2] := InputAry[Temint,2];
   end;

for J := 1 to porodlmt do                  {Porod Approximation Regression}
   begin
     Temint := NofInData-PorodLmt+J;
     IniVal[J,1] := ln(InPutAry[TemInt,1]);
     if InputAry[temInt,2] <=0 then
        begin
          wrtln(#7+'     >>Error [Porod Fitting] : Y value is less than 0. No logarithm.');
          goto 3exit;
        end;
     iniVal[J,2] := Ln(InputAry[TemInt,2]);
   end;

LinReg(IniVal, PorodLmt, Aconst, Pcoef, CorelCf);
Str(Aconst:10,AconstStr);
Str(Pcoef:10:6, Pcoefstr);
str(PorodLmt:4,NumStr);
```

```
   Str(CorelCf:10:6, CorelCfStr);
   WrtLn('         *Porod Region was fitted by Power Approximation Law.');
   wrtln('              *Intercept : '+Aconststr+'    *Power: '+Pcoefstr);
   wrtln('              *No of Data: '+numStr+'    *Correl.Coef: '+CorelCFstr);
   if (CorelCf < 0.0) or (CorelCf > 1.0) then
      begin
       wrtln(#7+'     >>Error [Porod Fitting] : Correlation Coeff is out of Range.');
       goto 3exit;
      end;

   NumPorod := trunc((FitLimit-InPutAry[NofInData,1])/SpResol);
   Temcount1 := NofInData + NumGuinier + 1;       {Porod Approximation Fitting}
   TemCount2 := NofInData + NumGuinier + NumPorod;
   for J := TemCount1 to TemCount2 do
      begin
        Outputary[J,1] := SpResol * (J);
        Outputary[J,2] := exp(Aconst) * exp(Pcoef*Ln(Outputary[J,1]));
      end;
   NofOutData := temCount2;
   exit;

3exit:                                                  {Error in extrapolation}
   Wrtln (#7+'     >>Error [Extrapolation Module]: Extrapolation Skipped');
   NofOutdata := NofIndata;
   for J := 1 to NofInData do                          {Collecting original data}
      begin
        OutputAry[J,1] := InputAry[J,1];
        OutputAry[J,2] := InputAry[J,2];
      end;
end;                                                                  {Extrapol}



(*************************************************************)
(*              Initialization Module                        *)
(*                   June 6, 1987                            *)
(*************************************************************)

Procedure Ini(var Tem:PlotArray; last:integer);
                                                {Procedure for initialization}
var
   p :integer;

begin     {ini}
   for p := 1 to last do
     begin
       Tem[p,1] := 0;
       Tem[p,2] := 0;
```

```
    end;
end;    {ini}

(*************************************************************)
(*              Main calculation Module                      *)
(*                   July 6, 1987                            *)
(*************************************************************)
Procedure MainAction( FileName   : String12);

var
   XY, LorXY, Splinexy, FitXY   : Plotarray;
   GamorgXY, Gamlorxy, gamfitxy : Plotarray;
   LorfitXY, gamlorfitXY        : Plotarray;
   FullNum                      : integer;
   DesiredNo, datlength         : integer;  {desired no of Splined data}
   Orginitial, temreal          : real;
   TemStr1, TemStr2, numstrg    : String12;
   Strg                         : String80;

begin
   Get_Data(FileName,XY,datlength);
   str(datlength:3,numstrg);
   Strg :='  '+numstrg+' of K and I values were collected from '+FileName+'.';
   wrtln(strg);
   if (datlength > 30) then  {Manupulate data only when data of 30 or larger}
   begin
      Orginitial:= InitialK;       {that is 0.006}
      Datlength := MinIndex(XY,Datlength-20,datlength);
      str(Datlength:3,Numstrg);
      Strg :='       * '+NumStrg+' data sets are to be considered.';
      wrtln(Strg);
      wrtln('      Writing Original data.........');
      filename := copy(FileName,1,5) +'Org.dat';
      write_data(FileName,XY,DatLength);

 (* Getting DistDist from original uncorrected data set. *)
(*    ini(GamOrgxy,Gammax);
      wrtln('      Getting DistDist value from orginal data.......'); {Gamma of Org}
      DistDist(xy,GamOrgxy,datlength,Gammax);
      Filename := Copy(FileName,1,5) +'PDO.prn';
      write_data(Filename,Gamorgxy,Gammax);
*)

      wrtln('      Doing spline correction.......');         {Spline correction}
      if Orginitial < XY[1,1] then                          {comp w/ XY[1,1]}
         Orginitial := Trunc(XY[1,1]/SpResol+1)*SpResol;
      temreal := Trunc(XY[datlength,1]/Spresol)*SpResol;    {Last data X}
      DesiredNo := Trunc((Temreal-orginitial)/ Spresol)+1;
      Str(orginitial:10,TemStr1);
```

```
      Str(Temreal:10,Temstr2);
      wrtln('          * Initial K(sp) value: '+TemStr1+'   * Final K(sp) value: '+Temstr2);
      makespline(XY,datlength,Orginitial,temreal,SplineXY,DesiredNo);
      Filename := Copy(FileName,1,5) +'spl.dat';
      write_data(Filename,splinexy,DesiredNo);

      wrtln('      Data Fitting for initial and tail part.......');{Extra Fitting}
      ExtraPol(SplineXY,DesiredNo,FitXY,FullNum);
      Filename := Copy(FileName,1,5) +'fit.prn';
      write_data(Filename,Fitxy,FullNum);

      Ini(GamFitXY,Gammax);
      wrtln('      Getting DistDist value from Fitted original data.......');{Gamma for fit}
      DistDist(Fitxy,GamFitxy,FullNum,Gammax);
      Filename := Copy(FileName,1,5) +'PDF.prn';
      write_data(Filename,GamFitxy,Gammax);

(* Lorentz Correction and Gamma Correlation function from original Lorentz Data*)

(*    wrtln('      Doing LORENTZ correction......');  {Lorentz correction}
      lorentz(XY,datlength,LorXY);
      Filename := Copy(FileName,1,5) +'lor.dat';
      write_data(Filename,Lorxy,Datlength);

      wrtln('      Getting DistDist value from Original Lorentz data.......'); {Gamma Lor}
      DistDist(Lorxy,gamlorxy,datlength,Gammax);
      Filename := Copy(FileName,1,5) +'LPO.prn';
      write_data(Filename,Gamlorxy,Gammax);
*)
(* Lorentz Correction and Gamma Correlation function from Fitted Lorentz Data*)

      wrtln('      Doing LORENTZ correction for fitted data......');  {Lorentz correction}
      lorentz(FitXY,FullNum,LorFitXY);
      Filename := Copy(FileName,1,5) +'lft.prn';
      write_data(Filename,LorFitxy,FullNum);

      wrtln('      Getting DistDist value from fitted Lorentz data.......'); {Gamma Lor}
      DistDist(LorFitxy,gamlorfitxy,fullnum,Gammax);
      Filename := Copy(FileName,1,5) +'LPF.prn';
      write_data(Filename,GamlorFitXy,Gammax);

   end;

end;    {Main action}


(*************************************************************)
(*              Inner Shell Main Module                      *)
(*                   July 16, 1987                           *)
```

```
(*************************************************************)
Procedure ShellIn;

var
   FileNo,code                : integer;
   FileName                   : String12;
   DirPath                    : String80;
   Guindicate                 : char;
   Inputindicate              : char;


(**************Nested Procedure*****************************)
procedure Inner;
begin
  clrscr;                                                {ChDir & Dir Checkup}
  Write('      Do you want to look at directory (Y/N)? ');
  read(Kbd,indicate);
  writeln;
  if upcase(indicate) = 'Y'  then
    begin
      while (upcase(indicate) = 'Y') do
        begin
          write('                        Enter Directory Path : ');
          Readln(DirPath);
          chdir(DirPath);
          ShowDir('.\*.*');
          writeln;
          Write(' Do you want to look at other directory (Y/N)? ');
          read(Kbd,indicate);
          writeln;
        end;
    end;
  writeln;
  writeln(#7+'* * * * * * * * * * * * * * * * * * * * * * * * * * * * * * * * * * * * * *');

  write(' What is initial filename (without ext(.PRN))? ');
  readln(Filename);
  Filename := Filename + '.PRN';inifile := FileName;
  write('    What is last filename (without ext(.PRN))? ');
  readln(LastFile);
  LastFile := LastFile + '.PRN';
  writeln;
  write(' Do you want to fit the Guinier Region with Simple Power Law (Y/N)? ');
  readln(Guindicate);
  GuinierYes :=True;
  if Upcase(Guindicate) <>'Y' then
     begin
        GuinierYes := true;
        writeln('   * Guinier Region will be fitted with Guinier Law.');
```

```
        writeln(lst,'   * Guinier Region will be fitted with Guinier Law.');
      end
   else
      begin
         GuinierYes := False;
         writeln('   * Guinier Region will be fitted with Simple Power Law.');
         writeln(lst,'   * Guinier Region will be fitted with Simple Power Law.');
      end;
end;   {Nested procedure Inner}

begin   { Main}
   textmode(c80);                                          {initial Screen}
   clrscr;
   showtime(TimeStr);
   gotoxy(20,7);Writeln('Current Date > ', DateStr);
   gotoxy(20,8);Writeln('Current Time > ', TimeStr);
   gotoXY(5,10);writeln('ïëëëëëëëëëëëëëëëëëë<<< SAXS CORELATION FUNCTION
>>>ëëëëëëëëëëëëëëë¡');
   gotoXY(5,11);writeln('* Correlation Function from Lorentz corrected and original data
set*');
   gotoXY(5,12);writeln('*                          By Young Lee
*');
   gotoXY(5,13);writeln('*                         July 17, 1987
*');
   gotoXY(5,14);writeln('*
*');
   gotoXY(5,15);writeln('*      This program utilizes a extensive amount of LOOP.
*');
   gotoXY(5,16);writeln('*      So, It takes at least several minutes for each data set.
*');
   gotoXY(5,17);writeln('*      You should turn on the printer which will keep permanent
*');
   gotoXY(5,18);writeln('*      record for the whole procedure.
*');
   gotoXY(5,19);writeln('*
*');
   gotoXY(5,20);writeln('åëëëëëëëëëëëëëëëëë>  Press Any Key To Proceed.
<ëëëëëëëëëëëëëëëëf');
   read;
   repeat until Keypressed;
   inner;
   write(' Is above input O.K. (Y/N)? ');
   Read(Kbd,inputindicate); writeln;
   if upcase(inputindicate) <> 'Y' then
      begin
         while(upcase(inputindicate) <> 'Y') do
            begin
              inner;
              write(' Is above input O.K. (Y/N)? ');
```

```
            Read(Kbd,inputindicate); writeln;
          end;
      end;

   clrscr;


   writeln(lst,'Starting SAXS analysis form ',inifile,' to ',lastfile);
   GOTOXY(1,10);

   repeat
      MainAction( Filename);
      val(copy(Filename,1,5),FileNo,code);
      if code <>0 then
        begin
          wrtln(#7+'     >>Error in file name increment..');
          exit;
        end;
      FileNo := FileNo + 1;
      Str(FileNo,Filename);
      Filename := Filename + '.PRN';
   until Filename = lastFile;
   MainAction( Filename);
   Writeln(#7+'*.........Loop Finished.........*');
   Writeln(lst,'*.........Loop Finished.........*');
end;


(*************************************************************)
(*                    Main Module                            *)
(*                   July 16, 1987                           *)
(*************************************************************)
Begin  {Main}
   Showtime(Timestr);
   Showdate(DateStr);
   Getime(Hr1,Min1,Sec1);
   writeln(lst);
   writeln(lst,'* * * * * * * * * * * * * * * * * * * * * * * * * * * * * * * * * * * * * * * * * * * * * ');
   writeln(Lst,'                                                Current Date> ',DateStr);
   Writeln(Lst,'                                                Current Time> ',TimeStr);

   ShellIn;
   Write('            Do you want to run program again (Y/N) ?');
   read(kbd,MainIndic);
   if Upcase(Mainindic) = 'Y' then
      begin
         while Upcase(Mainindic) = 'Y' do
           begin
             ShellIn;
```

```
            Write('            Do you want to run the program again (Y/N) ?');
            read(kbd,MainIndic);
            writeln;
          end;
      end;
   Getime(Hr2,Min2,Sec2);
   showTime(TimeStr);
   writeln;writeln(lst);
   Writeln('          ............Program running Finished............');
   Writeln('                                          Current Time: ',TimeStr);
   Writeln(lst,'        ...................Program running Finished.............');
   Writeln(Lst,'                                          Current Time: ',TimeStr);


   writeln('  *ORG.PRN : Original data        PDO.PRN : P-DIS From Org data.');
   writeln('  *SPL.PRN : Spline   data       *PDF.PRN : P-DIS From FIT data.');
   writeln('  *FIT.PRN : Fitted   data        LPO.PRN : P-DIS From Org Lorntz data.');
   writeln('   LOR.PRN : Lorentz Org Data    *LPF.PRN : P-DIS From Fit Lorentz data.');
   writeln('  *LFT.PRN : Lorentz from corrected data.');
   writeln('Starting SAXS analysis form ',inifile,' to ',lastfile);


   writeln(lst,'  *ORG.PRN : Original data        PDO.PRN : P-DIS From Org data.');
   writeln(lst,'  *SPL.PRN : Spline   data       *PDF.PRN : P-DIS From FIT data.');
   writeln(lst,'  *FIT.PRN : Fitted   data        LPO.PRN : P-DIS From Org Lorntz data.');
   writeln(lst,'   LOR.PRN : Lorentz Org Data    *LPF.PRN : P-DIS From Fit Lorentz data.');
   writeln(lst,'  *LFT.PRN : Lorentz from fitted data.');
   writeln(lst,'Starting SAXS analysis form ',inifile,' to ',lastfile);



   SecDif := 3600.0 *Hr2+ 60.0 * Min2 + Sec2
             -( 3600.0 * Hr1+ 60.0 * Min1 + sec1);
   MinDif := Int(Secdif / 60);
   SecDif := (secdif - Mindif*60);
   Writeln('              Operation Time: ',
                          MinDif:4:0,' Minutes ',SecDif:3:0,' Seconds');
   Writeln(lst,'              Operation Time: ',
                          MinDif:4:0,' Minutes ',SecDif:3:0,' Seconds');
   writeln(lst);
end.
```

# VITA

Young D. Lee was born in Daejeon, Korea on June 20, 1957. He attended primary and junior high schools there and graduated from the Kyungbok High School at Seoul in January 1975. The following March he entered the Seoul National University and in June 1981 he received a Bachelor of Science degree in Textile Engineering. During his college years he served his military service in the Korean Army for two and a half years. Upon graduation he was employed as a textile engineer with Kolon International Corp. in Seoul, Korea.

In September 1982 the author came to the United States and began graduate studies in Polymer Engineering at the University of Tennessee. He received the Master of Science degree in Polymer Engineering in March 1985. At the same university he received the Doctor of Philosophy degree in Polymer Engineering in August 1989.

While attending the University of Tennessee, the author was a member of the Phi Kappa Phi, SPE, ACS and IEEE. He was elected as the president of Korean Student Association in 1984-1985.